SOLID STATE THERMAL DECOMPOSITION OF AMIDE COMPLEXES OF NICKEL(II) CHLORIDE

THESIS

Submitted in fulfilment of

the requirements for the degree of

DOCTOR OF PHILOSOPHY

of

Rhodes University

by

Aubrey Ndifelani Nelwamondo

December 1996

ABSTRACT

The thermal decompositions of a series of amide complexes of nickel(II) chloride have been studied. Thermochemical, kinetic, structure and solid-state stability correlations have been investigated.

Complexes containing homologous amide ligands (L) of the form $NiLC\ell_2$, $Ni_3L_2C\ell_6$, $Ni_3LC\ell_6$, $NiL_2C\ell_2(2H_2O)$ and $ML_2C\ell_2$ (where M = Ni(II), Co(II) or Cu(II)) have been prepared. Chemical analysis, spectral and thermogravimetric measurements were used to characterize the complexes and their decomposition stoichiometries.

Three sets of reactions were identified as yielding stable products in a single step:

(i) $NiLC\ell_2\ (s) \rightarrow NiC\ell_2\ (s) + L\ (g)$

(ii) $Ni_3L_2C\ell_6\ (s) \rightarrow 3NiC\ell_2\ (s) + 2L\ (g)$

(iii) $Ni_3LC\ell_6\ (s) \rightarrow 3NiC\ell_2\ (s) + L\ (g)$

Characterization of the processes in the $ML_2C\ell_2$ and $NiL_2C\ell_2(2H_2O)$ complexes was not straightforward. Reaction enthalpies (ΔH) were determined using DSC. The orders of the reaction onset temperatures (T_e), peak temperatures (T_{max}) and ΔH_L values for the $NiLC\ell_2$ system were: N-methylacetamide < acetamide < N-methylformamide, suggesting the importance of steric hindrance of the methyl-substituent groups in the amide skeleton. In the $Ni_3L_2C\ell_6$, $NiL_2C\ell_2(2H_2O)$ and $ML_2C\ell_2$ systems no simple orders could be deduced. The T_e and T_{max} sequences obtained from analogous metal(II) chloride complexes indicated that the copper(II) complexes were the least stable.

The kinetics of the loss of L from $NiLC\ell_2$ complexes were investigated using isothermal TG, non-isothermal TG and DSC measurements. The contracting geometry models described the course of the decompositions in the most satisfactory manner. Apparent activation energies (E_a) were estimated from Arrhenius plots of rate coefficients from: (i) an approximate zero-order relationship, (ii) the contracting-area (**R2**) and contracting-volume (**R3**) equations, (iii) a new empirical (**B2**) expression, (iv) the half-life ($^1/t_{0.5}$) and (v) the characteristic feature of the rate-time curve ($^1/t_{max/2}$). The non-dependence of E_a on the rate equation used supports the reliability of the kinetic parameters.

Non-isothermal experiments were analyzed by the Coats-Redfern, the modified Borchardt-Daniels and the Kissinger methods. Arrhenius parameters were in keeping with results from the isothermal kinetic measurements.

The values of E_a obtained for the $NiLC\ell_2$ system increased with an increase in basicity of the amide ligands. No straightforward correlation was found between E_a and T_e, T_{max}, ΔH_L or spectral properties.

ACKNOWLEDGEMENTS

I am indebted to Professors M. E. Brown and D. J. Eve for inspiration, able guidance and constant encouragement throughout this project. I lack words to express my heart-felt thanks for the efforts they put out so as to ensure the success of this project.

I would also like to thank:

- the Foundation for Research and Development (FRD) and, especially, the manager of the **IRDP**, Ms T. Morolo, for the research grant and sustained interest in this project.
- Mrs M. Maksa of the CSIR (Mattek division) for performing the elemental analyses.
- staff of the Chemistry Departments at *UFH* and *RU* for their encouragement. Mention has to be made to Dr. G. Watkins, for useful discussion of the far-IR spectra.
- fellow students and friends who contributed in their own different ways to make this possible.

Finally, I wish to convey my gratitude to the members of my family whose encouragement was a motivating factor: Mike, Blossom, Royal, Edith, ... A thina maipfi a u ni livhuwa ngao!

Contents

List of Tables

CHAPTER 9

CHAPTER 10

CHAPTER 13

List of Figures

CHAPTER 10

CHAPTER 12

CHAPTER 13

List of Amide Ligands used in the present study

Amide ligand	Abbreviation	Formula
Formamide	*fa*	CH_3NO
N-Methylformamide	*nmf*	C_2H_5NO
N-Ethylformamide	*nef*	C_3H_7NO
N,N-Dimethylformamide	*dmf*	C_3H_7NO
N,N-Diethylformamide	*def*	$C_5H_{11}NO$
Acetamide	*aa*	C_2H_5NO
N-Methylacetamide	*nma*	C_3H_7NO
N-Ethylacetamide	*nea*	C_4H_9NO
N,N-Dimethylacetamide	*dma*	C_4H_9NO
Propionamide	*pa*	C_3H_7NO
N-Methylpropionamide	*nmp*	C_4H_9NO
N,N-Dimethylpropionamide	*dmp*	$C_5H_{11}NO$
N,N-Diethylpropionamide	*dep*	$C_7H_{15}NO$
Butyramide	*ba*	C_4H_9NO
Isobutyramide	*iba*	C_4H_9NO

CHAPTER 1

MOTIVATION OF THIS WORK

1.1 Introduction

Thermal methods of analysis are standard techniques for studying the thermochemistry and kinetics of reactions of solid compounds. Thermogravimetry (TG), differential scanning calorimetry (DSC) and differential thermal analysis (DTA) are the most commonly used techniques. The possibility of correlating the parameters obtained from these thermoanalytical techniques with the nature (steric and electronic effects) of the coordinated ligands and the strengths of the metal-volatile ligand bonds has been explored by investigating the spectral, thermochemical and kinetic aspects of the decompositions of a series of alkyl-substituted amide complexes of nickel(II) chloride.

1.2 Background

Thermochemical, kinetic, spectroscopic and stability correlation studies of solid metal halide complexes have been the subject of several investigations [1-10]. DTG, DSC or DTA thermal decomposition parameters such as T_e (the procedural decomposition onset temperature), T_{max} (peak temperature), ΔH (change in enthalpy) and E_a (apparent activation energy) have been described in relation to the strengths of metal-volatile ligand bonds, structure and IR properties.

In the thermal decomposition studies of $PdL_2C\ell_2$ complexes with pyridine and with several alkyl-substituted pyridine derivatives, Farran *et al.* [5] reported a linear relation between E_a and pK_b. In their thermal study of cobalt(II) halide complexes with a series of alkyl-substituted pyridine ligands, Thornton *et al.* [7] reported higher values of T_{max} for smaller coordination numbers. They suggested that T_{max} was influenced by the stereochemistry of the complexes. Siracusa *et al.* [2] reported a linear relation between the UO_2 group stretching vibrational frequency and E_a in a series of uranyl-amide derivatives. Carstens *et al.* [1] studied the thermal decompositions of UO_2LF_2 complexes with a series of amide ligands. These authors found no simple relationship between E_a and ΔH, T_{max} or IR spectral properties. More rarely, solid state decomposition studies have been used [11-13] to study substitution mechanisms, that is dissociative and associative mechanisms.

1.3 Motivation

The organic ligands that have attracted most interest in thermal decomposition studies of metallo-organic complexes have been nitrogen donor molecules, particularly pyridine and its alkyl-substituted derivatives, as well as imidazoles. Reports on metallo-amide complexes are limited [14-16]. The monoligand complexes of type MLX_2 (where M is a transition metal, X a halogen and L a simple amide) cannot be readily prepared, with the result that there have been no systematic investigations of the monoligand complexes. The first examples of nickel(II) chloride complexes containing one amide ligand for each nickel ion have been prepared in this study. We have also prepared new complexes of the types: $NiL_2C\ell_2(2H_2O)$, $ML_2C\ell_2$, $Ni_3L_2C\ell_6$ and $Ni_3LC\ell_6$. Elemental, spectral and thermogravimetric measurements were used to characterize the complexes.

Possible relationships between the strengths of the metal-amide bonds (of complexes prepared from a homologous series of amide ligands), the thermal decomposition parameters, and spectroscopic properties have been investigated. Variation of the alkyl constituent, *i.e.* methyl, ethyl or propyl, in the amide skeleton makes it possible to investigate the steric and inductive effects.

Outline of the stages of this investigation:

- Preparation and elemental analyses of amide complexes of nickel(II) chloride.
- Determination of the nature of the nickel-amide coordination using uv-visible-NIR diffuse reflectance and IR vibrational spectroscopies.
- Thermal studies and comparison of thermochemical parameters for different amide ligands coordinated similarly to the nickel(II) chloride, *i.e.* similar composition and geometrical configuration.
- Kinetic studies of solid-state decompositions, determination of activation energy (E_a) and attempts to determine the decomposition mechanisms.
- Investigation of the influence of the nature of the amide ligands (*i.e.* steric and electronic effects) on the thermal stabilities of their corresponding nickel(II) complexes; including the examination of any correlation between the thermochemical, spectral and kinetic properties.

- Comparison of the thermal behaviour and stabilities of $NiC\ell_2$-amide complexes with similar complexes formed with other metal(II) chlorides.

Our preliminary exploration suggested that the following sets of reactions were occurring:

(i)..... $NiL_2C\ell_2(2H_2O)$ (s) → $NiLC\ell_2$ (s) + $2H_2O$ (g) + L(g),

(ii)..... $NiLC\ell_2$ (s) → $NiC\ell_2$ (s) + L (g),

(iii)..... $3NiL_2C\ell_2$ (s) → $Ni_3L_2C\ell_6$ (s) + 4L (g),

(iv)..... $Ni_3L_2C\ell_6$ (s) → $3NiC\ell_2$ (s) + 2L (g), and

(v)..... $Ni_3LC\ell_6$ (s) → $3NiC\ell_2$ (s) + L (g)

where L is a simple amide ligand.

Reactions of types (ii), (iv) and (v) were most suitable for detailed thermochemical investigation since decompositions were completed in single stage, with presumably simple stoichiometry. A number of the amide ligands formed stable complexes of the type $NiLC\ell_2$, and the released ligands do not decompose during the decomposition of the complexes. The $NiLC\ell_2$ complexes were most suitable for kinetic investigation.

A somewhat similar choice of system for kinetic investigation (MLX_2 system) has been reported for the amide complexes of dioxodifluorouranium(VI) [1], but uranium is not an ideal choice of central coordinating atom. Kinetic measurements and the subsequent data analysis were made under restricted experimental conditions.

CHAPTER 2

BACKGROUND OF THERMAL ANALYSIS TECHNIQUES

2.1 Introduction

The International Confederation for Thermal Analysis and Calorimetry (ICTAC) defines *thermal analysis* as [17,18] " *a group of techniques in which a physical property of a substance is measured as a function of temperature whilst the substance is subjected to a controlled temperature program* ". Thermal analysis techniques are applied to numerous areas of research [17,19]. Use of a single technique often provides inadequate information and complementary techniques are valuable [18,20]. The two main techniques used in this work are:

- Thermogravimetry (TG), where the physical property is mass; and
- Differential Scanning Calorimetry (DSC), which involves measurement of enthalpy changes.

The historical and theoretical aspects of the two techniques have been discussed by many authors [18,21,22].

2.2 Thermogravimetry (TG)

In thermogravimetry, the sample mass is determined as a function of temperature or time. For a mass change to be detected, a volatile component must be evolved or absorbed by the sample. Two modes of operation [23] will be examined in this review:

- Dynamic thermogravimetry - in which the sample temperature is changed in a programmed manner, commonly at a linear rate; and
- Isothermal thermogravimetry - where the sample mass is measured as a function of time at a constant temperature.

A plot of mass change *versus* temperature (or time) is termed the thermogravimetric curve or simply TG curve. A typical TG curve is shown in Figure 2.1. The TG curve in Figure 2.1 is characteristic of a single-stage reaction of the form

$$(\text{solid})_1 \rightarrow (\text{solid})_2 + \text{gas} \qquad 2.1$$

For TG experiments at constant heating rate, a plateau (ℓ) indicates constant mass. The start and end of a decomposition stage can be defined by two successive mass

change plateaus. Three temperature points may be selected as useful characteristics of any single-stage non-isothermal reaction:

- T_e (onset temperature) - where the cumulative mass-change reaches a magnitude detectable by a thermobalance. This is often termed the *procedural* decomposition onset temperature,
- T_{max} (maximum decomposition rate temperature) - where the rate of the cumulative mass loss or gain attains its maximum value, and
- T_f (final temperature) - at which the cumulative mass change reaches its maximum value, corresponding to complete reaction.

The temperature limits of the plateau described are not properties of the sample alone. They apply only to the particular condition of that pyrolysis. For example, in an endothermic decomposition, T_e, T_{max} and T_f increase with the heating rate. The total temperature range of reaction may shift towards lower temperatures when one or more of the following experimental factors is decreased: the sample mass, the linear heating rate, the size of the particles of the substance, the thickness of the sample layer, or the pressure of the gaseous reaction product. Several other factors may influence the position of the characteristic temperatures and are described elsewhere [18,22,24]. The use of the term " *decomposition temperature* " to mean either T_e or T_{max} is confusing.

A plot of the rate of mass loss *versus* temperature (or time) is referred to as the derivative thermogravimetric (DTG) curve. An example of a DTG curve is depicted in Figure 2.1. The curve is obtained from the TG curve by numerical differentiation of the digital TG signal. Dynamic derivative thermogravimetry is recommended [18,24] as a first method to be used in the exploration of the thermal behaviour of initially solid substances. Two overlapping reactions often present an ill-defined TG curve, whereas the corresponding DTG curve may indicate where the stages can be divided. DTG curves bear a strong resemblance to DSC (and DTA) curves and hence permit comparisons to be made. The height of the DTG peak at any temperature gives the rate of mass-change at that temperature [18]. This may be useful in kinetic studies.

The change in mass resulting from evolution of gas is related to the dimensionless extent of decomposition (α) by:

$$\alpha = (m_o - m)/(m_o - m_f) \qquad 2.2$$

where m_o is the initial mass of sample, m is mass at time t, and m_f is the final mass. TG data is usually converted to a curve of α *versus* time or temperature for kinetic analysis.

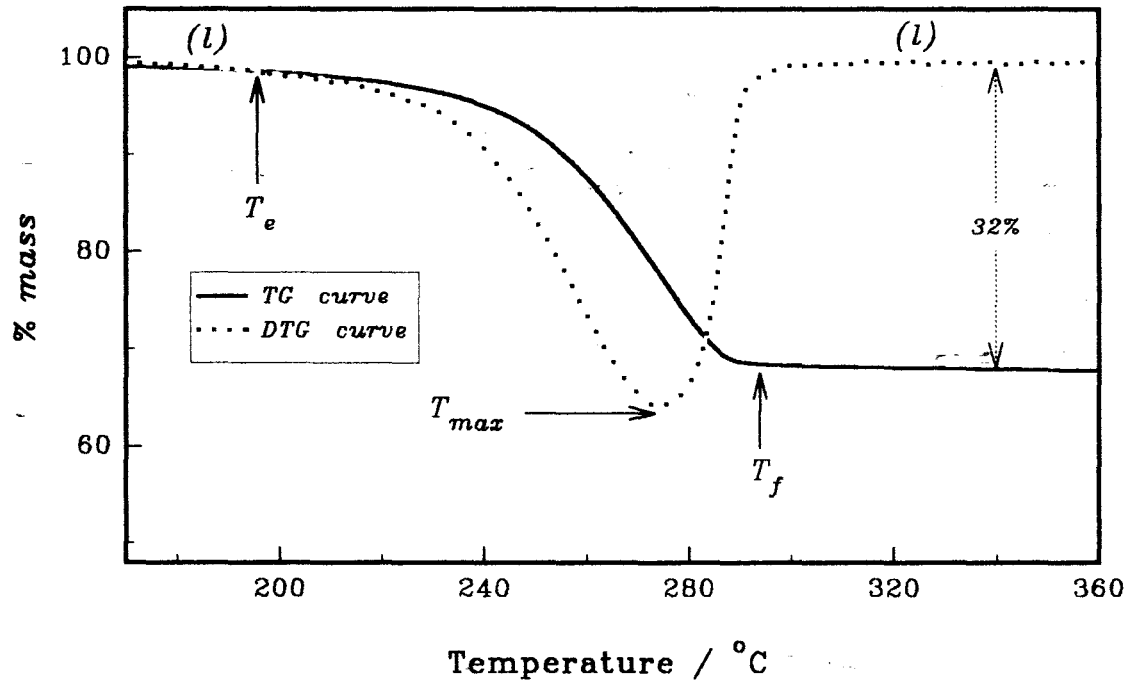

Figure 2.1: Typical TG and DTG curves showing onset temperature of about 195°C, T_{max} around 275°C, and T_f of about 295°C. The approximate mass loss is 32%.

2.3 Differential scanning calorimetry (DSC)

In differential scanning calorimetry (DSC), the temperature difference between the sample and the reference material, $(T_s - T_r)$, is maintained at zero by supplying heat to either the sample or reference during a reaction. For example, when an endothermic transition occurs, the energy absorbed by the sample is replenished by increased input to the sample to maintain the temperature balance. A recording of the balancing energy yields a direct calorimetric measurement of the energy of transition [23]. An external standard with known enthalpy of fusion (ΔH_{fus}) is needed to calibrate the temperature scale and the area response of the calorimeter. In DSC measurements an empty pan is usually used as reference.

Figure 2.2 illustrates a typical DSC curve, for an endothermic reaction of the type shown by equation (2.1). The flat baseline of the DSC curve indicate temperature ranges

in which no transition occurs, while excursions (peaks) above (or below) the baseline represent endothermic (or exothermic) transitions. The amplitude of the DSC trace from the baseline position is a direct measure of energy input (endo) or output (exo) and the area (A) under the peak is proportional to the total transition energy [23,25]. The enthalpy of reaction is obtained directly from the area under the curve. The heat capacity of the sample may be determined from the magnitude of the baseline displacement.

2.4 Quantitative aspects of DSC

DSC is widely used in the determination of enthalpies of reaction, as well as in isothermal and rising temperature kinetic studies [18]. The area enclosed by the DSC curve peak (*cf.* Figure 2.2) is directly proportional to the enthalpy change,

$$\text{Area} = m(\Delta H)/K_{cal.} \qquad 2.3$$

where ΔH is the enthalpy change, m is the mass of sample and K_{cal} is the calibration constant. $K_{cal.}$ is determined by calibration of the system with compounds having known enthalpies of reaction (or transition), and is temperature independent. The pure metals commonly used as standards, and their corresponding enthalpies of fusion are listed in Table 2.1.

The calculation of the extent of reaction (α) at temperature T, or at time t, from a DSC run requires the determination of the partial area (a) under the curve up to that point and the total peak area (A)

$$\alpha = a/A \qquad 2.4$$

The areas a and A are obtained by numerical integration of the DSC signal as a function of temperature or time.

Table 2.1: Some commonly used DSC calibrants [23].

Substance	Temperature / °C	Enthalpy of fusion ΔH_{fus} / J g^{-1}
Indium	156.6	28.5
Tin	231.9	60.3
Zinc	419.4	108.4

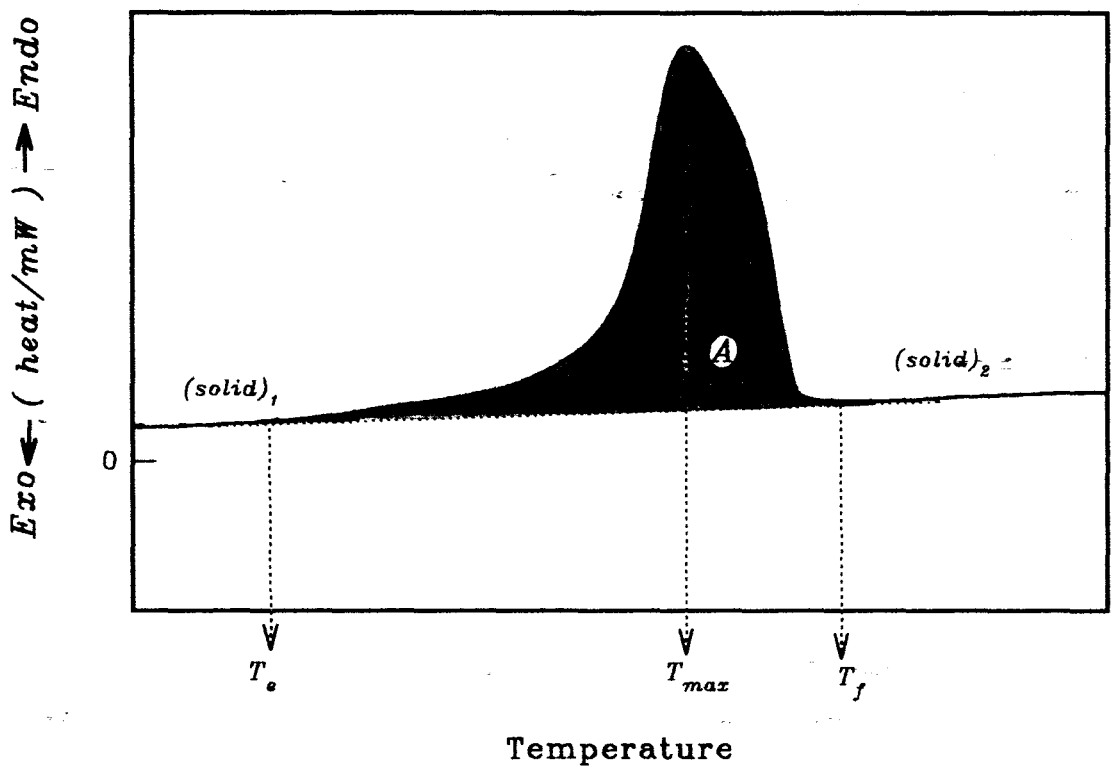

Figure 2.2: A typical DSC curve showing the characteristic temperatures. The shaded area, A, is a measure of the enthalpy of an endothermic transiton.

2.5 Decomposition enthalpy of metallo-organic complexes

Some published works [9,26,27] use as the basis for the evaluation of the decomposition enthalpy (ΔH_1) reactions of the type

$$ML_nX_2\ (s) \rightarrow MX_2\ (s) + nL\ (g) \qquad 2.5$$

Ideally, the strength of metal-volatile ligand bond should be obtained from calculation of the enthalpy (ΔH_2) of the hypothetical reaction

$$ML_nX_2\ (g) \rightarrow MX_2\ (g) + nL\ (g) \qquad 2.6$$

such that

$$\Delta H_2 = \Delta H_1 - \{ \Delta H_{subl}(ML_nX_2) + \Delta H_{subl}(MX_2) \} \qquad 2.7$$

where $\Delta H_{subl}(ML_nX_2)$ and $\Delta H_{subl}(MX_2)$ are the enthalpies of sublimation of ML_nX_2 and MX_2, respectively.

In most practical work, strengths of metal-volatile ligand bonds are compared on the assumption that differences between the enthalpies of sublimation of MX_2 and ML_nX_2 (respectively) are nearly constant [28] so that ΔH_1 can be used as an approximate estimate of the strengths of the metal-volatile ligand bonds. The relationship requires that enthalpies of decomposition be compared at the same temperature. Specific heat capacities (C_p) are, however, commonly not available for reactants and products. For a particular decomposition, variations of C_p values with temperature are small [9,26], so that comparison of decomposition enthalpies should be permissible within the experimental uncertainties of the data.

Only enthalpies of decompositions of complexes of the same stoichiometric type and of similar geometrical configuration should be compared, because the bonding possibilities between the same central atom and the volatile ligand in different types of coordination polyhedra vary (*e.g.* octahedral, tetrahedral, *etc.*).

CHAPTER 3

BACKGROUND THEORY OF SOLID STATE KINETICS

This chapter reviews the processes that control the rates of solid state reactions: nucleation, interface advance (growth) and diffusion.

3.1 The fundamentals of solid state kinetics

3.1.1 Introduction

Solid state decomposition takes place in several stages that may involve [22,29,32]:

- the destruction of one chemical compound and the formation of others,
- the formation of crystallization centres and their growth,
- the adsorption-desorption of gaseous products,
- the diffusion of gases,
- heat transfer, *etc.*

The rate-determining process may change with extent of decomposition. Several physical variables are known to influence the overall process [18]. These include: the physical state of the sample, compactness, particle size, character of the atmosphere and the heat conductivities of furnace atmosphere.

Studies of solid state decompositions may provide information on the mechanisms [30] by characterisation of reaction intermediates and product compositions. Studies of reaction rates may be of value in establishing the most efficient conditions that can be exploited in production [31].

Kinetic investigations of thermal decompositions may be made under dynamic or isothermal conditions. For reactions described by equation (2.1), isothermal rate equations have been derived based on reactions controlled either by the movement of a phase boundary, by nucleation followed by growth of nuclei, *etc.* [18,22,32].

3.1.2 Nucleation and growth of nuclei

Many solid decompositions are initiated at strained regions of the crystal such as lattice

defects or dislocations [22]. These regions at which reaction first commences are called nucleation sites. Nucleation may be defined as the initial establishment of a new and discrete product particle within the solid reactant. The process is accompanied by very little escape of gaseous product. Predictions of the rate at which gaseous product is evolved are derived from further nucleation and growth of nuclei. Two types of chemical changes may be involved [33]:

- the chemical transformation of constituents (*e.g.* ions or molecules) of the reactant into the constituents of the product, and
- recrystallization of reacted material to the lattice structure of the product phase.

One or both of these processes result in the generation of an active reactant-product interface at which reaction occurs preferentially. The relative ease of further nucleation has an important influence on the kinetics of reaction. If nucleation is rapid, all reactant surfaces will be rapidly covered by product, and the resultant interface advances inwards giving rise to a deceleratory yield-time curve. Where nucleation occurs relatively slowly, a sigmoid yield-time curve is observed.

Experimental identification of the chemical changes that contribute to nucleation is difficult [34] because nucleation sites are changed beyond recognition by the formation of the product particle. Nuclei are themselves microscopically identifiable because of the textural changes that accompany reaction. Cracks resulting from loss of material also appear. Recrystallization may yield small particles with crystallite textures that scatter light and the opaque intranuclear material may be recognizable.

High magnification microscopic examinations of the interface zones, corroborated with evidence from suitable observations, have been used to develop a classification scheme for interfacial nucleus functions [35]. Three classes of nucleus were suggested. These are:

Functional nuclei: The product directly promotes the chemical change. The reaction is induced by strain and / or heterogeneous catalytic breakdown of a chemisorbed intermediate at the reactant-product interface.

Fluid-flux nuclei: These are interfacial structures that temporarily retain some of a volatile product that has been condensed into a liquid. Chemical reactions and / or recrystallization take place from within the nuclei.

Fusion nuclei: These result from temporary and locally restricted melting of product that is accompanied by the dissolution of the solid reactant in the expanding fluid

formed. Reactions that proceed within the melt are capable of explaining the predominantly sigmoid α *versus* time curves.

Rates of growth of nuclei below the microscopic detection limit may be different from those subsequently attained. After initial deviations, all nuclei within a particular reactant sample are assumed to grow at the same rate [34,36]. When there is unrestricted growth of nuclei in three dimensions ($\lambda = 3$) the interface expands outwards in increasing hemispheres of active interface. When the solid is in the form of thin crystals (or has a layer structure), nucleus growth is likely to be restricted to two dimensions ($\lambda = 2$).

3.1.3 Diffusion processes in reactions of solids

Diffusion processes participate in many types of chemical changes involving solids. Two reaction models in which diffusion is a dominant kinetic control were described by Galwey *et al.* [33]:

- Decompositions controlled by the diffusive escape of product, and
- Reactions between solids where a solid product is formed between the reactants, so that progress is maintained by transport across the barrier layer.

Transport may be a dominant control in a structure that is not reorganized directly as a result of the chemical change [22]. Such reactions are often characterized by *anisotropy* of the interface advance. In layered structures, where migrations are exclusively in the interlayer planes, ease of movement is determined by the dimensions of the intracrystalline channels.

3.1.4 Isothermal rate equations

The relationship between the reacted fraction, α, and the time of reaction, t, under isothermal conditions is usually derived from the assumption [32,37,38] that the reaction rate is a function of the degree of conversion expressed by

$$d\alpha/dt = k(T)\, f(\alpha) \qquad 3.1$$

where k(T) is the rate coefficient. On integration, equation (3.1) leads to a function of the form

$$g(\alpha) = kt \qquad 3.2$$

The conversion function, $f(\alpha)$, is assumed to take various forms. For instance

$$f(\alpha) = (\alpha)^m (1 - \alpha)^n \qquad 3.3$$

where m and n are constants (referred to as the homogeneity factors [37,39]). Several generalized functions have been suggested [38,40,41] for describing a larger variety of thermal curves. Examples include:

$$d\alpha/dt = k (\alpha)^m (1 - \alpha)^n [- \ell n (1 - \alpha)]^p \quad 3.4a$$

and

$$d\alpha/dt = k (\alpha)^{1-p} (1 - \alpha)^{1-q} \quad 3.4b$$

Equation (3.3) is often simplified to [37,42]

$$f(\alpha) = (1 - \alpha)^n \quad 3.5$$

where the homogeneity factor m is assumed to be zero. In analogy with homogenous reactions, n is called the reaction order.

3.2 Conversion functions, f(α)

3.2.1 Classification

The conversion functions, f(α), used in solid state kinetics may be classified into one or other of the following broad categories [38,43]:

- Phase boundary controlled reactions;
- Reactions controlled by nucleation and growth of nuclei; and
- Diffusion controlled reactions.

3.2.2 Phase boundary controlled reactions

The general derivative equation which relates the rate to the extent of reaction is of the form

$$\upsilon = d\alpha/dt = k f(\alpha) = k(1 - \alpha)^n \quad 3.6$$

Values of $n = 0, ½, {}^2/_3$ and unity have special physical significance in solid state reactions [42,44,45]. The physical interpretations for the various values of n are:

n* = *0 : very slow diffusion of the evolved gaseous component from the reactant into the surroundings. Several different reaction models are reported [22] to be distinguishable from microscopic observations of reacting substances.

***n* = ½** : decomposition begins with rapid surface nucleation and is controlled by the geometric advance of the reaction interface at the edges of a disc, or a plate-

like particle, into the bulk of the reactant particle [21,32]. The model is referred to as the contracting-area or cylinder model (**R2**).

$n = {}^{2}/_{3}$: decomposition on an ideal spherical surface of a reactant particle, not hindered by diffusion, proceeds uniformly towards its centre. This model is referred to as the contracting-volume or sphere model (**R3**).

$n = 1$: assumes equal decomposition probability by all the reactant constituents during the entire process. This is unlikely in practice.

Integration of equation (3.6) leads to [46]

$$1 - (1 - \alpha)^{1-n} = (1 - n)kt \; ; \; n \neq 1 \qquad 3.7$$

Therefore when

$$n = {}^{1}/_{2} : \quad 1 - (1 - \alpha)^{1/2} = ({}^{1}/_{2})kt \qquad 3.8$$

$$n = {}^{2}/_{3} : \quad 1 - (1 - \alpha)^{1/3} = ({}^{1}/_{3})kt \qquad 3.9$$

$$n = {}^{1}/_{3} : \quad 1 - (1 - \alpha)^{2/3} = ({}^{2}/_{3})kt$$

$$n = 0 : \quad \alpha = kt \qquad 3.10$$

When $n = 1$, integration of equation (3.6) yields the first-order kinetic expression

$$-\ell n(1 - \alpha) = kt \qquad 3.11$$

3.2.3 Reactions controlled by nucleation and growth of nuclei

Detailed treatment of the laws governing the rate of appearance of nuclei and their subsequent growth have been given by many authors [32,47,48]. Two α,t relationships concerned with nuclei growth are frequently quoted as applicable up to $(d\alpha/dt)_{max}$. These are:

The power law [49], of the general form

$$\alpha = (kt)^{m} \qquad 3.12$$

or its derivative form

$$d\alpha/dt = mk(\alpha)^{(m-1)/m}$$

According to the power law, normal growth of nuclei is assumed without overlapping of the decomposition zones. The integer m is given by $m = \beta + \lambda$ where β is the number of stages in the nucleation process (*i.e.* 1, 2 or 3) and λ is the number of dimensions in which the growth occurs.

The exponential law [48] is based on random or branching nucleation followed by normal growth without overlap. It also holds up to $(d\alpha/dt)_{max}$ and takes the form

$$\alpha = \exp(kt) \qquad 3.13$$

or

$$d\alpha/dt = k(\alpha)^m$$

Both of the above models allow for unrestricted growth of nuclei.

Two factors exert major restrictions upon nucleus development [22,48,50]. These are:

- Impingement or coalescence of developed nuclei; and
- Ingestion of undeveloped nucleation sites.

Coalescence refers to the loss of interface resulting from the coming together of two or more growing reaction zones, sometimes (incorrectly) referred to as " overlap of nuclei ". Ingestion is the elimination of a possible nucleation site by the growth of an existing nucleus.

Theoretical treatments based on nucleation-and-growth have been associated with the names Johnson, Mehl, Avrami, Erofeev, Kohlmogorov, *etc.* [30,51,52]. The resulting rate equation is sometimes referred to as the JMAK or the KEKAM equation.

The JMAK equation

Erofeev [48] put forward an equation of the form

$$(1 - \alpha) = \exp[-(kt)^n] \qquad 3.14$$

The derivative equation is

$$d\alpha/dt = n(k)^n(t)^{n-1}(1 - \alpha)$$

When $n = 2$, this is said to correspond to two-dimensional growth; $n = 3$ implies three-dimensional growth; and $n = 4$ has been interpreted in terms of two stage nucleation. Avrami [52] presented a similar equation with $n = 3$ for the specific case of the coalescence of three-dimensional growth nuclei with initial random nucleation. The JMAK equation has been commonly given as [53-55]

$$[- \ell n(1 - \alpha)]^{1/n} = kt \qquad 3.15$$

where $k = (k')^{1/n}$. It is a common mistake in the literature to use k' instead of $(k')^{1/n}$. The most direct method for determining n from α *versus* time data should be plots of $\ell n [- \ell n(1 - \alpha)]$ against $\ell n(t)$. $\ell n(\ell n)$ plots are always very insensitive, however, and the recommended approach [20] is to plot $[- \ell n(1 - \alpha)]^{1/n}$ against time

for various values of n.

Prout-Tompkins rate equation

The Prout-Tompkins rate equation is based on two alternative models [22,38]:

- the development of needle or laminar nuclei which undergo branching with interference between the nuclei growing in one or two dimensions.
- the development of cracks in the reactant phase because of strains in the vicinity of each established reaction interface.

The two models are consistent with a strongly acceleratory nucleation law. The treatment given by Prout and Tompkins is based on symmetrical sigmoid α *versus* time curves with the point of inflection at $\alpha = 0.50$. The Prout-Tompkins equation is:

$$\ell n\{ \alpha/(1 - \alpha)\} = kt \qquad 3.19$$

or its derivative form

$$d\alpha/dt = k\alpha(1 - \alpha)$$

The modified Prout-Tompkins equation is [38]:

$$\ell n\{ \alpha/(1 - \alpha)\} = k\, \ell n(t) \qquad 3.20$$

or

$$d\alpha/dt = k\alpha^m(1 - \alpha)^n; \quad \text{where } m < \text{unity} < n$$

The second form was derived on the basis of a variation in the rate of branching with time.

3.2.4 Diffusion-controlled rate equations

Diffusion-controlled reactions are commonly classified according to the number of dimensions into which the transport process occurs [56].

One-dimensional diffusion

A one-dimensional transport process with constant diffusion coefficient gives rise to the *parabolic law* [48]

$$\alpha^2 = kt \qquad 3.21$$

The derivative equation is of the form

$$(d\alpha/dt) = 2k\alpha \qquad 3.22$$

Two-dimensional diffusion

A two-dimensional transport process into a cylinder with no volume change during the reaction follows the equation [57]

$$(1 - \alpha)\ell n(1 - \alpha) + \alpha = kt \qquad 3.23$$

or its derivative form

$$(d\alpha/dt) = k [- \ell n(1 - \alpha)]^{-1}$$

Three-dimensional diffusion

Three-dimensional transport in a spherical particle, in its simplest form leads to the equation proposed by Jander [56,58]

$$\{ 1 - (1 - \alpha)^{1/3} \}^2 = kt \qquad 3.24$$

The derivative form is

$$(d\alpha/dt) = 3k(1 - \alpha)^{2/3} [2\{ 1 - (1 - \alpha)^{1/3}\}]^{-1}$$

A more detailed treatment by Ginstling and Brounshtein [58], that takes into account the dimensions and shape of the reacting particle, leads to

$$(1 - 2\alpha/3) - (1 - \alpha)^{2/3} = kt \qquad 3.25$$

or

$$(d\alpha/dt) = 3k [2\{ (1 - \alpha)^{-1/3} - 1\}]^{-1}$$

3.2.5 Summary of main solid state decomposition rate equations

The main $g(\alpha)$ and $f(\alpha)$ functions used to characterize solid state reactions are summarized in Table 3.1. The labelling scheme commonly used in the literature is employed. The expressions are grouped according to the rate controlling process assumed in their derivations [60]. The characteristic observed shapes of isothermal α *versus* time curves are illustrated in Figure 3.1. Detailed plots have been presented by Brown and co-workers [33,59]. Typical isothermal rate ($\upsilon = d\alpha/dt$) *versus* α and rate *versus* time curves are also given, Figures 3.2, 4.1 and 4.2.

Table 3.1: Integral, g(α), and derivative, f(α), kinetic expressions used in solid-state decompositions.

Symbols	$g(\alpha) = kt$	$f(\alpha) = (1/k)(d\alpha/dt)$	$d\alpha/dt = \upsilon = f(t)$*
(a) Acceleratory α-time curves: *Reactions controlled by nucleation & unrestricted growth*			
P1	$(\alpha)^{1/m}$, $m = \beta + \lambda$	$m(\alpha)^{(m-1)/m}$	$mk(kt)^{m-1}$
E1	$\ln(\alpha)$	α^m	$[\exp(kt)]^m$
(b) Sigmoid α-time curves: *Reactions controlled by nucleation-and-growth*			
An	$[-\ell n(1-\alpha)]^{1/n}$	$n[-\ell n(1-\alpha)^{(n-1)/n}](1-\alpha)$	$n(k)^n (t)^{n-1} \exp[-(kt)^n]$
B1	$\ell n[\alpha/(1-\alpha)]$	$\alpha(1-\alpha)$	$k \exp(-kt)[1 - \exp(-kt)^{-2}$
(c) Deceleratory α-time curves:			
Based on geometrical models			
R2	$2[1-(1-\alpha)^{1/2}]$	$(1-\alpha)^{1/2}$	$k[1-(1/2)kt]$
R3	$3[1-(1-\alpha)^{1/3}]$	$(1-\alpha)^{2/3}$	$k[1-(1/3)kt]^2$
Diffusion-controlled reactions			
D1	α^2	$1/2(1/\alpha)$	$1/2\ (k/t)^{1/2}$
D2	$(1-\alpha)\ell n(1-\alpha) + \alpha$	$[-\ell n(1-\alpha)]^{-1}$	reverse calc. #
D3	$[1-(1-\alpha)^{1/3}]^2$	$3(1-\alpha)^{2/3}[2\{1-(1-\alpha)^{1/3}\}]^{-1}$	$3/[2(k/t)^{1/2}\{1-(kt)^{1/2}\}^2]$
D4	$(1-2\alpha/3)-(1-\alpha)^{2/3}$	$3[2\{(1-\alpha)^{-1/3}-1\}]^{-1}$	reverse calc. #
Based on order of reaction			
F0	α	1	k
F0.33	$(3/2)[1-(1-\alpha)^{2/3}]$	$(1-\alpha)^{1/3}$	$k[1-(2/3)kt]^{1/2}$
F1	$-\ell n(1-\alpha)$	$(1-\alpha)$	$k \exp(-kt)$
F2	$(1-\alpha)^{-1} - 1$	$(1-\alpha)^2$	$k/(kt+1)^2$

* refer to Chapter **4** (**§4.2.3**) for details.

calculated values of time at set values of α.

Acceleratory equations
(see Table 3.1a)

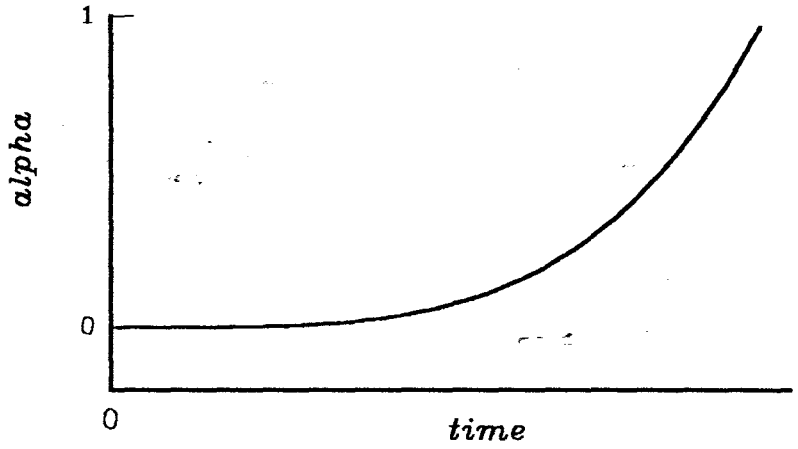

Sigmoid equations
(see Table 3.1b)

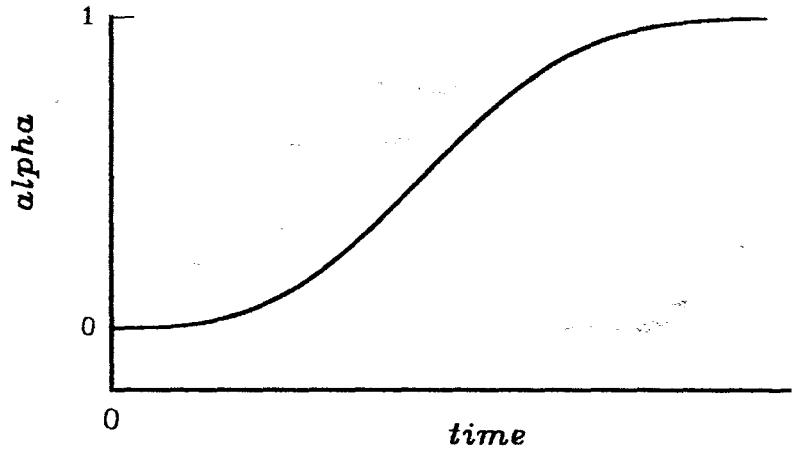

Deceleratory equations
(see Table 3.1c)

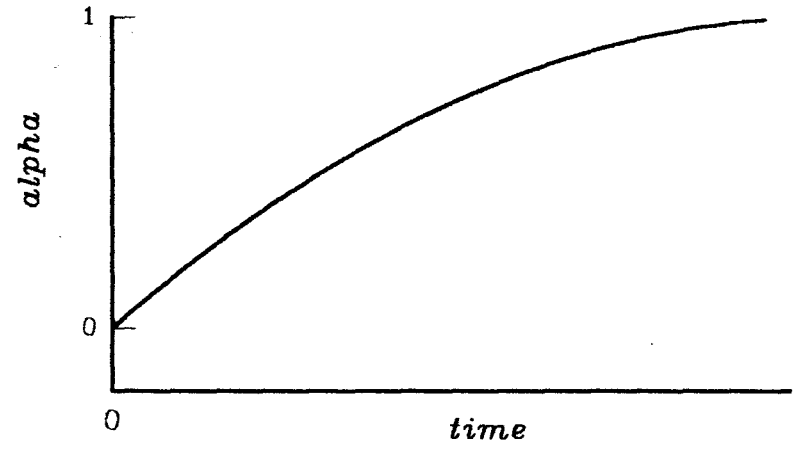

Figure 3.1: Characteristic shapes of alpha versus time curves for the most frequently reported groups of rate equations (see also Figures 4.1 and 4.2).

Acceleratory equations
(see Table 3.1a)

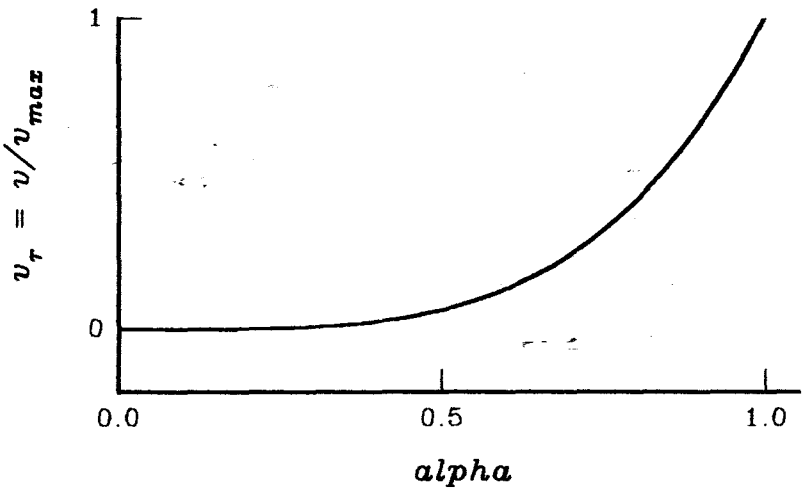

Sigmoid equations
(see Table 3.1b)

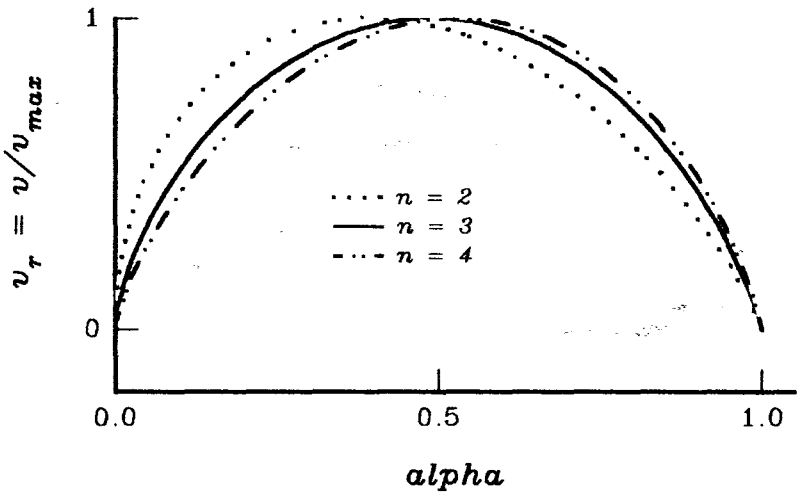

Deceleratory equations
(see Table 3.1c)

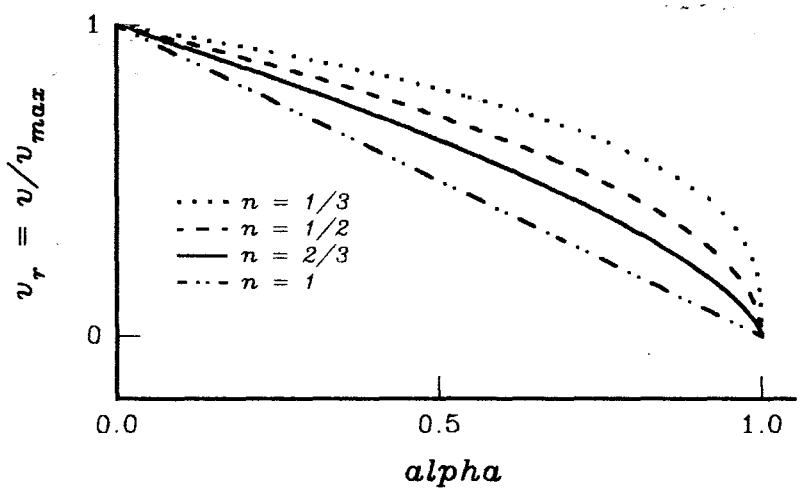

Figure 3.2: Characteristic shapes of rate versus alpha curves for the most frequently reported groups of rate equation, i.e P1, An and Rn .

3.3 Empirical expressions

In examining the results of isothermal kinetic experiments, it is not uncommon to encounter rate *versus* time curves of the overall shape shown in Figure 3.3, but with different concave down curvatures. The usual range of kinetic models does not provide for such behaviour (*e.g.* refs. 22, 30, 61 and 62). The sigmoid, geometric and diffusion models all provide a rather gentle approach to completion, whereas the curve in Figure 3.3 indicates a rather abrupt termination.

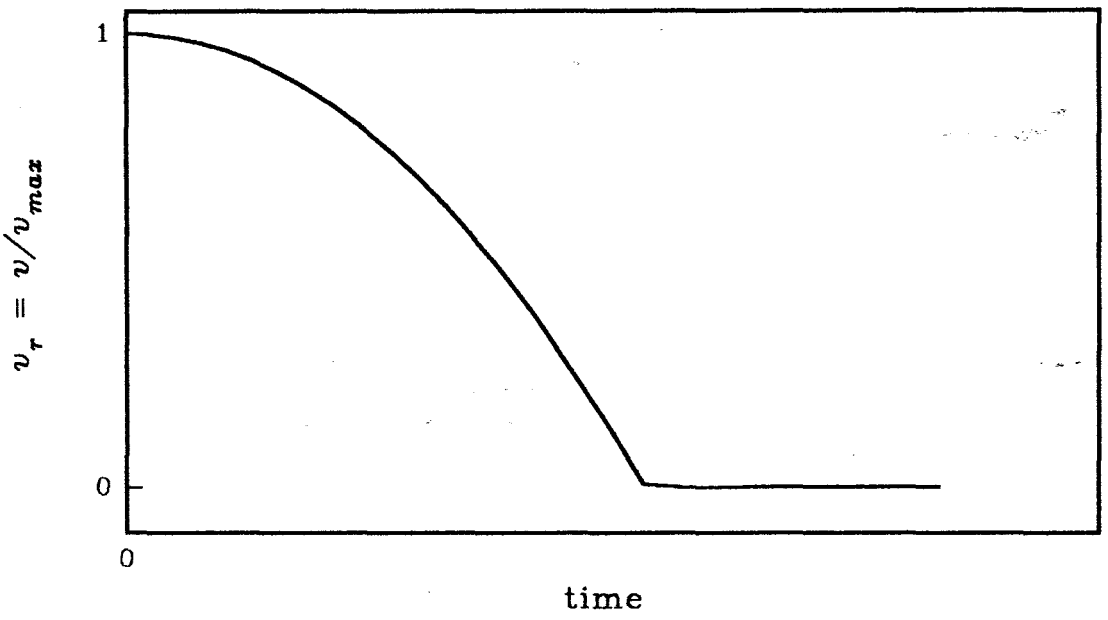

Figure 3.3: A rate versus time curve which might be encountered when examining results of isothermal kinetic experiments and which is not describable by the rate equations in Table 3.1.

An empirical rate equation which could give rise to this type of rate *versus* time curve at constant temperature is

$$d\alpha/dt = \upsilon = \upsilon_{max} [1 - (kt)^b] \qquad 3.26$$

(which will be referred to as the (**B2**) expression). Thus

$$\upsilon_r = \upsilon/\upsilon_{max} = 1 - (kt)^b$$

and

$$\ell n(1 - \upsilon_r) = b\, \ell n(k) + b\, \ell n(t) \qquad 3.27$$

or

$$(1 - \upsilon_r)^{1/b} = kt$$

When $t = 0$, $\upsilon_r = 1$ (its maximum value)

When $\upsilon = 0$, $t = 1/k$

Figure **3.4** shows the υ_r against time curves for values of b (= 2, 3 and 4).

Integration of

$$d\alpha = \upsilon_{max} [1 - (kt)^b]dt$$

between the limits $\alpha = 0$ at $t = 0$ and $\alpha = \alpha$ at $t = t$ gives

$$\alpha = \upsilon_{max} \{t - [k^b/(b+1)]\, t^{(b+1)}\}$$

$$= [\upsilon_{max} t/(b + 1)][b + 1 - (kt)^b] \qquad 3.28$$

The corresponding α against time curves for b values = 2, 3 and 4 are shown in Figure **3.5**. By calculating both υ_r and α at common values of t, it is possible to construct curves of υ_r against α.

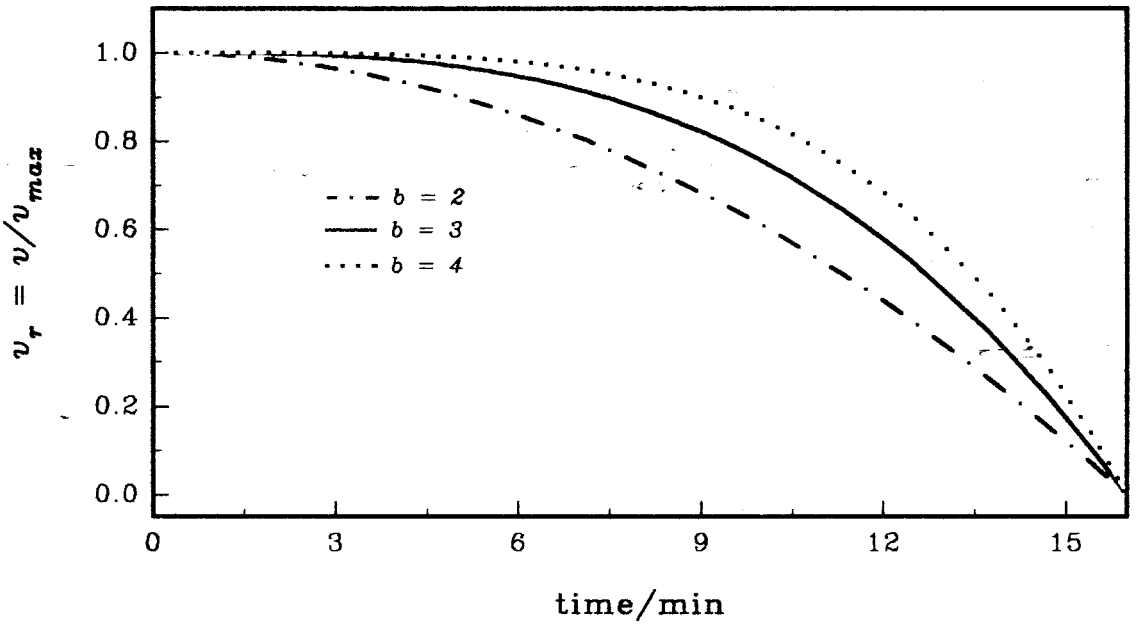

Figure 3.4: Calculated rate versus time curves for reactions conforming to the empirical (B2) expression (3.26), $\vartheta_r = 1 - (kt)^b$, using $k = 0.05\ min^{-1}$ and the different values of b shown.

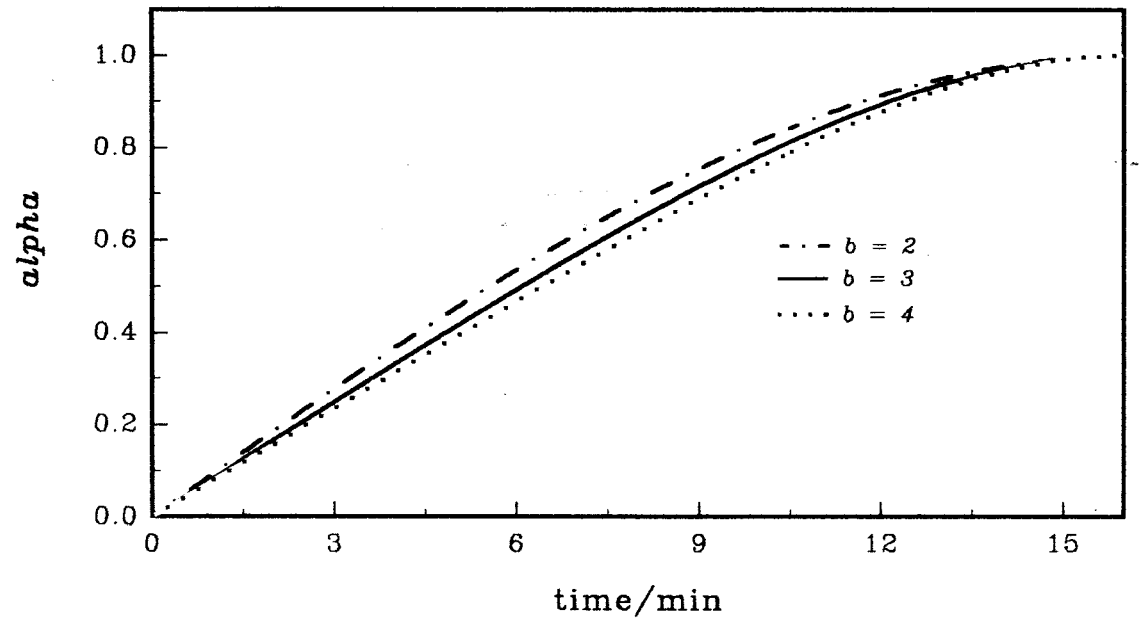

Figure 3.5: Calculated alpha versus time curves for reactions conforming to the empirical (B2) expression (3.26), using $k = 0.05\ min^{-1}$ and the b values shown.

CHAPTER 4

THE TREATMENT OF ISOTHERMAL KINETIC DATA

4.1 Overview

Isothermal thermogravimetry (TG) provides direct measurements of the extent of reaction (α), which enable the integrated rate equations of the form $g(\alpha) = kt$ to be tested for applicability. Some instrumental techniques (DSC in particular) permit the collection of sufficiently accurate data for kinetic analyses to be based on the derivative forms of the rate equations, $\upsilon = k\, f(\alpha)$, with the possible advantage of improved discrimination.

Vyazovkin *et al.* [63] suggested that the methods of kinetic data treatment be classified into two categories: namely (i) the methods of " discriminative " descriptions and (ii) the methods of " generalized " descriptions.

- The first named class, discrimination, refers to all the approaches used to compare competing formal models of the process in order to identify the " best " fitting model(s). Discrimination may be based on statistical methods of analysis and / or other physico-chemical information. Examples of the use of several such approaches in solving the inverse kinetic problem (IKP) are examined in section 4.2.
- The second class, generalized description, refers to the " synthesizing " of a general description from a set of competing models. This approach permits all the variety of descriptions to be considered in terms of individual models, reflecting different but equally important features of the process [64]. Examples are examined in §4.3.

Correlation analysis, a mathematical treatment starting from experimental data and seeking empirical relationships which can subsequently be interpreted theoretically, is another approach.

4.2 The method of discrimination

4.2.1 Introduction

This treatment of isothermal kinetic data uses statistical methods to identify a relationship between the measured α,t values and a number of different formal kinetic models (refer to Table 3.1) in order to distinguish the best fitting model. If

experimental data fit a rate expression *accurately* [31,63,65-67], then it is possible (but not certain) that the reaction may proceed by the kinetic model assumed in the derivation of the theoretical kinetic expression. Such results may be used to identify the spatial development of the reaction interface, *etc.* Kinetic conclusions should be supported by independent evidence such as microscopic observations [22,48].

Comparison of experimental plots of α against time or rate ($\upsilon = d\alpha/dt$) against time with theoretical curves (see Figures **3.1**, **4.1** and **4.2**) can be used to distinguish between applicability of the deceleratory and sigmoid models. The advantage of this approach is that only a limited number of rate equations need then be considered for further screening.

Methods of identification of the rate equation which provides the most satisfactory fit to the isothermal experimental α,t measurements include [30,59]:

- the examination of linearity of plots of calculated values of $g(\alpha)$ against time for each integrated model rate equation, $g(\alpha) = kt$;
- comparison of experimental plots of α against reduced-time with curves given by similar treatment for various kinetic model rate equations;
- examination of the plots of measured $(d\alpha/dt)$ values against α, against time or against the derivative function, $f(\alpha)$; and
- examination of the linearity of plots of ℓn(rate) against $\ell n(1 - \alpha)$, and the constancy of the apparent order, n.

These, and other related methods are described in greater detail below. The time scale may have to be corrected for any induction period to reaction, t_o.

4.2.2 The use of integrated rate equations

Testing the linearity of plots of g(α) against time

Deviation from linearity of plots of calculated $g(\alpha)$ values against time may be used to identify equations which merit more detailed consideration. Standard statistical criteria which are used to measure linearity across any defined α range include [59]:

- the correlation coefficient (r),
- the standard error of the slope of the regression line (s_b), and
- the standard error of the estimate of $g(\alpha)$ from t (s_{xy}).

Plots of residuals, $\{g(\alpha)_{expt.} - g(\alpha)_{theory}\}$, against time may also be used in identifying the

most appropriate rate expression. If an acceptable fit is obtained, the value of k (at that specified temperature), and its standard error can be determined from the slope of the *least-squares* fit.

Some points to note in applying this method are:

(i) The acceleratory region, where the power law may apply, can be tested by using either of the following plots:
- $\alpha^{1/m}$ against t, this should yield a straight line of slope k, or
- $\ell n(\alpha)$ *versus* $\ell n(t)$, this should be linear, with slope $^1/m$.

(ii) The equations deduced from reaction order considerations: equations (3.8), (3.9) and (3.11) are difficulty to distinguish, especially for lower α values ($\alpha \leq 0.5$). This might be expected since the integration of $d\alpha/dt = k(1 - \alpha)^n \approx k$ leads to $\alpha \approx kt$ (when α is small), which is independent of the apparent order, *n*.

(iii) The $g(\alpha)$ function for nucleation-and-growth (the JMAK equation (3.15)) may be tested using the equation

$$\ell n\,[-\ell n(1 - \alpha)] = n\,\ell n(t) \qquad 4.1$$

A plot of $\ell n\,[-\ell n(1 - \alpha)]$ against $\ell n(t)$ should yield a straight line of slope *n*. Such plots are, however, notoriously insensitive [68] and an error in t_o can significantly influence the apparent value of *n* [33].

Comparison of plots of α against reduced-time

This approach is attributed to Sharp *et al.* [42]. It involves the scaling of reaction time values to a reduced-time scale so as to allow the comparison of α *versus* $t_{red.}$ with theoretical curves for the commonly reported kinetic equations. The reduced-time is usually calculated as $t_{red.} = t/t_{0.5}$ where $t_{0.5}$ is the time at which $\alpha = 0.5$. Hence

$$k = g(0.5)/t_{0.5} \qquad 4.2$$

and

$$g(\alpha) = g(0.5)(t/t_{0.5}) = g(0.5)\,t_{red.} \qquad 4.3$$

where g(0.5) is a constant for a given function, $g(\alpha)$.

When experiments at different temperatures are isokinetic, *i.e.* follow the same rate equation, plots of α_e against $t_{red.}$ will all lie on a single curve [42]. Any systematic change in kinetic behaviour with change in temperature can be noticed.

Using the theoretical functions of α (see Table **4.1**), plots of α_m against $t_{red.}$ are constructed for the various functions to give *master* plots for comparison with the plots of α_e against $t_{red.}$. The closest fitting theoretical expression can be identified, although the method is susceptible to errors in the time scales [22]. Measured time values may have to be corrected by subtracting t_o, the induction period to onset of reaction (which may also include the time required to heat the reactant to the desired temperature).

Table 4.1: Values of α and $t/t_{0.5}$ for nine solid state formal models frequently encountered in the literature [21].

	Values of $t/t_{0.5}$ for the theoretical functions indicated								
α	R2	R3	F1	A2	A3	D1	D2	D3	D4
0.1	0.174	0.165	0.152	0.390	0.533	0.040	0.033	0.028	0.032
0.2	0.362	0.349	0.322	0.567	0.685	0.160	0.140	0.121	0.135
0.3	0.556	0.544	0.515	0.717	0.801	0.360	0.328	0.295	0.324
0.4	0.768	0.762	0.737	0.858	0.903	0.640	0.609	0.576	0.595
0.5	1.000	1.000	1.000	1.000	1.000	1.000	1.000	1.000	1.000
0.6	1.253	1.277	1.322	1.150	1.097	1.440	1.521	1.628	1.541
0.7	1.543	1.607	1.737	1.318	1.198	1.960	2.207	2.568	2.297
0.8	1.887	2.014	2.322	1.524	1.322	2.560	3.115	4.051	3.378
0.9	2.334	2.602	3.322	1.822	1.492	3.240	4.363	6.747	5.028

Three methods of linearization of reduced-time data may be used [22,42,69]:

- Plots of α_e against α_m obtained from common values of $(t/t_{0.5})$ will, for exact agreement between experimental and master data, yield a straight line which passes through the origin.
- Plots of $(t/t_{0.5})_m$ against $(t/t_{0.5})_e$ for matching values of α_e and α_m should also give a straight line.
- Plots of t_e against $(t/t_{0.5})_m$ should also give a straight line.

4.2.3 The use of derivative rate equations

The direct use of the derivative forms of the rate equations is becoming increasingly popular [30,31,61,62]. They may have the advantages of improved discrimination. Rate curves for a reaction are obtained from isothermal differential scanning calorimetry on

the assumption that the evolution or absorption of heat is a measure of the extent of reaction, or from isothermal derivative thermogravimetry.

The rate *versus* time curves for the deceleratory group of models have maximum rate (υ_{max}) at t = 0, while the bell-shaped rate *versus* time curves for the sigmoid group have υ_{max} at some time, $t_{max} > 0$ (see Figures **4.1** and **4.2**). Experimental plots of υ *versus* time can thus be used for initial broad separation of the kinetics.

From

$$(d\alpha/dt) = k(1 - \alpha)^n \qquad 4.4$$

upon taking natural logarithms

$$\ell n(d\alpha/dt) = n\, \ell n(1 - \alpha) + \ell n(k) \qquad 4.5$$

A plot of $\ell n(d\alpha/dt)$ against $\ell n(1 - \alpha)$ should thus yield a straight line of slope n and intercept $\ell n(k)$. If the simple plot based on equation (4.5) is not sufficient, then more specific equations may be tested [31,70], namely the diffusion-controlled model equations, the various JMAK-type equations, the power law, the Prout-Tompkins equation, *etc.*

Methods based on derivative form of the rate equations include [30,61,71]:

- comparison of the plots of $(d\alpha/dt)$ against time or against α with theoretical plots (Figures **3.2**, **4.1** and **4.2**). Experimental curves can be compared with curves constructed for each rate equation in Table **3.1**.
- testing the linearity of plots of experimental rate values against the derivative functions of the rate equations [30].

Methods requiring measurements of rate, t and / or α are examined in the following subsections.

(a) The power law

For the power law of the general form [49,60]

$$\alpha = (kt)^m \qquad 4.6$$

we have

$$[(\alpha)^{1/m}]/k = t$$

so that

$$d\alpha/dt = mk\,(\alpha)^{(m-1)/m} \qquad 4.7$$

A plot of $\ell n(d\alpha/dt)$ against $\ell n(\alpha)$ should thus permit the calculation of m from slope ($= 1 - 1/m$). Then, knowing m should permit the evaluation of k from

the intercept (= ℓn(k) + ℓn(m)).

(b) The JMAK equation

For the JMAK kinetic models

$$(1 - \alpha) = \exp[-(kt)^n] \qquad 3.14$$

the derivative form is

$$d\alpha/dt = n\,(k)^n\,(t)^{n-1}\,(1 - \alpha) \qquad 4.8$$

and the expression for ($d\alpha$/dt) as a function of t is written as

$$d\alpha/dt = n\,(k)^n\,(t)^{n-1}\exp\{-(kt)^n\} \qquad 4.9$$

Shapes of the rate against time curves for values of n of 1, 2, 3 and 4 are illustrated in Figure **4.1**. Except for $n = 1$ with υ_{max} at t = 0, the rate *versus* time curves have a maximum at some time ($t_{max} > 0$) satisfying

$$k\,t_{max} = \{(n-1)/n\}^{1/n} \qquad 4.10$$

(c) The reaction order rate equation

Processes following a simple rate equation of the form

$$d\alpha/dt = k(1 - \alpha)^n = k\,f(\alpha) \qquad 3.6$$

with n = 0, $^1/_3$, ½, $^2/_3$ and unity are briefly examined below, and the derivative forms of the rate equations are included in Table **3.1**. The rate against time curves are illustrated in Figure **4.2**.

The case n = 0 (zero-order) : $d\alpha/dt = \upsilon = k.$ 4.11

The rate remains constant from the start of the reaction and falls to zero when all the reactant is consumed.

The case n = ½ (contracting-area) : $\upsilon = k(1 - \alpha)^{½}$ 4.12

The integration of equation (4.12) leads to equation (3.8)

$$g(\alpha) = 1 - (1 - \alpha)^{½} = (½)kt$$

thus

$$(1 - \alpha)^{½} = 1 - (½)kt \qquad 4.13$$

Substitution into equation (4.12) gives

$$\upsilon = k[1 - (½)kt] = k - (½)(k)^2 t \qquad 4.14$$

Thus rate falls linearly until the reaction reaches completion (Figure **4.2**).

The case n = $^1/_3$ (one-third-order) : $\upsilon = k(1 - \alpha)^{1/3}$ 4.15

Integration of equation (4.15) leads to

$$g(\alpha) = 1 - (1 - \alpha)^{2/3} = (^2/_3)kt$$

and the rate-time expression is

$$\upsilon = k[1 - (^2/_3)kt]^{½} \qquad 4.16$$

The rate-time curve initially remains approximately linear, and falls gently to completion (see Figure **4.2**).

The case n = $^2/_3$ (contracting-sphere) : $\upsilon = k(1 - \alpha)^{2/3}$ 4.17

The treatment follows that for n = ½ (above)

$$g(\alpha) = 1 - (1 - \alpha)^{1/3} = (^1/_3)kt$$

and

$$(1 - \alpha)^{2/3} = [1 - (^1/_3)kt]^2 \qquad 4.18$$

such that

$$\upsilon = k[1 - (^1/_3)kt]^2 \qquad 4.19$$

The case n = 1 (first-order) : $\upsilon = k(1 - \alpha) = k - k\alpha$ 4.20

A plot of υ against α should thus be linear with slope -k (*cf.* Figure **3.2**). The rate-time relationship is of the form

$$\upsilon = k \exp(-kt) \qquad 3.11$$

and a plot of $\ell n(\upsilon)$ against time should be linear with slope -k .

When α is small equations (4.12), (4.15), (4.17), (4.20), *etc.*, takes the form of the zero-order equation (4.11). This leads to an approximately zero-order process

$$d\alpha/dt = \upsilon \approx k \qquad 4.21$$

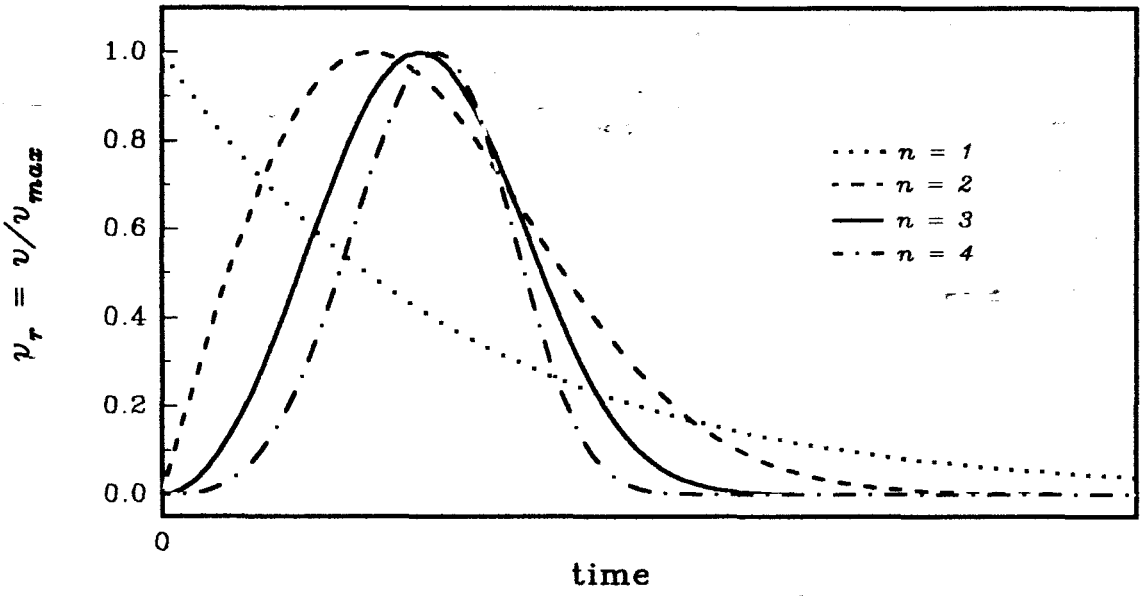

Figure 4.1: Calculated rate versus time curves for reactions conforming to the JMAK equation:
$da/dt = n(k)^n(t)^{n-1}\ exp[-(kt)^n\ ]$, $n = 1, 2, 3$ and 4.

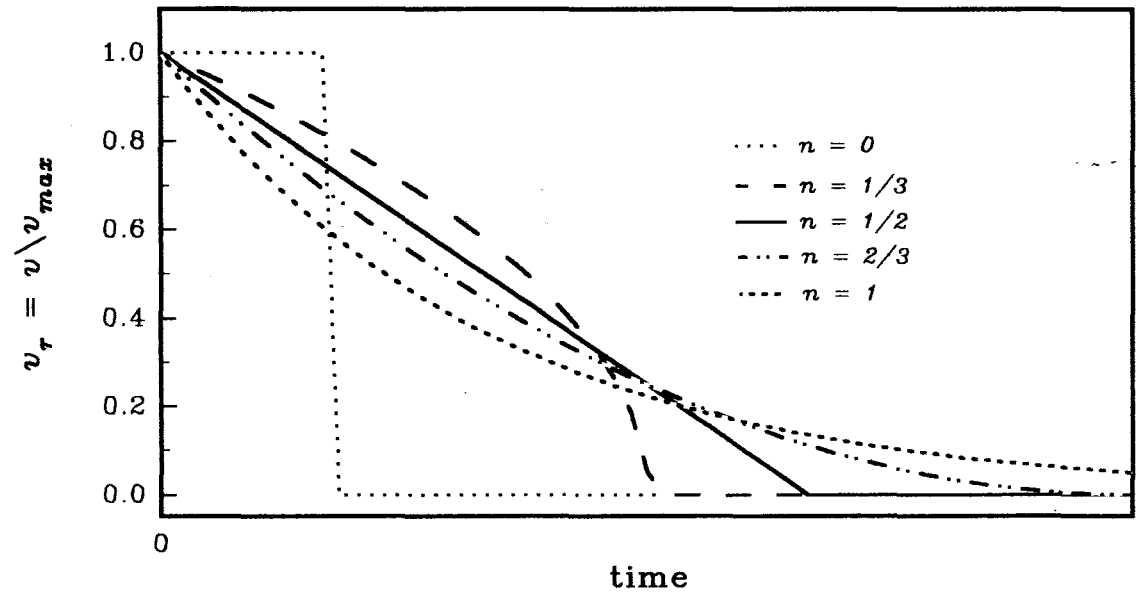

Figure 4.2: Calculated rate versus time curves for reactions conforming to the simple order rate equation:
$da/dt = k(1 - a)^n$, $n = 0,\ 1/3,\ 1/2,\ 2/3$ and 1.

(d) Plots of ($d\alpha/dt$) against the derivative function, $f(\alpha)$

Plot of the experimental ($d\alpha/dt$) value against the values of $f(\alpha)$, calculated for an appropriate function for each corresponding value of α will be linear, with slope $^1/k$. This method, put forward by Galwey *et al.* [30] deserves serious consideration since it provides better distinguishability amongst models with similar shapes of the α versus time curves: acceleratory, sigmoid or deceleratory. The distinguishability is particularly good for the sigmoid group of equations (**A2** to **A4**). Distinguishability between the geometric processes (**R2** and **R3**) still remains a problem.

4.2.4 Confirmation of the individual rate equation

The conclusion that the kinetic behaviour, $g(\alpha) = kt$, or $d\alpha/dt = kf(\alpha)$, observed for the reaction of interest, results from a particular geometric pattern of interface advance should be confirmed by independent evidence because kinetic interpretations are often ambiguous. For example, a fit of α *versus* time data to the **A3** equation can result either from instantaneous nucleation followed by three-dimensional growth (*i.e* $\beta = 0$, $\gamma = 3$ so that $n = 3$) or from linear nucleation accompanied by two-dimensional growth ($\beta = 1$, $\gamma = 2$ and again $n = 3$).

The most direct method of confirming kinetic deductions is by microscopic observation of the textural changes related to interface development within a sequence of partially-decomposed reactant samples [19,22,35]. For example, nucleation-and-growth processes, or interface development in the **R2** and **R3** models, can sometimes be identified [72]. The positive identification of intermediates can also be important in supporting a proposed chemical mechanism [73]. Additional indications of the reliability of kinetic analyses may be obtained by comparison of isothermal kinetic measurements with those obtained from non-isothermal experiments [63].

4.3 Methods of generalized model-type descriptions

A main criticism of the discrimination method is the limited group of rate equations used. It is claimed that the description of the experimental results may be improved by relaxing the restrictions on the models tested [38,63,64]. A more general rate equation known as the Sestak-Berggren equation has thus been suggested

$$f(\alpha) = \alpha^m (1 - \alpha)^n [-\ell n(1 - \alpha)]^p \qquad 3.4$$

Suitable choices of values of m, n and p result in all of the f(α) in Table 3.1 [38,63]. Equation (3.4) has been criticized [43,74,75] for containing redundant terms since no more than two parameters may be estimated with sufficient reliability.

A linear combination of several formal models has been suggested as a possible generalized description [41,76]. An example cited [41] involves the substitution of the JMAK-type models by the linear combination of power-law nucleation, interface controlled and the diffusion-controlled models.

4.4 The influence of temperature on reaction rate

4.4.1 Introduction

Temperature exerts a strong controlling influence over the rates of most chemical reactions. One or other form of the Arrhenius equation [22,77,78]

$$k = A \exp(- E_a/RT) \quad \text{or} \quad k = A' T^n \exp(-E_a/RT) \qquad 4.22$$

where E_a is the apparent activation energy and A is the pre-exponential factor, has found application for diverse rate processes that include both homogeneous and heterogeneous reactions [79]. Doubts have, however, been expressed regarding the reliability of the theoretical foundations for the application of the Arrhenius-type equations to chemical changes proceeding in the solid state [80-84].

Laidler [78] presented a critical discussion of the alternative functions which have been proposed, and the reasons why they have no advantages over the conventional equation.

4.4.2 The significance given to the Arrhenius parameters, E_a and A

The Arrhenius parameters calculated for reactions of solids are usually described in terms similar to those used in the collision theory of gaseous reactions. The activation process is identified with an energy barrier or threshold that must be surmounted to enable the occurrence of the bond redistribution steps required to convert reactants into products [79]. For nucleation and growth of nuclei, the value of E_a is composed of activation energies of mass transfer (diffusion) and factors arising from the thermodynamics of nucleation and / or growth. The frequency factor is a measure of the frequency of occurrence of the reaction situation and may

include the vibration frequency in the reaction coordinate [33].

Generally, it can be said that **A** can include many constants describing the initial state of the sample such as molecular mass, active surface and number of lattice imperfections, stoichiometric factors of chemical reaction, as well as computational and experimental artifacts [85].

The direct application of the Arrhenius equation to reactions of solid has been questioned [86-88]. Galwey and Brown [66,79] suggested that due allowance be made for the number of precursor species within the reaction zone, and the changing area of the reaction interface. Precise application to solids have been reported [89] for the diffusion of ions and studies concerned with the migrations of crystal imperfections.

In spite of the critical arguments against the applicability of Arrhenius-type equations in solid state reactions, experimenters continue reporting and comparing data obtained on the basis of the Arrhenius equation. Many workers suggest that the Arrhenius parameters have clear empirical significance. For example, values of E_a are useful in empirical testing of (i) hazards and explosives, (ii) oxidative stability, and (iii) optimization conditions during industrial synthesis and fabrication. From a purely practical perspective, their magnitudes provide a convenient comparative measure of reactivity and of temperature coefficients of reactions.

4.4.3 Evaluation of Arrhenius parameters from plots of $\ell n(k)$ against $^1/T$

The conventional approach to the determination of the kinetic parameters E_a and A has been first to determine isothermal α against time or rate (υ) *versus* time relationship at a series of different temperatures. Once the rate equation is established, and there is evidence that the reaction is isokinetic at different temperatures, a plot of $\ell n(k)$ *versus* $^1/T$ then gives a straight line whose slope and intercept give the apparent activation energy (E_a) and the pre-exponential factor (A) respectively.

4.4.4 Evaluation of E_a from plots of $\ell n(^1/t_s)$ against $^1/T$

The magnitude of $^1/t_s$, where t_s is the time scaling factor (for example $t_{0.5}$ when $\alpha = 0.5$), is proportional to the rate coefficient (k) at the temperature of the experiment.

From

$$g(\alpha) = kt$$

we have

$$g(0.5) = kt_{0.5} \qquad 4.23$$

and thus

$$k = g(0.5)/t_{0.5} \qquad 4.24$$

The reciprocals of the time scaling factor ($^1/t_s$) at several different temperatures can thus be used as quantitative measures of k to calculate the Arrhenius parameters without the necessity for identifying the kinetic model. Thus a plot of $\ell n(^1/t_s)$ against $^1/T$ should be linear with slope E_a. The intercept includes $\ell n\{g(\alpha)\}$ and does not directly yield the pre-exponential factor, **A**.

4.4.5 Evaluation of E_a from characteristic features of rate-time curves

A secondary feature of rate-time data of the deceleratory and the sigmoid α-time relationship (*cf.* § 4.2.3) is the time $t_{max/2}$ taken for the rate to drop to half its maximum value (*i.e.* $v_{max/2}$). The parameter $t_{max/2}$ can be obtained (when present) from DTG or DSC rate-time curves [61]. Measurements of its temperature dependence may be used in Arrhenius-type plots (*i.e.* $\ell n(^1/t_{max/2})$ *versus* $^1/T$) to calculate values for the apparent activation energy, without knowledge of the particular kinetic model that applies. The pre-exponential factor (A) is however not readily obtained since the measured quantities are only proportional to the rate coefficient.

4.5 The apparent kinetic compensation effect

The apparent compensation effect (CE) has been described in terms of the observed changes in the Arrhenius parameters of either: (i) one substance under varying experimental conditions (*e.g.* changes in sample mass, particle size and measuring conditions) or (ii) of a series of different substances similar in structure, under identical conditions. The basic equation is of the form [39,90]

$$\ell n(A) = bE_a + c \qquad 4.25$$

where **b** and **c** are constants. This is described as compensation because, in a set of data obeying equation (4.25), the decrease in reaction rate expected to result from an increase in E_a is offset by an increase in the magnitude of $\ell n(A)$. The occurrence of a compensation effect may also be confirmed from Arrhenius plots of $\ell n(k)$ *versus* $^1/T$ (equation 4.26), if the different straight lines for a series of reactions intersect in a single point (the isokinetic temperature [91])

$$\ell n(A) = E_a/RT_{iso} + \ell n(k_{iso}) \quad 4.26$$

where k_{iso} is the isokinetic rate coefficient and T_{iso} is the isokinetic temperature.

Two similar, but non-equivalent definitions of compensation are currently in use. Some authors refer to the linear relation between $\ell n(A)$ and E_a (Figure **4.3**), whilst others require the existence of an isokinetic temperature, T_{iso} (see Figure **4.4**) [85,91-95]. The apparent compensation effect has also been linked to artifacts produced by either the inadequate processing of data or lack of control of experimental conditions.

Several attempts [96-99] have been made to determine the physico-chemical factors that result in the empirically observed behaviour. A shared view seems to be that the *compensation effect* is a consequence of a common rate-controlling factor occurring within the same temperature range for a group of related reactions.

Zsako's viewpoint [98] is that **b** is related to the strength of the bond being broken when gaseous products are formed. A small value of **b** has been associated with rupturing of a strong bond. Constant **c** is suggested to be related to the structure of, and defects in, the starting material, or to the mobility of constituents of the crystal.

Other authors [81,84] have suggested that the Arrhenius equation is responsible for the observed linear relation between $\ell n(A)$ and E_a. Exner [81] suggested that compensation is observed only because it is impossible to determine **A** by means of an independent experiment, but it is calculated with E_a using the Arrhenius based relationship. Any error in the calculated value of E_a is thus accompanied by a corresponding change in the value of **A**. Garn's viewpoint [82] is that the appearance of the compensation effect may be regarded as a confirmation of the opinion that the Arrhenius equation cannot, in principle, be applied to describe solid-state reactions.

Agrawal [91] has suggested that the CE be classified into the "true" and "false" compensation. True compensation should arise from physico-chemical factors. False compensation refers to computational and experimental artifacts. The occurrence of true compensation is confirmed through the existence of the isokinetic temperature. The failure of a series of reactions to display a single point of concurrence confirms a false compensation effect.

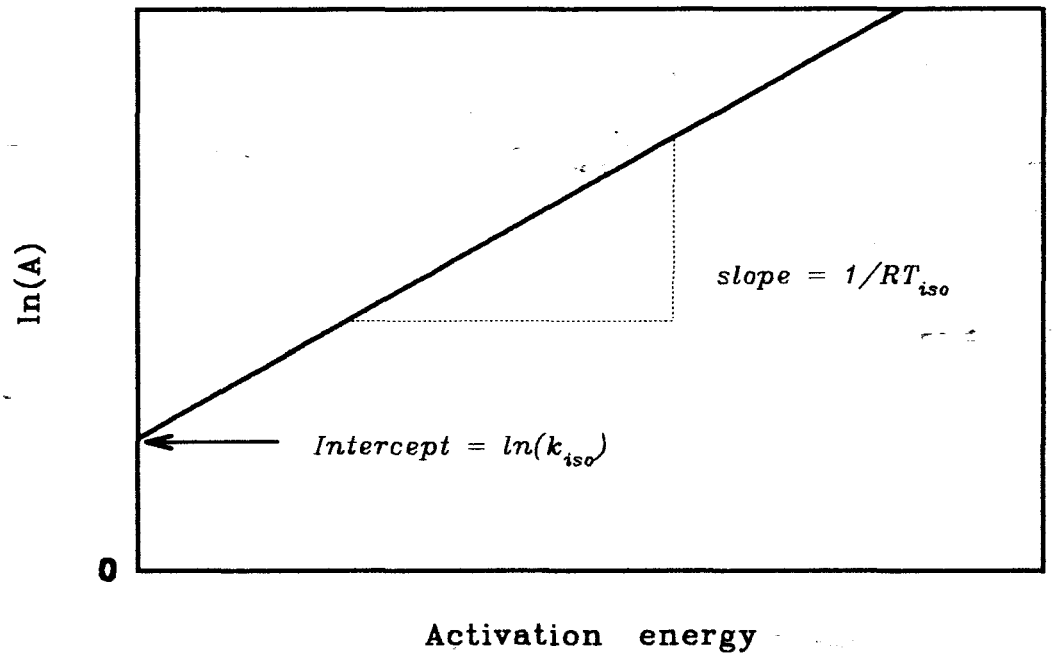

Figure 4.3: Representation of a plot generally accepted to establish the existence of compensation effect.

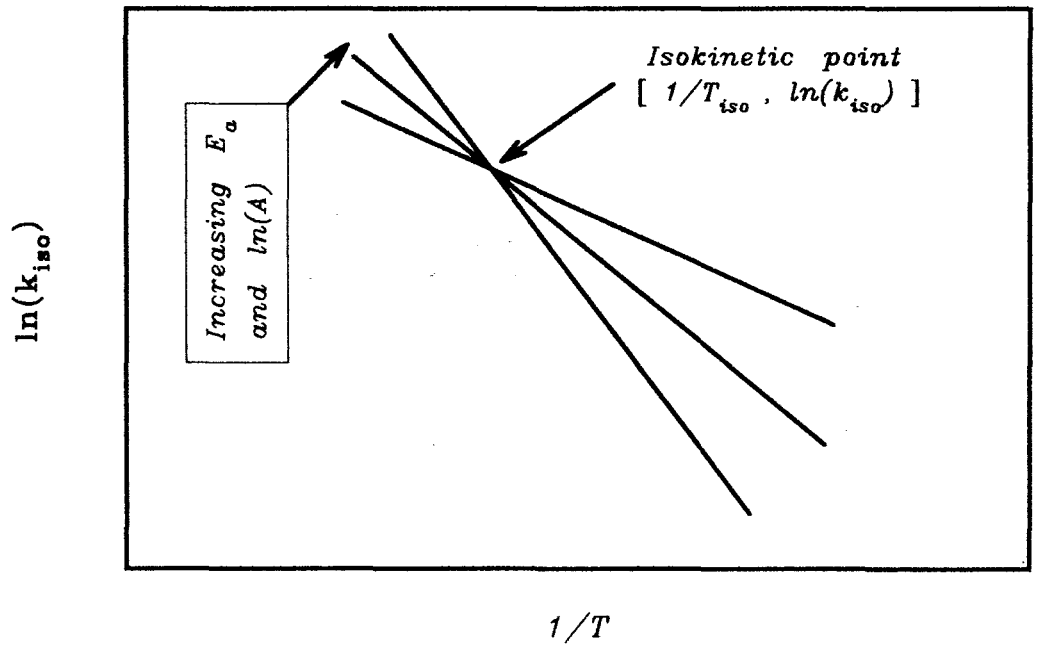

Figure 4.4: Representation of Arrhenius plot in the existence of an isokinetic temperature. The single point of concurrence has been associated with the occurence of " true " compensation effect.

According to Agrawal [91] and Koga's classification scheme [85] a " false " CE may arise from:

- comparison of $\ell n(A)$ and E_a values obtained by varying the kinetic model,
- errors resulting from various mathematical approximations of rate equations,
- experimental errors such as inaccurate temperature measurements and temperature gradients within the sample, and
- comparison of $\ell n(A)$ and E_a for a single substance decomposed under a variety of conditions.

Muraleedharan [95], Zsako *et al.* [100] and others [92] have challenged the existence of an isokinetic temperature as a criterion for establishing a " true " compensation effect. Muraleedharan's viewpoint is that uncertainties in the kinetic parameters convert the point of concurrence into an intersecting domain, which may be wide. The position of T_{iso} was proposed as an alternative criterion. The author suggested that for false compensation T_{iso} will be within the experimental temperature range. According to Zsako's " perturbation " analysis, for Agrawal's procedure to be true the regression correlation coefficient (r) for the plot of $\ell n(A)$ *versus* E_a must be unity.

CHAPTER 5

NON-ISOTHERMAL KINETICS

5.1 Introduction

Kinetic analyses of non-isothermal experiments are important because many natural and industrial processes proceed non-isothermally. Non-isothermal methods may offer some advantages over conventional isothermal methods [18,68,101].

Non-isothermal methods offer no zero-time error since it is possible to determine the reaction onset temperature precisely. The reaction onset temperature is however dependent upon experimental conditions. Support comes from the Arrhenius equation where, even at low temperatures, k is not exactly zero.

Considerably fewer data are required for a non-isothermal experiment. A single sample may be sufficient to scan the entire temperature range, while a new sample is needed in every isothermal experiment.

5.2 The fundamentals

Many non-isothermal methods of kinetic analysis are in use. The methods may be grouped into two main classes based on their mathematical background: derivative and integral (approximation) methods. Most treatments are based on the combination of the three equations:

$$d\alpha/dt = k\, f(\alpha)$$

$$k = A \exp(- E_a/RT)$$

$$T = T_o + \beta t$$

and the assumption that $d\alpha/dT = (d\alpha/dt)(dt/dT)$.

A is the pre-exponential factor, E_a is the apparent activation energy, R is the gas constant, β (= dT/dt) is the constant heating rate, and T_o is the starting temperature of the experiment. Combination of the three equations gives

$$d\alpha/f(\alpha) = (A/\beta) \exp(- E_a/RT)\, dT \qquad 5.1$$

Taking natural logarithms gives

$$\ell n\{(d\alpha/dT)/f(\alpha)\} = - E_a/RT + \ell n(A/\beta) \qquad 5.2$$

In derivative methods, the left-hand side of equation (5.2) is essentially plotted against the reciprocal of the absolute temperature, and the activation energy can be derived from the slope, and A from the intercept.

Integration of equation (5.1) between the limits $\alpha = 0$ at $T = T_o$ and α at some temperature (T) leads to equation (5.3)

$$g(\alpha) = \int_o^{\alpha} d\alpha/f(\alpha) = \int_{T_o}^{T} (A/\beta) \exp(- E_a/RT)\, dT \qquad 5.3$$

Two main difficulties arise: (i) the analytical form of the function $f(\alpha)$ is generally unknown, and (ii) the right-hand of equation (5.3) does not reduce to a finite form upon integration. Different mathematical approximations for evaluating the integral have been described in the literature [102-106], and there is a steady flow of " refined " formulations and computational schemes.

5.3 Derivative methods

Derivative methods include difference-derivative methods and methods based on different heating rates. The most frequently used [19,75] are reviewed.

5.3.1 Difference-derivative methods

An example is the method first introduced by Freeman and Carroll [107]. It is a difference-derivative method involving differences in rate, and attempts to determine both the order of reaction and the activation energy. The method follows from equation (5.1) by arbitrarily choosing $f(\alpha) = (1 - \alpha)^n$. Differentiation of equation (5.2) with respect to $d\ell n(1 - \alpha)$ leads to

$$\left\{\frac{d\ell n[\beta(d\alpha/dT)]}{d\ell n\,(1 - \alpha\,)}\right\} = - \left\{\frac{(E_a/R)\, d(^1/T)}{d\ell n(1 - \alpha)}\right\} + n \qquad 5.4a$$

or

$$\left\{\frac{\Delta\ell n[\beta(d\alpha/dT)]}{\Delta\ell n(1 - \alpha)}\right\} = - \left\{\frac{(E_a/R)\, \Delta(^1/T)}{\Delta\ell n(1 - \alpha)}\right\} + n \qquad 5.4b$$

Therefore a plot of the left-hand side of either equation (5.4a) or (5.4b) against $\{[d(^1/T)]/d\ell n(1 - \alpha)\}$, or $\{\Delta(^1/T)/\Delta\ell n(1 - \alpha)\}$ should yield a straight line with slope $- E_a/R$ and intercept equal to *n*.

The assumption of a simple reaction order, n, may be improved [107,108] by use of a less formal model. For example, in nucleation-and-growth the general function is given by $f(\alpha) = (1 - \alpha)[-\ell n(1 - \alpha)]^p$ such that

$$\left\{\frac{\Delta \ell n[\beta(d\alpha/dT)/(1 - \alpha)]}{\Delta \ell n[-\ell n(1 - \alpha)]}\right\} = - (E_a/R)\left\{\frac{\Delta(^1/T)}{\Delta \ell n[-\ell n(1 - \alpha)]}\right\} + p \qquad 5.5$$

Sestak *et al.* [108] have criticized the accuracy of the graphical determination of $d\alpha/dT$ which depends on various factors such as heating rate, absolute linearity of heating rate, *etc.* Criado *et al.* [109] demonstrated that the Freeman and Carroll method cannot discriminate between reaction order kinetics and other kinetic models.

5.3.2 Methods based on thermal curves obtained at different heating rates

The Kissinger (peak temperature) method

Kissinger [110] published a method which requires several thermal curves (*e.g.* DTG or DSC) obtained at different heating rates (β). Values of the temperature at the curve maximum (T_{max}) are measured. The equation then used is (*cf.* equation (5.15)).

$$\ell n(\beta/T^2_{max}) = - E_a/RT_{max} + \ell n(AR/E_a) \qquad 5.6$$

The value of E_a can then be determined from the slope of a plot of $\ell n(\beta/T^2_{max})$ *versus* $^1/T_{max}$. From their examination of Kissinger's method, Tang *et al.* [101] reported that validity of the method is limited to n being close to unity.

The isoconversional methods

Isoconversional methods are based on the use of the temperature values for the same α value obtained at different heating rates (β) [31,111-113]. Several examples are possible, based on equation (5.1). The commonly used equation is

$$\ell n[\beta(d\alpha/dT)] = - E_a/RT + \ell n[A\, f(\alpha)] \qquad 5.7$$

The values of E_a and $[A\, f(\alpha)]$ can be determined from a plot of $\ell n[\beta(d\alpha/dT)]$ against $^1/T$, at a particular value of α, from several experiments at different heating rates. The formal model $f(\alpha)$ has to be identified before the pre-exponential factor (A) can be estimated. The analytical form of $f(\alpha)$ is however difficult to determine. Some authors [93,94] have reported the estimation of the pre-exponential factor using the "apparent" compensational relationship (refer to **§ 4.5**).

At moderate heating rates (5 to 20°C min^{-1}) and for E_a values of about 100 kJ mol^{-1}, the Kissinger method is practically isoconversional with $\alpha_{max} \approx 0.60$ [114,115]. Generally, the conversion degree α_{max} at T_{max} depends on the heating rate.

Methods for obtaining $f(\alpha)$, based on one thermal curve, have been criticized for assuming that $f(\alpha) \approx$ constant in a wide α interval (*e.g.* 0.05 to 0.80 in the Piloyan method) [132,133]. The dependence of E_a on the degree of conversion (α) remains a problem in the treatment of kinetic data using isoconversional methods.

5.4 Integral methods

Many alternative methods, using a series expansion as an approximation for the temperature integral, equation (5.3), have been proposed and discussed [102-106,118,119]. Amongst the commonly used methods are those originally developed by Murray and White, by Doyle, and by Coats and Redfern.

Using equation (5.3) and the notation $x = E_a/RT$, Murray and White [103] and Doyle [105] assumed low α values at low temperature and substituted zero for T_o to obtain

$$g(\alpha) = (A/\beta) \int_o^T \exp(-E_a/RT)\, dT = - \int_o^y (AE_a/\beta R)\, [\exp(-x)/x^2]\, dx \qquad 5.8$$

which, after integration, can be written as

$$g(\alpha) = (AE_a/\beta R)\, p(x) \qquad 5.9$$

where $$p(x) = - \int_o^y [\exp(-x)/x^2]\, dx \qquad 5.10$$

Murray and White made use of the asymptotic expansion:

$$p(x) = [\exp(x)/x^2][1 + (2!/x) + (3!/x^2) + (4!/x^3) + \ldots] \qquad 5.11$$

to obtain (after ignoring all but the first two terms of the expansion)

$$g(\alpha) = (ART^2/\beta E_a)(1 - 2RT/E_a) \exp(-E_a/RT) \qquad 5.12$$

The rest of the treatment is based on a lengthy trial-and-error curve-fitting which requires that $g(\alpha)$, E_a and A be known or assumed. For this reason, other authors have chosen to utilize other relationships [102,104,106,110].

Doyle calculated $\ell n[p(x)]$ values for a wide range of x values, and found that within the limits $20 < (E_a/RT) < 60$ the following approximation applies:

$$\ell n[p(x)] \approx -5.332 - 1.052(E_a/RT) \qquad 5.13$$

Substitution of equations (5.13) into (5.9) gives equation (5.14)

$$\ell n[g(\alpha)] = \ell n(AE_a/\beta R) - 5.332 - 1.052(E_a/RT) \qquad 5.14$$

The main difficulty in applying equation (5.14) is the dependence of p(x) on both the temperature and the activation energy. Other attempts to simplify Doyle's method have been made by Zsako [39], Sestak [120], Satava [68], and others [108,118,121]; and tables of p(x) as a function of E_a and T have been made available [39,68,105,118].

The asymptotic expansion usually attributed to Coats and Redfern [106] gives

$$g(\alpha) = (ART^2/\beta E_a)[1 - 2RT/E_a] \exp(-E_a/RT) \qquad 5.12$$

Upon ignoring the variation of $(1 - 2RT/E_a)$ compared to $(ART^2/\beta E_a)$

$$g(\alpha) = (ART^2/\beta E_a)\exp(-E_a/RT) \qquad 5.15$$

which may be written in logarithmic form as

$$\ell n[g(\alpha)/T^2] = -E_a/RT + \ell n(AR/\beta E_a) \qquad 5.16$$

In the analyses of thermal curves, the linearity of plots of $\ell n[g(\alpha)/T^2]$ against $^1/T$ has often been taken as sufficient proof of choice of the correct form of $g(\alpha)$. However, the values of **A** are seriously in error, particularly as $E_a/2RT$ gets smaller.

Criado and Morales [122] showed that use of $g(\alpha) = [-\ell n(1 - \alpha)]^{1/n}$, yields the same linear correlation between $\ell n[g(\alpha)/T^2]$ and $^1/T$ for values of $n = 1$, 2 and 3. They also showed that data for any reaction following the JMAK or Prout-Tompkins model must necessarily be describable as a first-order reaction. From their examination of the Coats and Redfern method, Sestak and co-workers [108] reported that the magnitude of E_a was strongly dependent on the form of $g(\alpha)$ chosen for the data analysis.

Ozawa [123] proposed a method based on thermal curves obtained at different heating rates. This author utilized equation (5.14) to obtain

$$\ell n(\beta_1) + 1.052(E_a/RT_1) = \ell n(\beta_2) + 1.052(E_a/RT_2) \qquad 5.17$$

where T_1 and T_2 are the temperature values for the same value of α obtained at different heating rates, β_1 and β_2. Equation (5.17) can be written as

$$\ell n(\beta_2/\beta_1) = 1.052(E_a/R\Delta T) \qquad 5.18$$

where $(^1/\Delta T) = (^1/T_1 - {}^1/T_2)$. Therefore a plot of $\ell n(\beta_2/\beta_1)$ against $(^1/\Delta T)$ for a selected value of α should yield a straight line, the slope of which give E_a.

Other series expansions for the temperature integral have been proposed based on asymptotic expansion of either $\exp(-E_a/RT)$ or $^1/T$, in the vicinity of an arbitrarily chosen reference temperature (*e.g.* T_{max}).
For example:

(i) van Krevelen *et al.* [102] made use of $\exp(-E_a/RT)$ to obtain

$$\ell n\{g(\alpha)\} = (E_a/RT^2_{max})(T - T_{max}) \qquad 5.19$$

(ii) Horowitz and Metzger [104] made use of $^1/T$ to obtain

$$\ell n\{g(\alpha)\} = \{(E_a/RT_{max}) + 1\}\ell n(T) + \ell n(B) \qquad 5.20$$

where $B = (A/\beta)[(E_a/RT_{max}) + 1]^{-1} (0.368/T_{max})^{E_a/RT_{max}}$

Equations (5.19) and (5.20) are mathematically contradictory [37], since $\ell n\{g(\alpha)\}$ cannot be a linear function of both $\ell n(T)$ and T. Both methods have been shown to be less accurate [75] than the Coats and Redfern method.

CHAPTER 6

REVIEW OF STUDIES OF METALLO-AMIDE COMPLEXES

6.1 Introduction

Transition metal halides react with amide ligands to form complexes of various compositions. Studies reported in the literature were mainly concerned with the preparation and structural investigations [124-131]. Much attention has been given to the N,N-dimethylacetamide (*dma*) and N,N-dimethylformamide (*dmf*) because of their potential use as organic solvents.

Aliphatic amides (Table **8.1**) are described as resonance hybrids of the primary structures

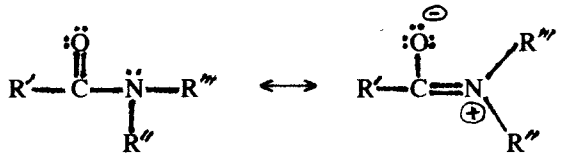

I II

where R′ is H, methyl, ethyl, propyl, *etc.* R″ and R‴ are H's or alkyl groups such as methyl or ethyl, or one alkyl group and hydrogen. Such molecules present two possible coordination centres, either oxygen or nitrogen. In N-substituted amides the coordination through nitrogen is thought to involve steric interaction, while less steric hindrance is expected when coordination is through the oxygen atom [128]. Ligands of different donor strength are possible, on the basis of inductive effects, because replacement of hydrogen by an alkyl group should change the basicity of the carbonyl oxygen. Restricted rotation in N-substituted amides, leading to the planar form **II**, will depend on the nature of R′, R″ and R‴.

The effect of changing R′ from H to CH_3 on the visible absorption spectra of *dmf* and *dma* chromium(III)-amide complexes (refer to Table **8.1** for the amide ligands abbreviations) has been reported by Rollison *et al.* [127].

The conditions of formation, the compositions and structures of amide complexes of types $ML_nX_2(yH_2O)$, with ratios MX_2 : L = 1:4, 1:5 or 1:6 (where M = Mn(II), Fe(II), Co(II) or Ni(II) and L = N,N-dimethylformamide, N,N-dimethylbutyramide, formamide N,N-diethylformamide, N,N-dimethylacetamide, N-methylacetamide, N-methyfomamide or acetamide and X = halide) have been described [126,129,131]. Analogous complexes formed with two moles of aliphatic amide per metal(II) ion are rare [128,131]. No

studies of transition metal complexes containing aliphatic amide ligands (in Table **8.1**) of the form MLX_2, $Ni_3L_2C\ell_6$ and $Ni_3LC\ell_6$ have been reported in the literature.

6.2 The preparation of metal-amide complexes

6.2.1 $ML_6(C\ell O_4)_2$ complexes

Drago *et al.* [124] reported the syntheses of several amide complexes of nickel(II) and chromium(II) perchlorate. Complexes were prepared from aqueous solutions of metal perchlorate by treatment with a *seven-fold* mole ratio of an appropriate amide, followed by pumping off the volatile material under reduced pressure. The following complexes were isolated as solids by extracting the oily products with ether, followed by ethanol: $[Ni(nmf)_6](C\ell O_4)_2$, $[Ni(dmf)_6](C\ell O_4)_2$, $[Cr(aa)_6](C\ell O_4)_2$ and $[Cr(dma)_6](C\ell O_4)_2$.

Infrared spectra of *nujol* mulls suggested coordination through carbonyl oxygen from the negative shifts of the carbonyl frequency ($\hat{\upsilon}_{C=O}$) of the complexes, relative to $\hat{\upsilon}_{C=O}$ of corresponding amide. Elemental analyses, and visible and near-infrared spectra provided evidence for six-coordinate, octahedral species. The constancy of the intensity ratio of the absorption bands due to $^3T_1(P) \leftarrow {}^3A_2(F)$ to $^3T_1(F) \leftarrow {}^3A_2(F)$ transitions was taken as additional evidence for the existence of octahedral nickel(II). Their reported visible and near-infrared spectral data are shown in Table **6.1**. The basicity of the employed amide, as estimated from their inductive effects, was of the order:

$$nmf \sim aa < nma \sim dmf < def < dma.$$

Calculated Dq values for the octahedral complexes were found not to follow the inductive order, but produced the series:

$$nma < dma < aa < nmf \sim def < dmf$$

The authors explained the differences in the calculated Dq values on the basis of the steric requirements of the alkyl-substituent groups. Non-substituted amides were expected to experience less steric repulsion, leading to stronger interaction with the metal ion and hence larger Dq values.

Table 6.1: Visible and near-infrared spectra of $[NiL_6](C\ell O_4)_2$ complexes [124]

Ligand	Solvent	Band assignments / 10^3 cm^{-1}			Dq / cm^{-1}
		$^3T_{1g}(P) \leftarrow {}^3A_{2g}(F)$	$^3T_{2g}(F) \leftarrow {}^3A_{2g}(F)$	$^3T_{1g}(F) \leftarrow {}^3A_{2g}(F)$	
nmf	*nmf*	8.38	13.66 ; 14.70	25.00	838
dmf	*dmf*	8.50	13.60 ; 14.90	25.00	850
def	*def*	8.40	13.70 ; 14.95	25.13	840
aa	*acetone*	8.24	13.37 ; 14.70	24.51	824
dma	$CH_2C\ell_2$	7.58	12.74 ; 14.70	23.81	758
dmbu	*dmbu*	7.49	12.02 ; 14.55	23.81	749
nma	*nma*	7.52	12.66 ; 14.58	23.70	752

6.2.2 M(*dma*)$_2$Cℓ_2(yH_2O) complexes

Bull *et al.* [128] described the preparation of N,N-dimethylacetamide complexes of several different transition metal chlorides. Complexes were prepared by the method of Drago *et al.* [124], using a large excess of N,N-dimethylacetamide. The reported complexes were $ML_2C\ell_2(yH_2O)$, where M is a transition metal and $y = 0$ to 6.

Infrared spectra of the complexes showed a shift of the $\hat{\upsilon}_{C=O}$ to lower frequencies, indicating coordination through the carbonyl oxygen atom. No attempts to obtain ligand field spectra of the complexes were made in their first study.

In a follow-up study made by Madan *et al.* [130], a number of amide complexes were prepared with cobalt(II) halide and perchlorate. Complexes were prepared by the addition of an excess of N,N-dimethylacetamide ligand to the respective cobalt(II) salts. Precipitates were treated according to the method of Drago *et al.* [124], or a slight modification thereof. The complexes isolated were: Co(*dma*)$_2C\ell_2$, Co(*dma*)$_2Br_2$, Co(*dma*)$_2I_2$ and $[Co(dma)_6](C\ell O_4)_2$.

From a study of the visible and near-infrared spectra and magnetic moments of the complexes, the authors suggested that [Co(*dma*)$_2C\ell_2$], [Co(*dma*)$_2Br_2$] and [Co(*dma*)$_2I_2$] complexes were tetrahedrally coordinated, while $[Co(dma)_6](C\ell O_4)_2$ exhibited octahedral coordination.

6.2.3 $Ni(aa)_nC\ell_2(yH_2O)$ complexes

Stone *et al.* [131] reported the preparation of $Ni(aa)_4C\ell_2(2H_2O)$ complexes. Visible and near-infrared spectral analysis suggested an approximately octahedral environment for the nickel(II) ion. IR spectra showed a lowering of the $\hat{\upsilon}_{C=O}$ vibration upon complex formation, suggesting coordination *via* the carbonyl oxygen atom. Acetamide was reported [126,129] to form other types of complexes with nickel(II), namely $Ni(aa)_6C\ell_2$ and $Ni(aa)_4C\ell_2(H_2O)$. Nickel-oxygen bonding was suggested in all the complexes. Upon coordination, the acetamide $\hat{\upsilon}_{C=O}$ stretching frequency was lowered from 1690 cm^{-1} to 1672 cm^{-1} and the $\hat{\upsilon}_{N-H}$ vibration shifted from 1605 to 1586 cm^{-1}, in agreement with the proposed nickel-oxygen bonding. The $\hat{\upsilon}_{Ni-O}$ was assigned to the band at 535 cm^{-1}. Hydrogen-bonding between the NH_2 and $C\ell$ was also suggested.

6.2.4 $CrC\ell_3$-amide complexes

Rollison *et al.* [127] synthesized several chromium(III)-amide complexes by azeotropic distillation of a benzene solution of $[Cr(H_2O)_4C\ell_2]C\ell$ and N,N-dimethylacetamide or N,N-dimethylformamide. Their reaction mixture was refluxed and stirred. Complexes were reported to form as soon as the water was distilled off. Resultant complexes were dried over P_2O_5 in a desiccator. They obtained several violet $CrL_3C\ell_3$ complexes and a green $[CrL_4C\ell_2]C\ell$ complex. Some of the $CrC\ell_3$-amide complexes isolated were reported to decompose rapidly on contact with atmospheric moisture. Variants of the synthetic procedure were tried in unsuccessful attempts to obtain solid identifiable complexes with N,N-diethylacetamide, N,N-dibutylacetamide, N,N-diphenylacetamide, N-phenylacetamide, N-phenylformamide, *etc.*

IR spectra suggested coordination through the oxygen atom from the negative shift (about 40 cm^{-1}) of the carbonyl frequencies of the complex from those of the corresponding amide ligands. The observations were consistent with some previously reported studies [125]. The authors were however unable to deduce the geometrical configuration of the prepared complexes from their visible absorption spectra.

6.3 The thermal decompositions of metallo-amide complexes

No quantitative thermal decomposition studies of amide complexes of transition metals could be found in the literature. Reports by Allan *et al.* [15,16] were all semi-

quantitative. They reported [15] the preparation of cobalt(II), nickel(II) and copper(II) chloride complexes with acrylamide, C_3H_5NO. The $Ni(C_3H_5NO)_2C\ell_2$, $Co(C_3H_5NO)_2C\ell_2$ and $Co(C_3H_5NO)_2C\ell_2$ complexes were isolated from hot ethanol solutions by treatment with a metal to ligand mole ratio of 1:2. From a study of the visible and near-infrared diffuse reflectance spectra and magnetic moments of the complexes, the authors suggested polymeric octahedral structures for $Ni(C_3H_5NO)_2C\ell_2$ and a tetrahedral structure for the cobalt(II) and copper(II) complexes. The spectral and magnetic data are shown in Table **6.2**. IR spectra suggested metal-nitrogen bonding in all the complexes. The absorption bands due to $\hat{\upsilon}_{N-H}$ were lowered upon complexation, while the $\hat{\upsilon}_{C=C}$ and $\hat{\upsilon}_{C=O}$ bands showed little change.

In another study by Allan *et al.* [16], complexes of type $ML_2C\ell_2$ were isolated on mixing anthranilamide, $C_7H_8N_2O$, with a metal chloride in a 2:1 mole ratio in ethanol solution. Visible and near-infrared reflectance spectra and magnetic properties suggested that the $Ni(C_7H_8N_2O)_2C\ell_2$ and $Co(C_7H_8N_2O)_2C\ell_2$ complexes exhibited octahedral structures. The IR $\hat{\upsilon}_{N-H}$ vibrations of the amine group were at lower frequencies in the complexes than in the free ligand. The $\hat{\upsilon}_{C=O}$ and $\hat{\upsilon}_{N-H}$ vibrations of the amide group were shifted to lower and higher frequencies respectively. These observations were interpreted in terms of coordination of the nickel(II) and cobalt(II) ions through the carbonyl oxygen atom. The $Cu(C_3H_5NO)_2C\ell_2$ was thought to consist of two parallel chains of copper atoms bonded to the chlorine atom, whilst the anthranilamide molecules were bonded (by the nitrogen atom of the amine group) above and below the plane of the copper-chloride chains. IR absorption bands assignment suggested coordination of nitrogen atom of the amine group to the copper(II) ion. Upon complexation, the $\hat{\upsilon}_{N-H}$ bands due to amine group shifted to lower frequencies, while the $\hat{\upsilon}_{C=O}$ and $\hat{\upsilon}_{N-H}$ bands of the amide group shifted to higher frequencies.

The thermal decompositions of the acrylamide and anthranilamide complexes of the metal(II) chloride were studied [15,16], in static air, using TG and DTA methods. The hydrated complexes lost water, followed by organic ligands, to give metal oxides as final products. The $Co(C_7H_8NO)_2C\ell_2$ and $Cu(C_7H_8NO)_2C\ell_2$ complexes decomposed *via* the formation of $M(C_7H_8NO)C\ell_2$ species. The intermediate then underwent an exothermic reaction with loss of the remaining anthranilamide and chlorine, to give M_3O_4. All the other complexes showed single-stage thermal decomposition curves for the removal of the amide ligands. No thermochemical and kinetic data were reported.

Table 6.2: Diffuse reflectance spectra and magnetic moments of acrylamide and anthranilamide complexes of metal(II) chloride [15,16].

Complexes	Band assignments / 10^3 cm^{-1}			μ(BM)
(a) Nickel(II)				
Octahedral	$^3T_{2g}(F) \leftarrow {}^3A_{2g}(F)$	$^3T_{1g}(F) \leftarrow {}^3A_{2g}(F)$	$^3T_{1g}(P) \leftarrow {}^3A_{2g}(F)$	
$Ni(C_3H_5NO)_2C\ell_2$	7.194	13.389	23.148	2.76
$Ni(C_7H_8N_2O)_2C\ell_2$	8.620	15.492	26.428	3.16
(b) Cobalt(II)				
Octahedral	$^4T_{2g} \leftarrow {}^4T_{1g}(F)$	$^4A_{2g} \leftarrow {}^4T_{1g}(F)$	$^4T_{1g}(P) \leftarrow {}^4T_{1g}(F)$	
$Co(C_7H_8N_2O)_2C\ell_2$	7.692	14.814	18.518	4.84
$Co(C_7H_8N_2O)C\ell_2$	8.403	13.072	19.230	5.02
Tetrahedral	$^4T_1(F) \leftarrow {}^4A_2(F)$	$^4T_1(P) \leftarrow {}^4A_2(F)$		
$Co(C_3H_5NO)_2C\ell_2$	7.300	14.598		4.20
(c) Copper(II)				
Octahedral	$^2T_{2g}(D) \leftarrow {}^2E_g(D)$			
$Cu(C_7H_8N_2O)_2C\ell_2$	13.071			1.62
$Cu(C_7H_8N_2O)C\ell_2$	13.889			1.56
Tetrahedral				
$Cu(C_3H_5NO)_2C\ell_2$	6.410 ; 24.986			2.02

6.4 The kinetics of thermal decompositions of metal-amide complexes

6.4.1 Introduction

In thermal analysis, the use of the procedural onset temperature (T_e), the peak temperature (T_{max}) and the enthalpy change (ΔH) of decomposition as characteristic measures of the strengths of the metal-volatile ligand bonds is not universally accepted. Some published work [3-6,10,12,132,133] insists that E_a, the average excess of energy a reactant must have in order to react, is the parameter that is more closely connected with the strength of the broken bond.

6.4.2 $UO_2L_2(NO_3)_2$ complexes

Siracusa *et al.* [2] reported the preparation, spectroscopic and thermal decompositions of uranyl nitrate with acetamide, N,N-dimethylformamide, urea, nitrosodimethylaniline, pyridine-N-oxide and water. The aim was to see whether E_a for removal of ligands can be correlated with the donor properties of the ligands and the asymmetric stretching frequency ($\hat{\upsilon}_3$) of the O-U-O group. Complexes of the general formula $UO_2L_2(NO_3)_2$ were prepared by mixing ethanol solutions of $UO_2(H_2O)_6(NO_3)_2$ with an excess of an appropriate ligand.

Thermal decompositions were studied using TG and DTA. The proposed thermal decomposition stoichiometry was

$$UO_2L_2(NO_3)_2\ (s) \rightarrow UO_2L_x(NO_3)_2(s) + yL\ (g);\ 1 \leq x \leq 2 \text{ and } 0 \leq y \leq 1$$

$$UO_2L_x(NO_3)_2\ (s) \rightarrow UO_3\ (s) + \text{gaseous products}$$

Thermochemical and kinetic parameters were obtained from thermoanalytical curves relating to the first decomposition step (Table 6.3). E_a values calculated using a number of non-isothermal methods of kinetic analysis were comparable. The thermal data were correlated with the strengths of the UO_2-volatile ligand bonds. A linear relationship was found between E_a and $\hat{\upsilon}_3$, namely $\hat{\upsilon}_3 = 892.8 + 1.67E_a$.

Table 6.3: Asymmetric stretching frequency ($\hat{\upsilon}_3$) and thermal data for the first decomposition step of $UO_2L_2(NO_3)_2$ complexes [2].

Ligand (L)	$\hat{\upsilon}_3$ / cm^{-1}	Onset temperature T_e / °C	Activation energy E_a / kJ mol^{-1}
acetamide	942	186	123
dimethylacetamide	932	156	95
urea	952	185	147
H_2O	943	110	129

6.4.3 UO_2LF_2 complexes

A few complexes of the form UO_2LF_2, where L = acetamide, N-methylacetamide, N,N-dimethylacetamide, N,N-dimethylformamide, urea, N,N-dimethylurea, and N,N,N,N-

tetramethylurea, have been prepared [1,134,135] by mixing ethanol solutions of uranyl fluoride and the appropriate ligand in a 1:1 (or excess ligand) mole ratio. Precipitates were washed with ethanol, followed by acetone. The complex $UO_2(urea)F_2$ could only be precipitated from aqueous methanol solution. $UO_2(urea)_2F_2$ was obtained by heating a mixture of uranyl fluoride and urea in a 1:10 molar ratio, in methanol. A decrease in the C=O stretching frequency, coupled with an increase of the C-N frequency in relation to the free amide, were observed from the IR spectra of complexes. This was interpreted as indicating coordination through oxygen. Detection of terminal or bridging fluoride groups was reported to be impossible because of absorptions due to ligand in the expected IR region.

For kinetic investigations, Carstens and co-workers [1] chose, from many complexes prepared with a series of amide ligands, only those which decomposed in a single step without decomposition of the released ligand. That is

$$UO_2LF_2\ (s) \rightarrow UO_2F_2\ (s) + L(g)$$

The most suitable kinetic expression for all the complexes investigated was reported to be the contracting area equation, $\{1 - (1 - \alpha)^{1/2}\} = (1/2)kt$. Calculated E_a values were compared with the IR stretching frequencies, decomposition enthalpies and the DTG peak temperatures (T_{max}) of the reactions. The thermal decomposition parameters are shown in Table **6.4**. No simple correlation was found between E_a and any of the physical parameters used.

Table 6.4: Thermal decomposition parameters for the reaction [1]
$UO_2LF_2\ (s) \rightarrow UO_2F_2\ (s) + L\ (g)$

Ligand (L)	DTG T_{max} / °C	Enthalpy of decomposition ΔH_L / kJ mol^{-1}	E_a / kJ mol^{-1}
acetamide	274	85	125
N-methylacetamide	314	91	150
N,N-dimethylacetamide	314	95	128
N,N-dimethylformamide	275	90	134
N,N-dimethylurea	345	163	173
N,N,N,N-tetramethylurea	311	96	166

CHAPTER 7

REVIEW OF THERMAL DECOMPOSITIONS OF OTHER METALLO-ORGANIC COMPLEXES

7.1 Introduction

A range of transition metal halide complexes of organic ligands (metallo-organics) have been reported in the literature. Their thermal behaviour has been described in relation to the nature and strengths of the metal-volatile ligand bonds, structure and IR spectral properties [136-138]. Whilst most of the studies have been qualitative, a few have yielded thermochemical and kinetic data. The transition metal halide complexes formed with pyridine have been extensively studied and may be used as model complexes.

7.2 $PdL_2C\ell_2$ complexes

Farran and co-workers [5] have studied the thermal decompositions of palladium(II) chloride complexes with pyridine, 2-methylpyridine, 3-methylpyridine, 4-methylpyridine, 3,4-dimethylpyridine and 2,6-dimethylpyridine, using TG and DSC. Their aim was to examine the effect of the basicity of the ligands on the enthalpies and the activation energies of the decompositions. Complexes of type $PdL_2C\ell_2$ lost two ligands in a single step, to give $PdC\ell_2$. Activation energies were determined by the method of Thomas and Clarke [139]. The thermal data are given in Table 7.1.

No relationship was found between the enthalpy values (ΔH) for the decomposition and any other property of the complexes. With only a few exceptions, exhibited by complexes with 4-methylpyridine and with 3,4-dimethylpyridine, a linear relationship was observed between the pK_b values of the ligands and the decomposition activation energy (E_a). Calculated E_a values increased with increase in basicity of the ligands. The procedural onset temperatures (T_e) of the decompositions decreased with increasing basicity. This was explained in terms of the *trans* influence of one ligand in the square planar complexes, which caused the first ligand to be lost more easily than the second. The opposing trends indicated by the E_a and T_e values were explained in terms of the difficulties associated with the method of Thomas and Clarke [139], used to determine E_a.

Table 7.1: Thermal decomposition data for the reaction [5]

$PdL_2C\ell_2$ (s) → $PdC\ell_2$ (s) + 2L (g)

Ligand (L)	pK_b	T_e / °C	ΔH / kJ mol^{-1}	E_a / kJ mol^{-1}
pyridine	8.78	272	74	39
2-methylpyridine	8.04	277	118	197
3-methylpyridine	8.37	246	33	126
4-methylpyridine	8.02	310	34	307
2,4-dimethylpyridine	7.21	283	27	303
3,4-dimethylpyridine	7.54	294	23	383
3,5-dimethylpyridine	7.85	295	37	203
2,6-dimethylpyridine	7.28	290	18	338

7.3 $AgL_2(NO_3)$ complexes

Akhavein *et al.* [6] studied the thermal decomposition of solid complexes of silver nitrate with 2,4-dimethylpyridine, 3,4-dimethylpyridine, 3,5-dimethylpyridine, 3-methylpyridine and 4-cyanopyridine. Their aim was to determine the effects of the basicity of the ligands on the activation energies of decomposition. Complexes of general formula $AgL_2(NO_3)$ were prepared. The kinetics of the thermal decompositions were investigated using TG and DSC techniques. Rate coefficients were calculated from first-order kinetic plots of $-\ell n(1-\alpha)$ *versus* time. The thermal decomposition parameters are shown in Table 7.2.

For most complexes, continued heating produced a strong exothermic peak due to reaction of the melted complex with the aluminium pan. Higher basicity of the ligand gave rise to higher apparent activation energies (E_a). Plots of $\ell og(k)$ against pK_b indicated a linear relation for the complexes formed by the ligands with no methyl substituent on the 4-position. The deviating behaviour of the 2,4-dimethylpyridine and 3,4-dimethylpyridine complexes was explained on the basis of increased π-bonding resulting from a resonance structure which offered possibilities of multiple bonding of the silver ion to the ligands.

Table 7.2: Thermal decomposition data for the reaction [6]

$$AgL_2(NO_3)\ (s) \rightarrow Ag(NO_3)\ (s) + 2L\ (g)$$

Ligand (L)	pK_b	T_{melt} / °C	Enthalpy of fusion ΔH_{fus} / kJ mol^{-1}	E_a / kJ mol^{-1}
pyridine	8.78	84	23	-
2-methylpyridine	8.04	115	33	-
3-methylpyridine	5.68	125	41	54
4-cyanopyridine	1.90	-	-	99
2,4-dimethylpyridine	6.99	120	35	119
2,6-dimethylpyridine	6.75	-	-	129
3,4-dimethylpyridine	6.50	147	35	72
3,5-dimethylpyridine	6.34	150	44	78

7.4 $CdL_nC\ell_2$ complexes

The decompositions of picoline complexes of cadmium(II) chloride have been investigated by House and co-workers [140], using DSC. Their aim was to study the thermal stabilities of the complexes, and to determine the enthalpies (ΔH) and activation energies (E_a) of the decompositions. Complexes of the types $CdL_2C\ell_2$ and $CdLC\ell_2$ (where L = α-picoline, β-picoline or γ-picoline) were prepared.

$CdL_2C\ell_2$ (where L = β-picoline or γ-picoline) decomposed in three steps corresponding to the loss of one, one-third, and two-thirds of a molecule of ligand, respectively. The decomposition pattern of Cd(*α-picoline*)$C\ell_2$ was dependent on the sample mass. For large sample masses (*e.g.* 8 to 10 mg), one-third of α-picoline was lost first. When sample masses less than 5 mg were used, two-thirds of α-picoline was lost first. The effect of sample size was suggested to be due to differences in the diffusion rates of the greater amounts of free ligand liberated from larger samples.

The thermal parameters are summarized in Table 7.3. Enthalpy values (ΔH) determined for the various decompositions were compared with similar values reported by Beech and co-workers [26], for the decomposition of the Cd(*pyridine*)$_2C\ell_2$ complex. The slightly higher ΔH values for the Cd(*picoline*)$_2C\ell_2$ system were accounted for on the grounds that methylpyridine may be slightly more basic than pyridine. The following thermal

stability order of the complexes was established on the basis of T_e values for the first decomposition step:

α-picoline < β-picoline < γ-picoline.

Table 7.3: Thermal decomposition data for the CdL_nCl_2 complexes [140]

Ligand (L)	Stoichiometry*	Onset temp. T_e / °C	Enthalpy of decomposition ΔH / kJ mol^{-1}	E_a / kJ mol^{-1}
β-picoline	(A)	381	75	83
γ-picoline	(A)	391	68	89
pyridine	(A)	-	65	-
α-picoline	(B)	481	21	-
β-picoline	(B)	458	23	-
γ-picoline	(B)	499	24	230
pyridine	(B)	-	47	-
α-picoline	(C)	512	41	130
β-picoline	(C)	519	23	-
γ-picoline	(C)	556	40	-

* (A) $CdL_2C\ell_2$ (s) → $CdLC\ell_2$ (s) + L (g)

(B) $CdLC\ell_2$ (s) → $CdL_{2/3}C\ell_2$ (s) + $(^1/_3)$L (g)

(C) $CdL_{2/3}C\ell_2$ (s) → $CdC\ell_2$ (s) + $(^2/_3)$L (g)

7.5 $NiL_2(NCS)_2$ complexes

Jona and co-workers [11-13] reported the thermochemical and kinetic properties of $NiL_2(NCS)_2$, where L = pyridine, α-picoline, β-picoline, quinoline or 2,6-lutidine. The decomposition enthalpies (ΔH) were determined using DSC. The thermochemical data are summarized in Table 7.4.

From the decreasing values of ΔH, the following order of the strengths of the nickel-volatile ligand bonds was suggested:

for ***square-planar*** , α-picoline < quinoline(I) < 2,6-lutidine

for ***pseudooctahedral***, quinoline(II) < β-picoline < pyridine

The kinetics of the thermal decompositions of pseudooctahedral and square-planar complexes were investigated under isothermal conditions using TG. Kinetic results were interpreted in terms of the contracting-volume (**R3**) model, with supportive evidence from microscopic observation of the partially-decomposed complexes. The authors reported that the overall decomposition rate was controlled by the chemical process. The calculated activation energies (E_a) are included in Table **7.4**.

For pseudooctahedral complexes, $E_a < \Delta H$, while in the square-planar complexes $\Delta H < E_a$. The differences between E_a and ΔH were explained in terms of a substitution process in the coordination sphere. The following decomposition route was proposed for pseudooctahedral complexes:

$NiL_2(NCS)_2 \rightarrow NiL(NCS)_2$ (C.N.5) $\rightarrow NiL(NCS)_2$ (C.N.6) $\rightarrow Ni(NCS)_2$ (C.N.5)

$Ni(NCS)_2$ (C.N.5) $\rightarrow Ni(NCS)_2$ (C.N.6)

Table 7.4: Thermal decomposition data for the $NiL_2(NCS)_2$ complexes [11]

Ligand (L)	T_e /°C (DTA ; DTG)	T_{max} / °C (DTA ; DTG)	ΔH / kJ mol^{-1}	E_a / kJ mol^{-1}
Square-planar				
α-picoline *	392 ; 360	453 ; 438	102	95
2,6-lutidine *	428 ; 412	494 ; 472	126	117
quinoline(I) #	437 ; 405	475 ; 462	119	129
Pseudooctahedral				
pyridine *	475 ; 450	557 ; 532	132	199
quinoline(II) *	413 ; 390	471 ; 460	116	102
β-picoline #	458 ; 412	515 ; 478	123	116

* $NiL_2(NCS)_2$ (s) $\rightarrow$ $Ni(NCS)_2$ (s) + 2L (g)

\# $NiL_2(NCS)_2$ (s) $\rightarrow$ $NiL(NCS)_2$ (s) + L (g) $\rightarrow$ $Ni(NCS)_2$ (s) + 2L (g)

7.6 CuL_2X_2 complexes

Langfelderova [8] investigated the influence of "*distortion isomerism*" on the courses of thermal decompositions of CuL_2X_2 complexes (refer to Table 7.5 for the ligands L and counter-ions X). The evaluation was based on T_{max} values of the first DTA endotherm. Studies indicated that the degree of distortion of the coordination polyhedron increased with increasing σ-donor ability of the alkyl derivatives of ammonia, and the steric requirements of the ligands. Thermal stability decreased with increasing degree of distortion of the coordination polyhedron, from L = methylamine (*ma*) through ethylamine (*ea*) to diethylamine (*da*). This corresponded with the change in structural configuration from the pseudooctahedral $Cu(ma)_2C\ell_2$, through the distorted tetragonal bipyramid $Cu(ea)_2C\ell_2$, to the square-planar $Cu(da)_2C\ell_2$. The observations were not consistent with the view of enhanced thermal stability of a complex with increasing basicity of the ligand. A summary of the visible absorption spectra and thermochemical data is given in Table 7.5.

From evaluation of published data, including decomposition T_{max}, $\hat{\upsilon}_{max}$ of $d \rightarrow d$ transitions and pK_b values (Table 7.5), a number of observations were noted:

- The relationship between T_{max} and Cu-N bond strength is not simple.
- The differences between degrees of distortion of the coordination polyhedra (in complexes with similar stoichiometric composition) led to different decomposition stoichiometries.
- Thermal stability is related to both the strength of the copper-volatile ligand bond and the differences in the distortion of the coordination polyhedron.
- In evaluating thermal stability for reactions of the type

$$CuL_nX_2\ (s) \rightarrow CuX_2\ (s) + nL\ (g), \text{ where } X = C\ell \text{ or NCS}$$

one cannot exclude the influence of physical factors, nor the effect of secondary interactions within the crystal lattice.

7.7 MX_2-picoline complexes

Liptay *et al.* [141,142] reported a number of thermal decomposition studies of metal halide complexes formed with picoline. Metals used were nickel(II), cobalt(II), manganese(III), cadmium(II), copper(II) and zinc(I). The thermal investigation was mainly concerned with the observation of phase changes, the establishment of

decomposition stoichiometry and the spectral characterisation of intermediates. The authors suggested that solid decomposition was favoured when the complex formed intermediates with M-X→ M bridges (where X = Cℓ or Br). The tendency to form metal-halide bridges increased with increase in the electron density of the halide.

Stability deductions were based on the order of increasing number of ligands per metal atom in complexes prepared from a large excess of ligand. The following order of the metal-*picoline* bond strengths was established:

α-picoline < β-picoline < γ-picoline,

Table 7.5: The spectral and thermal decomposition data for copper(II) complexes with amines, pyridine or substituted pyridine derivatives [8].

Ligand (L) in CuL_2X_2	ligand pK_b	$\bar{\upsilon}_{max}$ / 10^3 cm^{-1} d → d transition	T_{max} for first DTA endotherm
$CuL_2C\ell_2$			
methylamine	3.37	14.0	140
ethylamine	3.22	15.3	130
diethylamine	2.89	18.8 14.8	100
pyridine	-	14.7	130
γ-picoline	-	14.8	140
$CuL_2(NCS)_2$			
pyridine	8.78	15.6	110
α-picoline	8.04	13.0 ; 16.6	60
β-picoline	8.37	17.1	110
γ-picoline	8.02	16.2	110
2,3-lutidine	7.43	14.1	70
2,4-lutidine	7.37	17.2	65
2,6-lutidine	7.28	14.5; 16.7; 19.7	65
3,4-lutidine	7.54	13.1 ; 16.3	100
3,5-lutidine	7.85	13.2 ; 16.3	100

The thermal decomposition of $[Ni(py)_4]C\ell_2$ was shown (from simultaneous TG, DTG and DTA) to occur in several steps. Intermediates with various stoichiometric compositions

were observed. X-ray powder diffraction and IR studies of the decomposition intermediates suggested: $[Ni(py)_2]C\ell_2$, $[Ni(py)]C\ell_2$ and $[Ni(py)_{2/3}]C\ell_2$. However, no thermal decomposition parameters were reported.

7.8 ML_nX_2 complexes

The preparation, stereochemistry and the thermal decompositions of cobalt(II), nickel(II), and copper(II) complexes with 2-ethylpyridine, 3-ethylpyridine, and 4-ethylpyridine have been reported [143-145]. Cobalt complexes with 3-ethylpyridine and 4-ethylpyridine had the stoichiometry CoL_4X_2, and complexes with 2-ethylpyridine had the stoichiometry CoL_2X_2. $CoL_4X_2(2H_2O)$ complexes, where L = 3-ethylpyridine and X = Br or I, were dehydrated at 45°C overnight. Visible and near-infrared spectra, and magnetic moments suggested octahedral structures for the CoL_4X_2 and tetrahedral structures for the CoL_2X_2 complexes. Nickel formed complexes of stoichiometry NiL_2X_2, which were suggested to have octahedral structures. Copper complexes had the stoichiometry CuL_2X_2, and octahedral structures involving halogen bridging were suggested. The presence of an ethyl-substituent group in the 2-position of the pyridine ring (*i.e.* in 2-ethylpyridine) led to the formation of complexes containing fewer molecules of base to metal atom, ML_2X_2. Steric factors were thought to play a more dominant role than the electron donating power of nitrogen.

TG and DTA thermal decomposition curves were presented. The CoL_4X_2 complexes decomposed to CoL_2X_2 and then to the metal halide. The decomposition pattern differs from that for the corresponding metal(II) chloride and bromide complexes of methylpyridines [141,142]. However, complexes of nickel with methylpyridines and those with ethylpyridines showed similar decomposition patterns. The proposed reaction scheme was

$$NiL_4X_2\ (s) \rightarrow NiL_2X_2\ (s) + 2L\ (g) \rightarrow NiX_2\ (s) + 2L\ (g)$$

Allan and co-workers [146] reported the thermal decompositions of cobalt(II), nickel(II) and copper(II) complexes with 2-methylpyridine, 3-methylpyridine, 4-methylpyridine, 2-ethylpyridine, 3-ethylpyridine and 4-ethylpyridine. An intermediary phase with three nickel atoms for every two ligands ($Ni_3L_2X_6$) was suggested. The decompositions of nickel(II) chloride and bromide complexes followed the stoichiometry

$$NiL_4X_2\ (s) \rightarrow NiL_2X_2\ (s) \rightarrow Ni_3L_2X_6\ (s) \rightarrow NiX_2\ (s) + 4L\ (g)$$

TG and DTA curves of the CoL_2X_2 and CuL_2X_2 complexes showed no formation of intermediates. No thermal decomposition data were reported.

Thornton *et al.* [7] reported the thermal decompositions of $Co(R\text{-}py)_2X_2$ complexes, where *R-py* are alkyl-substituted pyridine derivatives and X = Cℓ or Br. In general, cobalt(II) chloride complexes started to decompose at lower temperatures and the decompositions extended over a wider temperature range than the corresponding cobalt(II) bromide analogues. A possible explanation given for the greater stability of the $Co(R\text{-}py)_2Br_2$ complexes was the ease of polarizability of the bromine atom. This was thought to allow for cobalt-nitrogen bond strengthening by encouraging back-bonding from the cobalt to the nitrogen in pyridine. Evidence was obtained from the work of Wong [147], who showed (from calculations of the force constants of metal-nitrogen bonds in $[Zn(py)_2C\ell_2]$ and $[Zn(py)_2Br_2]$) that the zinc-nitrogen bond in the bromo complex was stronger than in the chloro complex. The decomposition onset temperature (T_e) was also influenced by the stereochemistry of the complexes. Higher onset temperatures were found for smaller coordination numbers. No thermochemical or kinetic data were reported.

7.9 MX_2-imidazole complexes

Thermal decompositions of metal-imidazole complexes have been studied using TG, DSC, MS or high temperature X-ray powder diffraction techniques [9,148-151]. van Dam *et al.* [9] prepared complexes of formula $Ni(Iz)_nX_2$ (where Iz = imidazole, n = 1, 2, 4 or 6, and X = Cℓ, Br, I or NCS). $[Ni(Iz)_6]X_2(yH_2O)$ complexes lost water below 80°C with an enthalpy value close to the sublimation energy of ice. In $[Ni(Iz)_4(2H_2O)]X_2$ and $[Ni(Iz)_2(2H_2O)C\ell_2]$ complexes, the water molecules were held more firmly and were only completely removed above 130°C, with enthalpies higher than the value for the sublimation of ice.

Decomposition enthalpies were determined for several reactions of the general form:

$$Ni(Iz)_nX_2\ (s) \rightarrow Ni(Iz)_{n-p}X_2\ (s) + pIz\ ,\quad \text{where } p = 1, 2, 3, \ldots, n$$

ΔH_{Iz} values (*i.e.* enthalpies of reactions per mole of Iz) were used as indicators of the stability of the nickel-imidazole binding, after a correction was made for the sublimation enthalpies of the released ligands. The decomposition enthalpies are summarized in Table **7.6**.

A number of observations are noted:

- For the single step loss of six imidazole ligands, values of ΔH_{Iz} were in the order: NCS < Cℓ < Br < I, which corresponds with the trend of the observed melting points of the starting complexes.
- Square planar complexes of type $[Ni(Iz)_4X_2]$ (where X = Br or I) indicated stronger nickel-imidazole binding than the octahedral $[Ni(Iz)_4C\ell_2]$ and $[Ni(Iz)_4(NCS)_2]$ complexes.
- A comparison of ΔH_{Iz} values with similar data previously reported for pyridine complexes suggested that imidazole and pyridine were similarly bound to the nickel(II) ion. The only notable differences were the higher ΔH_L values for the square-planar complexes which were thought to be partly due to hydrogen-bonding effects.

Table 7.6: Reaction enthalpies of the imidazole complexes of nickel(II) chloride [9]

Reaction	ΔH_L / kJ mol^{-1} of ligand
$Ni(Iz)_2C\ell_2$ (s) → $NiC\ell_2$ (s) + 2L (g)	104
$Ni(Iz)_2Br_2$ (s) → $NiBr_2$ (s) + 2L (g)	109
$Ni(Iz)_2(NCS)_2$ (s) → $Ni(NCS)_2$ (s) + 2L (g)	95
$Ni(Iz)C\ell_2$ (s) → $NiC\ell_2$ (s) + L (g)	109
$Ni(Iz)Br_2$ (s) → $NiBr_2$ (s) + L (g)	119
$Ni(Iz)(NCS)_2$ (s) → $Ni(NCS)_2$ (s) + L (g)	99

van Berkum *et al.* [150] studied the thermal decompositions of CuX_2 complexes with imidazole and with N-methylimidazole. Complexes of type CuL_nX_2 (where n = 2 or 4 and X = Cℓ or Br) were prepared. The decompositions were complex and no simple ligand losses were observed. The losses of ligands and redox reactions occurred simultaneously, resulting in the formation of copper metal.

The thermal decompositions, in air, of N-methylimidazole and 2-methylimidazole complexes with chromium(III) halide were complex [151,152]. The differences in thermal behaviour of the N-methylimidazole and 2-methylimidazole complexes were explained in terms of the positions of the methyl-substituent in the imidazole skeleton. The presence of hydrogen bonding between the nitrogen atom in the imidazole ligand of a complex

and a halogen atom of a neighbouring complex was thought to contribute to the observed differences.

The following observations with regard to the magnitudes of the ΔH_L values were noted:

- From the decompositions of the chromium(III) chloride complexes, N-methylimidazole was found to be held more strongly than imidazole. This was explained in terms of the stronger basicity of N-methylimidazole.
- In the decompositions of complexes of the type CrL_5X_3, ΔH values increased from X = Cℓ to Br. This was explained in terms of the different degrees of polarizability of the halide (Cℓ < Br) and their different effective contributions to the metal-ligand π-dative bond.

CHAPTER 8

PREPARATION OF AMIDE COMPLEXES OF NICKEL(II) CHLORIDE

8.1 Introduction

Several nickel(II) chloride complexes were prepared with a series of amide ligands. Elemental analyses, *i.e.* nickel, carbon, hydrogen and nitrogen content, were used to determine the stoichiometric compositions of the complexes. Thermogravimetry was also used to characterise the complexes. The environment of the nickel(II) ions were deduced from visible and near-infrared diffuse reflectance spectra. IR vibrational spectral analysis was used to investigate the nickel-amide coordination.

8.2 Preparation of complexes

8.2.1 Materials

The amide ligands used are listed in Table 8.1. These were obtained from Aldrich Chemical Company and were used without further purification. The anhydrous nickel(II) chloride was also a commercially obtained reagent-grade chemical.

8.2.2 Preparation methods

Five types of chloro nickel(II)-amide complexes were prepared:

Type (I): $NiL_2C\ell_2(2H_2O)$, where L = *nmf*, *aa* or *nma*

Type (II): $NiLC\ell_2$, where L = *nmf*, *aa* or *nma*

Type (III): $NiL_2C\ell_2$, where L = *dmf*, *nef*, *fa*, *pa*, *ba* or *iba*

Type (IV): $Ni_3L_2C\ell_6$, where L = *dmf*, *nef*, *def*, *pa* or *dma*

Type (V): $Ni_3LC\ell_6$, where L = *dmp*.

Two preparative methods were used: **method (A)** and **method (B)** (see below). **Method (A)** was used to prepare complexes of types (I), (III) and (V), as well as certain type (IV) complexes. **Method (B)** was used to obtain complexes of types (II) and (IV).

Table 8.1: Properties of the amide ligands used in the present study.

Amide ligand	Abbreviation	Formula	M_w / g mol^{-1}	ρ /g cm^{-3}	bp(mp)/ °C
Formamide	(fa)	CH_3NO	45.0	1.13	210
N-Methylformamide	(nmf)	C_2H_5NO	59.1	1.00	198 - 200
N-Ethylformamide	(nef)	C_3H_7NO	73.1	0.95	202 - 204
N,N-Dimethylformamide	(dmf)	C_3H_7NO	73.1	0.95	153
N,N-Diethylformamide	(def)	$C_5H_{11}NO$	101.2	0.91	61 - 63
Acetamide	(aa)	C_2H_5NO	59.1	-	(79 - 81)
N-Methylacetamide	(nma)	C_3H_7NO	73.1	-	(27 - 30)
N-Ethylacetamide	(nea)	C_4H_9NO	87.1	0.92	90 - 92
N,N-Dimethylacetamide	(dma)	C_4H_9NO	87.1	0.94	163 - 166
Propionamide	(pa)	C_3H_7NO	73.1	-	(75 - 78)
N-Methylpropionamide	(nmp)	C_4H_9NO	87.1	0.93	146
N,N-Dimethylpropionamide	(dmp)	$C_5H_{11}NO$	101.2	0.92	174 - 175
N,N-Diethylpropionamide	(dep)	$C_7H_{15}NO$	129.2	0.90	77
Butyramide	(ba)	C_4H_9NO	87.1	-	(114 - 116)
Isobutyramide	(iba)	C_4H_9NO	87.1	-	(127 - 129)

Method (A): Preparation of types **(I)**, **(III)**, **(IV)** and **(V)** complexes

Complexes were prepared with slight modifications of the standard approaches reported in the literature [7,15,16]. The preparation was based on the general reaction

$$NiC\ell_2 + 2L \rightarrow NiL_2C\ell_2$$

where L is a simple amide. A nickel(II) chloride to ligand molar ratio of approximately 1:2 was used. About 0.03 moles of nickel(II) chloride was dissolved in about 20 cm^3 of boiling ethanol. Sufficient deionized water was added dropwise to dissolve the salt. The calculated amount of an amide ligand, dissolved in 20 cm^3 of warm ethanol, was slowly added to the nickel chloride solution with stirring. The hot solution was filtered through sintered glass and the filtrate was allowed to cool to room temperature.

Precipitation of the product occurred either immediately or after the mixture was decreased in volume by evaporation, until about 20 to 30 cm^3 remained. Usually, pure crystals formed only after repeated washing of an oily product with anhydrous ether

and storage of the crude product over P_2O_5 under reduced pressure. The prepared complexes were recrystallized from a mixture of anhydrous ethanol and ether, dried over P_2O_5, and then finally stored in a desiccator over silica gel.

Method (B): Preparation of types **(II)** and **(IV)** complexes

A single preparative route was followed to convert $NiL_2C\ell_2(2H_2O)$ or $NiL_2C\ell_2$ to $NiLC\ell_2$ or $Ni_3L_2C\ell_6$ complexes, respectively. About 2 g of an appropriate complex, depending on availability, was placed in a flat surfaced porcelain dish in a closed oven and heated to a fixed predetermined temperature (estimated from DTG curves) for several hours. The heating period was dependent on obtaining an approximately constant mass after repeated weighing, as well as yielding the " correct " elemental analysis results given in Table **8.3**. The complexes prepared, the starting complex and the drying temperature are shown in Table **8.2** .

Table 8.2: Starting complex and drying temperature used to prepare the $NiLC\ell_2$ or $Ni_3L_2C\ell_6$ complexes.

Preparation of $NiLC\ell_2$

$Ni(nmf)_2C\ell_2(2H_2O)$	$\xrightarrow[\text{(about 10 h)}]{120^\circ C}$	$Ni(nmf)C\ell_2$
$Ni(aa)_2C\ell_2(2H_2O)$	$\xrightarrow[\text{(about 6 h)}]{120^\circ C}$	$Ni(aa)C\ell_2$
$Ni(nma)_2C\ell_2(2H_2O)$	$\xrightarrow[\text{(about 6 h)}]{100^\circ C}$	$Ni(nma)C\ell_2$

Preparation of $Ni_3L_2C\ell_6$

$Ni(dmf)_2C\ell_2$	$\xrightarrow[\text{(about 8 h)}]{120^\circ C}$	$Ni_3(dmf)_2C\ell_6$
$Ni(nef)_2C\ell_2$	$\xrightarrow[\text{(about 5 h)}]{120^\circ C}$	$Ni_3(nef)_2C\ell_6$
$Ni(pa)_2C\ell_2$	$\xrightarrow[\text{(about 6 h)}]{100^\circ C}$	$Ni_3(pa)_2C\ell_6$

8.3 Apparatus

8.3.1 Elemental analyses

Nickel(II) ion was determined by a standard addition method using a Unicam-939 AA spectrophotometer [153]. Carbon, hydrogen and nitrogen analyses were performed at CSIR, MATTEK division, using a Carlo-Erba Microanalyser, model 1106.

8.3.2 Spectral characterisation

Uv-visible-NIR diffuse reflectance spectra

Diffuse reflectance spectra were obtained on a Beckman 5240, uv-visible-NIR spectrophotometer with a **198845** integrating sphere accessory. The instrument was interfaced to a personal computer running on a spectrophotometer automatic sampling controller software. Magnesium oxide was used as the reference standard.

Infrared (IR) absorption spectra

IR spectra were obtained using the KBr technique (2500 to 400 cm^{-1}) and CsI discs (400 to 200 cm^{-1}) on a Perkin-Elmer FT-IR spectrophotometer, 2000 System. Test spectra recorded on the same samples using the *nujol* mull method, did not show marked differences from the halide discs spectra.

8.3.3 Thermal measurements

Thermogravimetry (TG)

Simultaneous TG and DTG were carried out with a Perkin-Elmer TGA-7 instrument, interfaced to a personal computer. The TG instrument was calibrated with magnetic standards using the Curie point method [23]. Both linear temperature rise and isothermal modes were used.

The experimental conditions were: 2 to 3 mg of sample; heating rate 20°C min^{-1} from 30 to 400°C; open platinum crucible; flow rate of high purity nitrogen, about 20 cm^3 min^{-1}. For isothermal kinetic measurements, the heating rate to a predetermined reaction temperature was 200°C min^{-1}.

Differential scanning calorimetry (DSC)

A Perkin-Elmer DSC-7 Differential Scanning Calorimeter, interfaced to a personal computer, was calibrated using pure indium and pure tin as reference materials. A linear temperature rise mode was used.

About 2 to 3 mg samples of starting complex were heated from 40 to 400°C at 20°C min^{-1} in flowing nitrogen. Aluminium pans with lids, but uncrimped, were used. An empty aluminium pan was used as reference. For non-isothermal kinetic studies, heating rates from 5 to 30°C min^{-1} were used, with the sample mass kept constant at about 2 mg.

The DSC curves were corrected by subtracting the baseline measured in a blank run. Enthalpy changes were obtained from the DSC peak area using numerical integration.

Microscopic and visual examinations of thermal processes

The thermal behaviour of selected complexes was examined, in static air and at rising temperature, using the hot-stage of an Ortholux Leitz microscope apparatus. Gram-size samples of partially decomposed complexes and their final decomposition products (for spectral analysis and visual inspections) were prepared by heating the respective complexes in a Carbolite **MTF 12/18B** tube furnace, in flowing nitrogen.

8.4 Analytical results

The prepared complexes and their analytical data are shown in Table **8.3**. The elemental compositions found are in reasonable agreement with the calculated values. The amounts of ligand were determined from TG mass loss data.

8.5 Visible and near-infrared diffuse reflectance spectra

Visible and near-infrared diffuse reflectance spectra were recorded for all the starting complexes and the stable new phases produced by thermal decomposition. The spectra are shown in Figures **8.1.1** to **8.1.6** of Appendix **I**. Spectra of anhydrous $NiC\ell_2$ and of the decomposition residue of the various types of the amide complexes of nickel(II) chloride are included for comparison.

Spectral band assignments (Table **8.4**) are used to predict the geometrical structures about the nickel(II) ions. The ground state for a nickel(II) ion (d^8) in a regular octahedral field is $^3A_{2g}(F)$. Spectral bands at about 7000 to 10,500 cm^{-1} are assigned to the $^3T_{2g}(F)$ transition ($\hat{\upsilon}_1$); at 11,500 to 16,000 cm^{-1} to the $^3T_{1g}(F)$ transition ($\hat{\upsilon}_2$); and at 21,500 to 24,000 cm^{-1} to the $^3T_{1g}(P)$ transition ($\hat{\upsilon}_3$) [154,155]. The spectra are nearly similar to the spectrum of anhydrous $NiC\ell_2$, suggesting that the average environment is dominated by chloride anions.

Two forms of octahedral arrangement are suggested by the visible and near-infrared reflectance spectra of the $NiL_2C\ell_2$ complexes (Figures **8.1.3** and **8.1.5**). $Ni(fa)_2C\ell_2$ and $Ni(dmf)_2C\ell_2$ had an intense orange colour and their spectra are different from those of the other $NiL_2C\ell_2$ complexes. The complexes with L = *pa, nef, ba* or *iba* have similar spectra. The split of the $\hat{\upsilon}_2$ transition (to $^3T_{1g}$) band suggests that the transition to the $^1E_g(D)$ level gained intensity through configurational interaction with the $^3T_{1g}(F)$ level [155]. The spectra are similar to those of the related nickel(II)-amide complexes reported by other workers [15,16,124], for which additional evidence was used to support octahedral coordination. Chloride bridges are anticipated, and the octahedra proposed have a D_{2h} symmetry character. Other authors [156-160] have suggested that splitting of the $\hat{\upsilon}_1$ band could results from a tetragonal distortion to a symmetry approaching D_{4h}.

Octahedral complexes of formulae $NiLC\ell_2$ and $Ni_3L_2C\ell_6$ have been postulated to have chain structures with chloride bridging between nickel(II) ions [146,161].

8.6 Infrared (IR) absorption spectra

IR spectra were recorded for all the complexes using KBr or CsI discs. The usual range was 2500 to 200 cm^{-1}. IR spectra are shown in Figures **8.2.1** to **8.2.10** of Appendix I. The inclusion of spectra of free amide ligands allowed for the identification of those changes in absorption band position due to nickel-amide coordination. Table **8.5** shows assignments of the amide **I** ($\hat{\upsilon}_{C=O}$), the amide **II** ($\hat{\upsilon}_{N-H}$) and the amide **III** ($\hat{\upsilon}_{C-N}$) frequencies [125-131,162].

The frequencies of the IR absorption band assignments indicate a negative shift of the $\hat{\upsilon}_{C=O}$ stretch (about 8 to 45 cm^{-1}) and a positive shift of the $\hat{\upsilon}_{C-N}$ stretch (about 8 to 60 cm^{-1}) on complex formation. The $\Delta\hat{\upsilon}_{C=O}$ and $\Delta\hat{\upsilon}_{C-N}$ values (see Table **13.1**) are consistent with similar values reported by other workers [163-166]. The amide ligands are thus coordinated to the nickel ion through the carbonyl oxygen atom.

Tentative assignments of $\tilde{\upsilon}_{Ni\text{-}C\ell}$ and $\tilde{\upsilon}_{Ni\text{-}O}$ stretching vibrations are shown in Table **8.6**. The $\tilde{\upsilon}_{Ni\text{-}C\ell}$ vibrations were assigned following (primarily) related reports [167-175]. The assignments have been notably assisted by observing: (i) the halogen sensitivity of some of the bands, and (ii) the effects of varying the amide ligand in the complex. Two strong $\tilde{\upsilon}_{Ni\text{-}C\ell}$ bands are expected due to the $NiC\ell_2$ deformations. If the $\tilde{\upsilon}_{M\text{-}X}$ bands separation frequencies reported by Dorrity *et al.* [175] are assumed to hold for the present series of amide complexes, then the assignment of one $\tilde{\upsilon}_{Ni\text{-}C\ell}$ mode is consistent with reports that bridging $\tilde{\upsilon}_{M\text{-}X}$ vibrations also appear below 200 cm^{-1} [170-172,176]. Such bands fall outside the lower frequency range of the detector (mirTGS) used. Unassigned bands are listed in Table **8.6** as " other bands ".

Table 8.3: Analytical data for the amide complexes of nickel(II) chloride.

Prep. method	Complex stoichiometry	% Nickel Found (Calc.)	% Nitrogen Found (Calc.)	% Carbon Found (Calc.)	% Hydrogen Found (Calc.)	% Ligand Found (Calc.)
(a) $NiL_2C\ell_2(2H_2O)$						
A	$Ni(nmf)_2C\ell_2(2H_2O)$	19.6 (20.7)	10.3 (9.9)	17.7 (16.9)	4.7 (5.0)	55.6 (54.3)
A	$Ni(aa)_2C\ell_2(2H_2O)$	22.0 (20.7)	9.5 (9.9)	16.3 (16.9)	4.6 (5.0)	54.8 (54.3)
A	$Ni(nma)_2C\ell_2(2H_2O)$	20.1 (18.8)	9.4 (9.0)	22.2 (23.1)	6.0 (5.8)	57.9 (58.4)
(b) $NiLC\ell_2$						
B	$Ni(nmf)C\ell_2$	32.4 (31.1)	7.3 (7.4)	12.4 (12.7)	2.6 (2.7)	32.2 (31.3)
B	$Ni(aa)C\ell_2$	31.4 (31.1)	6.8 (7.4)	11.7 (12.7)	2.6 (2.7)	30.8 (31.3)
B	$Ni(nma)C\ell_2$	29.3 (29.0)	6.6 (6.9)	16.8 (17.8)	3.5 (3.5)	35.8 (36.1)
(c) $NiL_2C\ell_2$						
A	$Ni(fa)_2C\ell_2$	25.2 (26.7)	12.6 (12.8)	10.9 (10.9)	2.8 (2.8)	40.7 (41.0)
A	$Ni(dmf)_2C\ell_2$	19.4 (21.3)	9.7 (10.2)	26.3 (26.1)	5.1 (5.1)	54.7 (53.0)
A	$Ni(nef)_2C\ell_2$	19.3 (21.3)	9.8 (10.2)	25.4 (26.1)	5.2 (5.1)	53.5 (53.0)
A	$Ni(pa)_2C\ell_2$	20.8 (21.3)	10.0 (10.2)	26.0 (26.1)	5.3 (5.1)	53.5 (53.0)
A	$Ni(ba)_2C\ell_2$	17.5 (19.3)	8.0 (9.2)	28.0 (31.6)	5.8 (6.0)	56.9 (57.3)
A	$Ni(iba)_2C\ell_2$	16.9 (19.3)	8.2 (9.2)	28.2 (31.6)	5.8 (6.0)	55.7 (57.3)
(d) $Ni_3L_2C\ell_6$						
B	$Ni_3(dmf)_2C\ell_6$	32.4 (32.9)	5.0 (5.2)	13.1 (13.5)	2.8 (2.6)	27.0 (27.3)
A	$Ni_3(dma)_2C\ell_6$	33.2 (32.9)	5.8 (5.0)	18.1 (17.1)	3.7 (3.2)	29.7 (30.9)
A	$Ni_3(def)_2C\ell_6$	31.4 (32.6)	4.6 (4.7)	19.3 (20.3)	3.8 (3.8)	34.7 (34.2)
B	$Ni_3(nef)_2C\ell_6$	31.9 (32.9)	5.2 (5.2)	14.8 (13.5)	3.1 (2.6)	28.9 (27.3)
B	$Ni_3(pa)_2C\ell_6$	32.5 (32.9)	4.9 (5.2)	12.3 (13.5)	2.7 (2.6)	27.6 (27.3)
(e) $Ni_3LC\ell_6$						
A	$Ni_3(dmp)C\ell_6$	36.6 (35.9)	4.6 (4.7)	17.2 (20.3)	3.6 (3.8)	21.9 (20.6)

Table 8.4: Visible and near-infrared diffuse reflectance spectra of the amide complexes of nickel(II) chloride.

Complex	Colour	Band assignments / 10^3 cm^{-1}		
		$^3T_{2g}(F) \leftarrow {}^3A_{2g}(F)$ ($\hat{\upsilon}_1$)	$^3T_{1g}(F) \leftarrow {}^3A_{2g}(F)$ ($\hat{\upsilon}_2$)	$^3T_{1g}(P) \leftarrow {}^3A_{2g}(F)$ ($\hat{\upsilon}_3$)
$NiC\ell_2$	brown	7.223	11.696; 12.826	22.222
(a) $NiLC\ell_2$				
$Ni(nmf)C\ell_2$	brown	7.249	11.838	22.388
$Ni(aa)C\ell_2$	brown	7.238	11.413	22.089
$Ni(nma)C\ell_2$	brown	7.236	11.415	22.028
(b) $NiL_2C\ell_2(2H_2O)$				
$Ni(nmf)C\ell_2(2H_2O)$	orange	7.249	11.780	22.329
$Ni(aa)_2C\ell_2(2H_2O)$	orange	7.267	11.846	22.477
$Ni(nma)_2C\ell_2(2H_2O)$	orange	7.252	12.124	23.371
(c) $Ni_3L_2C\ell_6$				
$Ni_3(dmf)_2C\ell_6$	brown	7.259	11.701	22.047
$Ni_3(dma)_2C\ell_6$	brown	7.252	11.627	21.989
$Ni_3(nef)_2C\ell_6$	brown	7.232	11.531	21.885
$Ni_3(pa)_2C\ell_6$	brown	7.221	11.375	21.770
$Ni_3(def)_2C\ell_6$	brown	7.247	11.586	21.738
(d) $NiL_2C\ell_2$				
$Ni(fa)_2C\ell_2$	intense-orange	7.286	11.885	22.311
$Ni(dmf)_2C\ell_2$	intense-orange	7.267	12.556	23.077
$Ni(nef)_2C\ell_2$	blue-green	7.271	14.167; 15.200	22.074
$Ni(pa)_2C\ell_2$	blue-green	7.556	14.196; 15.334	23.280
$Ni(ba)_2C\ell_2$	blue-green	7.460	14.328; 15.236	21.985
$Ni(iba)_2C\ell_2$	blue-green	7.258	14.279; 15.243	21.985
(e) $Ni_3LC\ell_6$				
$Ni_3(dmp)C\ell_6$	brown	7.285	11.739	21.744

Table 8.5: Assignment of infrared absorption bands of the amide complexes of nickel(II) chloride (2500 to 400 cm^{-1}).

Ligand (L) in ↓	Infrared vibrational frequencies / cm^{-1}					
	Amide I		Amide II		Amide III	
	free L	complex	free L	complex	free L	complex
(a) $NiLC\ell_2$						
nmf	1668	1655	1544	1534	1247	1294
aa	1684	1660	1636	1576	1400	1460
nma	1659	1633	1565	1569	1300	1311
(b) $NiL_2C\ell_2(2H_2O)$						
nmf	1668	1652	1544	1541	1247	1262
aa	1684	1663	1636	1578	1400	1466
nma	1659	1629	1565	1564	1300	1308
(c) $Ni_3L_2C\ell_6$						
dmf	1674	1656	1501	1494	1095	1113
dma	1639	1620	1502	1518	1401	1430
nef	1667	1653	1539	1546	1245	1268
pa	1661	1652	1629	1584	1421	1471
def	1669	1640	1439	1456	1111	1123
(d) $NiL_2C\ell_2$						
dmf	1674	1651	1501	1500	1095	1118
nef	1667	1647	1539	1537	1245	1252
fa	1691	1694	1606	1585	1309	1345
pa	1661	1653	1629	1586	1421	1472
ba	1670	1655	1634	1587	1425	1466
iba	1672	1654	1644	1593	1429	1479
(e) $Ni_3LC\ell_6$						
dmp	1644	1603	1498	1501	1402	1411

Table 8.6: Assignment of far-IR absorption bands of the amide complexes of nickel(II) chloride (400 to 200 cm^{-1}).

Ligand (L) in ↓	Far-infrared vibrational frequencies / cm^{-1}		
	$\hat{\upsilon}_{Ni\text{-}C\ell}$ (bridging)	$\hat{\upsilon}_{Ni\text{-}O}$ (nickel-oxygen)	other bands (unassigned)
(a) $NiLC\ell_2$			
nmf	226	367	215
aa	220	357	
nma	226	366	214
(b) $NiL_2C\ell_2(2H_2O)$			
nmf	226	368	213
aa	222	380	
nma	225	353	217
(c) $Ni_3L_2C\ell_6$			
dmf	220	402	
dma	224	346	207
nef	222	398	208
pa	223	351	
def	223	396	205
(d) $NiL_2C\ell_2$			
dmf	222	393	209
nef	221	397	207
fa	233	352	
pa	228	360	209
ba	223	497	
iba	219	377	204
(e) $Ni_3LC\ell_6$			
dmp	216	346	204

CHAPTER 9

THERMAL DECOMPOSITION OF NICKEL(II)-AMIDE COMPLEXES

9.1 Introduction

The thermal decomposition stoichiometries and enthalpies of all the characterised complexes were determined from TG and DSC curves. Simple, non-overlapping decomposition patterns were observed for $NiLC\ell_2$, $Ni_3L_2C\ell_6$ and $Ni_3LC\ell_6$ complexes. DSC curves of the $NiL_2C\ell_2$ and $NiL_2C\ell_2(2H_2O)$ complexes were relatively complicated.

9.2 Type (I) complexes: $NiL_2C\ell_2(2H_2O)$

The TG, DTG and DSC curves are shown in Figures **9.1.1** to **9.1.3**. For $Ni(nmf)_2C\ell_2(2H_2O)$ and $Ni(aa)_2C\ell_2(2H_2O)$, loss of the first amide ligand occurs after dehydration. The $NiL_2C\ell_2$ intermediate could not be isolated by isothermal heating of the starting complex. For $Ni(nma)_2C\ell_2(2H_2O)$, TG and DTG curves suggest simultaneous loss of $2H_2O$ and the first *nma* molecule, but the DSC curve shows three endotherms. TG mass loss data are consistent with the decomposition scheme

$$NiL_2C\ell_2(2H_2O)\ (s) \rightarrow NiLC\ell_2\ (s) + 2H_2O\ (g) + L\ (g)$$

$$NiLC\ell_2\ (s) \rightarrow NiC\ell_2\ (s) + L\ (g)$$

The thermal decomposition data are collected in Table **9.1**.

9.3 Type (II) complexes: $NiLC\ell_2$

TG and DSC curves, Figures **9.2.1** to **9.2.3**, indicate that in $NiLC\ell_2$ complexes the ligand L is removed completely in a single endothermic step. Thermal decomposition occurs over a narrow temperature range (about 30°C) with a well defined TG inflection.

$$NiLC\ell_2\ (s) \rightarrow NiC\ell_2\ (s) + L\ (g)$$

The thermal decomposition data are given in Table **9.2**.

Table 9.1: Thermal decomposition data for the reactions

$$NiL_2C\ell_2(2H_2O)\ (s) \rightarrow NiLC\ell_2\ (s) \rightarrow NiC\ell_2\ (s) + 2H_2O\ (g) + 2L\ (g)$$

Complex	Fragment lost			DTG Temp. / °C		ΔH_{2L} / kJ mol^{-1}
	Formula	% mass loss		T_e	T_{max}	
Residue		Found	Calc.			
$Ni(nmf)_2C\ell_2$	*nmf*	22.4	23.0	136	148	
	nmf	24.3	23.0	248	268	147
residue		53.3	54.0			
$Ni(aa)_2C\ell_2$	*aa*	24.0	23.0	197	215	
	aa	22.6	23.0	231	235	132
residue		53.4	54.0			
$Ni(nma)_2C\ell_2$	*nma*	-	26.5	-	-	
	nma	27.4	26.5	217	227	-
residue		44.6	47.0			

Table 9.2: Thermal decomposition data for the reaction

$$NiLC\ell_2\ (s) \rightarrow NiC\ell_2\ (s) + L\ (g)$$

Complex	Fragment lost			DTG Temp. / °C		ΔH_L / kJ mol^{-1}
	Formula	% mass loss		T_e	T_{max}	
Residue		Found	Calc.			
$Ni(nmf)C\ell_2$	*nmf*	32.2	31.3	243	271	67
residue		67.8	68.7			
$Ni(aa)C\ell_2$	*aa*	30.8	31.3	228	244	63
residue		69.2	68.7			
$Ni(nma)C\ell_2$	*nma*	35.8	36.1	215	230	60
residue		64.2	63.9			

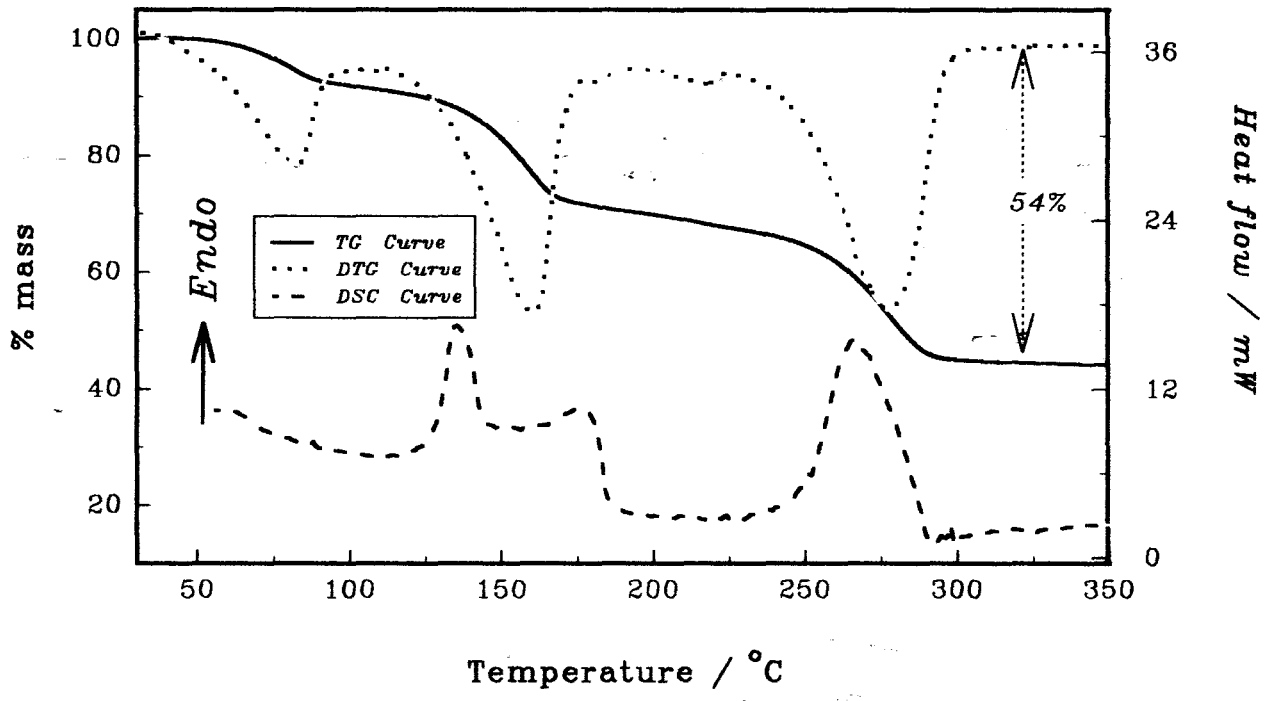

Figure 9.1.1: TG, DTG and DSC curves for $Ni(nmf)_2Cl_2(2H_2O)$ heated at 20°C min^{-1} in flowing N_2 .

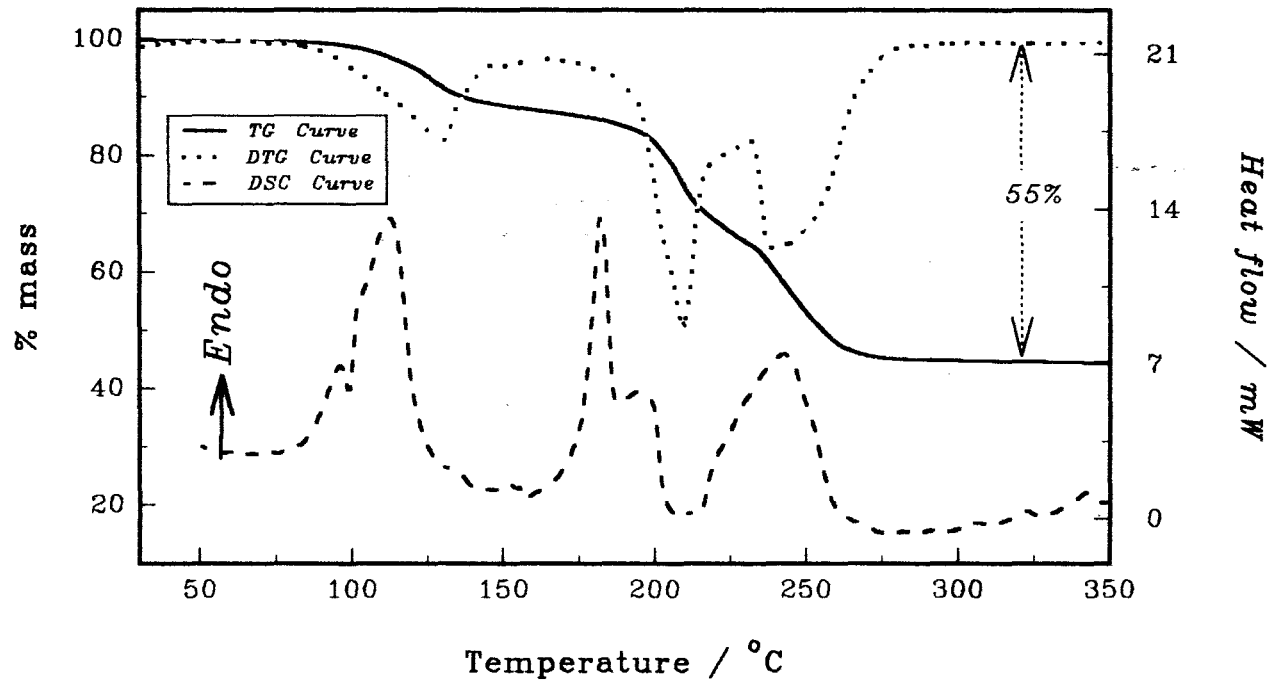

Figure 9.1.2: TG, DTG and DSC curves for $Ni(aa)_2Cl_2(2H_2O)$ heated at 20°C min^{-1} in flowing N_2 .

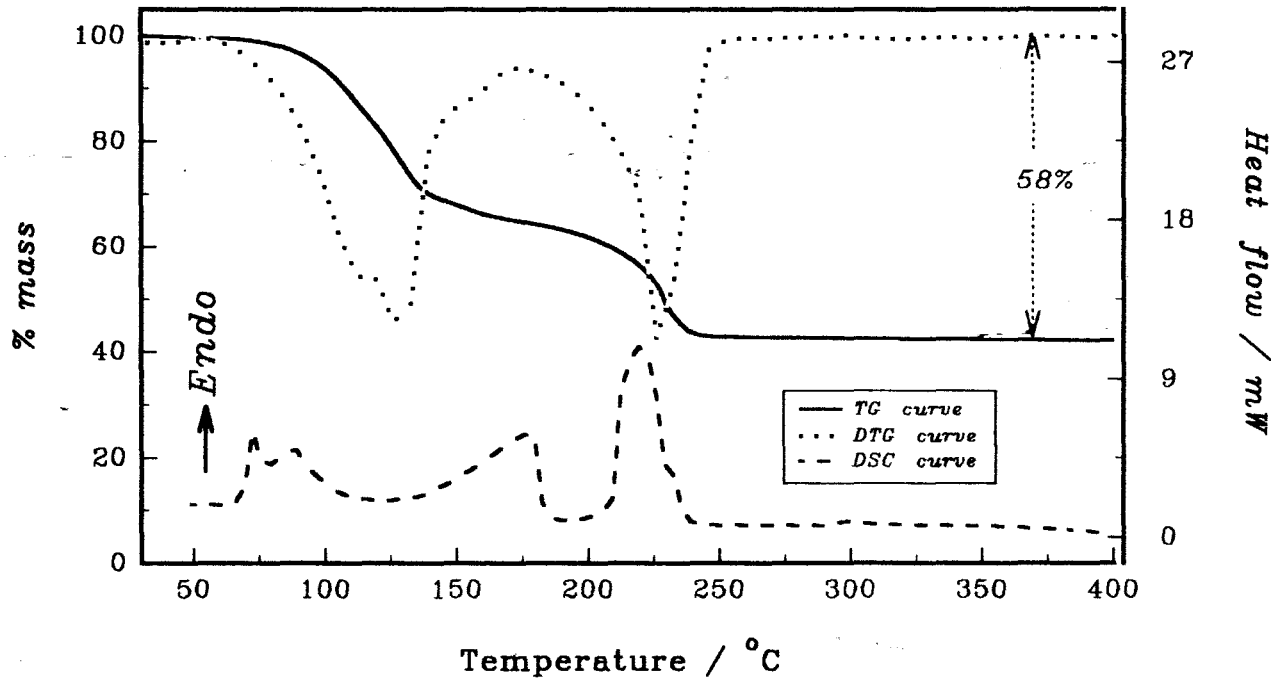

Figure 9.1.3: TG, DTG and DSC curves for $Ni(nma)_2Cl_2(2H_2O)$ heated at 20°C min^{-1} in flowing N_2 .

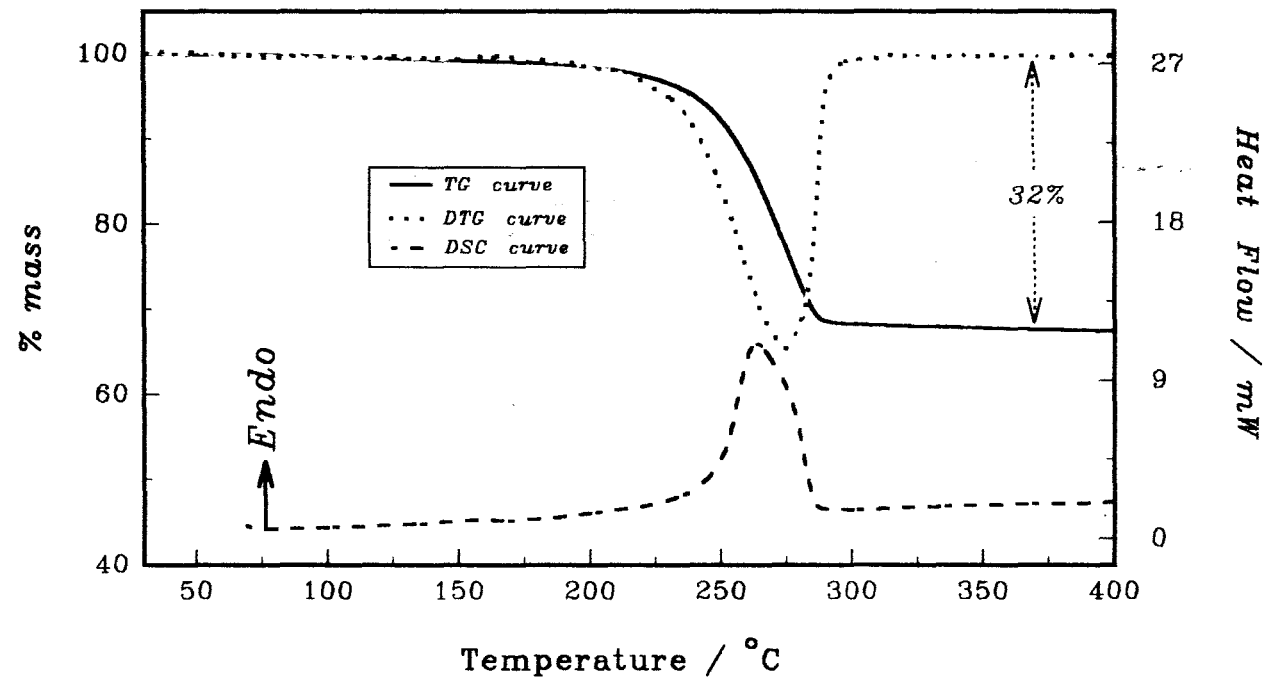

Figure 9.2.1: TG, DTG and DSC curves for $Ni(nmf)Cl_2$ heated at 20°C min^{-1} in flowing N_2 .

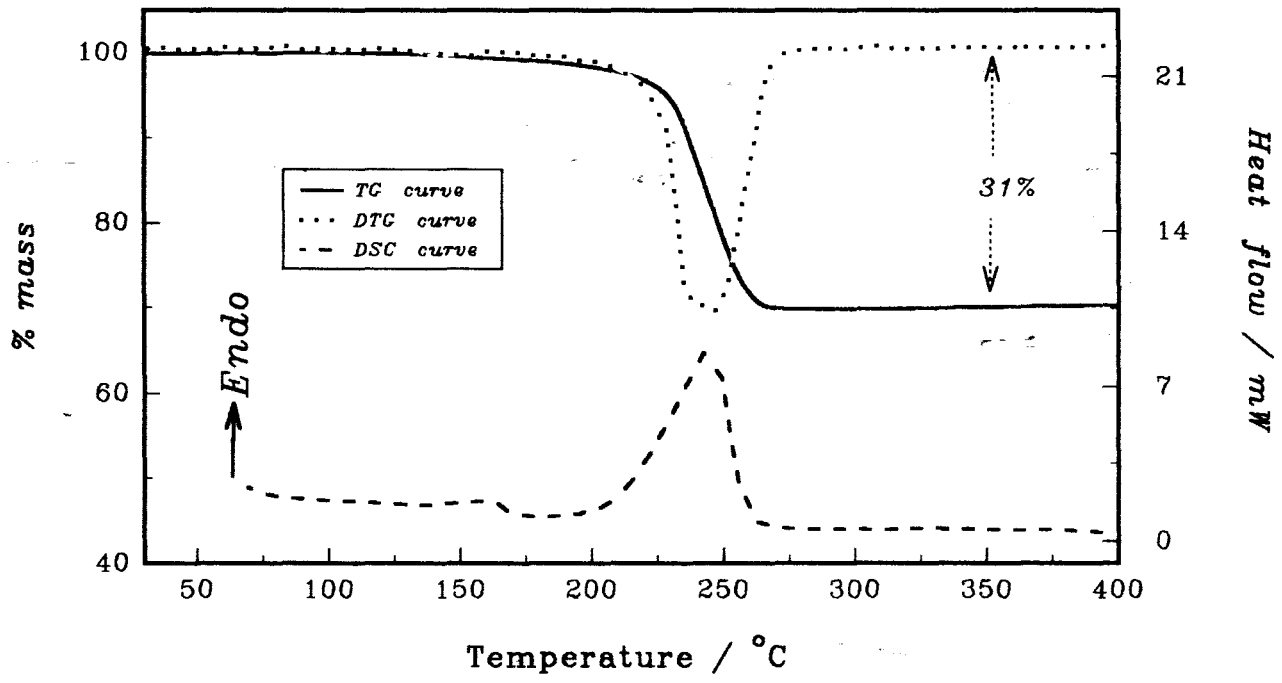

Figure 9.2.2: TG, DTG and DSC curves for $Ni(aa)Cl_2$ heated at 20°C min^{-1} in flowing N_2 .

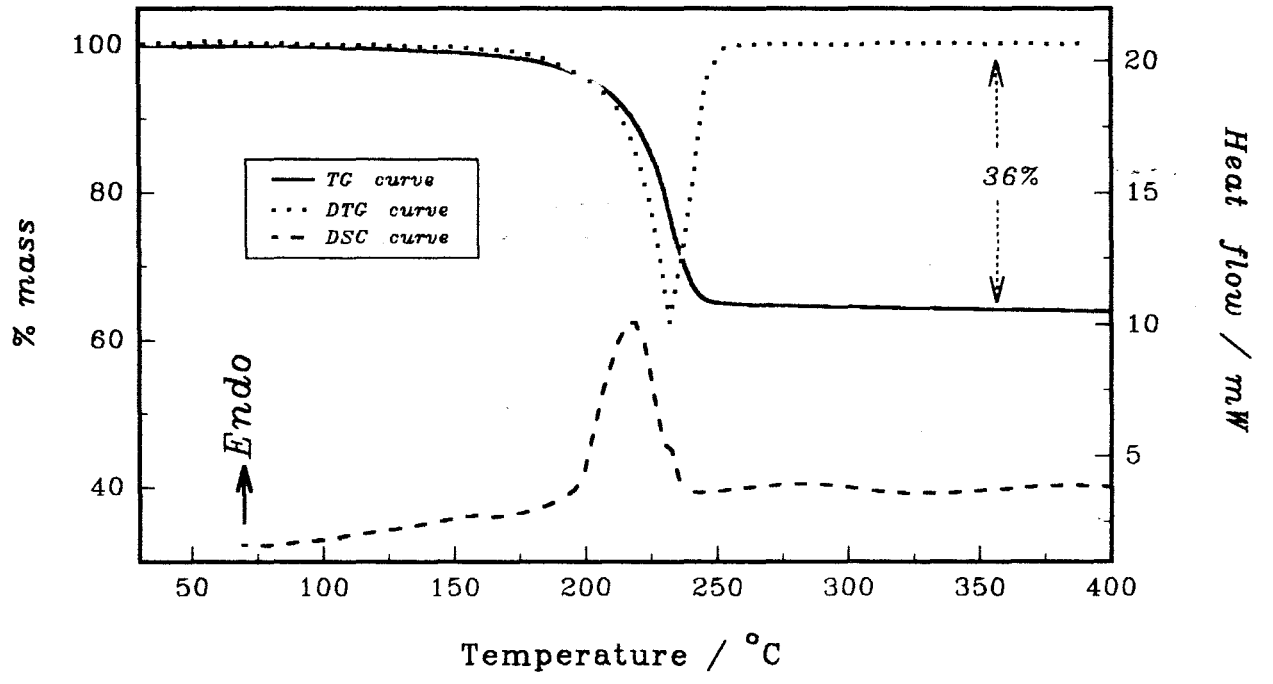

Figure 9.2.3: TG, DTG and DSC curves for $Ni(nma)Cl_2$ heated at 20°C min^{-1} in flowing N_2 .

9.4 Type (III) complexes: $NiL_2C\ell_2$

The TG and DTG curves, Figures **9.3.1** to **9.3.6**, indicate two decomposition steps. The two stages partially overlap for some of the complexes. Mass losses observed for the first step are consistent with the formation of a moderately stable $Ni_3L_2C\ell_6$ intermediate. The $Ni_3L_2C\ell_6$ intermediates were subsequently isolated and characterized using chemical and spectral methods (see Table **8.3**). The characterization results and the mass loss data in Table **9.3** are consistent with the decomposition scheme

$$3NiL_2C\ell_2\ (s) \rightarrow Ni_3L_2C\ell_6\ (s) + 4L\ (g)$$
$$Ni_3L_2C\ell_6\ (s) \rightarrow 3NiC\ell_2\ (s) + 2L\ (g)$$

The DSC curves, Figures **9.3.1** to **9.3.6**, indicate complex overlapping endotherms. The sharpness of the first DSC endotherm, Figures **9.3.4** to **9.3.6**, suggests melting. The diffuse reflectance spectra of the $Ni_3L_2C\ell_6$, when compared with their respective $NiL_2C\ell_2$ starting complexes (Figures **8.1.3** to **8.1.5**), indicate that the removal of ligand molecules is accompanied by structural rearrangements.

Under a hot stage microscope, the blue-green starting $NiL_2C\ell_2$ complexes (where L is *iba, ba, pa* or *nef*) appeared darker between about 136 to 154°C and then turned brown. The occurrence of melting could not be ascertained owing to the very deep colour of the complexes. Visual inspection of larger quantities of the partially decomposed complexes prepared in a tube furnace confirmed melting.

9.5 Type (IV) complexes: $Ni_3L_2C\ell_6$

TG, DTG and DSC curves, Figures **9.4.1** to **9.4.5**, indicate that the ligands are removed completely in a single endothermic step.

$$Ni_3L_2C\ell_6\ (s) \rightarrow 3NiC\ell_2\ (s) + 2L\ (g)$$

The thermal decomposition data are shown in Table **9.4**.

9.6 Type (V) complexes: $Ni_3LC\ell_6$

The DSC curve for the decomposition of the only $Ni_3LC\ell_6$ complex, $Ni_3(dmp)C\ell_6$, showed a single broad endotherm. The corresponding one-step TG mass loss is

consistent with the loss of *dmp* to give $NiC\ell_2$ residue.

$$Ni_3(dmp)C\ell_6\ (s) \rightarrow 3NiC\ell_2\ (s) + dmp\ (g)$$

TG, DTG and DSC curves are shown in Figure **9.5.1**. The decomposition data are given in Table **9.5**.

Table 9.3: Thermal decomposition data for the reactions

$$3NiL_2C\ell_2\ (s) \rightarrow Ni_3L_2C\ell_6\ (s) \rightarrow 3NiC\ell_2\ (s) + 6L\ (g)$$

Complex	Fragment lost			DTG Temp. / °C		ΔH_{6L} / kJ mol^{-1}
	Formula	% mass loss		T_e	T_{max}	
Residue		Found	Calc.			
$3Ni(fa)_2C\ell_2$	4*fa*	27.6	27.3	233	256	
	2*fa*	13.0	13.7	282	292	415
residue		59.4	59.0			
$3Ni(dmf)_2C\ell_2$	4*dmf*	36.7	35.3	89	107	
	2*dmf*	18.0	17.7	233	252	389
residue		45.3	47.0			
$3Ni(nef)_2C\ell_2$	4*nef*	37.2	35.3	144	168	
	2*nef*	16.4	17.7	241	257	322
residue		46.4	47.0			
$3Ni(pa)_2C\ell_2$	4*pa*	37.7	35.3	153	179	
	2*pa*	15.8	17.7	200	205	305
residue		46.5	47.0			
$3Ni(ba)_2C\ell_2$	4*ba*	41.2	38.2	163	191	
	2*ba*	15.7	19.1	218	229	256
residue		43.1	42.7			
$3Ni(iba)_2C\ell_2$	4*iba*	38.0	38.2	158	198	
	2*iba*	18.7	19.1	214	217	237
residue		43.3	42.7			

Table 9.4: Thermal decomposition data for the reaction

$$Ni_3L_2C\ell_6\ (s) \rightarrow 3NiC\ell_2\ (s) + 2L\ (g)$$

Complex	Fragment lost			DTG Temp. / °C		ΔH_{2L} / kJ mol^{-1}
	Formula	% mass loss		T_e	T_{max}	
Residue		Found	Calc.			
$Ni_3(dmf)_2C\ell_6$	*2dmf*	27.0	27.3	234	260	108
residue		73.0	72.7			
$Ni_3(dma)_2C\ell_6$	*2dma*	29.7	30.9	239	248	92
residue		70.3	69.1			
$Ni_3(nef)_2C\ell_6$	*2nef*	28.9	27.3	217	259	94
residue		71.1	72.7			
$Ni_3(pa)_2C\ell_6$	*2pa*	27.6	27.3	182	207	91
residue		72.4	72.7			
$Ni_3(def)_2C\ell_6$	*2def*	34.7	34.2	250	274	90
residue		65.3	65.8			

Table 9.5: Thermal decomposition data for the reaction

$$Ni_3(dmp)C\ell_6\ (s) \rightarrow 3NiC\ell_2\ (s) + dmp\ (g)$$

Complex	Fragment lost			DTG Temp. / °C		ΔH_L / kJ mol^{-1}
	Formula	% mass loss		T_e	T_{max}	
Residue		Found	Calc.			
$Ni_3(dmp)C\ell_6$	*dmp*	21.9	20.6	176	206	61
residue		78.1	79.4			

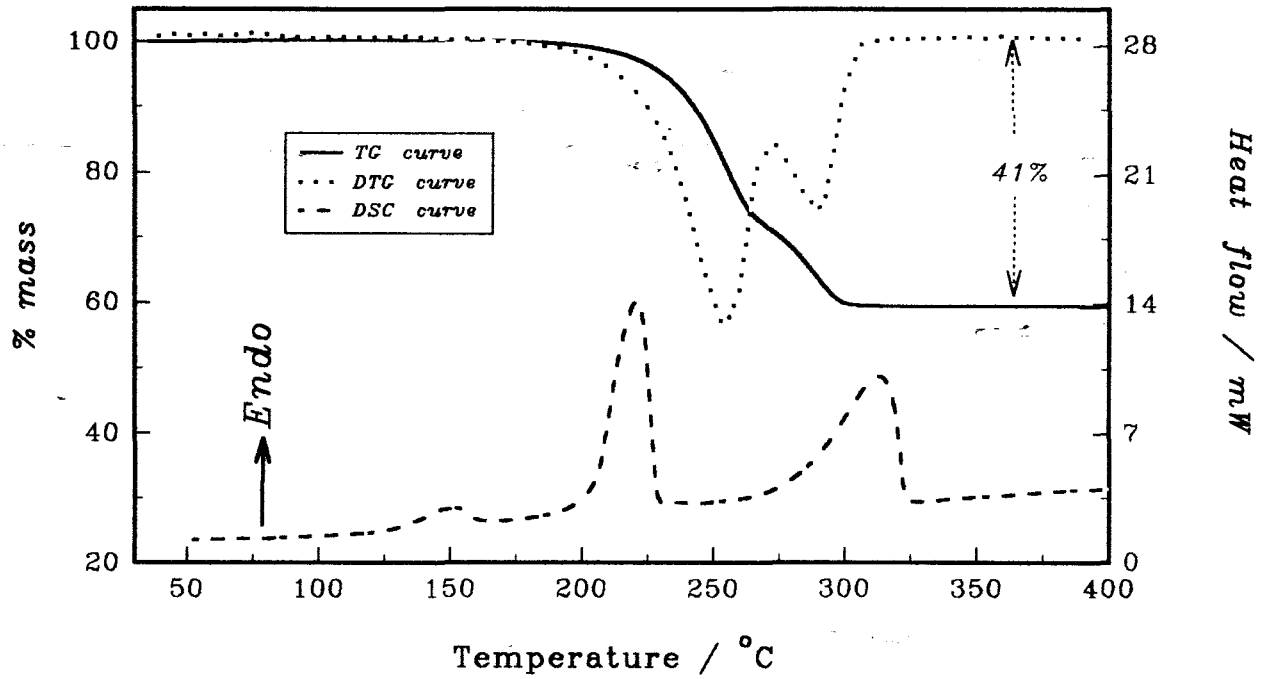

Figure 9.3.1: TG, DTG and DSC curves for $Ni(fa)_2Cl_2$ heated at 20°C min^{-1} in flowing N_2 .

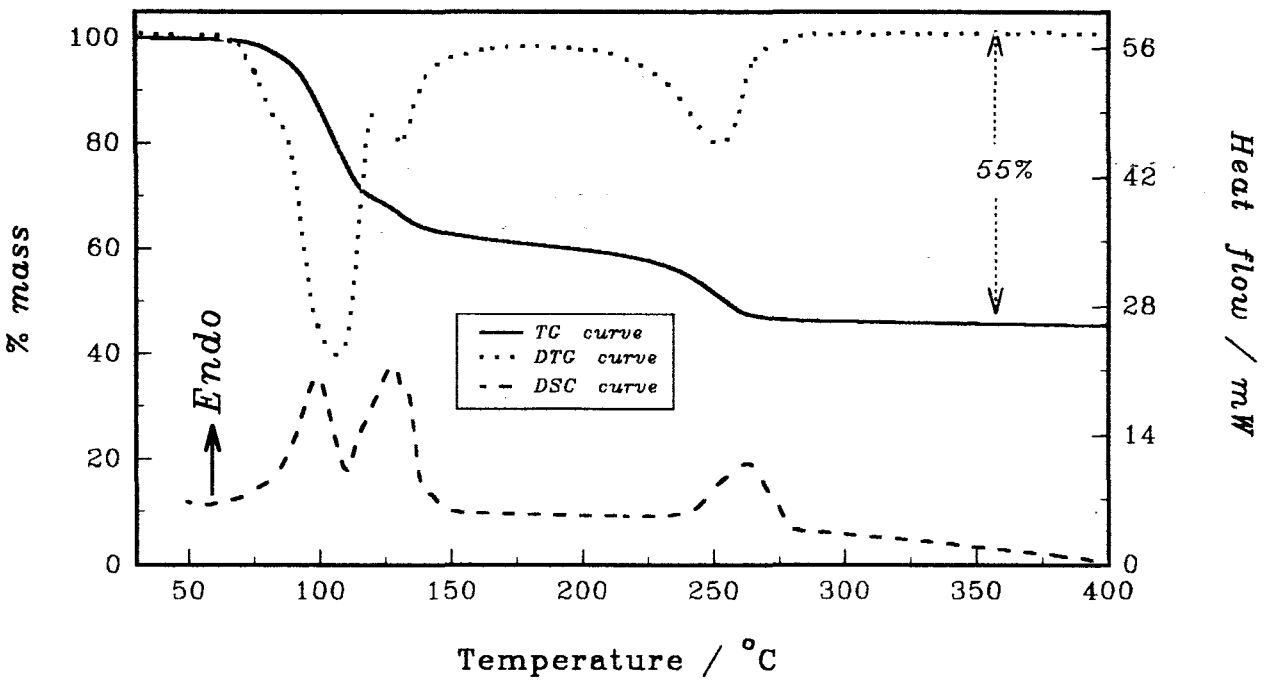

Figure 9.3.2: TG, DTG and DSC curves for $Ni(dmf)_2Cl_2$ heated at 20°C min^{-1} in flowing N_2.

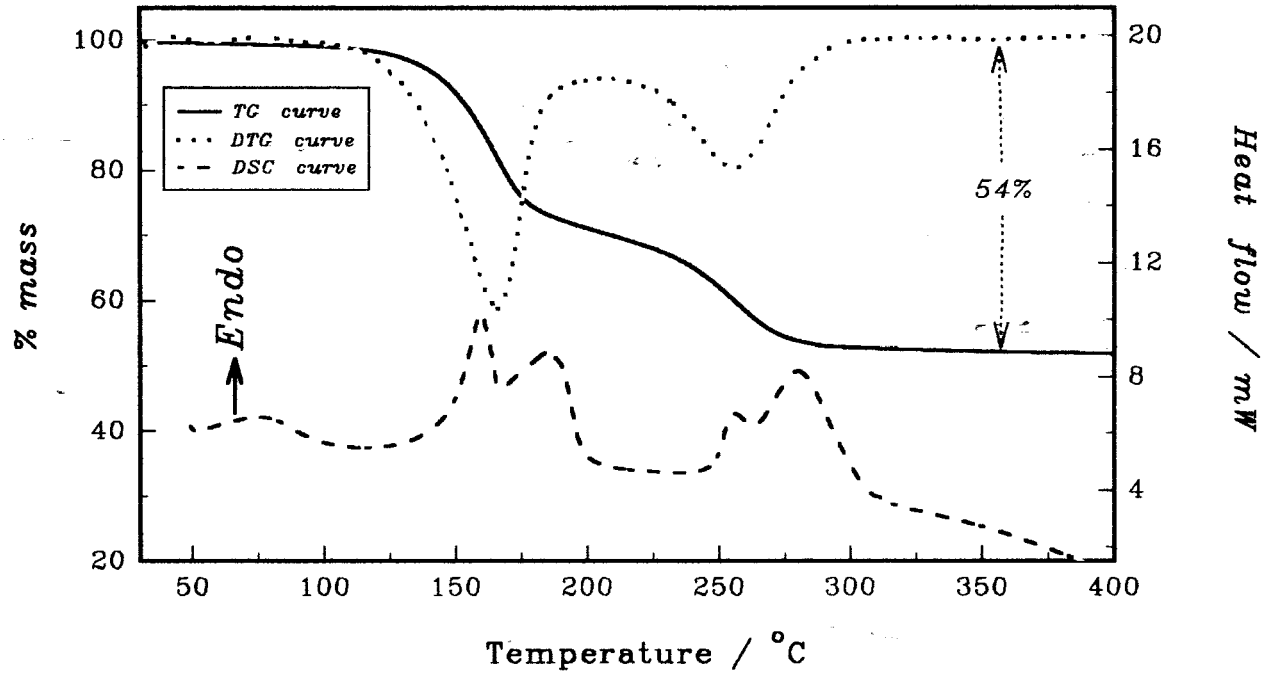

Figure 9.3.3: TG, DTG and DSC curves for $Ni(nef)_2Cl_2$ heated at $20^{\circ}C\ min^{-1}$ in flowing N_2 .

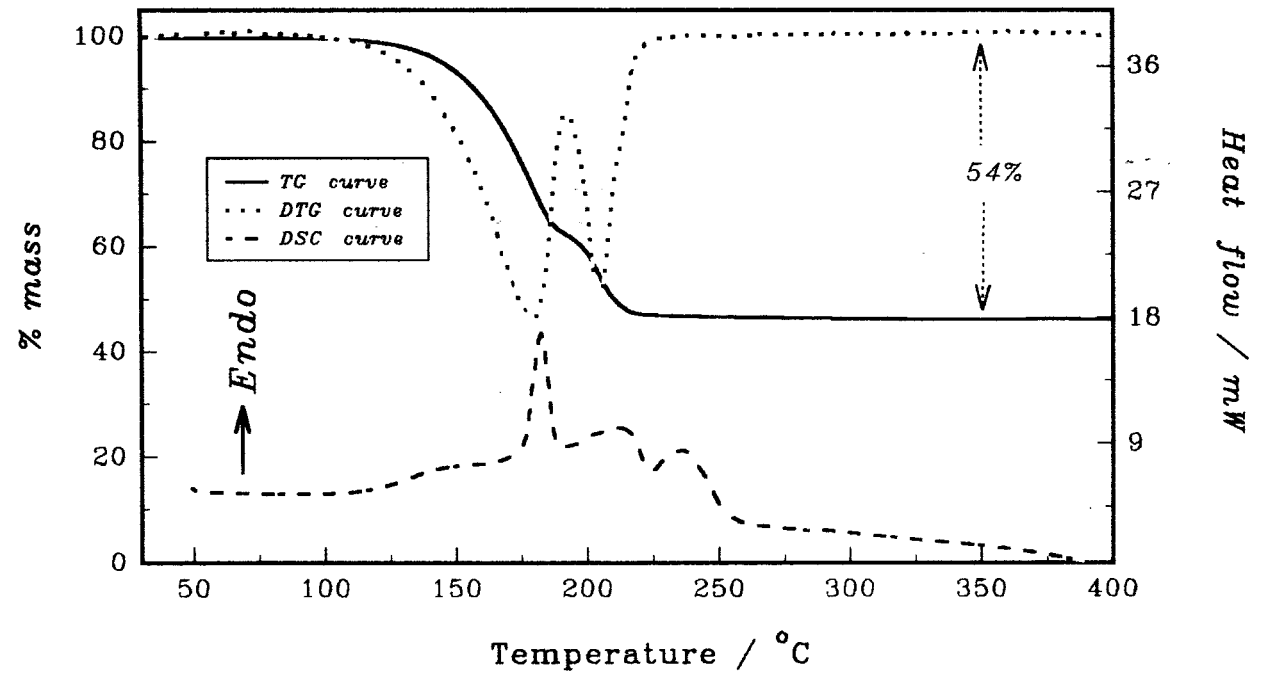

Figure 9.3.4: TG, DTG and DSC curves for $Ni(pa)_2Cl_2$ heated at $20^{\circ}C\ min^{-1}$ in flowing N_2 .

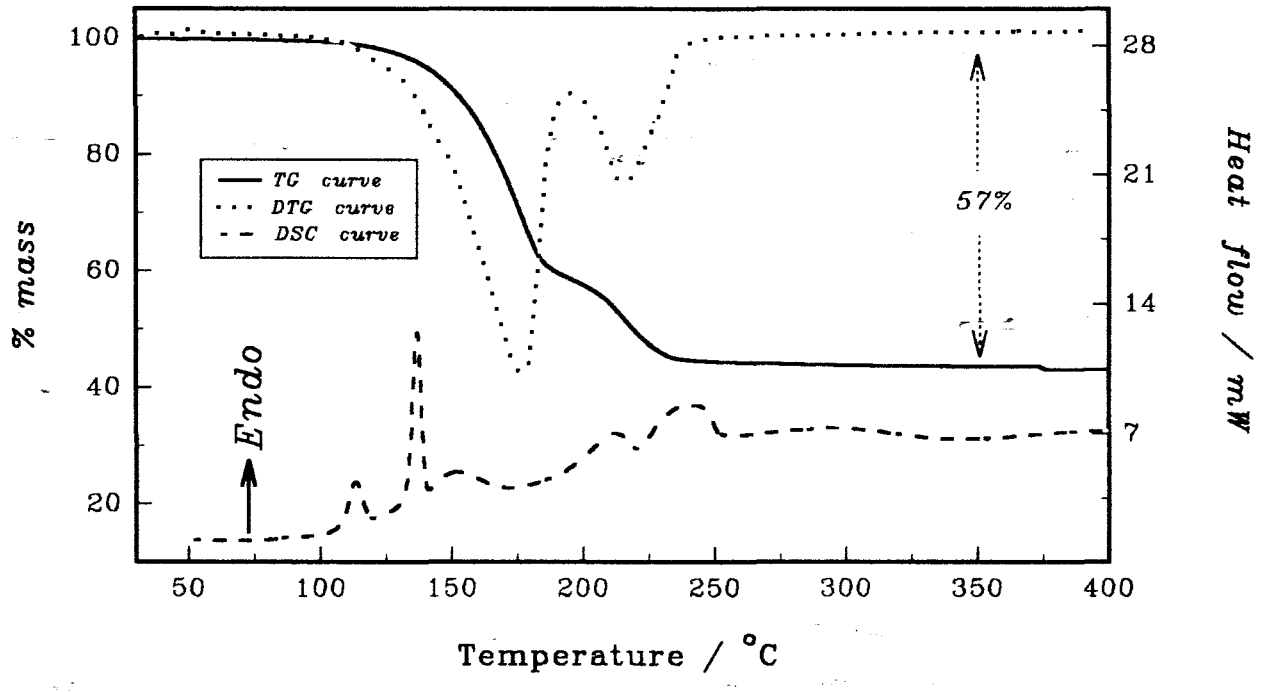

Figure 9.3.5: TG, DTG and DSC curves for $Ni(ba)_2Cl_2$ heated at 20°C min^{-1} in flowing N_2 .

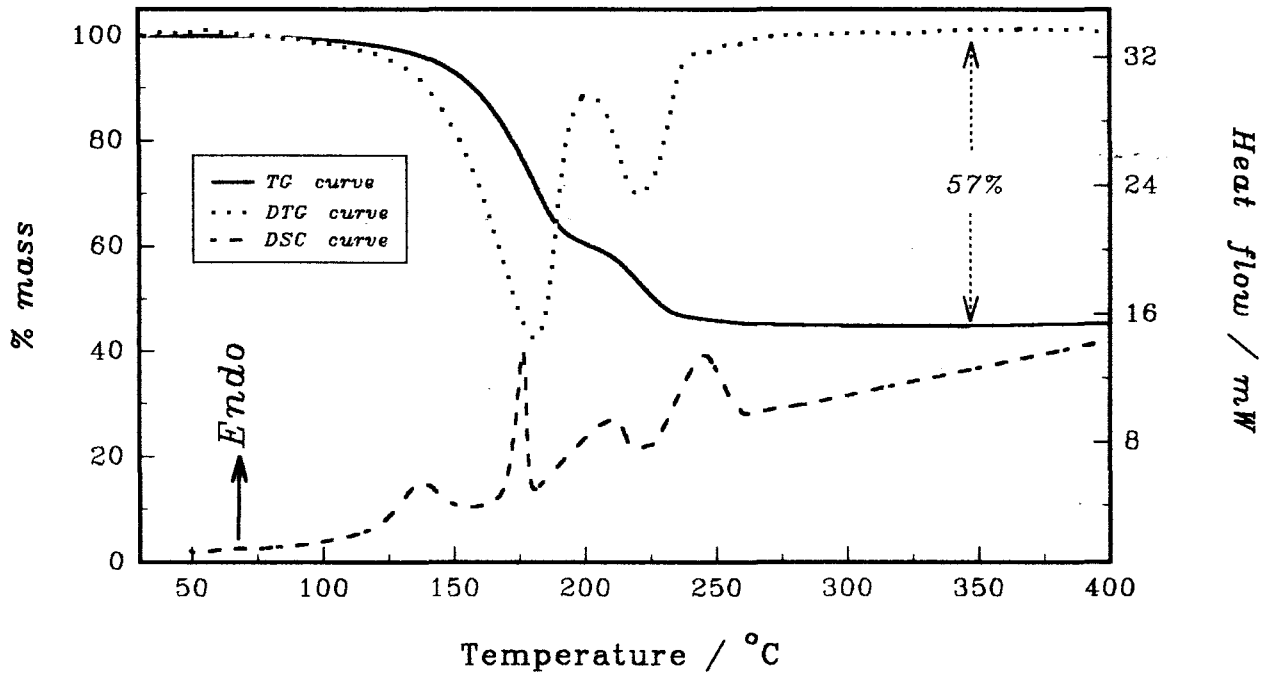

Figure 9.3.6: TG, DTG and DSC curves for $Ni(iba)_2Cl_2$ heated at 20°C min^{-1} in flowing N_2 .

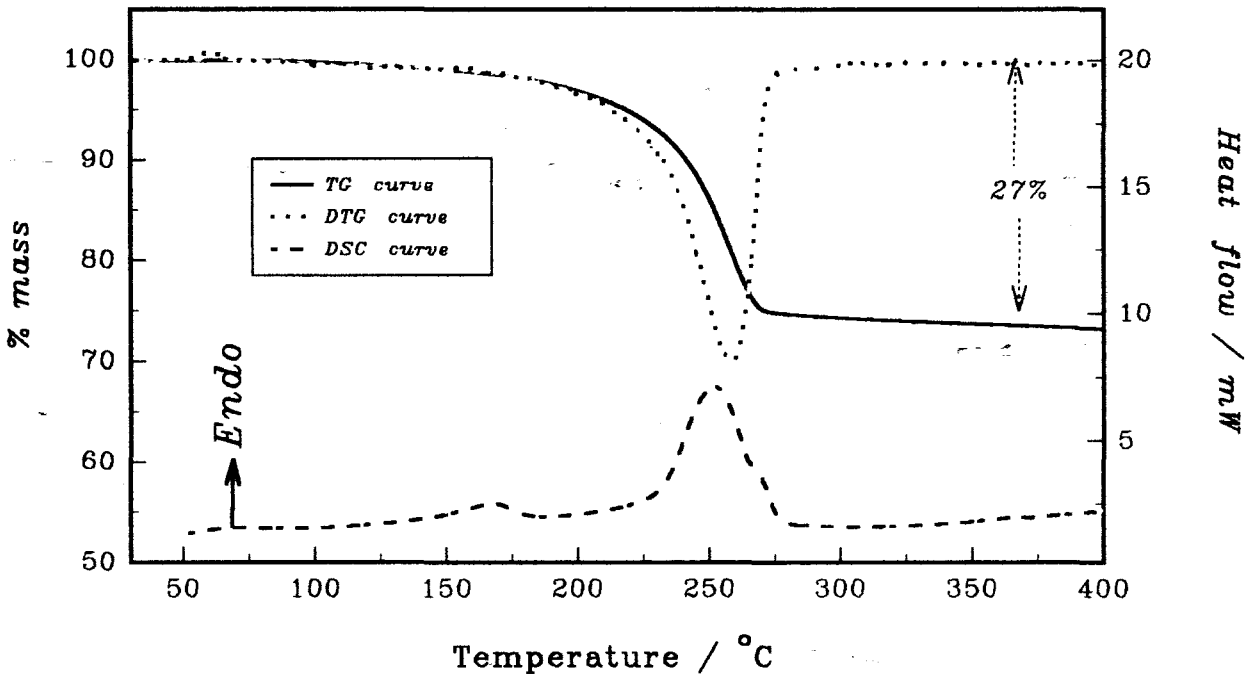

Figure 9.4.1: TG, DTG and DSC curves for $Ni_3(dmf)_2Cl_6$ heated at 20°C min^{-1} in flowing N_2 .

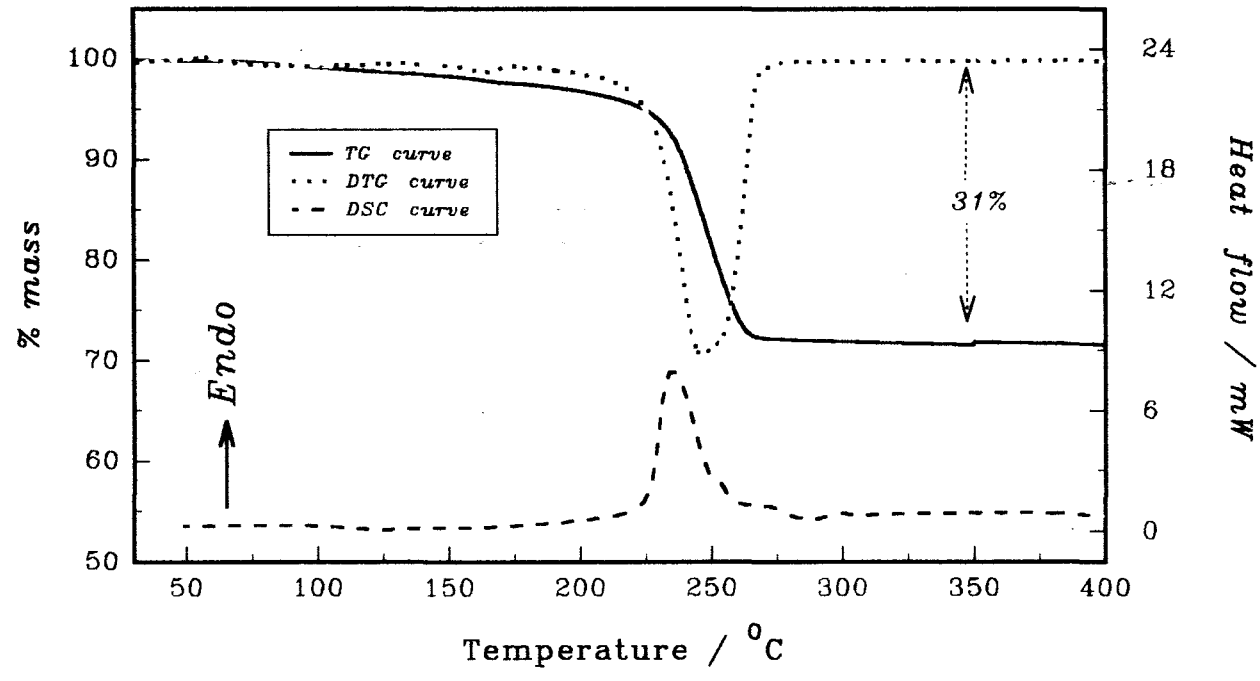

Figure 9.4.2: TG, DTG and DSC curves for $Ni_3(dma)_2Cl_6$ heated at 20°C min^{-1} in flowing N_2 .

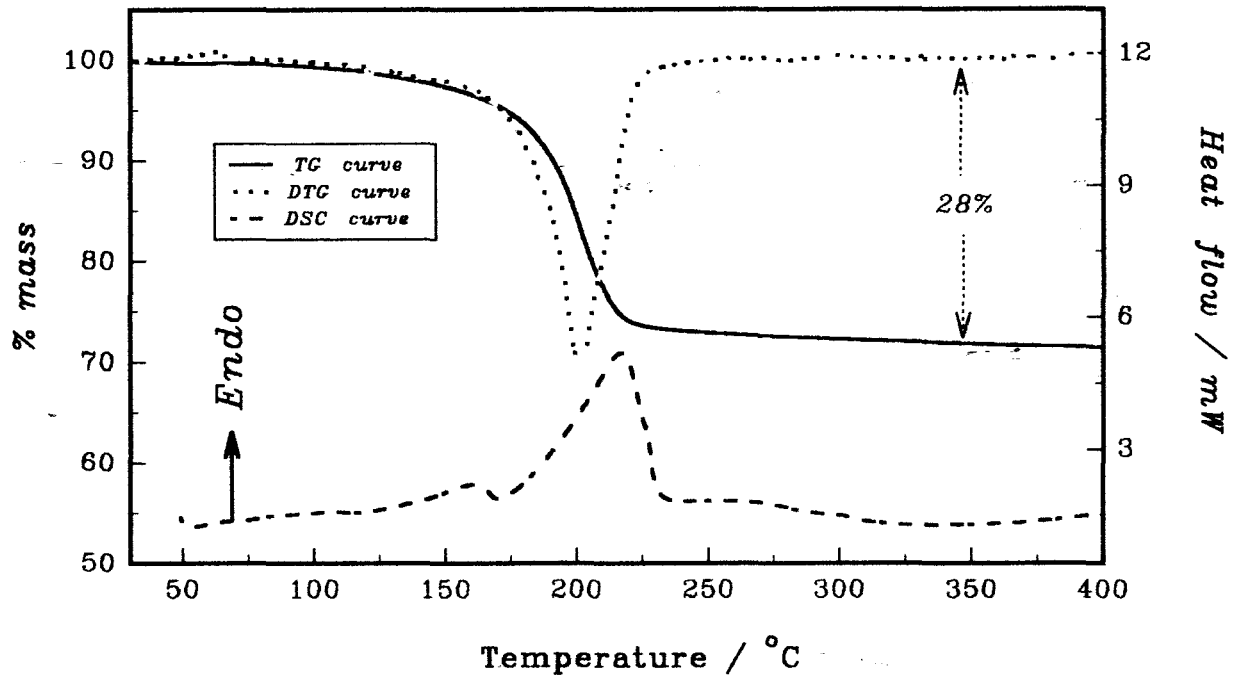

Figure 9.4.3: TG, DTG and DSC curves for $Ni_3(pa)_2Cl_6$ heated at 20°C min^{-1} in flowing N_2 .

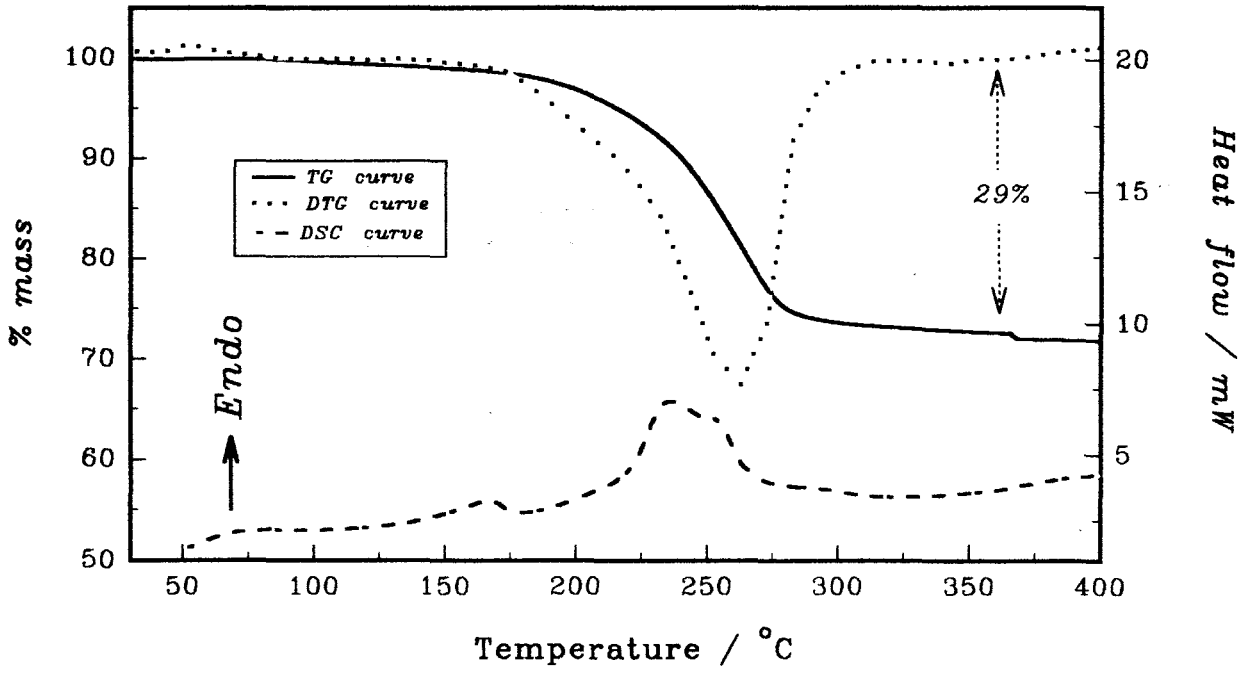

Figure 9.4.4: TG, DTG and DSC curves for $Ni_3(nef)_2Cl_6$ heated at 20°C min^{-1} in flowing N_2 .

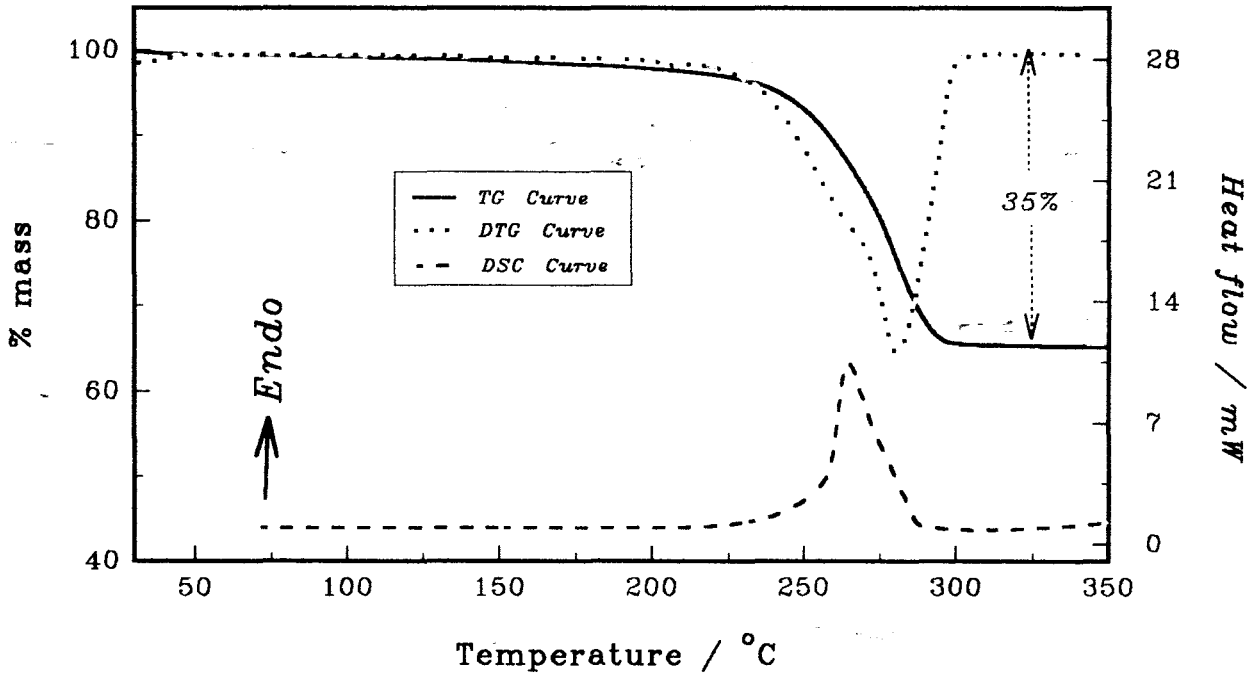

Figure 9.4.5 TG, DTG and DSC curves for $Ni_3(def)_2Cl_6$ heated at 20°C min^{-1} in flowing N_2 .

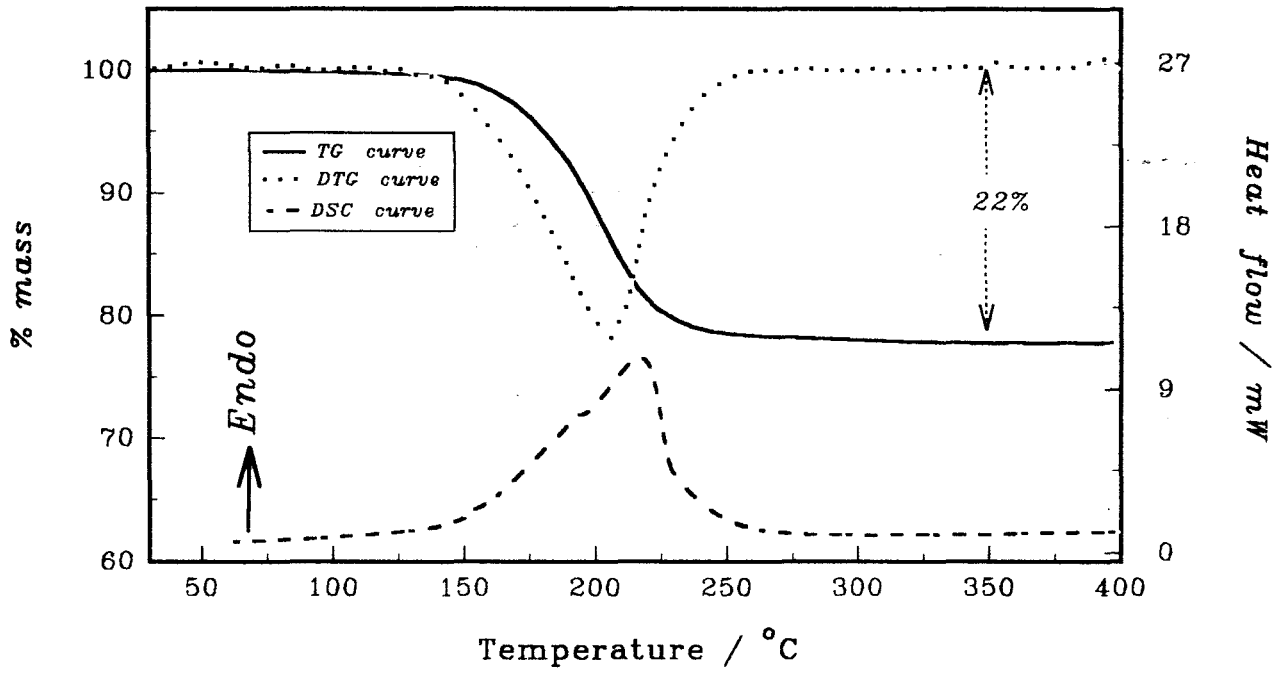

Figure 9.5.1: TG, DTG and DSC curves for $Ni_3(dmp)Cl_6$ heated at 20°C min^{-1} in flowing N_2 .

CHAPTER 10

KINETICS OF ISOTHERMAL DECOMPOSITION OF $NiLC\ell_2$ COMPLEXES

10.1 Introduction

The studies of decomposition stoichiometry reported in **Chapter 9** showed that in a nitrogen atmosphere the pseudooctahedral $NiLC\ell_2$ complexes decomposed in a single endothermic step

$$NiLC\ell_2(s) \rightarrow NiC\ell_2(s) + L(g)$$

The kinetics of the thermal decompositions of $NiLC\ell_2$, where L = N-methylformamide (*nmf*), N-methylacetamide (*nma*), or acetamide (*aa*), were studied by following the mass losses for the removal of L using isothermal TG. The onset temperatures of decomposition, determined from the non-isothermal DTG curves of the *nmf*, *aa* and *nma* complexes (see Figures **10.1.1a**, **10.2.1a** and **10.3.1a**), were used as a guide in choosing the isothermal reaction temperatures. The initial rapid heating rate to the selected isothermal reaction temperature was 200°C min^{-1}. Mass losses were converted to fractional reaction, α *versus* time data using

$$\alpha = (m_o - m)/(m_o - m_f) \qquad 10.1$$

where m_o = initial mass of sample, m = mass at time t and m_f = final mass. The first derivative of alpha with respect to time ($d\alpha/dt$) was calculated using a nine point Savitsky-Golay function [178].

10.2 Isothermal analysis

10.2.1 Methods of analysis

Kinetic models which gave acceptable descriptions of the isothermal results were established using several methods.

Rate ($\upsilon = d\alpha/dt$) *versus* time, and rate *versus* α plots were generated. Where necessary, a correction for the short "*warming-up*" period (t_o) required by the instrument to reach the isothermal reaction temperature was made, so that

$$t = t_e - t_o \quad \text{and} \qquad 10.2$$

$$\alpha = (\alpha_e - \alpha_o)/(1 - \alpha_o) \qquad 10.3$$

where α_e and t_e are the experimental values and $\alpha = \alpha_o$ at $t = t_o$. Comparison of the experimental plots of rate *versus* alpha (or time) with theoretical plots confirmed that the decompositions were mainly deceleratory. A secondary feature of the rate *versus* time data of the deceleratory (and sigmoid) group is the time $t_{max/2}$ taken for the rate to drop to half its maximum value. $t_{max/2}$ values estimated at a series of constant temperatures were used in Arrhenius-type plots, *i.e.* $\ell n(^1/t_{max/2})$ against $^1/T$, to determine the apparent activation energies of the reactions.

If a rate equation of simple reaction order

$$d\alpha/dt = kf(\alpha) = k(1 - \alpha)^n \qquad 10.4$$

applies, then when α is small, $(1 - \alpha) \approx 1$ and $(1 - \alpha)^n \approx 1$, so that

$$d\alpha/dt \approx k \qquad 10.5$$

Values of k estimated from slopes of the approximately linear initial portions of plots of α against time were used in the Arrhenius plots to evaluate E_a and A.

Alternatively, if equation (10.4) applies, a plot of ℓn(rate) against $\ell n(1 - \alpha)$ will be linear, with slope n (the apparent order of reaction), and intercept ℓn(k). This approach was used to test for applicability of the **R2** ($n = 0.50$), **R3** ($n = 0.67$) and **F1** ($n = 1.00$) models.

For an isokinetic process, if the times required to attain a series of α_i values at several different (isothermal) temperatures are determined, then it is possible to superimpose the plots of α_i against reduced-time obtained by dividing the actual time values by the respective times required to attain a specified percentage conversion, such as $t_{0.5}$ at 50% conversion, *i.e.* $t_{red.} = t/t_{0.5}$. Good agreement was obtained on plotting α_e against $t_{red.}$. The standard deviation of individual α_i values from the arithmetical mean (α_{mean}) was used to assess the isokinetic character of the reduced-time plots. The standard deviation (δ) is defined as

$$\delta = [\ \Sigma(\alpha_i - \alpha_{mean})^2 / s\ ]^{½} \qquad 10.6$$

where s is the number of experimental α_i data taken at a common value of $t/t_{0.5}$ for the calculation of α_{mean}.

Comparison of the experimental plots of α against $t_{red.}$ with theoretical curves allowed a limited number of kinetic functions to be identified as giving a close fit to the experimental results. The very slight differences in some functions (*e.g.* **R3** and **R2**) generally made it difficult to make an unambiguous choice of rate equation for the experimental data.

Values of $t_{0.5}$ estimated at several different (isothermal) temperatures were used in Arrhenius-type plots (*i.e.* $\ell n(^1/t_{0.5})$ against $^1/T$) to evaluate the apparent activation energies of the decompositions, without the necessity for identifying the kinetic model (refer to **§4.4.4**). The intercept includes $\ell n\{g(\alpha)\}$ and does not directly yield $\ell n(A)$.

Kinetic functions identified as providing the most reasonable fit of experimental values with theoretical ones on the basis of the plots of α *versus* $t_{red.}$ were subjected to a further screening, using the linearity of plots of $g(\alpha)$ against time. Assessment of the precision of the fit of data to the **R3**, **R2** and **F1** models is based on the standard error of the slope (s_b) and the correlation coefficient (r). Close similarity of the s_b and r values generally made it difficult to distinguish between applicability of the **R2** and **R3** models.

Rate coefficients calculated using the contracting geometry rate equations (Table **3.1**) were subsequently used in appropriate integrated expressions:

$$\alpha_{calc.} = 1 - [1 - (\tfrac{1}{2})kt]^2 \text{ , when } n = \tfrac{1}{2} \qquad 10.7$$

$$\alpha_{calc.} = 1 - [1 - (^2/_3)kt]^3 \text{ , when } n = {}^2/_3 \qquad 10.8$$

and $$\alpha_{calc.} = 1 - \exp(-kt) \text{ , when } n = 1 \qquad 10.9$$

to obtain calculated α *versus* time curves. Comparison of the calculated and experimental α against time curves often permitted a distinction between applicability of the **R2** and **R3** models.

Rate coefficients (k) calculated from the slopes of $g(\alpha)$ against time plots were used in Arrhenius plots to calculate the apparent activation energy (E_a) and the pre-exponential factor (**A**).

10.2.2 Plots of alpha against time

Figures **10.1.1b**, **10.2.1b** and **10.3.1b** illustrate the types of α against time plots obtained for the complexes with *nmf*, *aa* and *nma* (respectively) at different constant temperatures. The curves are initially approximately linear over an appreciable α range (*e.g.* $0.00 \leq \alpha \leq 0.35$). Equation (10.5) thus applies and $\alpha \approx kt$. Slopes of the linear portion of these plots were determined using the least squares fit, and the results are collected in Tables **10.1.1**, **10.2.1** and **10.3.1**. Figures **10.1.2a**, **10.2.2a** and **10.3.2a** show the Arrhenius plots constructed using these approximately zero-order rate coefficients (k) calculated over the most extensive α range found to give acceptable straight lines. The calculated apparent activation energies are given in Tables **10.1.2**, **10.2.2** and **10.3.2**.

10.2.3 Plots of alpha against reduced-time

The plots of α_e against $t_{red.}$ shown in Figures **10.1.3a**, **10.2.3a** and **10.3.3a** indicate that the reactions are isokinetic in the temperature ranges investigated. The arithmetic means (α_{mean}) were calculated at three different $t/t_{0.5}$ values and the standard deviations (δ) of α_i's from α_{mean} determined using equation (10.6). Results are shown in Tables **10.1.3**, **10.2.3** and **10.3.3**.

Examples of the experimental reduced-time plots, compared with theoretical curves for a selected number of kinetic expressions, are shown in Figures **10.1.4**, **10.2.4** and **10.3.4**. Plots of $g(\alpha)$ *versus* time were subsequently examined for only a selected number of kinetic functions (*i.e.* **R2**, **R3** and **F1**).

Plots of $\ell n(^1/t_{0.5})$ against $^1/T$ are shown in Figures **10.1.2b**, **10.2.2b** and **10.3.2b**. The apparent activation energies calculated are included in Tables **10.1.2**, **10.2.2** and **10.3.2**.

10.2.4 Testing for the deceleratory models (R2, R3 and F1)

Experimental α *versus* time data were substituted into the contracting-area (**R2**), contracting-volume (**R3**) or first-order (**F1**) equations (see Table **3.1**). The plots in Figures **10.1.5**, **10.2.5** and **10.3.5** illustrate the typical dependencies of $g(\alpha)$ on the time for each of the three complexes, and also show the α range over which the plots are approximately linear. The linearity of plots over the ranges $0.00 \leq \alpha \leq 0.85$ and $0.00 \leq \alpha \leq 0.95$ was used to assess the precision of the fit of data. The phase boundary controlled models yielded approximately linear plots over the most extensive

α ranges (Tables **10.1.4**, **10.2.4** and **10.3.4**). Figures **10.1.2c-d**, **10.2.2c-d** and **10.3.2c-e** show the Arrhenius plots constructed using k values from the acceptable $g(\alpha)$ functions. The apparent activation energies and the pre-exponential factors are collected in Tables **10.1.2**, **10.2.2** and **10.3.2**.

With the form of $g(\alpha)$ established, values of k, determined using the **R2**, **R3** or **F1** models over the most extensive α range found to give acceptable straight lines, were substituted into either equation (10.7), (10.8) or (10.9) and the corresponding values of α were calculated for the possible orders of unity, one-half or two-thirds. Plots of $\alpha_{calc.}$ and α_e *versus* time are shown in Figures **10.1.6**, **10.2.6** and **10.3.6** for the *nmf*, *aa* and *nma* complexes, respectively.

10.2.5 Plots of rate against α and rate against time

Plots of rate ($\upsilon = d\alpha/dt$) *versus* time and rate *versus* alpha are shown in Figures **10.1.7**, **10.2.7** and **10.3.7**. In general, $\upsilon = \upsilon_{max}$ at $t = 0$. Estimated values of $t_{max/2}$ are plotted as $\ell n\{^1/(t_{max/2})\}$ against $^1/T$ (Figures **10.1.2e**, **10.2.2e** and **10.3.2f**) and the calculated apparent activation energies are included in Tables **10.1.2**, **10.2.2** and **10.3.2**. The intercept includes $\ell n\{g(\alpha)\}$ and does not directly yield the pre-exponential factor.

Figures **10.1.8**, **10.2.8** and **10.3.8** show the plots of ℓn(rate) against $\ell n(1 - \alpha)$ for the *nmf*, *aa* and *nma* complexes, respectively. Results of the application of this test are collected in Tables **10.1.5**, **10.2.5** and **10.3.5**.

10.2.6 Use of the empirical (B2) expression

Analysis of isothermal TG rate data for the Ni(*nma*)Cℓ_2 complex was also performed using the empirical (**B2**) expression (refer to Chapter **3**, §**3.3**). Equation (3.26) was written in suitable form to yield a straight line plot. That is

$$(1 - \upsilon_r)^{1/b} = kt \qquad 10.10$$

or

$$\ell n(1 - \upsilon_r) = b\,\ell n(t) + b\,\ell n(k) \qquad 3.27$$

Typical plots of $\ell n(1 - \upsilon_r)$ against $\ell n(t)$ are shown in Figure **10.3.9a-b**, and the corresponding values of b calculated over $0.05 \leq \alpha \leq 0.85$ are given in Table **10.3.7** of Appendix **IV**. Rate coefficients from plots of $(1 - \upsilon_r)^{1/b}$ against time, using $b = 2$, are shown in Table **10.3.6**. Figure **10.3.2g** shows a typical Arrhenius plot constructed using k values over $0.05 \leq \alpha \leq 0.85$. The apparent activation energies and

the pre-exponential factors are collected in Table **10.3.2.**

Table 10.1.1: Approximate zero-order rate coefficients and $^1/t_{0.5}$ values for the decomposition of Ni(*nmf*)Cℓ_2 at different constant temperatures.

	α-range: 0.00 - 0.25		α-range: 0.00 - 0.30		10^3 s / $t_{0.5}$
T /°C	k / 10^{-3} s^{-1}	r	k / 10^{-3} s^{-1}	r	
245	3.548 ± 0.001	0.9999	3.530 ± 0.002	0.9998	6.510
243	4.116 ± 0.006	0.9990	4.057 ± 0.007	0.9983	7.214
240	4.099 ± 0.010	0.9989	4.031 ± 0.011	0.9976	6.994
238	2.276 ± 0.003	0.9993	2.259 ± 0.002	0.9992	4.139
235	2.955 ± 0.002	0.9999	2.938 ± 0.003	0.9998	5.411
233	2.247 ± 0.003	0.9995	2.223 ± 0.004	0.9991	4.033
230	2.419 ± 0.003	0.9995	2.394 ± 0.003	0.9992	4.410
228	1.324 ± 0.002	0.9993	1.308 ± 0.002	0.9989	2.344
225	1.894 ± 0.003	0.9995	1.873 ± 0.003	0.9991	3.367
223	0.829 ± 0.001	0.9990	0.817 ± 0.001	0.9983	1.458
220	1.147 ± 0.002	0.9989	1.130 ± 0.002	0.9982	1.994
218	1.101 ± 0.002	0.9988	1.083 ± 0.003	0.9980	1.890
215	0.468 ± 0.001	0.9967	0.457 ± 0.001	0.9952	0.784
212	0.457 ± 0.001	0.9985	0.434 ± 0.001	0.9986	0.784
210	0.624 ± 0.001	0.9982	0.612 ± 0.002	0.9971	1.047
208	0.326 ± 0.000	0.9986	0.321 ± 0.000	0.9981	0.567
205	0.335 ± 0.001	0.9985	0.331 ± 0.001	0.9981	0.590
200	0.223 ± 0.000	0.9990	0.220 ± 0.000	0.9987	0.395

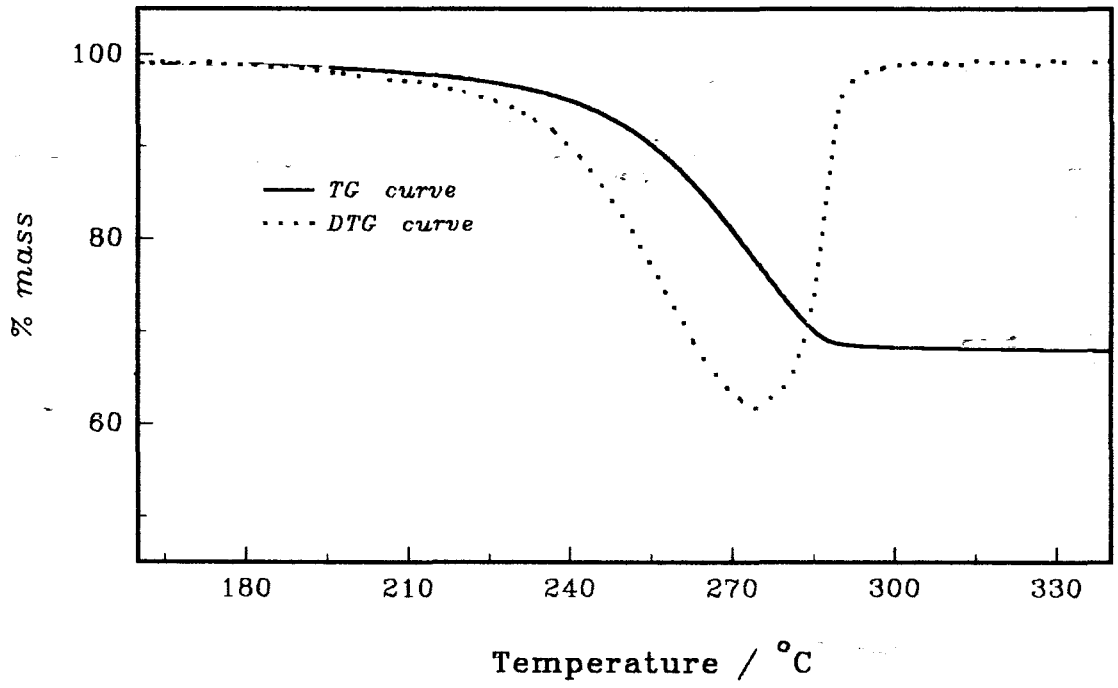

Figure 10.1.1a : TG and DTG curves for the decomposition of $Ni(nmf)Cl_2$ heated at $20^{\circ}C\ min^{-1}$ in flowing N_2 .

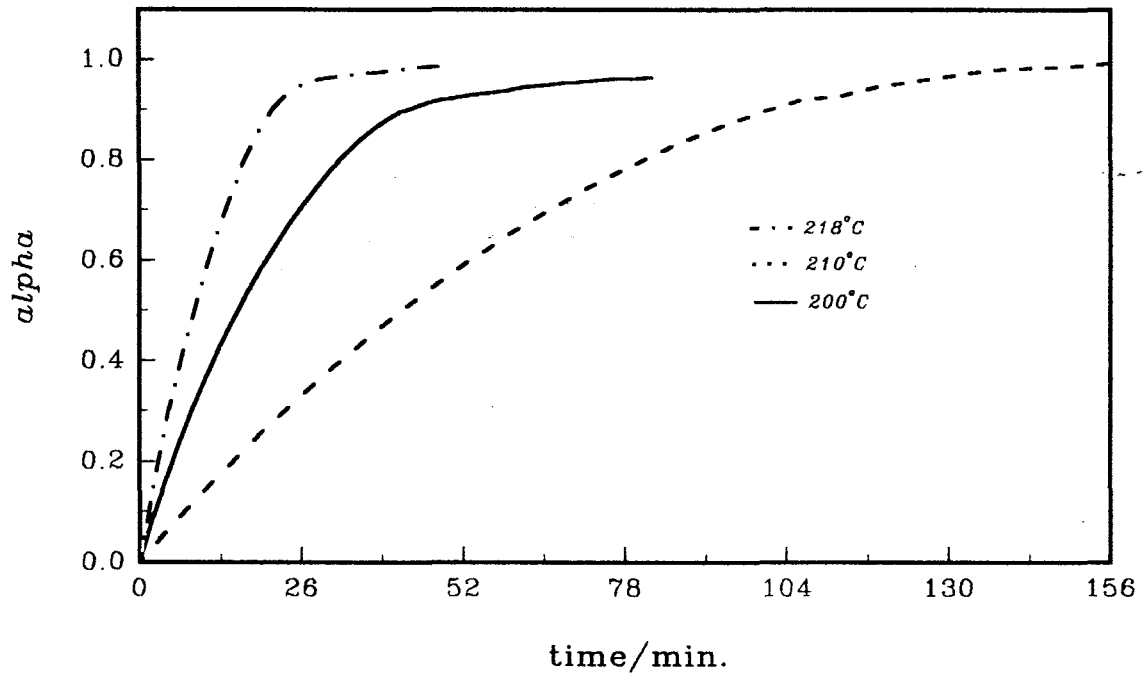

Figure 10.1.1b: Alpha versus time plots for the decomposition of $Ni(nmf)Cl_2$ at $218^{\circ}C$, $210^{\circ}C$, and $200^{\circ}C$.

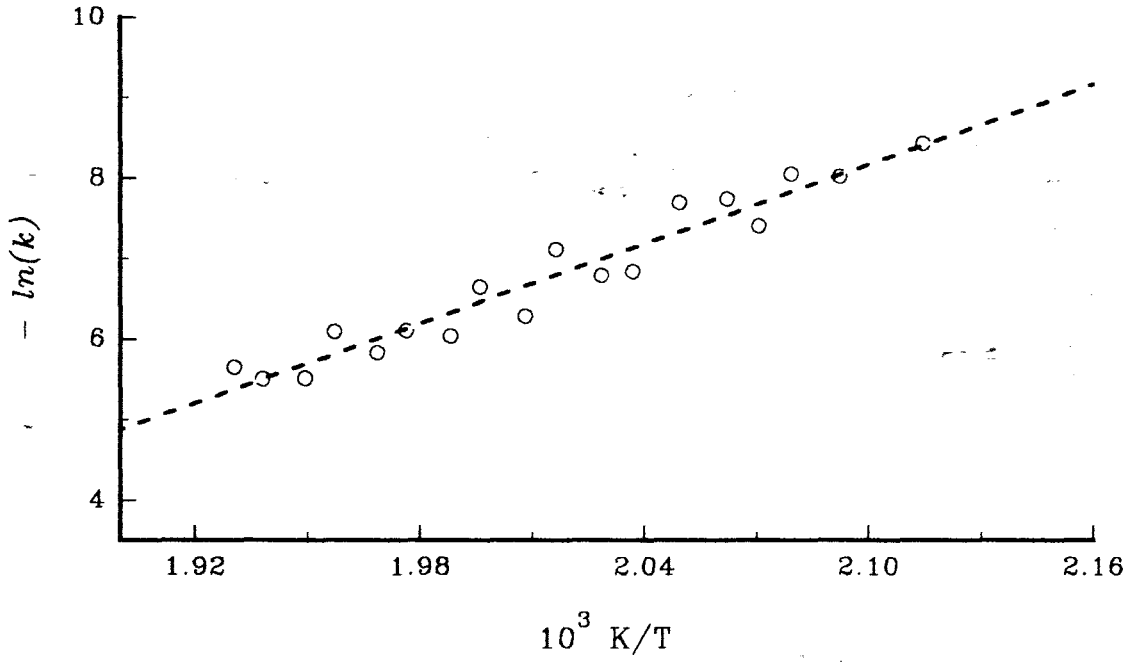

Figure 10.1.2a: Arrhenius plot for the decomposition of $Ni(nmf)Cl_2$ using approximate zero-order rate coefficients for $0.00 \leq \alpha \leq 0.30$.

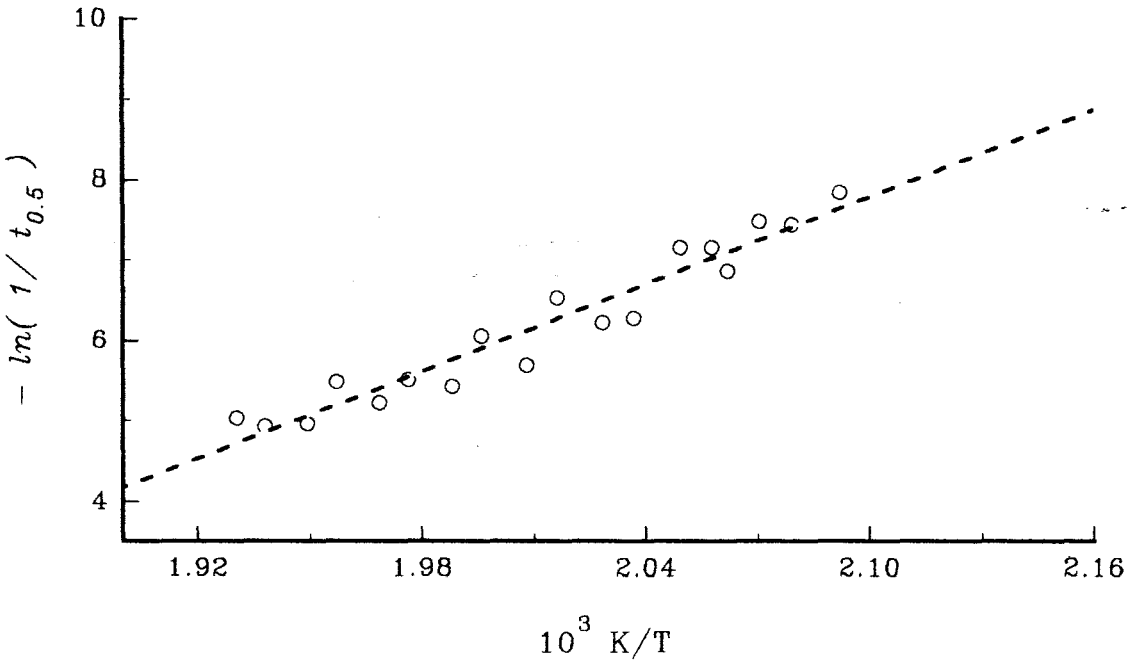

Figure 10.1.2b: Arrhenius plot for the decomposition of $Ni(nmf)Cl_2$ using rate coefficients based on $1/t_{0.5}$.

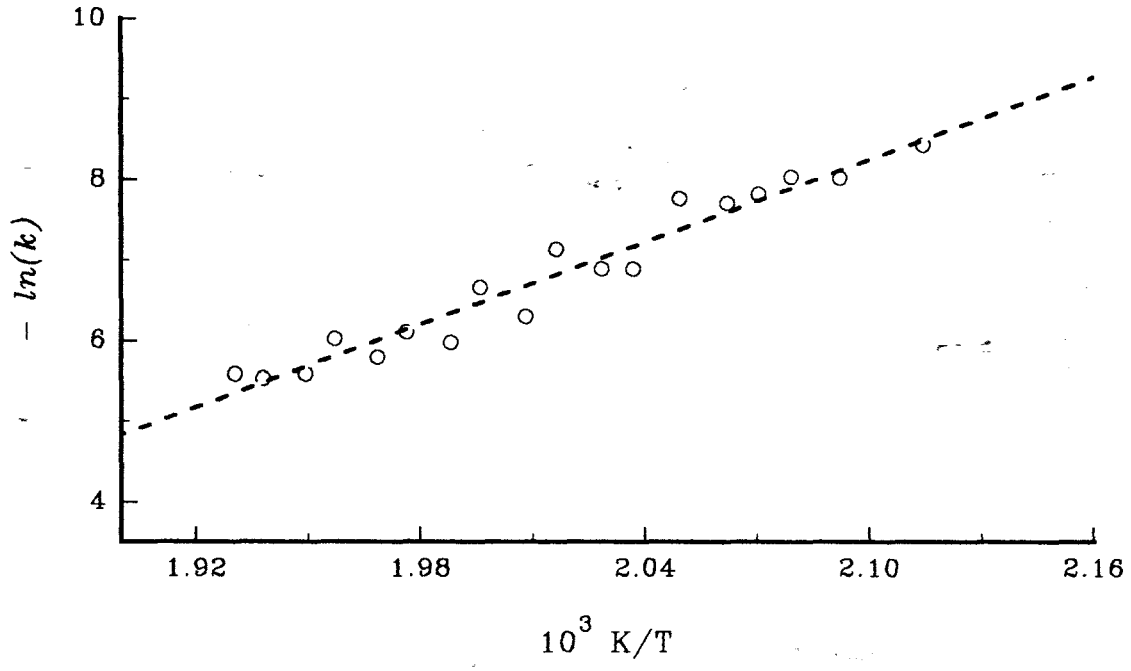

Figure 10.1.2c: Arrhenius plot for the decomposition of $Ni(nmf)Cl_2$ using rate coefficients from the R2 equation for $0.00 \leq \alpha \leq 0.95$.

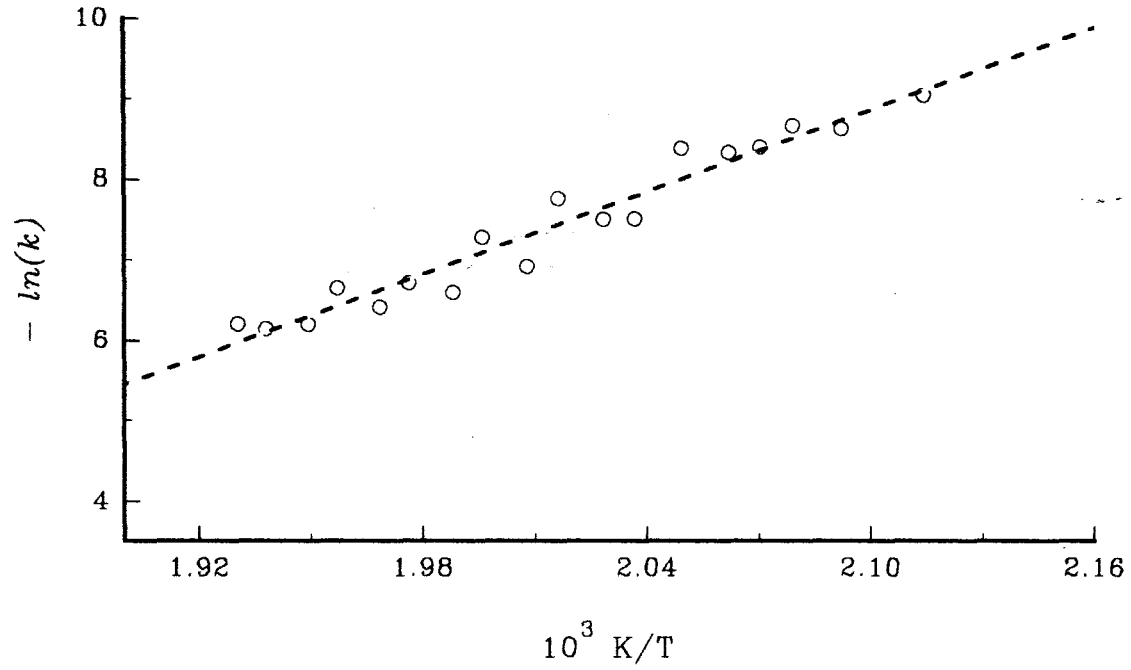

Figure 10.1.2d: Arrhenius plot for the decomposition of $Ni(nmf)Cl_2$ using rate coefficients from the R3 equation for $0.00 \leq \alpha \leq 0.95$.

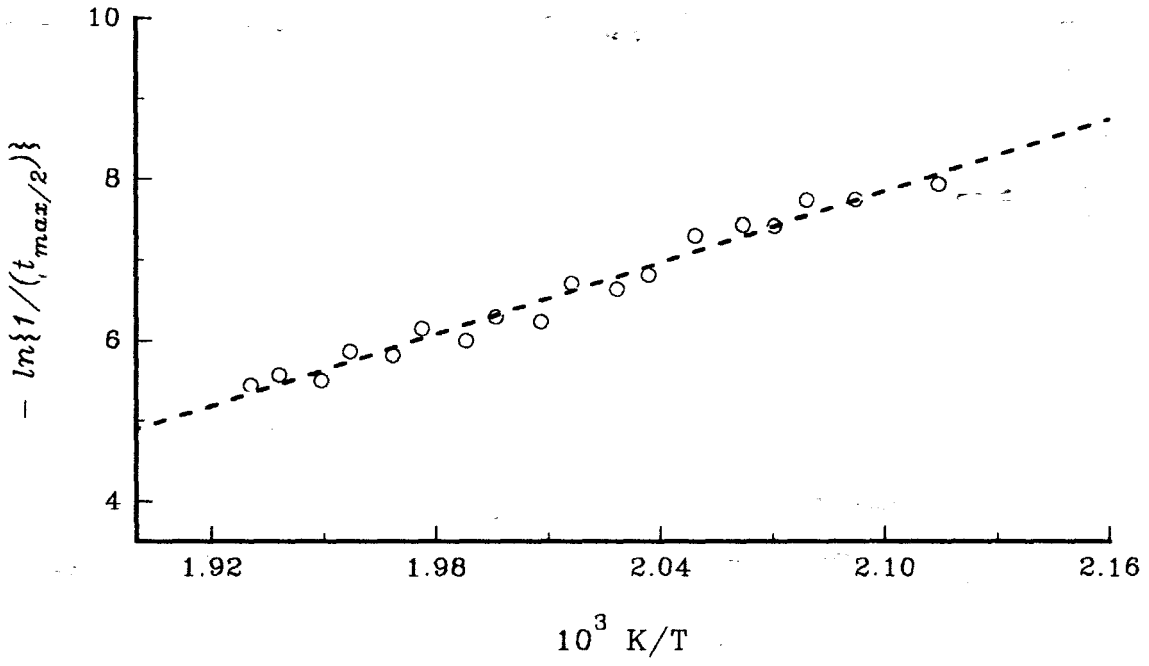

Figure 10.1.2e: Arrhenius plot for the decomposition of $Ni(nmf)Cl_2$ using rate coefficients based on $1/(t_{max/2})$

Table 10.1.2: Arrhenius parameters for the isothermal decomposition of Ni(*nmf*)Cℓ_2 calculated using different methods of kinetic analysis.

Models	α-range	E_a / kJ mol^{-1}	r	ℓn(A/s^{-1})*
Zero-order	0.00 - 0.30	137 ± 9	0.9341	26.5 ± 0.1
	0.00 - 0.25	136 ± 9	0.9344	26.3 ± 0.1
Half-lives	-	138 ± 9	0.9364	(27.4 ± 0.1)
R2 model	0.00 - 0.95	142 ± 8	0.9468	27.7 ± 0.1
	0.00 - 0.90	140 ± 8	0.9403	27.2 ± 0.1
	0.00 - 0.85	140 ± 8	0.9388	27.2 ± 0.1
R3 model	0.00 - 0.95	142 ± 8	0.9456	27.0 ± 0.1
	0.00 - 0.90	140 ± 8	0.9408	26.5 ± 0.1
	0.00 - 0.85	140 ± 8	0.9387	26.5 ± 0.1
υ_{max} **based**	-	124 ± 5	0.9711	(23.3 ± 0.1)

* the values in parentheses include ℓn{g(α)}

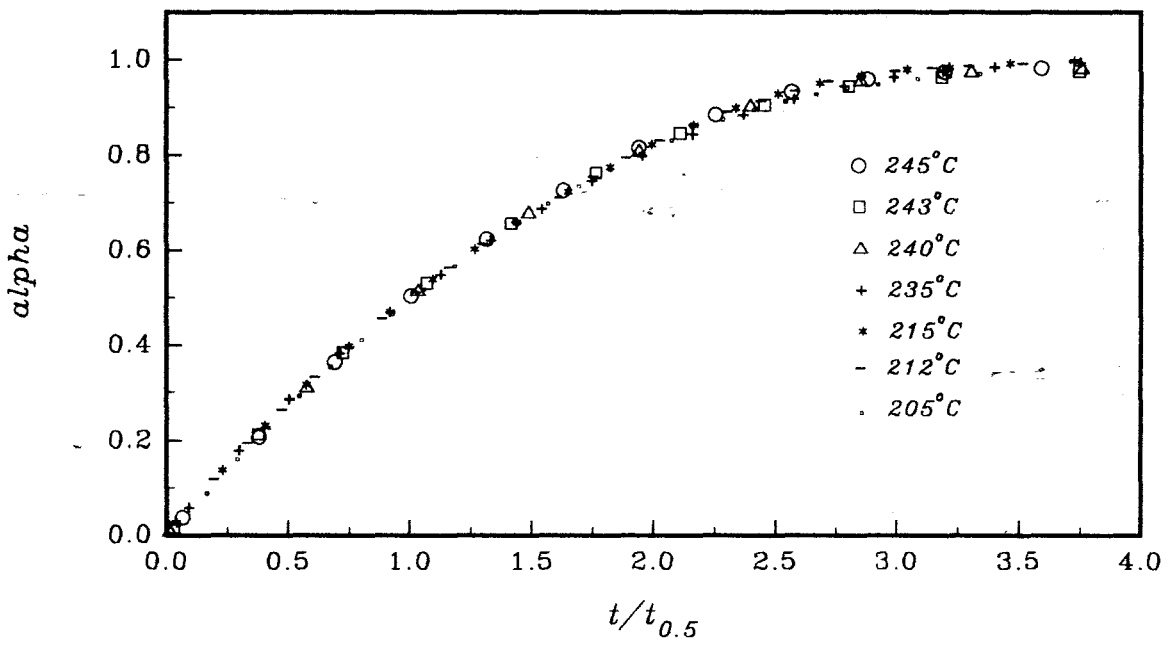

Figure 10.1.3a: Comparison of reduced–time plots for the decomposition of $Ni(nmf)Cl_2$ at a series of constant temperatures (see Figure 10.1.3b of Appendix II for more plots).

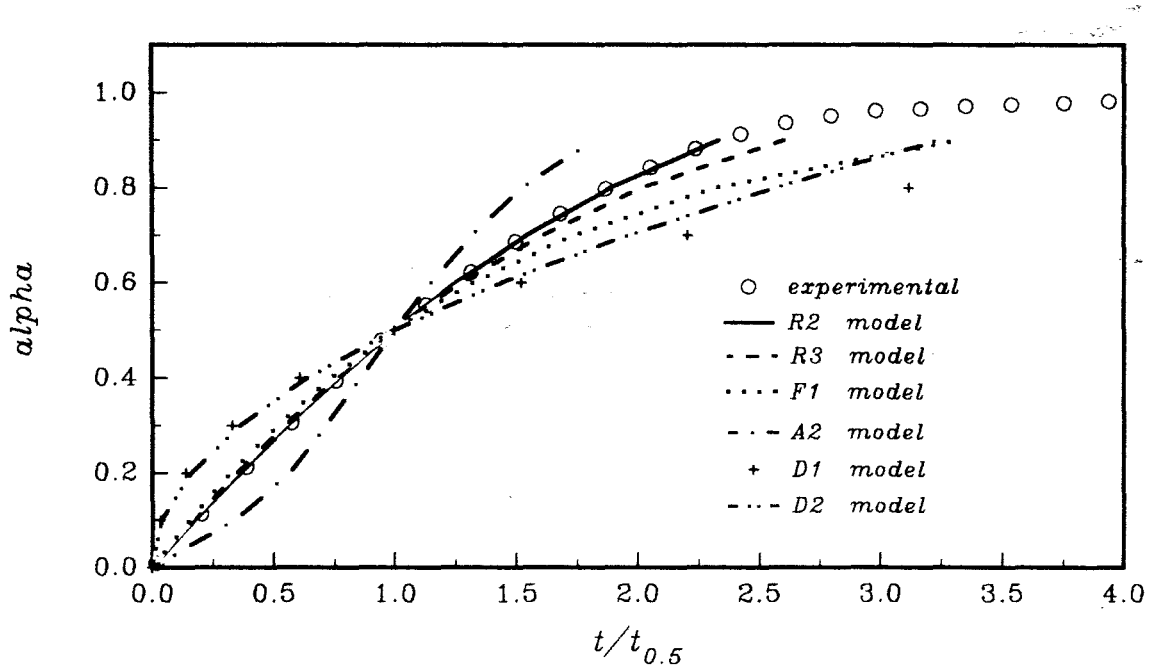

Figure 10.1.4a: Reduced–time plots for the decomposition of $Ni(nmf)Cl_2$ at 230°C, compared with calculated plots for various kinetic models (see also Figure 10.1.4b of Appendix II).

Table 10.1.3: The α_i, α_{mean} and the standard deviation (δ) of α_i values used to confirm the isokinetic behaviour of the decomposition of Ni(*nmf*)Cℓ_2 at different constant temperatures. The test was made using α_i taken at three distinct $t/t_{0.5}$ values of 0.5, 2.0 or 3.5.

T / °C	α at $t/t_{0.5} = 0.5$	α at $t/t_{0.5} = 2.0$	α at $t/t_{0.5} = 3.5$
245	0.270	0.828	0.980
243	0.276	0.821	0.971
240	0.279	0.811	0.972
238	0.271	0.833	0.992
235	0.271	0.821	0.978
233	0.271	0.823	0.973
230	0.270	0.830	0.975
228	0.274	0.811	0.982
225	0.273	0.813	0.976
223	0.275	0.811	0.986
220	0.279	0.807	0.960
218	0.280	0.818	0.964
215	0.283	0.810	0.990
212	0.279	0.823	0.993
210	0.284	0.795	0.933
208	0.278	0.824	0.979
205	0.276	0.821	0.984
200	0.273	0.818	0.988
α_{mean} =	**0.276**	**0.818**	**0.976**
δ =	**0.004 ± 0.001**	**0.009 ± 0.002**	**0.011 ± 0.003**

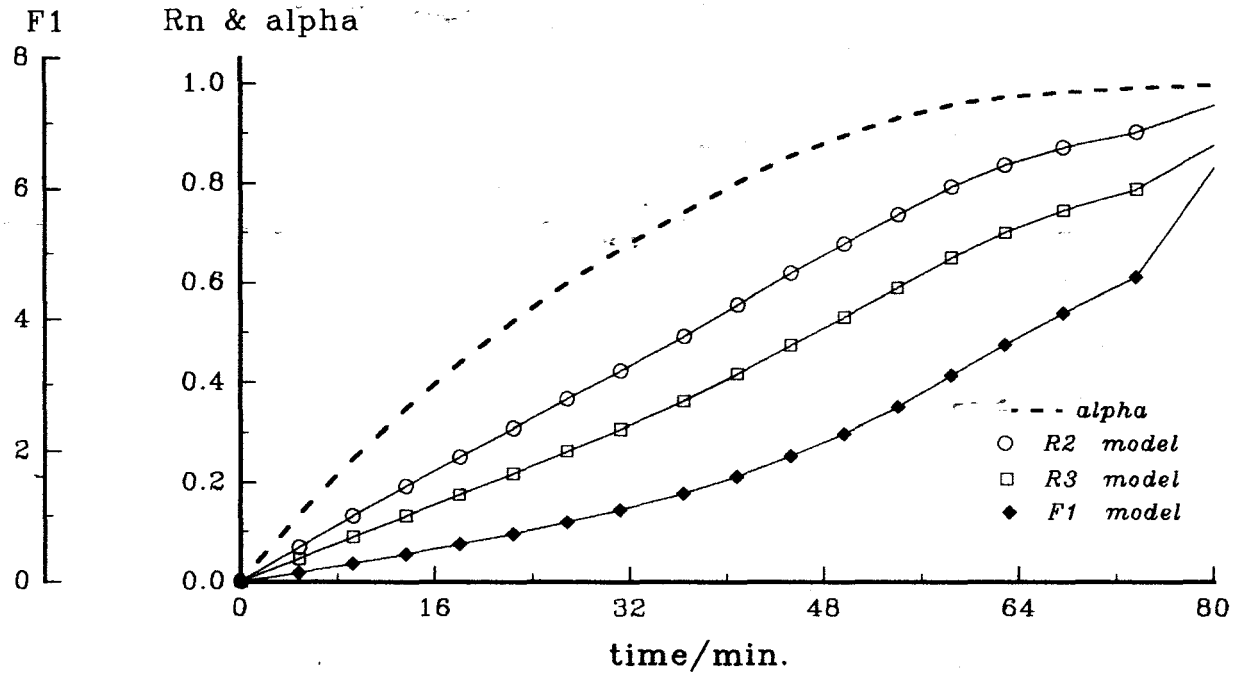

Figure 10.1.5a: Plots of g(α) versus time for the decomposition of $Ni(nmf)Cl_2$ at 212°C. The α–time curve is included to show the range of α over which g(α) is approximately linear (see also Figures 10.1.5b–r of Appendix II).

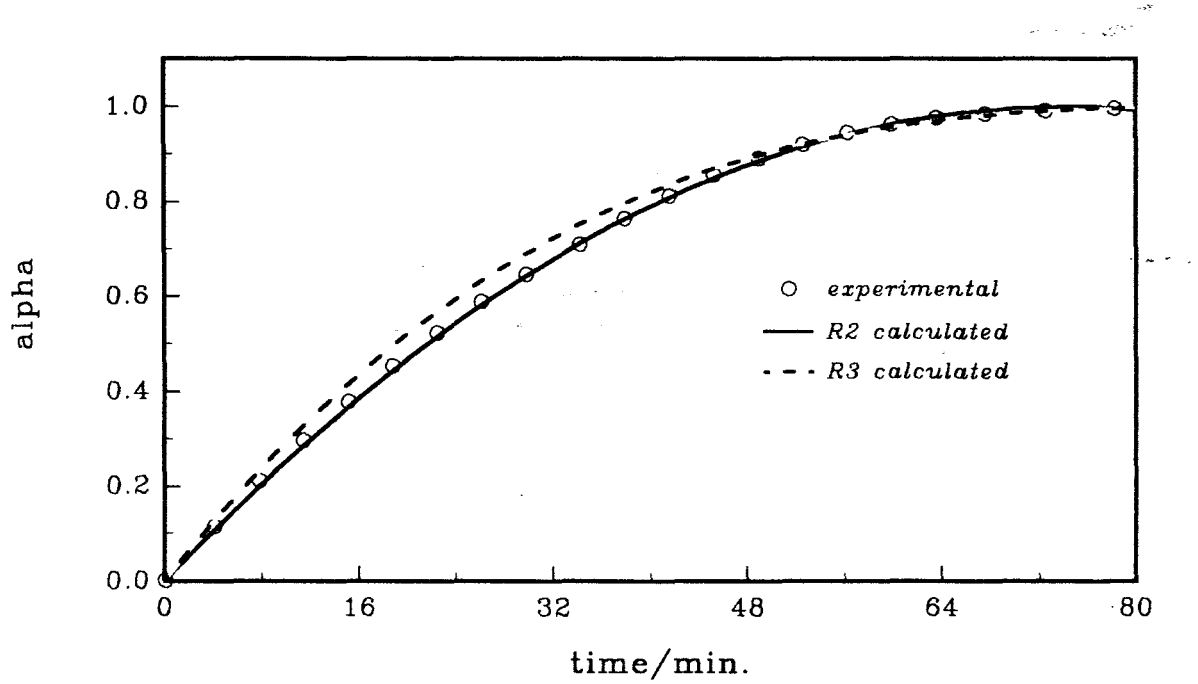

Figure 10.1.6a: Plots of $\alpha_{calc.}$ versus time using the R2 and R3 models, compared with α_e versus time data for the decomposition of $Ni(nmf)Cl_2$ at 212°C (see also Figures 10.1.6b–r of Appendix II).

Table 10.1.4: Rate coefficients for the decomposition of Ni(*nmf*)Cℓ_2 at different constant temperatures calculated using the **R2** or **R3** rate expression over $0.00 \leq \alpha \leq 0.95$.#

	R2 model		**R3 model**	
T / °C	k / 10^{-3} s^{-1}	r	k / 10^{-3} s^{-1}	r
245	3.774 ± 0.003	0.9996	4.559 ± 0.008	0.9979
243	3.980 ± 0.007	0.9980	4.841 ± 0.005	0.9992
240	3.773 ± 0.004	0.9982	4.590 ± 0.006	0.9994
238	2.430 ± 0.001	0.9998	2.930 ± 0.005	0.9974
235	3.064 ± 0.004	0.9994	3.719 ± 0.007	0.9984
233	2.252 ± 0.005	0.9982	2.737 ± 0.004	0.9991
230	2.542 ± 0.003	0.9991	3.082 ± 0.006	0.9983
228	1.281 ± 0.002	0.9990	1.550 ± 0.002	0.9991
225	1.850 ± 0.003	0.9989	2.242 ± 0.003	0.9991
223	0.798 ± 0.001	0.9991	0.963 ± 0.001	0.9990
220	1.020 ± 0.003	0.9938	1.252 ± 0.002	0.9988
218	1.022 ± 0.003	0.9970	1.241 ± 0.002	0.9991
215	0.426 ± 0.000	0.9995	0.515 ± 0.001	0.9983
212	0.451 ± 0.000	0.9999	0.543 ± 0.001	0.9958
210	0.404 ± 0.003	0.9452	0.506 ± 0.003	0.9650
208	0.326 ± 0.000	0.9999	0.389 ± 0.001	0.9973
205	0.331 ± 0.000	0.9991	0.402 ± 0.000	0.9987
200	0.219 ± 0.000	0.9984	0.266 ± 0.000	0.9987

refer to Appendix II for the results of the other α ranges tested.

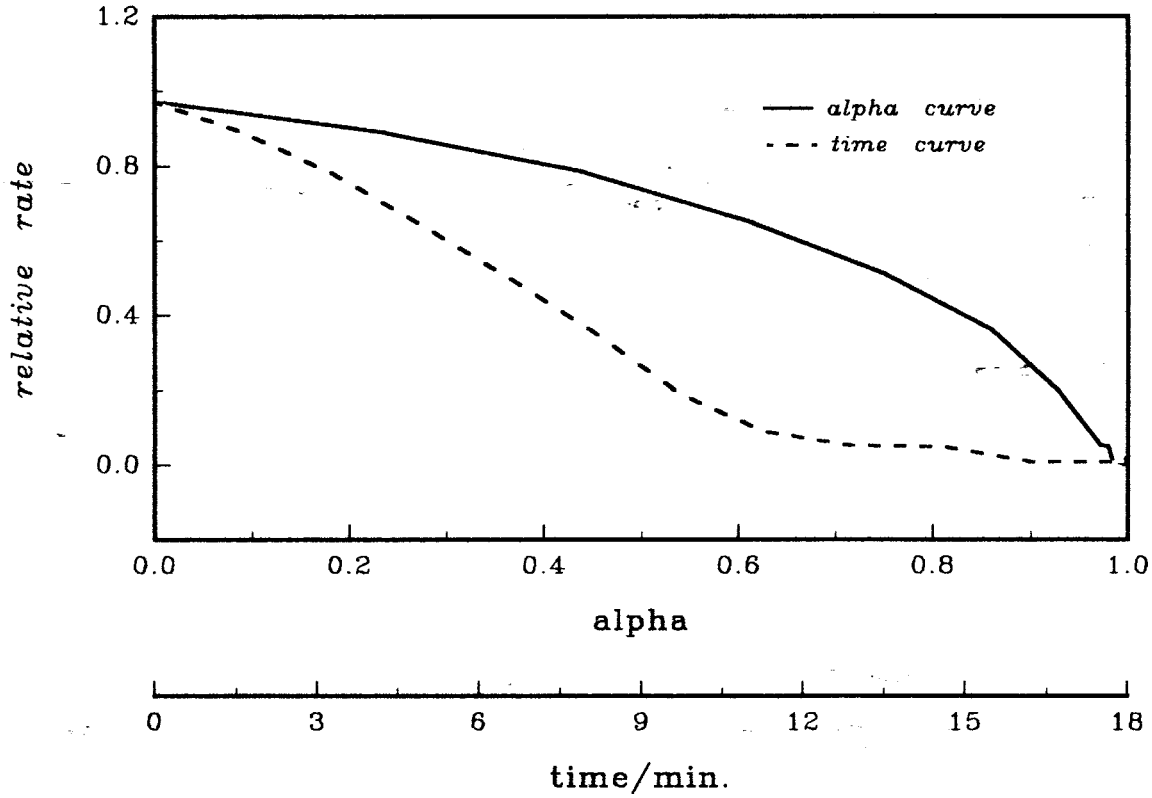

Figure 10.1.7a: Plots of rate versus alpha and rate versus time for the decomposition of $Ni(nmf)Cl_2$ at 230°C (see also Figures 10.1.7b–r of Appendix II).

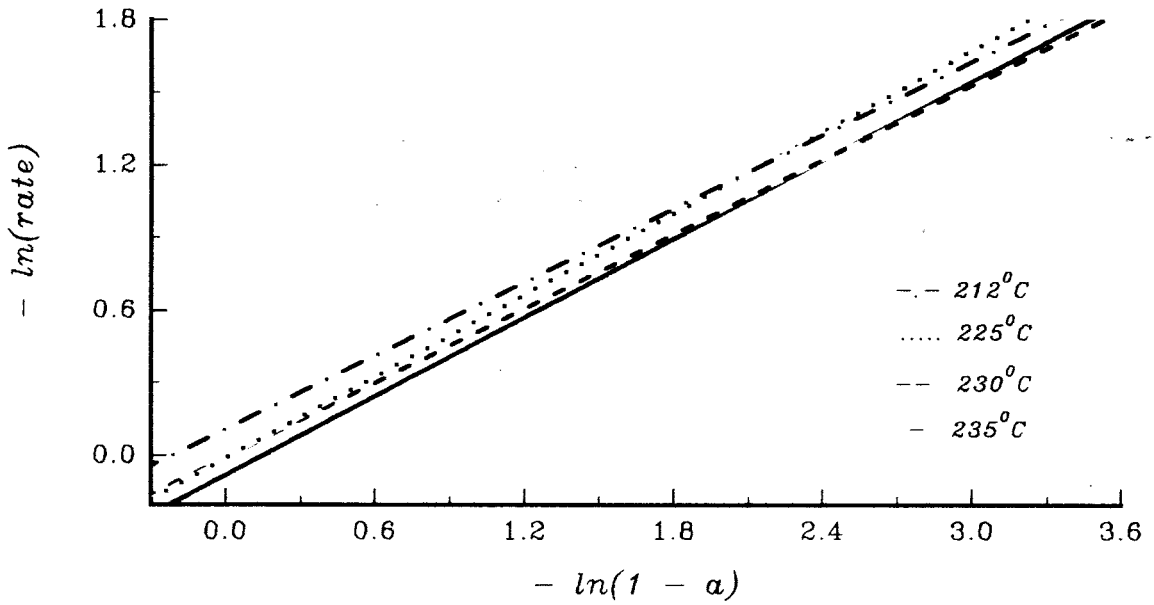

Figure 10.1.8a: Regression lines of ln(rate) versus $\ln(1 - \alpha)$ for the isothermal decomposition of $Ni(nmf)Cl_2$ (see also Figure 10.1.8b of Appendix II).

Table 10.1.5: Kinetic data for the decomposition of Ni(*nmf*)Cℓ_2 at different constant temperatures: (i) $t_{max/2}$, estimated from the rate versus time curves and used to obtain E_a from a plot of $\ell n\{^1/(t_{max/2})\}$ against $^1/T$; (ii) *n*, the apparent order obtained from plots of ℓn(rate) against $\ell n(1 - \alpha)$ over $0.03 \leq \alpha \leq 0.90$.

	Plots of rate *versus* time		Plots of ℓn(rate) *versus* $\ell n(1 - \alpha)$	
T / °C	10^3 s /$(t_{max/2})$	$-\ell n\{^1/(t_{max/2})\}$	order *n*	r
245	4.352	5.437	0.577 ± 0.005	0.9436
243	3.805	5.573	0.696 ± 0.010	0.8750
240	4.105	5.497	0.668 ± 0.006	0.9647
238	2.854	5.861	0.554 ± 0.005	0.9275
235	2.987	5.815	0.583 ± 0.004	0.9855
233	2.361	6.149	0.667 ± 0.009	0.9320
230	2.480	6.002	0.623 ± 0.005	0.9625
228	1.840	6.300	0.603 ± 0.003	0.9873
225	1.952	6.241	0.621 ± 0.004	0.9838
223	1.217	6.713	0.616 ± 0.006	0.9021
220	1.302	6.644	0.617 ± 0.004	0.9824
218	1.097	6.817	0.731 ± 0.009	0.9384
215	0.669	7.310	0.581 ± 0.006	0.9221
212	0.585	7.446	0.510 ± 0.004	0.9651
210	0.597	7.425	0.685 ± 0.004	0.9840
208	0.435	7.740	0.545 ± 0.005	0.9358
205	0.432	7.750	0.636 ± 0.006	0.9378
200	0.358	7.938	0.562 ± 0.009	0.8723

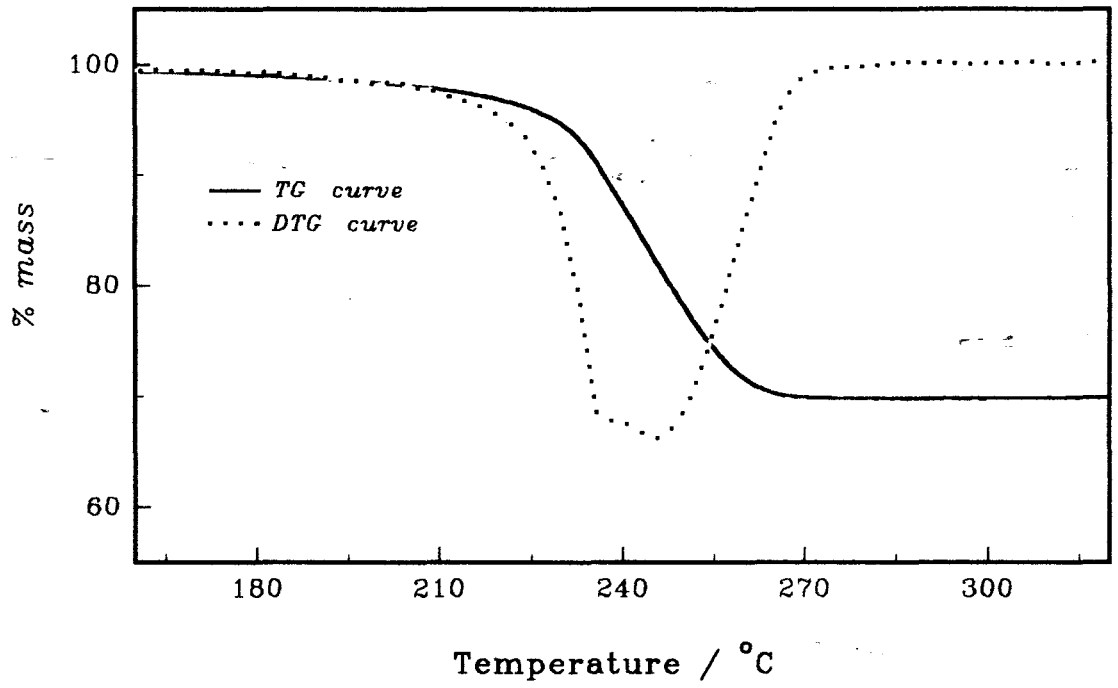

Figure 10.2.1a: TG and DTG curves for the decomposition of $Ni(aa)Cl_2$ heated at 20°C min^{-1} in flowing N_2 .

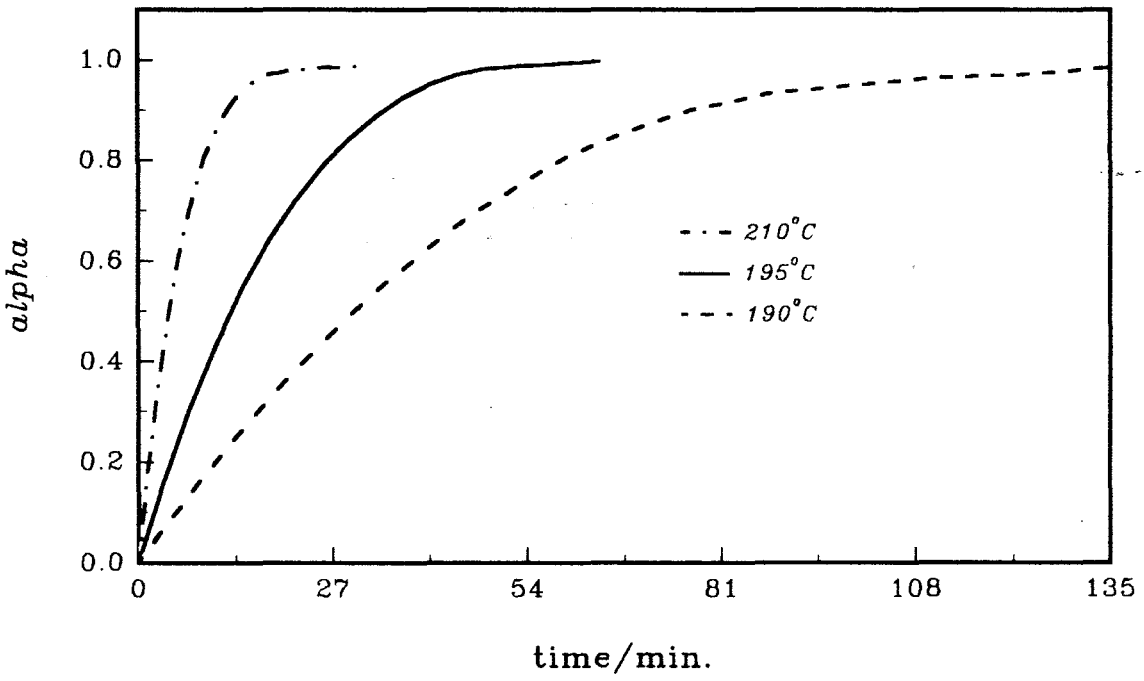

Figuire 10.2.1b: Alpha versus time plots for the decomposition of $Ni(aa)Cl_2$ at 210°C, 195°C and 190°C .

Table 10.2.1: Approximate zero-order rate coefficients and $^1/t_{0.5}$ values for the decomposition of Ni(*aa*)Cℓ_2 at different constant temperatures.

	α-range: 0.00 - 0.30		α-range: 0.00 - 0.33		10^3 s / $t_{0.5}$
T /°C	k / 10^{-3} s^{-1}	r	k /10^{-3} s^{-1}	r	
235	13.144 ± 0.044	0.9972	13.000 ± 0.046	0.9966	22.709
230	6.737 ± 0.017	0.9981	6.682 ± 0.017	0.9977	11.904
228	4.695 ± 0.015	0.9964	4.650 ± 0.015	0.9962	8.333
225	7.149 ± 0.035	0.9954	7.091 ± 0.030	0.9958	12.255
223	5.429 ± 0.020	0.9969	5.350 ± 0.021	0.9975	9.194
220	3.050 ± 0.005	0.9986	3.027 ± 0.005	0.9983	5.434
218	2.539 ± 0.007	0.9971	2.513 ± 0.007	0.9966	4.433
215	1.347 ± 0.002	0.9983	1.333 ± 0.003	0.9976	2.385
213	1.428 ± 0.004	0.9961	1.407 ± 0.005	0.9948	2.131
210	2.161 ± 0.003	0.9991	2.145 ± 0.004	0.9988	3.858
208	1.055 ± 0.003	0.9963	1.044 ± 0.003	0.9961	1.832
205	1.580 ± 0.002	0.9996	1.571 ± 0.002	0.9993	2.841
203	0.762 ± 0.001	0.9984	0.756 ± 0.001	0.9980	1.361
200	1.165 ± 0.004	0.9987	1.153 ± 0.004	0.9980	2.058
195	0.723 ± 0.001	0.9988	0.717 ± 0.001	0.9984	1.284
193	0.257 ± 0.000	0.9999	0.256 ± 0.000	0.9998	0.575
190	0.309 ± 0.001	0.9979	0.306 ± 0.001	0.9977	0.558
190*	0.383 ± 0.001	0.9991	0.380 ± 0.001	0.9986	0.681

* run in replicate.

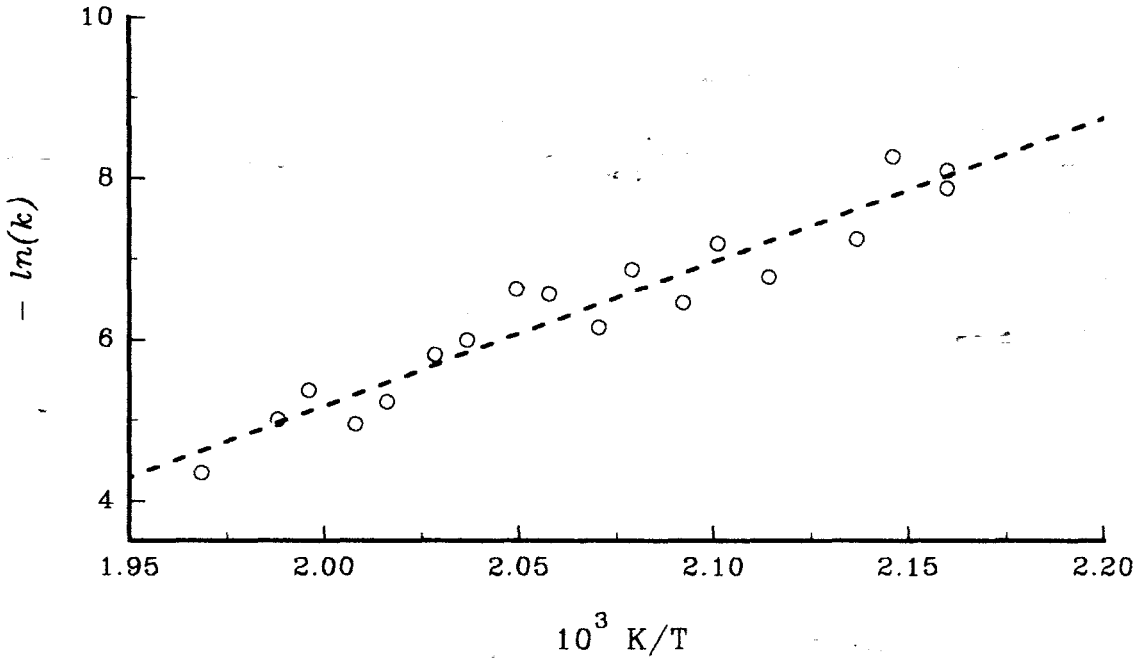

Figure 10.2.2a: Arrhenius plot for the decomposition of $Ni(aa)Cl_2$ using approximate zero-order rate coefficients for $0.00 \leq \alpha \leq 0.33$.

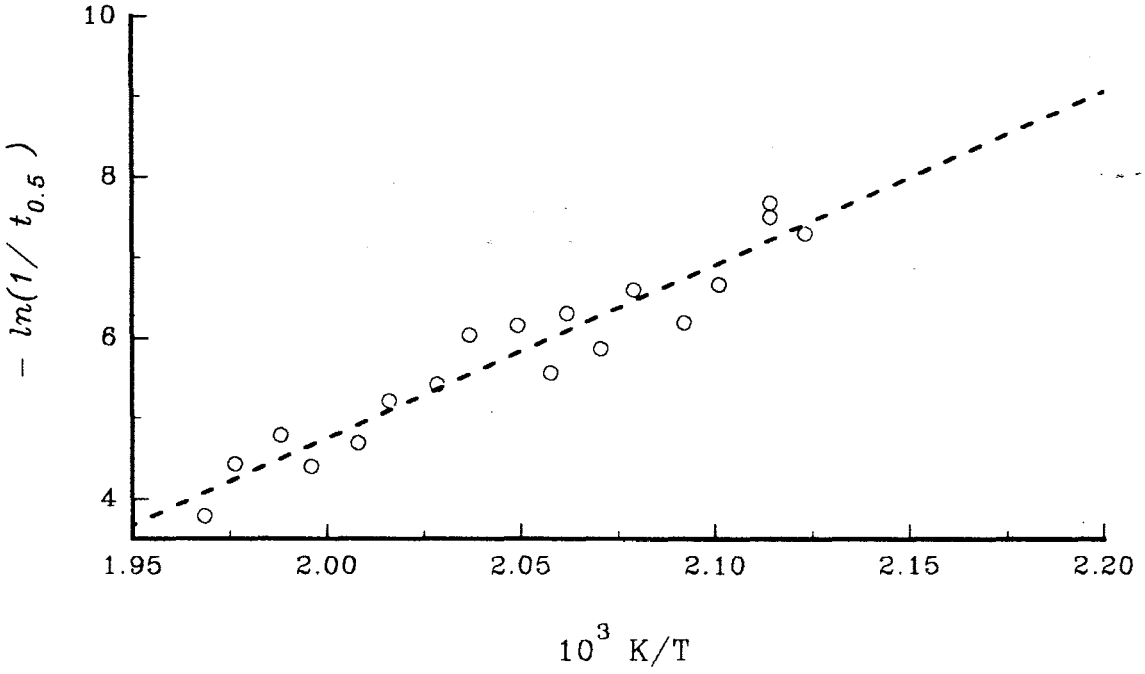

Figure 10.2.2b: Arrhenius plot for the decomposition of $Ni(aa)Cl_2$ using rate coefficients based on $1/t_{0.5}$.

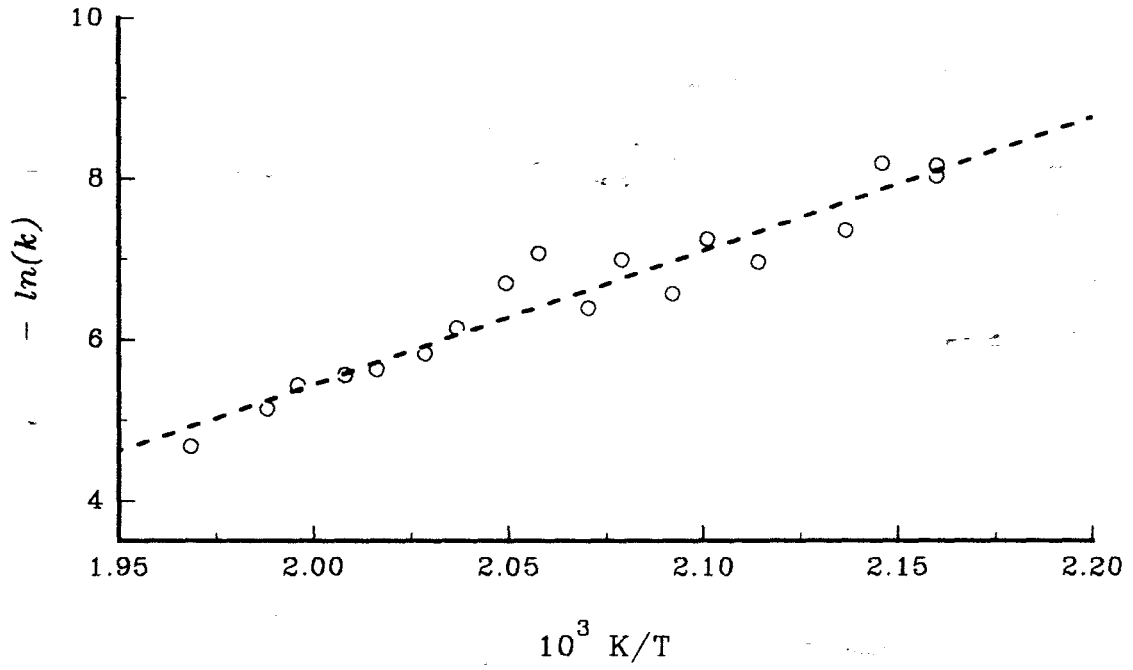

Figure 10.2.2c: Arrhenius plot for the decomposition of $Ni(aa)Cl_2$ using rate coefficients from the R2 equation for $0.00 \leq \alpha \leq 0.95$.

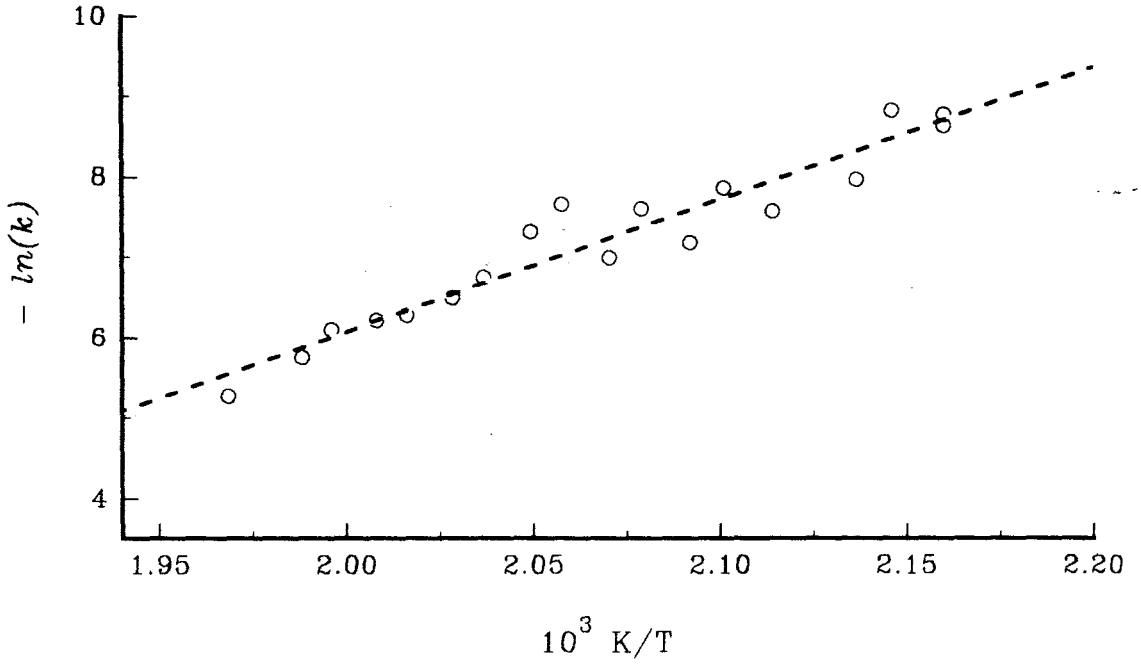

Figure 10.2.2d: Arrhenius plot for the decomposition of $Ni(aa)Cl_2$ using rate coefficients from the R3 equation for $0.00 \leq \alpha \leq 0.95$.

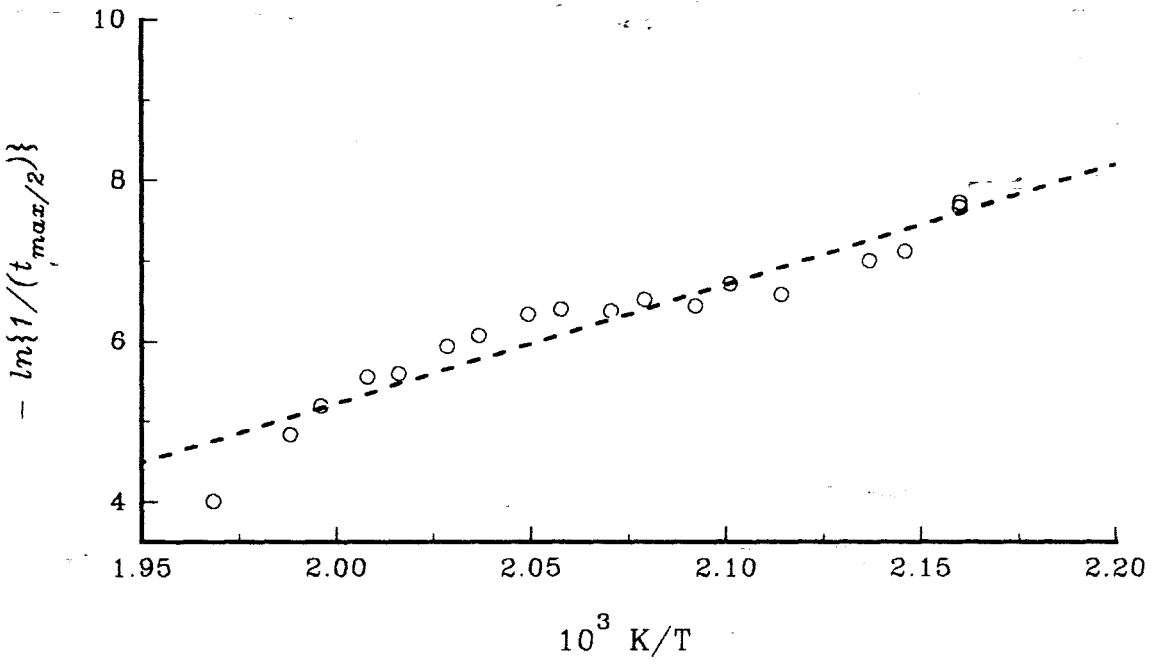

Figure 10.2.2e: Arrhenius plot for the decomposition of $Ni(aa)Cl_2$ using rate coefficients based on $1/(t_{max/2})$.

Table 10.2.2: Arrhenius parameters for the isothermal decomposition of Ni(*aa*)Cℓ_2 calculated using different methods of kinetic analysis.

Model	α-range	E_a / kJ mol^{-1}	r	ℓn(A/s^{-1})*
Zero-order	0.00 - 0.33	148 ± 11	0.9177	30.4 ± 0.2
	0.00 - 0.30	148 ± 11	0.9180	30.6 ± 0.2
Half-lives	-	144 ± 11	0.9172	(26.6 ± 0.1)
R2 model	0.00 - 0.95	138 ± 10	0.9239	27.6 ± 0.1
	0.00 - 0.90	142 ± 10	0.9314	28.8 ± 0.1
	0.00 - 0.80	145 ± 10	0.9256	29.7 ± 0.1
R3 model	0.00 - 0.95	137 ± 10	0.9232	30.0 ± 0.1
	0.00 - 0.90	141 ± 10	0.9313	27.9 ± 0.1
	0.00 - 0.80	144 ± 10	0.9251	28.8 ± 0.1
υ_{max} based	-	123 ± 10	0.9064	(21.5 ± 0.1)

* the values in parentheses include {g(α)}

Table 10.2.3: The α_i, α_{mean} and the standard deviation (δ) of α_i values used to confirm the isokinetic behaviour of the decomposition of Ni(*aa*)Cℓ_2 at different constant temperatures. The test was made using α_i values taken separately at $t/t_{0.5}$ ratios of 0.5, 2.0 and 3.5.

T / °C	α at $t/t_{0.5} = 0.5$	α at $t/t_{0.5} = 2.0$	α at $t/t_{0.5}=3.5$
235	0.284	0.770	0.938
230	0.279	0.790	0.967
228	0.275	0.791	0.967
225	0.285	0.763	0.883
223	0.285	0.771	0.902
220	0.275	0.800	0.982
218	0.279	0.797	0.961
215	0.278	0.799	0.984
213	0.284	0.787	0.921
210	0.276	0.778	0.946
208	0.280	0.801	0.968
205	0.276	0.792	0.978
203	0.274	0.801	0.983
200	0.276	0.781	0.957
195	0.276	0.791	0.975
193	0.263	0.812	0.991
190	0.273	0.804	0.959
190*	0.278	0.786	0.963
α_{mean} =	**0.278**	**0.790**	**0.957**
δ =	**0.005 ± 0.001**	**0.013 ± 0.003**	**0.028 ± 0.007**

* run in replicate

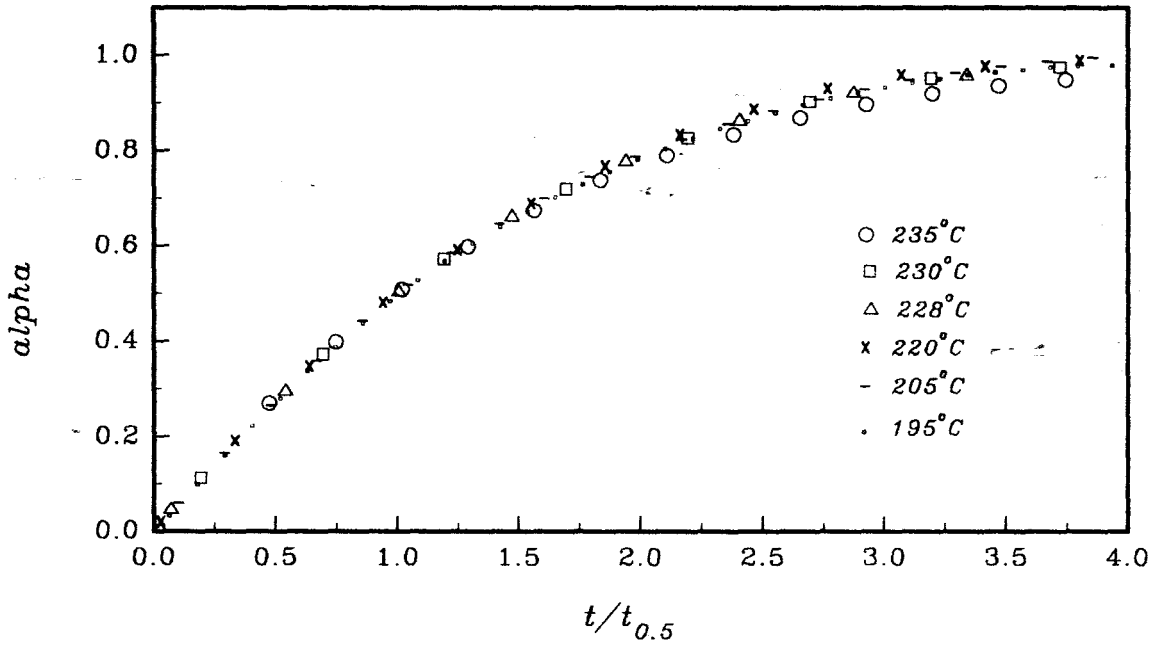

Figure 10.2.3a: Comparison of reduced-time plots for the decomposition of $Ni(aa)Cl_2$ at a series of constant temperatures .
(see also Figure 10.2.3b of Appendix III).

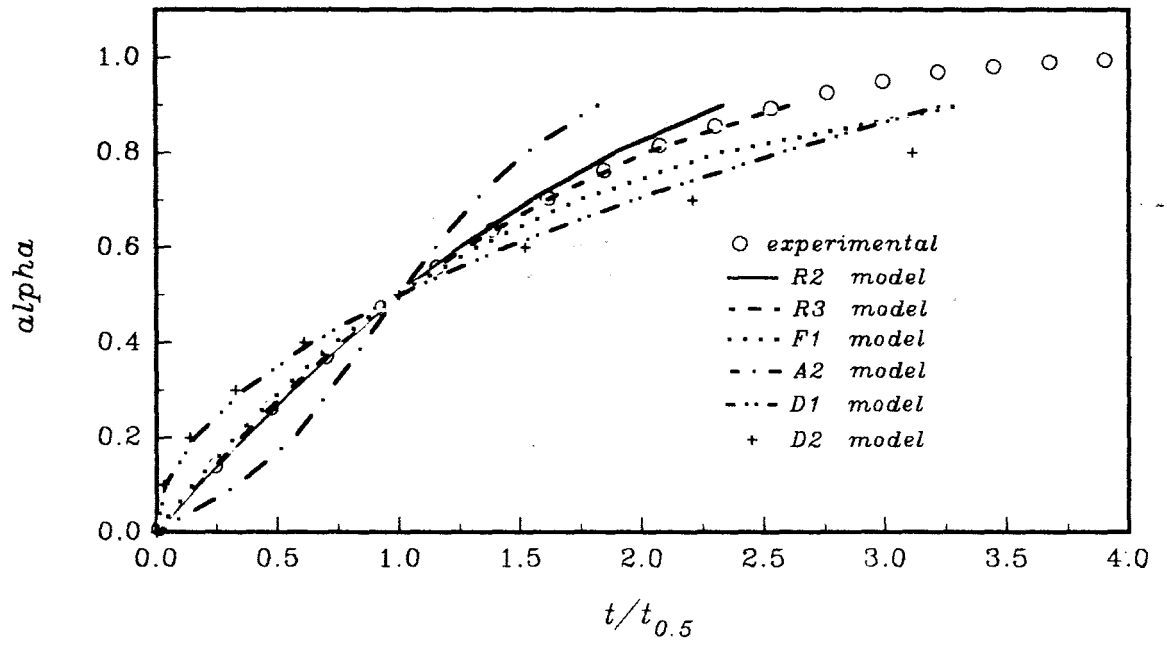

Figure 10.2.4a: Reduced-time plot for the decomposition of $Ni(aa)Cl_2$ at 215°C, compared with calculated plots for various kinetic models.
(see also Figure 10.2.4b of Appendix III).

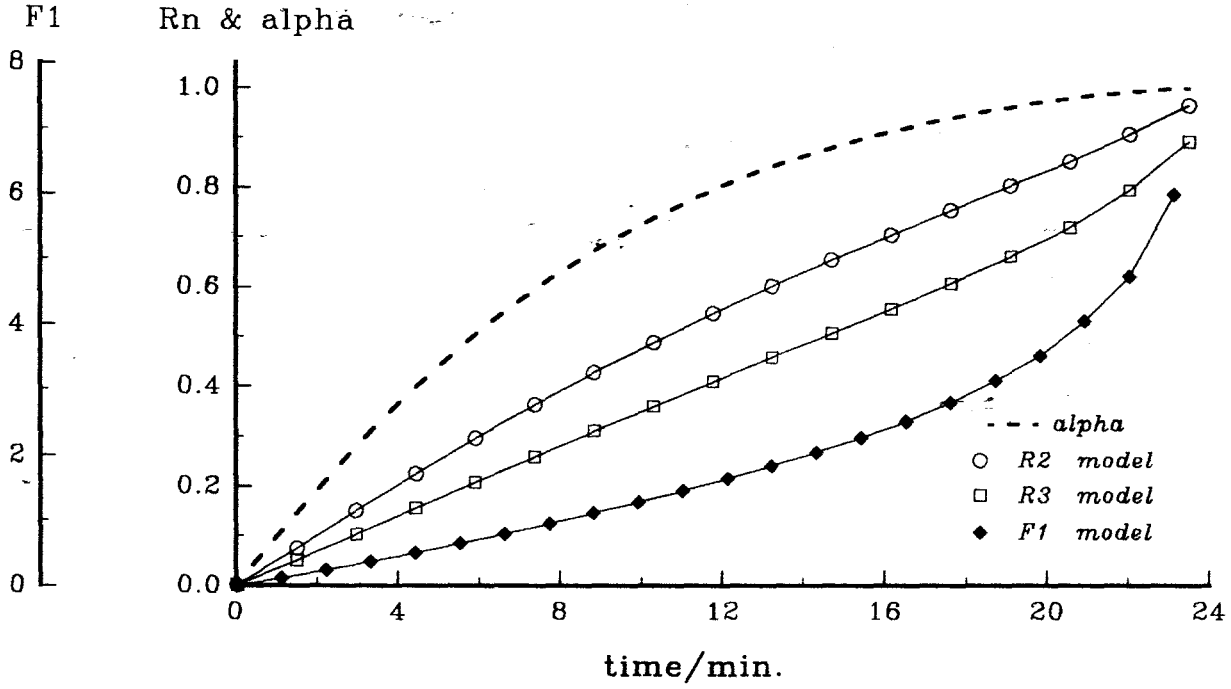

Figure 10.2.5a: Plots of $g(\alpha)$ versus time for the decomposition of $Ni(aa)Cl_2$ at 205°C. The α–time curve is included to show the range of α over which $g(\alpha)$ is approximately linear (see also Figures 10.2.5b–r of Appendix III).

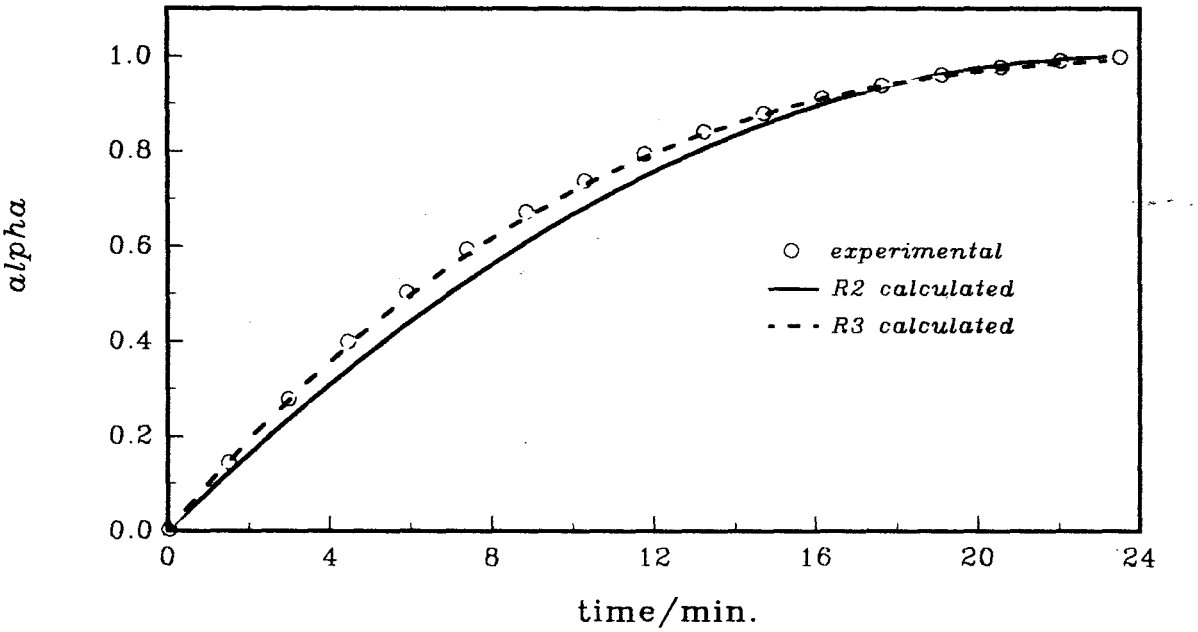

Figure 10.2.6a: Plots of $\alpha_{calc.}$ versus time using the R2 and R3 models, compared with α_e versus time data for the decomposition of $Ni(aa)Cl_2$ at 205°C (see also Figures 10.2.6b–r of Appendix III).

Table 10.2.4: Rate coefficients for the decomposition of Ni(*aa*)Cℓ_2 at different constant temperatures calculated using the **R3** or **R2** rate expressions over $0.00 \leq \alpha \leq 0.95$.#

	R2 model		**R3 model**	
T / °C	k / 10^{-3} s^{-1}	r	k / 10^{-3} s^{-1}	r
235	9.333 ± 0.068	0.9785	11.534 ± 0.049	0.9926
230	5.849 ± 0.021	0.9945	7.119 ± 0.005	0.9998
228	4.367 ± 0.011	0.9868	5.034 ± 0.003	0.9994
225	3.839 ± 0.051	0.8597	4.505 ± 0.053	0.7632
223	3.578 ± 0.027	0.8702	4.207 ± 0.026	0.8648
220	2.961 ± 0.004	0.9949	3.401 ± 0.001	0.9997
218	2.162 ± 0.008	0.9927	2.645 ± 0.003	0.9992
215	1.232 ± 0.002	0.9973	1.496 ± 0.001	0.9998
213	0.854 ± 0.009	0.9223	1.063 ± 0.009	0.9480
210	1.684 ± 0.009	0.9834	2.070 ± 0.006	0.9954
208	0.918 ± 0.003	0.9941	1.121 ± 0.001	0.9996
205	1.410 ± 0.005	0.9944	1.713 ± 0.001	0.9998
203	0.714 ± 0.001	0.9977	0.864 ± 0.001	0.9996
200	0.949 ± 0.007	0.9896	1.160 ± 0.003	0.9983
195	0.642 ± 0.002	0.9955	0.780 ± 0.000	0.9999
193	0.279 ± 0.000	0.9995	0.331 ± 0.001	0.9983
190	0.287 ± 0.001	0.9935	0.347 ± 0.000	0.9989
190*	0.327 ± 0.001	0.9929	0.399 ± 0.000	0.9995

refer to Appendix **III** for the results of the other α ranges examined.

* run in replicate.

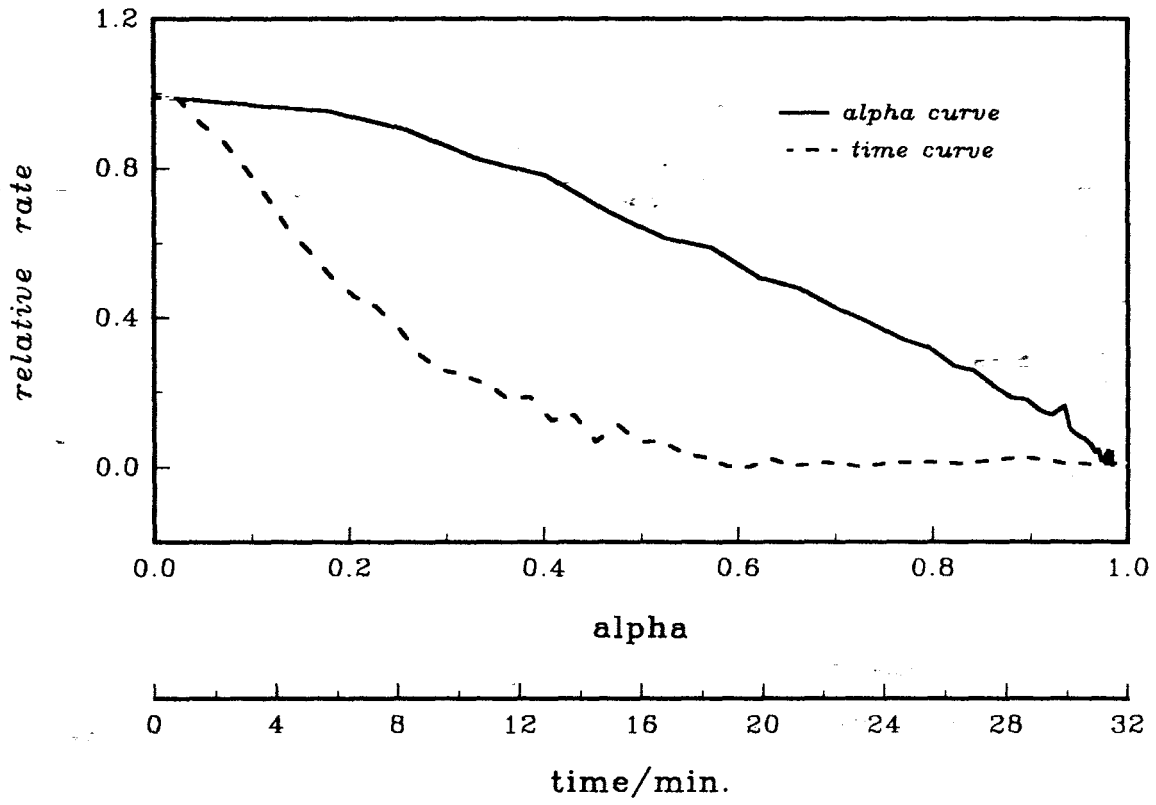

Figure 10.2.7a: Plots of rate versus alpha and rate versus time for the decomposition of $Ni(aa)Cl_2$ at 210°C (see also Figures 10.2.7b–r of Appendix III).

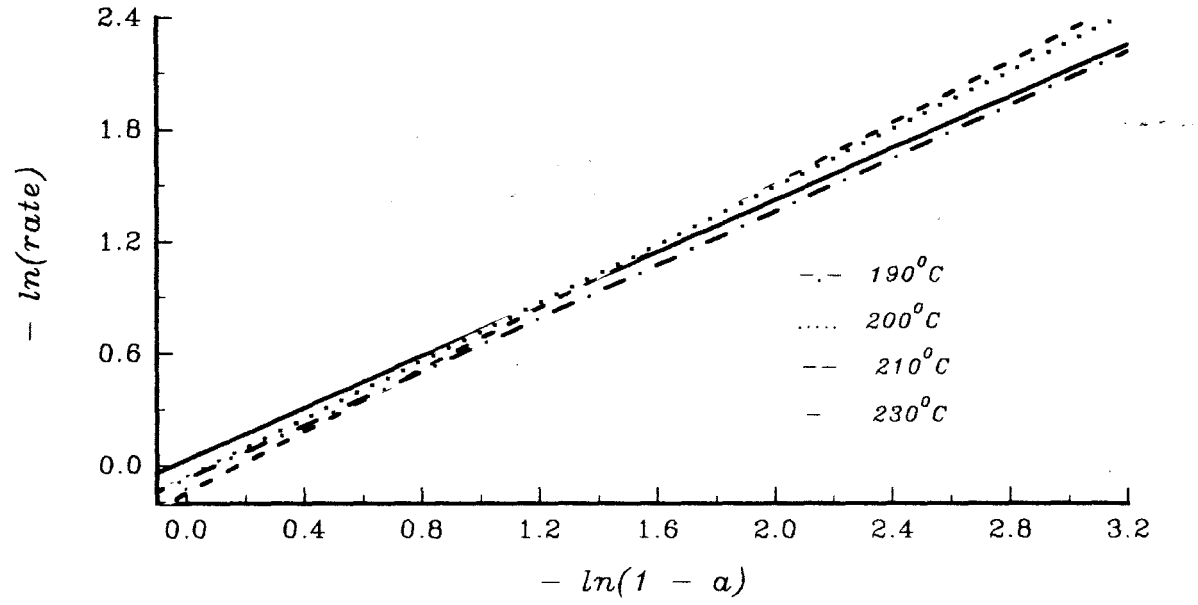

Figure 10.2.8a: Regression lines of ln(rate) versus $\ln(1-\alpha)$ for the isothermal decomposition of $Ni(aa)Cl_2$ (see also Figure 10.2.8b of Appendix III).

Table 10.2.5: Kinetic data for the decomposition of Ni(*aa*)Cℓ_2 at different constant temperatures: (i) $t_{max/2}$, estimated from rate *versus* time curves and used to obtain E_a from a plot of $\ell n\{^1/(t_{max/2})\}$ against $^1/T$; (ii) *n*, the apparent order derived from plots of ℓn(rate) against $\ell n(1 - \alpha)$ over $0.03 \leq \alpha \leq 0.90$.

	Plots of rate *versus* time		Plots of ℓn(rate) *versus* $\ell n(1 - \alpha)$	
T / °C	10^3 s /($t_{max/2}$)	- $\ell n\{^1/(t_{max/2})\}$	order *n*	r
235	8.315	4.007	0.848 ± 0.003	0.9952
230	7.937	4.836	0.700 ± 0.004	0.9880
228	5.556	5.193	0.715 ± 0.007	0.9683
225	3.876	5.555	0.959 ± 0.026	0.8678
223	3.704	5.599	0.837 ± 0.015	0.9177
220	2.646	5.937	0.633 ± 0.007	0.9283
218	2.315	6.071	0.711 ± 0.006	0.9713
215	1.773	6.336	0.660 ± 0.007	0.9408
213	1.667	6.398	0.745 ± 0.009	0.9482
210	1.701	6.377	0.869 ± 0.009	0.9447
208	1.475	6.520	0.692 ± 0.007	0.9504
205	1.603	6.437	0.680 ± 0.003	0.9926
203	1.217	6.713	0.596 ± 0.006	0.9358
200	1.389	6.580	0.758 ± 0.003	0.9971
195	0.911	7.003	0.677 ± 0.003	0.9866
193	0.813	7.116	0.533 ± 0.005	0.9264
190	0.444	7.720	0.610 ± 0.012	0.8271
190*	0.472	7.660	0.736 ± 0.005	0.9808

* run in replicate

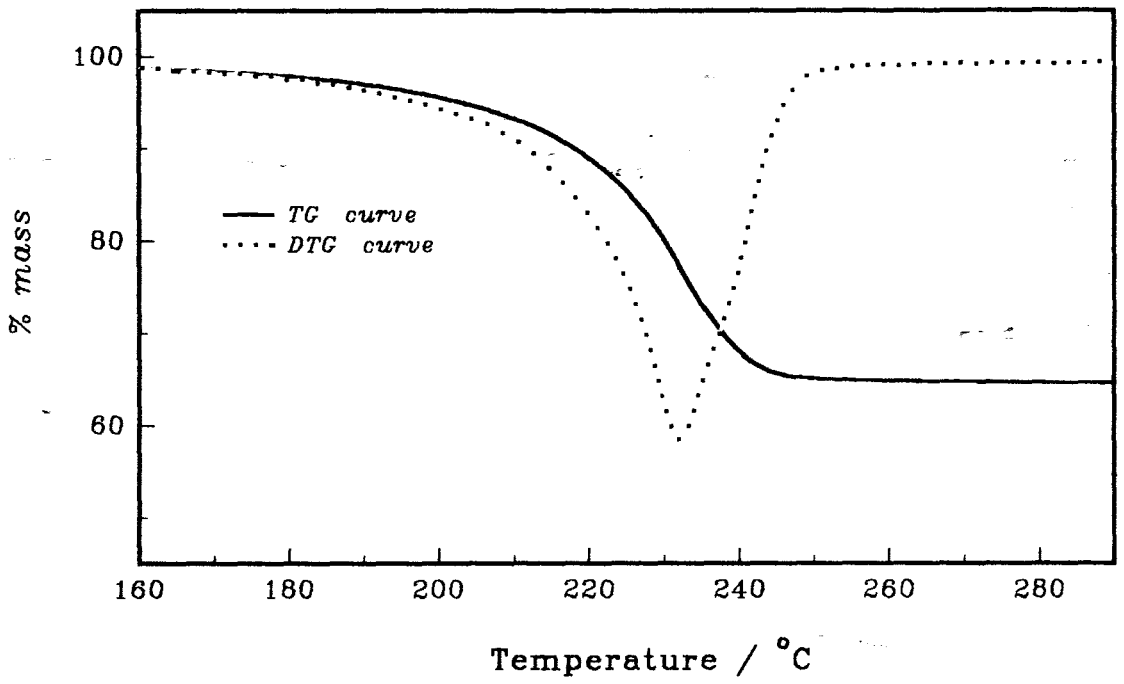

Figure 10.3.1a: TG and DTG curves for the decomposition of $Ni(nma)Cl_2$ heated at 20°C min^{-1} in flowing N_2.

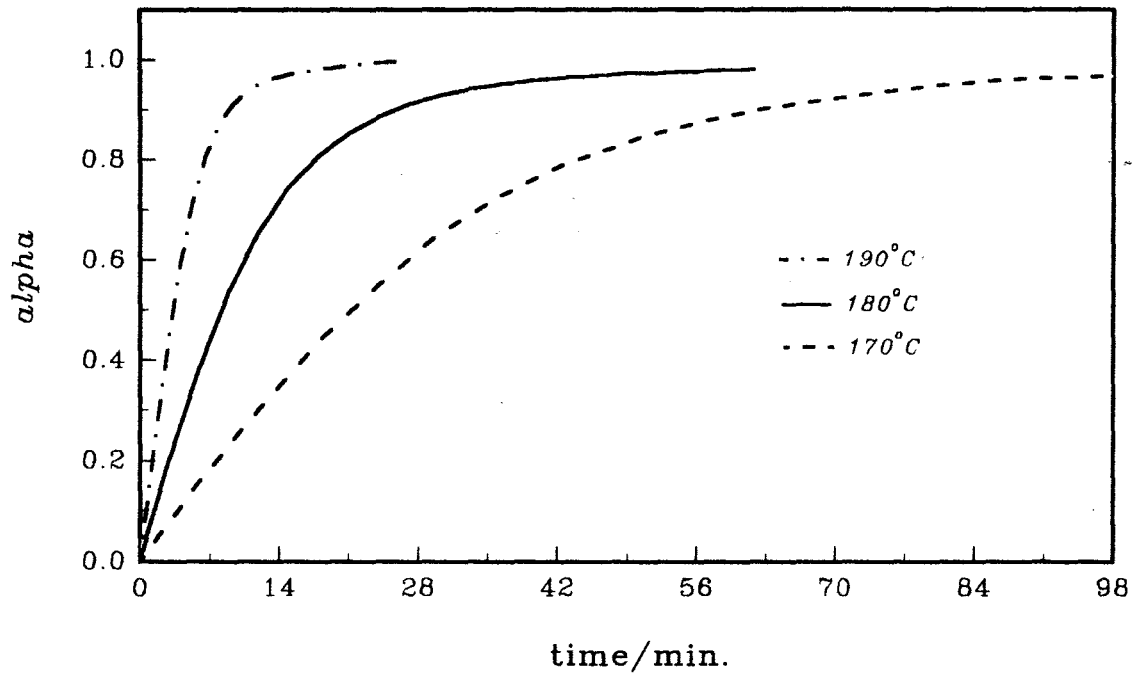

Figure 10.3.1b: Alpha versus time plots for the decomposition of $Ni(nma)Cl_2$ at 190°C, 180°C and 170°C.

Table 10.3.1: Approximate zero-order rate coefficients and $^{1}/t_{0.5}$ values for the decomposition of Ni(*nma*)Cℓ_2 at different constant temperatures.

	α-range: 0.00 - 0.30		α-range: 0.00 - 0.35		10^3 s / $t_{0.5}$
T / °C	k /10^{-3} s^{-1}	r	k /10^{-3} s^{-1}	r	
210	11.861 ± 0.020	0.9993	11.729 ± 0.024	0.9987	21.553
208	8.658 ± 0.017	0.9991	8.579 ± 0.018	0.9988	15.873
205	7.920 ± 0.019	0.9988	7.820 ± 0.022	0.9982	14.209
200	7.791 ± 0.018	0.9993	7.706 ± 0.022	0.9988	13.889
200*	4.934 ± 0.003	0.9999	3.912 ± 0.004	0.9997	7.375
198	4.500 ± 0.014	0.9981	4.432 ± 0.015	0.9974	6.884
195	3.358 ± 0.004	0.9996	3.343 ± 0.004	0.9995	6.219
193	2.919 ± 0.005	0.9991	2.901 ± 0.006	0.9985	5.342
190	2.643 ± 0.001	0.9999	2.634 ± 0.002	0.9999	5.001
188	1.997 ± 0.002	0.9997	1.990 ± 0.002	0.9996	3.731
185	1.660 ± 0.003	0.9995	1.644 ± 0.003	0.9989	3.051
183	0.837 ± 0.003	0.9952	0.828 ± 0.003	0.9953	1.570
180	1.114 ± 0.002	0.9993	1.103 ± 0.002	0.9990	2.028
178	0.836 ± 0.001	0.9993	0.829 ± 0.001	0.9991	1.543
175	0.870 ± 0.006	0.9998	0.687 ± 0.001	0.9996	1.268
175*	0.732 ± 0.001	0.9987	0.727 ± 0.001	0.9985	1.321
173	0.478 ± 0.000	0.9998	0.476 ± 0.001	0.9996	0.873
170	0.431 ± 0.001	0.9994	0.428 ± 0.001	0.9991	0.780
170*	0.492 ± 0.001	0.9988	0.489 ± 0.001	0.9987	0.895

* run in replicate

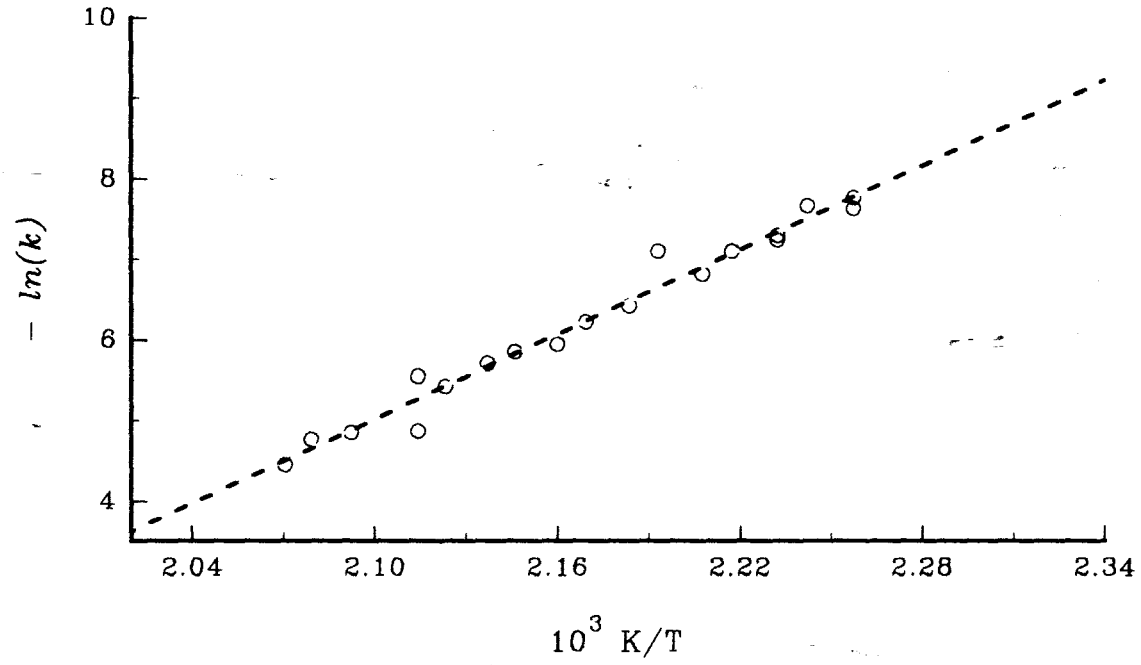

Figure 10.3.2a: Arrhenius plot for the decomposition of $Ni(nma)Cl_2$ using approximate zero-order rate coefficients for $0.00 \leq \alpha \leq 0.35$.

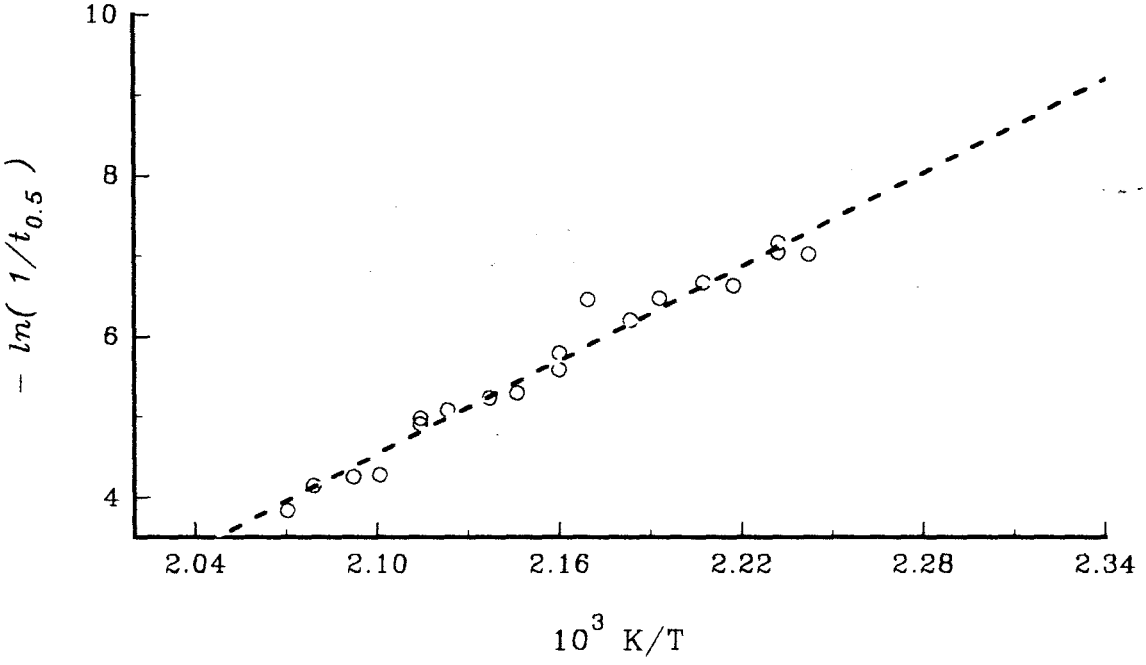

Figure 10.3.2b: Arrhenius plot for the decomposition of $Ni(nma)Cl_2$ using rate coefficients based on $1/t_{0.5}$.

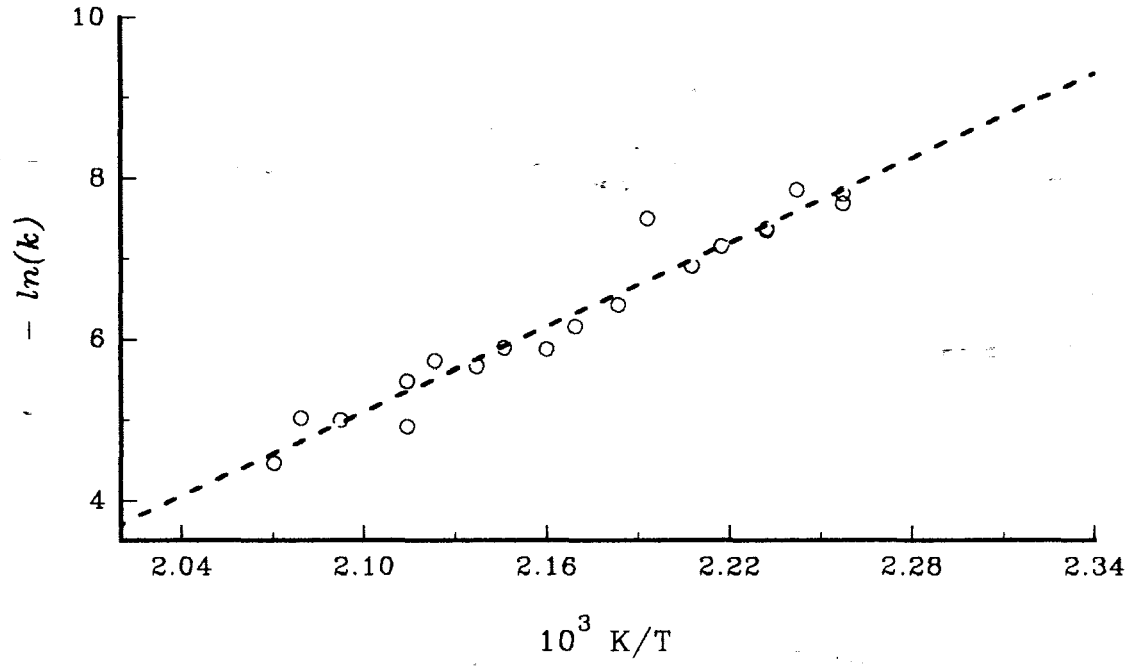

Figure 10.3.2c: Arrhenius plot for the decomposition of $Ni(nma)Cl_2$ using rate coefficients from the R2 equation for $0.00 \leq \alpha \leq 0.85$.

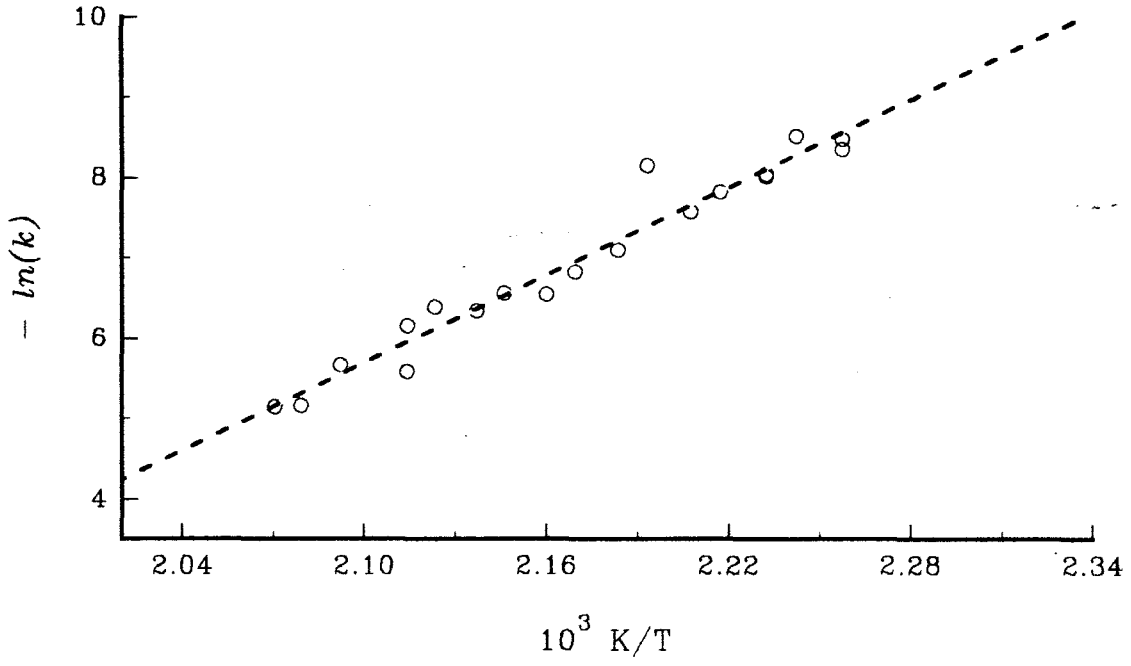

Figure 10.3.2d: Arrhenius plot for the decomposition of $Ni(nma)Cl_2$ using rate coefficients from the R3 equation for $0.00 \leq \alpha \leq 0.85$.

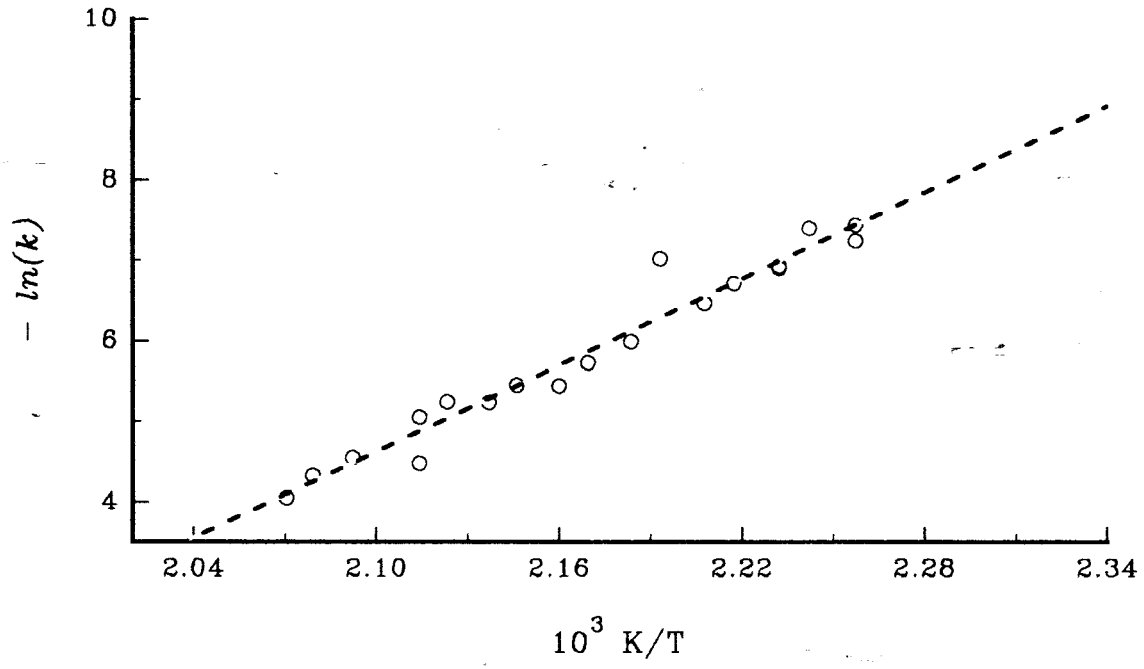

Figure 10.3.2e: Arrhenius plot for the decomposition of $Ni(nma)Cl_2$ using rate coefficients from the F1 equation for $0.00 \leq \alpha \leq 0.85$.

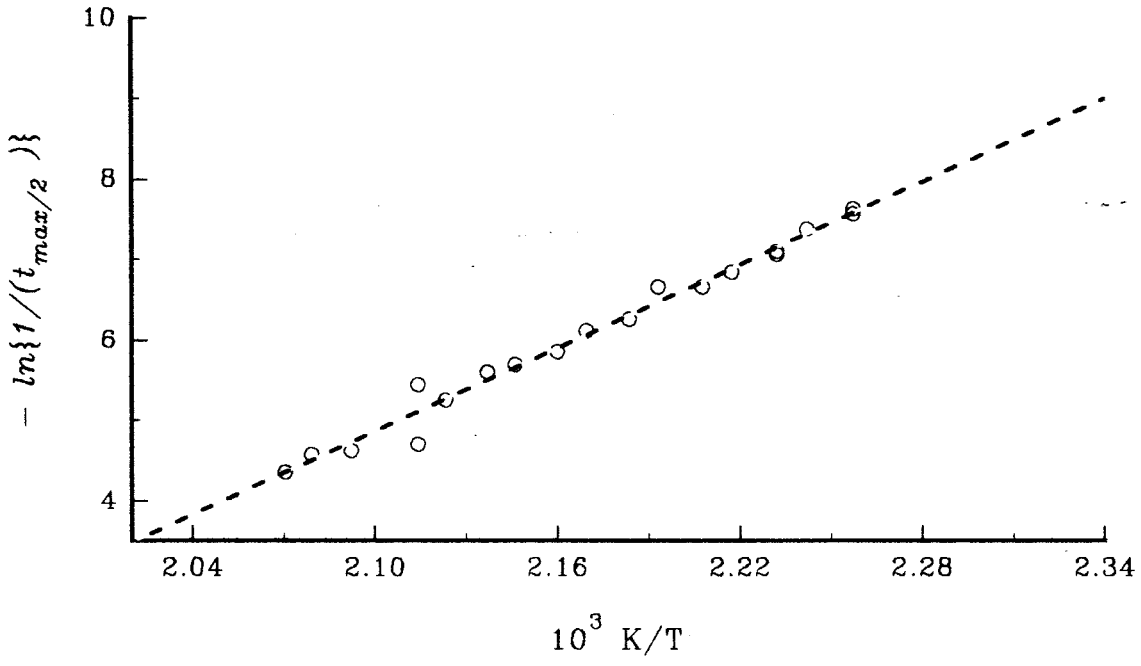

Figure 10.3.2f: Arrhenius plot for the decomposition of $Ni(nma)Cl_2$ using rate coefficients based on $1/(t_{max/2})$.

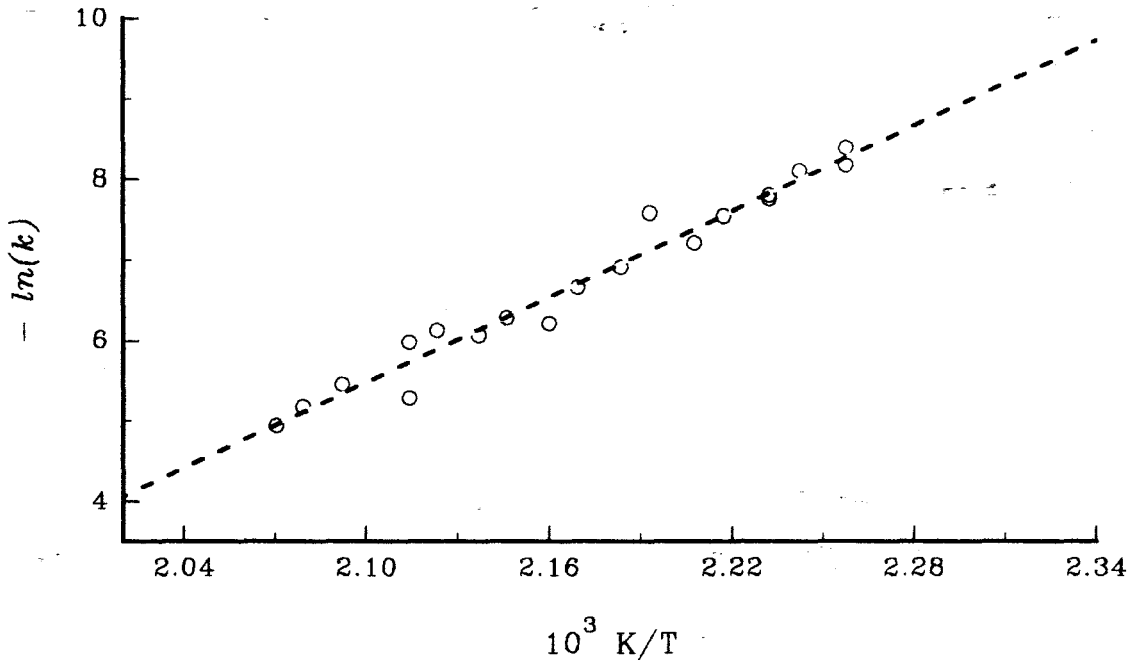

Figure 10.3.2g: Arrhenius plot for the decomposition of $Ni(nma)Cl_2$ using rate coefficients from the (B2) expression, $(1 - v_r)^{1/2} = kt$, over the range $0.00 \leq \alpha \leq 0.80$.

Table 10.3.2: Arrhenius parameters for the isothermal decomposition of Ni(*nma*)Cℓ_2, calculated using different methods of kinetic analysis.

Model	α-range	E_a / kJ mol^{-1}	r	ℓn(A/s^{-1})*
Zero-order	0.00 - 0.35	145 ± 6	0.9741	13.8 ± 0.1
	0.00 - 0.30	146 ± 6	0.9741	13.8 ± 0.1
Half-lives	-	145 ± 6	0.9750	(13.9 ± 0.1)
R2 model	0.00 - 0.85	145 ± 9	0.9454	13.7 ± 0.1
	0.00 - 0.80	147 ± 7	0.9633	13.9 ± 0.1
R3 model	0.00 - 0.85	151 ± 8	0.9536	14.1 ± 0.1
	0.00 - 0.80	146 ± 7	0.9640	13.6 ± 0.1
F1 eqn.	0.00 - 0.95	150 ± 9	0.9410	14.5 ± 0.1
	0.00 - 0.85	149 ± 8	0.9563	14.3 ± 0.1
	0.00 - 0.80	147 ± 7	0.9658	14.1 ± 0.1
υ_{max} based	-	144 ± 5	0.9819	(13.7 ± 0.1)
B2 eqn.	0.05 - 0.85	147 ± 7	0.9663	31.7 ± 0.2
	0.05 - 0.75	145 ± 6	0.9702	31.6 ± 0.2
	0.05 - 0.70	141 ± 6	0.9695	31.8 ± 0.2

* the values in parentheses include ℓn{g(α)}

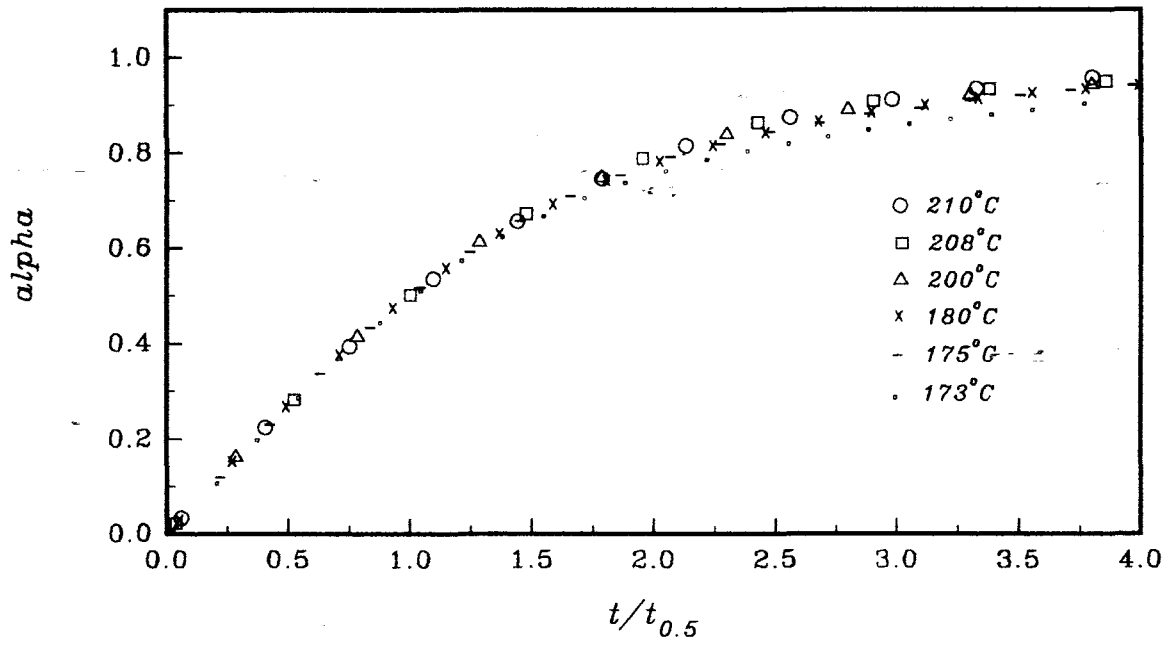

Figure 10.3.3a: Comparison of reduced–time plots for the decomposition of $Ni(nma)Cl_2$ at a series of constant temperatures.
(see also Figure 10.3.3b of Appendix IV).

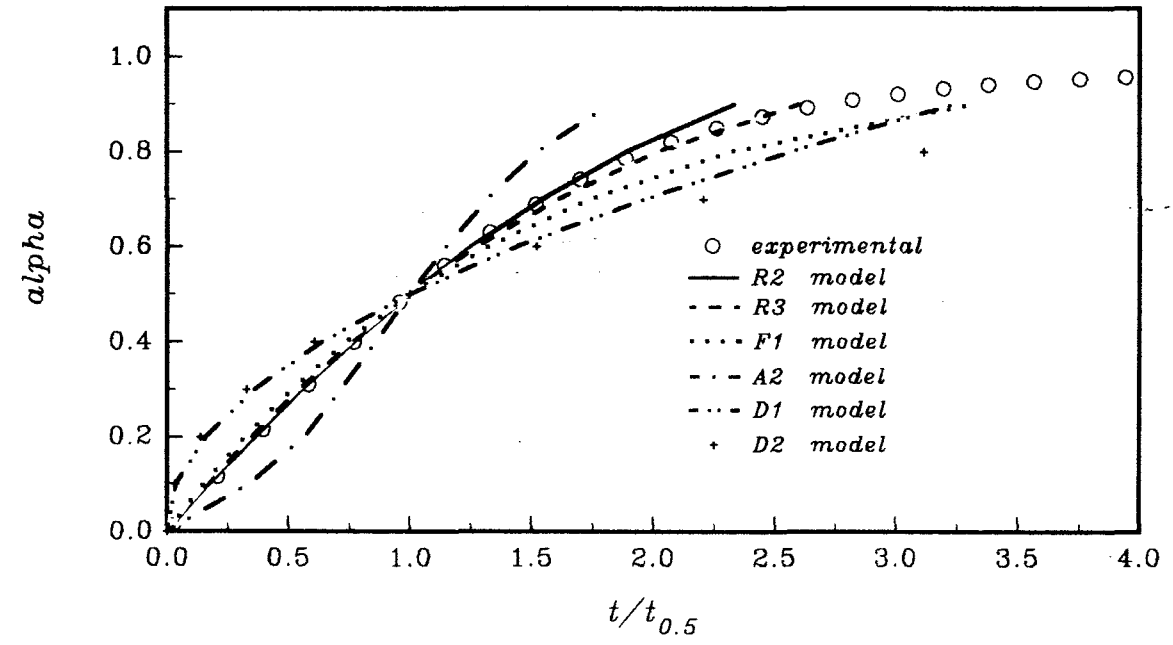

Figure 10.3.4a: Reduced–time plot for the decomposition of $Ni(nma)Cl_2$ at 195°C, compared with calculated plots for various kinetic models.
(see also Figure 10.3.4b of Appendix IV).

Table 10.3.3: The α_i, α_{mean} and the standard deviation (δ) of α_i values used to confirm the isokinetic behaviour of the decomposition of Ni(*nma*)Cℓ_2 at different constant temperatures. The test was made using α_i values taken separately at $t/t_{0.5}$ ratios of 0.5, 2.0 and 3.5.

T / °C	α at $t/t_{0.5} = 0.5$	α at $t/t_{0.5} = 2.0$	α at $t/t_{0.5} = 3.5$
210	0.273	0.792	0.943
208	0.267	0.799	0.938
205	0.276	0.770	0.906
200	0.278	0.793	0.933
200	0.266	0.806	0.945
198	0.268	0.785	0.924
195	0.268	0.807	0.944
193	0.270	0.787	0.931
190	0.262	0.808	0.948
188	0.266	0.814	0.956
185	0.268	0.793	0.933
183	0.283	0.789	0.934
180	0.270	0.776	0.921
178	0.270	0.784	0.916
175	0.270	0.780	0.920
175*	0.273	0.775	0.912
173	0.272	0.762	0.894
170	0.275	0.789	0.933
170*	0.270	0.788	0.938
α_{mean} =	**0.271**	**0.789**	**0.930**
δ =	**0.005 ± 0.001**	**0.013 ± 0.003**	**0.015 ± 0.004**

* run in replicate

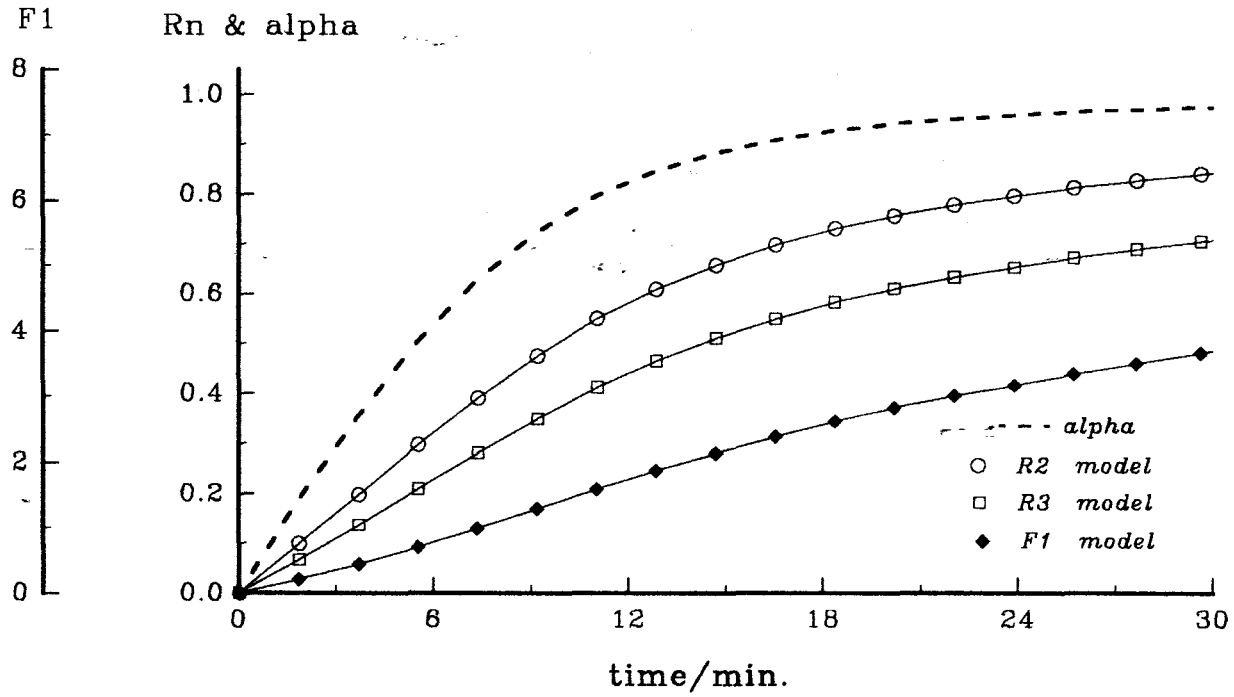

Figure 10.3.5a: Plots of g(α) versus time for the decomposition of $Ni(nma)Cl_2$ at 185°C. The α–time curve is included to show the range of α over which g(α) is approximately linear (see also Figures 10.3.5b–s of Appendix IV).

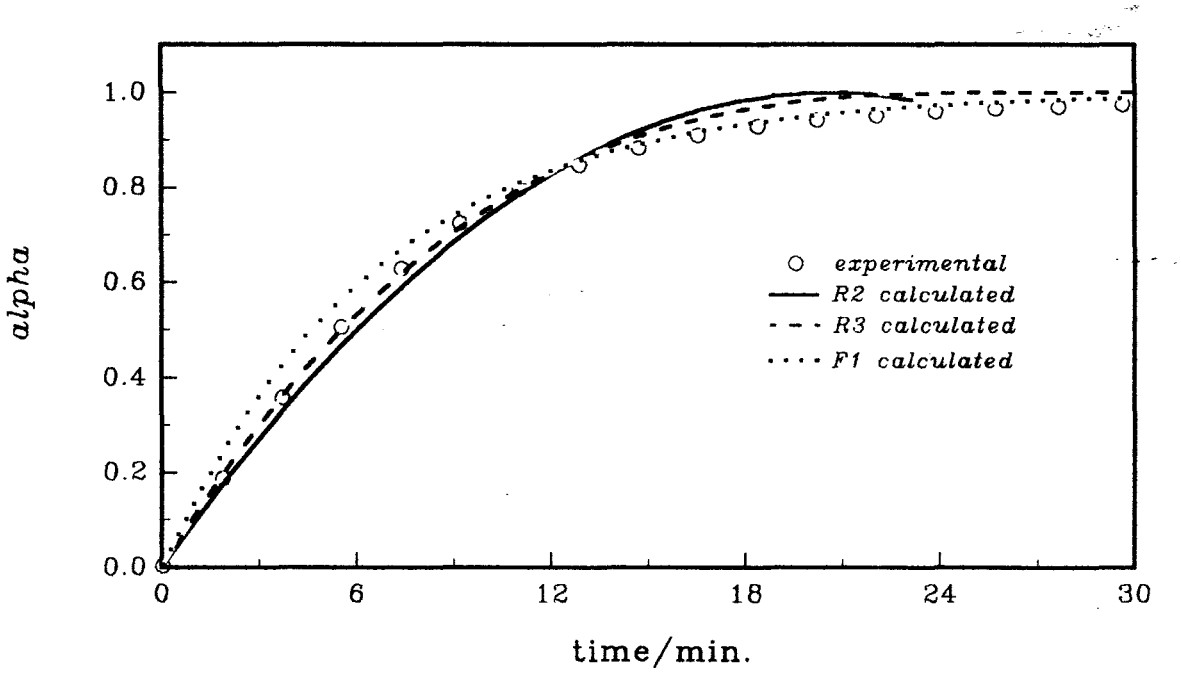

Figure 10.3.6a: Plots of $\alpha_{calc.}$ versus time using various kinetic models, compared with α_e versus time data for the decomposition of $Ni(nma)Cl_2$ at 185°C.
(see also Figures 10.3.6b–s of Appendix IV).

Table 10.3.4: Rate coefficients for the decomposition of Ni(*nma*)Cℓ_2 at different constant temperatures calculated using the **R2**, **R3** or **F1** rate expression over $0.00 \leq \alpha \leq 0.85$.#

	R2 model		**R3 model**		**F1 model**	
T/ °C	k / 10^{-3} s^{-1}	r	k / 10^{-3} s^{-1}	r	k / 10^{-3} s^{-1}	r
210	11.512 ± 0.044	0.9962	13.157 ± 0.022	0.9993	17.469 ± 0.063	0.9966
208	6.575 ± 0.033	0.9993	12.887 ± 0.017	0.9964	13.228 ± 0.054	0.9958
205	6.754 ± 0.054	0.9854	7.798 ± 0.043	0.9930	10.584 ± 0.018	0.9993
200	7.301 ± 0.049	0.9936	8.398 ± 0.030	0.9982	11.311 ± 0.045	0.9978
200*	4.165 ± 0.013	0.9974	4.771 ± 0.007	0.9994	6.372 ± 0.031	0.9941
198	3.259 ± 0.033	0.9739	3.781 ± 0.029	0.9848	5.259 ± 0.008	0.9974
195	3.474 ± 0.010	0.9975	3.983 ± 0.005	0.9995	5.328 ± 0.023	0.9942
193	2.784 ± 0.013	0.9939	3.200 ± 0.008	0.9982	4.304 ± 0.012	0.9976
190	2.831 ± 0.009	0.9974	3.243 ± 0.005	0.9993	4.331 ± 0.020	0.9940
188	2.134 ± 0.004	0.9988	2.441 ± 0.003	0.9997	3.250 ± 0.017	0.9918
185	1.623 ± 0.006	0.9952	1.864 ± 0.004	0.9988	2.503 ± 0.008	0.9940
183	0.558 ± 0.006	0.9426	0.651 ± 0.006	0.9581	0.903 ± 0.005	0.9811
180	1.006 ± 0.006	0.9893	1.159 ± 0.004	0.9956	1.565 ± 0.003	0.9991
178	0.787 ± 0.004	0.9898	0.906 ± 0.003	0.9957	1.221 ± 0.002	0.9986
175	0.632 ± 0.004	0.9887	0.729 ± 0.003	0.9952	0.986 ± 0.002	0.9990
175*	0.647 ± 0.004	0.9870	0.750 ± 0.003	0.9940	1.014 ± 0.002	0.9990
173	0.391 ± 0.003	0.9752	0.452 ± 0.001	0.9854	0.618 ± 0.001	0.9973
170	0.412 ± 0.002	0.9937	0.472 ± 0.001	0.9981	0.593 ± 0.014	0.9924
170*	0.465 ± 0.002	0.9936	0.535 ± 0.001	0.9981	0.720 ± 0.002	0.9978

refer to Appendix **IV** for the results of the other α ranges examined.

* run in replicate.

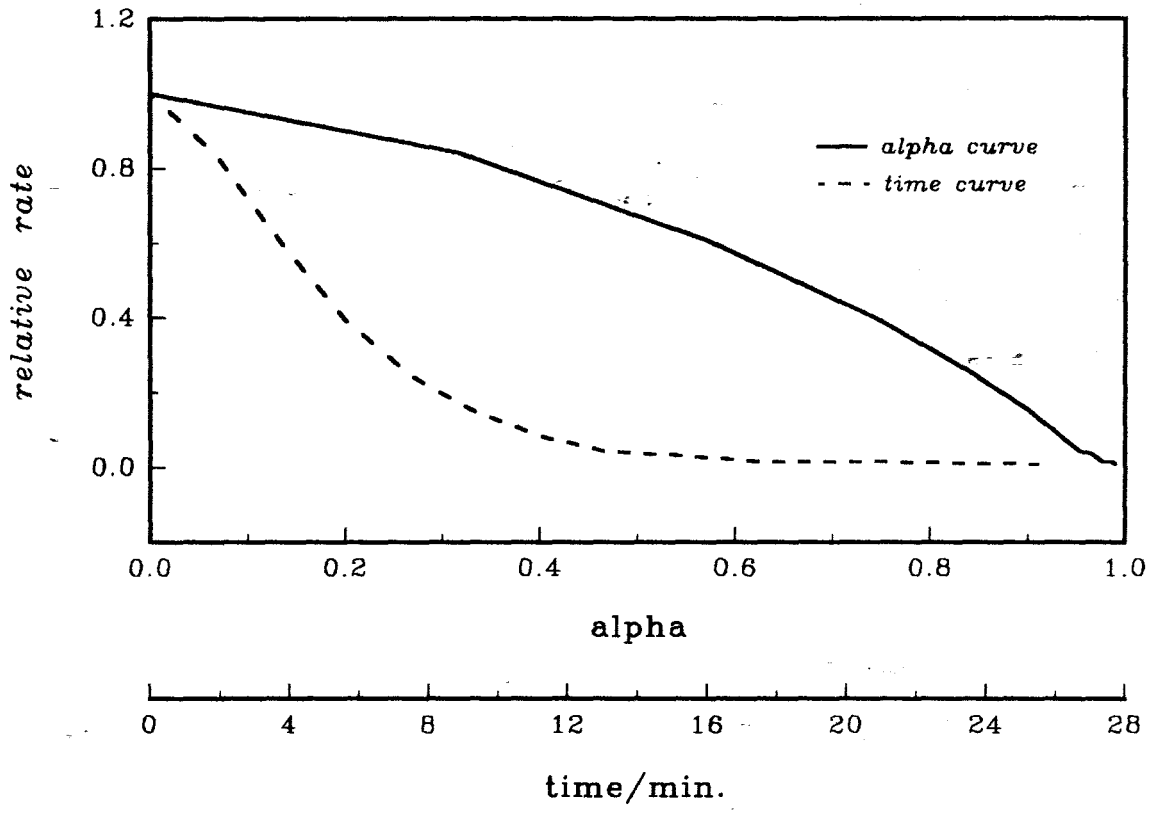

Figure 10.3.7a: Plots of rate versus alpha and rate versus time for the decomposition of Ni(nma)Cl_2 at 193°C (see also Figures 10.3.7b–s of Appendix IV).

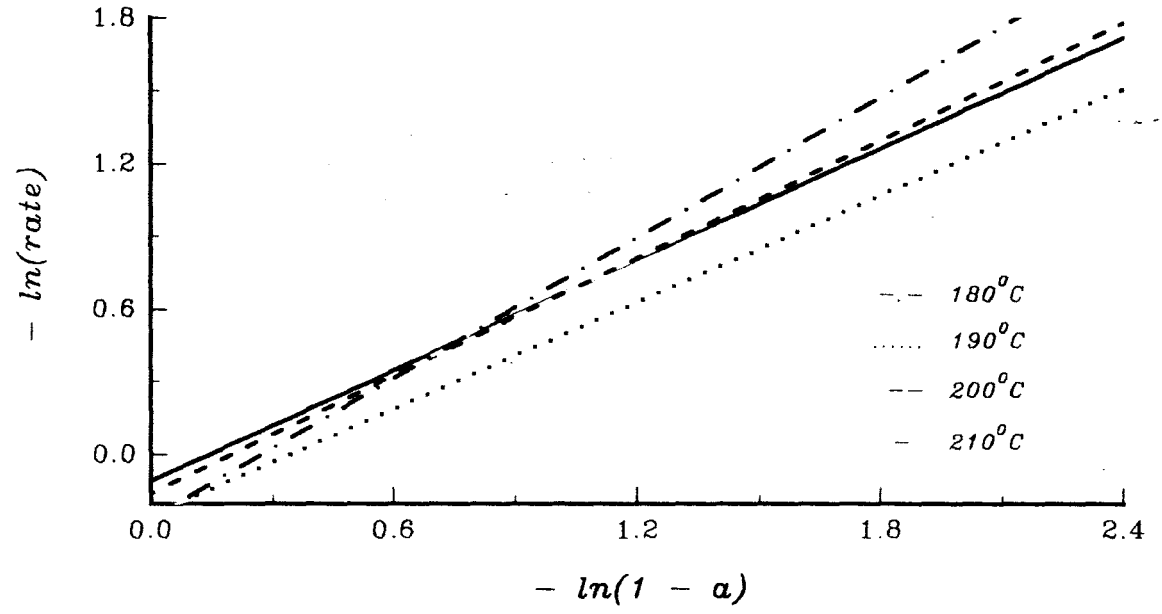

Figure 10.3.8a: Regression lines of ln(rate) versus ln(1 − α) for the isothermal decomposition of Ni(nma)Cl_2 (see also Figure 10.3.8b of Appendix IV).

Table 10.3.5: Kinetic data for the decomposition of Ni(*nma*)Cℓ_2 at different constant temperatures: (i) $t_{max/2}$, estimated from the rate *versus* time curves and used to obtain E_a from a plot of $\ell n\{^1/(t_{max/2})\}$ against $^1/T$; (ii) *n*, the apparent order derived from plots of ℓn(rate) against $\ell n(1 - \alpha)$ over $0.03 \leq \alpha \leq 0.80$.

	Plots of rate *versus* time		Plots of ℓn(rate) *versus* $\ell n(1 - \alpha)$	
T / °C	10^3 s /$(t_{max/2})$	$-\ell n\{^1/(t_{max/2})\}$	order *n*	r
210	12.820	4.357	0.734 ± 0.008	0.9730
208	10.288	4.578	0.686 ± 0.008	0.9752
205	9.804	4.078	0.902 ± 0.011	0.9718
200	9.058	4.705	0.762 ± 0.009	0.9799
200*	4.318	5.447	0.621 ± 0.012	0.9191
198	5.208	5.258	0.960 ± 0.014	0.9699
195	3.687	5.603	0.650 ± 0.008	0.9654
193	3.360	5.698	0.753 ± 0.009	0.9638
190	2.874	5.854	0.641 ± 0.010	0.9435
188	2.213	6.115	0.590 ± 0.007	0.9615
185	1.909	6.262	0.714 ± 0.007	0.9718
183	1.284	6.660	0.748 ± 0.014	0.8988
180	1.280	6.663	0.851 ± 0.009	0.9703
178	1.068	6.842	0.826 ± 0.013	0.9148
175	0.821	7.107	0.834 ± 0.012	0.9445
175*	0.855	7.066	0.834 ± 0.012	0.9445
173	0.629	7.383	0.789 ± 0.013	0.9281
170	0.485	7.635	0.772 ± 0.013	0.9062
170*	0.514	7.575	0.778 ± 0.008	0.9636

* run in replicate

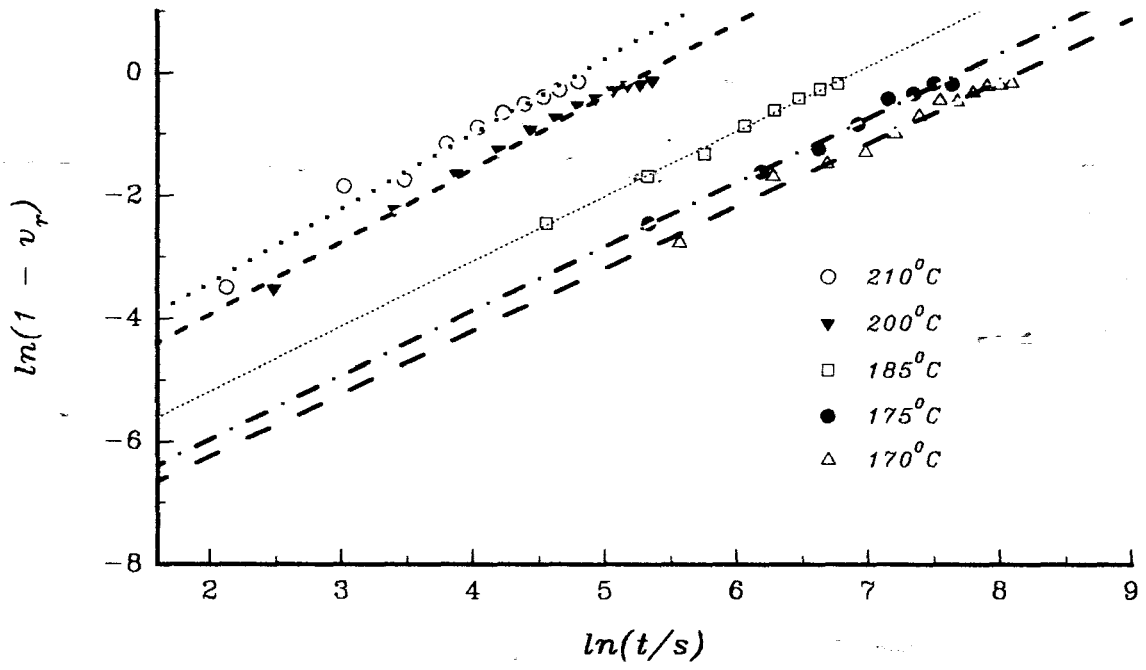

Figure 10.3.9a: Plots of $\ln(1 - v_r)$ versus $\ln(t/s)$ for the decomposition of $Ni(nma)Cl_2$ at different constant temperatures for $0.05 \leq \alpha \leq 0.85$.

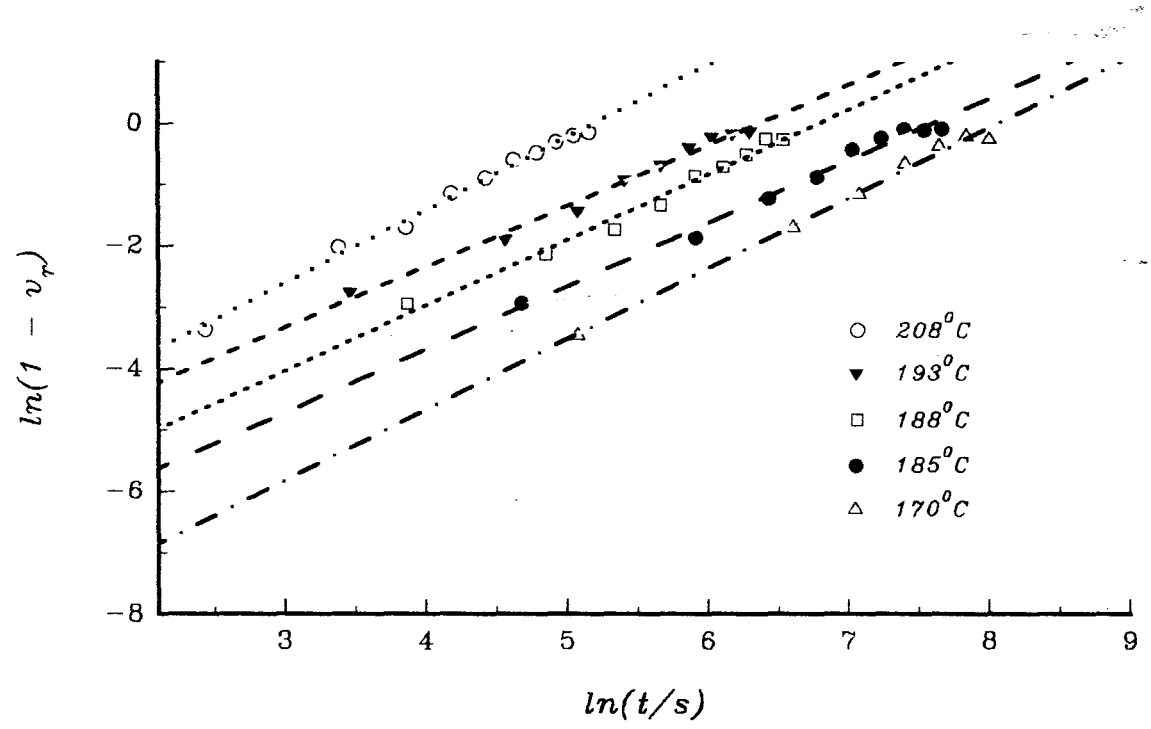

Figure 10.3.9b: Plots of $\ln(1 - v_r)$ versus $\ln(t/s)$ for the decomposition of $Ni(nma)Cl_2$ at different constant temperatures for $0.05 \leq \alpha \leq 0.85$.

Table 10.3.6: Rate coefficients for the decomposition of N(*nma*)Cℓ_2 at different constant temperatures calculated using the new empirical (**B2**) expression, $\upsilon_r = 1 - (kt)^b$, with $b = 2$ or 3, for $0.05 \leq \alpha \leq 0.85$.#

	$b = 2$		$b = 3$	
T / °C	k / 10^{-3} s^{-1}	r	k / 10^{-3} s^{-1}	r
210	7.188 ± 0.080	0.9712	6.099 ± 0.097	0.9426
208	5.665 ± 0.062	0.9755	4.962 ± 0.089	0.9362
205	4.298 ± 0.058	0.9656	3.492 ± 0.068	0.9318
200	5.091 ± 0.079	0.9712	4.424 ± 0.104	0.9366
200*	2.547 ± 0.051	0.9185	2.225 ± 0.052	0.8933
198	2.189 ± 0.044	0.9168	1.749 ± 0.044	0.8788
195	2.341 ± 0.019	0.9837	2.081 ± 0.029	0.9545
193	1.869 ± 0.017	0.9804	1.601 ± 0.022	0.9558
190	2.010 ± 0.017	0.9819	1.848 ± 0.023	0.9647
188	1.283 ± 0.012	0.9786	1.127 ± 0.014	0.9595
185	0.992 ± 0.008	0.9806	0.837 ± 0.010	0.9556
183	0.507 ± 0.006	0.9475	0.417 ± 0.006	0.9253
180	0.738 ± 0.008	0.9688	0.637 ± 0.010	0.9313
178	0.529 ± 0.007	0.9494	0.445 ± 0.007	0.9260
175	0.412 ± 0.005	0.9566	0.340 ± 0.005	0.9320
175*	0.432 ± 0.005	0.9612	0.355 ± 0.005	0.9426
173	0.304 ± 0.003	0.9562	0.252 ± 0.003	0.9344
170	0.229 ± 0.004	0.9277	0.186 ± 0.004	0.9857
170*	0.284 ± 0.003	0.9568	0.236 ± 0.003	0.9237

refer to Appendix **IV** for the results of the other α ranges examined.

* run in replicate.

CHAPTER 11

NON-ISOTHERMAL KINETICS OF DECOMPOSITION OF Ni(*nmf*)Cℓ_2

11.1 Introduction

Rising temperature studies may yield kinetic parameters which are inconsistent with those obtained from isothermal measurements [19,108], and comparisons may help to provide information on the physical meanings of the kinetic parameters.

Isothermal kinetic measurements of the decomposition of Ni(*nmf*)Cℓ_2 were supplemented by a non-isothermal kinetic investigation using TG and DSC experiments. The TG curve, Figure **11.1a**, for the decomposition of a small (about 2 mg) sample was obtained in flowing stream of N_2 at a flow rate of about 20 cm^3 min^{-1}. The constant heating rate was 20°C min^{-1}. The constant DSC heating rates were varied from 5 to 30°C min^{-1}.

The fractional conversion (α) and the rates ($\upsilon = d\alpha/dt$) of reactions were calculated as before. Alpha *versus* temperature (T) and rate *versus* T plots for the Ni(*nmf*)Cℓ_2 complex are shown in Figure **11.1b**.

11.2 Methods of analysis

Three different methods of non-isothermal analysis were used: the Coats and Redfern, Borchardt and Daniels, and Kissinger methods.

(a) The Coats and Redfern method is based on the equation [106] (*cf.* eqn. (5.12)).

$$\ell n[g(\alpha)/T^2] = - E_a/RT + \ell n(AR/\beta E_a) \qquad 11.1$$

where β is the constant heating rate (dT/dt). A plot of $\ell n[g(\alpha)/T^2]$ against $^1/T$ should give a straight line when the correct $g(\alpha)$ is used for the calculation. Conversion functions of the type $f(\alpha) = (1 - \alpha)^n$ were tested with n = 0, $^1/_3$, $^1/_2$, $^2/_3$, 1 and 2. The analytical forms of $g(\alpha)$ obtained on the basis of the relation

$$g(\alpha) = \int_0^{\alpha} d\alpha/f(\alpha) \qquad 11.2$$

are listed below for the different values of n.

(i) $n = 0$: $g(\alpha) = \alpha$

(ii) $n = {}^1/_3$: $g(\alpha) = 1½ \{1 - (1 - \alpha)^{2/3}\}$

(iii) $n = ½$: $g(\alpha) = 2 \{1 - (1 - \alpha)^{½}\}$

(iv) $n = {}^2/_3$: $g(\alpha) = 3 \{1 - (1 - \alpha)^{1/3}\}$

(v) $n = 1$: $g(\alpha) = - \ell n(1 - \alpha)$

(vi) $n = 2$: $g(\alpha) = \alpha/(1 - \alpha)$

(b) The method originally developed by Borchardt and Daniels [179] is based on the relationship (*cf.* equation (5.1))

$$d\alpha/dT = (A/\beta) \exp(-E_a/RT) f(\alpha) \qquad 11.3$$

from which an expression for the rate constant may be written as

$$k = [\beta(d\alpha/dT)/f(\alpha)] \qquad 11.4$$

With the choice of $f(\alpha) = (1 - \alpha)^n$

$$k = [\beta(d\alpha/dT)/(1 - \alpha)^n] \qquad 11.5$$

and

$$\ell n(k) = \ell n[\beta(d\alpha/dT)/(1 - \alpha)^n] = - E_a/RT + \ell n(A) \qquad 11.6$$

Rate coefficients were calculated as functions of temperature using equation (11.6) with $n = 0$, ${}^1/_3$, ½, ${}^2/_3$, 1 or 2.

(c) The Kissinger (peak temperature) method is based on the equation [110]

$$\ell n(\beta/RT^2)_{max} = - E_a/RT_{max} + \ell n[(AR/E_a)(1 - 2RT/E_a)] \qquad 11.7$$

in which the subscript *max* signifies " peak " quantities (*cf.* equation 5.12). Therefore a plot of $\ell n(\beta/T^2)_{max}$ *versus* ${}^1/T_{max}$ for several thermal curves obtained at different heating rates (β) should yield a straight line of slope $- E_a/R$ (upon assuming that $1 \gg 2RT/E_a$).

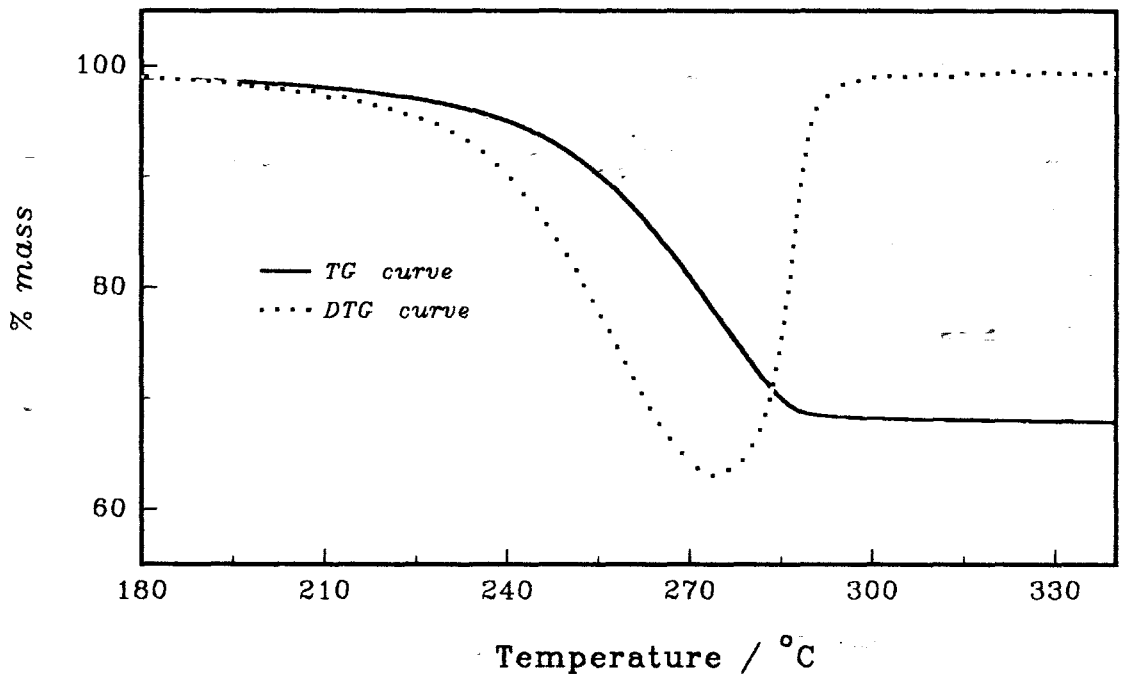

Figure 11.1a: TG and DTG curves for the decomposition of $Ni(nmf)Cl_2$ heated at $20^{\circ}C\ min^{-1}$ in flowing N_2.

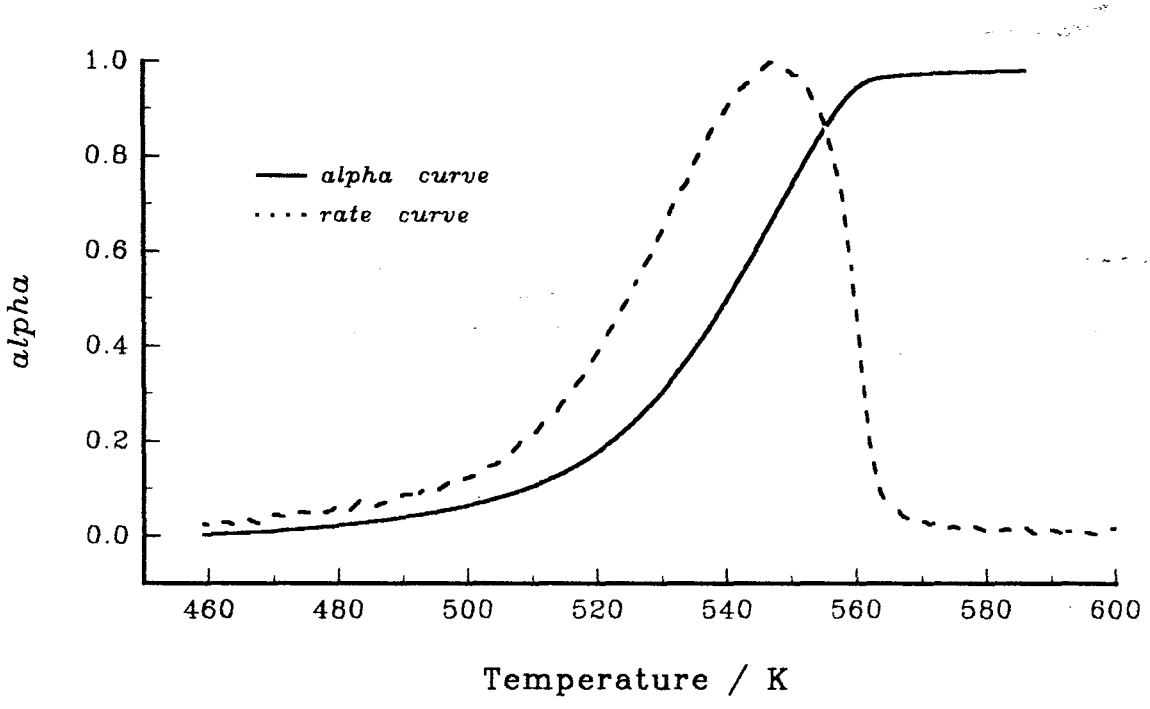

Figure 11.1b: Plots of α versus T and of rate versus T for the decomposition of $Ni(nmf)Cl_2$ heated at $20^{\circ}C\ min^{-1}$ in flowing N_2.

11.3 Non-isothermal analysis

11.3.1 The Coats and Redfern method

Figure 11.2 shows the Coats-Redfern analysis based on the TG data of Figure 11.1. The best straight lines are obtained over the temperature interval of 500 to 550 K, using smaller values of n (*i.e.* 0, $^1/_3$, ½ and $^2/_3$). The calculated E_a values are given in Table 11.1.

11.3.2 The Borchardt and Daniels method

Figure 11.3 shows plots of $\ell n(k)$ versus $^1/T$ according to the Borchardt and Daniels treatment, for the different values of n. The criterion of the best linearity singled out $n = {}^2/_3$ as the most probable order (Table 11.2).

11.3.3 The Kissinger (peak temperature) method

Typical DSC curves obtained at different heating rates are shown in Figure 11.4. Figure 11.5 shows the plot of $\ell n(\beta/T^2)_{max}$ *versus* $^1/T_{max}$. The calculated kinetic parameters are given in Table 11.3.

11.3.4 Comparison of the different methods of non-isothermal analysis

The Coats-Redfern method yielded comparable values of r, when using the various values of n,. This lack of sensitivity to the value of n could be an advantage when determining the value of E_a. The curvatures of the higher temperature region are more serious in the Borchardt-Daniels plots (Figure 11.3). The plots corresponding to $n = 1$ or 2 were non-linear. The high sensitivity to the value of n is an advantage when trying to find the formal rate equation.

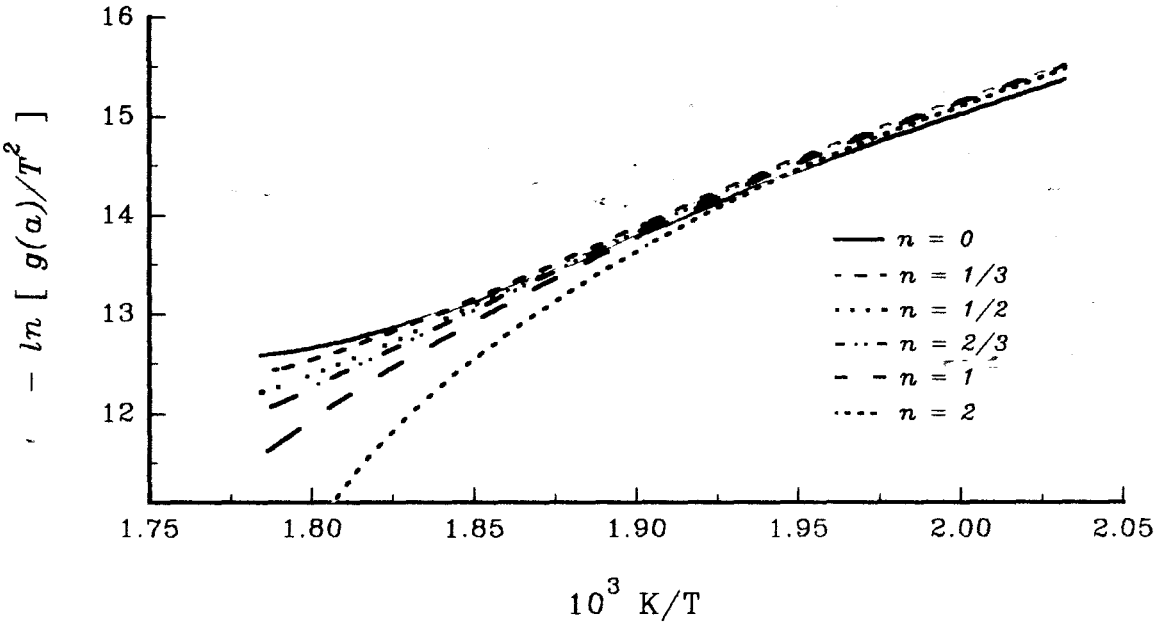

Figure 11.2: Arrhenius-type plots for the non-isothermal decomposition of Ni(nmf)Cl_2, using rate coefficients calculated from the Coats-Redfern method. The temperature range used is 500 to 560 K.

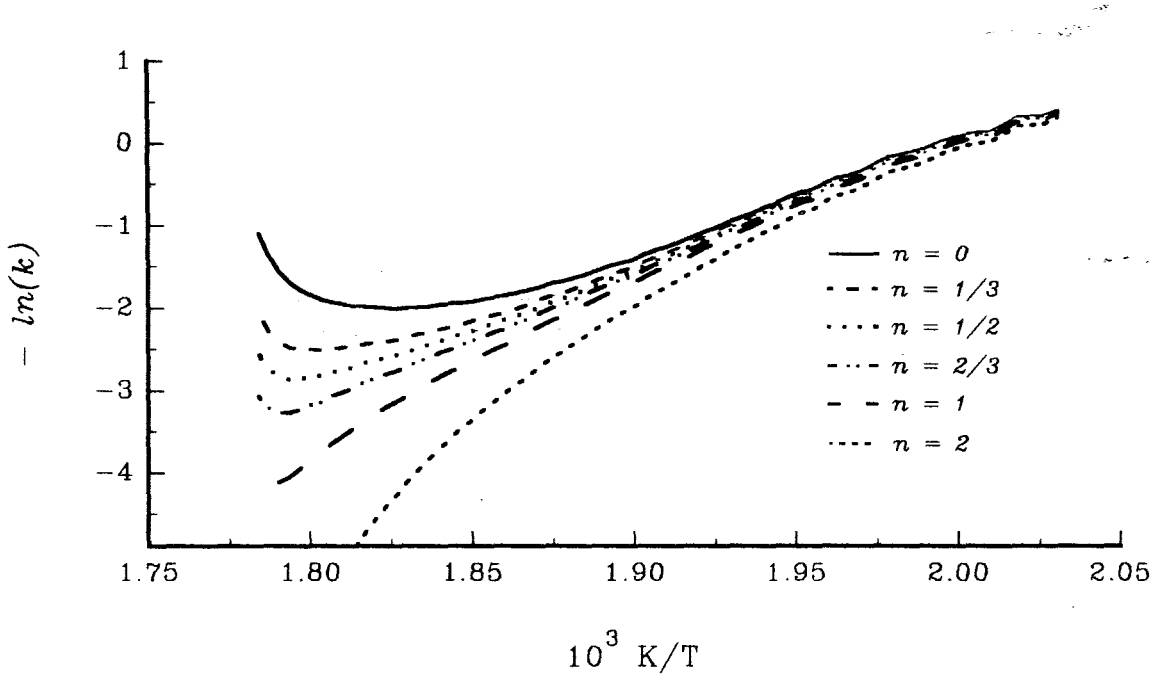

Figure 11.3: Arrhenius plots for the non-isothermal decomposition of Ni(nmf)Cl_2, using rate coefficients from the modified Borchardt-Daniels equation (11.6). The temperature range used is from 500 to 560 K.

Table 11.1: Apparent activation energies for the non-isothermal decomposition of Ni(*nmf*)$C\ell_2$ using the Coats-Redfern method over the separate α (temperature) ranges.

order *n*	E_a / kJ mol^{-1}	r	constant, *a**
(a) α-range: 0.06 - 0.80, *i.e.* 500 to 550 K			
0	104.7 ± 0.3	0.9988	10.15 ± 0.03
1/3	113.0 ± 0.3	0.9987	11.98 ± 0.03
½	116.7 ± 0.4	0.9981	12.87 ± 0.04
2/3	120.8 ± 0.5	0.9971	13.83 ± 0.05
1	129.2 ± 0.8	0.9940	15.82 ± 0.07
2	157.6 ± 1.9	0.9769	22.55 ± 0.17
(b) α-range: 0.06 - 0.90, *i.e.* 500 to 558 K			
0	102.6 ± 0.4	0.9974	9.66 ± 0.04
1/3	112.4 ± 0.3	0.9988	11.83 ± 0.03
½	116.9 ± 0.3	0.9985	12.92 ± 0.03
2/3	122.0 ± 0.5	0.9974	14.11 ± 0.05
1	132.7 ± 0.8	0.9931	16.63 ± 0.08
2	170.4 ± 2.5	0.9644	25.54 ± 0.24
(c) α-range: 0.06 - 0.95, *i.e.* 500 to 560 K			
0	100.7 ± 0.5	0.9954	9.21 ± 0.05
1/3	111.5 ± 0.3	0.9986	11.62 ± 0.03
½	116.8 ± 0.3	0.9987	12.88 ± 0.03
2/3	122.7 ± 0.4	0.9976	14.26 ± 0.05
1	135.3 ± 0.9	0.9920	17.23 ± 0.10
2	181.8 ± 3.1	0.9502	28.20 ± 0.33

* $a = -\ell n[AR/\beta E_a)(1 - 2RT/E_a)]$

Table 11.2: Apparent activation energies for the non-isothermal decomposition of Ni(*nmf*)$C\ell_2$ using the modified Borchardt-Daniels method over the separate α (temperature) ranges.

order *n*	E_a / kJ mol^{-1}	r	$\ell n(A)$
(a) α-range: 0.06 - 0.80, *i.e.* 500 to 550 K			
0	96.4 ± 0.7	0.9865	23.28 ± 0.13
1/3	118.8 ± 0.8	0.9920	28.56 ± 0.07
½	127.7 ± 0.5	0.9972	30.66 ± 0.05
2/3	136.5 ± 0.3	0.9993	32.76 ± 0.03
1	154.2 ± 0.6	0.9974	36.96 ± 0.06
2	207.2 ± 2.6	0.9749	49.55 ± 0.23
(b) α-range: 0.06 - 0.90, *i.e.* 500 to 558 K			
0	90.36 ± 2.0	0.9190	21.85 ± 0.20
1/3	113.1 ± 1.1	0.9839	27.24 ± 0.11
½	124.6 ± 0.6	0.9954	29.94 ± 0.06
2/3	136.0 ± 0.3	0.9994	32.64 ± 0.03
1	158.8 ± 0.9	0.9949	38.03 ± 0.09
2	227.2 ± 3.7	0.9563	54.21 ± 0.36
(c) α-range: 0.06 - 0.95, *i.e.* 500 to 560 K			
0	78.8 ± 2.8	0.8088	19.18 ± 0.30
1/3	106.2 ± 1.6	0.9576	25.63 ± 0.18
½	119.9 ± 1.1	0.9855	28.78 ± 0.11
2/3	133.6 ± 0.6	0.9967	32.10 ± 0.06
1	161.1 ± 0.9	0.9943	38.56 ± 0.10
2	243.3 ± 4.4	0.9426	57.93 ± 0.47

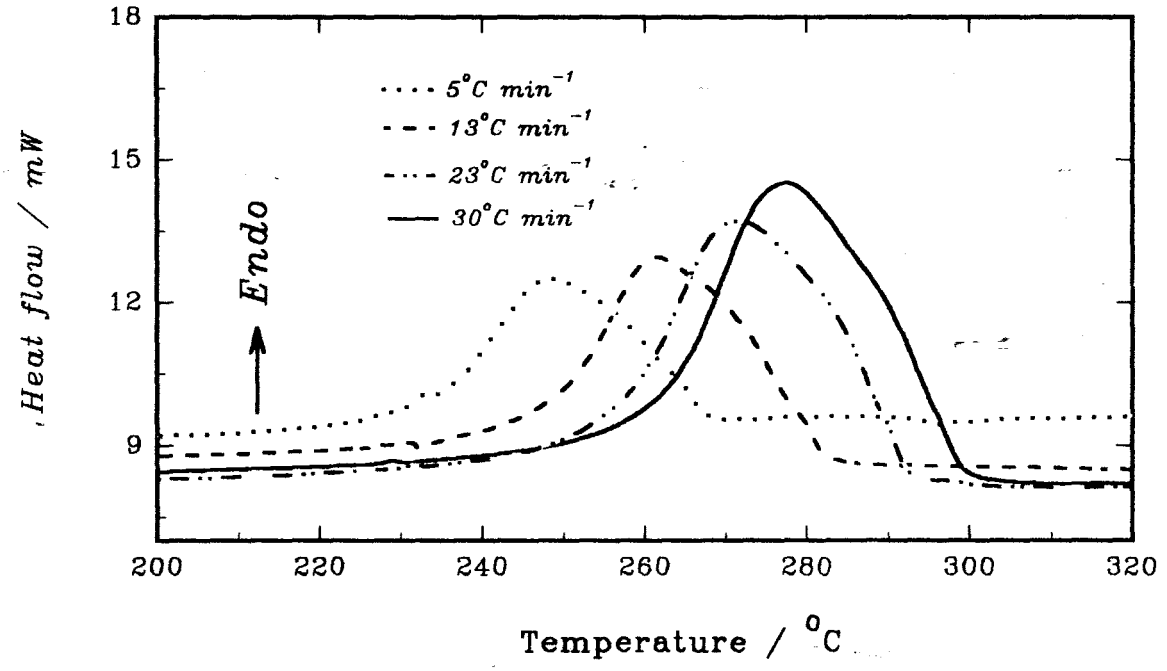

Figure 11.4: DSC curves for the decompoition of $Ni(nmf)Cl_2$ at different heating rates. The T_{max} values were used to calculate a value for the apparent activation energy using the Kissinger method.

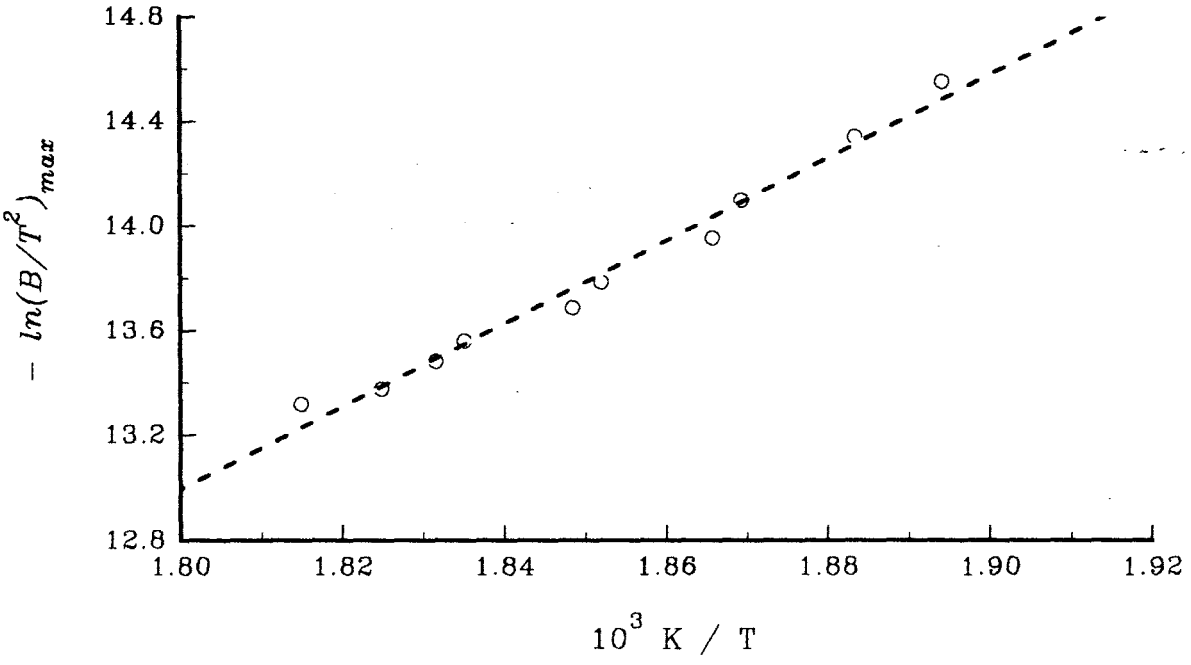

Figure 11.5: Arrhenius-type plot for the non-isothermal DSC kinetics of $Ni(nmf)Cl_2$ using the Kissinger method.

Table 11.3: Non-isothermal DSC data for the decomposition of Ni(*nmf*)$C\ell_2$ (β and T_{max}) and the apparent activation energy calculated using Kissinger's method.

β / °C min^{-1}	T_{max} / K	$-\ell n(\beta/T^2)_{max}$
5	522	15.00
8	528	14.55
10	531	14.34
13	535	14.10
15	536	13.96
18	540	13.79
20	541	13.69
23	545	13.56
25	546	13.48
28	548	13.38
30	551	13.32

E_a / kJ mol^{-1} = 141 ± 6 r = 0.9848 $\ell n(A)$ = 27.2 ± 0.7

CHAPTER 12

STUDIES OF OTHER CHLORO METAL(II)-AMIDE COMPLEXES

12.1 Introduction

The aim of this part of the investigation was to compare results of the amide complexes of nickel(II) chloride with related cobalt(II) and copper(II) complexes. The cobalt(II) and copper(II) chloride complexes were however difficult to handle and store. Most of them hydrolysed and decomposed rapidly on contact with atmospheric moisture. Spectroscopic and thermal measurements made using the relatively stable complexes are described.

12.2 Preparation and analytical results

12.2.1 Cobalt(II)-amide complexes

Five $CoL_2C\ell_2$ complexes were prepared using **method (A)** of Chapter 8 (§ 8.2.2). The complexes prepared and their analytical data are shown in Table 12.1.

Table 12.1: Analytical data for the amide complexes of cobalt(II) chloride

Prep. method	Complex stoichiometry	% Cobalt Found (Calc.)	% Nitrogen Found (Calc.)	% Carbon Found (Calc.)	% Hydrogen Found (Calc.)	% Ligand Found (Calc.)
A	$Co(fa)_2C\ell_2$	27.4 (26.8)	12.6 (12.7)	10.8 (10.9)	2.8 (2.8)	41.6 (41.0)
A	$Co(nma)_2C\ell_2$	20.5 (21.4)	9.7 (10.2)	25.0 (26.1)	5.2 (5.1)	52.0 (53.0)
A	$Co(dmf)_2C\ell_2$	19.5 (21.4)	8.6 (10.2)	25.6 (26.1)	5.1 (5.1)	53.4 (53.0)
A	$Co(dma)_2C\ell_2$	19.1 (19.4)	9.1 (9.2)	31.3 (31.6)	6.0 (6.0)	57.7 (57.3)
A	$Co(dmp)_2C\ell_2$	18.1 (17.7)	6.9 (8.4)	33.0 (36.2)	4.2 (3.3)	57.1 (60.9)

12.2.2 Copper(II)-amide complexes

Three $CuL_2C\ell_2$ complexes, where L = *aa*, *fa* or *iba*, were prepared using **method (A)** of **Chapter 8** (**§ 8.2.2**). Analytical data for the complexes are given in Table 12.2.

Table 12.2: Analytical data for the copper(II) chloride complexes

Prep. method	Complex stoichiometry	% Copper Found (Calc.)	% Nitrogen Found (Calc.)	% Carbon Found (Calc.)	% Hydrogen Found (Calc.)	% Ligand Found (Calc.)
A	$Cu(aa)_2C\ell_2$	25.1 (25.2)	10.4 (11.1)	17.8 (19.0)	3.8 (4.0)	47.3 (46.8)
A	$Cu(fa)_2C\ell_2$	27.1 (28.4)	12.0 (12.5)	10.5 (10.7)	2.7 (2.7)	43.0 (40.1)
A	$Cu(iba)_2C\ell_2$	22.4 (20.6)	8.6 (9.1)	30.2 (31.1)	5.8 (5.9)	54.5 (56.4)

12.3 Visible and near-infrared diffuse reflectance spectra

12.3.1 Cobalt(II)-amide complexes

Visible and near-infrared diffuse reflectance spectra of the $CoL_2C\ell_2$ complexes and anhydrous (octahedral) $CoC\ell_2$ are shown in Appendix **V**, Figures **12.1.1** and **12.1.2**. Table **12.3** gives the main bands. The ground state of octahedrally coordinated cobalt(II) is $^4T_{1g}$ and three main bands are often observed, corresponding to transitions to the electronic states $^4T_{2g}(F)$, $^4A_{2g}(F)$ and $^4T_{1g}(P)$ [155]. The ground state of tetrahedral cobalt(II) is $^4A_2(F)$ and two bands are expected between about 5000 and 20,000 cm^{-1}, corresponding to transitions to the excited states $^4T_1(F)$ and $^4T_1(P)$ [156,177].

Visible and near-infrared spectra of the mauve $Co(fa)_2C\ell_2$ and the blue $Co(nma)_2C\ell_2$ complexes suggest an octahedral environment for the cobalt(II) ions. The spectra are similar to the spectrum of anhydrous $CoC\ell_2$. The ratios of $\hat{\upsilon}_2/\hat{\upsilon}_1$ (≈ 2.0) conform to the usual value from octahedral assignment [155]. Spectra of the $Co(dmf)_2C\ell_2$, $Co(dma)_2C\ell_2$ and $Co(dmp)_2C\ell_2$ complexes (Figure **12.1.2**) are typical of cobalt(II) ion in a tetrahedral environment [154]. The $Co(dma)_2C\ell_2$ complex isolated by Madan *et al.* [130] also exhibited a tetrahedral coordination.

12.3.2 Copper(II)-amide complexes

Visible and near-infrared diffuse reflectance spectra of the $CuL_2C\ell_2$ complexes and $CuC\ell_2$ (octahedral) are shown in Figure **12.1.3** of Appendix **V**. Table **12.4** gives the main bands.

The visible region reflectance spectra of the $CuL_2C\ell_2$ complexes show a broad band

around 13,000 cm^{-1}. This suggests an octahedral coordination for the copper(II) ions. The spectra of Cu(*iba*)$_2C\ell_2$ and anhydrous $CuC\ell_2$ exhibited two bands. The higher energy bands are possibly due to charge transfer.

12.4 Infrared (IR) absorption spectra

The IR spectra (Figures 12.2.1 to 12.2.5) were recorded using KBr or CsI discs method over the range of 2500 to 200 cm^{-1}. Assignments of the $\hat{\upsilon}_{C=O}$ (amide I), $\hat{\upsilon}_{N-H}$ (amide II), $\hat{\upsilon}_{C-N}$ (amide III), $\hat{\upsilon}_{M-O}$ (metal-oxygen), and $\hat{\upsilon}_{M-C\ell}$ (metal-chloride) bands are shown in Tables 12.5 and 12.6 (far-IR). Results indicate that the amide ligands are coordinated to the metal(II) ions through the carbonyl oxygen atom (*cf.* **§8.6**).

Table 12.3: Visible and near-infrared diffuse reflectance spectra of the $CoL_2C\ell_2$ complexes.

Complex	**Colour**	**Band assignments / 10^3 cm^{-1}**		
(a) Octahedral		$^4T_{2g}(F) \leftarrow {}^4T_{1g}(F)$	$^4A_{2g}(F) \leftarrow {}^4T_{1g}(F)$	$^4T_{1g}(P) \leftarrow {}^4T_{1g}(F)$
		($\hat{\upsilon}_1$)	($\hat{\upsilon}_2$)	($\hat{\upsilon}_3$)
$CoC\ell_2$	blue	6.291	12.980	16.892
Co(fa)$_2C\ell_2$	mauve	5.808	13.356	16.112(sh); 19.299
Co(nma)$_2C\ell_2$	blue	6.293	11.933	15.567; 18.573(sh)
(b) Tetrahedral		$^4T_1(F) \leftarrow {}^4A_2(F)$		$^4T_2(P) \leftarrow {}^4A_2(F)$
		($\hat{\upsilon}_2$)		($\hat{\upsilon}_3$)
Co(dmf)$_2C\ell_2$	royal blue	6.110		15.024
Co(dma)$_2C\ell_2$	royal blue	5.880		15.172; 19.588(sh)
Co(dmp)$_2C\ell_2$	royal blue	5.880		15.172

sh = shoulder

Table 12.4: Visible and near-infrared diffuse reflectance spectra of the $CuL_2C\ell_2$ complexes.

Complex	Colour	Band assignments / 10^3 cm^{-1}	
Octahedral		$^2T_{2g}(D) \leftarrow {}^2E_g(D)$	
$CuC\ell_2$	buff	13.057	24.404
$Cu(aa)C\ell_2$	green	12.969	-
$Cu(fa)_2C\ell_2$	green	13.018	-
$Cu(iba)_2C\ell_2$	gold	11.930	26.325

Table 12.5: Assignment of IR absorption bands of the $ML_2C\ell_2$ complexes.

Ligand (L) in ↓	Infrared vibrational frequencies / cm^{-1}					
	Amide I		Amide II		Amide III	
	free L	complex	free L	complex	free L	complex
(a) $CoL_2C\ell_2$						
nma	1659	1632	1565	1567	1300	1313
dmf	1674	1654	1501	1500	1095	1114
fa	1691	1692	1606	1585	1309	1345
dma	1639	1617	1502	1512	1401	1428
dmp	1644	1600	1498	1512	1402	1415
(b) $CuL_2C\ell_2$						
aa	1684	1665	1636	1586	1400	1452
fa	1691	1686	1606	1579	1309	1366
iba	1672	1652	1644	1577	1429	1479

Table 12.6: Assignment of far-IR absorption bands of the $ML_2C\ell_2$ complexes.

Ligand (L) in ↓	Far-infrared vibrational frequencies / cm^{-1}		
	$\hat{\upsilon}_{M\text{-}Cl}$ (metal-chloride)	$\hat{\upsilon}_{M\text{-}O}$ (metal-oxygen)	other bands (unassigned)
(a) $CoL_2C\ell_2$			
nma	224	351	247
dmf	247	311	216
fa	225	313	248
dma	248	305	220; 208
dmp	248	304	215
(b) $CuL_2C\ell_2$			
aa	226	352	207
fa	232	-	209
iba	221	399	211

12.5 Decomposition stoichiometries and thermal data

12.5.1 Introduction

TG measurements were made for all the characterized amide complexes with cobalt(II) or copper(II) chloride, $ML_2C\ell_2$. Gram-size samples of partially decomposed complexes and / or the decomposition residue (for visual inspection and spectral analysis) were prepared in a tube furnace in flowing nitrogen. With the only exception of $Co(fa)_2C\ell_2$, DSC measurements were prevented by the reaction of melted complex with the aluminium pan.

12.5.2 Cobalt(II)-amide complexes

Octahedral $CoL_2C\ell_2$ ***complexes***

Of the two octahedral $CoL_2C\ell_2$ complexes (where L = *fa* or *nma*), only $Co(fa)_2C\ell_2$ decomposed in two steps. The TG mass loss data in Table 12.7 are consistent with the decomposition scheme

$$Co(fa)_2C\ell_2\ (s) \rightarrow Co(fa)C\ell_2\ (s) + fa\ (g)$$
$$Co(fa)C\ell_2\ (s) \rightarrow CoC\ell_2\ (s) + fa\ (g)$$

The TG, DTG and DSC curves are shown in Figure 12.3.1

$Co(nma)_2C\ell_2$ showed a single stage TG decomposition to give $CoC\ell_2$ as end product.

$$Co(nma)_2C\ell_2\ (s) \rightarrow CoC\ell_2\ (s) + 2nma\ (g)$$

The TG and DTG curves are shown in Figure 12.3.2, and the thermal data are shown in Table 12.7.

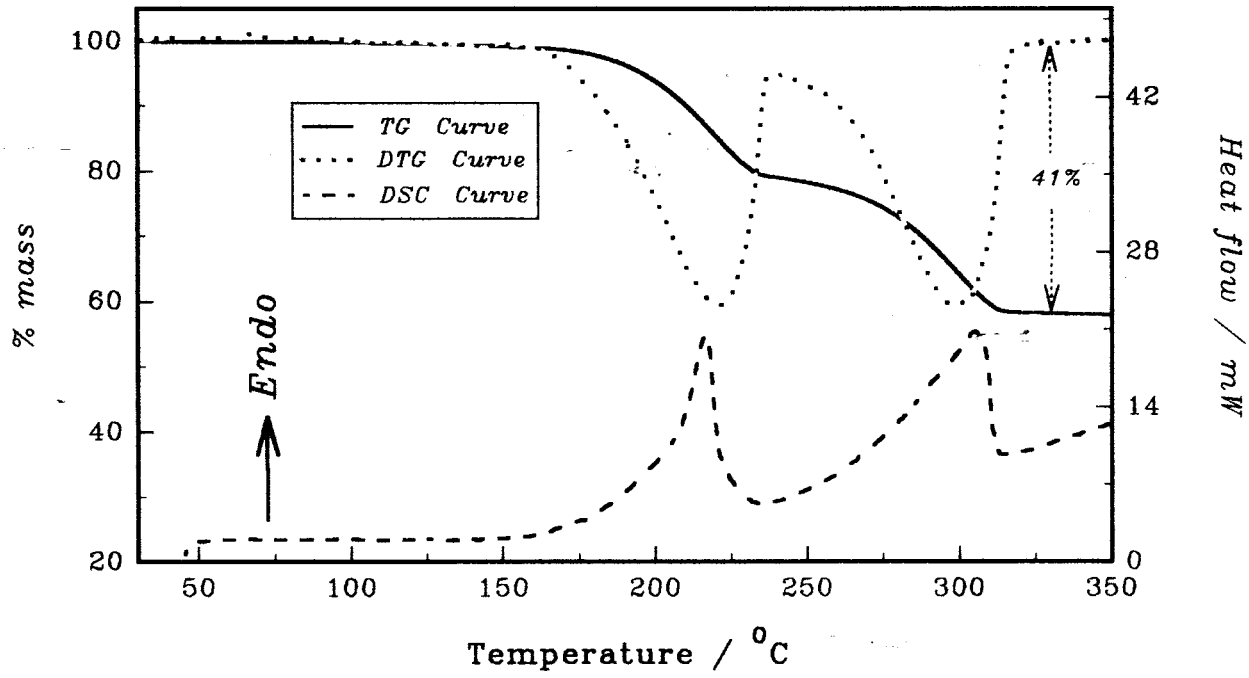

Figure 12.3.1: TG, DTG and DSC curves for $Co(fa)_2Cl_2$ heated at $20^{\circ}C\ min^{-1}$ in flowing N_2.

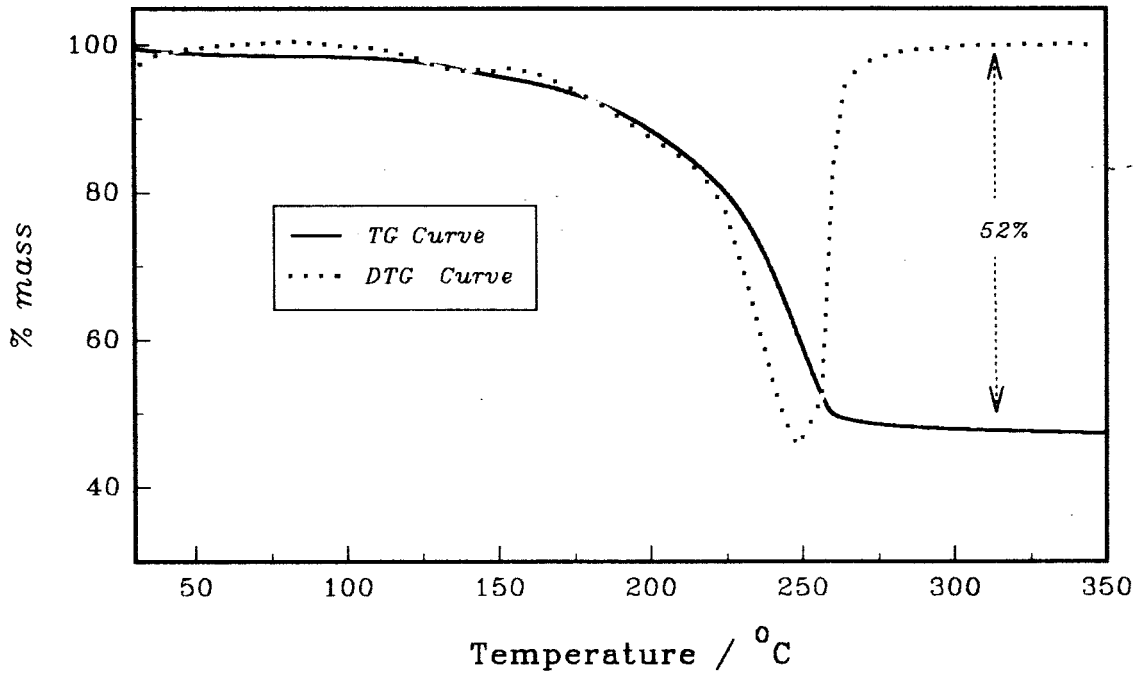

Figure 12.3.2: TG and DTG curves for $Co(nma)_2Cl_2$ heated at $20^{\circ}C\ min^{-1}$ in flowing N_2.

Table 12.7: Thermal decomposition data for the octahedral $CoL_2C\ell_2$ complexes.

Complex	Fragment lost			DTG Temp. / °C		ΔH_{2L} / kJ mol^{-1}
	Formula	% mass loss		T_e	T_{max}	
Residue		Found	Calc.			
$Co(fa)_2C\ell_2$	*fa*	20.4	20.5	194	221	
	fa	20.9	20.5	275	300	136
residue		58.7	59.0			
$Co(nma)_2C\ell_2$	2*nma*	52.3	53.0	217	248	-
residue		47.7	47.0			

Tetrahedral $CoL_2C\ell_2$ ***complexes***

The complexes with L = *dmf* or *dma* decomposed in two TG steps. The thermal analysis curves are shown in Figures **12.3.3** and **12.3.4**. For $Co(dmf)_2C\ell_2$, the mass loss data (Table **12.8**) are consistent with the decomposition scheme

$$3Co(dmf)_2C\ell_2\ (s) \rightarrow Co_3(dmf)_2C\ell_6\ (s) + 4dmf\ (g)$$
$$Co_3(dmf)_2C\ell_6\ (s) \rightarrow 3CoC\ell_2\ (s) + 2dmf\ (g)$$

For the complex with L = *dma*, the mass loss data (Table **12.8**) correspond to a loss of five ligands and a subsequent loss of one *dma* molecule per metal complex.

$$3Co(dma)_2C\ell_2\ (s) \rightarrow Co_3(dma)C\ell_6\ (s) + 5dma\ (g)$$
$$Co_3(dma)C\ell_6\ (s) \rightarrow 3CoC\ell_2\ (s) + dma\ (g)$$

$Co(dmp)_2C\ell_2$ showed a single-stage TG curve to give $CoC\ell_2$ as end product.

$$Co(dmp)_2C\ell_2\ (s) \rightarrow CoC\ell_2\ (s) + 2dmp\ (g)$$

The TG and DTG curves are shown in Figure **12.3.5**. The thermal decomposition data are given in Table **12.8**.

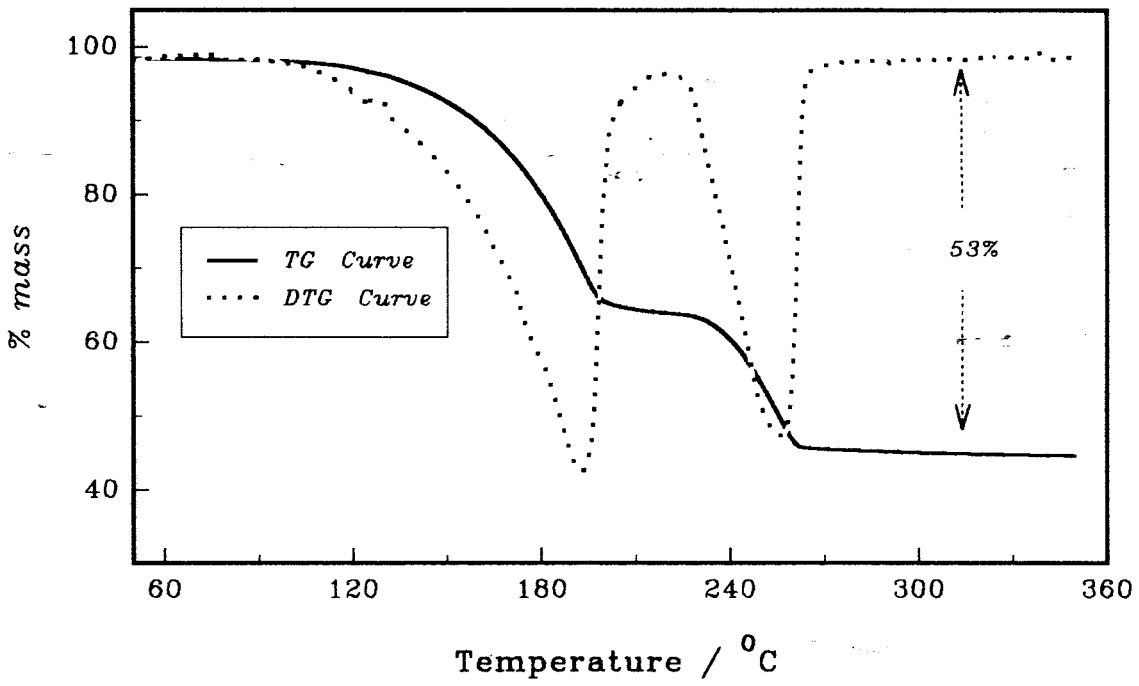

Figure 12.3.3: TG and DTG curves for $Co(dmf)_2Cl_2$ heated at $20^{\circ}C\ min^{-1}$ in flowing N_2.

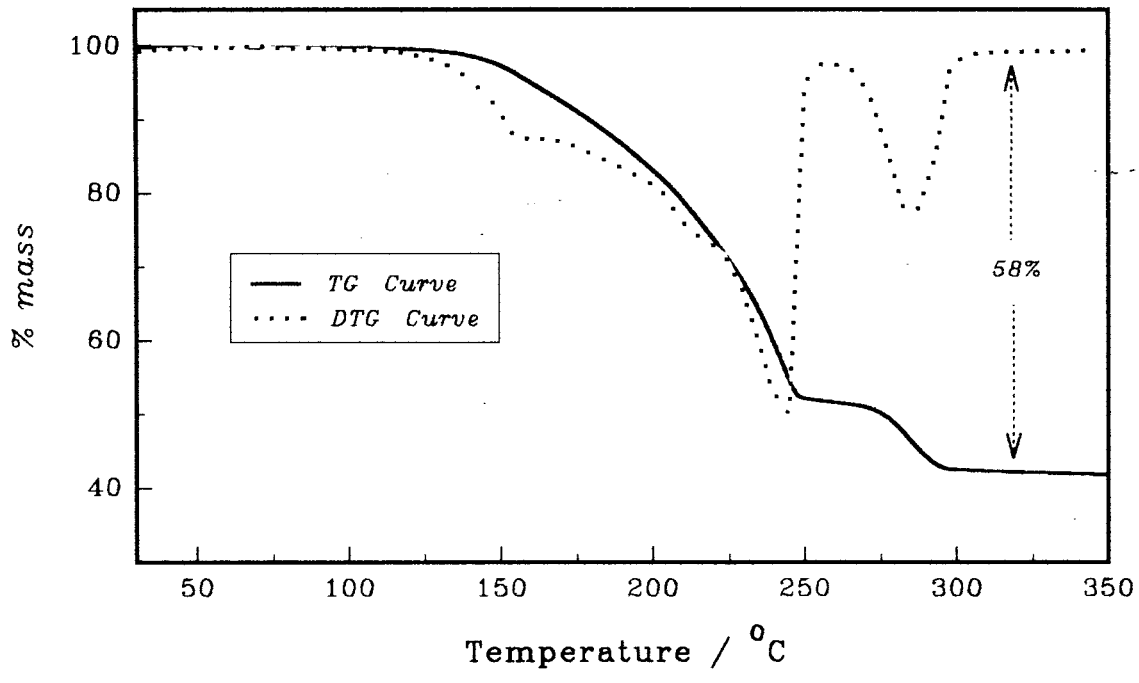

Figure 12.3.4: TG and DTG curves for $Co(dma)_2Cl_2$ heated at $20^{\circ}C\ min^{-1}$ in flowing N_2.

Table 12.8: Thermal decomposition data for the tetrahedral $CoL_2C\ell_2$ complexes.

Complex	Fragment lost			DTG Temp. / °C	
	Formula	% mass loss		T_e	T_{max}
Residue		Found	Calc.		
$3Co(dmf)_2C\ell_2$	4*dmf*	34.3	35.3	106	192
	2*dmf*	19.1	17.7	239	256
residue		43.6	47.0		
$3Co(dma)_2C\ell_2$	5*dma*	47.9	47.8	202	245
	dma	9.7	9.6	276	285
residue		42.4	42.6		
$Co(dmp)_2C\ell_2$	2*dmp*	57.1	60.9	210	240
residue		42.9	39.1		

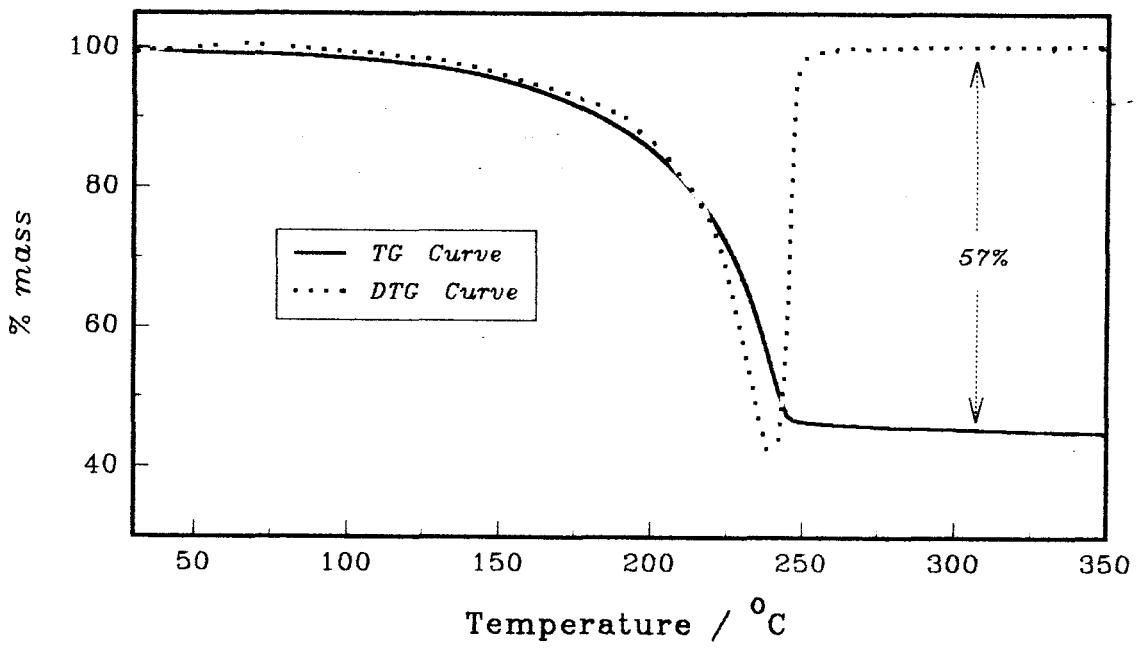

Figure 12.3.5: TG and DTG curves for $Co(dmp)_2Cl_2$ heated at 20°C min^{-1} in flowing N_2 .

12.5.3 Copper(II)-amide complexes

The complexes with L = *aa* or *fa* decomposed in two partially overlapping TG steps. The TG mass loss data (Table **12.9**) are consistent with the decomposition scheme

$$CuL_2C\ell_2\ (s) \rightarrow CuLC\ell_2\ (s) + L\ (g)$$
$$CuLC\ell_2\ (s) \rightarrow CuC\ell_2\ (s) + L\ (g)$$

The TG and DTG curves are shown in Figure **12.4.1** and **12.4.2**.

$Cu(iba)_2C\ell_2$ showed a single-stage TG curve to give $CuC\ell_2$ as end product.

$$Cu(iba)_2C\ell_2\ (s) \rightarrow CuC\ell_2\ (s) + 2iba\ (g)$$

The TG and DTG curves are shown in Figure **12.4.3**, and the thermal data are given in Table **12.9**.

Table 12.9: Thermal decomposition data for the octahedral $CuL_2C\ell_2$ complexes.

Complex	Fragment lost			DTG Temp. / °C	
	Formula	% mass loss		T_e	T_{max}
Residue		Found	Calc.		
$Cu(aa)_2C\ell_2$	*aa*	23.4	23.4	165	191
	aa	23.9	23.4	219	239
residue		52.7	53.2		
$Cu(fa)_2C\ell_2$	*fa*	20.1	20.1	182	205
	fa	22.9	20.1	233	248
residue		57.0	59.8		
$Cu(iba)_2C\ell_2$	2*iba*	54.5	56.4	193	220
residue		45.5	43.6		

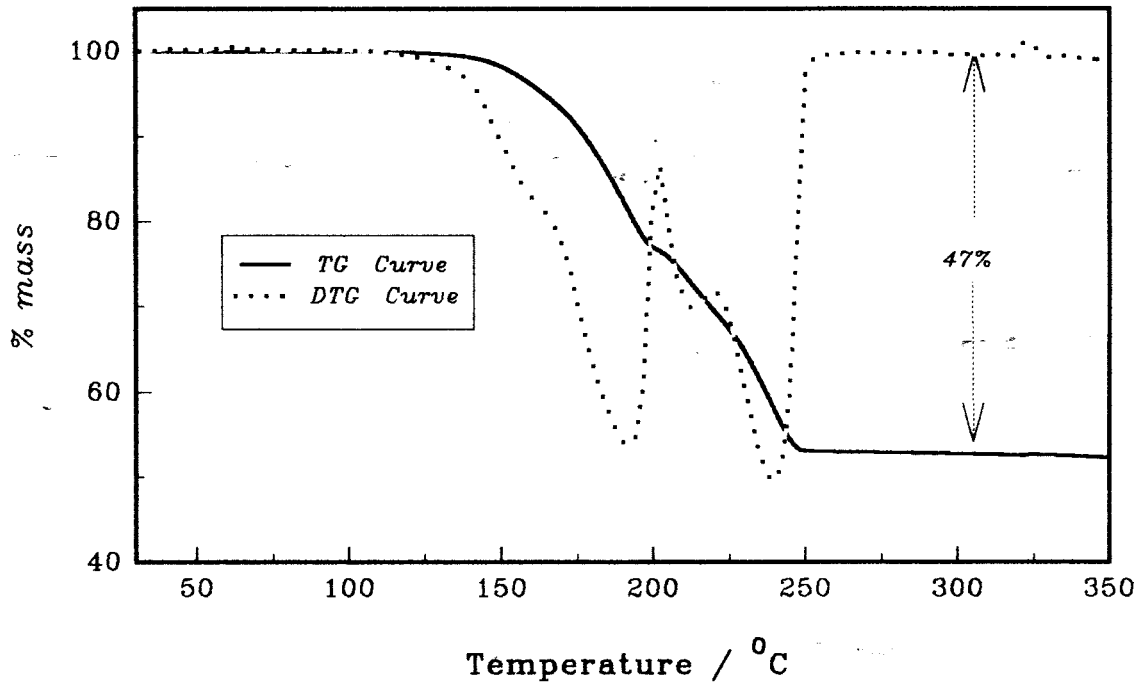

Figure 12.4.1: TG and DTG curves for $Cu(aa)_2Cl_2$ heated at $20^{\circ}C\ min^{-1}$ in flowing N_2 .

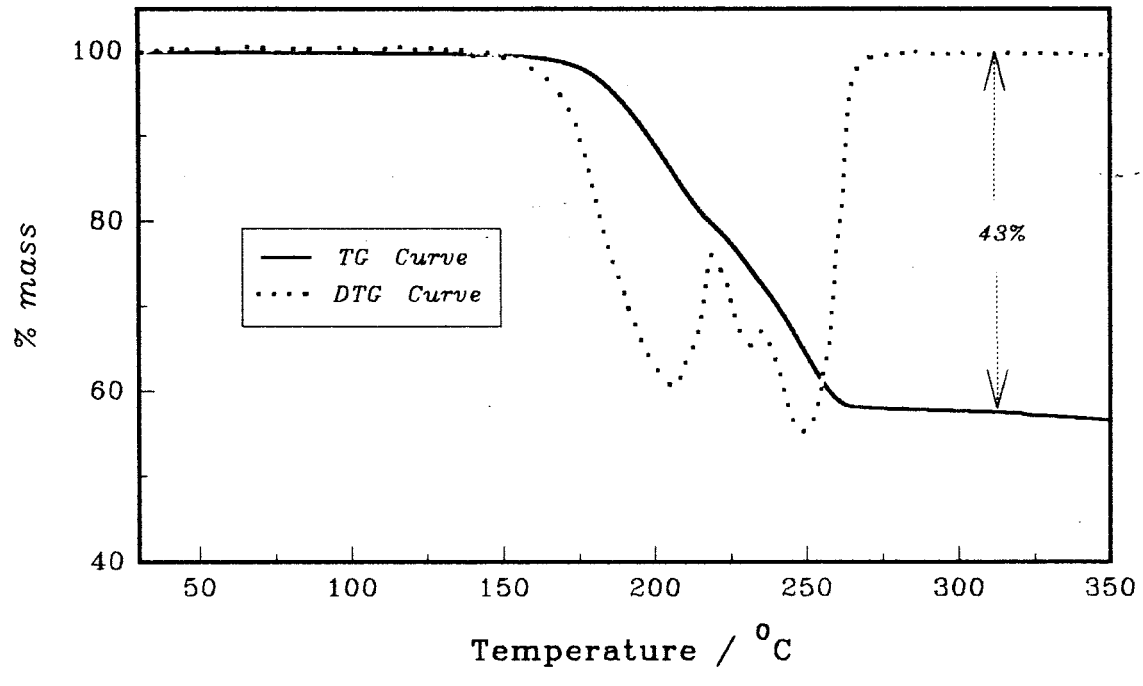

Figure 12.4.2: TG and DTG curves for $Cu(fa)_2Cl_2$ heated at $20^{\circ}C\ min^{-1}$ in flowing N_2 .

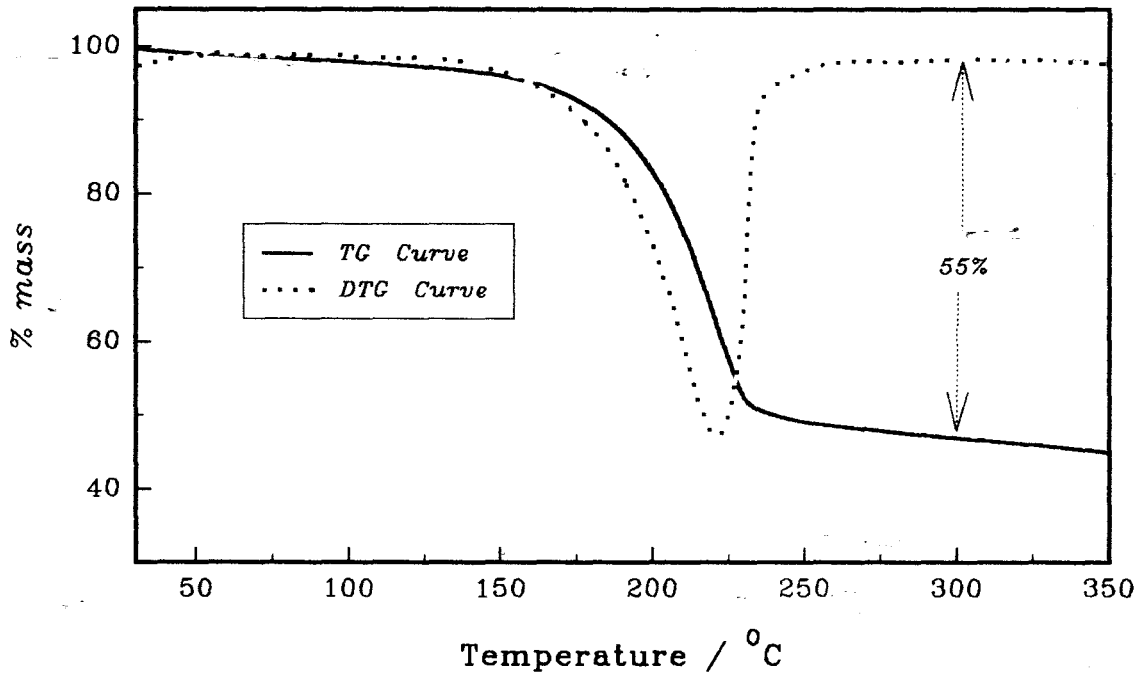

Figure 12.4.3: TG and DTG curves for $Cu(iba)_2Cl_2$ heated at $20^0C\ min^{-1}$ in flowing N_2 .

CHAPTER 13

DISCUSSION OF RESULTS

This chapter gives a discussion of the results of syntheses, spectroscopic and thermoanalytical studies.

13.1 Stoichiometries and structures of the complexes

The amides of interest in this study (refer to § **6.1** and § **8.2.1**) are of the general structural formula

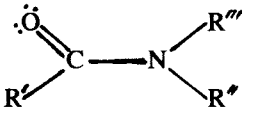

Here R′ is H, or an alkyl group such as methyl, ethyl or propyl. R″ and R‴ are H's, or groups such as methyl or ethyl, or one of these groups and hydrogen. The complexes prepared and their analytical data are given in Tables **8.3**, **12.1** and **12.2**.

The ligands (L) in $NiL_2C\ell_2(2H_2O)$ were N-methylformamide (*nmf*), N-methylacetamide (*nma*) or acetamide (*aa*). Thermoanalytical curves indicated that loss of water occurs below 120°C. This infers that the water molecules are held outside the coordination sphere [9,14,138]. Isothermal heating yielded corresponding complexes of the type $NiLC\ell_2$. Visible and near-infrared reflectance spectra suggested octahedral structures.

N-ethylformamide (*nef*), N,N-dimethylformamide (*dmf*), formamide (*fa*), propionamide (*pa*), butyramide (*ba*) and isobutyramide (*iba*), yielded octahedral complexes of the type $NiL_2C\ell_2$ from their respective ethanol solutions. Upon heating at selected constant temperatures, $NiL_2C\ell_2$ (where L = *nef*, *dmf* or *pa*) yielded octahedral complexes of the type $Ni_3L_2C\ell_6$. N,N-diethylformamide (*def*) and N,N-dimethylacetamide (*dma*) ligands yielded similar complexes from their respective ethanol solutions. $Ni_3(dmp)C\ell_6$ was the only complex of the type $Ni_3LC\ell_6$ characterized.

The cobalt(II) and copper(II) complexes had stoichiometries $CoL_2C\ell_2$ (where L = *fa*, *nma*, *dmf*, *dma* or *dmp*) and $CuL_2C\ell_2$ (where L = *fa*, *aa* or *iba*). Cobalt(II)-amide complexes were tetrahedrally coordinated, except for the complexes with formamide or N-methylacetamide, for which a distorted octahedral environment has been proposed. Visible region reflectance spectra of the $CuL_2C\ell_2$ complexes suggested a very distorted octahedral arrangement.

The actual structures of the various octahedral metal(II) chloride complexes are not known, but it is postulated that there is considerable chloride bridging (Figure 13.1). The assignment of the $\upsilon_{M\text{-}Cl}$ vibration (Table 13.1) are in agreement with assignments made for similar vibrations in related complexes [161,180-182], for which halide bridging has been suggested.

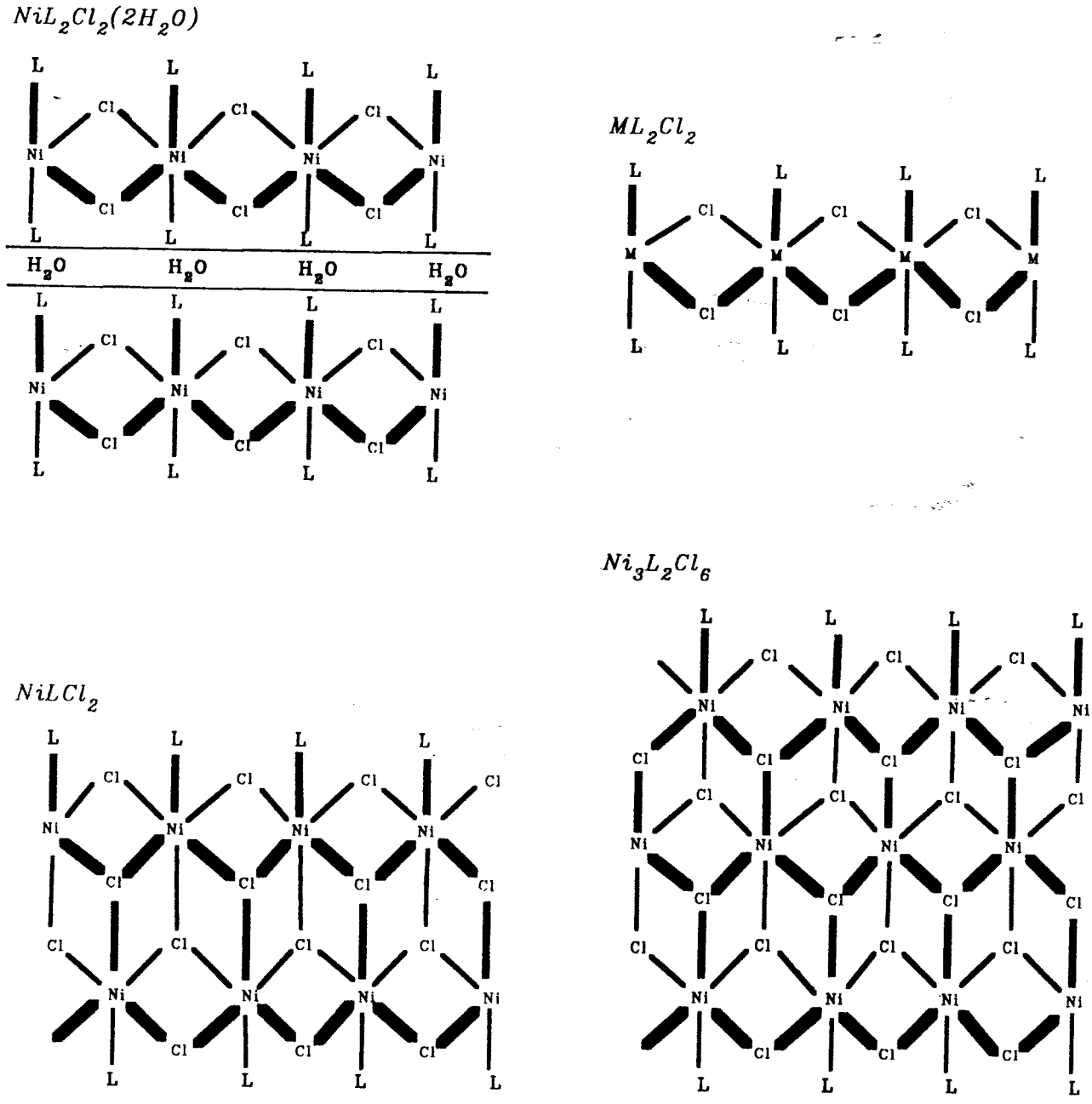

Figure 13.1: Postulated structures of the octahedral $NiL_2C\ell_2(2H_2O)$, $ML_2C\ell_2$, $NiLC\ell_2$ and $Ni_3L_2C\ell_6$ complexes.

Table 13.1: Summary of IR frequencies ($\Delta\tilde{\upsilon}_{C=O}$, $\tilde{\upsilon}_{M-O}$, $\tilde{\upsilon}_{M-Cl}$ and $\Delta\tilde{\upsilon}_{C-N}$) for the MCl_2-amide complexes.

Ligand (L) in	$-\Delta\tilde{\upsilon}_{C=O}$ / cm^{-1}	$\tilde{\upsilon}_{M-O}$ / cm^{-1}	$\tilde{\upsilon}_{M-Cl}$ / cm^{-1}	$\Delta\tilde{\upsilon}_{C-N}$ / cm^{-1}
(a) $NiLCl_2$				
nmf	13	367	226	47
aa	24	357	220	60
nma	26	366	225	11
(b) $NiL_2Cl_2(2H_2O)$				
nmf	16	368	226	15
aa	21	380	222	66
nma	30	353	225	8
(c) $Ni_3L_2Cl_6$				
dmf	18	402	220	18
dma	19	346	224	29
nef	14	398	222	23
pa	9	351	223	50
def	29	396	223	12
(d) NiL_2Cl_2				
dmf	23	393	233	23
nef	20	397	221	7
fa	-3	352	222	36
pa	8	360	228	51
ba	15	397	223	41
iba	18	377	219	50
(e) $Ni_3(dmp)Cl_6$	41	346	216	9
(f) CoL_2Cl_2				
nma	27	351	224	13
dmf	20	311	247	19
fa	-1	313	225	36
dma	22	305	248	27
dmp	44	304	248	13
(g) CuL_2Cl_2				
aa	19	352	226	52
fa	5	-	232	57
iba	20	399	221	50

13.2 Thermal behaviour

13.2.1 Overview

DSC endotherms without corresponding DTG mass losses were presumed to involve either melting or a structural change. Hot-stage microscopy and visual examination of the partially decomposed complexes were used to ascertain fusion.

Nickel(II) chloride complexes of similar composition and geometrical configuration showed similar thermal behaviour. DSC curves of the $NiL_2C\ell_2(2H_2O)$ complexes showed three endothermic steps ($-2H_2O$; - L; - L). The $NiL_2C\ell_2$ complexes decomposed in two endothermic steps (- 4L; -2L for $3NiL_2C\ell_2$), often accompanied by fusion and structural rearrangements. The $NiLC\ell_2$, $Ni_3L_2C\ell_6$ and $Ni_3LC\ell_6$ complexes exhibited a single endothermic step to give $NiC\ell_2$. The thermal decomposition patterns are in accordance with the experience of other workers [138,140,145,146,183,184]. There are however two important differences concerning the $NiL_2C\ell_2(2H_2O)$ complexes: (i) the $NiLC\ell_2$ intermediate isolated by Mitra *et al.* [138] had a T_d symmetry, and (ii) transformed to $NiC\ell_2$ *via* two further intermediates.

$CoC\ell_2$-*amide* complexes of similar composition and geometrical structure showed different thermal behaviour. The octahedral $Co(fa)_2C\ell_2$ decomposed (in the solid state) *via* the formation of $Co(fa)C\ell_2$, whilst $Co(nma)_2C\ell_2$ decomposed (from a molten state) in a single step to give $CoC\ell_2$. The tetrahedral complexes with *dmf* or *dma* form $Co_3(dmf)_2C\ell_6$ and $Co_3(dma)C\ell_6$ species (respectively) from melts. $Co(dmp)_2C\ell_2$ decomposed (also from a melt) in a single step to give $CoC\ell_2$. The reaction stoichiometries differ from those of the corresponding nickel(II) chloride complexes, except for the complex of cobalt(II) with *dmf*. There are, however, two notable differences: (i) no signs of melting were detected in the $Ni(dmf)_2C\ell_2$ complex, and (ii) $Co(dmf)_2C\ell_2$ has a tetrahedral structure whilst $Ni(dmf)_2C\ell_2$ is octahedrally coordinated. The single-stage loss of 2L molecules from related $CoL_2C\ell_2$ complexes has been reported by other workers [141,142,145]. Intermediates of type $CoLC\ell_2$ have also been suggested [15,26,28].

$CuC\ell_2$-*amide* complexes of similar composition and structure to the Ni(II) complexes showed different thermal behaviour. The $Cu(fa)_2C\ell_2$ and $Cu(aa)_2C\ell_2$ complexes decomposed (from the solid state) *via* the formation of $CuLC\ell_2$ species. $Cu(iba)_2C\ell_2$ decomposed (from the melt) in a single step to give a molten product. Similar behaviour has been reported for related copper(II) complexes [16,141,142].

The thermal decompositions of solid reactants can be described by the following sets of reactions:

Set 1:

$$ML_2C\ell_2\,(s) \rightarrow MLC\ell_2\,(s) + L\,(g) \quad 1a$$
$$MLC\ell_2\,(s) \rightarrow MC\ell_2\,(s) + L\,(g) \quad 1b$$

Set 2:

$$3ML_2C\ell_2\,(s) \rightarrow M_3L_2C\ell_6\,(s) + 4L\,(g) \quad 2a$$
$$M_3L_2C\ell_6\,(s) \rightarrow 3MC\ell_2\,(s) + 2L\,(g) \quad 2b$$

Set 3:

$$3ML_2C\ell_2\,(s) \rightarrow M_3LC\ell_6\,(s) + 5L\,(g) \quad 3a$$
$$M_3LC\ell_6\,(s) \rightarrow 3MC\ell_2\,(s) + L\,(g) \quad 3b$$

Set 4:

$$ML_2C\ell_2\,(s) \rightarrow MC\ell_2\,(s) + 2L\,(g) \quad 4$$

T_e and T_{max} (for the first decomposition steps) were determined from the DTG curves, and ΔH_{zL} from the DSC curves. Values of the stoichiometric coefficient (z) of the released ligands and the measured enthalpy change were used to calculate the enthalpy per mole of amide ligand. That is, $\Delta H_L = \Delta H_{zL}/z$. Evaluation of ΔH_{zL} for the individual decomposition steps in some of the reactions proved difficult owing to the overlap of the DSC stages. This problem was overcome by estimating ΔH_L values on the basis of the release of all ligands, irrespective of the number of steps in a thermal process. Results are shown in Table 13.2.

13.2.2 The influence of the nature of the amide ligands on the thermal stabilities of their corresponding metal(II) complexes

One of the primary objectives of this work was to investigate the possible relationship between the nature of the amides (steric and electronic effects) and the thermal stabilities of their corresponding metal(II) chloride complexes. T_e, T_{max} and ΔH_L for complexes of similar compositions, geometrical structure and decomposition stoichiometry were examined as indicators of the strengths of the metal-amide bonds. It had to be assumed that (within such a set of closely related complexes) the crystal packing forces of the products are reasonable similar [4,26,27]. In the absence of heat capacity data to refer the enthalpies to one temperature, and following Beech *et al.* [26], it was assumed that the magnitude of the corrections of ΔH_L values to their respective mean temperatures could not be larger than the uncertainties associated with the ΔH values.

Reactions of Set (1)

Thermal data for reaction (**1b**), Table **13.2**, indicate the orders:

$NiLC\ell_2$ (i) T_e, *nma* < *aa* < *nmf*

(ii) T_{max}, *nma* < *aa* < *nmf*

(iii) ΔH_L, *nma* < *aa* < *nmf*

These sequences are consistent and reflect the order of decreasing steric hindrance of the methyl-substituent groups. The least stable complex, as suggested by the smallest values of ΔH_L, T_e and T_{max}, is Ni(*nma*)$C\ell_2$. This could be explained in terms of steric interaction involving the double methyl groups. When inductive effects are more important than steric effects, Ni(*nmf*)$C\ell_2$ will come below Ni(*aa*)$C\ell_2$ in the stability series, and *vice versa*. The present results therefore suggest that the methyl-substituent (attached to the carbonyl carbon atom) hinders effective interaction of the central nickel(II) ion with the carbonyl oxygen atom.

Less steric repulsion is expected from less bulky amides, leading to stronger interaction with the metal and higher frequencies of the $^3T_{2g}(F) \leftarrow {}^3A_{2g}$ transition ($\hat{\upsilon}_1$) [8,124,185]. The shift of the $\hat{\upsilon}_1$ band to higher wavenumbers (Table **8.4**) produced the sequence

nma (7 236 cm^{-1}) ~ *aa* (7 238 cm^{-1}) < *nmf* (7 249 cm^{-1})

This sequence is consistent with steric hindrance caused by the methyl-substituent groups. The differences in $\hat{\upsilon}_1$ values are however not well established.

Assuming that a higher IR carbonyl frequency band shift confirms a stronger inductive effect, $\Delta\hat{\upsilon}_{C=O}$ should increase from *nmf* to *nma* in accordance with the expected increase in bond order. The $\Delta\hat{\upsilon}_{C=O}$ values in Table **13.1** confirm this order. That is,

nmf (13 cm^{-1}) < *aa* (24 cm^{-1}) ~ *nma* (26 cm^{-1})

It can thus be concluded that, in the $NiLC\ell_2$ system, the quantities ΔH_L, T_e and T_{max} indicate a stronger influence of the steric rather than the inductive effects.

Thermal data for reactions (**1a+b**), Table **13.2**, indicate the orders:

$NiL_2C\ell_2(2H_2O)$ (i) T_e, *nmf* < *aa*

(ii) T_{max}, *nmf* < *aa*

(iii) ΔH_L, *aa* < *nmf*

$CuL_2C\ell_2$ (i) T_e, *aa* < *fa*
(ii) T_{max}, *aa* < *fa*

In the $NiL_2C\ell_2(2H_2O)$ system, the enthalpy and temperature sequences are at variance. The ΔH_L sequence is consistent with the steric order, whilst the temperature data suggest the importance of inductive factors. The $\Delta\hat{\upsilon}_{C=O}$ sequence

nmf (16 cm^{-1}) < *aa* (21 cm^{-1}) < *nma* (30 cm^{-1})

confirms the inductive order. Explanation of this apparent anomaly is difficult, owing largely to the lack of thermal data for the $Ni(nma)_2C\ell_2(2H_2O)$ complex.

For the decomposition of the $CuL_2C\ell_2$ complexes, lower T_e and T_{max} values were obtained for the complex with the more basic *aa* ($\Delta\hat{\upsilon}_{C=O} \approx 19\ cm^{-1}$) compared with the *fa* complex ($\Delta\hat{\upsilon}_{C=O} \approx 5\ cm^{-1}$). This is consistent with steric hindrance caused by the methyl-substituent in acetamide.

In the $CoL_2C\ell_2$ system, only $Co(fa)_2C\ell_2$ decomposed according to reactions (**1a+b**). However, $Co(fa)_2C\ell_2$, $Cu(fa)_2C\ell_2$, $Cu(aa)_2C\ell_2$ and $Ni(aa)_2C\ell_2$ have similar structures. The T_e and T_{max} values for reaction (**1a**) indicate the orders:

(i) loss of *fa*, $Cu(fa)_2C\ell_2$ < $Co(fa)_2C\ell_2$
(ii) loss of *aa*, $Cu(aa)_2C\ell_2$ < $Ni(aa)_2C\ell_2$

A possible explanation for the low thermal stability of the copper(II) complexes is the very distorted octahedral structure.

Reactions of Set (2)

Thermal data for reaction (**2b**), Table **13.2**, indicate the trends:

$Ni_3L_2C\ell_6$ (i) T_e, *pa* < *def* < *dmf* < *dma* < *nef*
(ii) T_{max}, *pa* < *def* < *dma* < *dmf* < *nef*
(iii) ΔH_L, *def* ~ *pa* ~ *dma* ~ *nef* < *dmf*

Lower ΔH_L values for the complexes with *def*, *dma* or *pa*, when compared to *nef* or *dmf*, are excellent evidence for the importance of steric hindrance caused by bulkier alkyl-substituent groups. That is, the experimental order suggests a general decrease in ΔH_L as steric hindrance become more important. The values of ΔH_L are however nearly similar, and no literature values could be found for comparison.

Table 13.2: Summary of thermal data for the various metal(II)-amide complexes

Complex	Reaction	T_e / °C	T_{max} / °C	ΔH_L / kJ mol^{-1} ligand
(a) octahedral $NiLC\ell_2$				
Ni(*nmf*)$C\ell_2$	(1b)	243	271	67
Ni(*aa*)$C\ell_2$	(1b)	228	244	63
Ni(*nma*)$C\ell_2$	(1b)	215	230	60
(b) octahedral $NiL_2C\ell_2(2H_2O)$				
Ni(*nmf*)$_2C\ell_2(2H_2O)$	(1a+b)	136	148	74
Ni(*aa*)$_2C\ell_2(2H_2O)$	(1a+b)	197	215	66
Ni(*nma*)$_2C\ell_2(2H_2O)$	(1a+b)	-	-	-
(c) octahedral $Ni_3L_2C\ell_6$				
Ni_3(*dmf*)$_2C\ell_6$	(2b)	217	259	51
Ni_3(*dma*)$_2C\ell_6$	(2b)	239	248	46
Ni_3(*nef*)$_2C\ell_6$	(2b)	250	274	47
Ni_3(*pa*)$_2C\ell_6$	(2b)	182	207	46
Ni_3(*def*)$_2C\ell_6$	(2b)	200	229	45
(d) octahedral $NiL_2C\ell_2$				
Ni(*fa*)$_2C\ell_2$	(2a+b)	233	256	69
Ni(*dmf*)$_2C\ell_2$	(2a+b)	89	107	64
Ni(*nef*)$_2C\ell_2$	(2a+b)	144	168	53
Ni(*pa*)$_2C\ell_2$	(2a+b)	153	179	50
Ni(*ba*)$_2C\ell_2$	(2a+b)	163	191	42
Ni(*iba*)$_2C\ell_2$	(2a+b)	158	198	40
(e) octahedral $Ni_3LC\ell_6$				
Ni_3(*dmp*)$C\ell_6$	(3b)	176	206	61
(f) octahedral $CoL_2C\ell_2$				
Co(*fa*)$_2C\ell_2$	(1a+b)	194	221	68
Co(*nma*)$_2C\ell_2$	(4)	217	248	-
(g) tetrahedral $CoL_2C\ell_2$				
Co(*dmf*)$_2C\ell_2$	(2a+b)	106	192	-
Co(*dma*)$_2C\ell_2$	(3a+b)	202	245	-
Co(*dmp*)$_2C\ell_2$	(4)	210	240	-
(h) octahedral $CuL_2C\ell_2$				
Cu(*aa*)$_2C\ell_2$	(1a+b)	165	191	
Cu(*fa*)$_2C\ell_2$	(1a+b)	182	205	
Cu(*iba*)$_2C\ell_2$	(4)	193	220	

The $\hat{\upsilon}_1$ values (Table **8.4**) suggest an interplay between steric and inductive factors.

pa (7221 cm^{-1}) < *nef* (7232 cm^{-1}) < *def* (7247 cm^{-1}) < *dma* (7252 cm^{-1}) < *dmf* (7252 cm^{-1})

The sequence, *def* < *dma* < *dmf*, supports the steric order, whilst *nef* < *def* (< *dma*) can best be explained in terms of stronger inductive effects.

The T_e series, *pa* < *dmf* < *dma*, suggests the importance of inductive effects. $\Delta\hat{\upsilon}_{C=O}$ data in Table **13.1** confirm this order:

pa (9 cm^{-1}) < *nef* (14 cm^{-1}) < *dmf* (18 cm^{-1}) ~ *dma* (19 cm^{-1}) < *def* (29 cm^{-1})

The T_{max} series, *def* < *dma* < *dmf* < *nef*, is consistent with the importance of steric effects; whilst *pa* < *def* can best be justified in terms of stronger inductive effects. Results for the $Ni_3LC\ell_6$ system therefore suggest that the quantities ΔH_L, T_e and T_{max} indicate an interplay between steric and inductive factors.

T_e and T_{max} for reaction (**2a**) and ΔH_L for reactions (**2a+b**), Table **13.2**, indicate the orders:

$NiL_2C\ell_2$ (i) T_e and T_{max}, *dmf* < *nef* < *pa* < *ba* ~ *iba* < *fa*

(ii) ΔH_L, *iba* ~ *ba* < *pa* ~ *nef* < *dmf* < *fa*

ΔH_L generally decreases with increase in size of the alkyl-substituent groups. Apart from the complex with *fa*, T_e and T_{max} generally increase with increase in basicity of the ligands. This is compatible with the inductive order produced by the $\Delta\hat{\upsilon}_{C=O}$ data,

pa (8 cm^{-1}) < *ba* (15 cm^{-1}) < *iba* (18 cm^{-1}) ~ *nef* (20 cm^{-1}) < *dmf* (23 cm^{-1})

The $Ni(dmf)_2C\ell_2$ and $Co(dmf)_2C\ell_2$ complexes have different structures: octahedral and tetrahedral coordinations, respectively.

Reactions of Sets (3) and (4)

Within set (**3**), no reasonable solid-state stability comparison is feasible. $Co(dma)_2C\ell_2$ showed a unique decomposition stoichiometry, whilst $Ni_3(dmp)C\ell_6$ and $Co_3(dma)C\ell_6$ contain different ligands and have octahedral and tetrahedral structures, respectively. Referring to set (**4**), $Co(nma)_2C\ell_2$ and $Cu(iba)_2C\ell_2$ exhibited octahedral structures, but with different amide ligands. $Co(dmp)_2C\ell_2$ has a tetrahedral structure.

13.2.3 Comparison between results of the present study and other related studies

Allowing for the different experimental conditions, there are some interesting trends between the findings of the present study and other studies. House *et al.* [140] reported ΔH values (Table **7.3**) for the $CdC\ell_2$-*picoline* system that were higher than those for the $CdC\ell_2$-*pyridine* system. The authors accounted for the higher values on the grounds that methylpyridine is more basic than pyridine. From studies of the $NiC\ell_2$-*imidazole* system, Losada *et al.* [151,152] reported that N-methylimidazole was held more strongly than imidazole. The authors advanced the basicity argument in favour of methylimidazole. In contrast to the above findings, Farran *et al.* [5] reported a decrease in T_e values with increasing basicity of alkyl-substituted pyridine ligands. The authors explained the observed T_e order in terms of a *trans* influence of one ligand, which can cause the first ligand to be lost more easily. Results of the present study do not support the enhancement of thermal quantities with increasing basicity of the amides. Instead, steric factors play a more important role in determining the magnitudes of ΔH_L, T_e and T_{max}. No simple relationship was found between $\Delta\hat{\upsilon}_{C=O}$ or $\hat{\upsilon}_1$ and the thermal quantities.

13.3 Kinetic results

13.3.1 Introduction

For the kinetic study, only those few complexes that decomposed in a single step without decomposition of the released ligand were chosen. These were the $NiLC\ell_2$ complexes, where L = N-methylformamide (*nmf*), acetamide (*aa*) or N-methylacetamide (*nma*). Kinetic data were analyzed using several different isothermal and non-isothermal methods (Chapters **10** and **11**). It was not possible to identify a single kinetic model which could describe the data over the entire conversion range ($0.0 \leq \alpha \leq 1.0$).

13.3.2 $NiLC\ell_2$ isothermal kinetic results

The decompositions started at maximum rates, *i.e.* $\upsilon = \upsilon_{max}$ at $t = 0$. The early portion of the rate against α curves is consistent with an approximately zero-order initial process. The plots of ℓn(rate) against $\ell n(1 - \alpha)$ are approximately linear over the range of $0.03 \leq \alpha \leq 0.90$ (Figures **10.1.8**, **10.2.8** and **10.3.8**). This approach offers the advantage that there is no constraint on the value of n. The apparent orders derived

lie in the region expected for the **R2** (0.50), **R3** (0.67) and **F1** (1.00) models (refer to Tables **10.1.5**, **10.2.5** and **10.3.5**).

Good agreement was obtained on plotting the experimental values of alpha (α_e) against reduced-time ($t/t_{0.5}$), indicating that the reactions are isokinetic over the temperature ranges studied (see Figures **10.1.3**, **10.2.3** and **10.3.3**). This isokinetic behaviour is confirmed by the small standard deviations (δ) of α_i's from their respective α_{mean}, obtained at various chosen ratios of $t/t_{0.5}$ (Tables **10.1.3**, **10.2.3** and **10.3.3**). This behaviour suggests that only one activated process is involved in the reaction [42].

Comparison of experimental data in the form of α against $t/t_{0.5}$, with similar curves calculated for various models indicated that coincidence with the *master* curve for the contracting geometry rate expressions is better than that for the first-order rate equation. Of the **R3** and **R2** models, it was difficult to distinguish the model giving a better fit when $0.00 \leq \alpha \leq 0.95$.

The plots of α against time are typical of deceleratory processes, best described by either the **R2**, **R3** or **F1** expressions. For decomposition of the Ni(*nmf*)$C\ell_2$ complex, the criterion of the best linearity, obtained from plots of $g(\alpha)$ against time, indicated that the **R3** and **R2** models give approximately straight lines at all temperatures investigated (Table **10.1.4**). It was thus difficult to make an unambiguous choice between the **R2** and **R3** equations. In the Ni(*aa*)$C\ell_2$ and Ni(*nma*)$C\ell_2$ complexes, highest correlation coefficients and smallest standard errors of slope were obtained when using the contracting-volume (**R3**) equation (Tables **10.2.4** and **10.3.4**). Obedience to the **F1** equation improved notably on going to higher α values. Beyond the α value of 0.95, the most satisfying fit changed from being the **R2** or **R3** to the **F1** model in all the complexes. Plots of $\alpha_{calc.}$ (calculated for the possible orders of unity, one-half or two-thirds) and α_e against time indicated best fit for $n = {}^2/_3$ in the most extensive α range in all the complexes (see Figures **10.1.6**, **10.2.6** and **10.3.6**). The fit of the kinetic data to deceleratory yield-time curves suggests that, at constant temperature, progress of the reactions is controlled by inward motion of the reactant-product interface.

The shapes of the experimental rate *versus* alpha curves of the Ni(*nma*)$C\ell_2$ complex are in qualitative accord with the theoretical curves calculated using the empirical (**B2**) expression (*cf.* Figures **3.4**, **3.5** and **10.3.9**). The quantitative applicability of equation (3.26), written in a straight line form

$$\ell n(1 - \upsilon_r) = b\, \ell n(t) + b\, \ell n(k) \qquad 3.27$$

was tested using plots of $\ell n(1 - \upsilon_r)$ against $\ell n(t)$, Figure **10.3.9**. Linear regression results indicated that the value of b is approximately equal to two (see Table **10.3.7** of Appendix **IV**). Plots of $(1 - \upsilon_r)^{1/b}$ against time yielded approximately straight lines when $b = 2$ (Table **10.3.6**). A kinetic model to explain this empirical behaviour has yet to be devised.

The Arrhenius parameters were estimated and compared for the reactions as obtained by the different methods of isothermal analysis: the plots of $\ell n(^1/t_{0.5})$ against $^1/T$; $\ell n\{^1/(t_{max/2})\}$ against $^1/T$; and $\ell n(k)$ against $^1/T$ (using k values calculated from the approximate zero-order, **R2**, **R3** or (**B2**) equations). The mean E_a values obtained are shown in Table **13.3**. Some trends which emerged from the E_a values include:

- Magnitudes of the apparent activation energies for a particular reaction are not very sensitive to the kinetic model used to calculate the rate coefficients.
- E_a values obtained for Ni(*nmf*)Cℓ_2 are somewhat similar to those of Ni(*aa*)Cℓ_2. Largest values are obtained for Ni(*nma*)Cℓ_2 using either of the models.
- Non-mechanistic approaches based on estimated values of $t_{0.5}$ or $t_{max/2}$ give rise to E_a values that are in good agreement with values calculated using mechanistic approaches (*e.g.* **R2**, **R3**, *etc.*). However, the apparent activation energies derived on the basis of the $t_{max/2}$ data are slightly and consistently lower than those from the other methods of analysis.

The fact that several different determinations of E_a from isothermal experiments lead to comparable values adds confidence to the methods employed and the results herein [32,151].

Apparent activation energies for the decomposition of other amide complexes have been reported [1,2]. Allowing for the different experimental conditions, there are noteworthy similarities between values of E_a calculated in the present study (Table **13.3**) and values reported by other workers. For example, Carstens *et al.* [1] fitted isothermal decomposition data for UO_2(*aa*)F_2 and UO_2(*nma*)F_2 to the contracting-area (**R2**) equation, and reported E_a values of 125 and 150 kJ mol^{-1}. In a related study, Siracusa *et al.* [2] found E_a of 123 kJ mol^{-1} for the decomposition of UO_2(*aa*)F_2. This adds confidence to results of the present study.

13.3.3 Ni(*nmf*)Cℓ_2 non-isothermal kinetic results

The linearity criteria obtained when using the Coats-Redfern equation with $n = ^1/_3$, $^1/_2$, or $^2/_3$ are nearly similar (Table **11.1**). It was therefore not possible to deduce,

unambiguously, the proper form of $g(\alpha)$. Other authors [122,186] have shown that the linearity of $\ell n[g(\alpha)/T^2]$ *versus* $^1/T$ of the Coats-Redfern equation is a necessary, but not a sufficient criterion to assign the correct form of $g(\alpha)$. Results obtained using the modified Borchardt-Daniels method indicate that the method may be advantageous when looking for the formal rate function, $f(\alpha)$. Plots corresponding to $n = {}^2/_3$ gave the best straight lines (Table **11.2**). This is in agreement with the choice of the **R3** equation based on results of the isothermal experiments.

An apparent activation energy of 141 ± 6 kJ mol^{-1} was obtained using the Kissinger method. The E_a value is similar to that derived from the isothermal analysis using the **R3** or **R2** model. Agreement between E_a values calculated using the Kissinger method and isothermal values has been reported in the literature [187,188].

13.3.4 Comparison between E_a and ΔH_L values for the decompositions of the $NiLC\ell_2$ complexes

The dependence of E_a values on the nature of the amide ligands was examined using the mean values obtained from the **R3** and from the **R2** models (Table **13.3**). Results indicate the order: N-methylformamide ~ acetamide < N-methylacetamide. This sequence suggests an increase in E_a with increase in basicity of the amide ligands. The $\Delta\upsilon_{C=O}$ values in Table **13.1** add confidence to the inductive order.

Theoretically, ΔH values contain contributions from several distinct chemical processes such as bond rupture, crystallization of the solid products and desorption of the gaseous products. E_a is expected to incorporate the maximum energy required for bond cleavage. The calculated E_a values are lower than the corresponding ΔH_L values, suggesting that the rate-controlling event is the nickel-amide bond cleavage [11-13]. It has been suggested [3-6,10,12,132] that E_a provides an assessment of the strength of metal-volatile ligand bond for decompositions that are chemically controlled. Farran *et al.* [5] reported an increase in E_a values with increase in basicity of the alkyl-substituted pyridine from decomposition studies of the $PdL_2C\ell_2$ complexes. Akhavein *et al.* [6] reported a similar trend from thermal decomposition studies of $AgL_2(NO_3)$ complexes with several alkyl-substituted pyridine. The E_a trend found in the present study is consistent with the above findings. In contrast, ΔH_L, T_e and T_{max} give an assessment of the steric factors. No simple correlation was found between E_a and the physical parameters investigated.

Table 13.3: Comparison of the mean E_a values calculated for the isothermal decompositions of the NiLCℓ_2 complexes using different methods of analysis.

Parameters	Ni(*aa*)Cℓ_2	Ni(*nma*)Cℓ_2	Ni(*nmf*)Cℓ_2
Model R3			
E_a / kJ mol^{-1}	141	149	141
r	0.927	0.959	0.942
Model R2			
E_a / kJ mol^{-1}	142	146	141
r	0.927	0.954	0.942
Zero-order			
E_a / kJ mol^{-1}	148	146	137
r	0.918	0.974	0.934
Model F1			
E_a / kJ mol^{-1}	-	149	-
r		0.954	
Half-life			
E_a / kJ mol^{-1}	144	145	138
r	0.917	0.975	0.936
$t_{max/2}$			
E_a / kJ mol^{-1}	123	144	124
r	0.906	0.982	0.971
B2 equation			
E_a / kJ mol^{-1}	-	144	-
r		0.969	

13.4 Conclusion

Complexes of general formulae: $NiL_2C\ell_2(2H_2O)$, $ML_2C\ell_2$, $NiLC\ell_2$, $Ni_3L_2C\ell_6$ and $Ni_3LC\ell_6$ (where L = acetamide (C_2H_5NO, *aa*), N-methylacetamide (C_3H_7NO, *nma*), formamide (CH_3NO, *fa*), N,N-dimethylacetamide (C_4H_9NO, *dma*), N-methylformamide (C_2H_5NO, *nmf*), N,N-dimethylformamide (C_3H_7NO, *dmf*), N-ethylformamide (C_3H_7NO, *nef*), propionamide (C_3H_7NO, *pa*), N,N-diethylformamide ($C_5H_{11}NO$, *def*), butyramide (C_4H_9NO, *ba*), isobutyramide (C_4H_9NO, *iba*) or N,N-dimethylpropionamide ($C_5H_{11}NO$, *dmp*); and M = Ni(II), Co(II) or Cu(II)) were prepared.

Near-infrared and visible reflectance spectra of the nickel(II) chloride complexes were consistent with an approximately octahedral environment around the nickel(II) ions. The $CoL_2C\ell_2$ complexes were tetrahedrally coordinated except for the complexes with formamide or N-methylacetamide, for which a distorted octahedral environment has been suggested. Visible region reflectance spectra of the $CuL_2C\ell_2$ complexes suggested a very distorted octahedral arrangement. The infrared (IR) $\hat{\upsilon}_{C=O}$ and $\hat{\upsilon}_{C\text{-}N}$ bands of the free amide ligands were shifted to lower and higher frequencies (respectively) upon complexation. This was taken to indicate coordination through the carbonyl oxygen atom. The $\Delta\hat{\upsilon}_{C=O}$ values were compatible with the estimated inductive orders of the various amide ligands. Far-IR $\hat{\upsilon}_{M\text{-}C\ell}$ band assignments suggested chloride bridging.

DSC curves and visual inspection suggested melting in most of the $ML_2C\ell_2$ complexes, which was also confirmed using hot-stage microscopy. No signs of melting were detected in the $Co(fa)_2C\ell_2$, $Ni(fa)_2C\ell_2$ and $Ni(dmf)_2C\ell_2$ complexes. Nickel(II) chloride complexes of similar composition and geometrical configuration led to similar thermal decomposition stoichiometry. The cobalt(II) and copper(II) complexes of similar compositions and coordination structures to the nickel(II) complexes showed very different thermal behaviour.

Thermal decompositions onset temperatures (T_e), peak temperatures (T_{max}) and enthalpies (ΔH_L) were compared for complexes with similar composition, geometrical structure and decomposition stoichiometry. ΔH_L values indicated the orders:

$NiLC\ell_2$ *system*, *nma* < *aa* < *nmf*

$Ni_3L_2C\ell_6$ *system*, *def* ~ *pa* ~ *dma* ~ *nef* < *dmf*

$NiL_2C\ell_2$ *system*, *iba* ~ *ba* < *pa* ~ *nef* < *dmf*

T_e and T_{max} values indicated the orders:

$NiLC\ell_2$ *system,*	*nma* < *aa* < *nmf*
$Ni_3L_2C\ell_6$ *system,*	*pa* < *def* < *dmf* ~ *dma* < *nef*
$NiL_2C\ell_2$ *system,*	*dmf* < *nef* < *pa* < *ba* ~ *iba*
$CuL_2C\ell_2$ *system,*	*aa* < *fa*

ΔH_L values generally decreased with increase in size of the alkyl-substituent groups in the amide skeleton. The T_e and T_{max} trends were justified in terms of interplay between steric and inductive effects. Ligand-field stabilisation energies were not well-enough established to permit correlations with the ΔH_L, T_e and T_{max} orders. IR carbonyl band frequency shifts ($\Delta\bar{\upsilon}_{C=O}$) were used to affirm that the ΔH_L, T_e and T_{max} values could not be direct measures of the basicity of the amide ligands coordinated to the metal(II) ion. T_e and T_{max} values for the first decomposition steps of the $ML_2C\ell_2$ complexes produced the orders:

$$Cu(fa)_2C\ell_2 < Co(fa)_2C\ell_2 < Ni(fa)_2C\ell_2$$
$$Cu(aa)_2C\ell_2 < Ni(aa)_2C\ell_2$$

The kinetics of the single-step loss of L from the $NiLC\ell_2$ complexes were investigated by measuring mass loss (using TG) and heat flow (using DSC). Rate data were most satisfactorily fitted to either the **R3** or **R2** equation. Analysis using the new empirical (**B2**) expression: $\upsilon_r = 1 - (kt)^b$, yielded reasonable results for the $Ni(nma)C\ell_2$ complex. Comparable E_a values were obtained using various isothermal and non-isothermal methods of analysis. Results of the Borchardt-Daniels equation: $\ell n(k) = \ell n[\beta(d\alpha/dT)/f(\alpha)]$, indicated that the method may offer some advantages when looking for the formal rate function, $f(\alpha)$.

Calculated E_a values for the $NiLC\ell_2$ system (using the **R3** model) generally increased with increase in basicity of the amide ligands:

N-methylformamide ~ acetamide < N-methylacetamide

E_a values were found to be lower than the corresponding ΔH_L values, indicating that cleavage of the nickel-amide bond could be the rate-controlling event. The order of E_a values was found not to coincide with that of the corresponding decomposition enthalpies (ΔH_L). No simple correlation was found between E_a, ΔH_L, T_e or T_{max} and the spectral properties of the complexes.

REFERENCES

1. Carstens P. A. B., Knoetze T. P. and van Vuuren C. P. J., Thermochim. Acta, **128** (1988) 237
2. Siracusa G., Abate L. and Maggiore R., Thermochim. Acta., **56** (1982) 333
3. Beech G., J. Chem. Soc. (A) (1969) 1903
4. Bonomo R. P., Gurrieri S., Musumeci S., Rizzarelli E. and Siracusa G., Thermochim. Acta, **9** (1974) 373
5. Farran R. and House J. E., J. Inorg. Nucl. Chem., **34** (1972) 2219
6. Akhavein A. and House J. E., J. Inorg. Nucl. Chem., **32** (1970) 1479
7. Thornton D. A., Verhoeven P. F. M., Desseyn H. O. and Hofmans H., Thermochim. Acta, **113** (1987) 161
8. Langfelderova H., J. Thermal Anal., **12** (1977) 413
9. Van Dam J. C., Hakvoort G., Jansen J. C. and Reedijk J., J. Inorg. Chem., **37** (1975) 713
10. Gurrieri S., Maggiore R., Musumeci S. and Siracusa G., Thermochim. Acta, **11** (1975) 73
11. Jona E., Sramko T., Ambrovic P. and Gazo J., J. Thermal Anal., **4** (1972) 153
12. Jona E., Jesenak V., Sramko T. and Gazo J., J. Thermal Anal., **5** (1973) 57
13. Jona E., Jesenak V., Sramko T. and Gazo J., J. Thermal Anal., **5** (1973) 389
14. De Beukeleer S. H. J., Desseyn H. O., Perlepes S. P. and Mullens J., Thermochim. Acta, **257** (1995) 149
15. Allan J. R., Paton A. D. and Turvey K., Thermochim. Acta, **196** (1992) 391
16. Allan J. R., McCloy B., Paton A. D., Smith W. E. and Gerrard D. L., Thermochim. Acta, **205** (1992) 127
17. Hill J. O., For Better Thermal Analysis and Calorimetry, ICTAC, Edn. III (1991)
18. Wendlandt W. W., Thermal Analysis, 3rd Edn., John Wiley and Sons, New York (1986)
19. Carr N. J. and Galwey A. K., Thermochim. Acta, **79** (1984) 323
20. Brown M. E., Galwey A. K. and Mohammed M. A., Thermochim. Acta, **127** (1988) 139
21. Keatch C. J. and Dollimore D., An Introduction to Thermogravimetry, Heyden, London (1975)
22. Brown M. E., Dollimore D. and Galwey A. K, in Bamford C. H and Tipper C. J. (Ed.), Comprehensive Solid State Kinetics, Vol. 22, Elsevier, Amsterdam (1980)
23. Perkin-Elmer, TG-7 / DSC-7 Operating Manual
24. Redfern J. P., in Mackenzie R. C. (Ed.), Differential Thermal Analysis, Vol. 1, Academic Press, New York (1970)
25. Speros D. M. and Woodhouse R. L., J. Phys. Chem., **67** (1963) 2164
26. Beech G., Mortimer C. T. and Tyler E. G., J. Chem. Soc., (A) (1969) 512
27. Beech G. and Kauffman G. B., Thermochim. Acta, **1** (1970) 93

28. Beech G. and Mortimer C. T., Chem. Soc. (A) (1967) 1115
29. Arnold M., Veress G. E., Paulik J. and Paulik F., J. Thermal Anal., **17** (1979) 507
30. Galwey A. K. and Brown M. E., Thermochim. Acta, **236** (1995) 1
31. Flynn J. H., J. Thermal Anal., **34** (1988) 367
32. Galwey A. K., Chemistry of Solids, Chapman and Hall, London (1967)
33. Galwey A. K. and Brown M. E., Handbook of Thermal Analysis and Calorimetry, " Principles and Practice", Vol. 1, in press
34. Galwey A. K., Jamieson D. M. and Brown M. E., J. Phys. Chem., **78** (1974) 2664
35. Galwey A. K., Thermochim. Acta, **96** (1985) 259
36. Dominey D. A., Morley H. and Young D. A., Trans. Faraday Soc., **61** (1965) 1246
37. Zsako J., J. Thermal Anal., **5** (1973) 239
38 Sestak J. and Berggren G., Thermochim. Acta, **3** (1971) 1
39. Zsako J., J. Phys. Chem., **72** (1968) 2406
40. Ng W. L., Aust. J. Chem., **28** (1975) 1169
41. Vyazovkin S. V. and Lesnikovich A. I., J. Thermal Anal., **36** (1990) 599
42. Sharp J. H., Brindley G. W. and Achar B. N. N., J. Amer. Ceram. Soc., **49** (1966) 379
43. Swaminathan V., Madhavan N. S and Radhamony D., Thermochim., Acta, **43** (1981) 371
44. Criado J. M., Gonzalez F. and Morales J., Thermochim. Acta, **12** (1975) 337
45. Tang T. B., Thermochim. Acta, **58** (1982) 373
46. Judd M. D. and Norris A. C., J. Thermal Anal., **5** (1973) 179
47. Jacobs P. W. M., Mater. Sci. Res., **4** (1969) 37
48. Erofeev B. V., Reactivity of Solids, Elsevier, Amsterdam (1961)
49. Young D. A., Decomposition of Solids, Perganon Press, Oxford (1966)
50. Satava V. and Skvara F., J. Amer. Ceram. Soc., **52** (1969) 591
51. Sestak J., J Thermal Anal., **16** (1979) 503
52. Avrami M., J. Chem. Phys., **7** (1939) 1103; **8** (1949) 212
53. Tanaka H., Thermochim. Acta, **48** (1981) 137
54. Criado J. M., Thermochim. Acta, **54** (1982) 159
55. Gorbachev V. M., J. Thermal Anal., **13** (1978) 509
56. Shewmon P. G., Diffusion in Solids, Mcgraw-Hill, New York (1963)
57. Holt J. B., Cutler J. B. and Wadsworth M. E., J. Amer. Ceram. Soc., **45** (1962) 133
58. Budnikov P. P. and Ginstling A. M., Principles of Solid State Chemistry, transl. from Russian, Gordon and Breach, New York (1968)
59. Brown M. E. and Galwey A. K., Thermochim. Acta, **29** (1979) 129
60. Jacobs P. W. M. and Tompkins F. C., in Garner W. E. (Ed.), Chemistry of the Solid State, Academic Press, New York (1955) Chap. 7
61. Brown M. E. and Galwey A. K., Anal. Chem., **61** (1989) 1136

62. Waters D. N. and Paddy J. L., Anal. Chem., **60** (1988) 53
63. Vyazovkin S. V. and Lesnikovich A. I., J. Thermal Anal., **32** (1987) 249
64. Vyazovkin S. V. and Lesnikovich A. I., J. Thermal Anal., **35** (1989) 2169
65. Flynn J. H., Brown M. E. and Sestak J., Thermochim. Acta, **40** (1987) 101
66. Galwey A. K., Thermochim. Acta, **96** (1985) 259
67. Skvara F. and Sestak J., J. Thermal Anal., **8** (1975) 477
68. Satava V., J. Thermal Anal., **5** (1973) 217
69. Jones L. F., Dollimore D. and Nicklin T., Thermochim. Acta, **13** (1975) 240
70. Brown M. E., Galwey A. K. and Po A. L. W., Thermochim. Acta, **220** (1993) 131
71. Brown M. E., Galwey A. K. and Po A. L. W., Thermochim. Acta, **203** (1992) 221
72. Galwey A. K., Koga N. and Tanaka H., J. Chem. Soc. Faraday Trans., **86** (1990) 531
73. Galwey A. K., Thermal Anal., **41** (1994) 267
74. Nolan P. S. and Lemay H. E., Thermochim. Acta, **6** (1973) 179
75. Chen D. T. Y. and Lai K. W., J. Thermal Anal., **20** (1981) 233
76. Vyazovkin S. V., Lesnikovich A. I. and Romanovsky I. S., J. Thermal Anal., **34** (1988) 85
77. Laidler K. J., J. Chem. Educ., **49** (1972) 343
78. Laidler K. J., J. Chem. Educ., **61** (1984) 494
79. Brown M. E. and Galwey A. K., Proc. R. Soc. Lond. **A**, **450** (1995) 501
80. Cordes H. F., J. Phys. Chem., **72** (1968) 2185
81. Exner O., Nature, **227** (1970) 366
82. Garn P. D., J. Thermal Anal., **7** (1975) 475
83. Garn P. D., J. Thermal Anal., **10** (1976) 99
84. Garn P.D., J. Thermal Anal., **13** (1978) 581
85. Koga N., Thermochim. Acta, **244** (1994) 1
86. Shlensky O. F., J. Thermal Anal., **20** (1979) 507
87. Garn P. D., Thermochim. Acta, **135** (1988) 71
88. Garn P. D., Thermochim. Acta, **160** (1990) 135
89. Jacobs P. W. M, Corish J. and Catlow C. R. A., J. Phys. Chem., **13** (1980) 1977
90. Zsako J. and Arz H. E., J. Thermal Anal., **6** (1974) 651
91. Agrawal K. R., J. Thermal Anal., **31** (1986) 73
92. Suarez M. P., Palermo A. and Aldao C. M., J. Thermal Anal., **41** (1994) 817
93. Pysiak J. and Sabalski B., J. Thermal Anal., **17** (1979) 287
94. Vyazovkin S. V. and Lesnikovich A. I., Thermochim. Acta, **128** (1988) 297
95. Muraleedharan R. V., J. Thermal Anal., **41** (1994) 53
96. Cremer E., Advan. Catal., **7** (1955) 75
97. Zsako J., J. Thermal Anal., **9** (1976) 101
98. Zsako J., Varhelyi C. S. and Szilagyi K., J. Thermal Anal., **7** (1975) 41

99. Linert W., Kurdjantsev A. B. and Schmid R., Aust. J. Chem., **36** (1983) 1903
100. Zsako J. and Somasekharan K. N., J. Thermal Anal., **32** (1987) 1277
101. Tang T. B. and Chaudhri M. M., J. Thermal Anal., **18** (1980) 247
102. van Krevelen D. W, van Herden C. and Huntjens F. T., Fuel, **30** (1951) 253
103. Murray P. and White J., Trans. Brit. Ceram. Soc., **54** (1955) 204
104. Horowitz H. H. and Metzger G., Anal. Chem., **35** (1963) 1464
105. Doyle C. D., J. Appl. Polymer Sci., **6** (1962) 639; **5** (1964) 285
106. Coats A. W. and Redfern J. P., Nature (London), **201** (1964) 68
107. Freeman E. S. and Carroll B., J. Phys. Chem., **62** (1958) 394; **73** (1969) 751
108. Sestak J., Satava V. and Wendlandt W. W., Thermochim. Acta, **17** (1973) 447
109. Criado J. M., Dollimore D. and Heal G. R., Thermochim. Acta, **54** (1982) 159
110. Kissinger H. E., Anal Chem., **29** (1957) 1702
111. Friedman H. L., J. Polymer Sci., **5** (1965) 183
112. Ozawa T., Thermochim. Acta, **100** (1986) 109
113. Arabien A., Santiago C. and Araiz A., J. Thermal Anal., **29** (1984) 1131
114. Torfs C. M., Deij L., Dorrepaal A. J. and Heijens J. C., Anal. Chem., **56** (1980) 247
115. Popescu C. and Segal E., Thermochim. Acta, **63** (1983) 381
116. Avramov L. K., Thermochim. Acta, **54** (1982) 337
117. Criado J. M. and Ortega A., J. Thermal Anal., **29** (1984) 1075
118. Gyulai G. and Greenhow E. J., Thermochim. Acta, **6** (1973) 239
119. Gyulai G. and Greenhow E. J., Talanta, **21** (1974) 131
120. Sestak J., Thermochim. Acta, **3** (1971) 150
121. Nowisz J. and Hajduk N., J. Thermal Anal., **13** (1978) 223
122. Criado J. M. and Morales J., Thermochim. Acta, **16** (1976) 382; **19** (1977) 305
123. Ozawa T., Bull Chem. Soc. Jap., **38** (1965) 1881
124. Drago R. S., Meek D. W., Joesten M. D. and Laroche L., Inorg. Chem., **2** (1963) 124
125. Archambault J. and Rivert R., J. Chem., **36** (1958) 1461
126. Stone M. E., Robertson B. E. and Stanley E., J. Chem. Soc. (A) (1971) 3632
127. Rollison C. L. and White R. C., Inorg. Chem., **1** (1962) 281
128. Bull W. E., Madan S. K. and Willis J. E., Inorg. Chem., **2** (1963) 303
129. Paul R. C., Chadha S. L. and Dev R., Indian J. Chem., **3** (1965) 364
130. Madan S. K. and Donohue A. M., J. Inorg. Nucl. Chem., **28** (1966) 1617
131. Stone M. E. and Johnson K. E., Can. J. Chem., **51** (1973) 1260
132. Bonomo R. P., Gurrieri S., Musumeci S., Rizzarelli E. and Siracusa G., Thermochim. Acta, **10** (1974) 119
133. Logvinenko V. A., Gegola O. V. and Myachina L. I., J. Thermal Anal., **14** (1978) 265
134. Dewan J. C., Edwards A. J., Slim D. R., Guerchais J. E. and Kergoat R., J. Chem. Soc. (Dalton Trans.), (1975) 2171

135. Chakravorti M. C. and Bharadway P. K., J. Inorg. Nucl. Chem., **40** (1978) 1643
136. Wendlandt W. W. and Smith J. P., The Thermal Properties of Transition Metal Amine Complexes, Elsevier, Amsterdam (1967)
137. Wendlandt W. W., Thermochim. Acta, **37** (1980) 89
138. Mitra S., De G. and Chaudhuri N. R., Thermochim. Acta., **66** (1983) 187
139. Thomas J. M. and Clarke T. A., J. Chem. Soc., (A) (1968) 457
140. House J. E. and Rohner A. L., Thermochim. Acta, **19** (1977) 119
141. Liptay G., Nagy G. and Borbely-Kuszmann A., Thermochim. Acta., **93** (1985) 97
142. Liptay G., Borbely-Kuszmann A. and Nagy G., J. Thermal Anal., **32** (1987) 91
143. Mohapatra B. K. and Rao D. V. R., Indian J. Chem., **9** (1971) 715
144. Mohapatra B. K., Indian J. Chem., **11** (1973) 698
145. Allan J. R. and Baillie G. M., J. Thermal Anal., **14** (1978) 291
146. Allan J. R., Brown D. H., Nuttal R. H. and Sharp D. W. A., J. Inorg. Nucl. Chem., **27** (1965) 1529
147. Wong P. T. T., Can. J. Chem., **52** (1974) 2005
148. van Ooyen J. A. C. and Reedijk J., J. Chem. Soc. (Dalton Trans.), (1978) 1170
149. Ranninger M. C. N., Andrade M. G. and Franco M. A. A., J. Thermal Anal., **14** (1978) 281
150. van Berkum J. G. and Hakvoort G., Thermochim. Acta, **43** (1981) 49
151. Sachez M. and Losada J., J. Thermal Anal., **28** (1983) 381
152. Losada J., Sanchez M., Gonzalez M. J., and Moran M., J. Inorg. Nucl. Chem., **43** (1981) 2269
153. Vogel A. I., A Textbook of Quantitative Inorganic Analysis, 4th Edtn., in Bassett J., Denney R. C., Jeffery G. H. and Mendham J. (Ed.), Longman, London (1979)
154. Figgis B. N. and Lewis J., Modern Coordination Chemistry, in Lewis J. and Wilkins R. G. (Ed.), Interscience, New York (1960)
155. Lever A. B. P., Inorganic Electronic Spectroscopy, Elsevier, London (1968)
156. Agnew N. H. Collin R. J. and Larkworthy L. F., J. Chem. Soc. (Dalton Trans.) (1974) 272
157. Lever A. B. P., Coord. Chem. Rev., **3** (1968) 129
158. Rowley D. A. and Drago R. S., Inorg. Chem., **6** (1967) 1092
159. Lever A. B. P and Nelson S. M., J. Chem. Soc., (1966) 859
160. Jona E., Sramko T. and Gazo J., Thermal Anal., 7 (1975) 551
161. Allan J. R., Brown D. H., Nuttal R. H. and Sharp D. W. A., J. Chem. Soc. (A) (1966) 1031
162. Miyazawa T., Shimanouchi T. and Mizushima S., J. Chem. Phys., **24** (1956) 408; **29** (1958) 611
163. Kraihanzel C. S. and Grenda S. C., Inorg. Chem., **4** (1965) 1037

164. Pace R. J., Williams J. and Williams R. L., J. Chem. Soc. (1961) 2196
165. Hertler W. R. and Muetterties E. L., Inorg. Chem., **5** (1966) 160
166. Jain S. C. and Rivest R., Can. J. Chem., **45** (1967) 139
167. Gropp A. H. and Letaw H., J. Chem. Phys., **21** (1953) 1621
168. Jungbauer M. A. J. and Curran C., Nature, **202** (1964) 290
169. Goldstein M. and Unsworth W. D., Spectrochim. Acta, **28A** (1972) 1297
170. Clark R. J. H. and Williams C. S., Inorg. Chem., **4** (1965) 350
171. Nuttal R. H., Talanta, **15** (1968) 157
172. Goodgame D. M. L., Goodgame M. and Weeks M. J., J. Chem. Soc. (1964) 5194
173. Goldstein M., Taylor F. B. and Unsworth W. D., J. Chem., Soc. Dalton (1972) 418
174. Goldstein M. and Unsworth W. D., Inorg. Chim. Acta, **4** (1970) 432
175. Dorrity I. A. and Orrell K. G., J. Inorg. Nucl. Chem., **36** (1974) 230
176. Clark R. J. H., Spectrochim. Acta, **21** (1965) 955
177. Allan J. R., Brown D. H., Nuttal R. H. and Sharp D. W. A., Inorg. Nucl. Chem., **26** (1964) 1895
178. Savitsky A. and Golay M. J. E., Anal. Chem., **36** (1964) 1627
179. Borchardt H. J. and Daniels F. J., J. Am. Chem. Soc., **79** (1957) 41
180. Carson B. R., Kenessey G., Allan J. R. and Liptay G., J. Thermal Anal., **45** (1995) 369
181. Allan J. R., Carson B. R., Gerrard D. L. and Hoey S., Thermochim. Acta, **153** (1989) 173
182. Allan J. R., Brown D. H., Nuttal R. H. and Sharp D. W. A., J. Inorg. Nucl. Chem. **27** (1965) 1865
183. Beech G. and Mortimer C. T., Chem. Soc. (**A**) (1967) 1111
184. Beech G., Mortimer C. T. and Tyler E. G., Chem. Soc. (**A**) (1967) 925
185. Lever A. B. P., J. Chem. (1963) 5042
186. Kassman A. J., Thermochim. Acta, **84** (1985) 89
187. Ocone L. R., Soulen J. R. and Block B. P., J. Nucl. Chem., **15** (1960) 79
188. Khanna Y. P. and Pearce E. M., J. Thermal Anal., **26** (1983) 107

APPENDIX I

Chapter 8

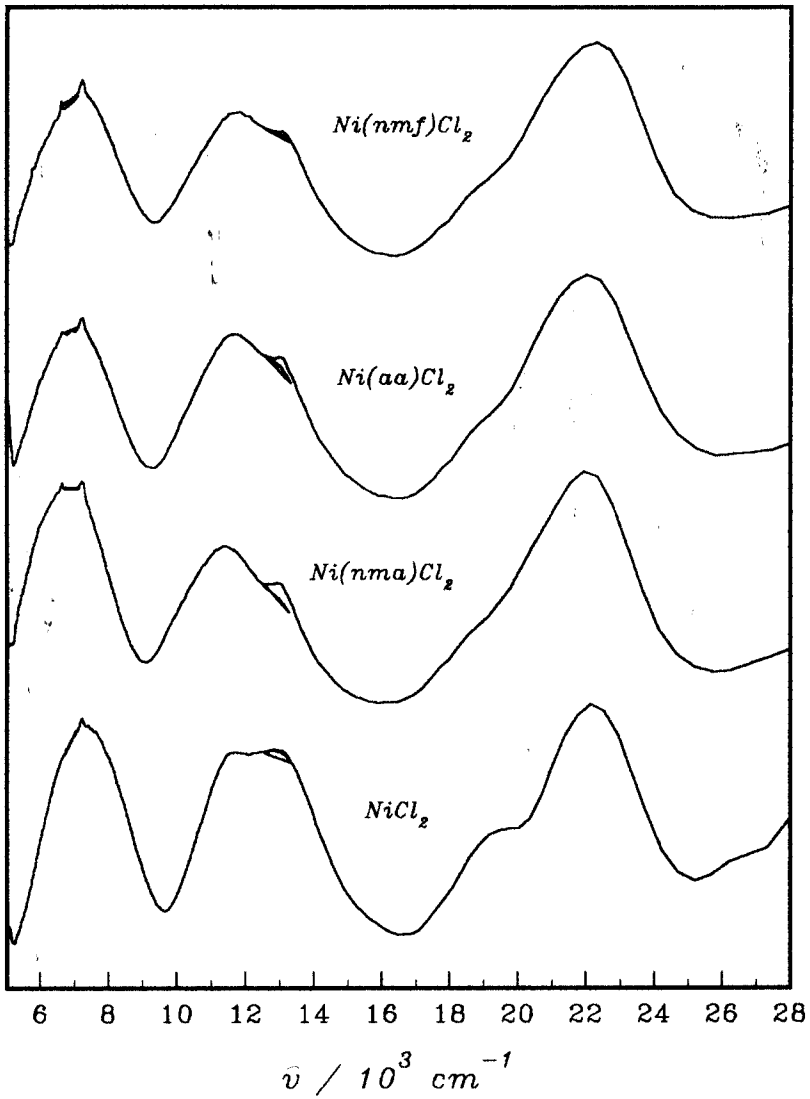

Figure 8.1.1: Diffuse reflectance spectra of the $NiLCl_2$ complexes, compared with spectrum of anhydrous $NiCl_2$.

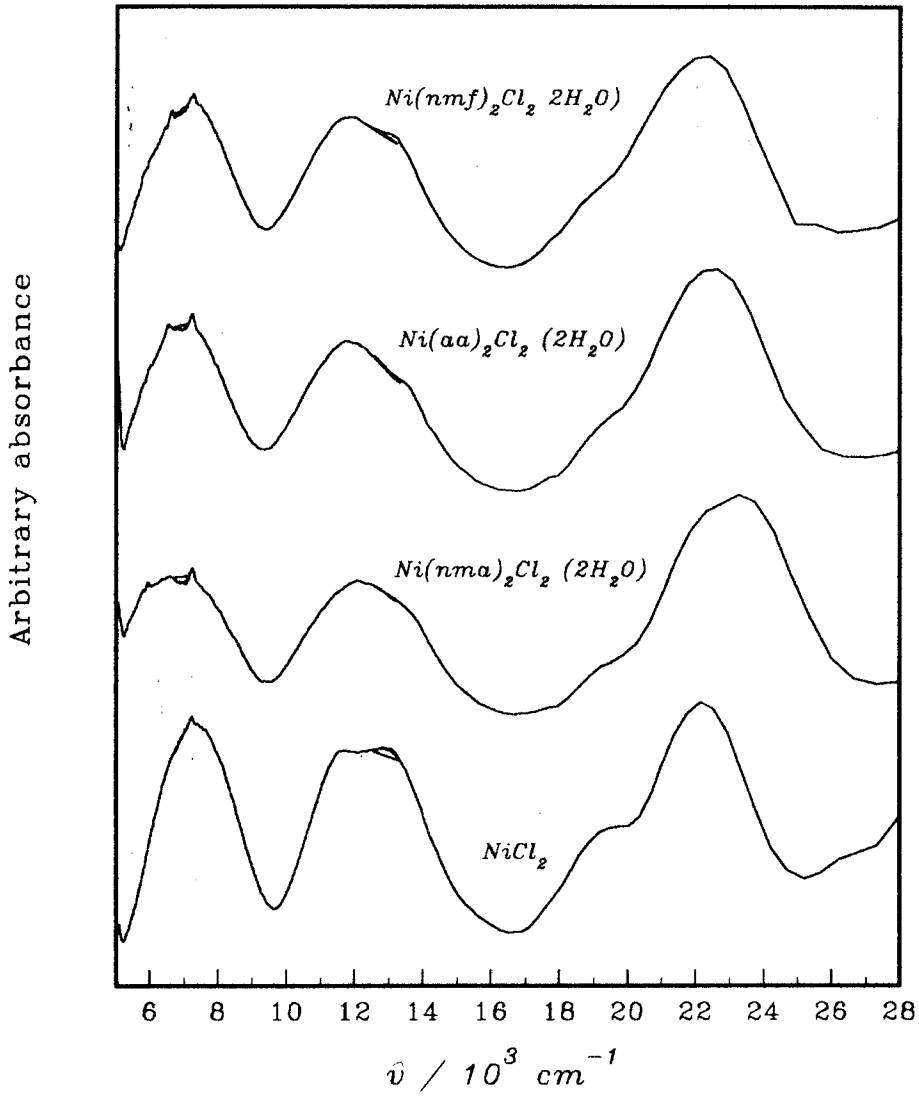

Figure 8.1.2: Diffuse reflectance spectra of the $NiL_2Cl_2(2H_2O)$ complexes, compared with spectrum of $NiCl_2$.

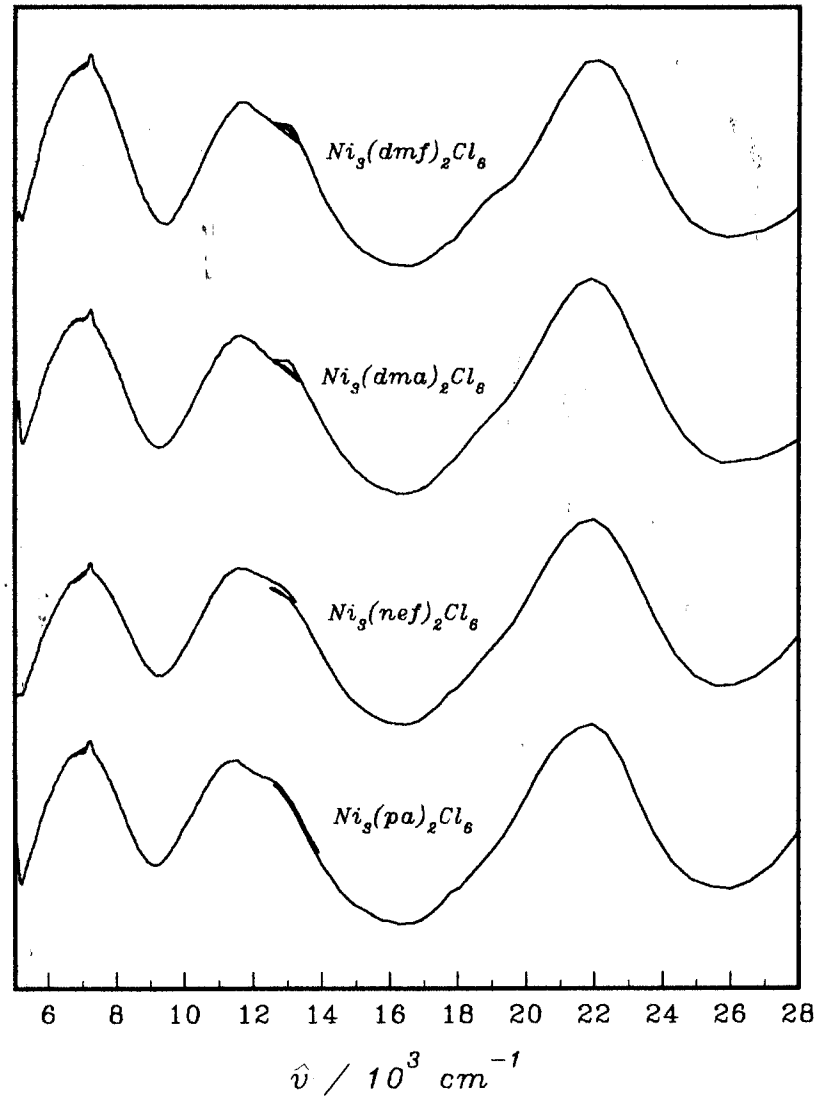

Figure 8.1.3: Diffuse reflectance spectra of the $Ni_3L_2Cl_6$ complexes (see also Figure 8.1.5).

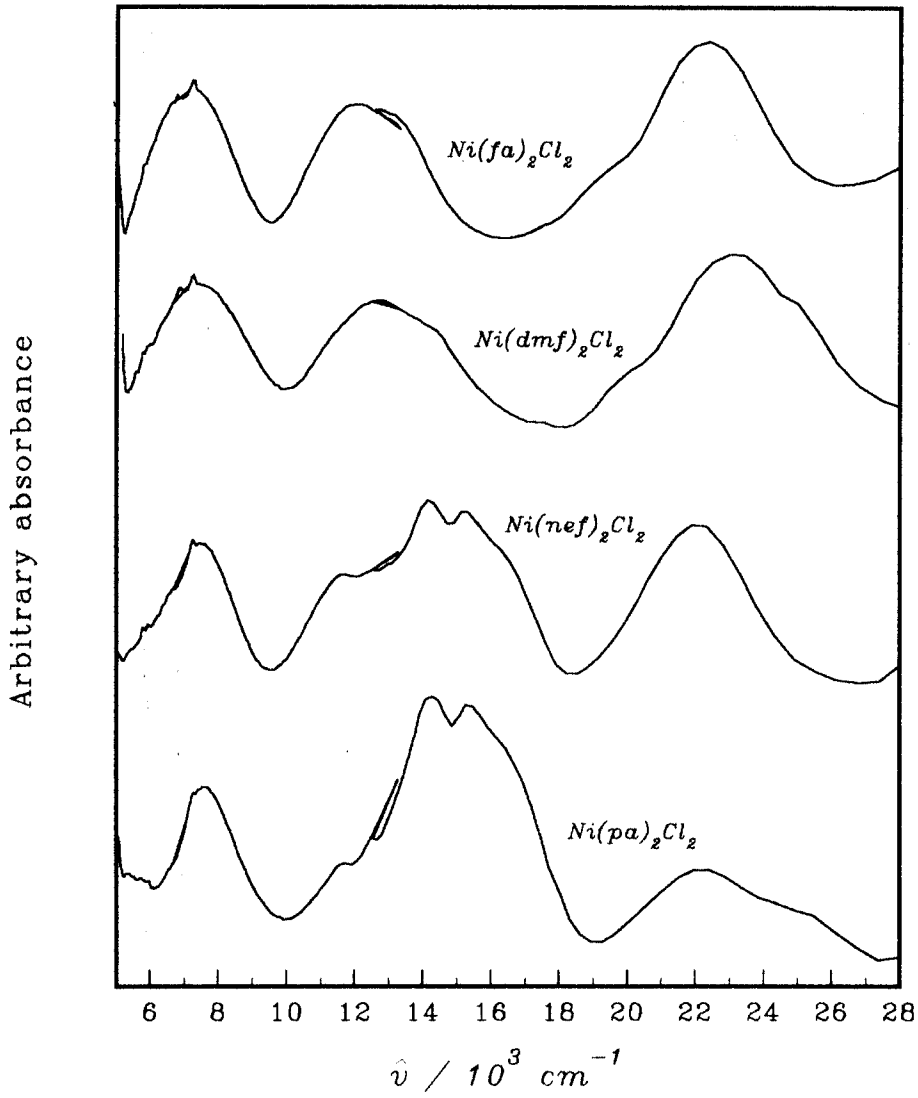

Figure 8.1.4: Diffuse reflectance spectra of the NiL_2Cl_2 complexes (see also Figure 8.1.5).

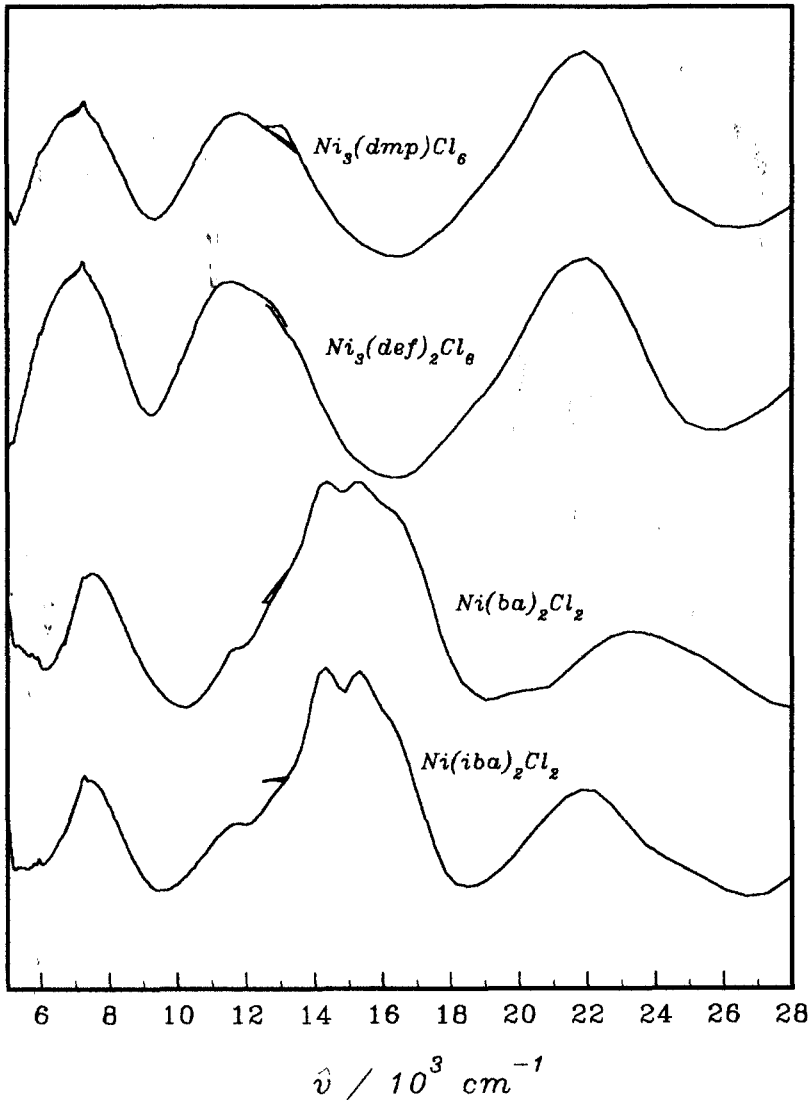

Figure 8.1.5: Diffuse reflectance spectra of the $Ni_3(dmp)Cl_2$, $Ni_3(def)_2Cl_6$, $Ni(ba)_2Cl_2$ and $Ni(iba)_2Cl_2$ complexes.

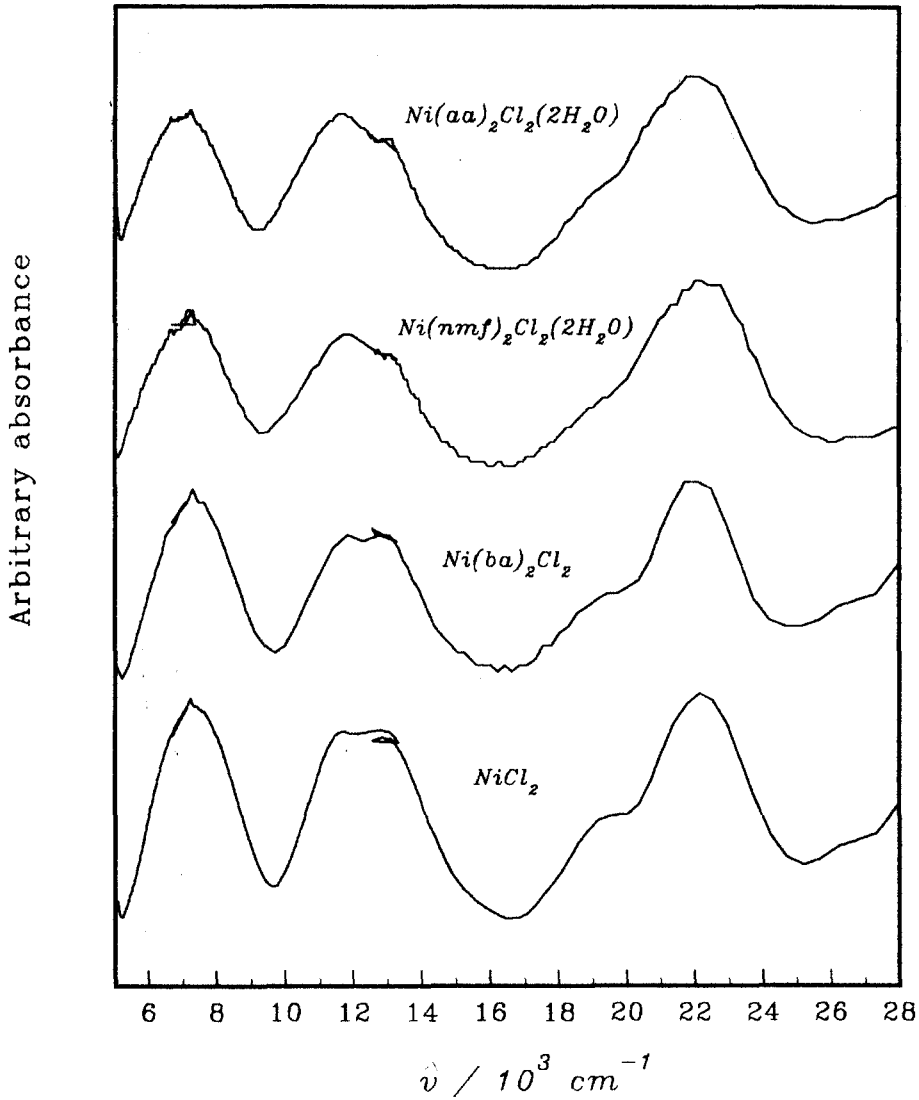

Figure 8.1.6a: Spectra of decomposition residue of the indicated complexes, compared with the spectrum of anhydrous $NiCl_2$.

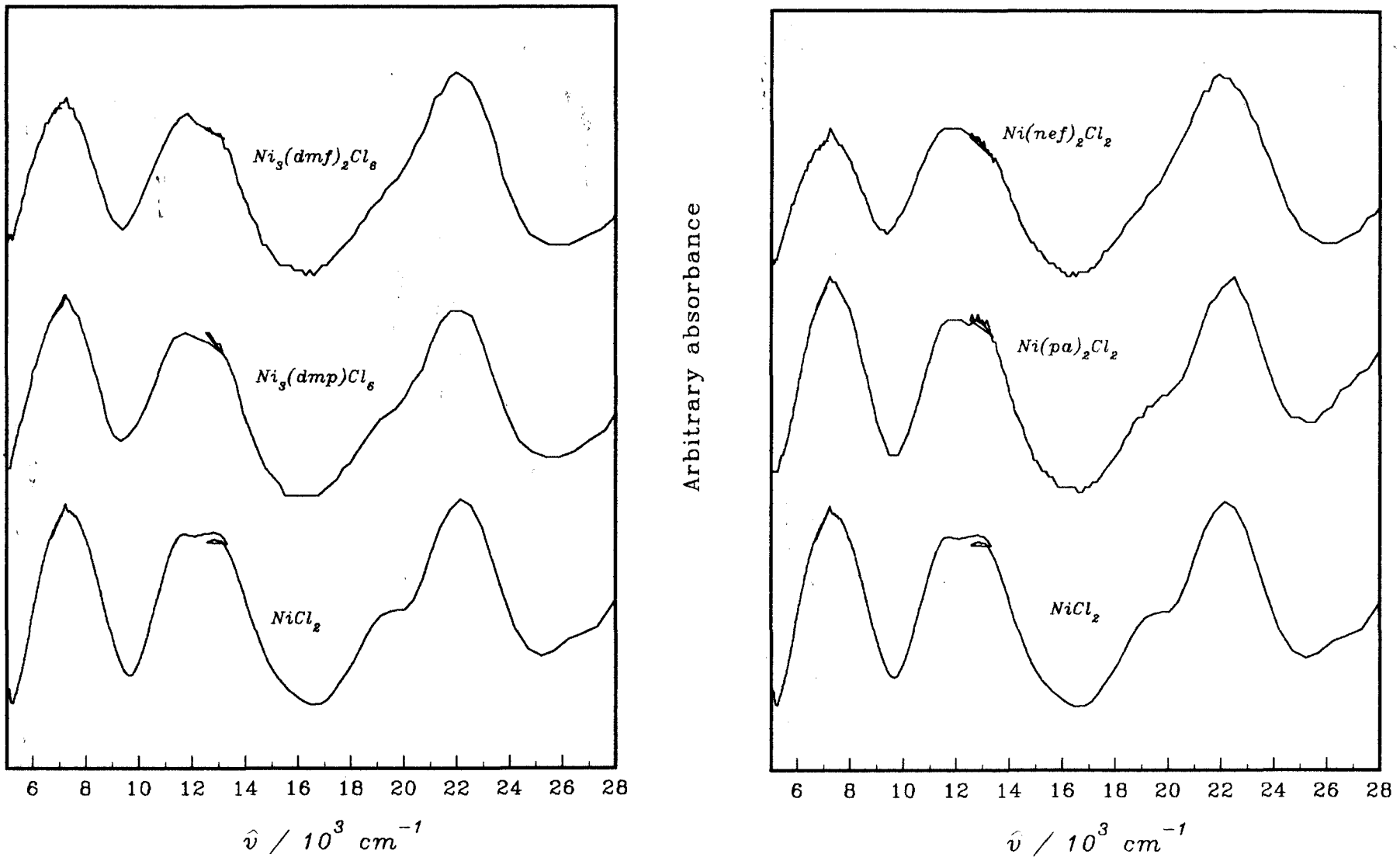

Figure 8.1.6b: Difuse reflectance spectra of decomposition residue of the indicated starting complexes, compared with the spectrum of anhydrous $NiCl_2$.

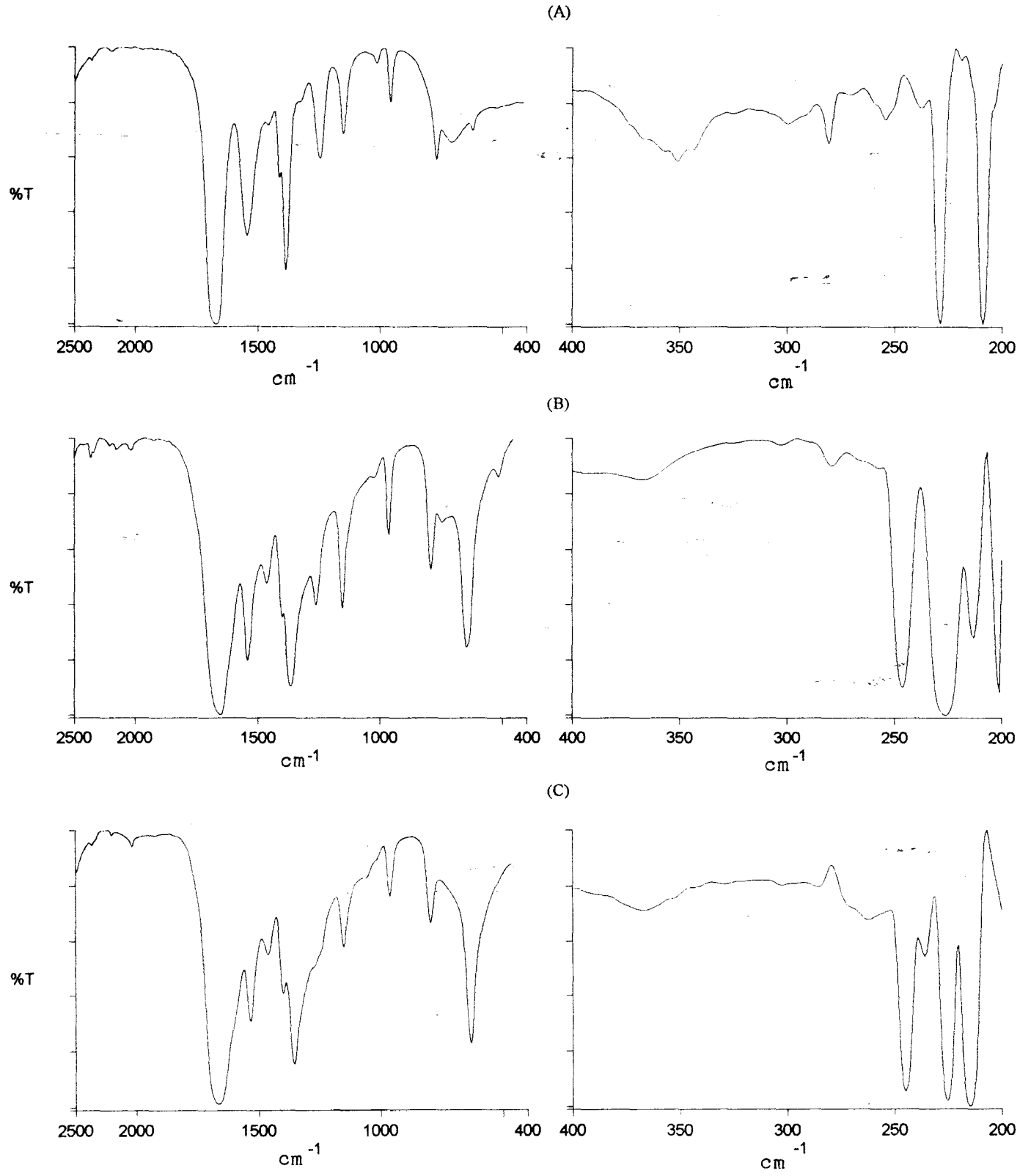

Figure 8.2.1: IR spectra of *nmf* (A), Ni(*nmf*)$_2$Cℓ_2(2H$_2$O) (B) and Ni(*nmf*)Cℓ_2 (C).

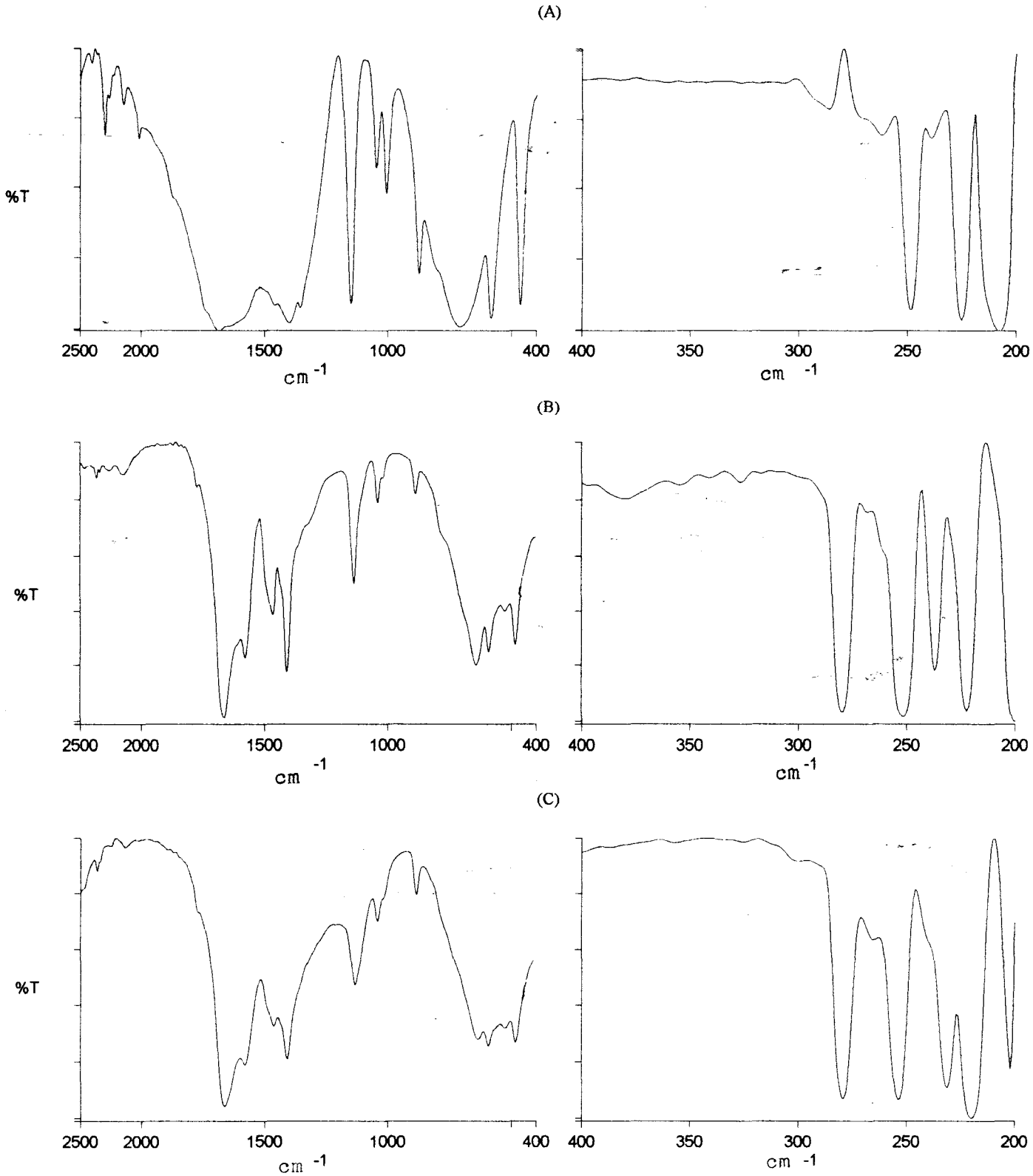

Figure 8.2.2: IR spectra of *aa* (A), $Ni(aa)_2C\ell_2(2H_2O)$ (B) and $Ni(aa)C\ell_2$ (C).

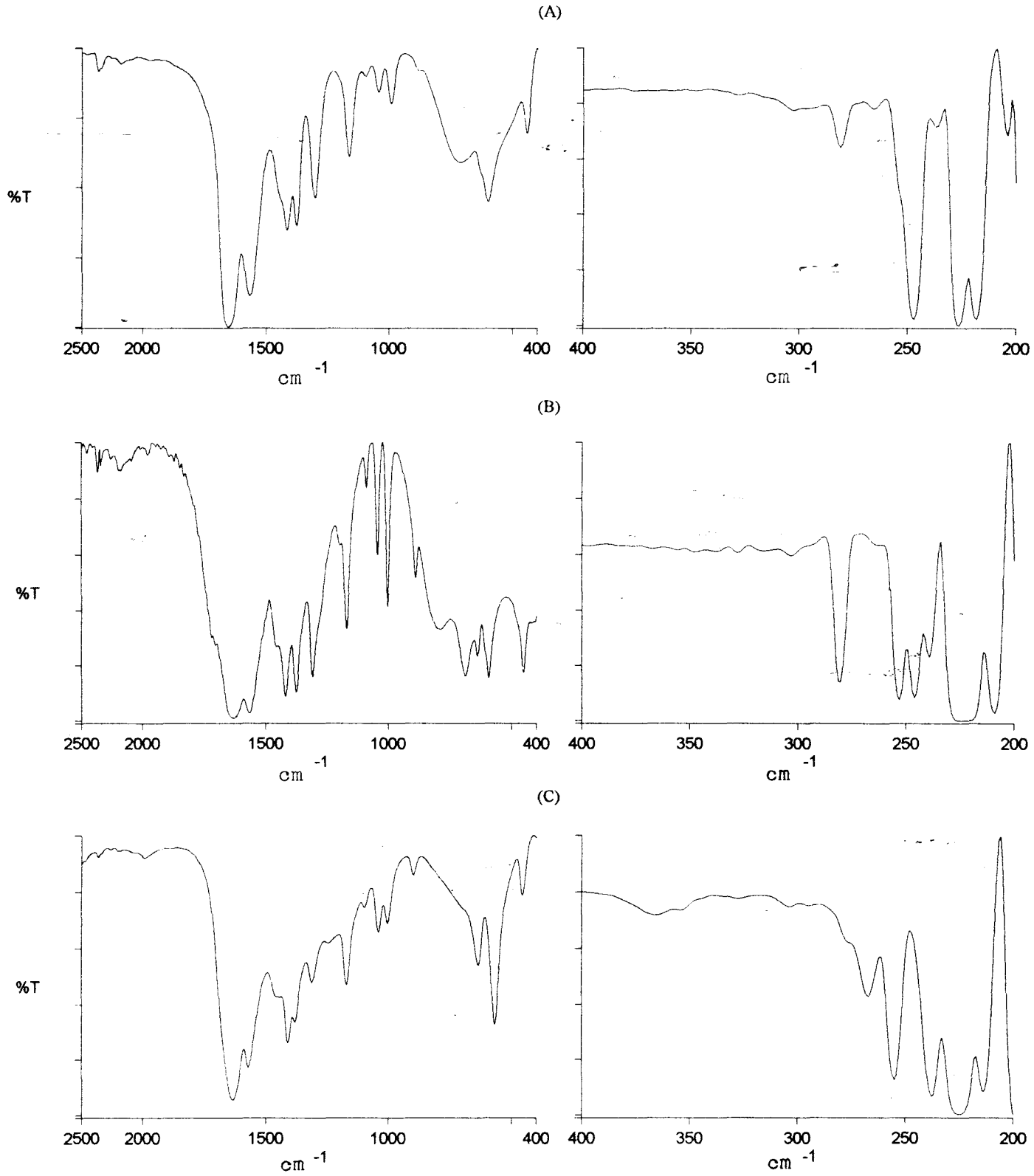

Figure 8.2.3: IR spectra of *nma* (A), Ni(*nma*)$_2$Cℓ_2(2H$_2$O) (B) and Ni(*nma*)Cℓ_2 (C).

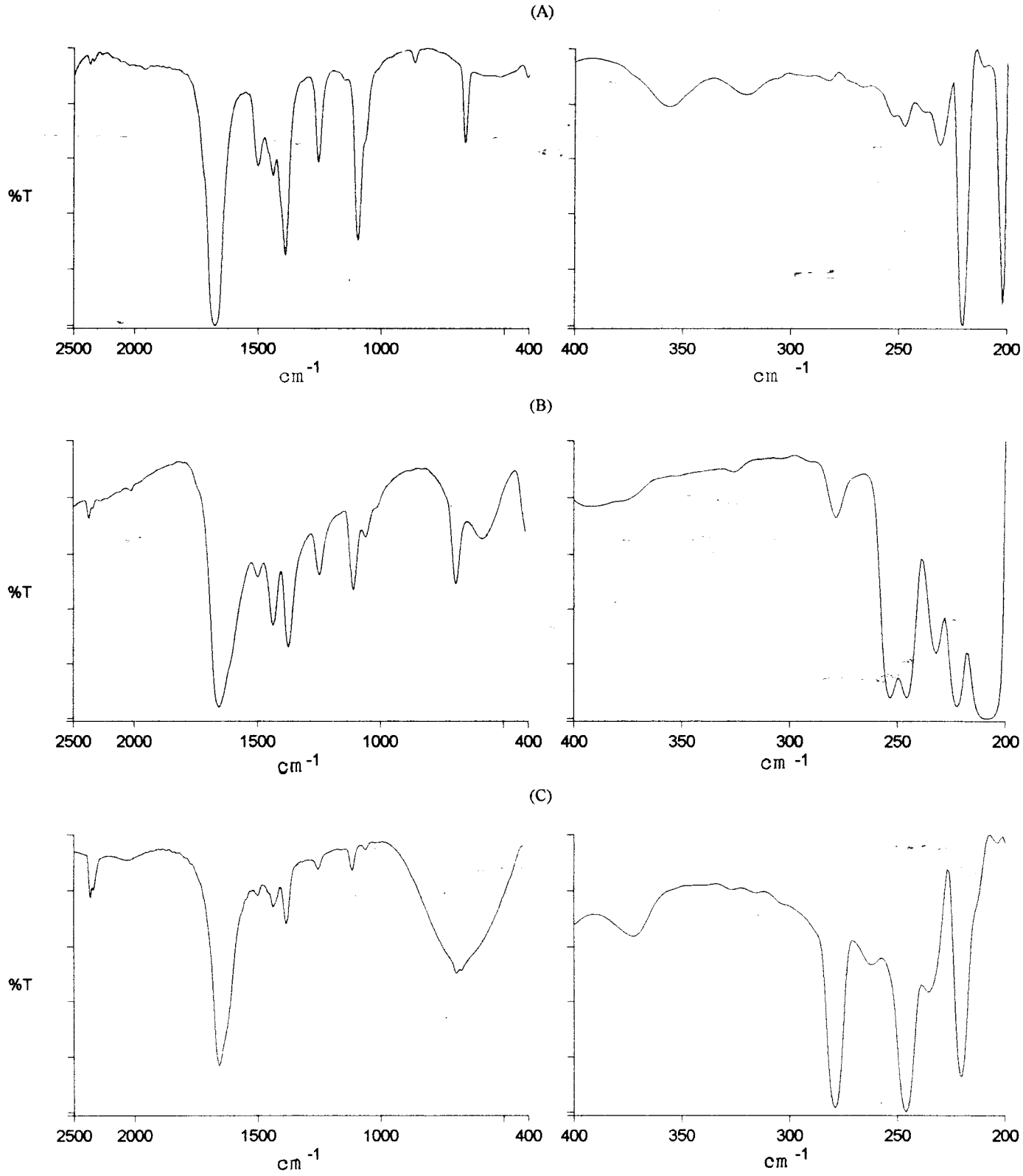

Figure 8.2.4: IR spectra of *dmf*(A), $Ni(dmf)_2C\ell_2$ (B) and $Ni_3(dmf)_2C\ell_6$ (C).

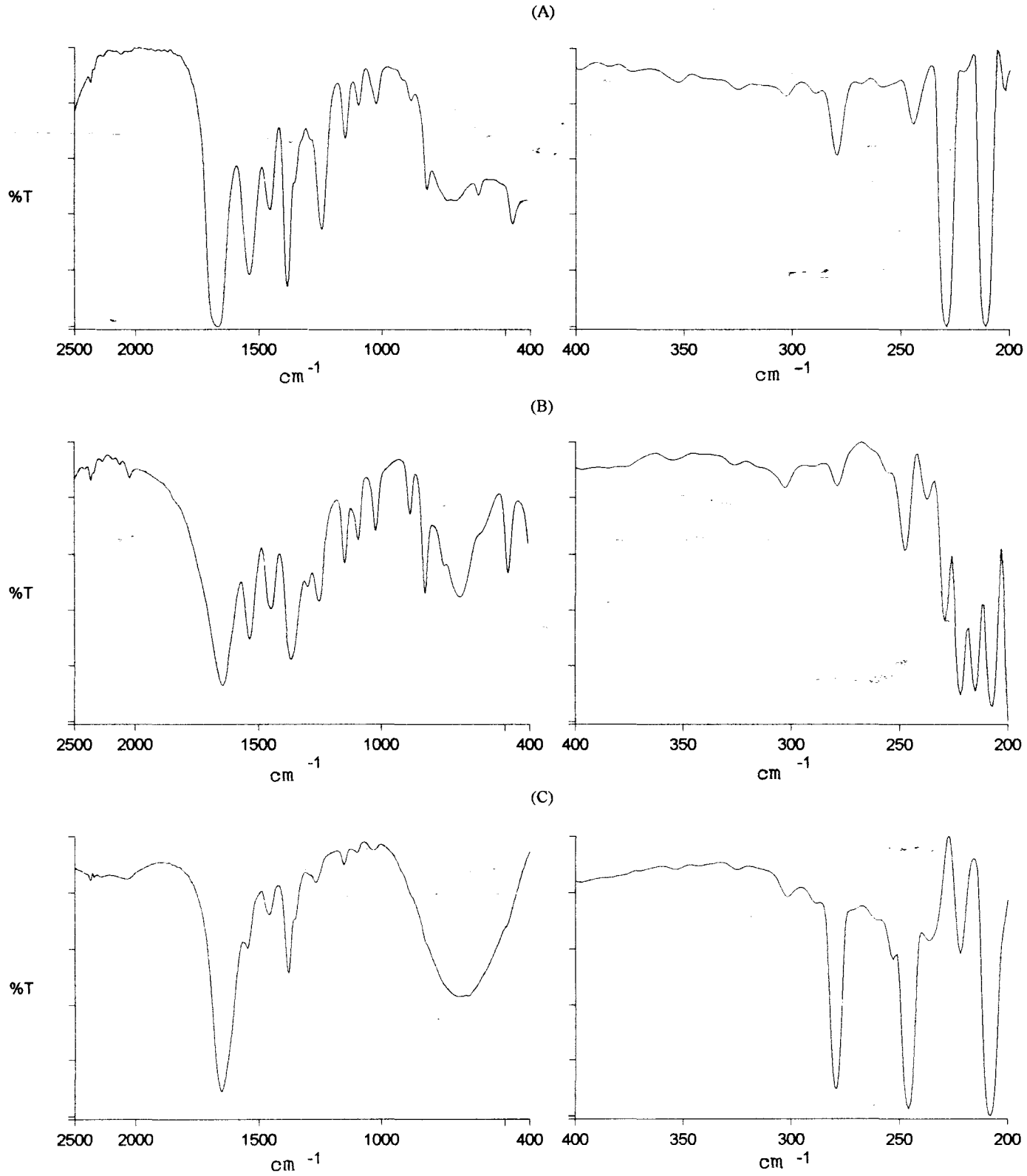

Figure 8.2.5: IR spectra of *nef* (A), $Ni(nef)_2C\ell_2$ (B) and $Ni_3(nef)_2C\ell_6$ (C).

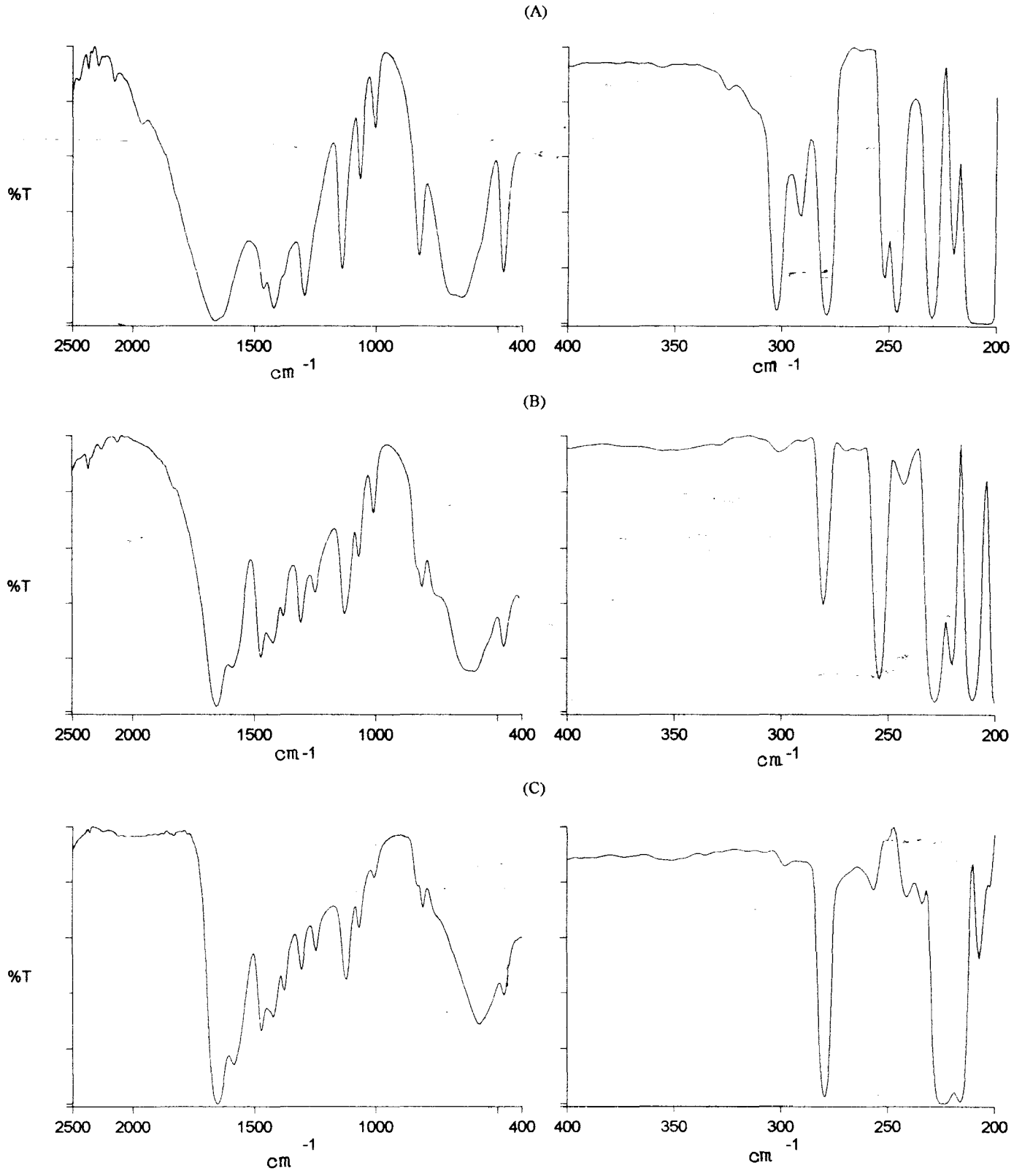

Figure 8.2.6: IR spectra of *pa* (A), $Ni(pa)_2C\ell_2$ (B) and $Ni_3(pa)_2C\ell_6$ (C).

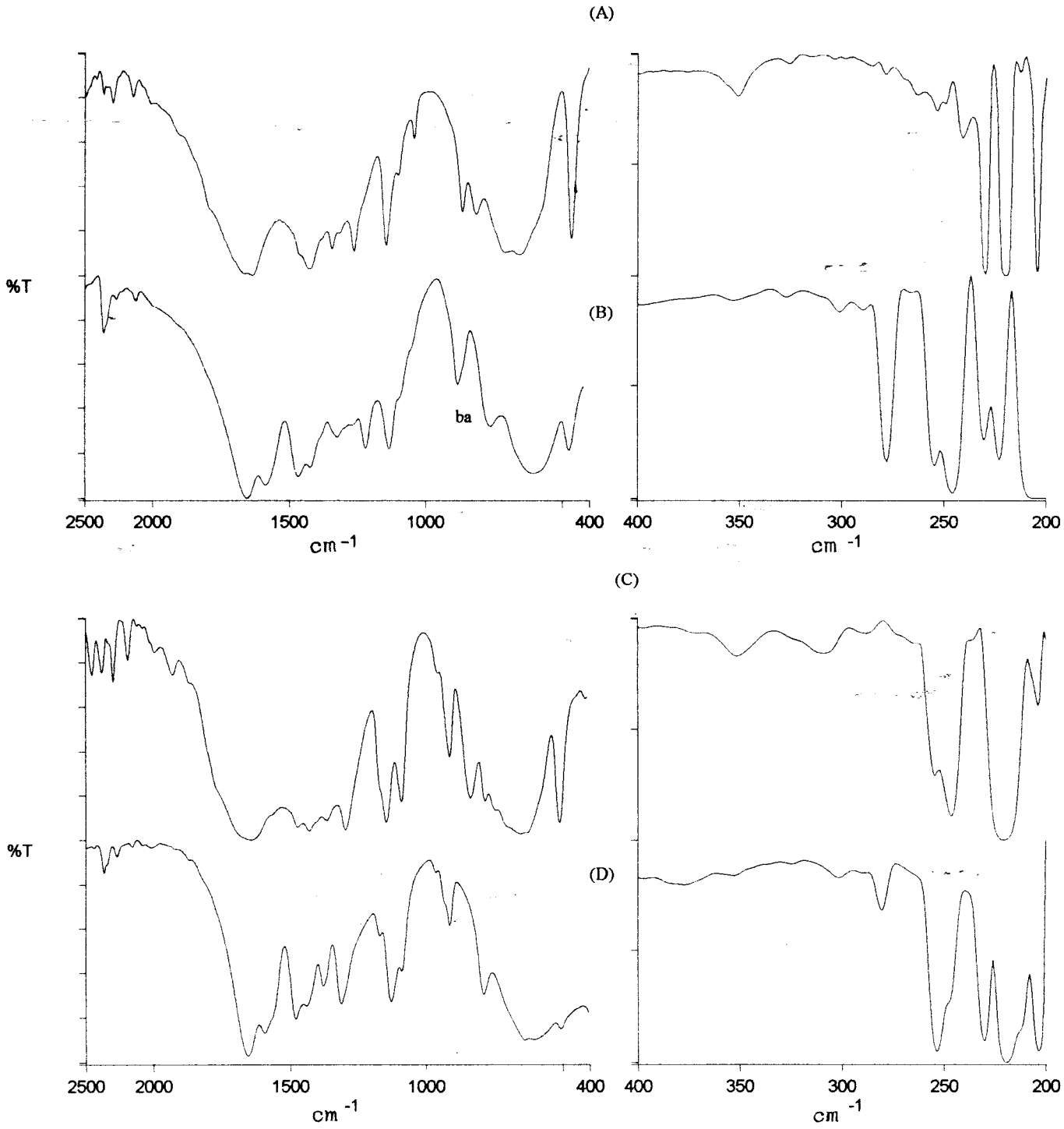

Figure 8.2.7: IR spectra of *ba* (A), $Ni(ba)_2C\ell_2$ (B), *iba* (C) and $Ni(iba)_2C\ell_2$ (D).

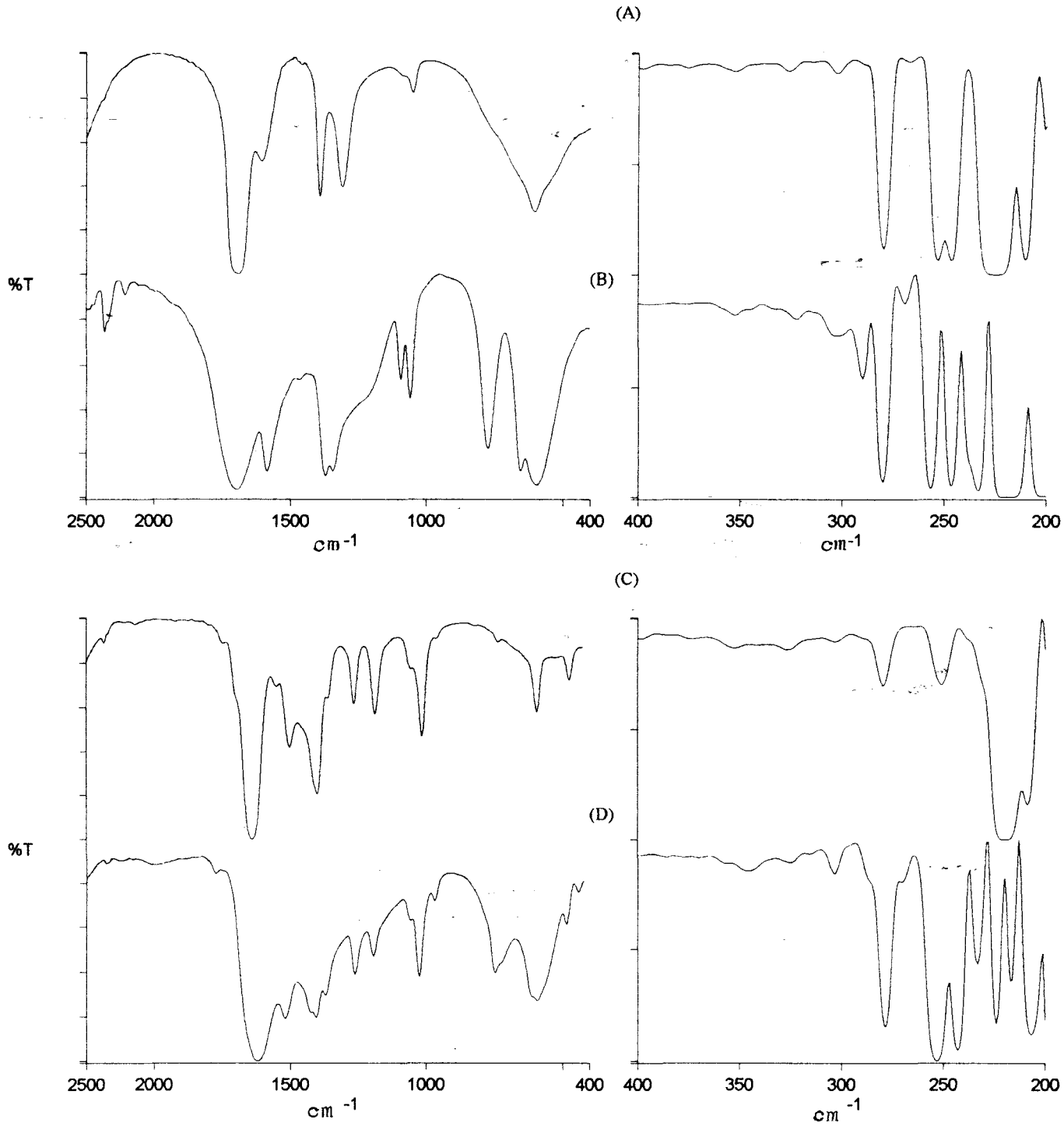

Figure 8.2.8: IR spectra of *fa* (A), $Ni(fa)_2C\ell_2$ (B), *dma* (C) and $Ni_3(dma)_2C\ell_6$ (D).

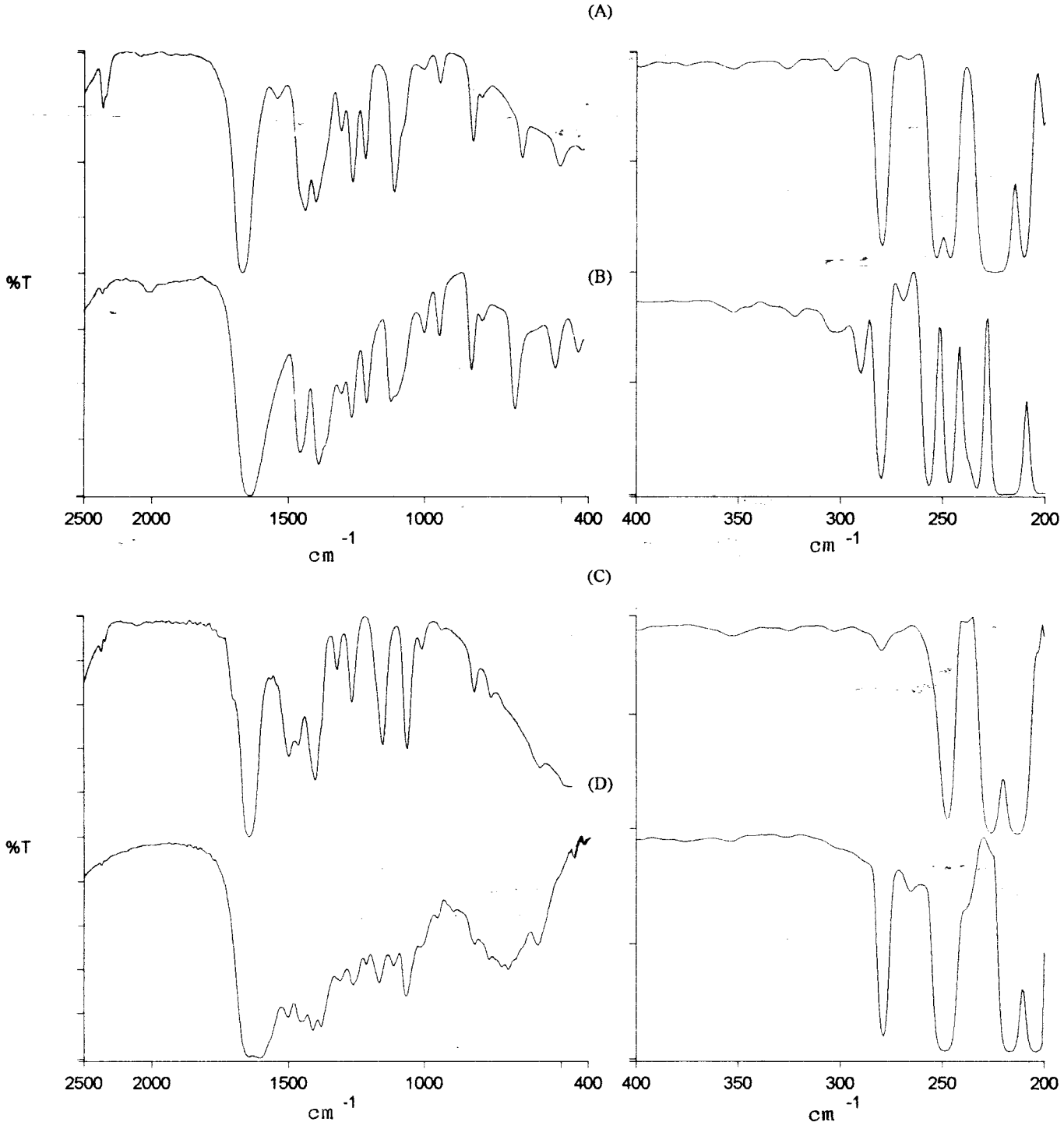

Figure 8.2.9: IR spectra of *def* (A), $Ni_3(def)_2C\ell_6$ (B), *dmp* (C) and $Ni_3(dmp)C\ell_6$ (D).

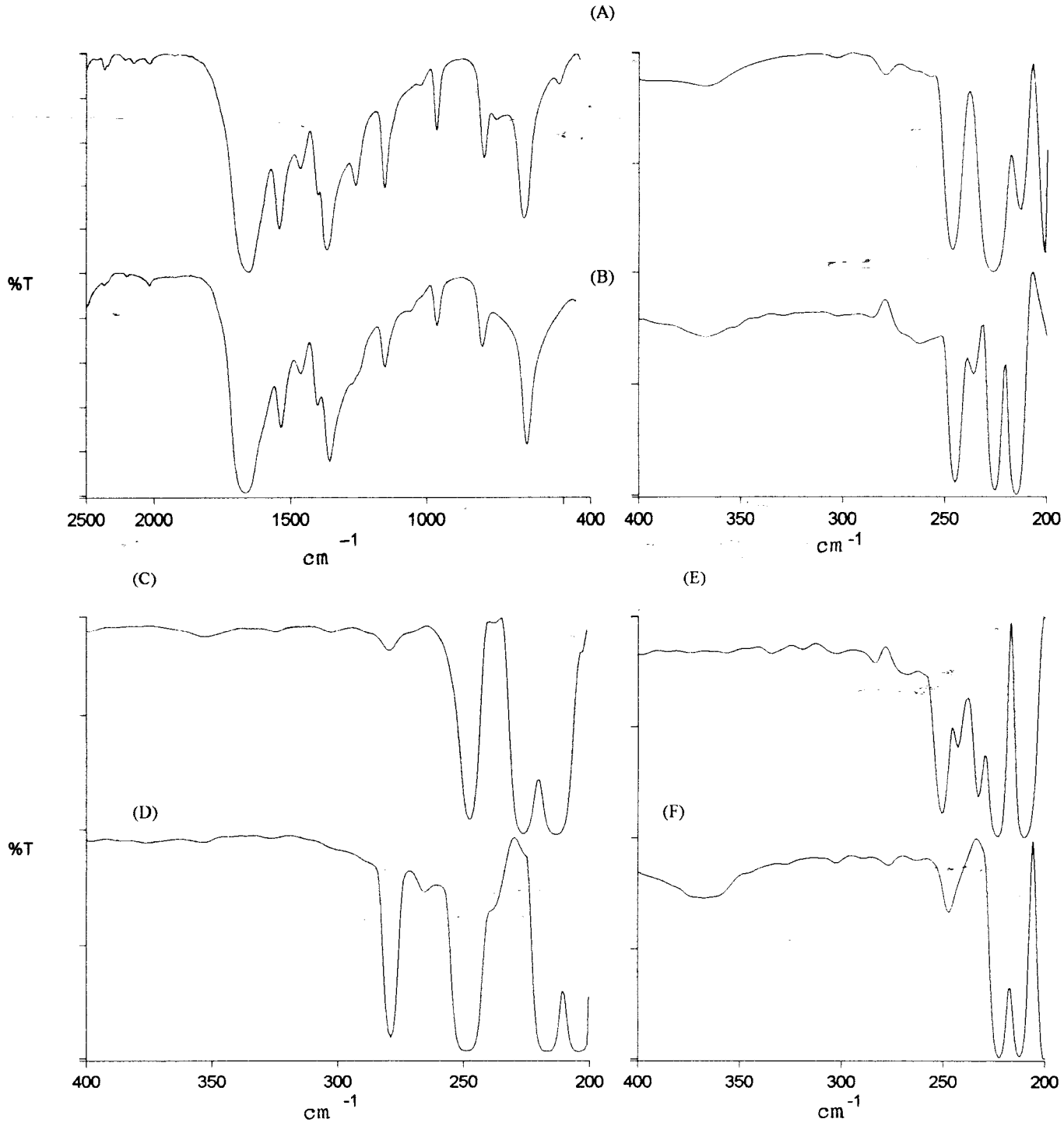

Figure 8.2.10: IR spectra of Ni(*nmf*)$C\ell_2(2H_2O)$ (A), Ni(*nmf*)$C\ell_2$ (B), compared with spectra of Ni(*nmf*)Br_2 (F), anhydrous $NiC\ell_2$ (C), $NiBr_2$ (D) and $CoC\ell_2$ (E).

APPENDIX II

Chapter 10

Table 10.1.4b: Rate coefficients for the decomposition of Ni(*nmf*)$C\ell_2$ at different constant temperatures calculated using the **R2** or **R3** rate expression over $0.00 \leq \alpha \leq 0.90$

	R2 model		**R3 model**	
T /°C	k / 10^{-3} s^{-1}	r	k / 10^{-3} s^{-1}	r
245	3.821 ± 0.001	1.0000	6.453 ± 0.008	0.9980
243	4.087 ± 0.003	0.9997	4.807 ± 0.007	0.9989
240	3.883 ± 0.005	0.9995	4.537 ± 0.006	0.9993
238	2.450 ± 0.001	1.0000	2.854 ± 0.005	0.9978
235	3.111 ± 0.002	0.9998	2.710 ± 0.007	0.9988
233	2.321 ± 0.002	0.9998	2.710 ± 0.005	0.9988
230	2.595 ± 0.001	1.0000	2.963 ± 0.006	0.9985
228	1.304 ± 0.001	0.9994	1.523 ± 0.002	0.9994
225	1.888 ± 0.002	0.9995	2.204 ± 0.003	0.9993
223	0.811 ± 0.001	0.9994	0.946 ± 0.001	0.9994
220	1.087 ± 0.001	0.9990	1.272 ± 0.001	0.9997
218	1.064 ± 0.001	0.9997	1.235 ± 0.002	0.9990
215	0.431 ± 0.000	0.9996	0.503 ± 0.001	0.9991
212	0.450 ± 0.000	0.9998	0.525 ± 0.001	0.9972
210	0.536 ± 0.001	0.9963	0.632 ± 0.000	0.9997
208	0.327 ± 0.000	1.0000	0.380 ± 0.001	0.9983
205	0.338 ± 0.000	0.9999	0.394 ± 0.001	0.9987
200	0.225 ± 0.000	0.9999	0.263 ± 0.000	0.9986

Table 10.1.4c: Rate coefficients for the decomposition of Ni(*nmf*)$C\ell_2$ at different constant temperatures calculated using the **R2** or **R3** rate expression over $0.00 \leq \alpha \leq 0.85$

	R2 model		**R3 model**	
T /°C	k / 10^{-3} s^{-1}	r	k / 10^{-3} s^{-1}	r
245	3.828 ± 0.001	1.0000	4.363 ± 0.007	0.9986
243	4.151 ± 0.002	0.9999	4.737 ± 0.007	0.9991
240	3.918 ± 0.005	0.9996	4.478 ± 0.006	0.9996
238	2.454 ± 0.001	1.0000	2.796 ± 0.005	0.9983
235	3.127 ± 0.002	0.9999	3.575 ± 0.007	0.9990
233	2.348 ± 0.001	1.0000	2.668 ± 0.005	0.9990
230	2.601 ± 0.000	1.0000	2.963 ± 0.006	0.9985
228	1.317 ± 0.001	0.9995	1.503 ± 0.001	0.9997
225	1.904 ± 0.002	0.9996	2.174 ± 0.003	0.9996
223	0.818 ± 0.001	0.9995	0.935 ± 0.001	0.9997
220	1.104 ± 0.001	0.9993	1.262 ± 0.001	0.9998
218	1.072 ± 0.001	0.9998	1.217 ± 0.002	0.9992
215	0.433 ± 0.000	0.9995	0.495 ± 0.000	0.9995
212	0.448 ± 0.000	0.9998	0.501 ± 0.001	0.9993
210	0.557 ± 0.001	0.9981	0.638 ± 0.000	1.0000
208	0.327 ± 0.000	0.9999	0.373 ± 0.000	0.9990
205	0.344 ± 0.000	0.9997	0.388 ± 0.000	0.9991
200	0.224 ± 0.000	0.9999	0.258 ± 0.000	0.9991

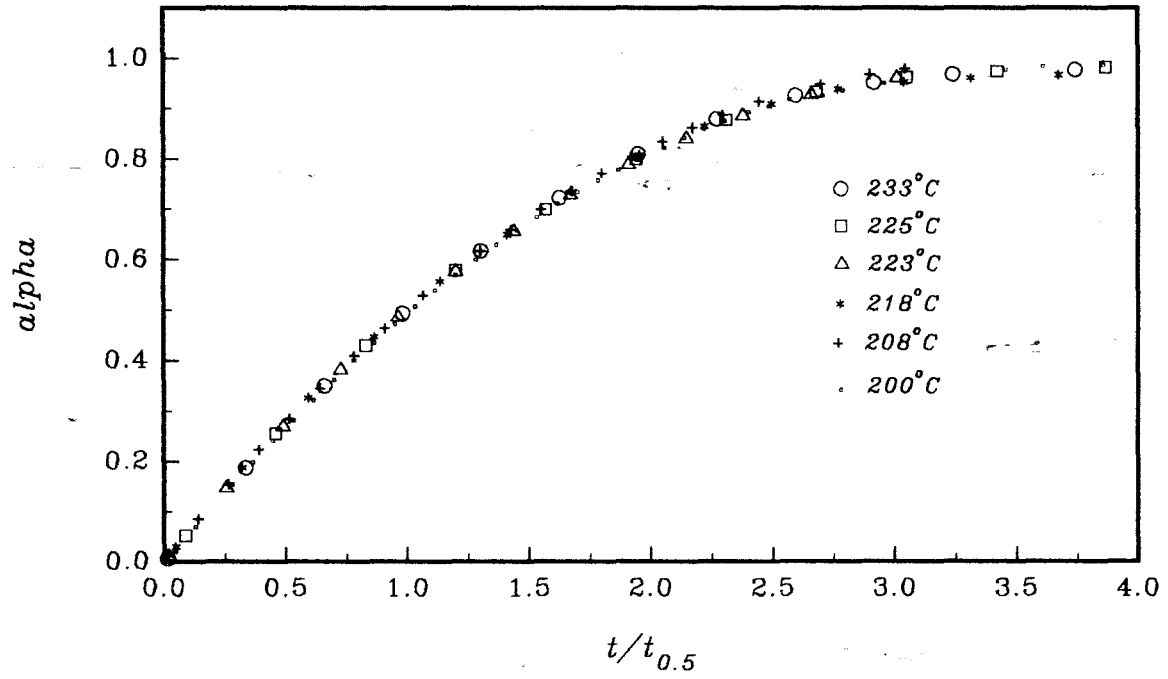

Figure 10.1.3b: Comparison of reduced–time plots for the decomposition of $Ni(nmf)Cl_2$ at a series of constant temperatures.

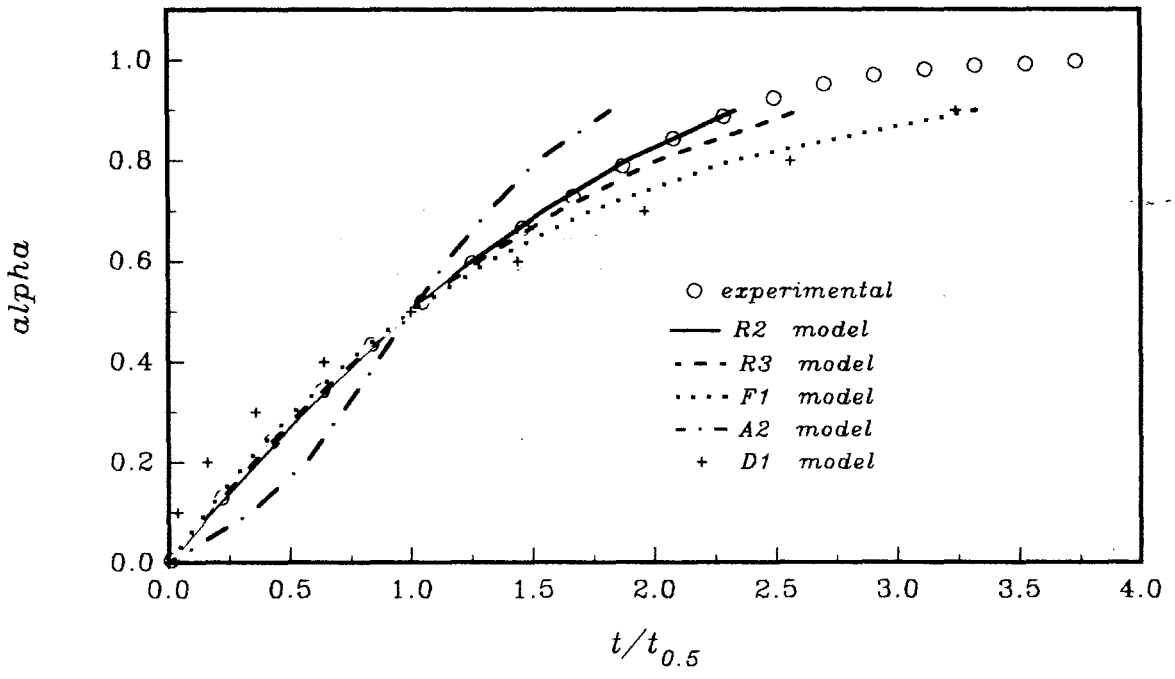

Figure 10.1.4b: Reduced–time plots for the decomposition of $Ni(nmf)Cl_2$ at 212°C, compared with calculated plots for various kinetic models.

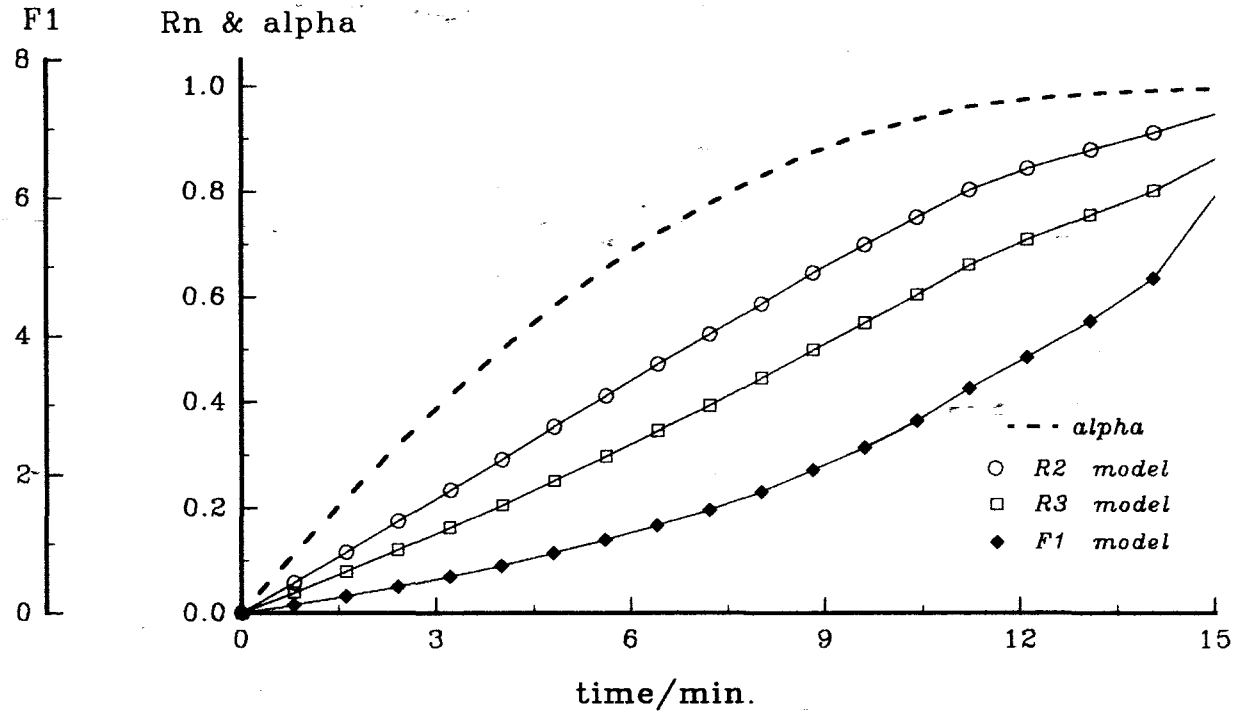

Figure 10.1.5b: Plots of $g(\alpha)$ versus time for the decomposition of $Ni(nmf)Cl_2$ at 238°C. The α–time curve is included to show the range of α over which $g(\alpha)$ is approximately linear.

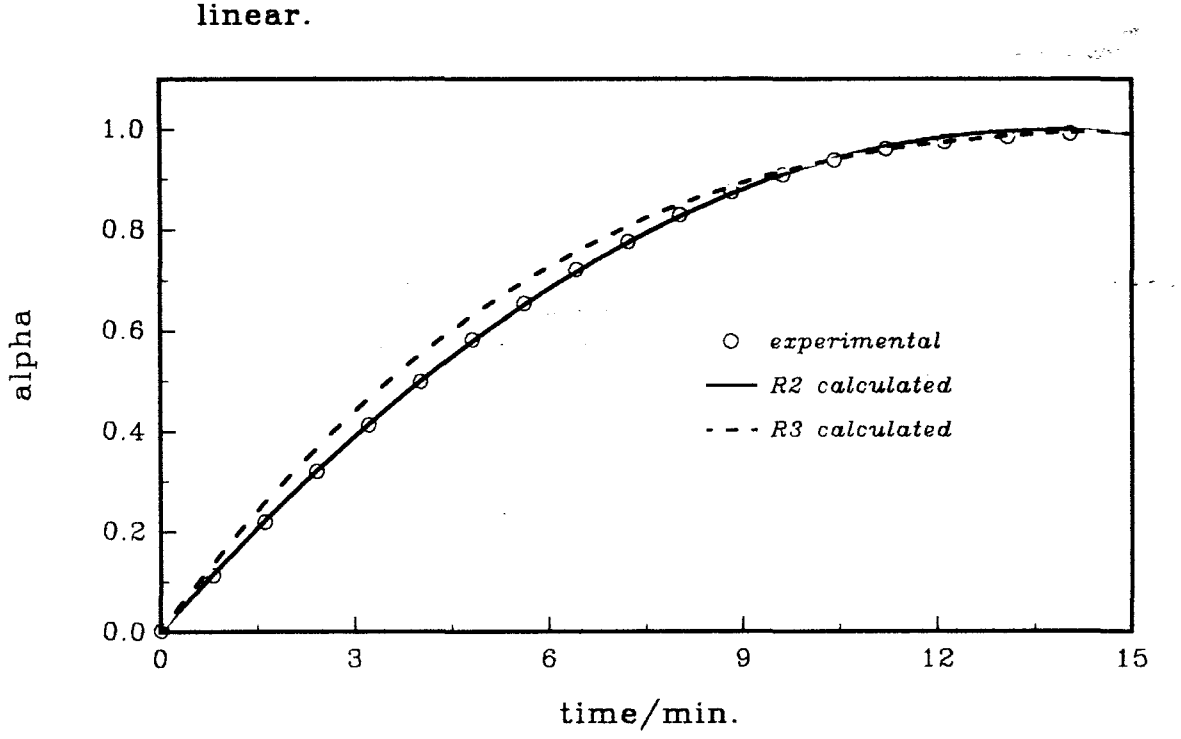

Figure 10.1.6b: Plots of $\alpha_{calc.}$ versus time using the R2 and R3 models, compared with α_e versus time data for the decomposition of $Ni(nmf)Cl_2$ at 238°C.

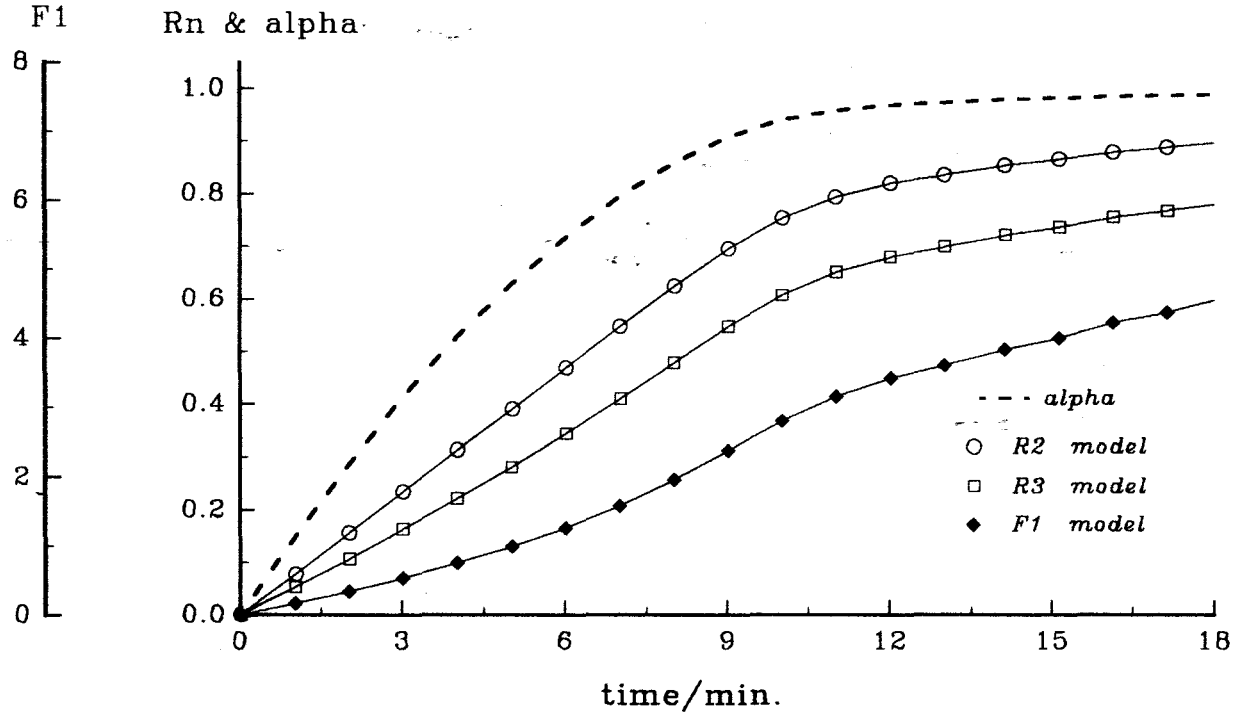

Figure 10.1.5c: Plots of $g(\alpha)$ versus time for the decomposition of $Ni(nmf)Cl_2$ at 230°C. The α–time curve is included to show the range of α over which $g(\alpha)$ is approximately linear.

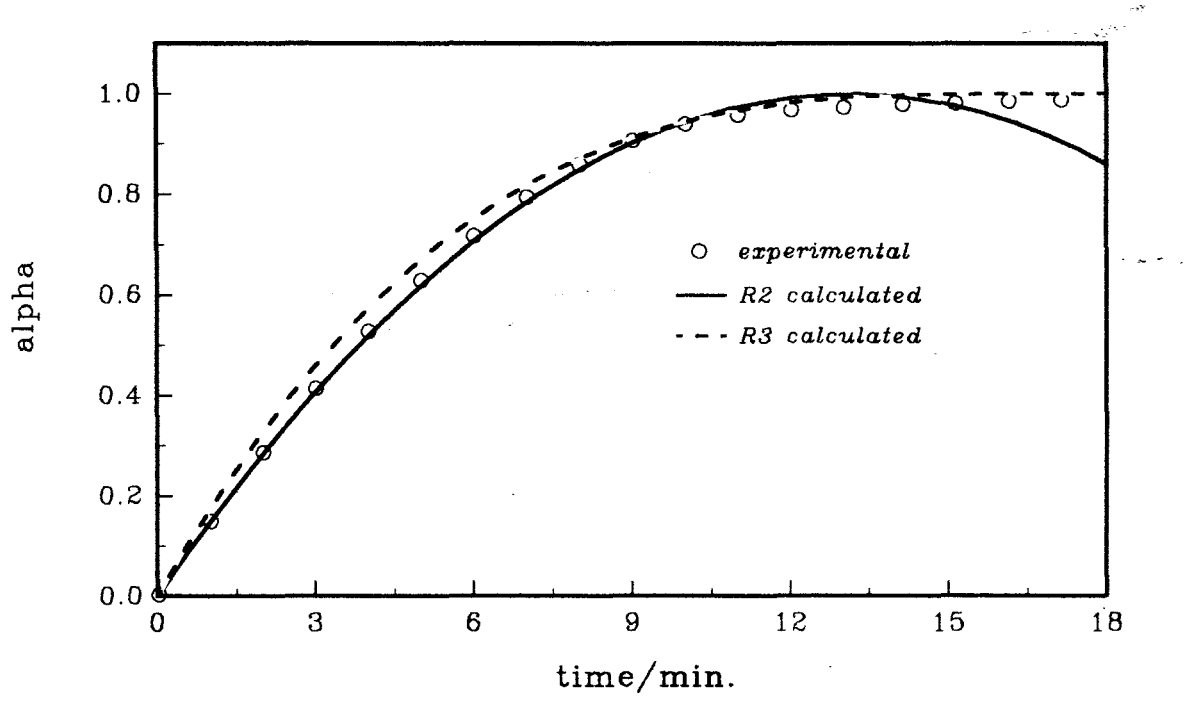

Figure 10.1.6c: Plots of $\alpha_{calc.}$ versus time using the R2 and R3 models, compared with α_e versus time data for the decomposition of $Ni(nmf)Cl_2$ at 230°C.

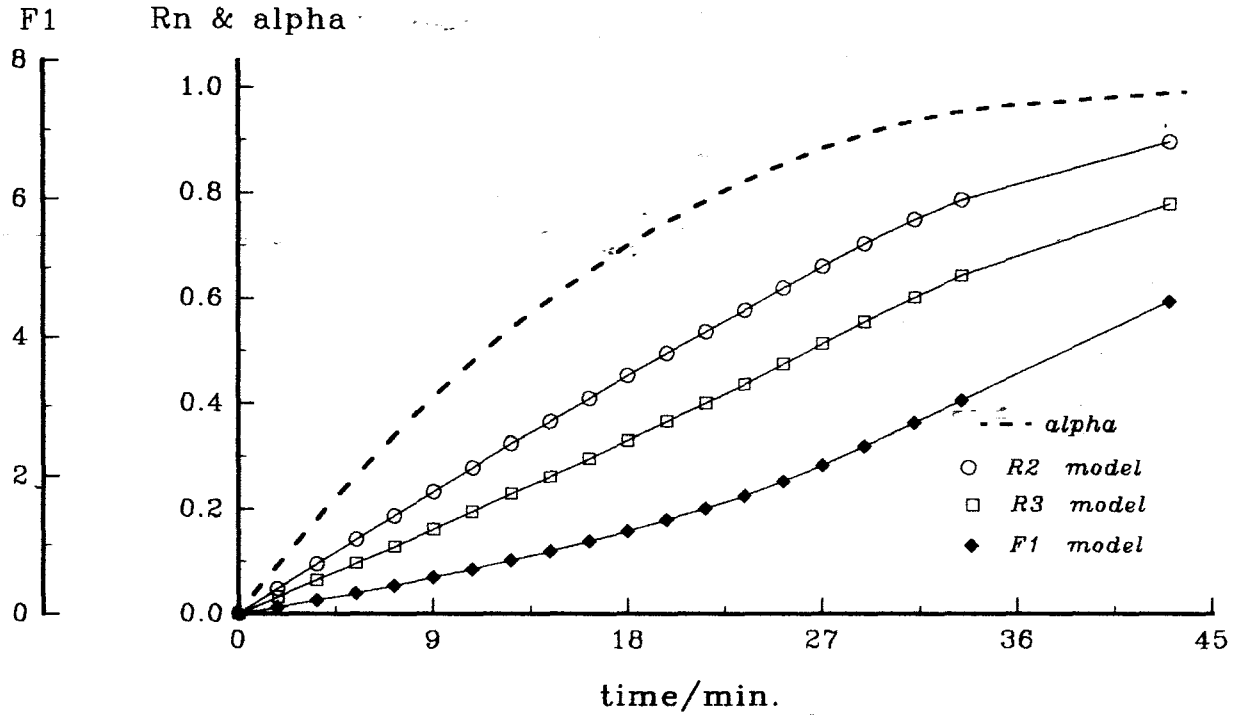

Figure 10.1.5d: Plots of $g(\alpha)$ versus time for the decomposition of $Ni(nmf)Cl_2$ at 223°C. The α–time curve is included to show the range of α over which $g(\alpha)$ is approximately linear.

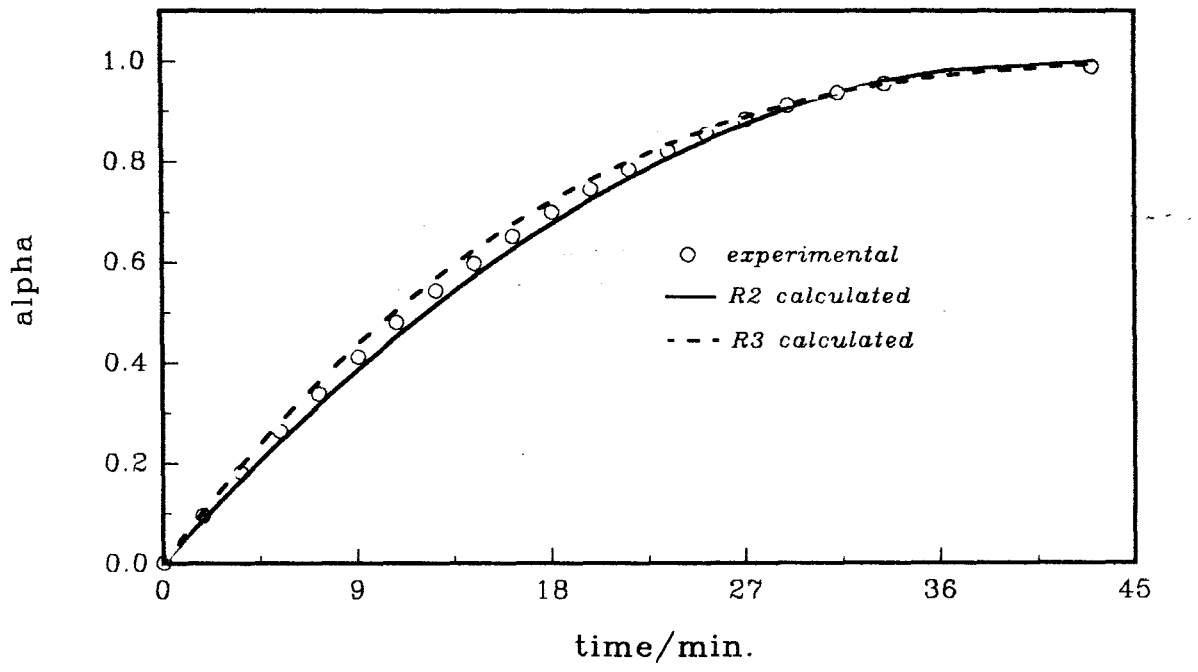

Figure 10.1.6d: Plots of $\alpha_{calc.}$ versus time using the R2 and R3 models, compared with α_e versus time data for the decomposition of $Ni(nmf)Cl_2$ at 223°C.

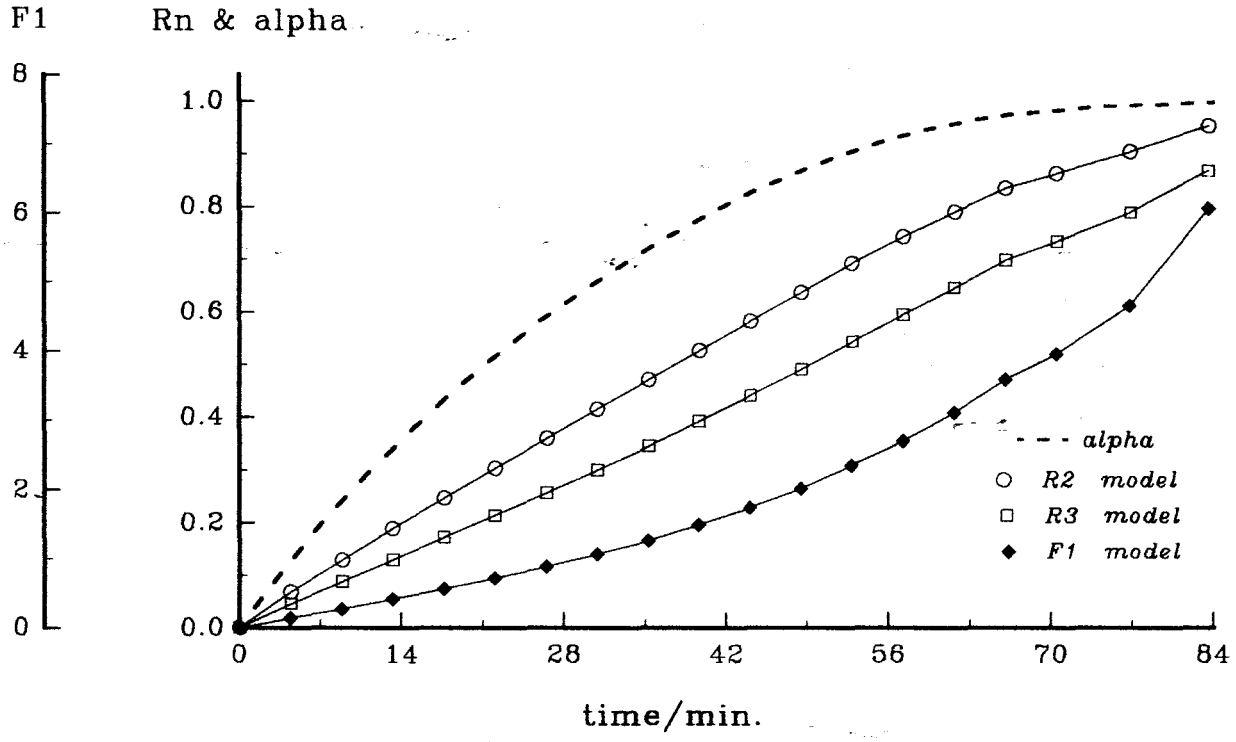

Figure 10.1.5e: Plots of $g(\alpha)$ versus time for the decomposition of $Ni(nmf)Cl_2$ at 215°C. The α–time curve is included to show the range of α over which $g(\alpha)$ is approximately linear.

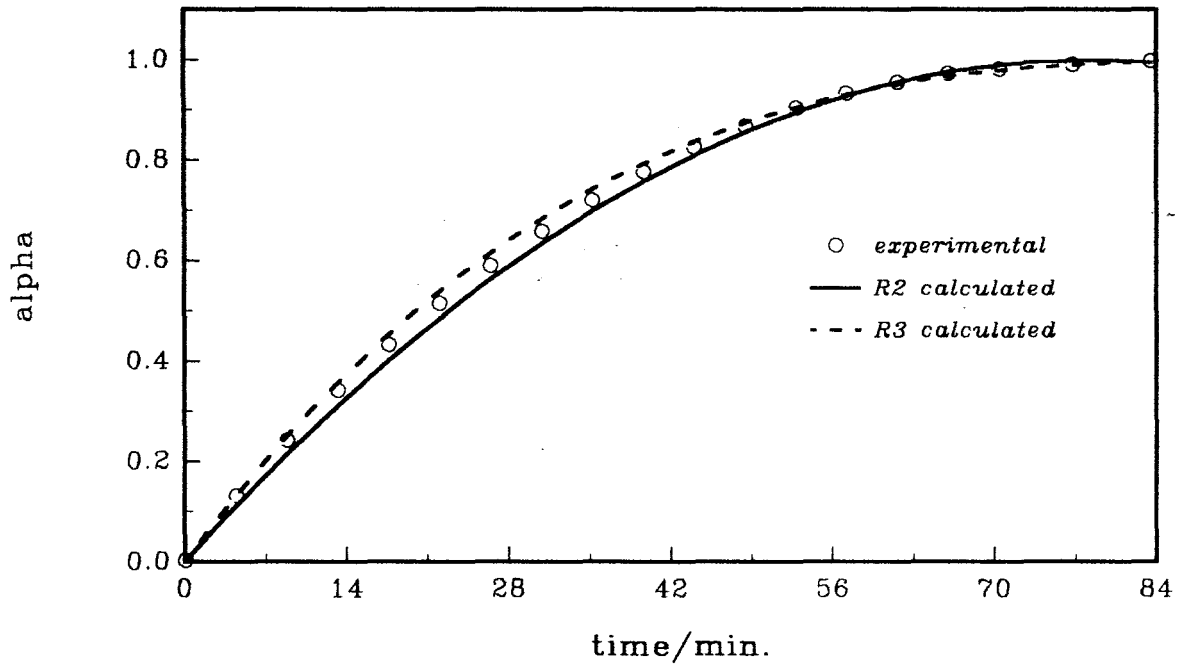

Figure 10.1.6e: Plots of $\alpha_{calc.}$ versus time using the R2 and R3 models, compared with α_e versus time data for the decomposition of $Ni(nmf)Cl_2$ at 215°C.

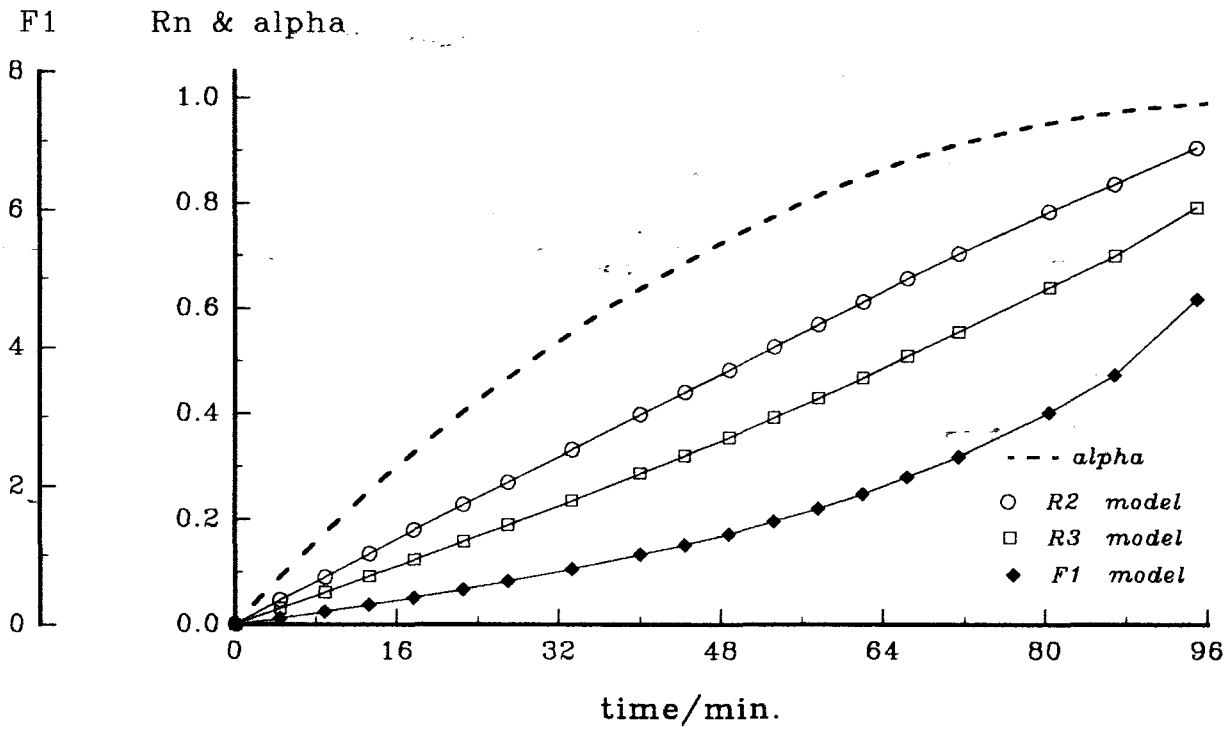

Figure 10.1.5f: Plots of g(α) versus time for the decomposition of $Ni(nmf)Cl_2$ at 208°C. The α–time curve is included to show the range of α over which g(α) is approximately linear.

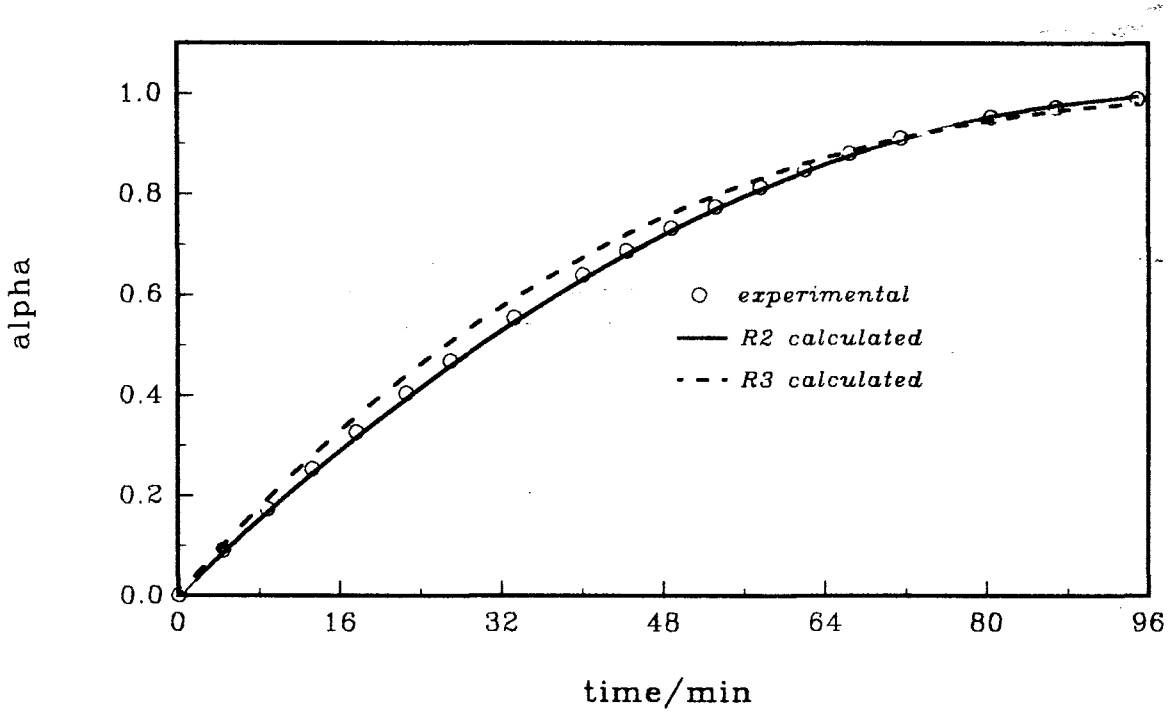

Figure 10.1.6f: Plots of $\alpha_{calc.}$ versus time using the R2 and R3 models, compared with α_e versus time data for the decomposition of $Ni(nmf)Cl_2$ at 208°C.

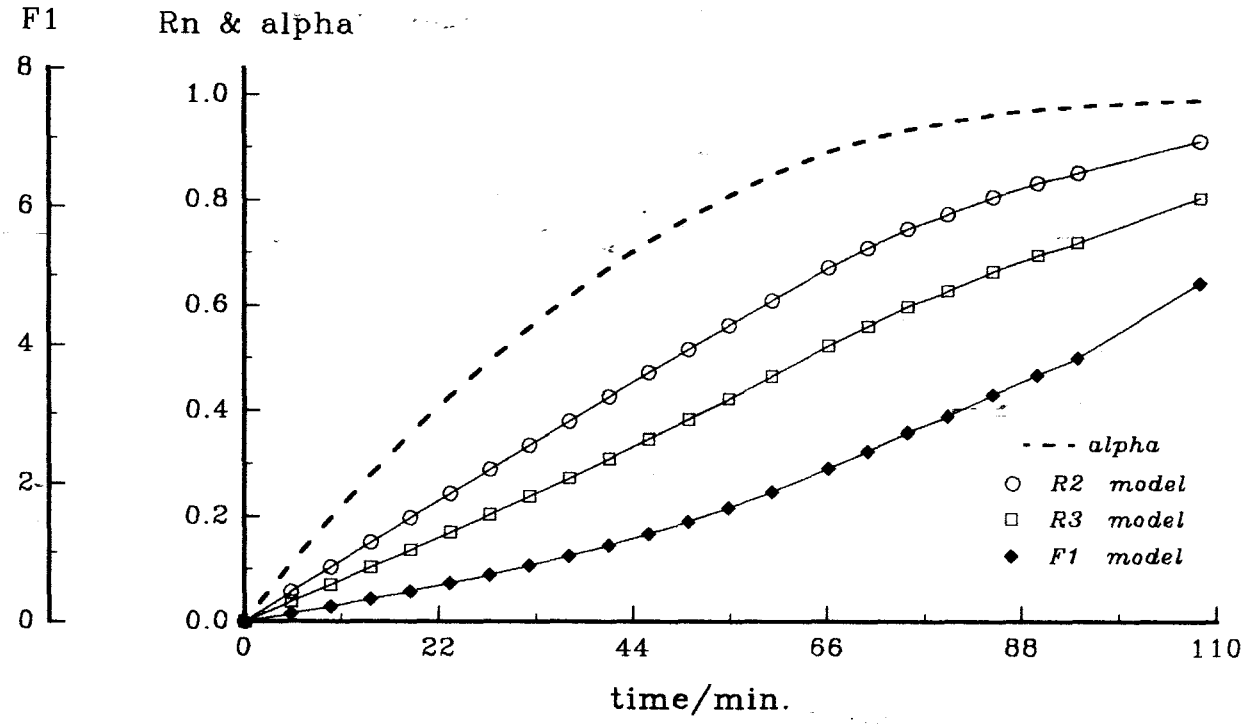

Figure 10.1.5g: Plots of $g(\alpha)$ versus time for the decomposition of $Ni(nmf)Cl_2$ at 205°C. The α–time curve is included to show the range of α over which $g(\alpha)$ is approximately linear.

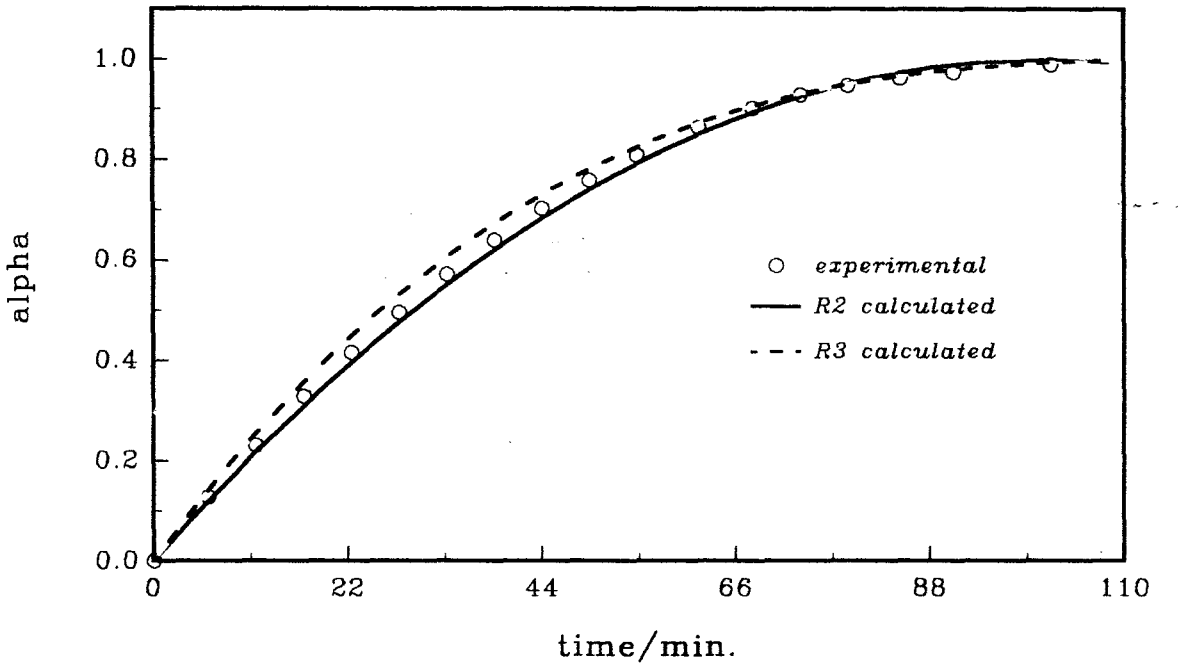

Figure 10.1.6g: Plots of $\alpha_{calc.}$ versus time using the R2 and R3 models, compared with α_e versus time data for the decomposition of $Ni(nmf)Cl_2$ at 205°C.

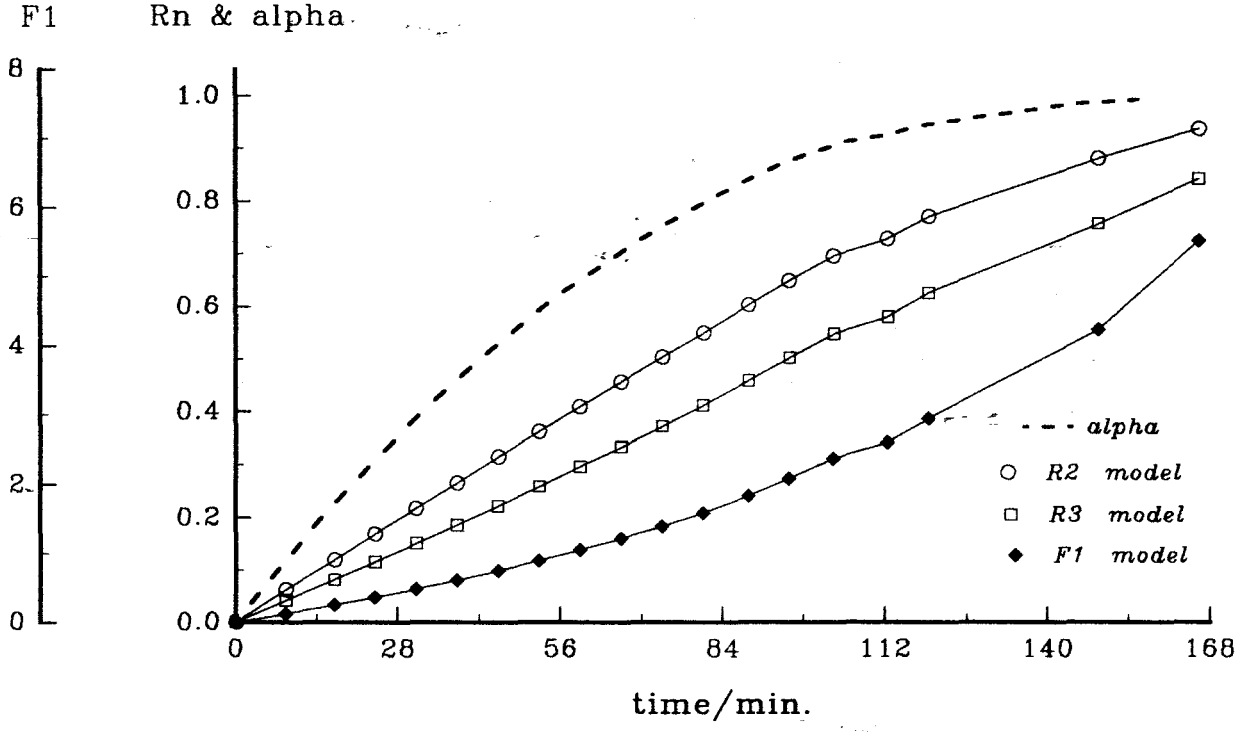

Figure 10.1.5h: Plots of $g(\alpha)$ versus time for the decomposition of $Ni(nmf)Cl_2$ at 200°C. The α–time curve is included to show the range of α over which $g(\alpha)$ is approximately linear.

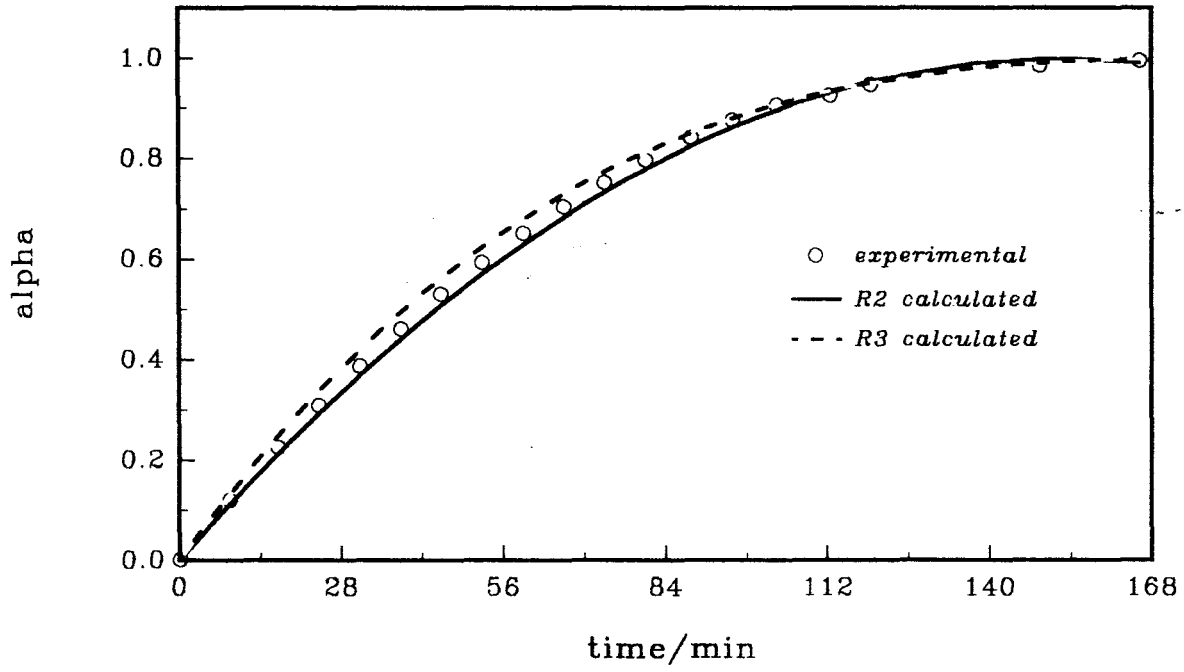

Figure 10.1.6h: Plots of $\alpha_{calc.}$ versus time using the R2 and R3 models, compared with α_e versus time data for the decomposition of $Ni(nmf)Cl_2$ at 200°C.

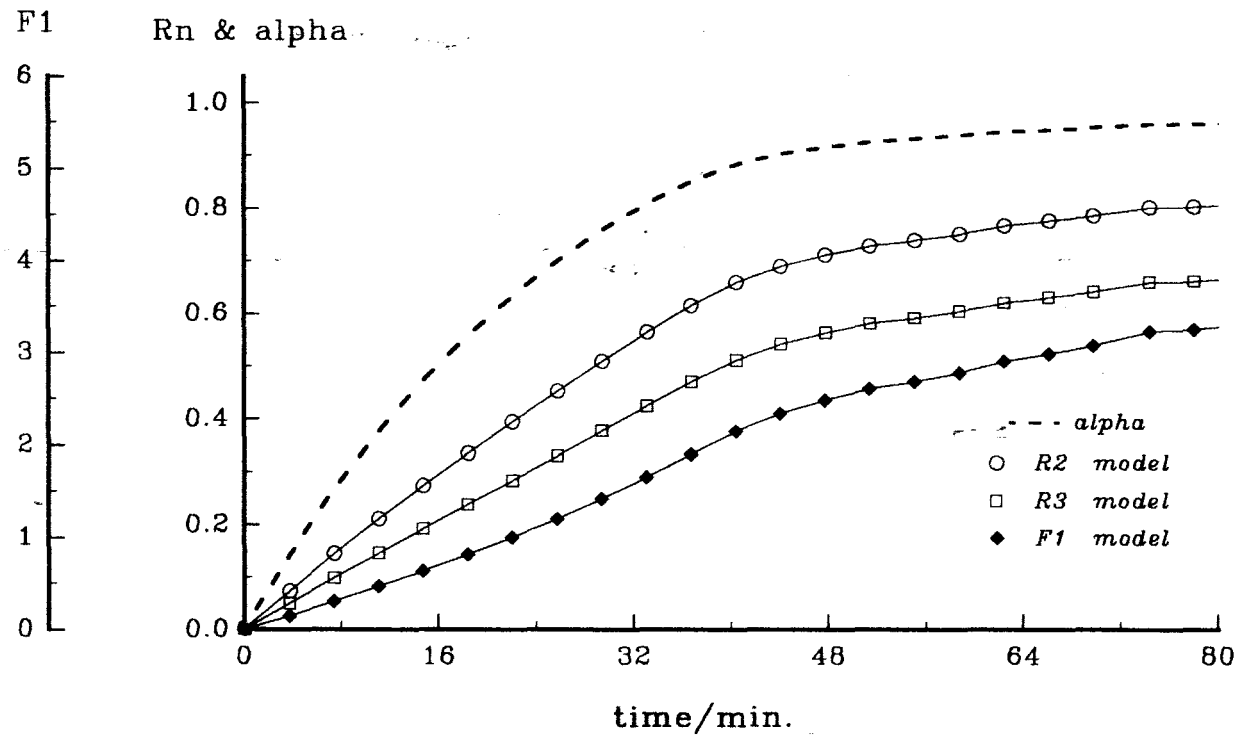

Figure 10.1.5i: Plots of $g(\alpha)$ versus time for the decomposition of $Ni(nmf)Cl_2$ at 210°C. The α–time curve is included to show the range of α over which $g(\alpha)$ is approximately linear.

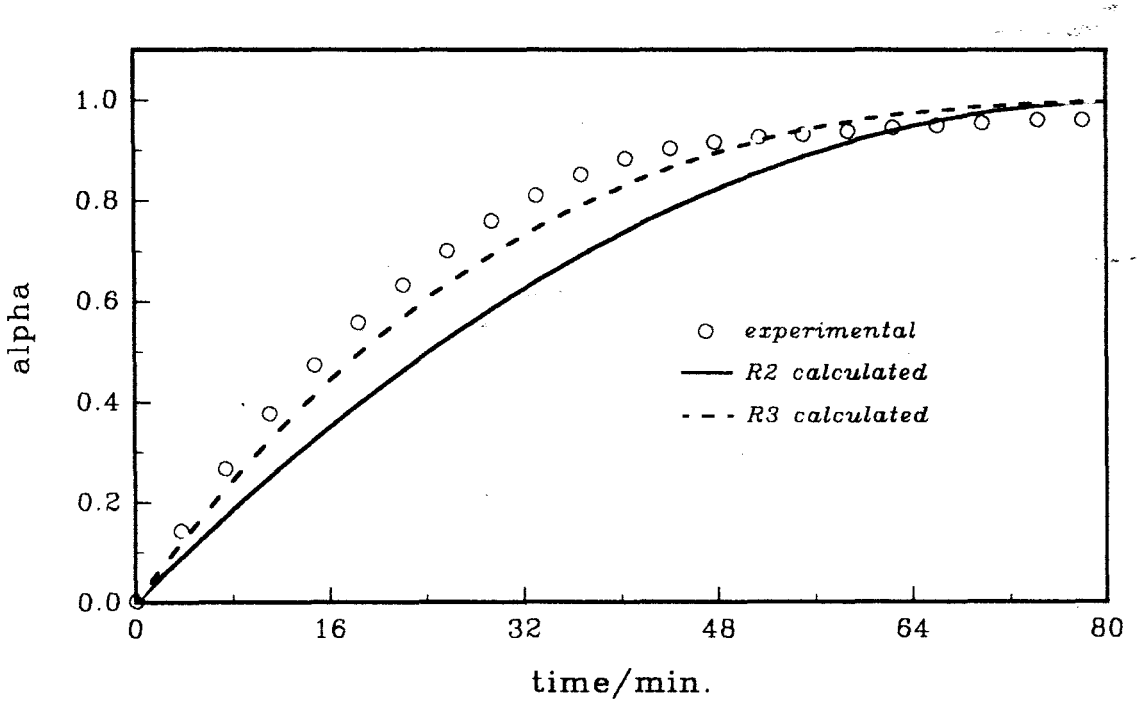

Figure 10.1.6i: Plots of $\alpha_{calc.}$ versus time using the R2 and R3 models, compared with α_e versus time data for the decomposition of $Ni(nmf)Cl_2$ at 210°C.

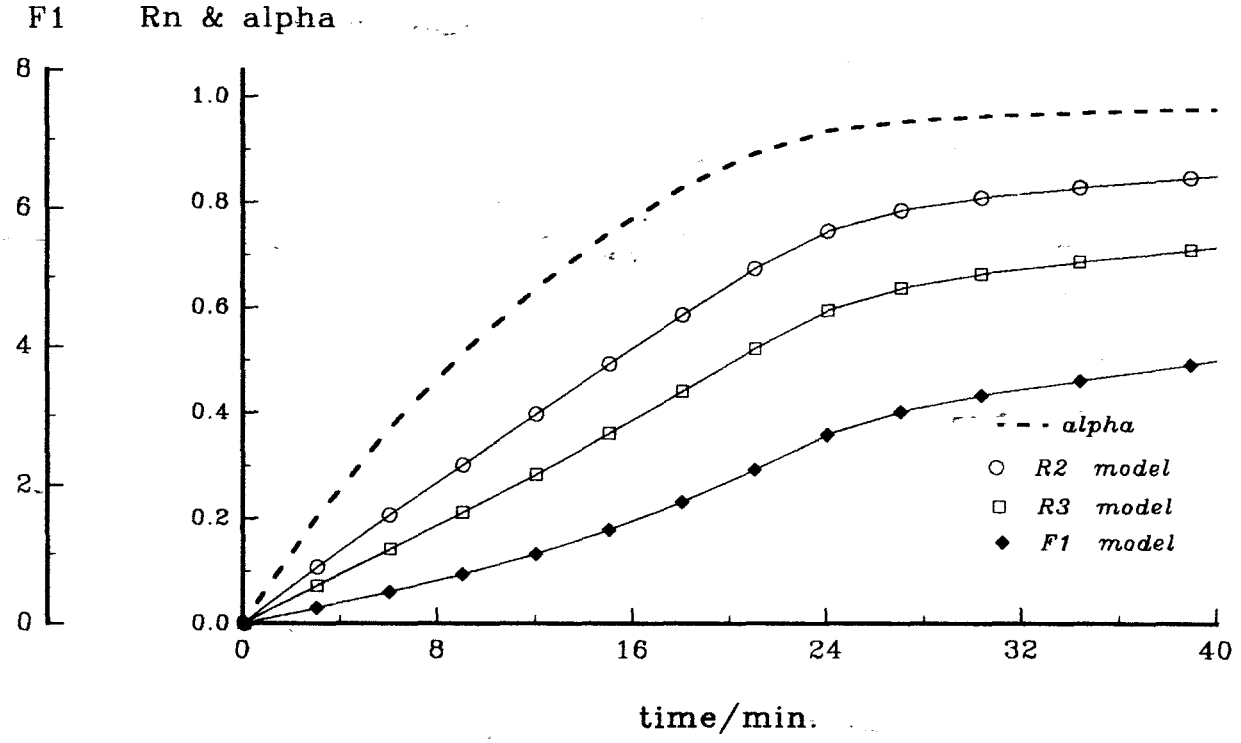

Figure 10.1.5j: Plots of $g(\alpha)$ versus time for the decomposition of $Ni(nmf)Cl_2$ at 218°C. The α–time curve is included to show the range of α over which $g(\alpha)$ is approximately linear.

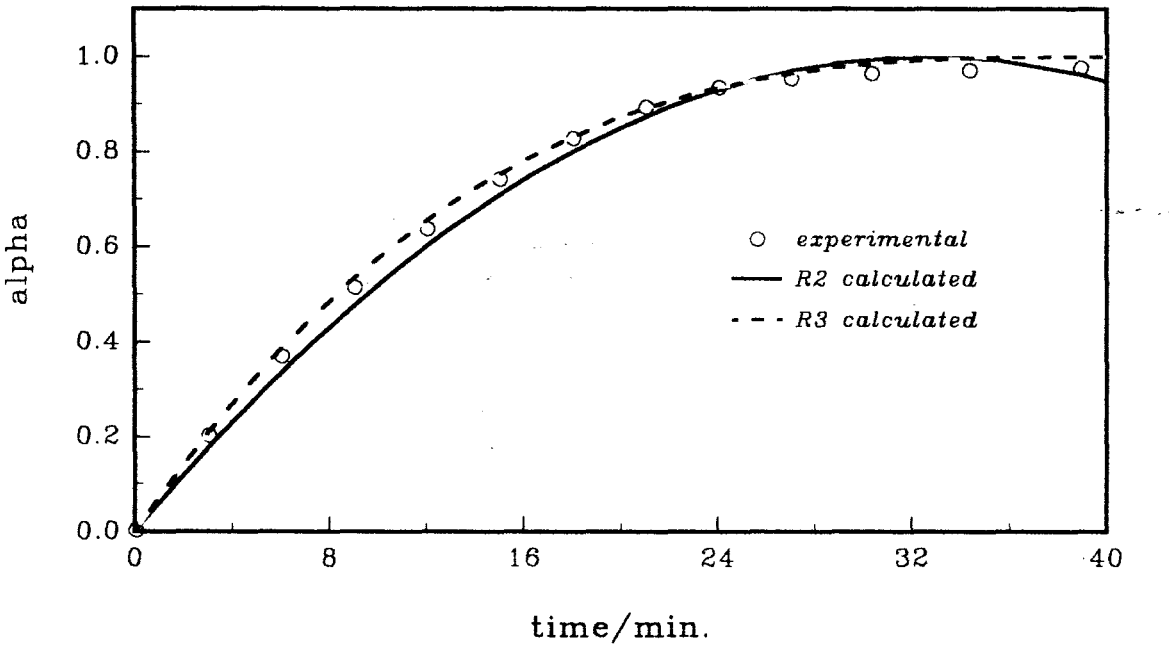

Figure 10.1.6j: Plots of $\alpha_{calc.}$ versus time using the R2 and R3 models, compared with α_e versus time data for the decomposition of $Ni(nmf)Cl_2$ at 218°C.

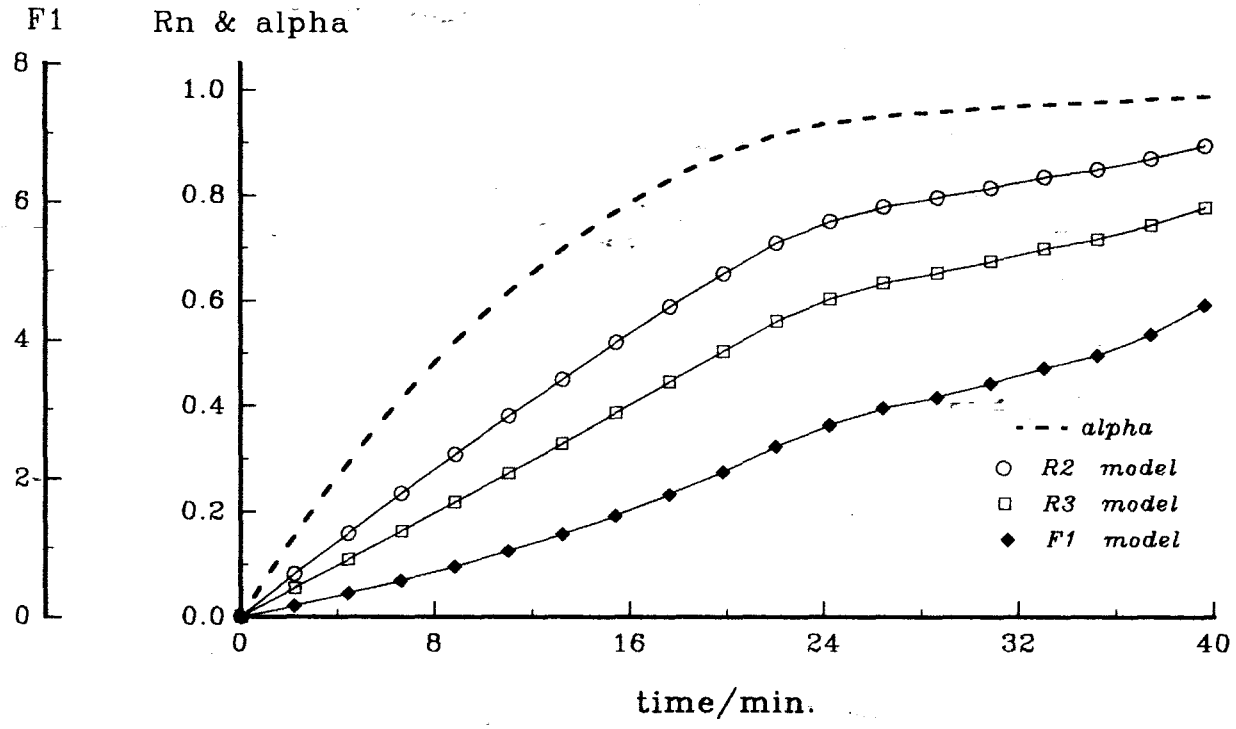

Figure 10.1.5k: Plots of $g(\alpha)$ against time for the decomposition of $Ni(nmf)Cl_2$ at 220°C. The α–time curve is included to show the range of α over which $g(\alpha)$ is approximately linear.

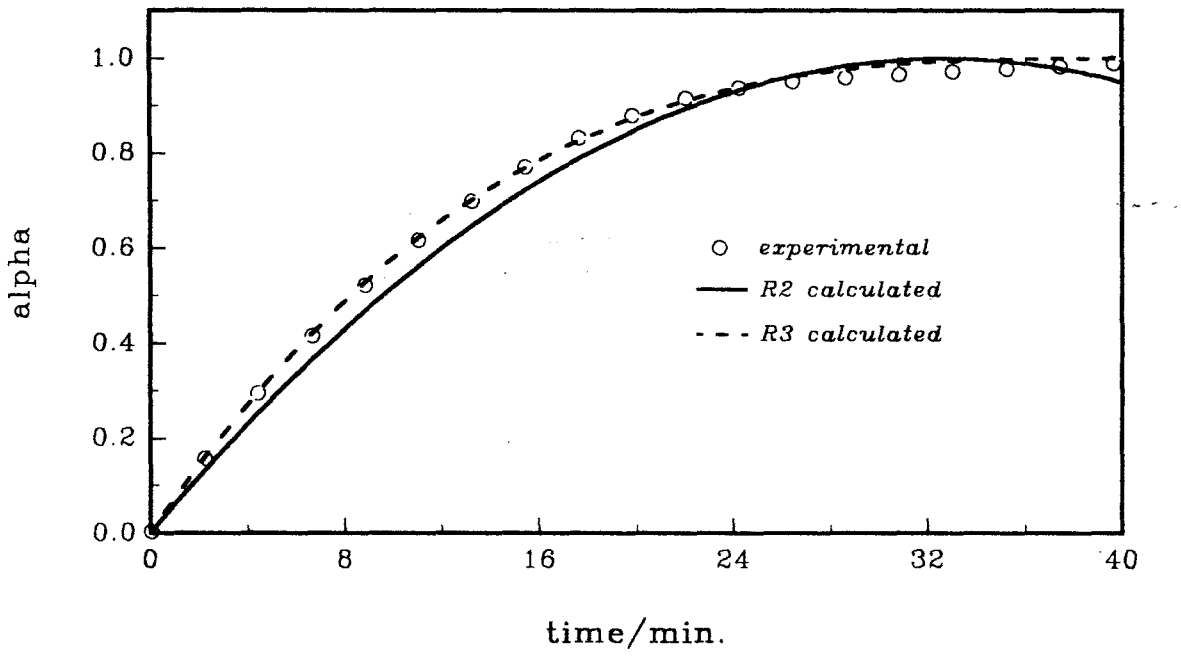

Figure 10.1.6k: Plots of $\alpha_{calc.}$ versus time using the R2 and R3 models, compared with α_e versus time data for the decomposition of $Ni(nmf)Cl_2$ at 220°C.

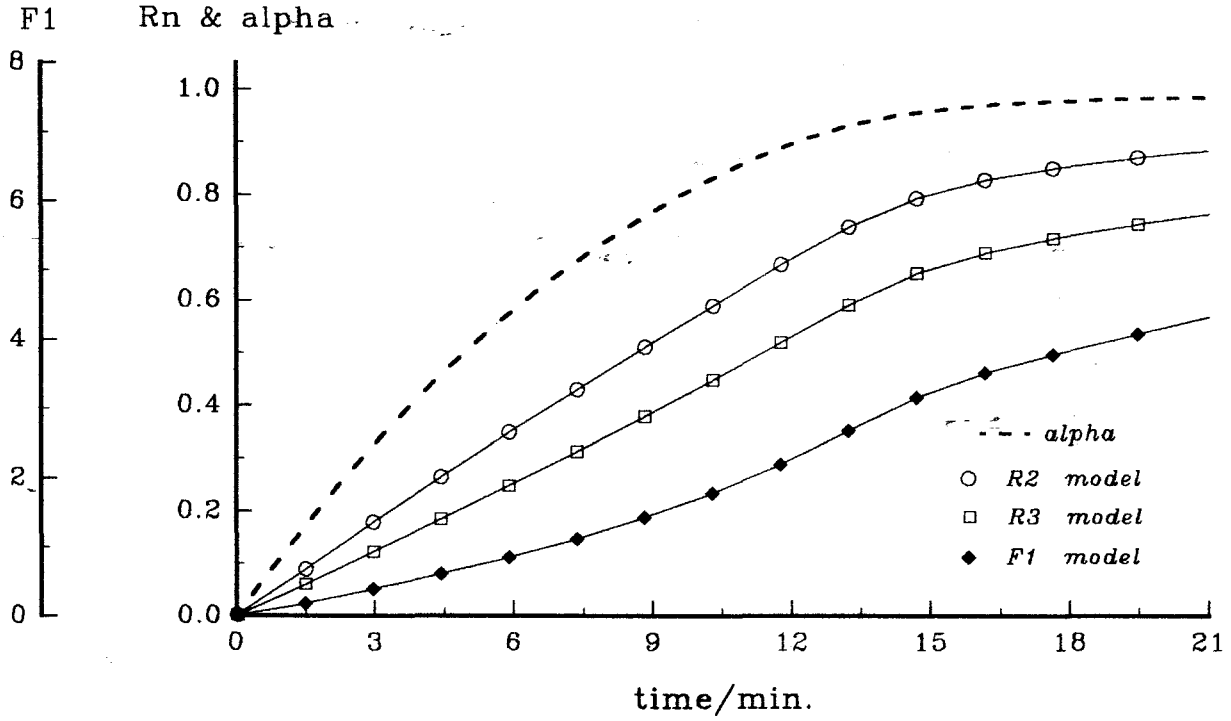

Figure 10.1.51: Plots of $g(\alpha)$ versus time for the decomposition of $Ni(nmf)Cl_2$ at 225°C. The α–time curve is included to show the range of α over which $g(\alpha)$ is approximately linear.

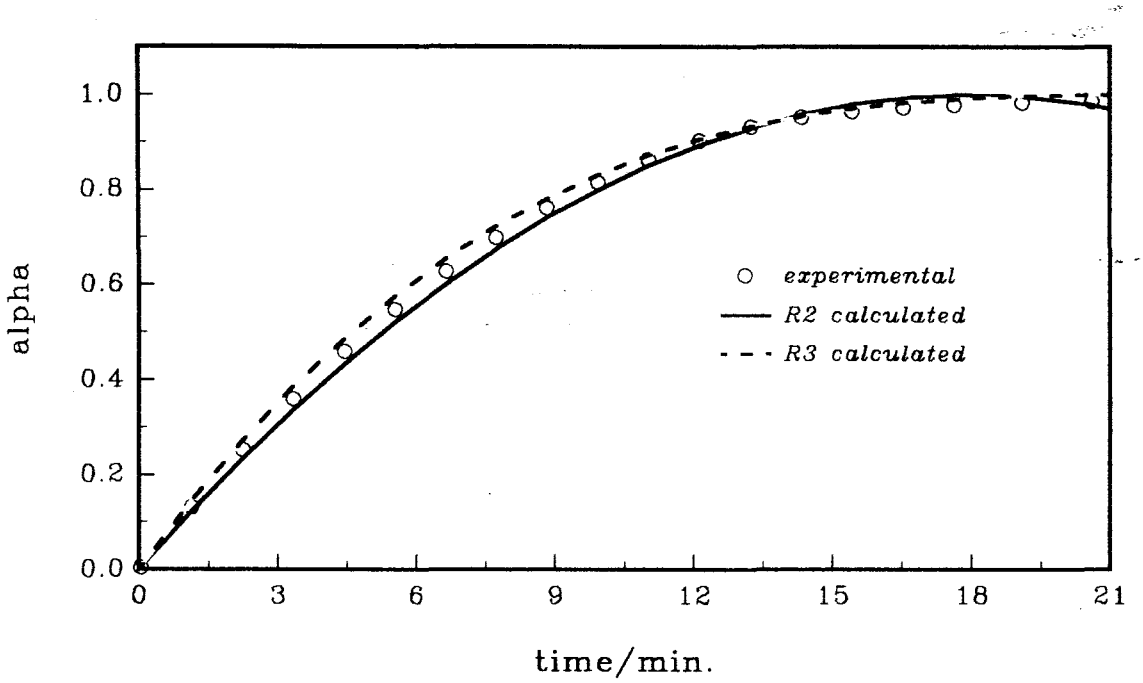

Figure 10.1.61: Plots of $\alpha_{calc.}$ versus time using the R2 and R3 models, compared with α_e versus time data for the decomposition of $Ni(nmf)Cl_2$ at 225°C.

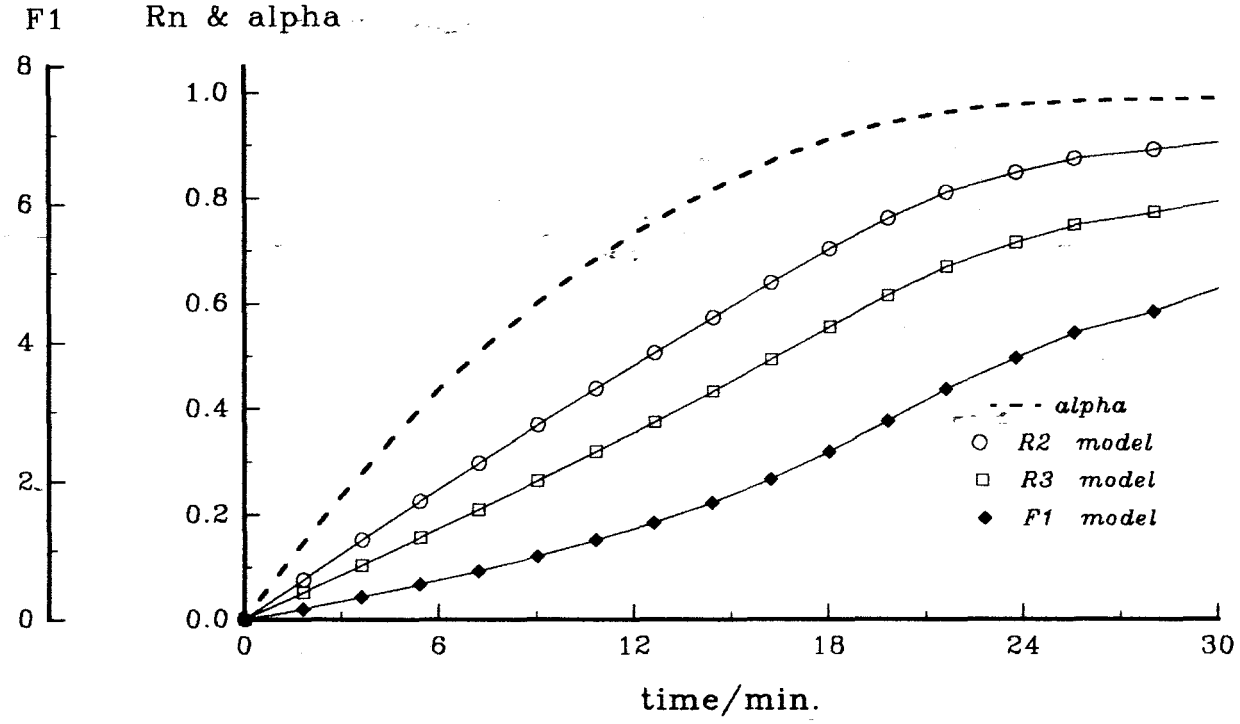

Figure 10.1.5m: Plots of $g(\alpha)$ versus time for the decomposition of $Ni(nmf)Cl_2$ at 228°C. The α–time curve is included to show the range of α over which $g(\alpha)$ is approximately linear.

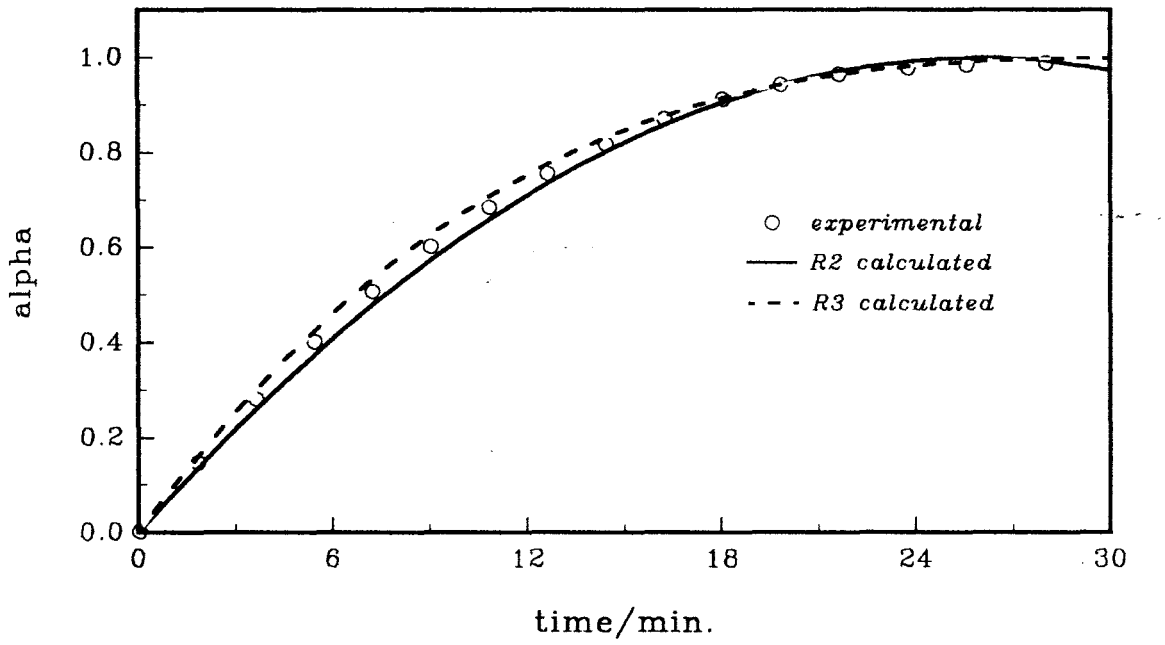

Figure 10.1.6m: Plots of $\alpha_{calc.}$ versus time using the R2 and R3 models, compared with α_e versus time data for the decomposition of $Ni(nmf)Cl_2$ at 228°C.

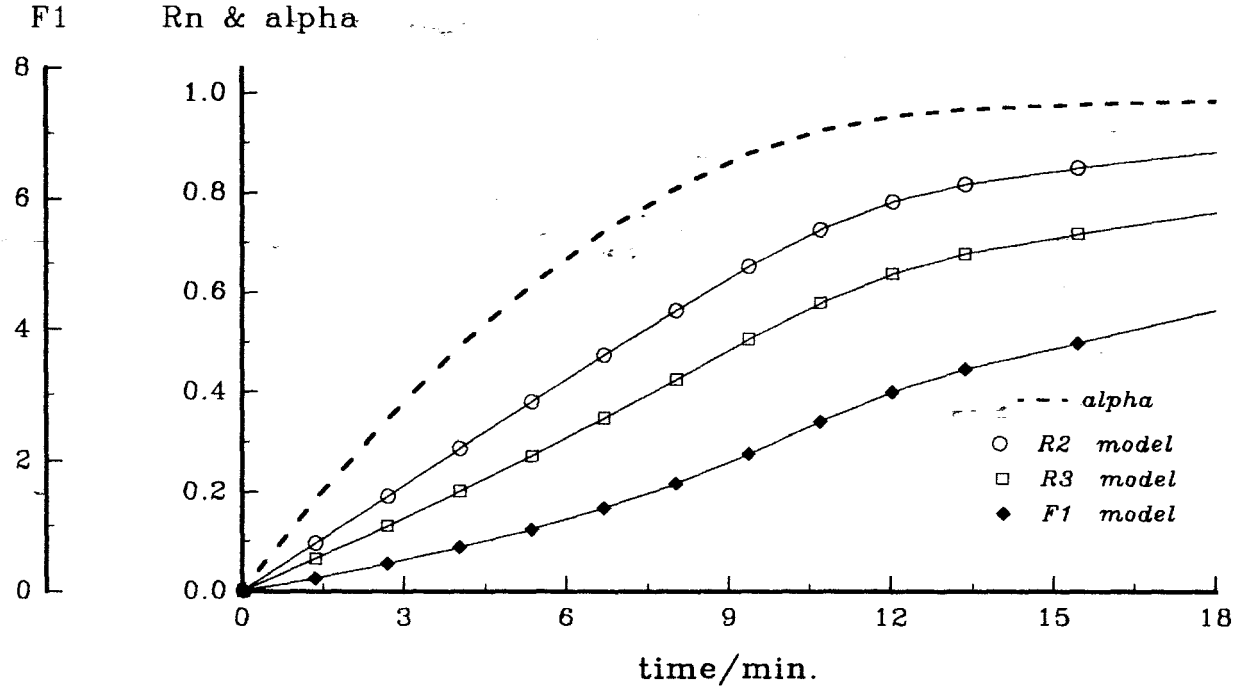

Figure 10.1.5n: Plots of g(α) versus time for the decomposition of $Ni(nmf)Cl_2$ at 233°C. The α–time curve is included to show the range of α over which g(α) is approximately linear.

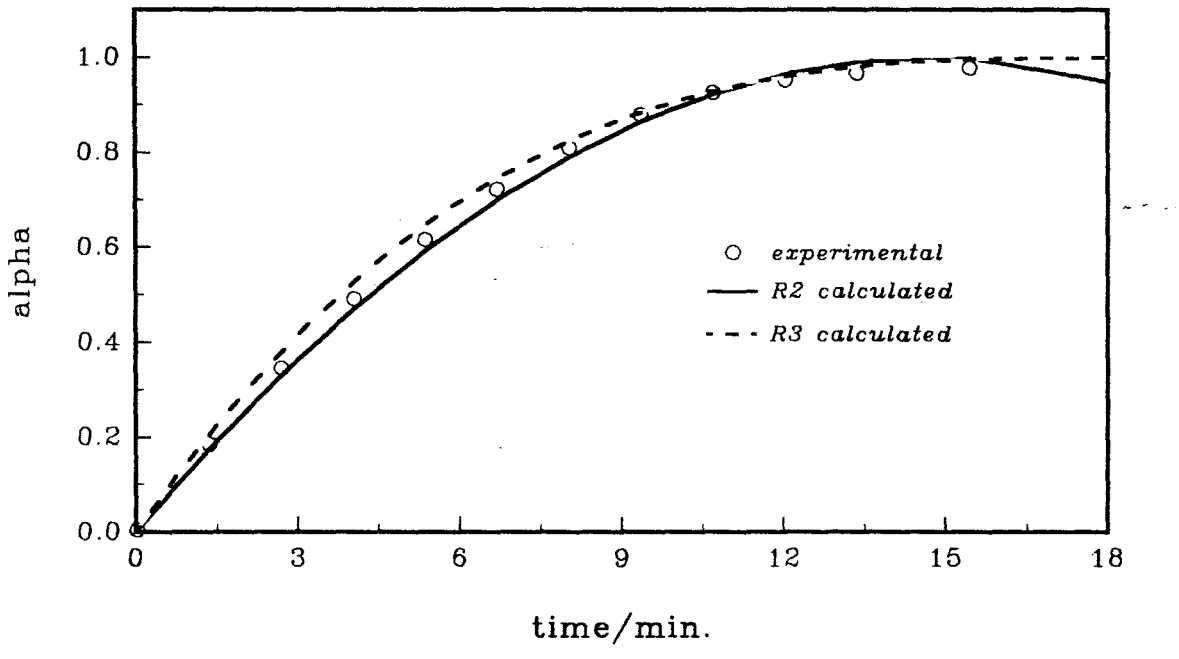

Figure 10.1.6n: Plots of $\alpha_{calc.}$ versus time using the R2 and R3 models, compared with α_e versus time data of the decomposition of $Ni(nmf)Cl_2$ at 233°C.

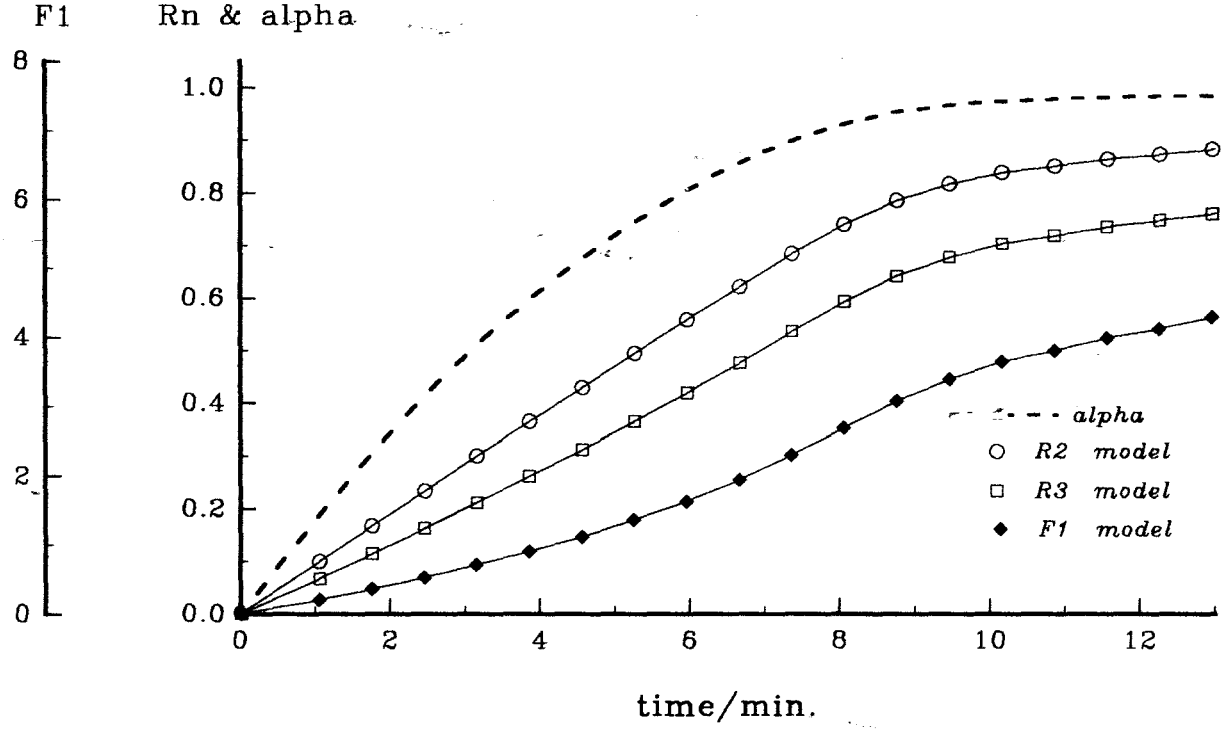

Figure 10.1.5o: Plots of g(α) versus time for the decomposition of $Ni(nmf)Cl_2$ at 235°C. The α–time curve is included to show the range of α over which g(α) is approximately linear.

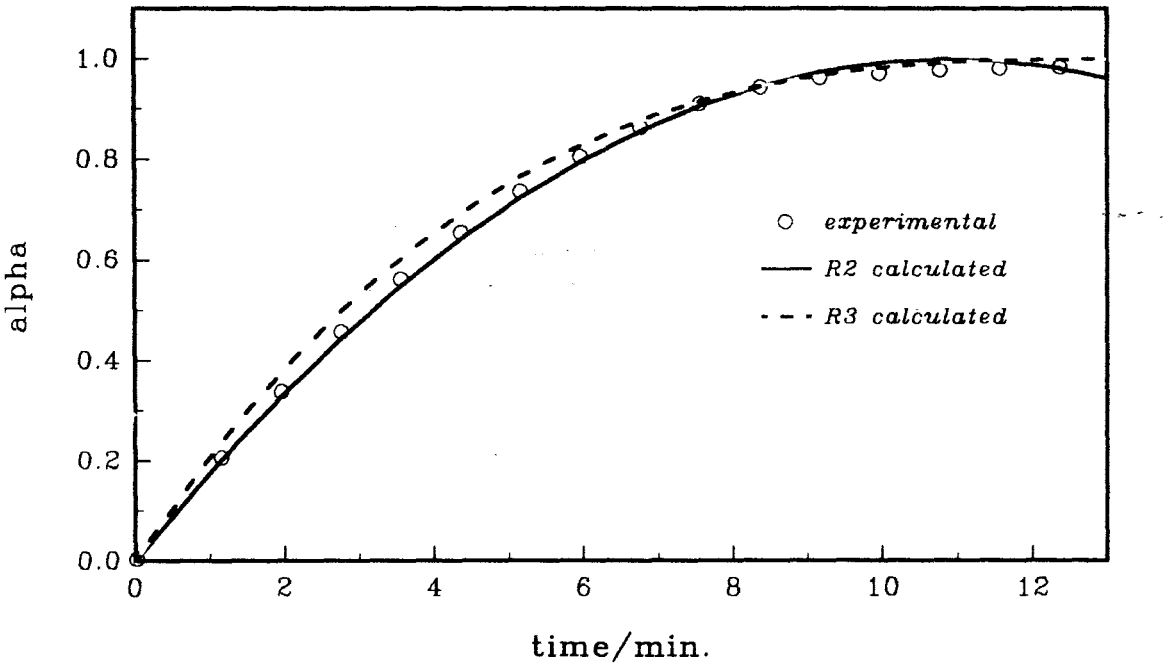

Figure 10.1.6o: Plots of $\alpha_{calc.}$ versus time using the R2 and R3 models, compared with α_e versus time data for the decomposition of $Ni(nmf)Cl_2$ at 235°C.

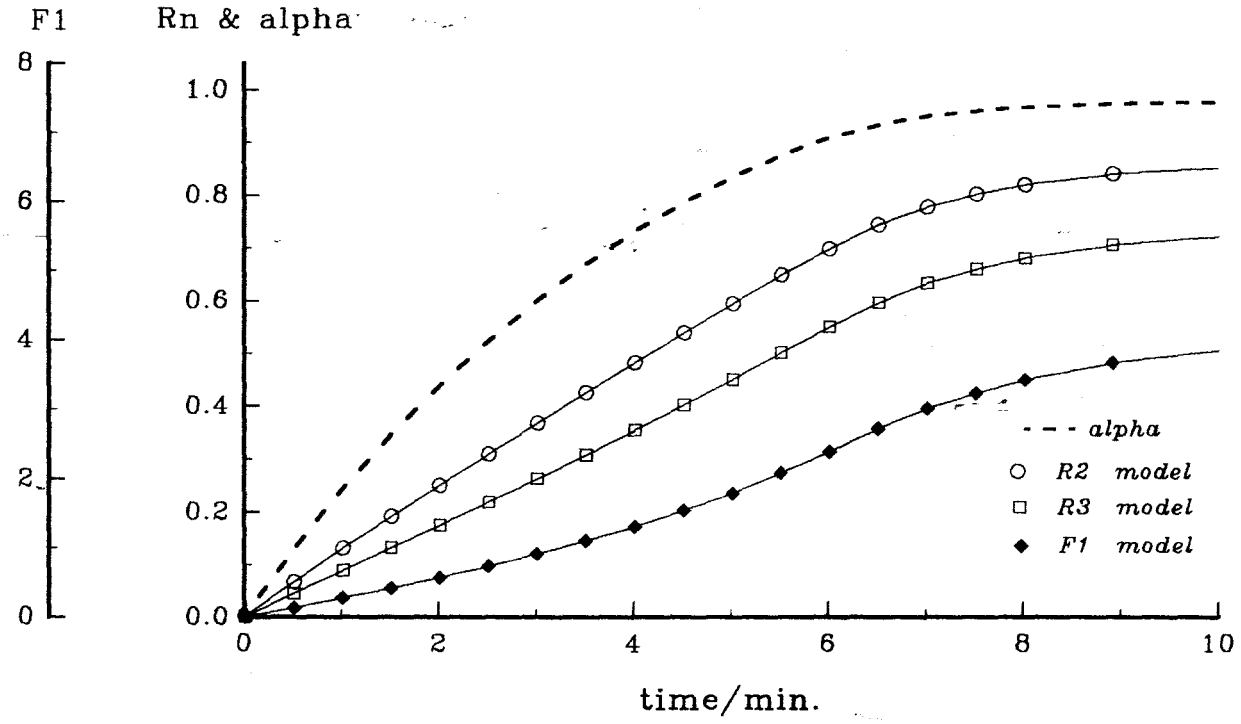

Figure 10.1.5p: Plots of $g(\alpha)$ versus time for the decomposition of $Ni(nmf)Cl_2$ at 240°C. The α–time curve is included to show the range of α over which $g(\alpha)$ is approximately linear.

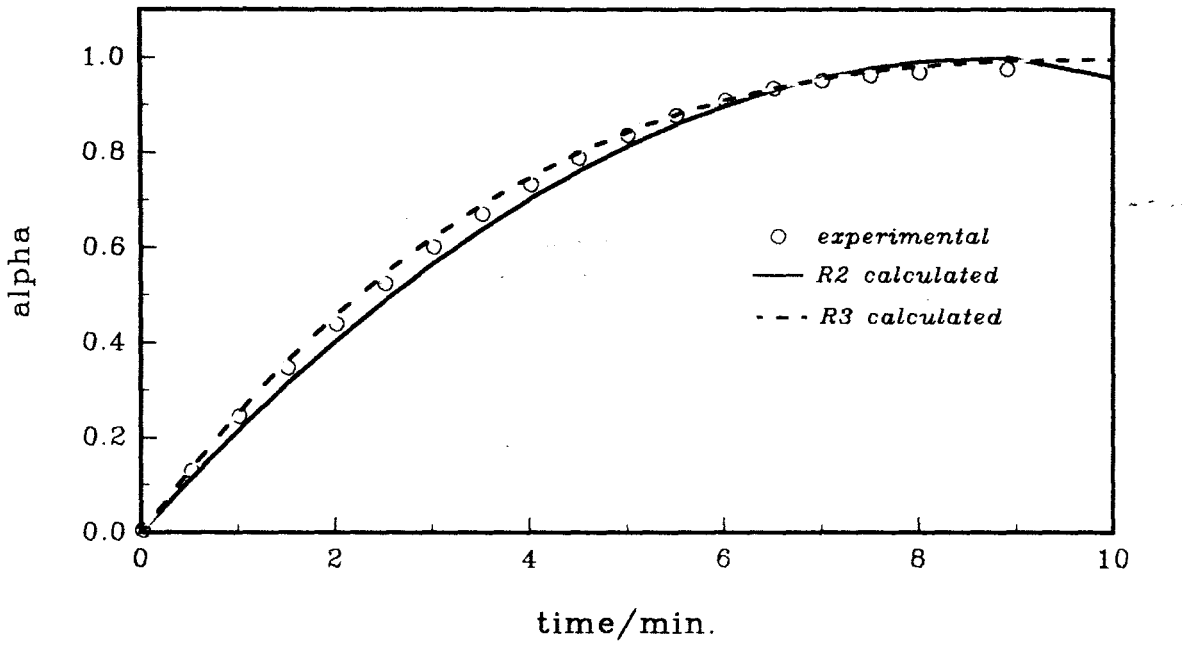

Figure 10.1.6p: Plots of $\alpha_{calc.}$ versus time using the R2 and R3 models, compared with α_e versus time data for the decomposition of $Ni(nmf)Cl_2$ at 240°C.

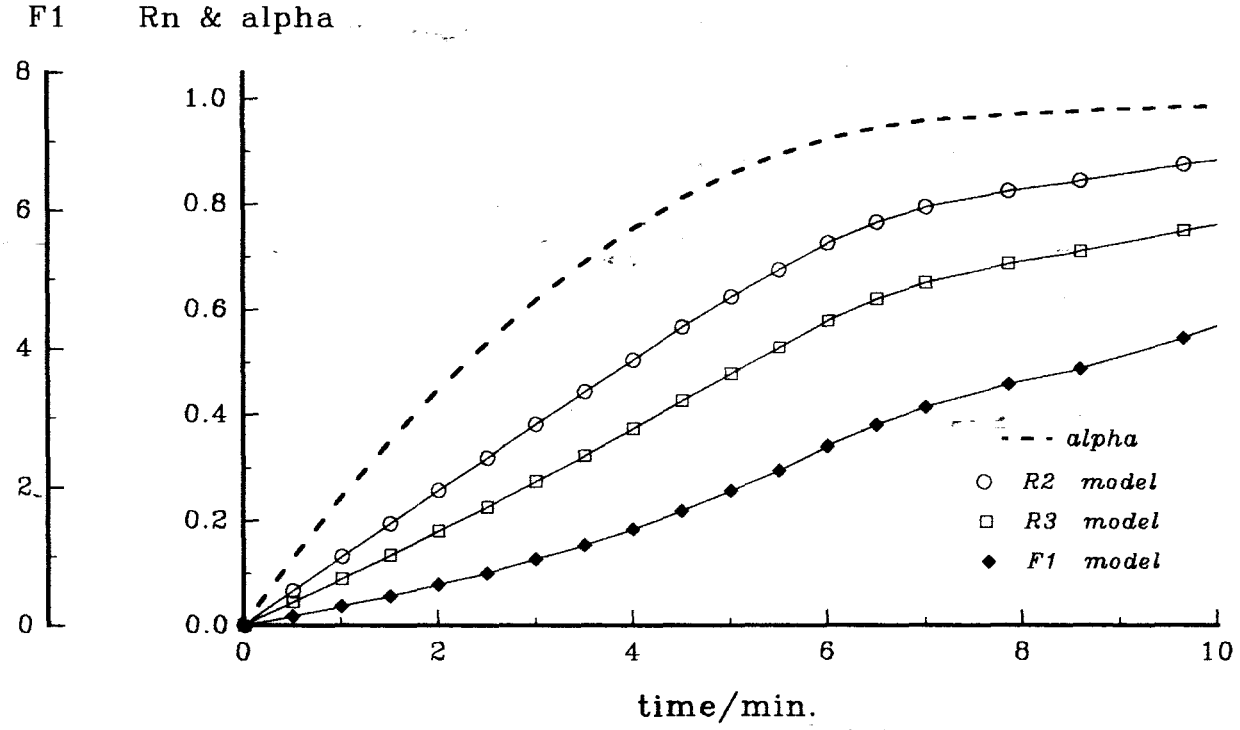

Figure 10.1.5q: Plots of $g(\alpha)$ versus time for the decomposition of $Ni(nmf)Cl_2$ at 243°C. The α–time curve is included to show the range of α over which $g(\alpha)$ is approximately linear.

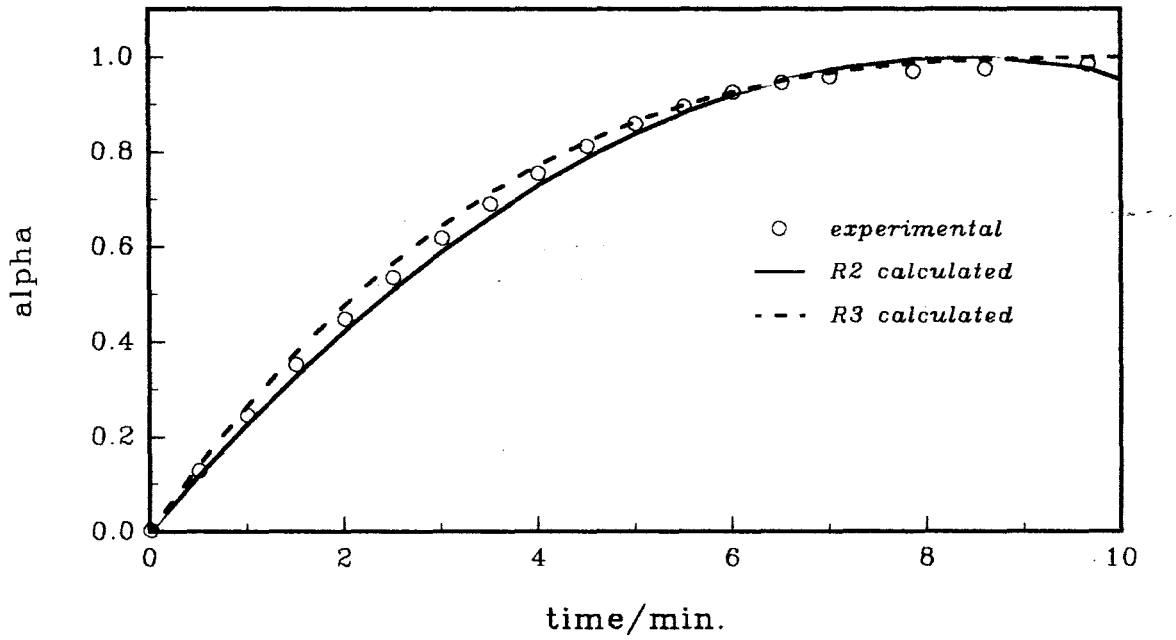

Figure 10.1.6q: Plots of $\alpha_{calc.}$ versus time using the R2 and R3 models, compared with α_e versus time data for the decomposition of $Ni(nmf)Cl_2$ at 243°C.

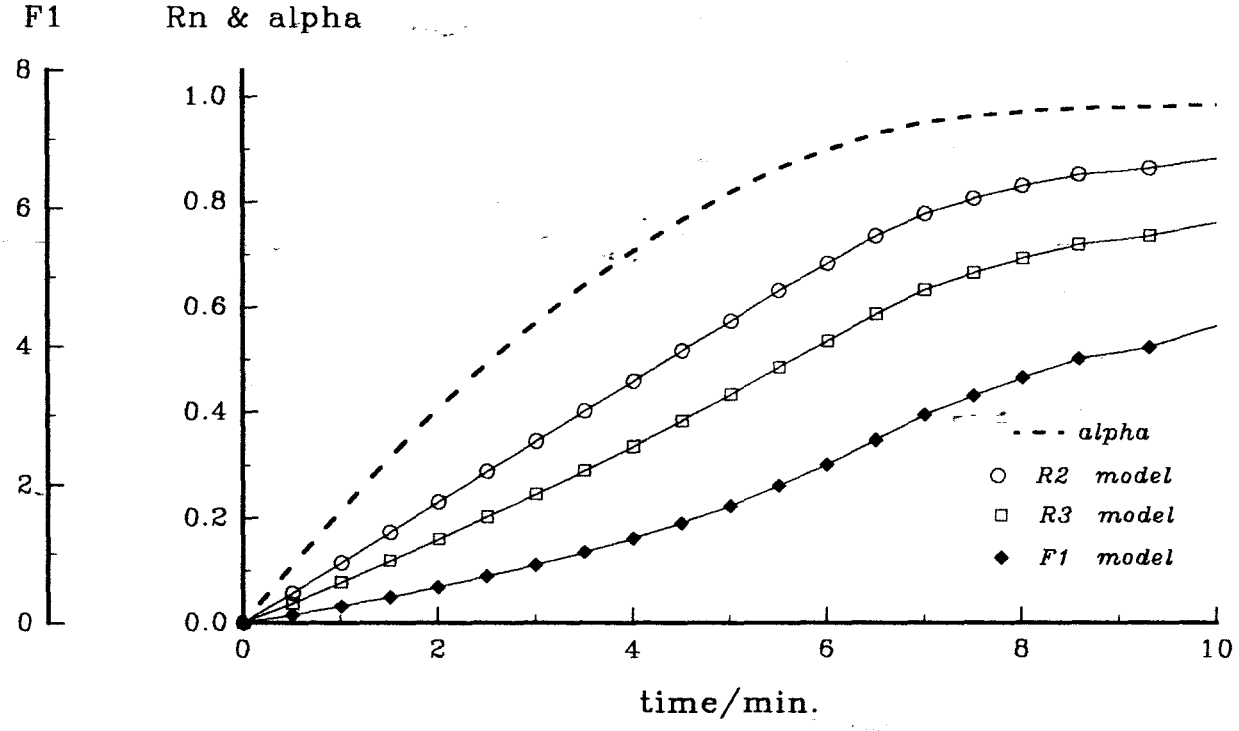

Figure 10.1.5r: Plots of $g(\alpha)$ versus time for the decomposition of $Ni(nmf)Cl_2$ at 245°C. The α–time curve is included to show the range of α over which $g(\alpha)$ is approximately linear.

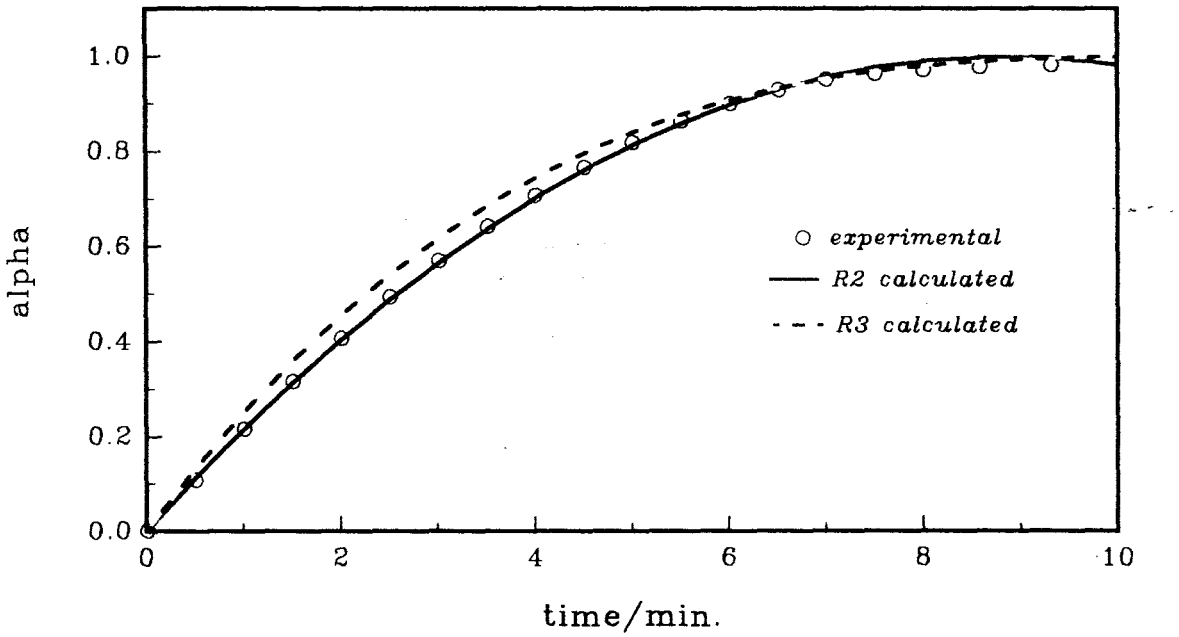

Figure 10.1.6r: Plots of $\alpha_{calc.}$ versus time using the R2 and R3 models, compared with α_e versus time data for the decomposition of $Ni(nmf)Cl_2$ at 245°C.

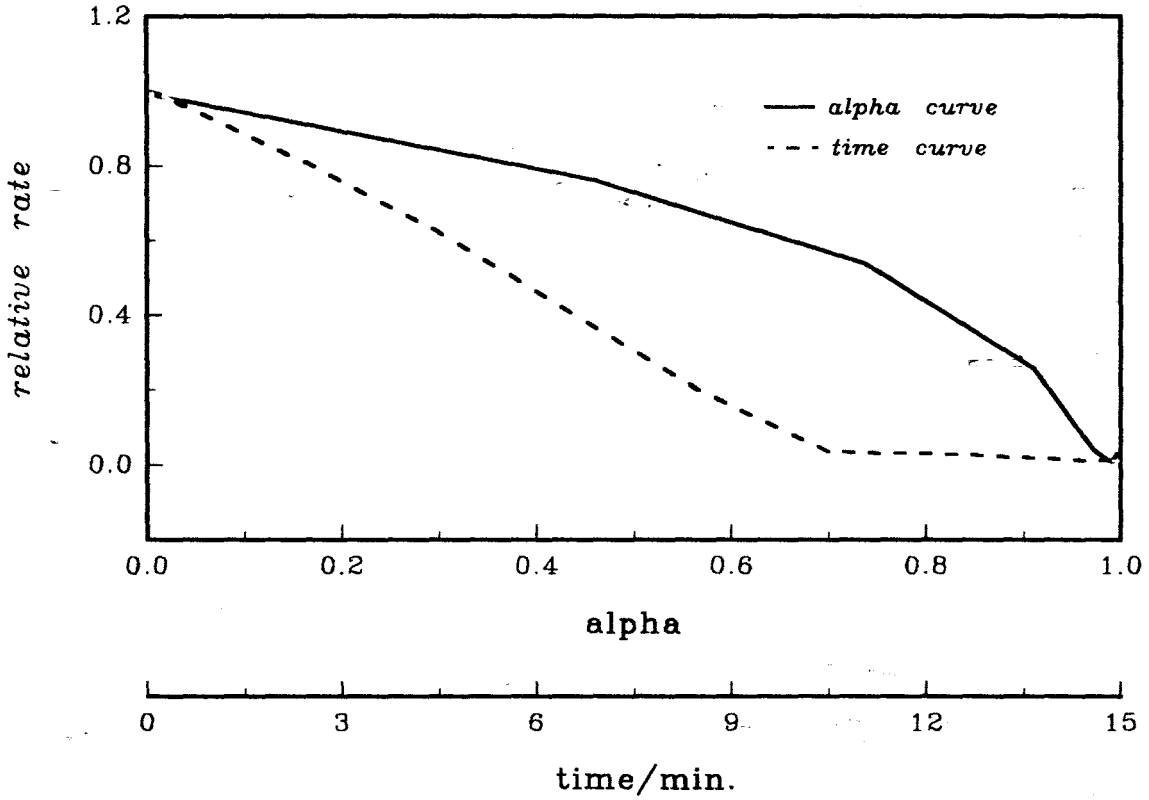

Figure 10.1.7b: Plots of rate versus alpha and rate versus time for the decomposition of $Ni(nmf)Cl_2$ at 235°C.

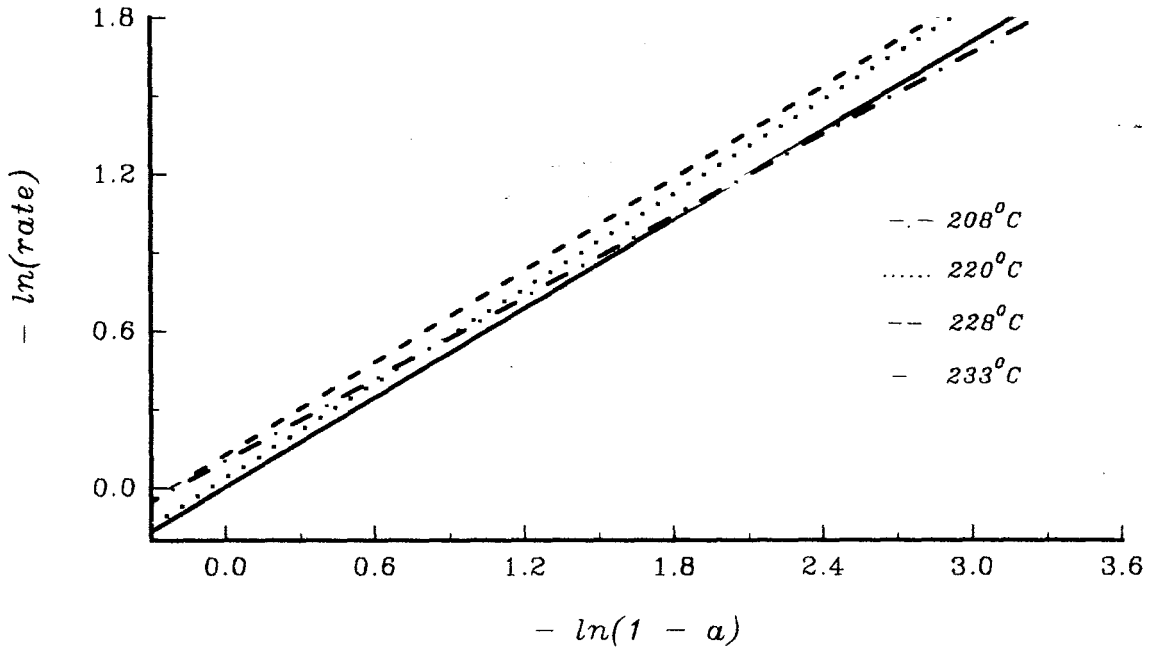

Figure 10.1.8b: Regression lines of ln(rate) versus $\ln(1 - \alpha)$ for the isothermal decomposition of $Ni(nmf)Cl_2$.

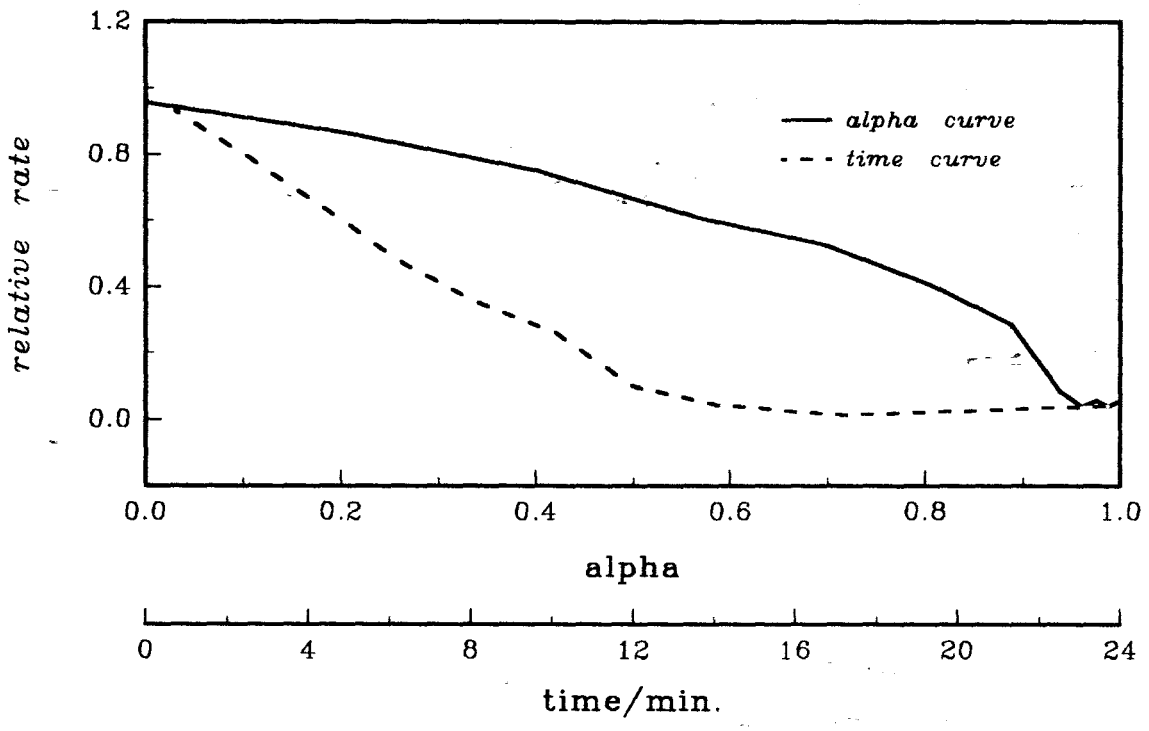

Figure 10.1.7c: Plots of rate versus alpha and rate versus time for the decomposition of $Ni(nmf)Cl_2$ at 233°C.

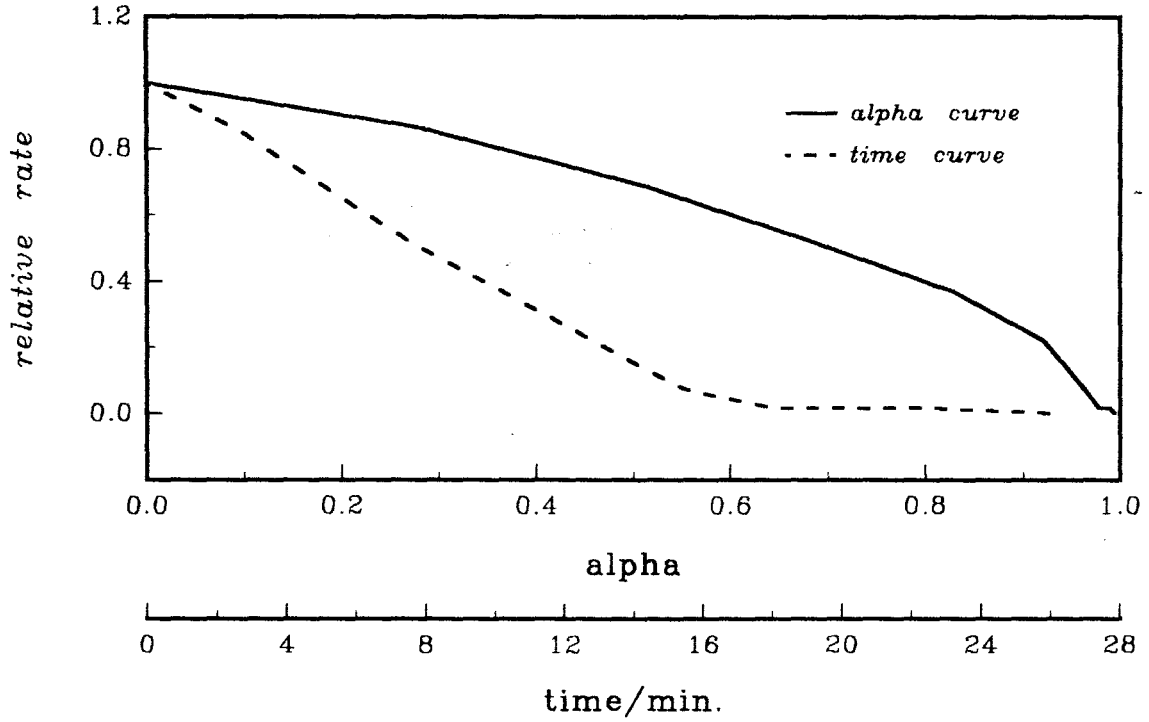

Figure 10.1.7d: Plots of rate versus alpha and rate versus time for the decomposition of $Ni(nmf)Cl_2$ at 225°C.

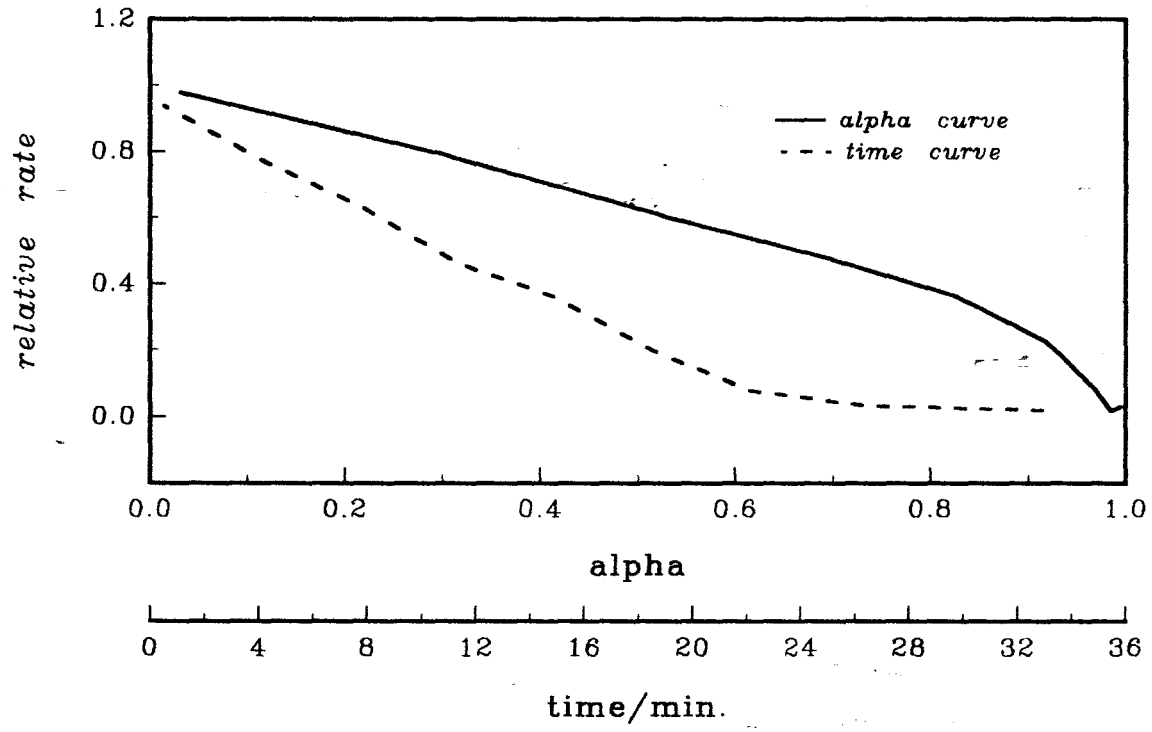

Figure 10.1.7e: Plots of rate versus alpha and rate versus time for the decomposition of $Ni(nmf)Cl_2$ at 228°C.

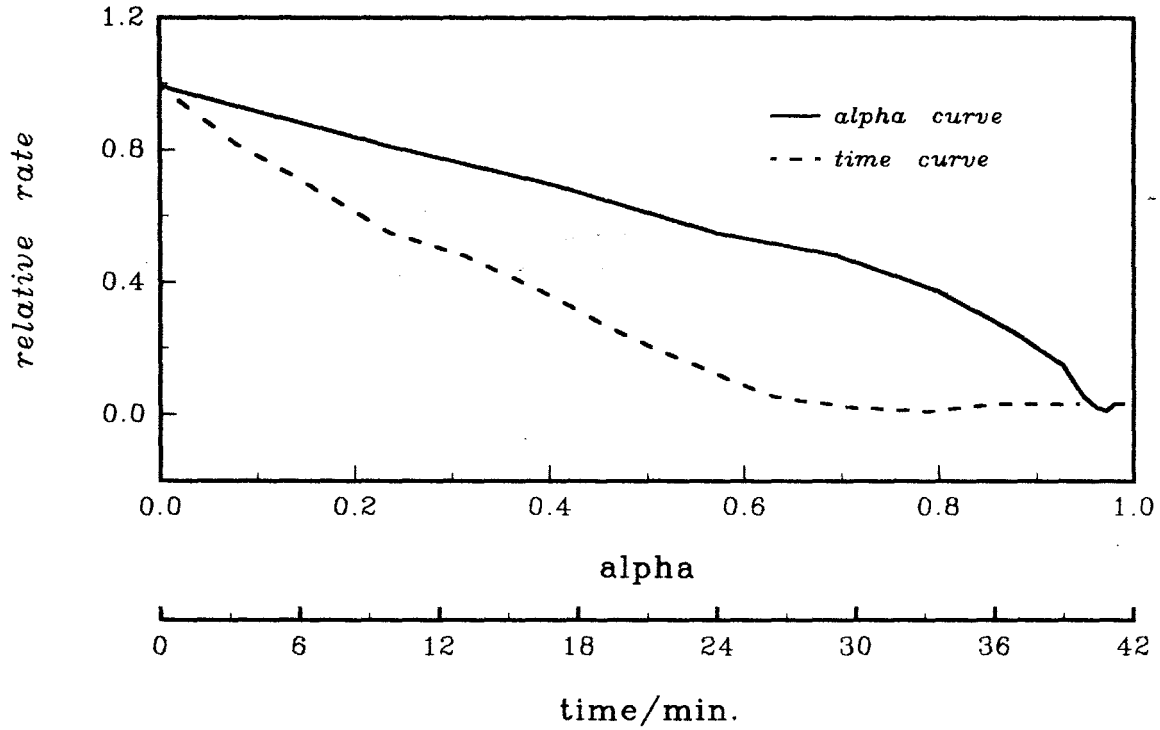

Figure 10.1.7f: Plots of rate versus alpha and rate versus time for the decomposition of $Ni(nmf)Cl_2$ at 220°C.

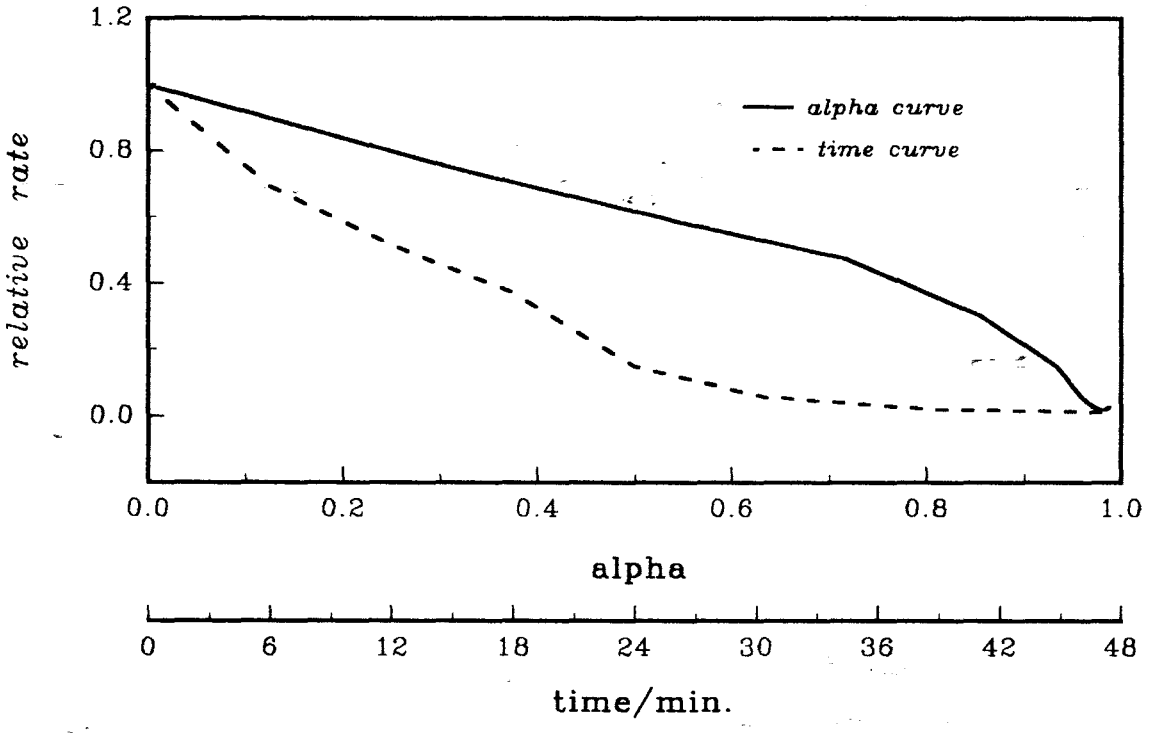

Figure 10.1.7g: Plots of rate versus alpha and rate versus time for the decomposition of $Ni(nmf)Cl_2$ at 218°C.

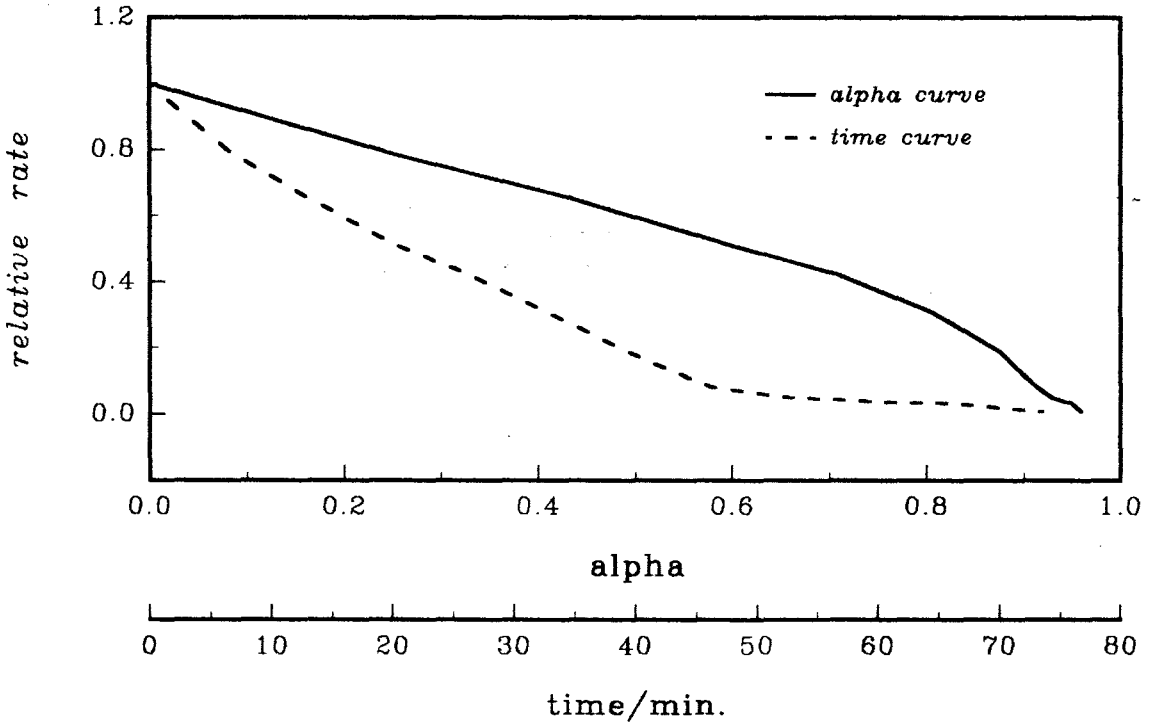

Figure 10.1.7h: Plots of rate versus alpha and rate versus time for the decomposition of $Ni(nmf)Cl_2$ at 210°C.

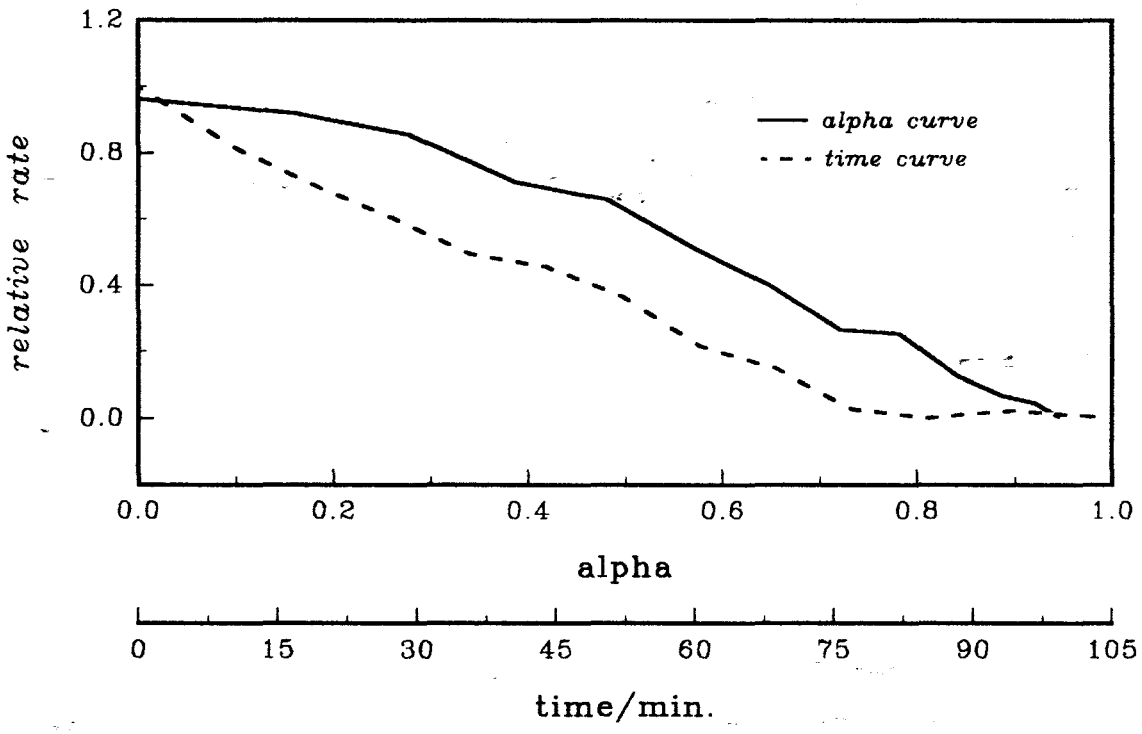

Figure 10.1.7i: Plots of rate versus alpha and rate versus time for the decomposition of $Ni(nmf)Cl_2$ at 200°C.

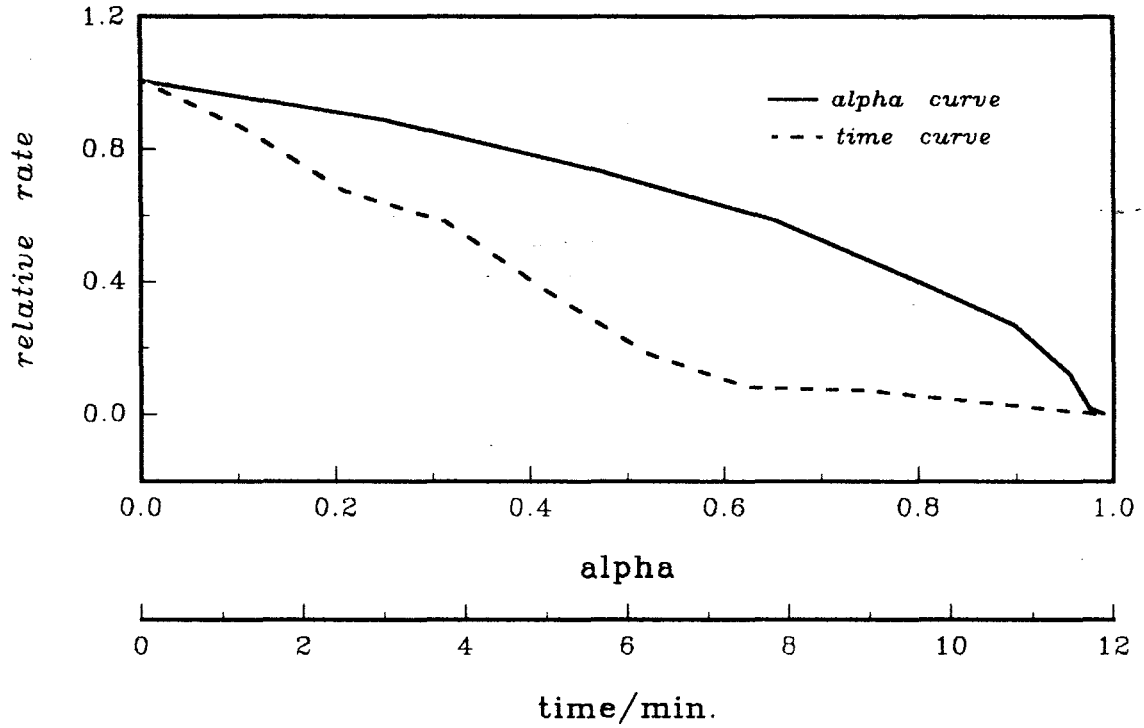

Figure 10.1.7j: Plots of rate versus alpha and rate versus time for the decomposition of $Ni(nmf)Cl_2$ at 243°C.

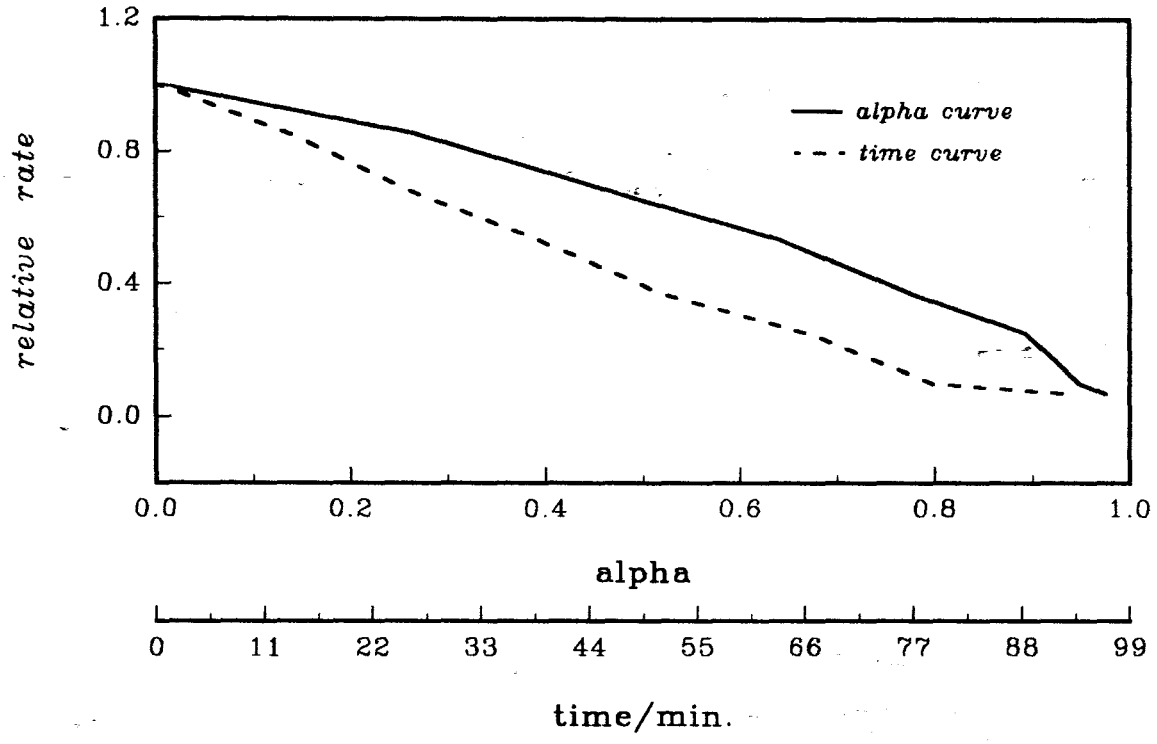

Figure 10.1.7k: Plots of rate versus alpha and rate versus time for the decomposition of $Ni(nmf)Cl_2$ at 205°C.

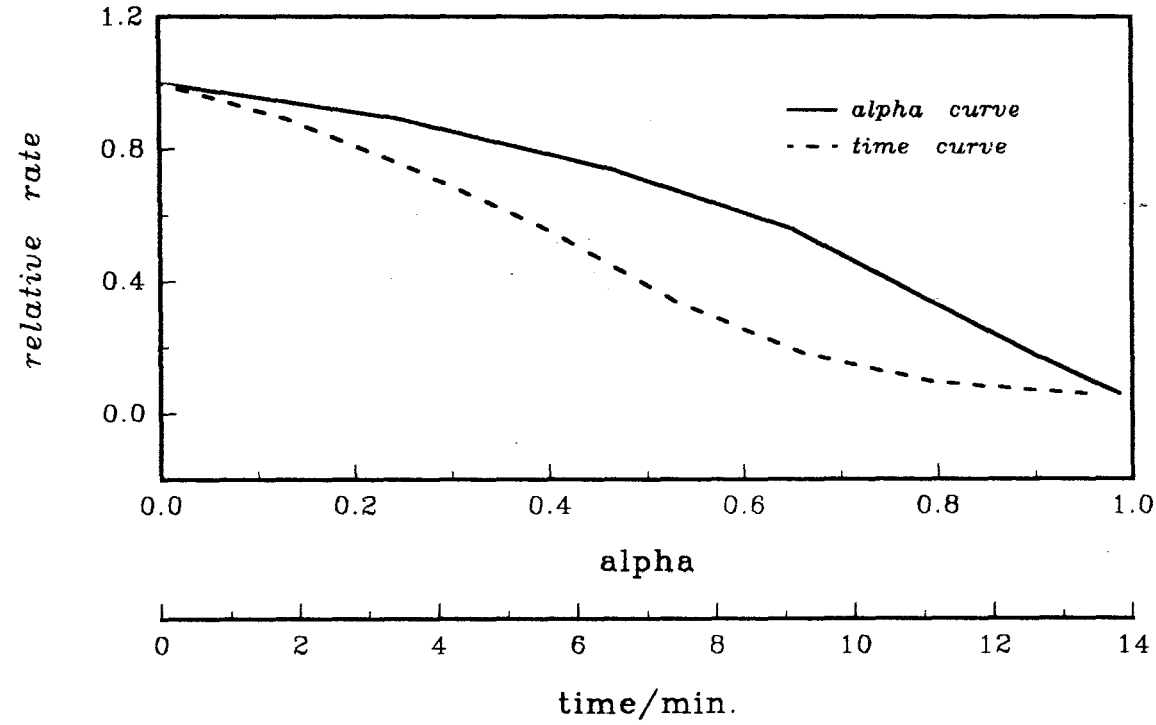

Figure 10.1.7l: Plots of rate versus alpha and rate versus time for the decomposition of $Ni(nmf)Cl_2$ at 238°C.

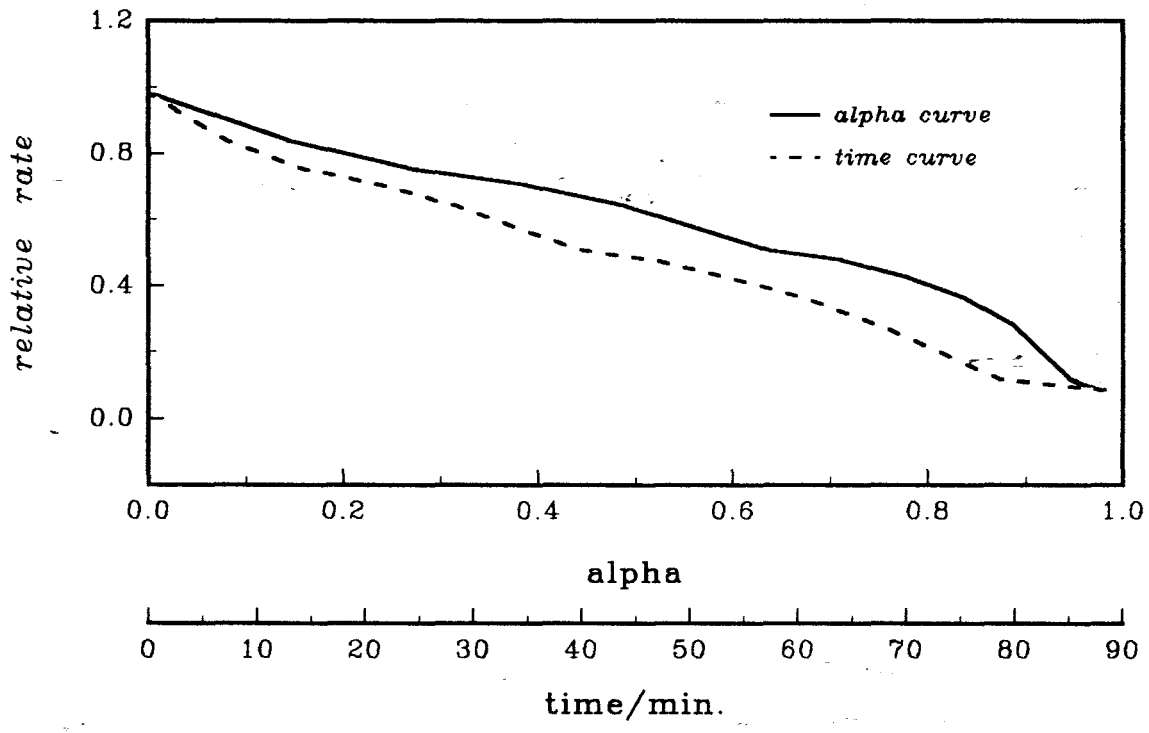

Figure 10.1.7m: Plots of rate versus alpha and rate versus time for the decomposition of $Ni(nmf)Cl_2$ at 208°C.

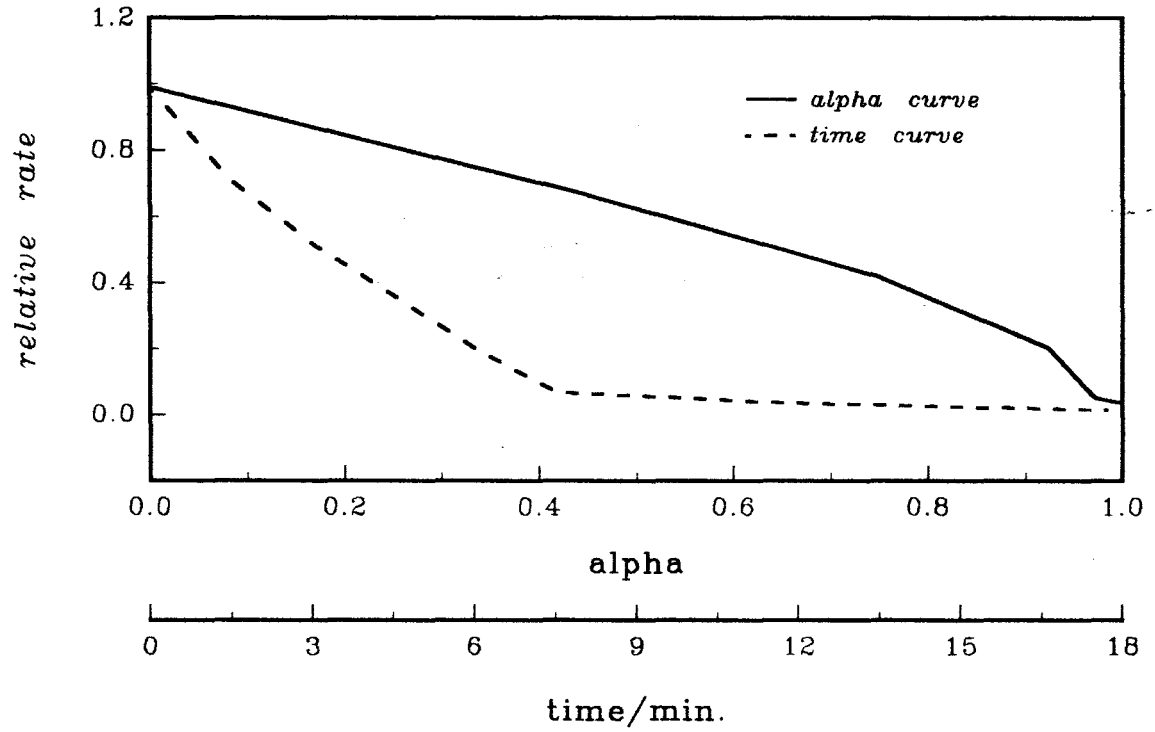

Figure 10.1.7n: Plots of rate versus alpha and rate versus time for the decomposition of $Ni(nmf)Cl_2$ at 240°C.

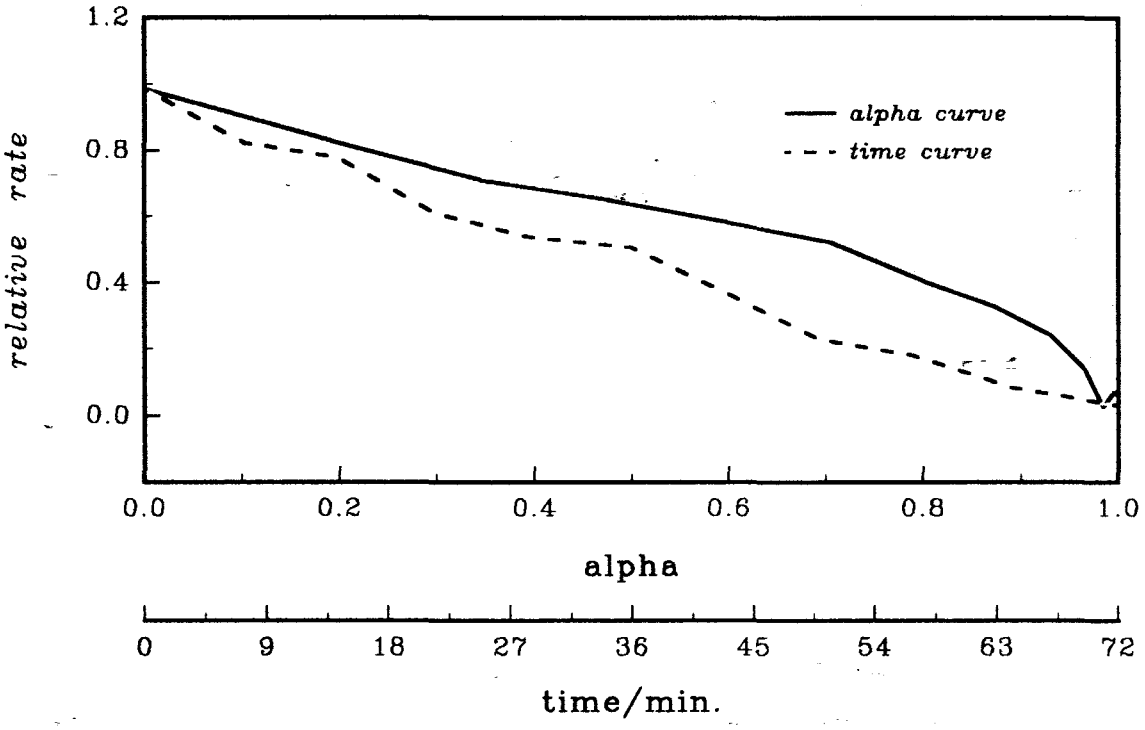

Figure 10.1.7o: Plots of rate versus alpha and rate versus time for the decomposition of $Ni(nmf)Cl_2$ at 215°C.

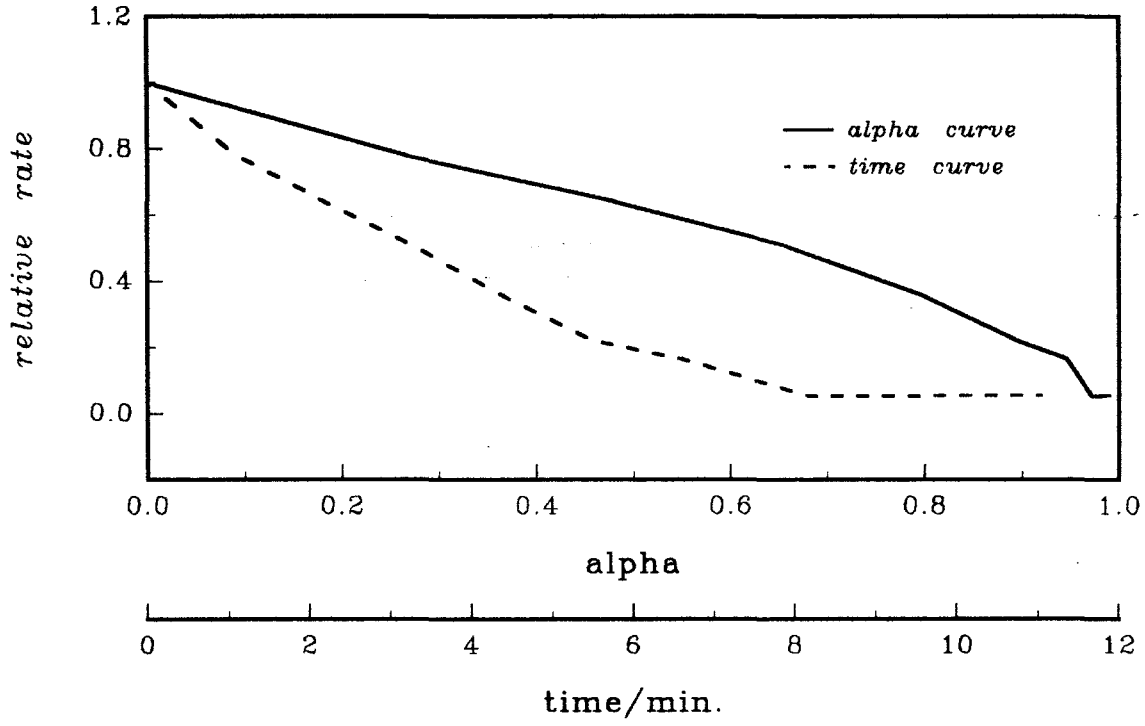

Figure 10.1.7p: Plots of rate versus alpha and rate versus time for the decomposition of $Ni(nmf)Cl_2$ at 245°C.

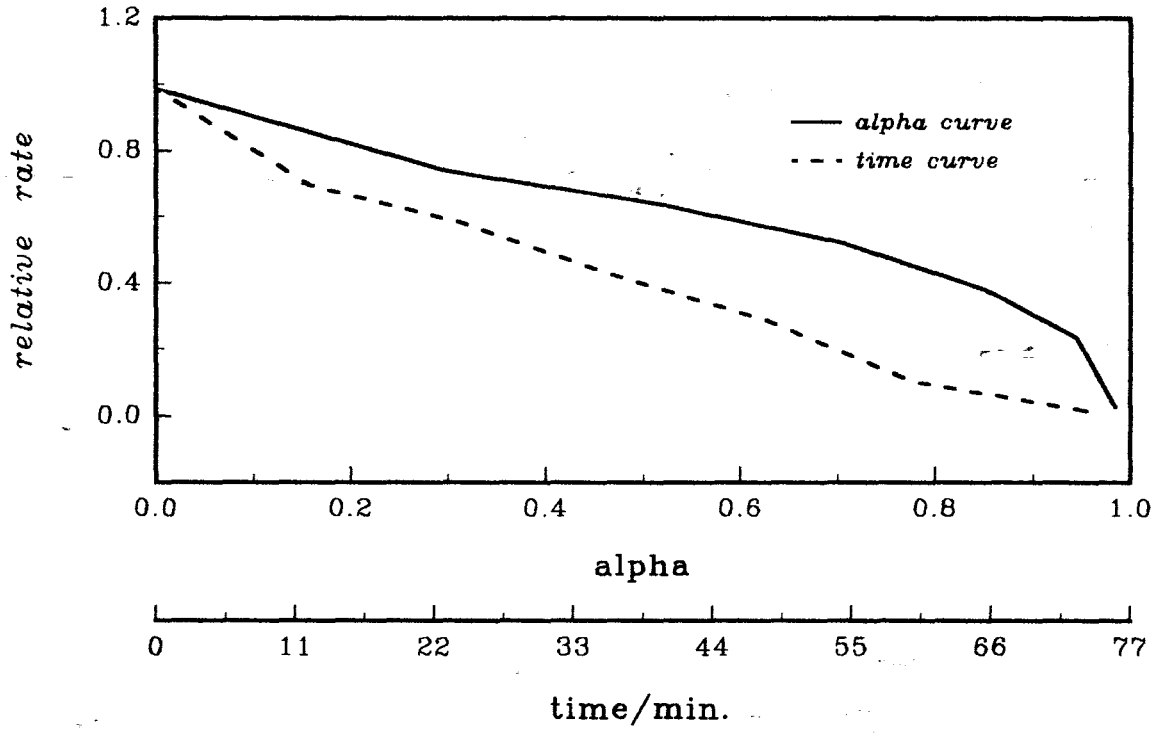

Figure 10.1.7q: Plots of rate versus alpha and rate versus time for the decomposition of $Ni(nmf)Cl_2$ at 212°C.

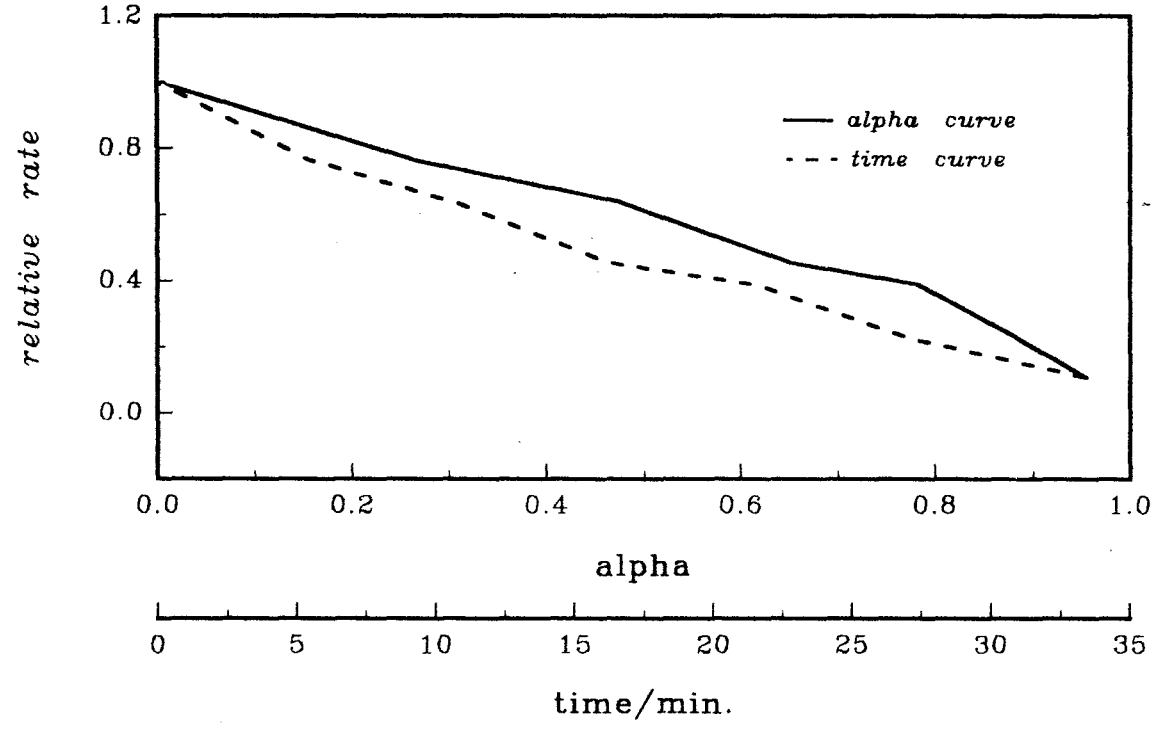

Figure 10.1.7r: Plots of rate versus alpha and rate versus time for the decomposition of $Ni(nmf)Cl_2$ at 223°C.

APPENDIX III

Chapter 10

Table 10.2.4b: Rate coefficients for the decomposition of Ni(*aa*)Cℓ_2 at different constant temperatures calculated using the **R2** or **R3** rate expression over $0.00 \leq \alpha \leq 0.90$

	R2 model		**R3 model**	
T / °C	k / 10^{-3} s^{-1}	r	k / 10^{-3} s^{-1}	r
235	10.493 ± 0.061	0.9893	12.391 ± 0.038	0.9969
230	6.109 ± 0.019	0.9964	7.170 ± 0.046	0.9999
228	4.519 ± 0.009	0.9925	5.079 ± 0.002	0.9997
225	5.329 ± 1.048	0.8353	5.976 ± 0.047	0.8826
223	4.341 ± 0.024	0.9270	4.931 ± 0.020	0.9628
220	3.019 ± 0.004	0.9965	3.381 ± 0.001	0.9999
218	2.300 ± 0.006	0.9970	2.702 ± 0.001	0.9999
215	1.265 ± 0.002	0.9979	1.484 ± 0.000	1.0000
213	1.130 ± 0.006	0.9844	1.347 ± 0.005	0.9937
210	1.847 ± 0.008	0.9905	2.177 ± 0.005	0.9975
200	0.969 ± 0.007	0.9928	1.138 ± 0.004	0.9986
208	1.470 ± 0.002	0.9975	1.725 ± 0.000	0.9999
205	0.737 ± 0.005	0.9960	0.861 ± 0.001	0.9998
203	1.010 ± 0.001	0.9990	1.188 ± 0.001	0.9996
195	0.666 ± 0.002	0.9966	0.781 ± 0.000	0.9999
193	0.283 ± 0.000	0.9998	0.331 ± 0.001	0.9983
190	0.302 ± 0.001	0.9981	0.354 ± 0.000	0.9998
190*	0.345 ± 0.001	0.9956	0.405 ± 0.000	0.9997

* run in replicate

Table 10.2.4c: Rate coefficients for the decomposition of Ni(*aa*)Cℓ_2 at different constant temperatures calculated using the **R2** or **R3** rate expression over $0.00 \leq \alpha \leq 0.85$.

	R2 model		**R3 model**	
T / °C	k / 10^{-3} s^{-1}	r	k / 10^{-3} s^{-1}	r
235	11.604 ± 0.054	0.9948	13.100 ± 0.032	0.9986
230	6.434 ± 0.017	0.9980	7.243 ± 0.005	0.9999
228	4.680 ± 0.008	0.9965	5.116 ± 0.002	0.9999
225	6.561 ± 0.026	0.9814	7.181 ± 0.017	0.9939
223	4.999 ± 0.015	0.9874	5.459 ± 0.009	0.9967
220	3.895 ± 0.003	0.9980	3.367 ± 0.001	0.9999
218	2.412 ± 0.005	0.9984	2.711 ± 0.001	0.9999
215	1.315 ± 0.002	0.9989	1.480 ± 0.000	1.0000
213	1.302 ± 0.003	0.9980	1.467 ± 0.001	0.9999
210	2.035 ± 0.007	0.9962	2.293 ± 0.004	0.9992
200	1.014 ± 0.006	0.9966	1.141 ± 0.003	0.9994
208	1.554 ± 0.002	0.9991	1.749 ± 0.001	0.9999
205	0.752 ± 0.004	0.9980	0.845 ± 0.001	0.9999
203	1.093 ± 0.001	0.9991	1.232 ± 0.000	0.9999
195	0.699 ± 0.002	0.9978	0.786 ± 0.001	0.9998
193	0.285 ± 0.000	1.0000	0.319 ± 0.000	0.9989
190	0.314 ± 0.000	0.9996	0.353 ± 0.000	0.9997
190*	0.366 ± 0.001	0.9975	0.412 ± 0.000	0.9997

* run in replicate

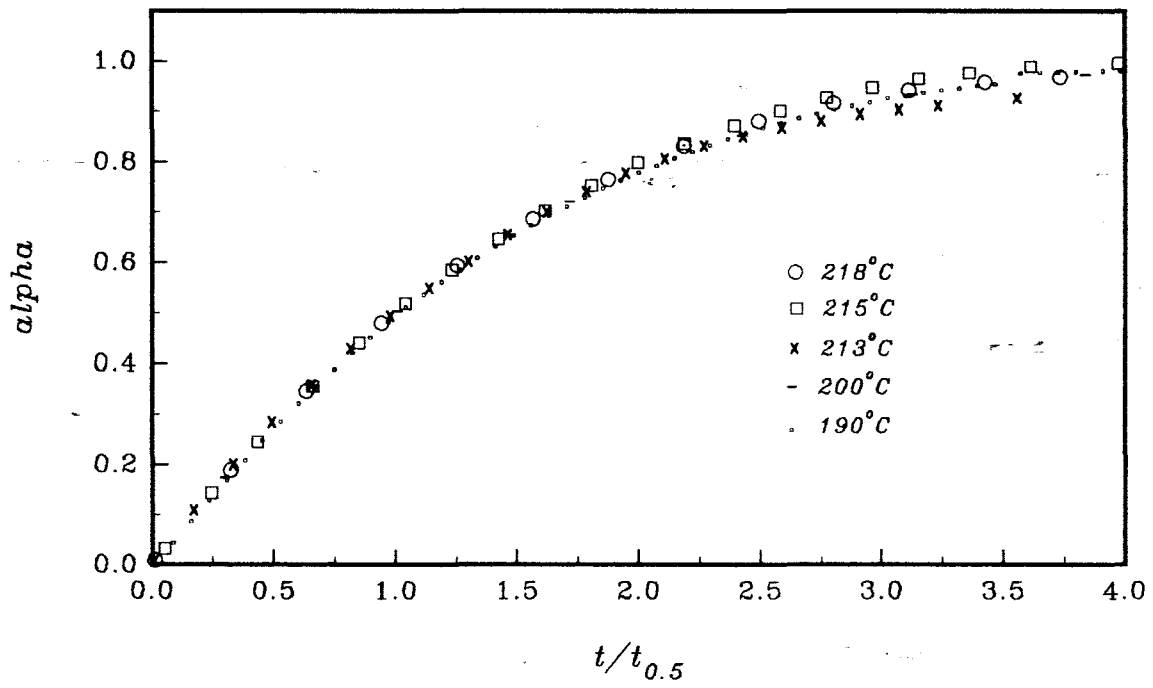

Figure 10.2.3b: Comparison of reduced–time plots for the decomposition of $Ni(aa)Cl_2$ at a series of constant temperatures.

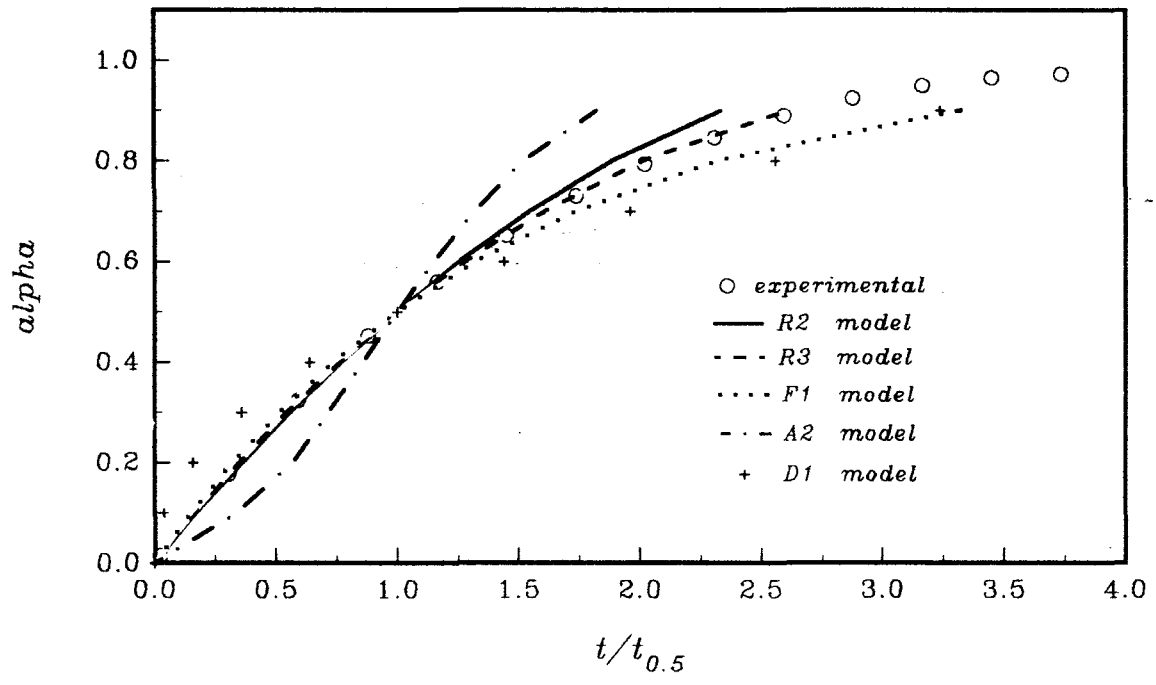

Figure 10.2.4b: Reduced–time plot for the decomposition of $Ni(aa)Cl_2$ at 230°C, compared with calculated plots for various kinetic models.

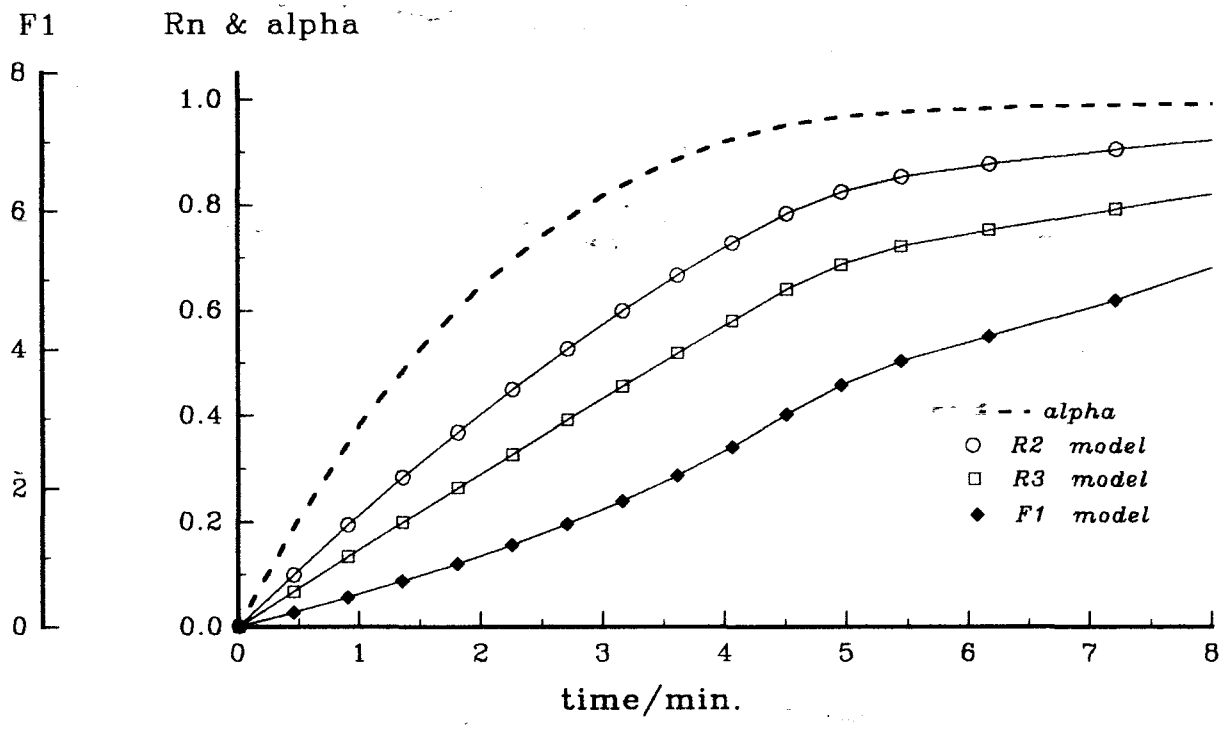

Figure 10.2.5b: Plots of g(α) versus time for the decomposition of $Ni(aa)Cl_2$ at 230°C. The α–time curve is included to show the range of α over which g(α) is approximately linear.

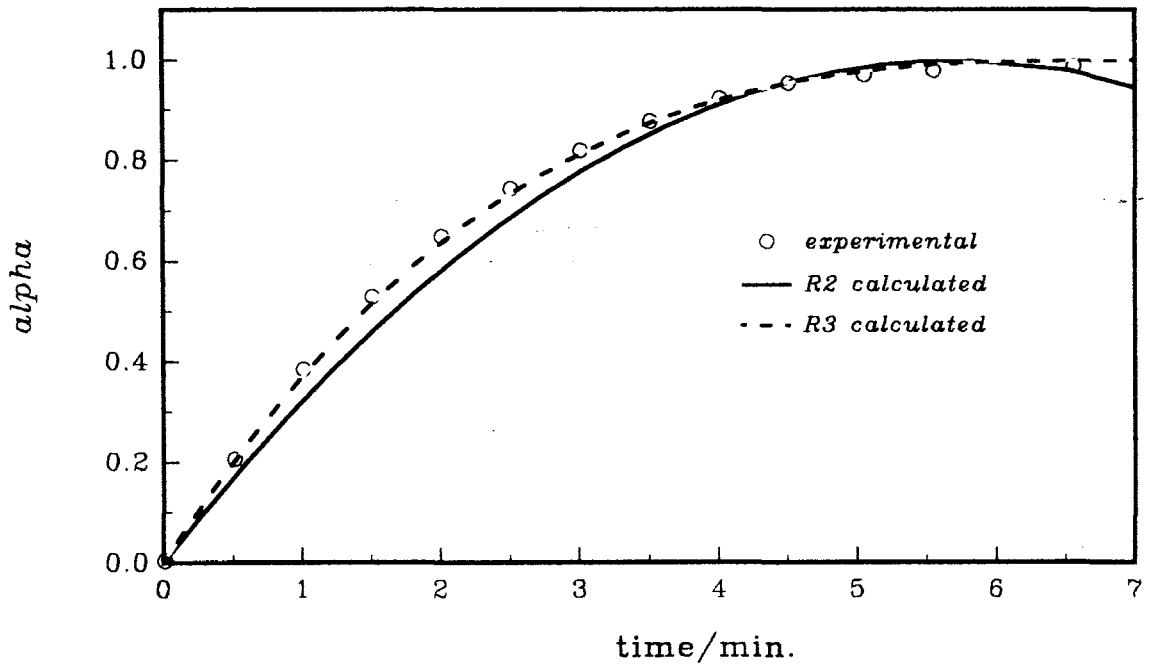

Figure 10.2.6b: Plots of $\alpha_{calc.}$ versus time using the R2 and R3 models, compared with α_e versus time data for the decomposition of $Ni(aa)Cl_2$ at 230°C.

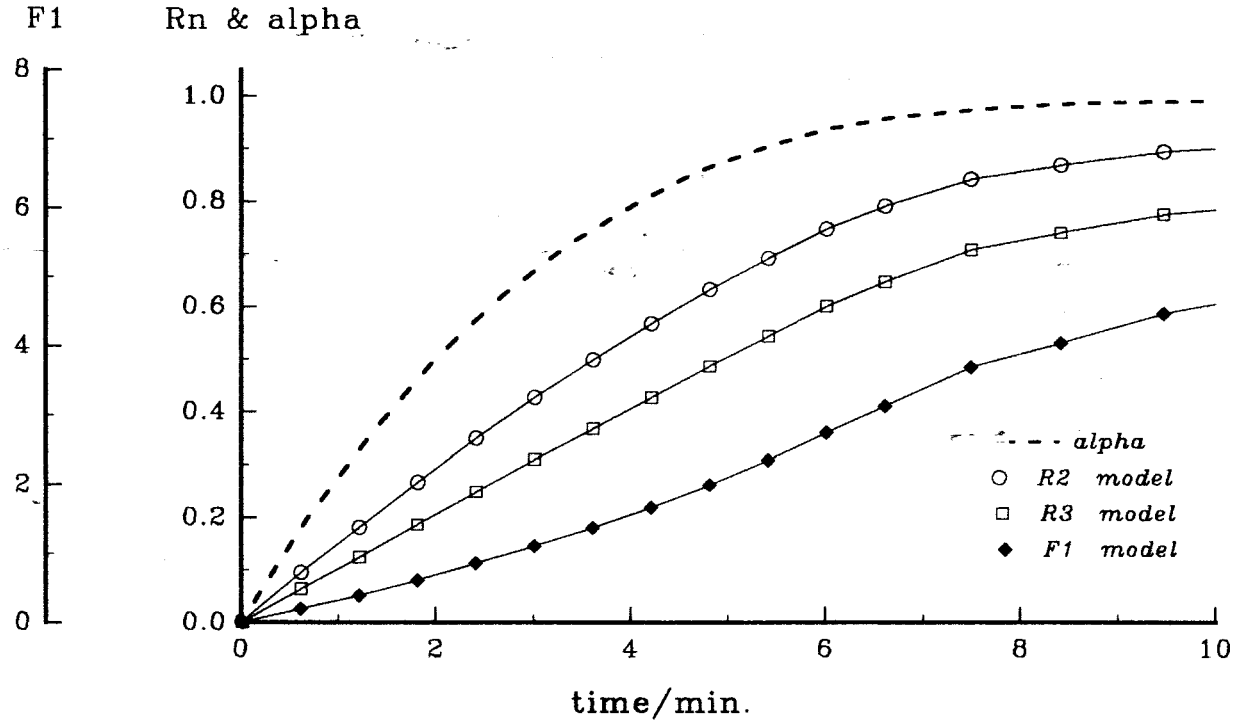

Figure 10.2.5c: Plots of g(α) versus time for the decomposition of $Ni(aa)Cl_2$ at 228°C. The α–time curve is included to show the range of α over which g(a) is approximately linear.

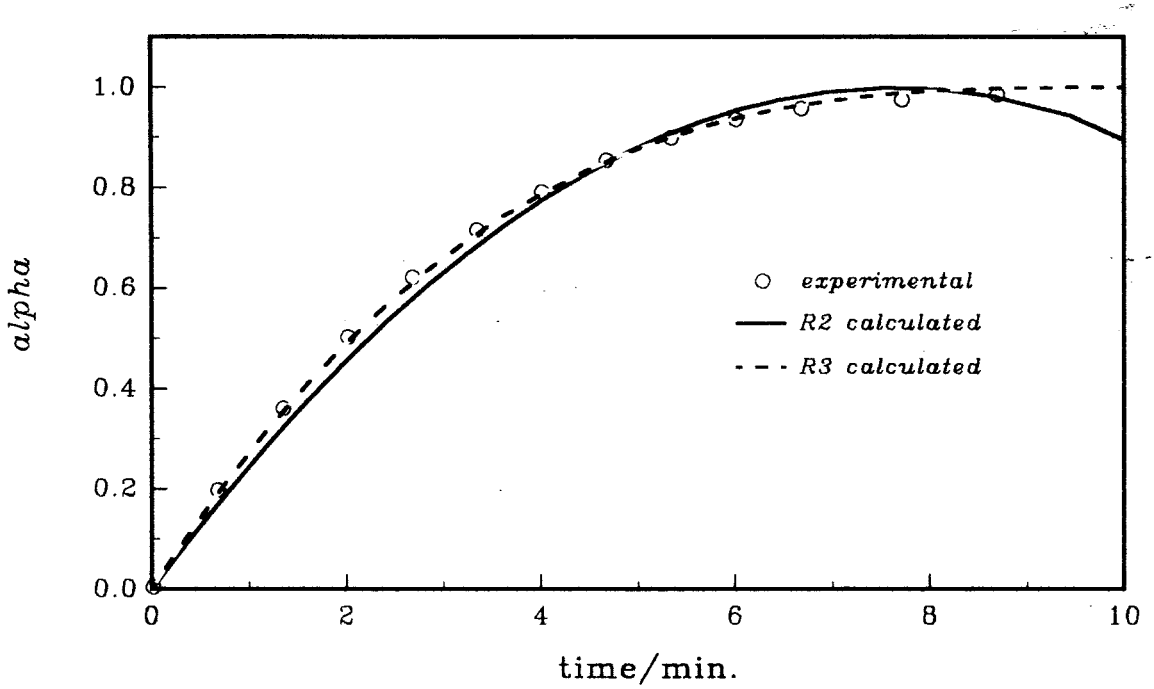

Figure 10.2.6c: Plots of $\alpha_{calc.}$ versus time using the R2 and R3 models, compared with α_e versus time data for the decomposition of $Ni(aa)Cl_2$ at 228°C.

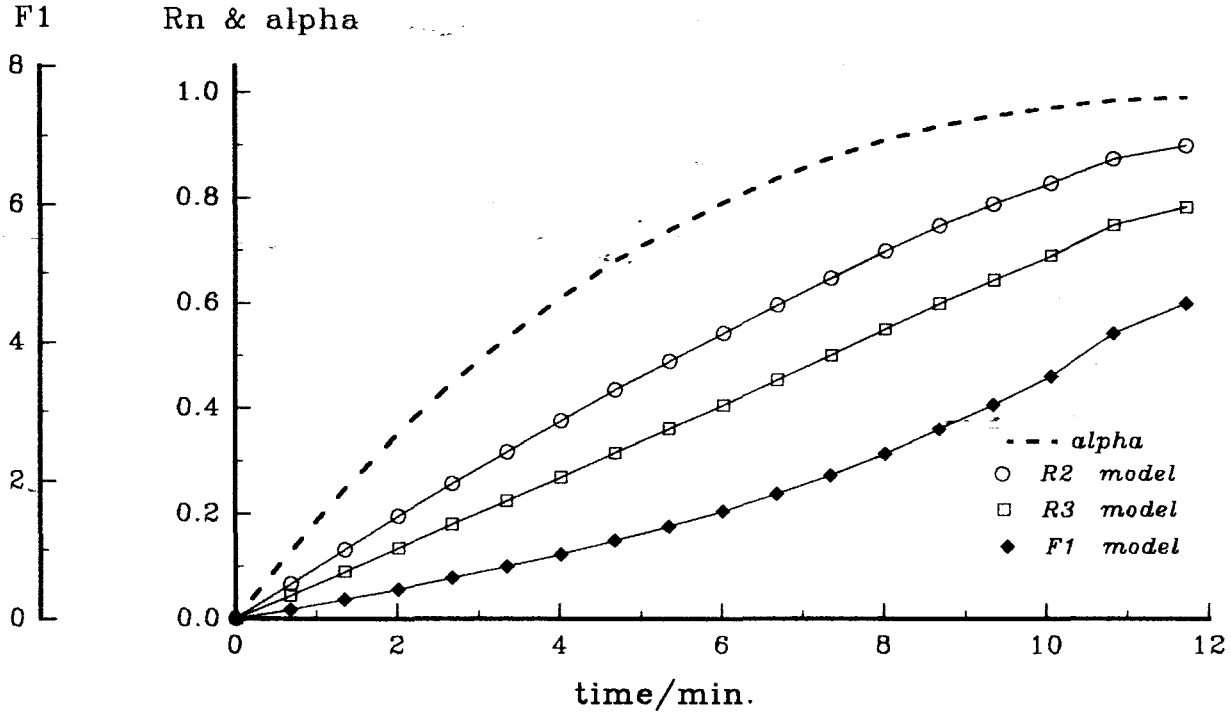

Figure 10.3.5d: Plots of $g(\alpha)$ versus time for the decomposition of $Ni(aa)Cl_2$ at 220°C. The α–time curve is included to show the range of α over which $g(\alpha)$ is approximately linear.

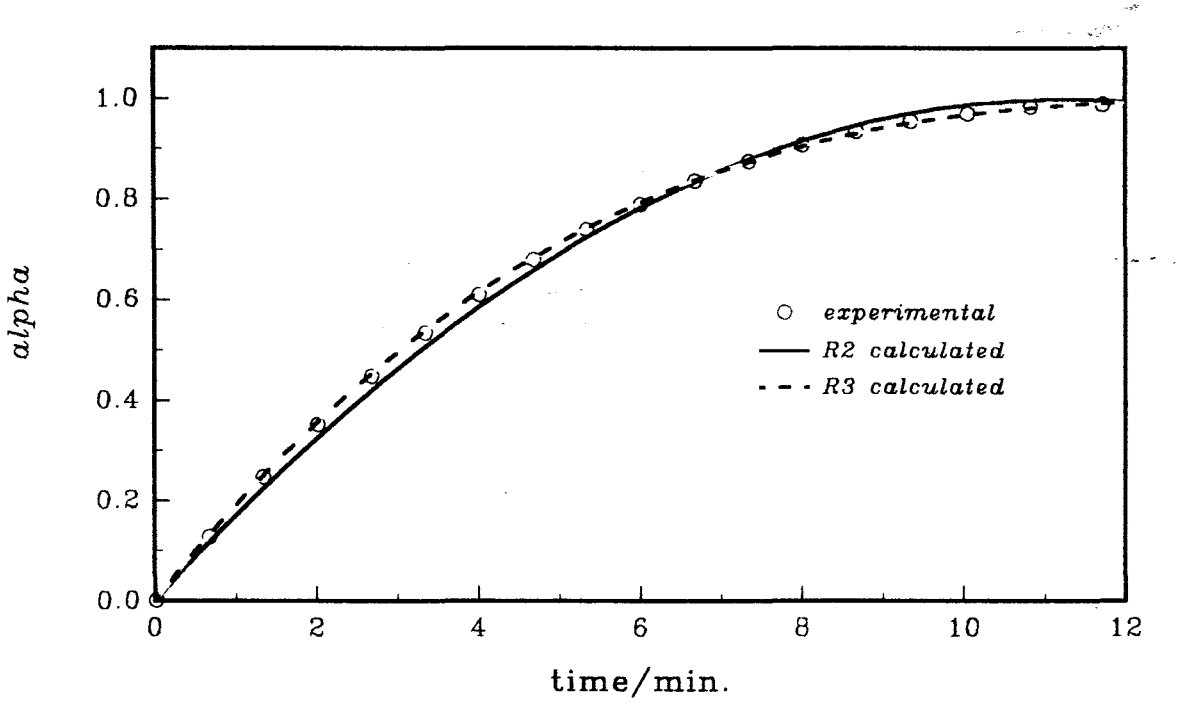

Figure 10.3.6d: Plots of $\alpha_{calc.}$ versus time using the R2 and R3 models, compared with α_e versus time data for the decomposition of $Ni(aa)Cl_2$ at 220°C.

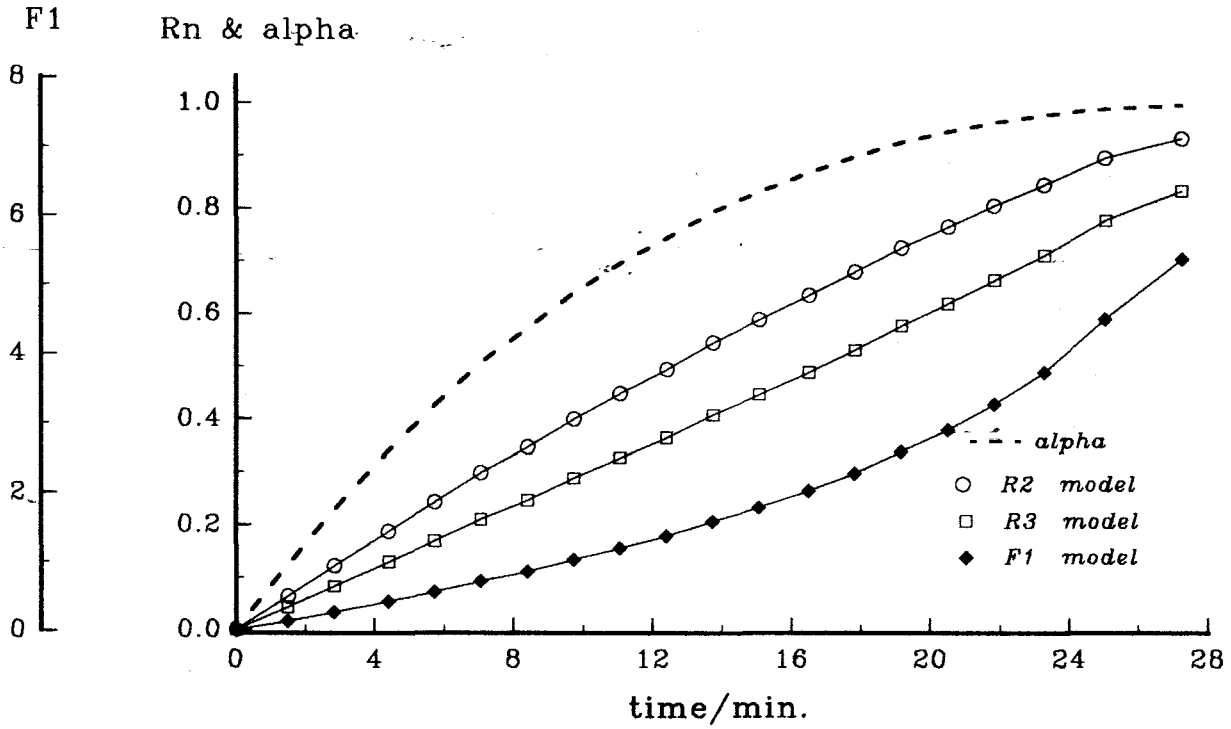

Figure 10.2.5e: Plots of g(α) versus time for the decomposition of $Ni(aa)Cl_2$ at 215°C. The α–time curve is included to show the range of α over which g(α) is approximately linear.

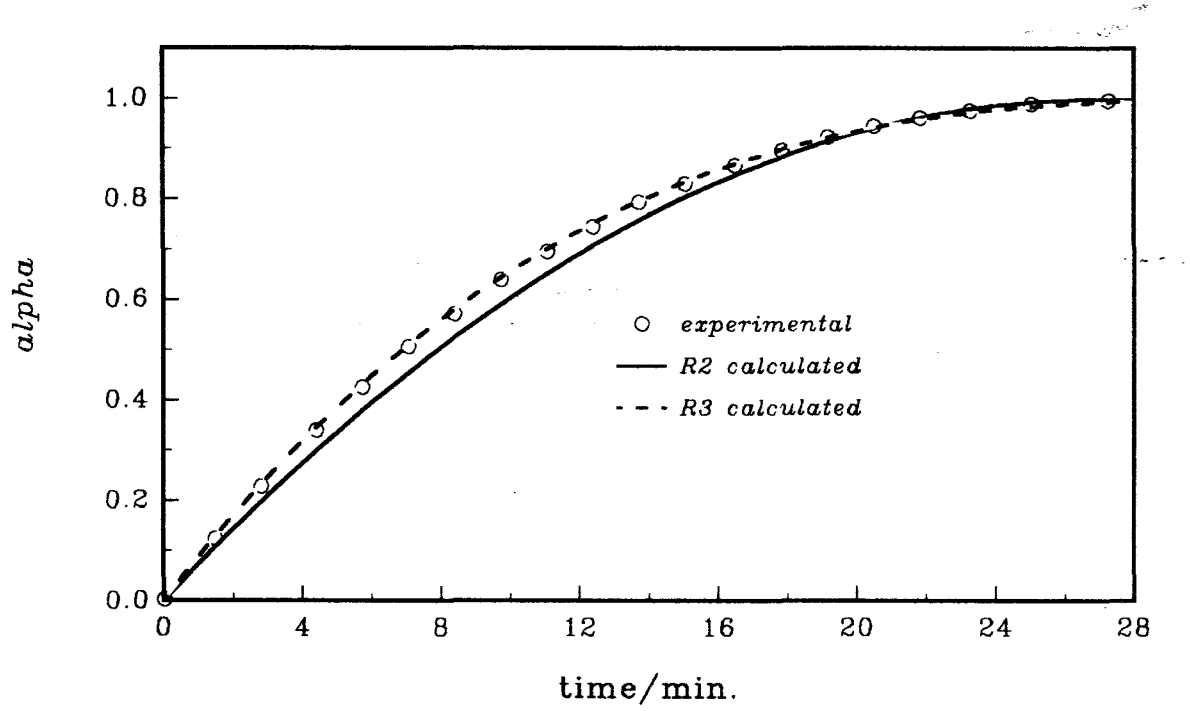

Figure 10.2.6e: Plots of $\alpha_{calc.}$ versus time using the R2 and R3 models, compared with α_e versus time data for he decomposition of $Ni(aa)Cl_2$ at 215°C.

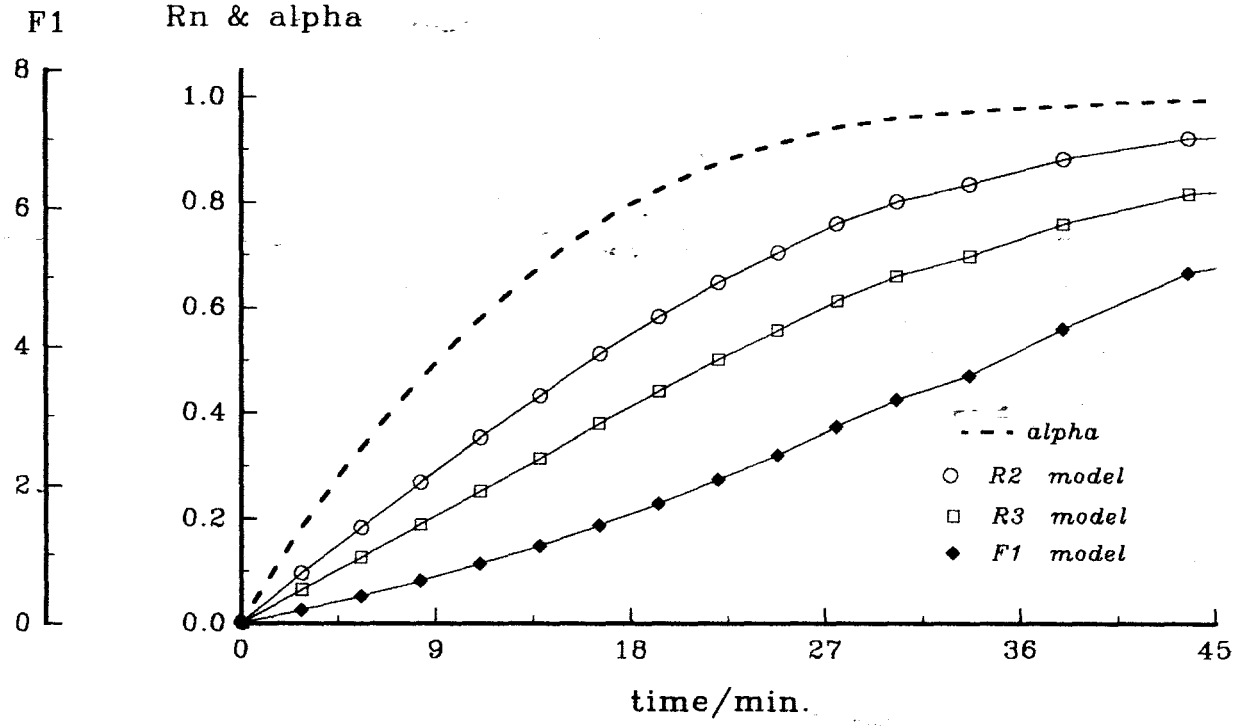

Figure 10.2.5f: Plots of $g(\alpha)$ versus time for the decomposition of $Ni(aa)Cl_2$ at 208°C. The α–time curve is included to show the range of α over which $g(\alpha)$ is approximately linear.

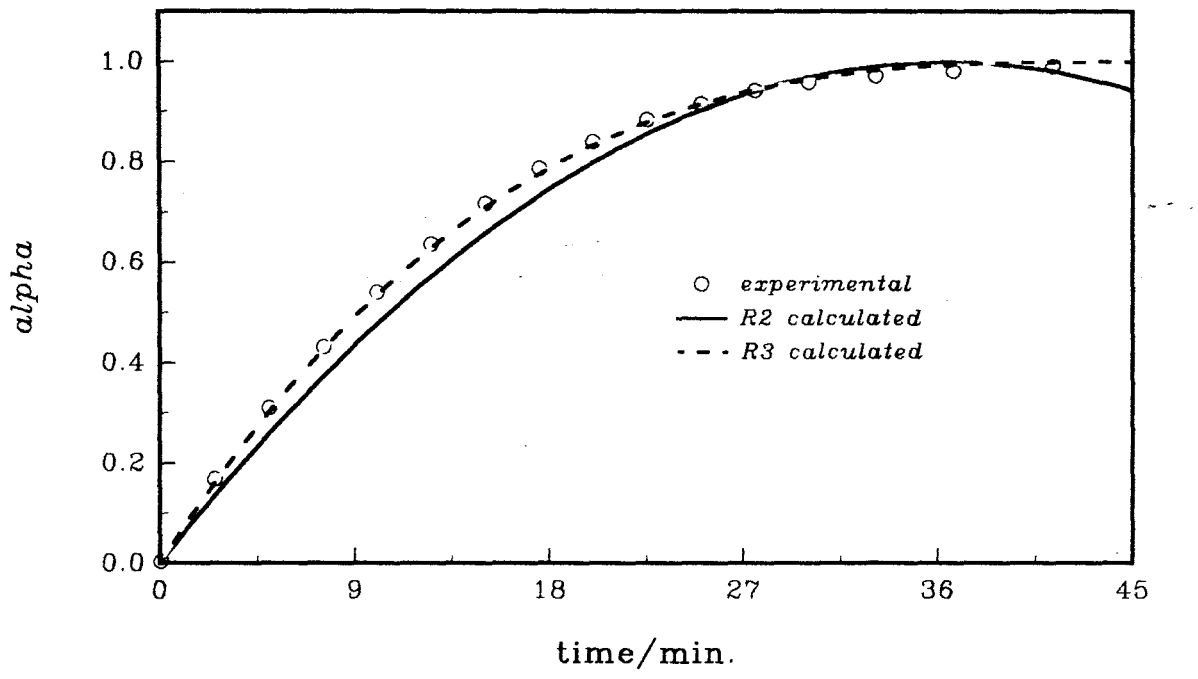

Figure 10.2.6f: Plots of $\alpha_{calc.}$ versus time using the R2 and R3 models, compared with α_e versus time data for the decomposition of $Ni(aa)Cl_2$ at 208°C.

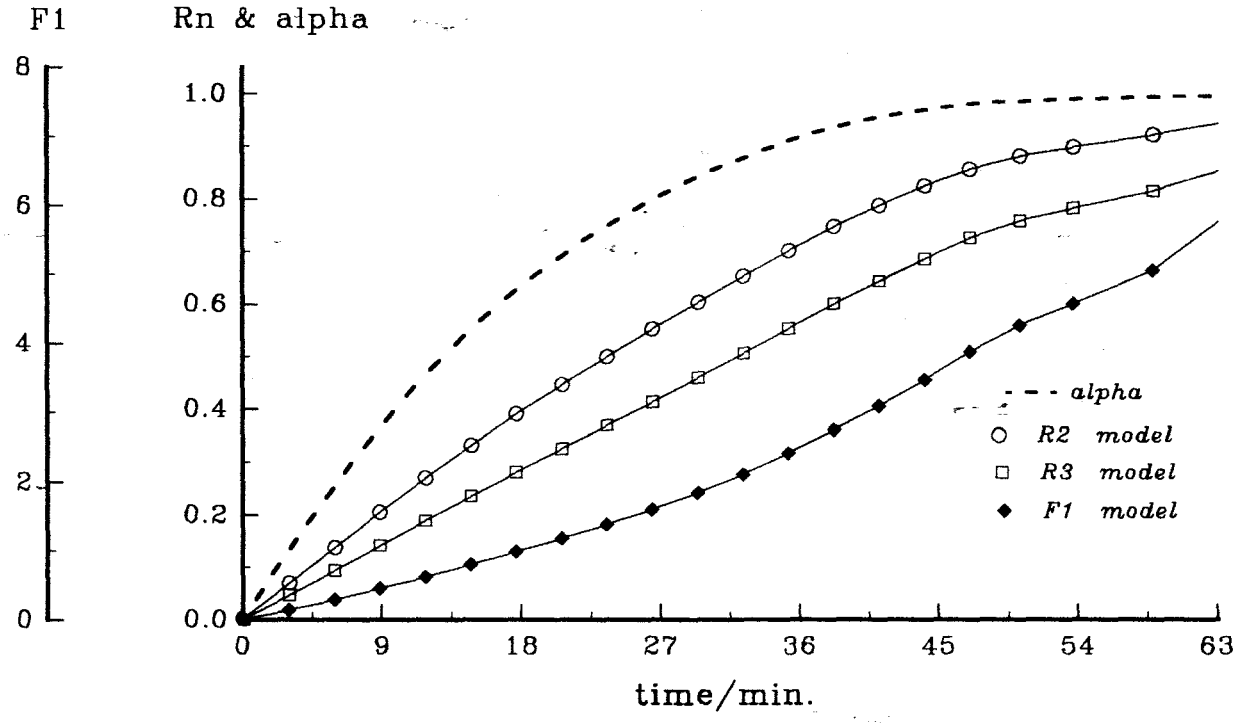

Figure 10.2.5g: Plots of $g(\alpha)$ versus time for the decomposition of $Ni(aa)Cl_2$ at 195°C. The α–time curve is included to show the range of α over which $g(\alpha)$ is approximately linear.

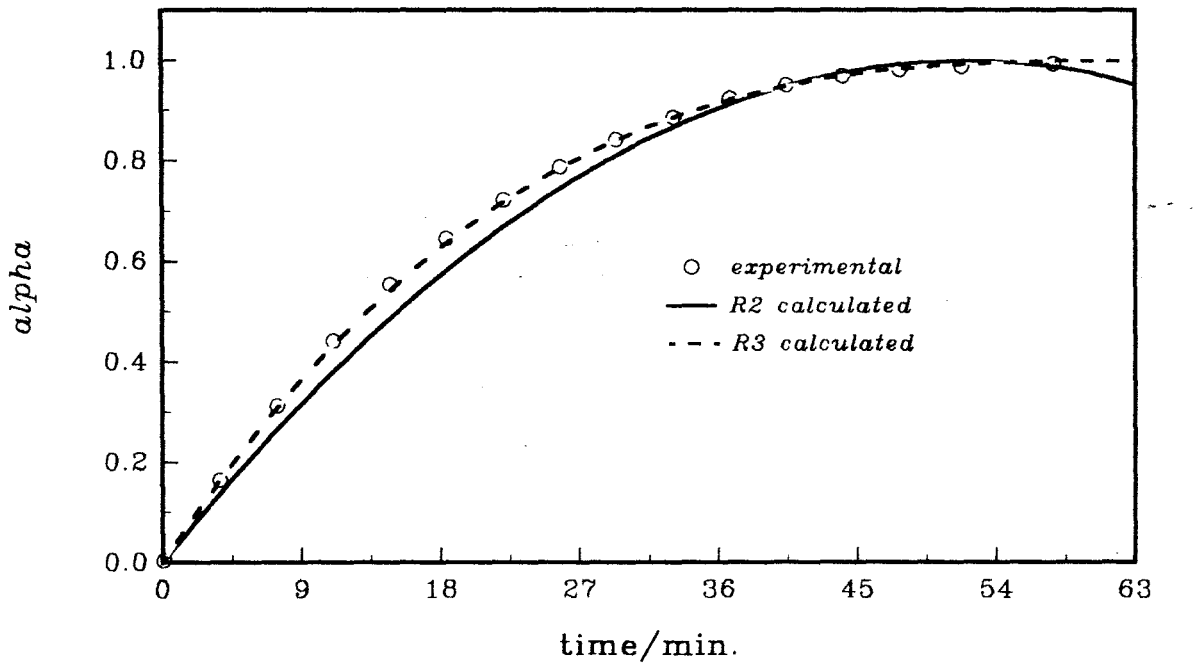

Figure 10.2.6g: Plots of $\alpha_{calc.}$ versus time using the R2 and R3 models, compared with α_e versus time data for the decomposition of $Ni(aa)Cl_2$ at 195°C.

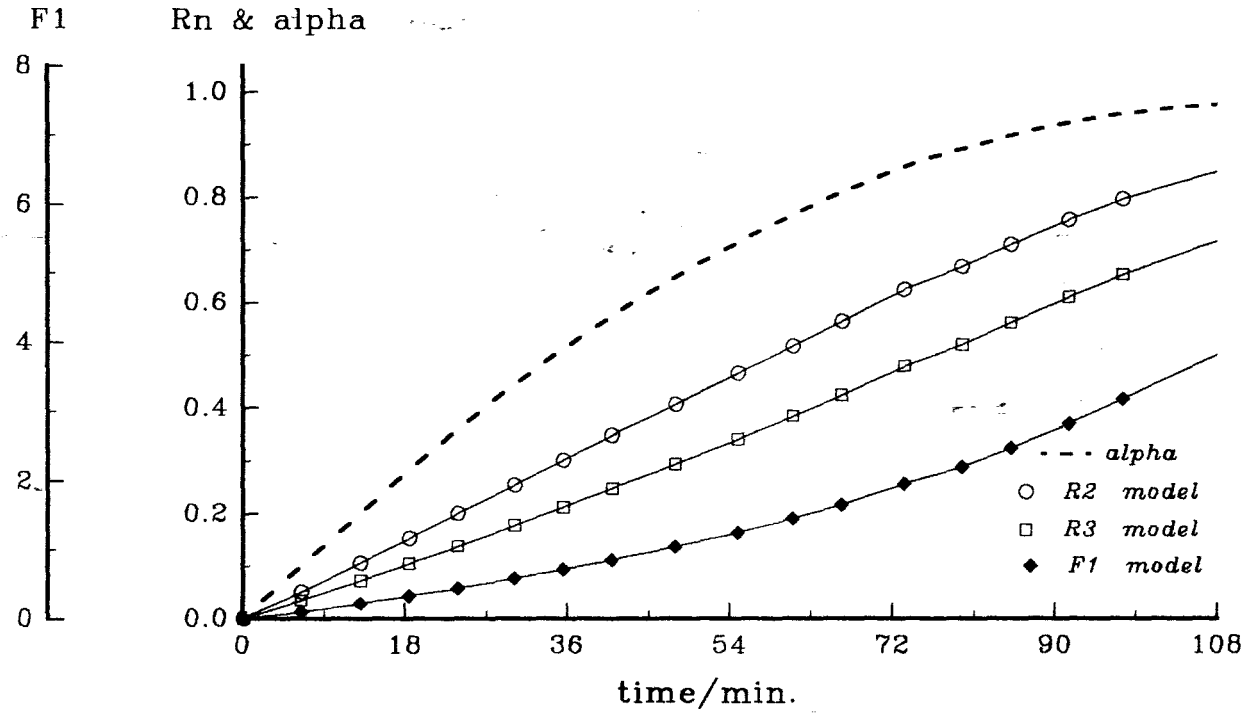

Figure 10.2.5h: Plots of g(α) versus time for the decomposition of $Ni(aa)Cl_2$ at 193°C. The α–time curve is included to show the range of α over which g(α) is approximately linear.

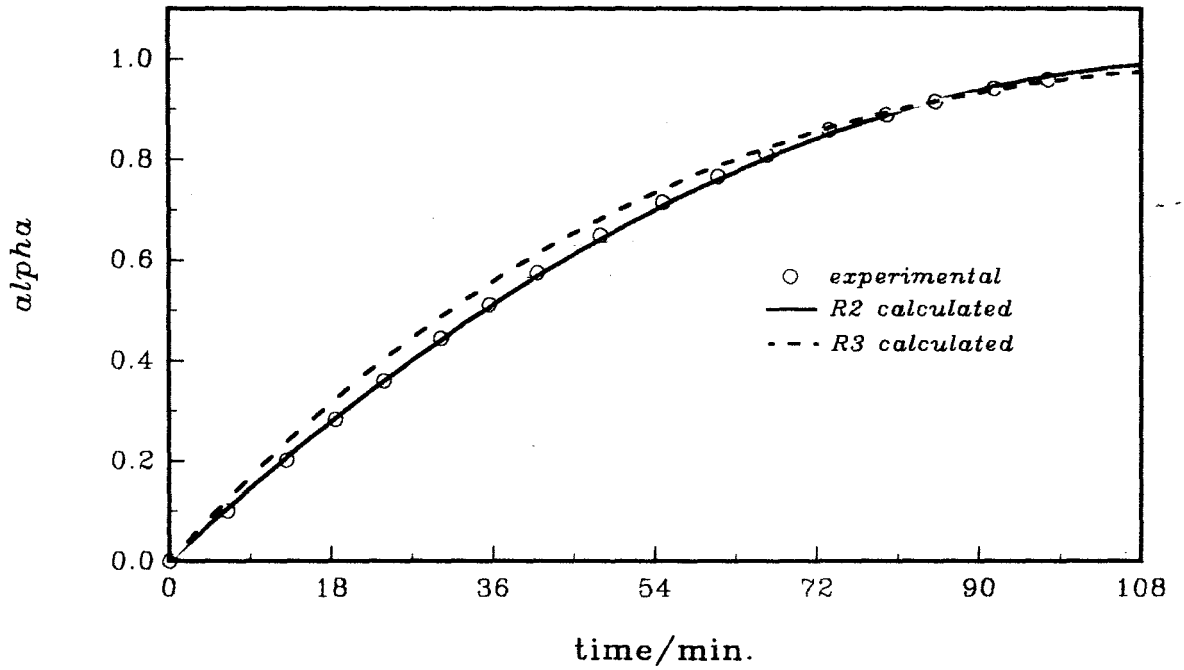

Figure 10.2.6h: Plots of $\alpha_{calc.}$ versus time using the R2 and R3 models, compared with α_e versus time data for the decomposition of $Ni(aa)Cl_2$ at 193°C

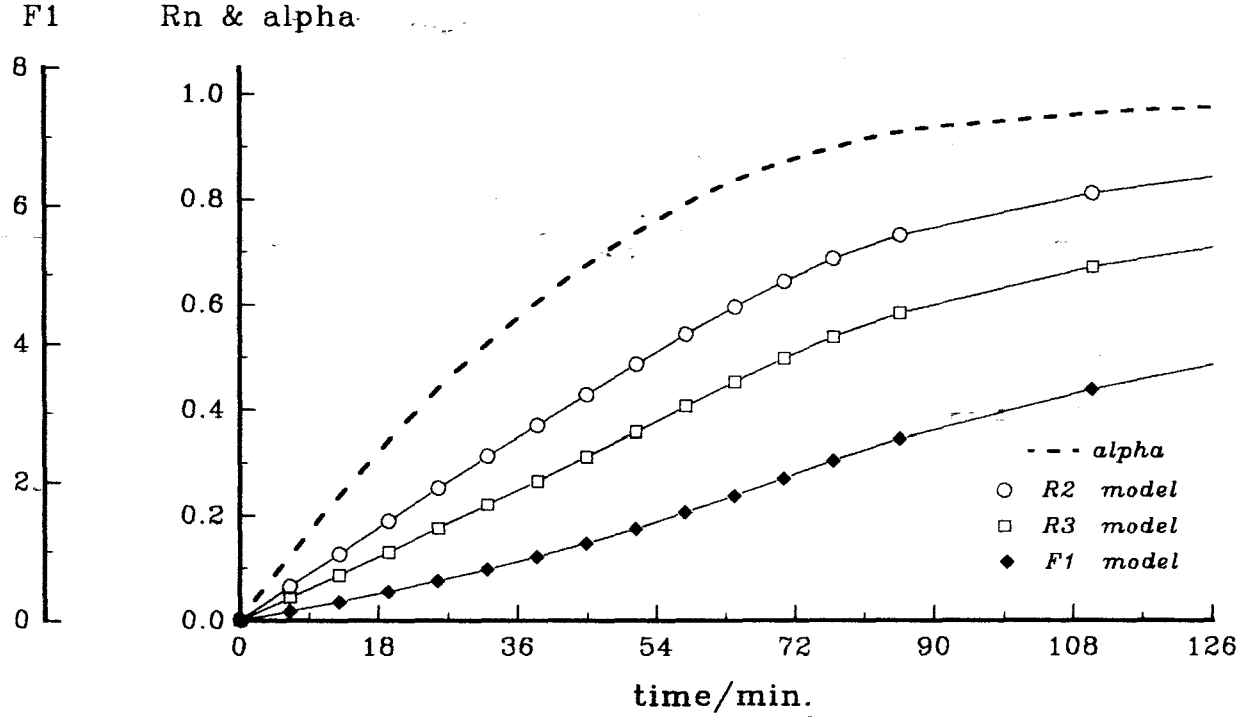

Figure 10.2.5i: Plots of $g(\alpha)$ versus time for the decomposition of $Ni(aa)Cl_2$ at 190°C. The α–time curve is included to show the range of α over which $g(\alpha)$ is approximately linear.

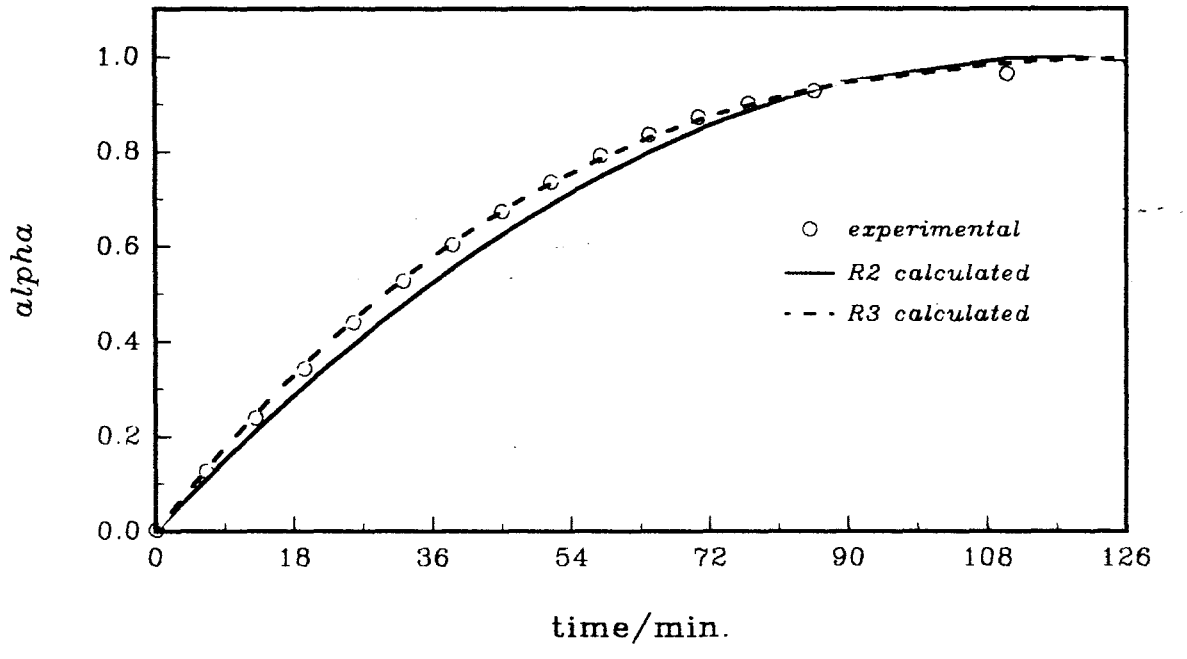

Figure 10.2.6i: Plots of $\alpha_{calc.}$ versus time using the R2 and R3 models, compared with α_e versus time data for the decomposition of $Ni(aa)Cl_2$ at 190°C.

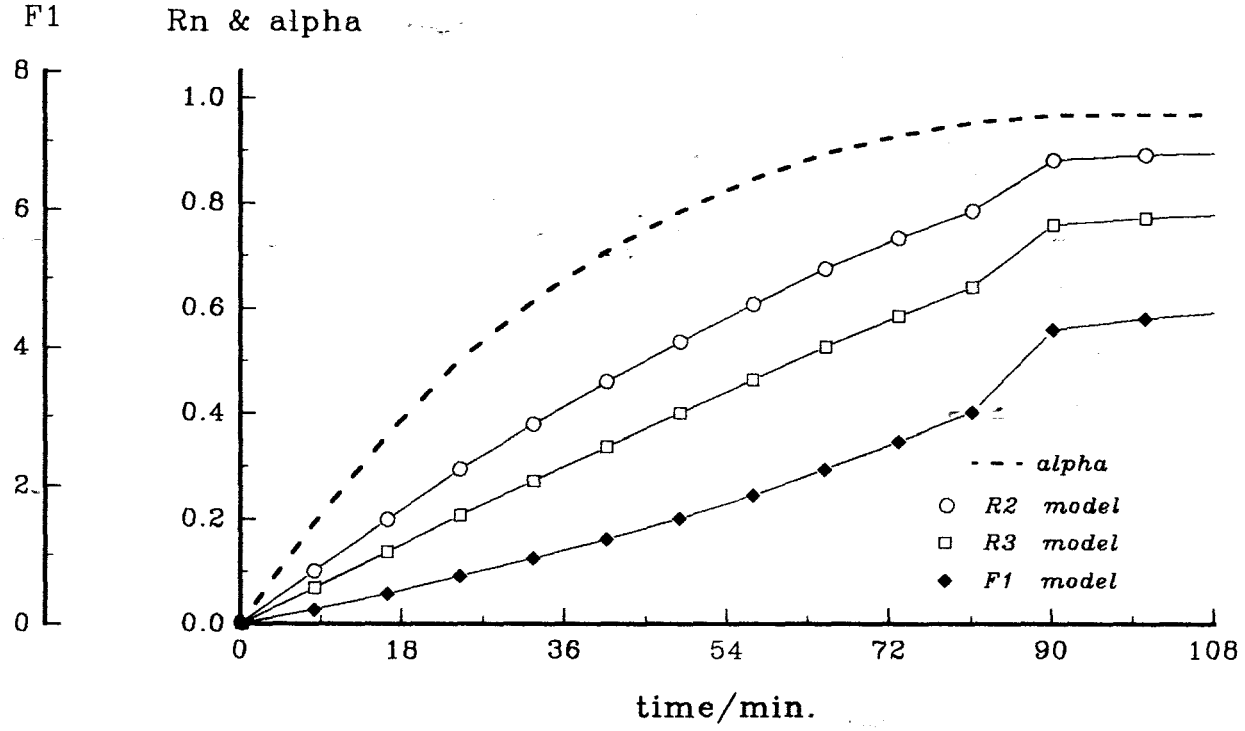

Figure 10.2.5j: Plots of $g(\alpha)$ versus time for the decomposition of $Ni(aa)Cl_2$ at 190°C.* The α–time curve is included to show the range of α over which $g(\alpha)$ is approximately linear.

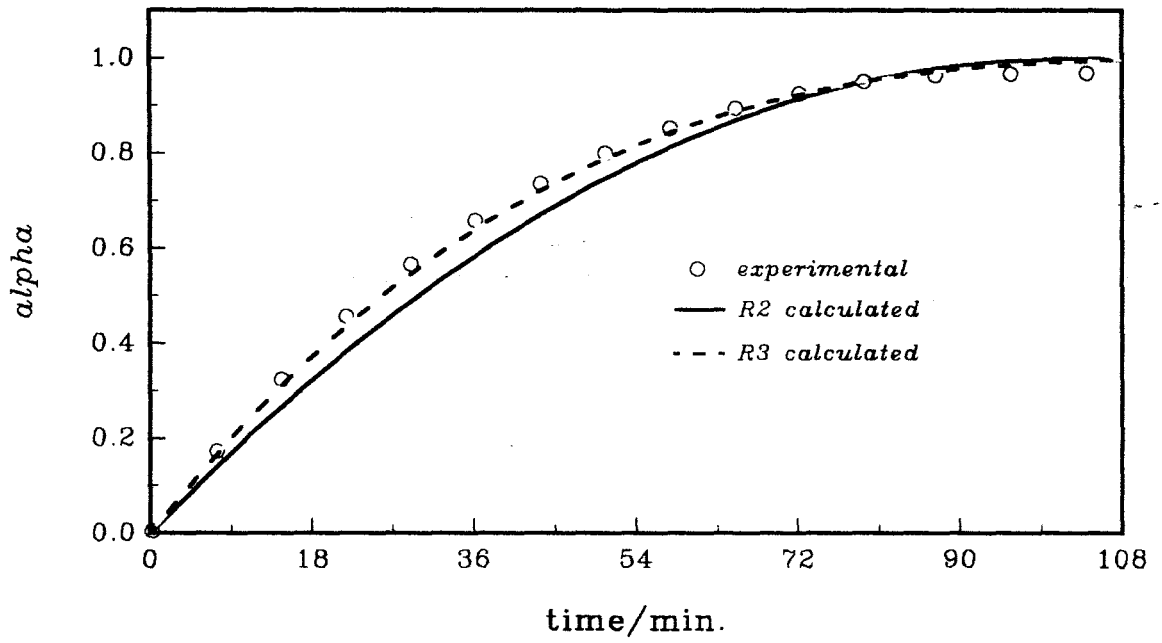

Figure 10.2.6j: Plots of $\alpha_{calc.}$ versus time using the R2 and R3 models, compared with α_e versus time data for the decomposition of $Ni(aa)Cl_2$ at 190°C.*

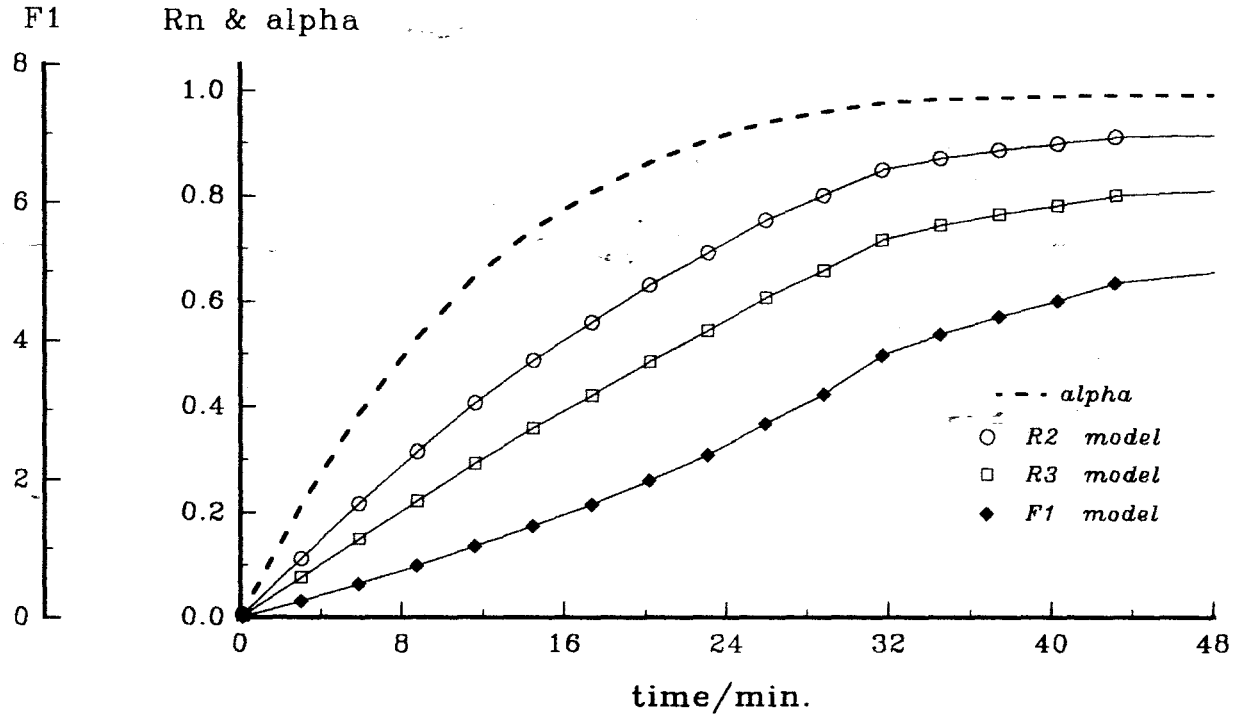

Figure 10.2.5k: Plots of $g(\alpha)$ versus time for the decomposition of $Ni(aa)Cl_2$ at 200°C. The α–time curve is included to show the range of α over which $g(\alpha)$ is approximately linear.

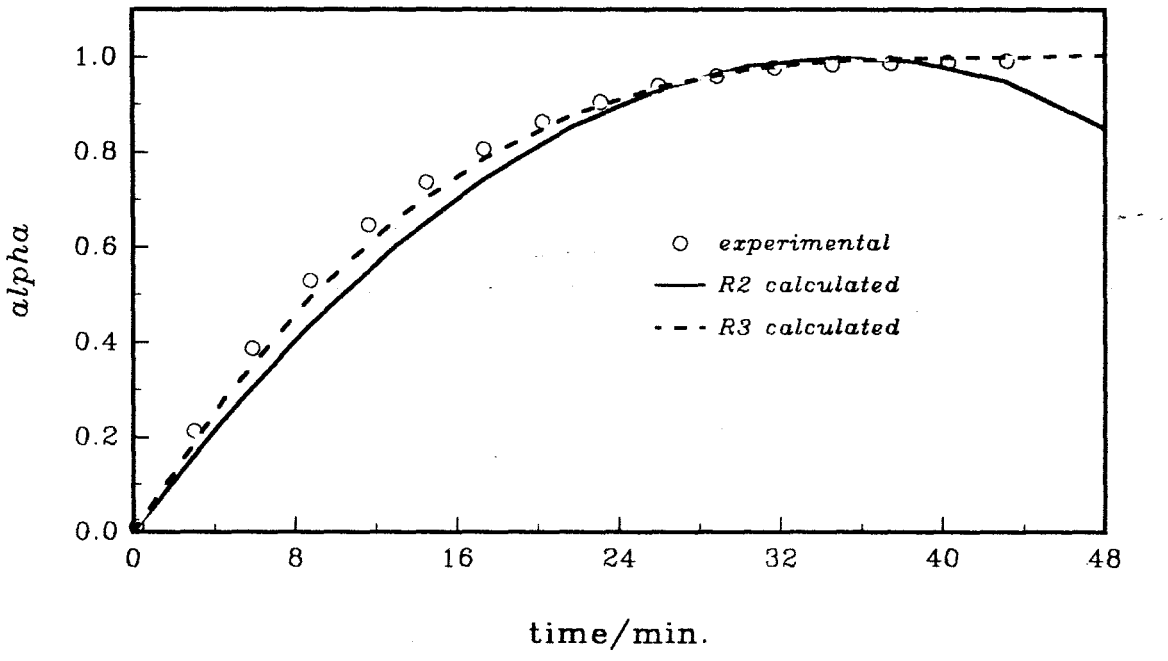

Figure 10.2.6k: Plots of $\alpha_{calc.}$ versus time using the R2 and R3 models, compared with α_e versus time data for the decomposition of $Ni(aa)Cl_2$ at 200°C.

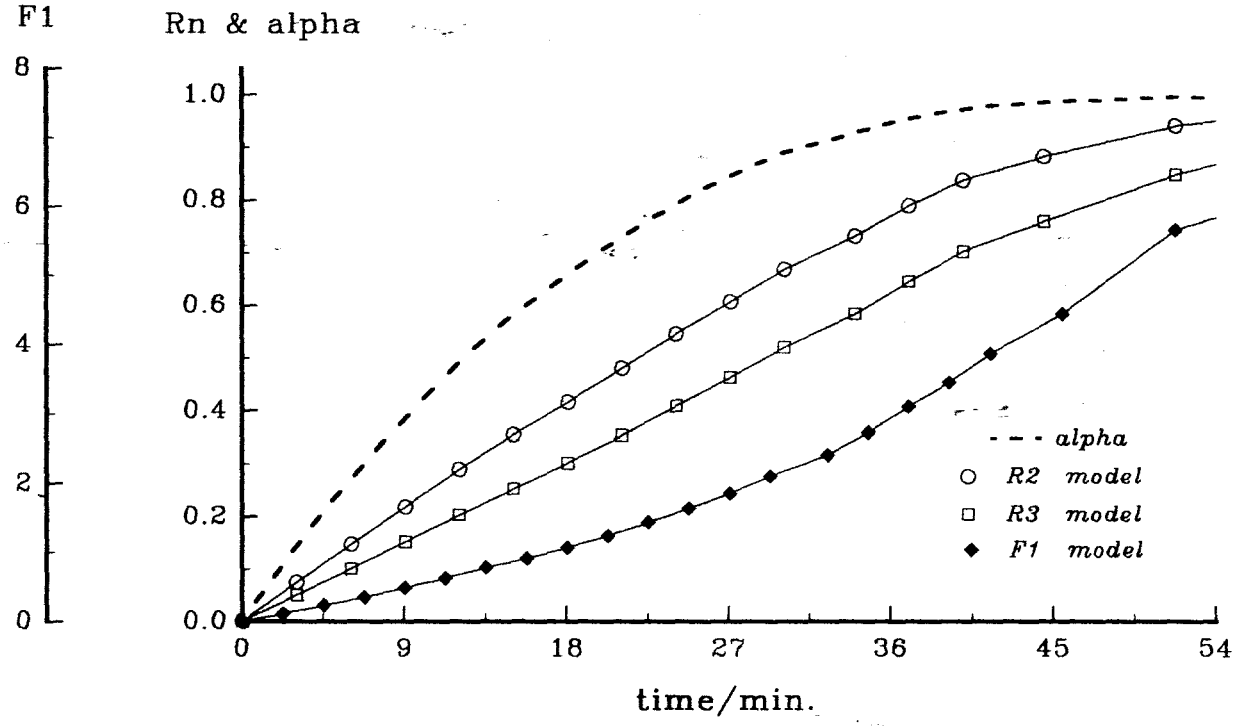

Figure 10.2.51: Plots of $g(\alpha)$ versus time for the decomposition of $Ni(aa)Cl_2$ at 203°C. The α–time curve is included to show the range of α over which $g(\alpha)$ is approximately linear.

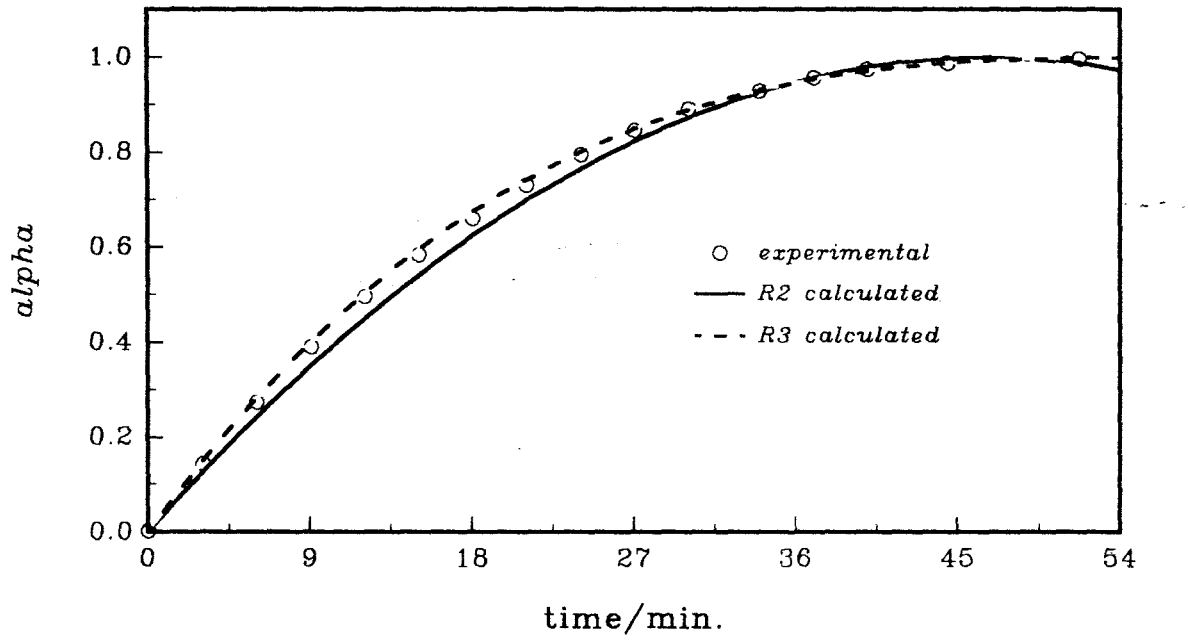

Figure 10.2.61: Plots of $\alpha_{calc.}$ versus time using the R2 and R3 models, compared with α_e versus time data for the decomposition of $Ni(aa)Cl_2$ at 203°C.

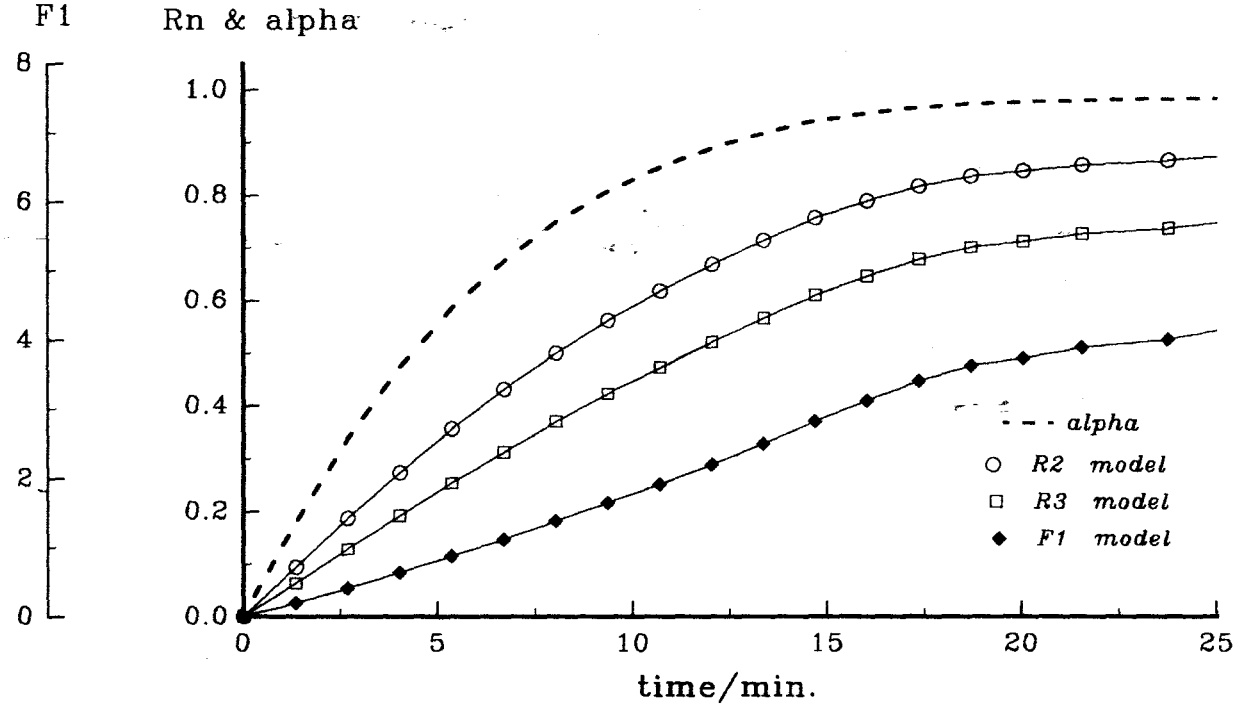

Figure 10.2.5m: Plots of $g(\alpha)$ versus time for the decomposition of $Ni(aa)Cl_2$ at 210°C. The α–time curve is included to show the range of α over which $g(\alpha)$ is approximately linear.

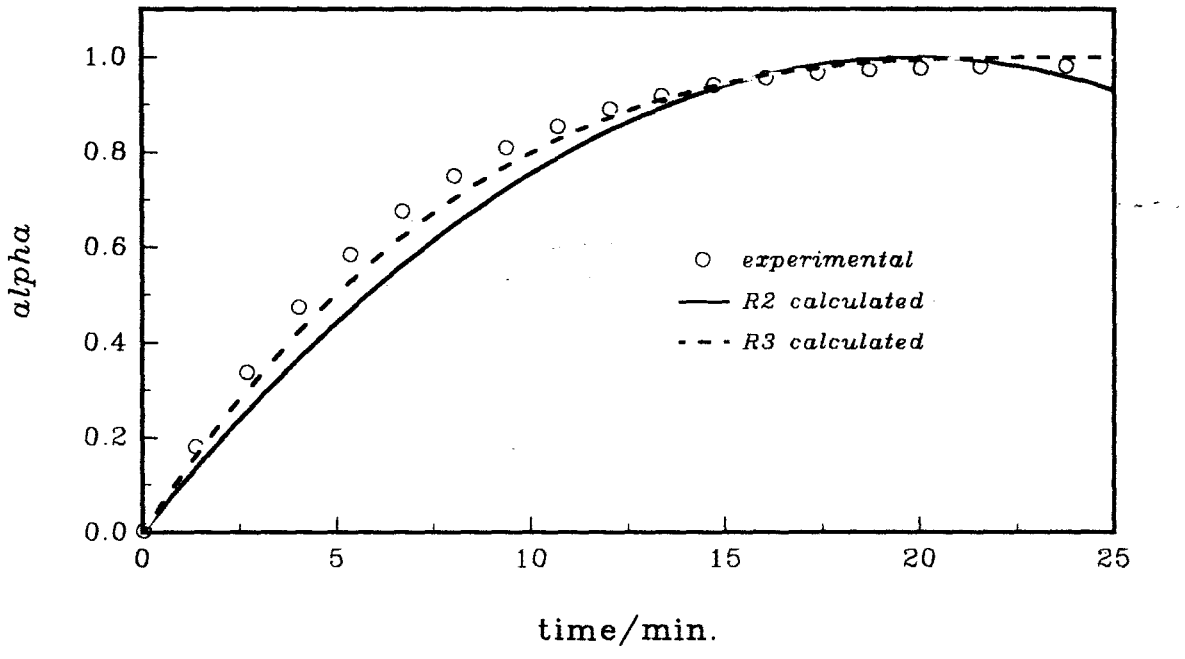

Figure 10.2.6m: Plots of $\alpha_{calc.}$ versus time using the R2 and R3 models, compared with α_e versus time data for the decomposition of $Ni(aa)Cl_2$ at 210°C.

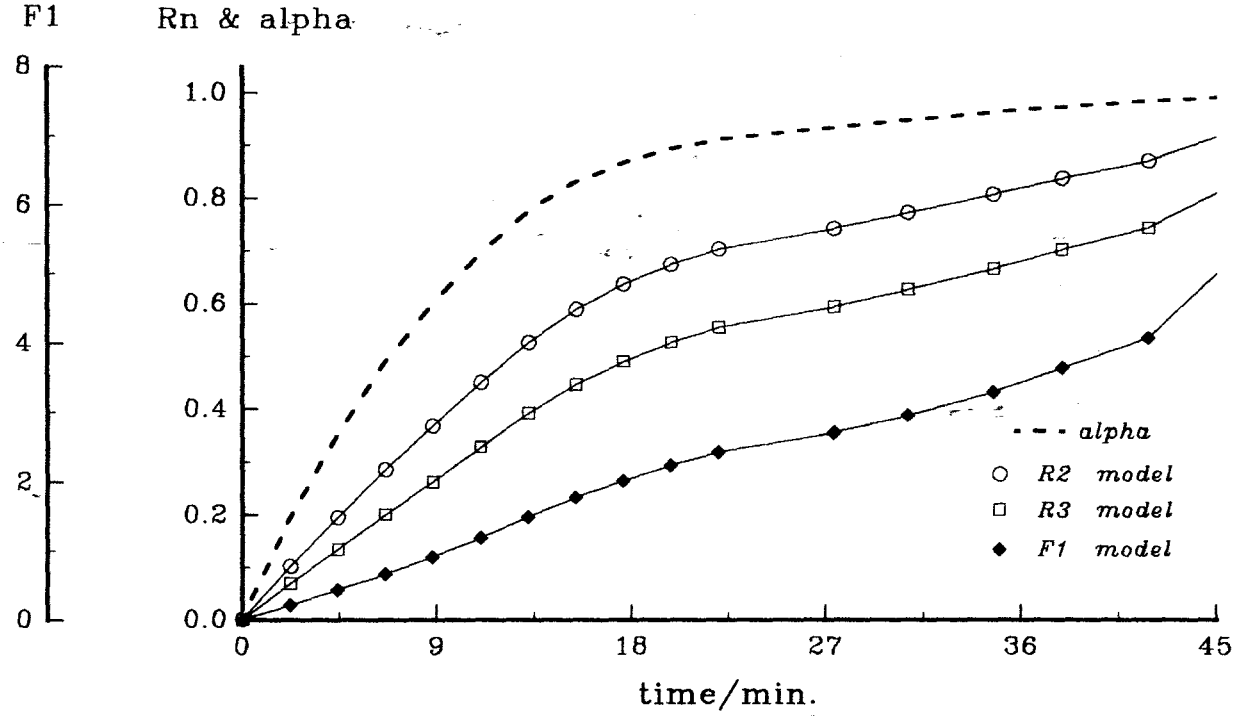

Figure 10.2.5n: Plots of g(a) versus time for the decomposition of $Ni(aa)Cl_2$ at 213°C. The α–time curve is included to show the range of α over which $g(\alpha)$ is approximately linear.

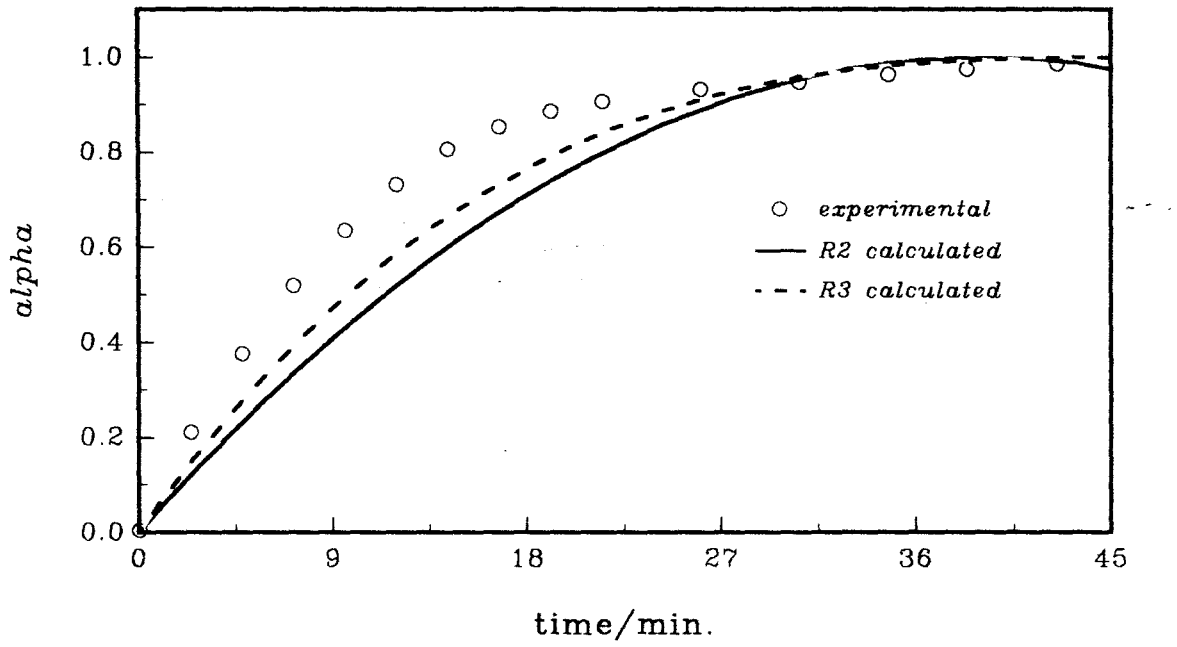

Figure 10.2.6n: Plots of $\alpha_{calc.}$ versus time using the R2 and R3 models, compared with α_e versus time data for the decomposition of $Ni(aa)Cl_2$ at 213°C.

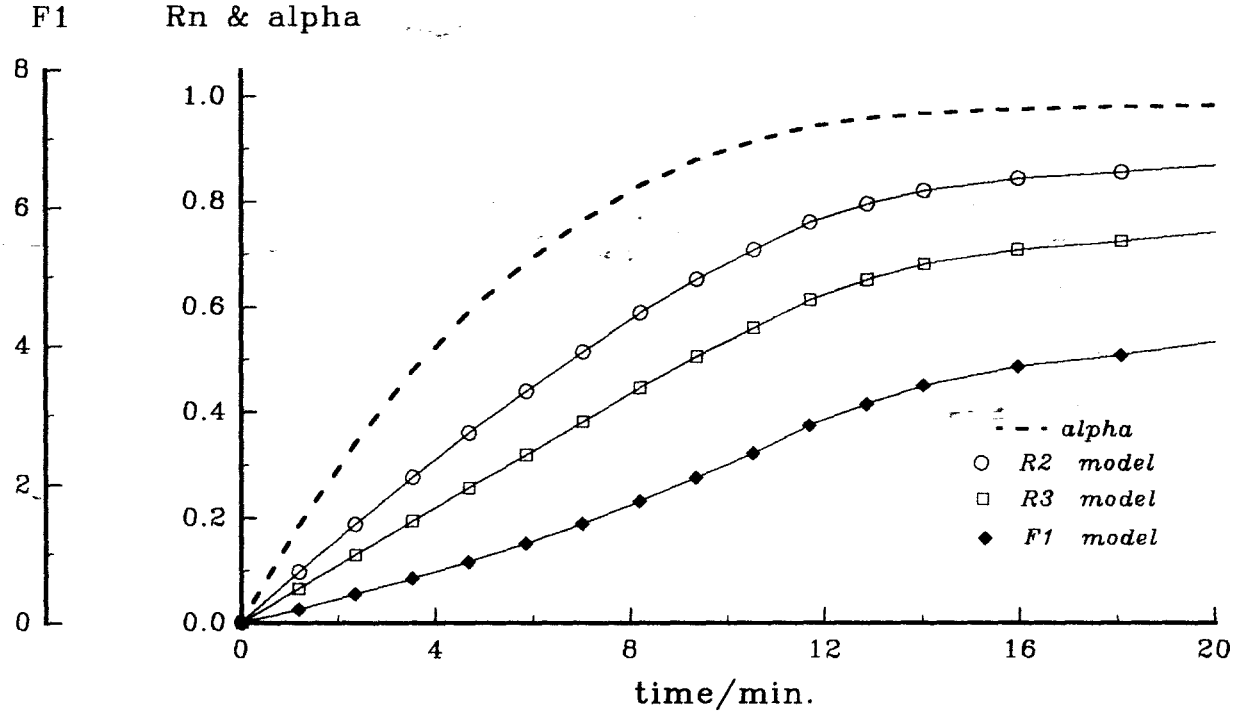

Figure 10.2.5o: Plots of $g(\alpha)$ versus time for the decomposition of $Ni(aa)Cl_2$ at 218°C. The α–time curve is included to show the range of α over which $g(\alpha)$ is approximately linear.

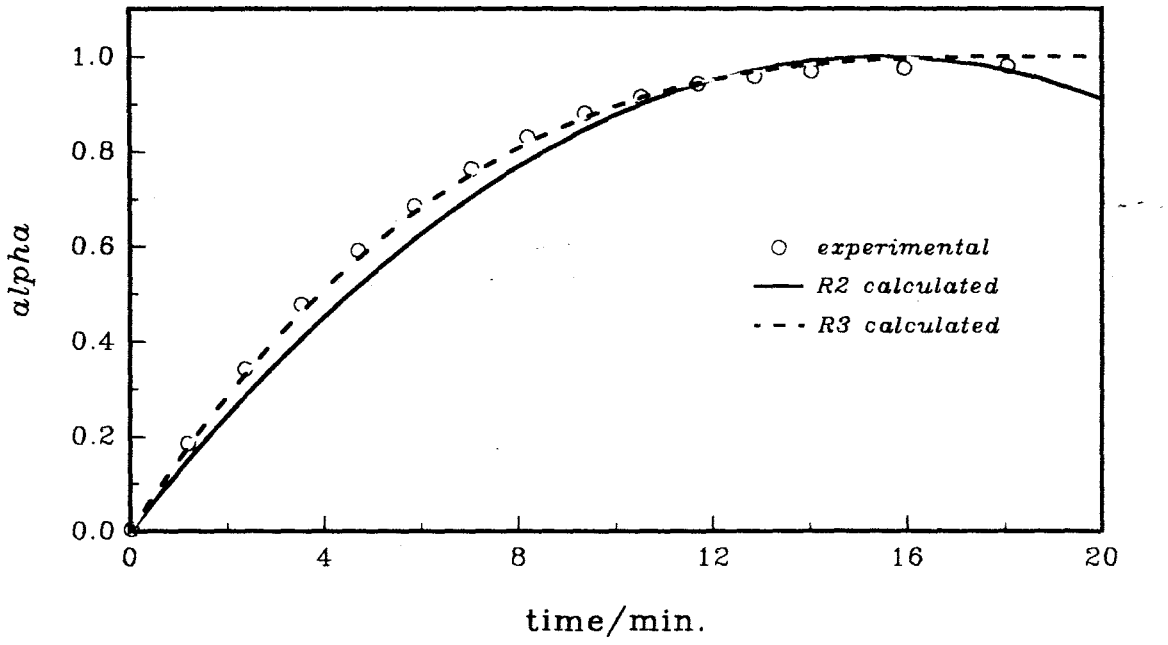

Figure 10.2.6o: Plots of $\alpha_{calc.}$ versus time using the R2 and R3 models, compared with α_e versus time data for the decomposition of $Ni(aa)Cl_2$ at 218°C.

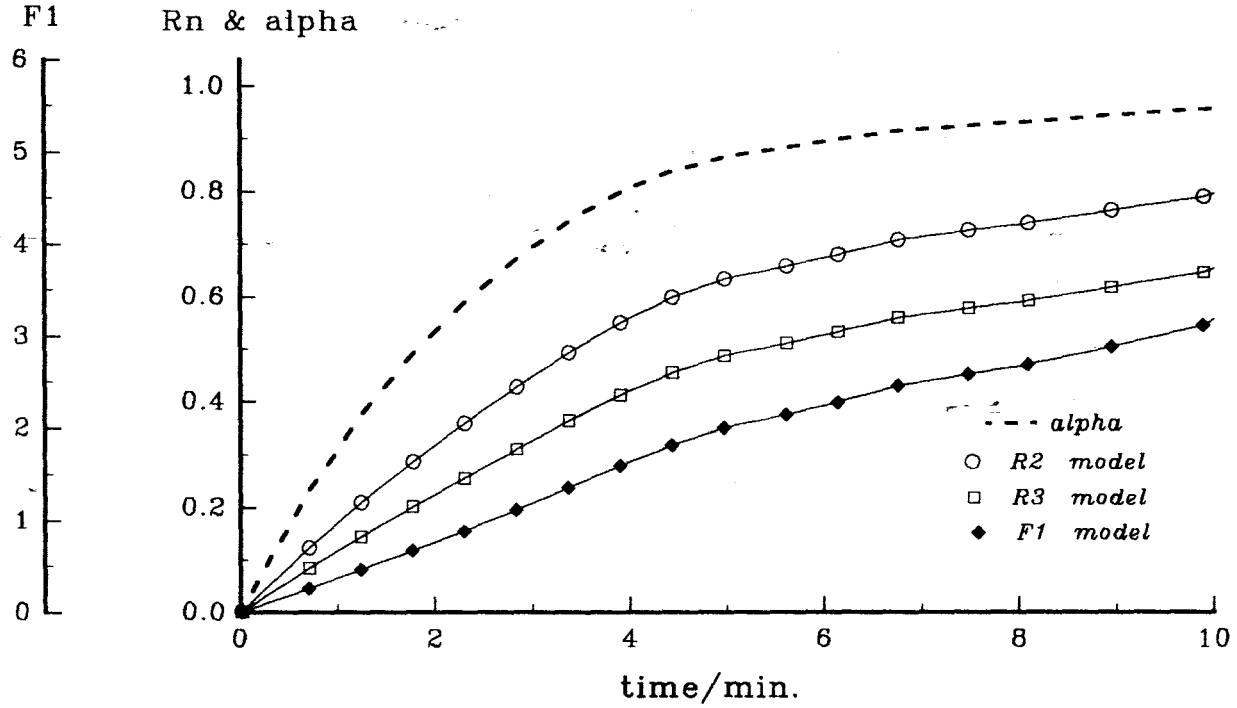

Figure 10.2.5p: Plots of $g(\alpha)$ versus time for the decomposition of $Ni(aa)Cl_2$ at 223°C. The α–time curve is included to show the range of α over which $g(\alpha)$ is approximately linear.

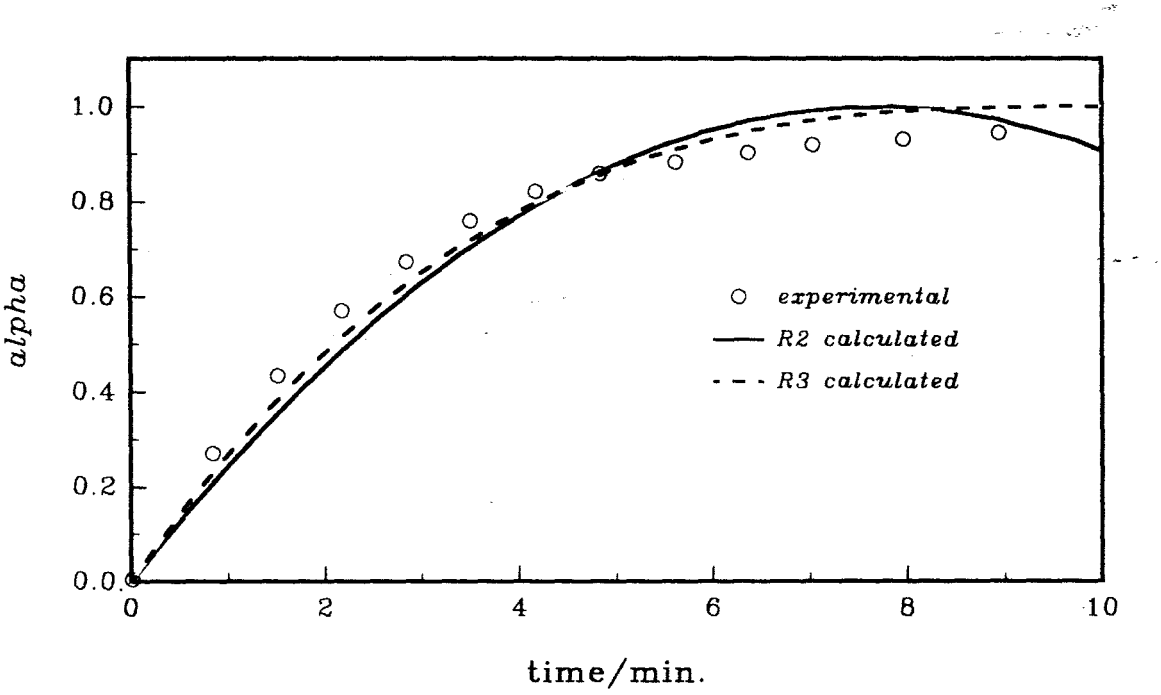

Figure 10.2.6p: Plots of $\alpha_{calc.}$ versus time using the R2 and R3 models, compared with α_e versus time data for the decomposition of $Ni(aa)Cl_2$ at 223°C.

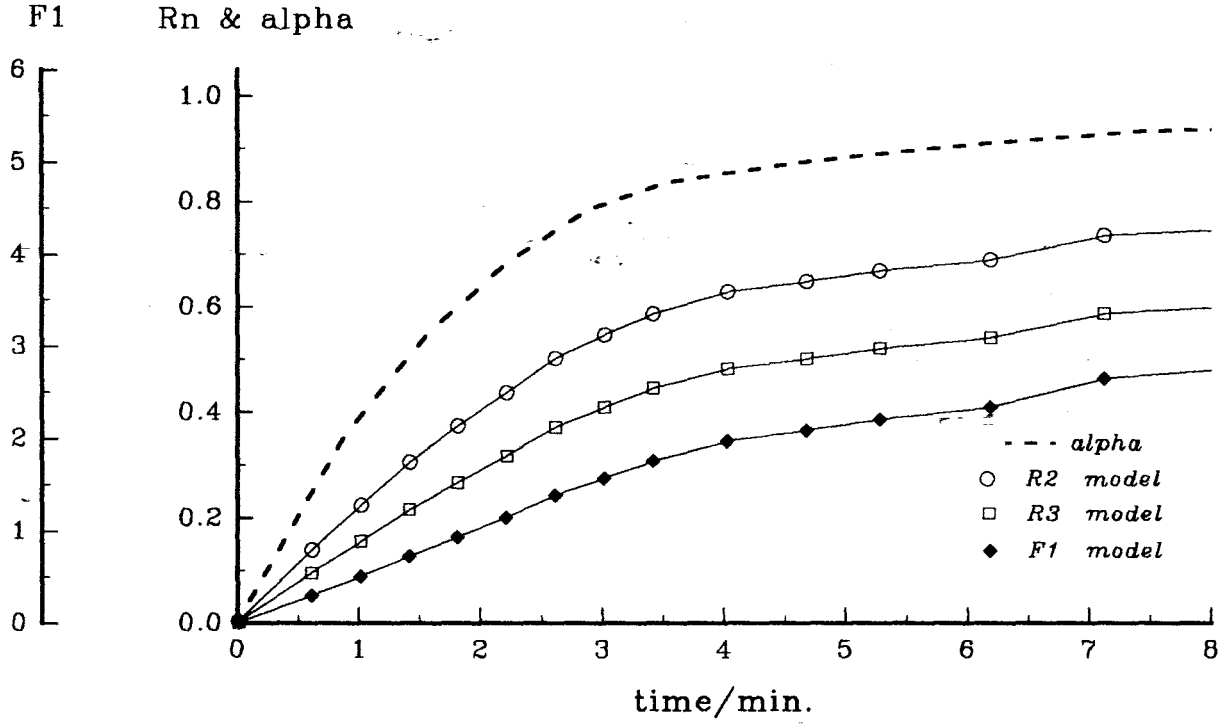

Figure 10.2.5q: Plots of $g(\alpha)$ versus time for the decomposition of $Ni(aa)Cl_2$ at 225°C. The α–time curve is included to show the range of α over which $g(\alpha)$ is approximately linear.

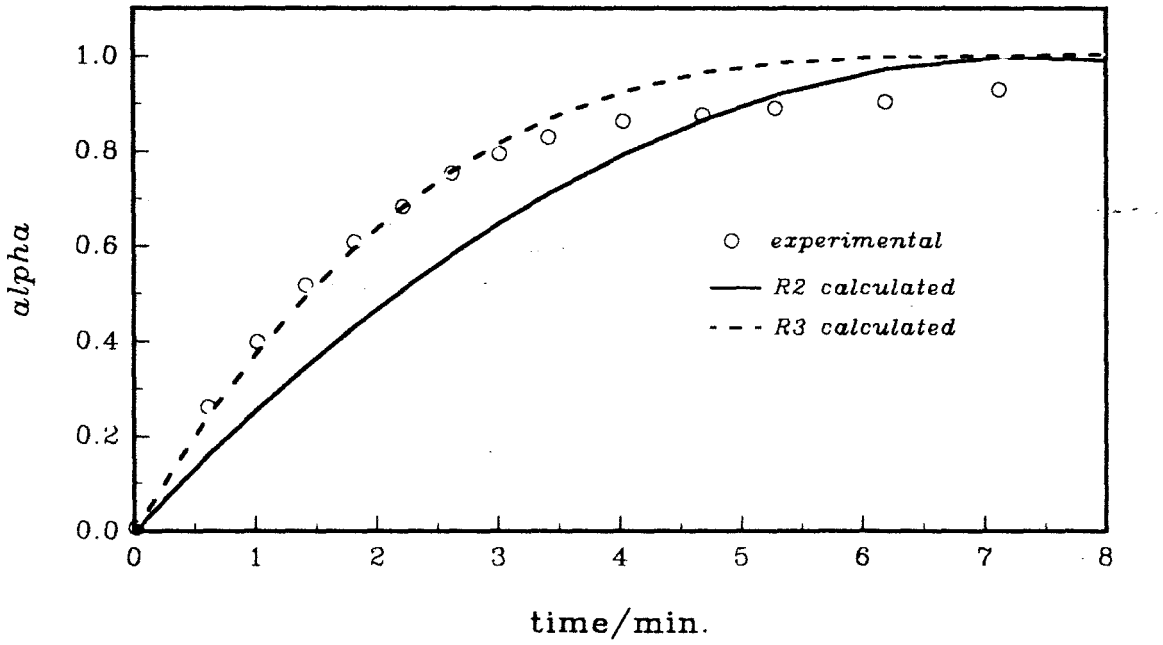

Figure 10.2.6q: Plots of $\alpha_{calc.}$ versus time using the R2 and R3 models, compared with α_e versus time data for the decomposition of $Ni(aa)Cl_2$ at 225°C.

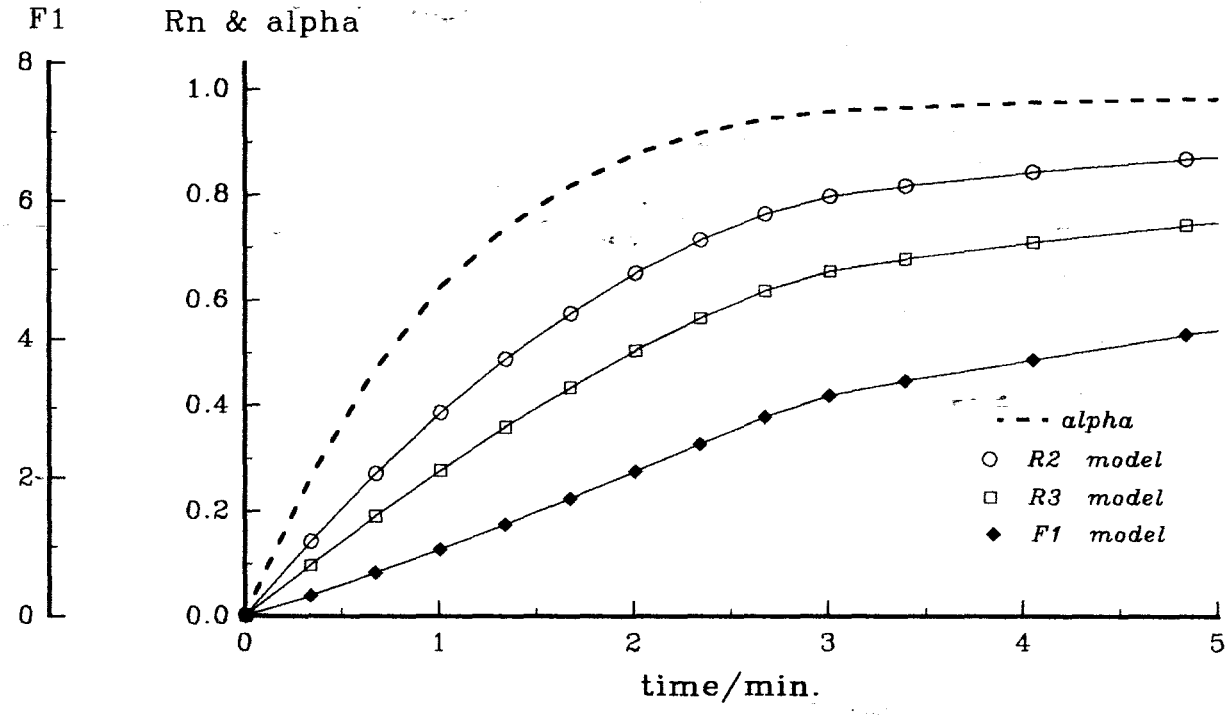

Figure 10.2.5r: Plots of $g(\alpha)$ versus time for the decomposition of $Ni(aa)Cl_2$ at 235°C. The α–time curve is included to show the range of α over which $g(\alpha)$ is approximately linear.

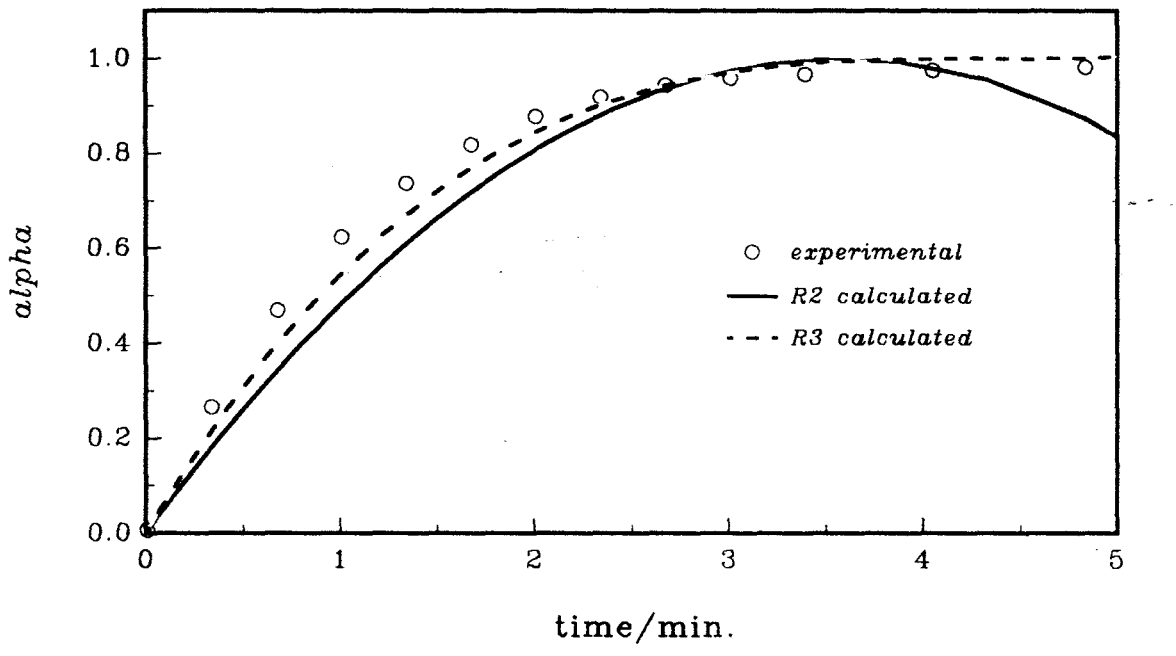

Figure 10.2.6r: Plots of $\alpha_{calc.}$ versus time using the R2 and R3 models, compared with α_e versus time data for the decomposition of $Ni(aa)Cl_2$ at 235°C.

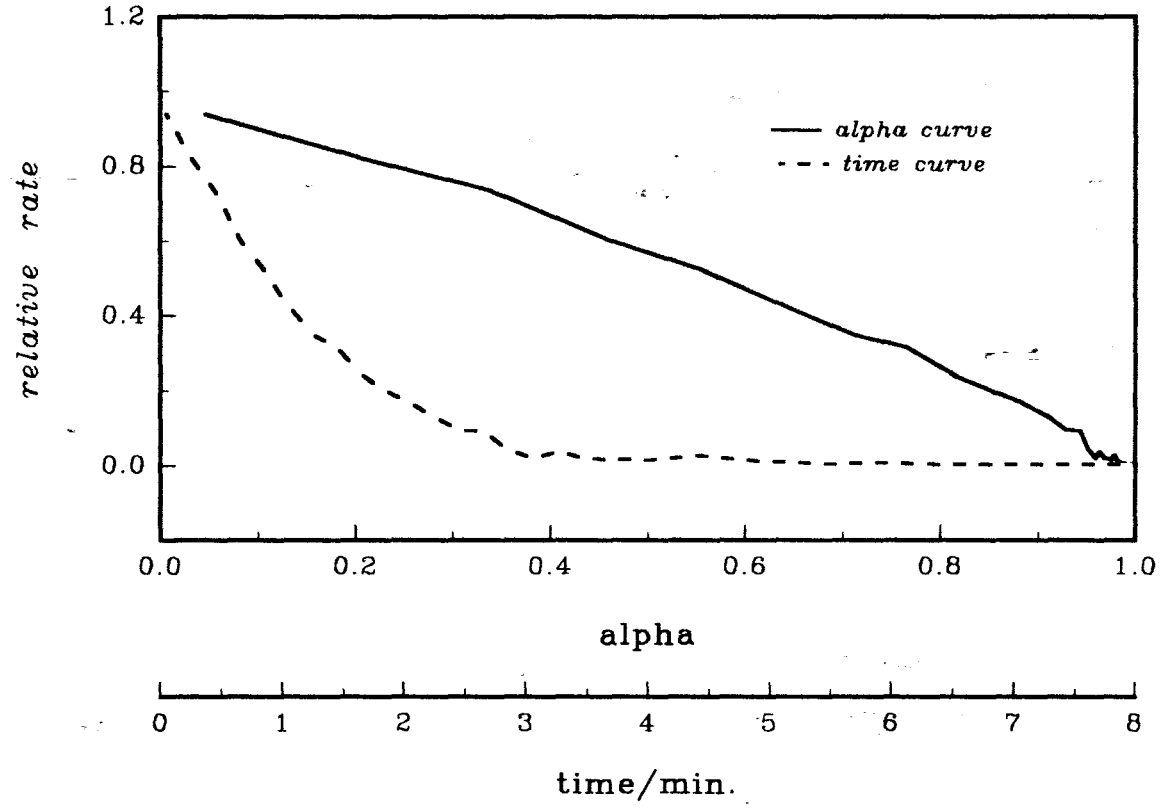

Figure 10.2.7b: Plots of rate vesus alpha and rate versus time for the decomposition of $Ni(aa)Cl_2$ at 235°C.

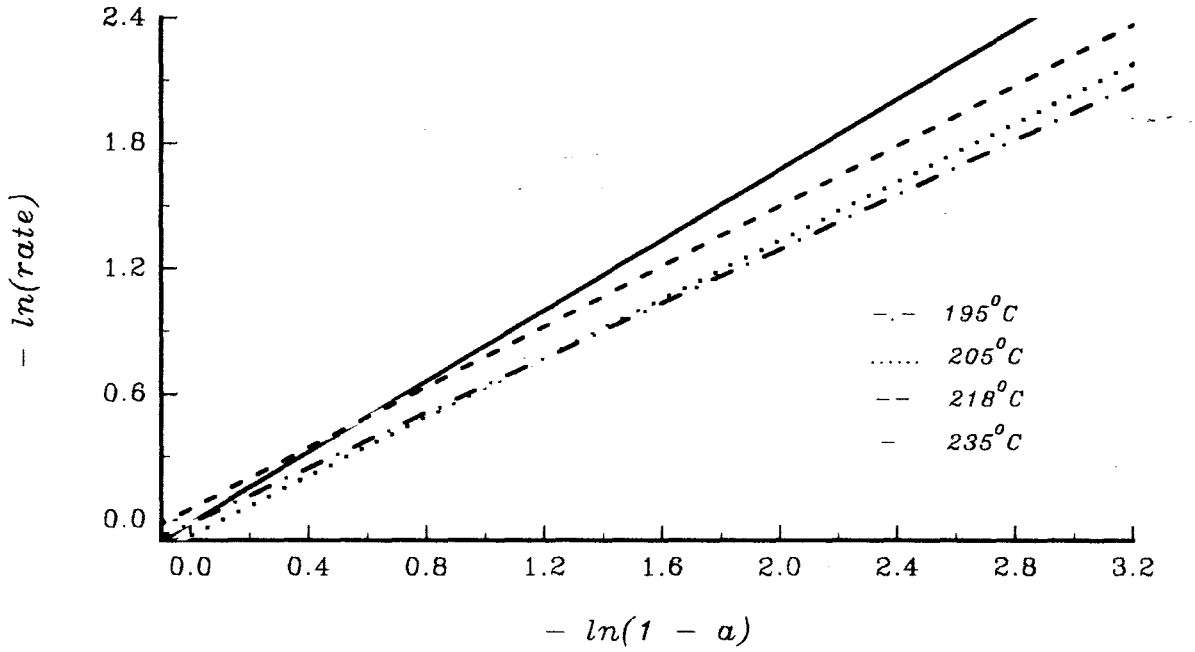

Figure 10.2.8b: Regression lines of ln(rate) versus $\ln(1 - \alpha)$ for the isothermal decomposition of $Ni(aa)Cl_2$.

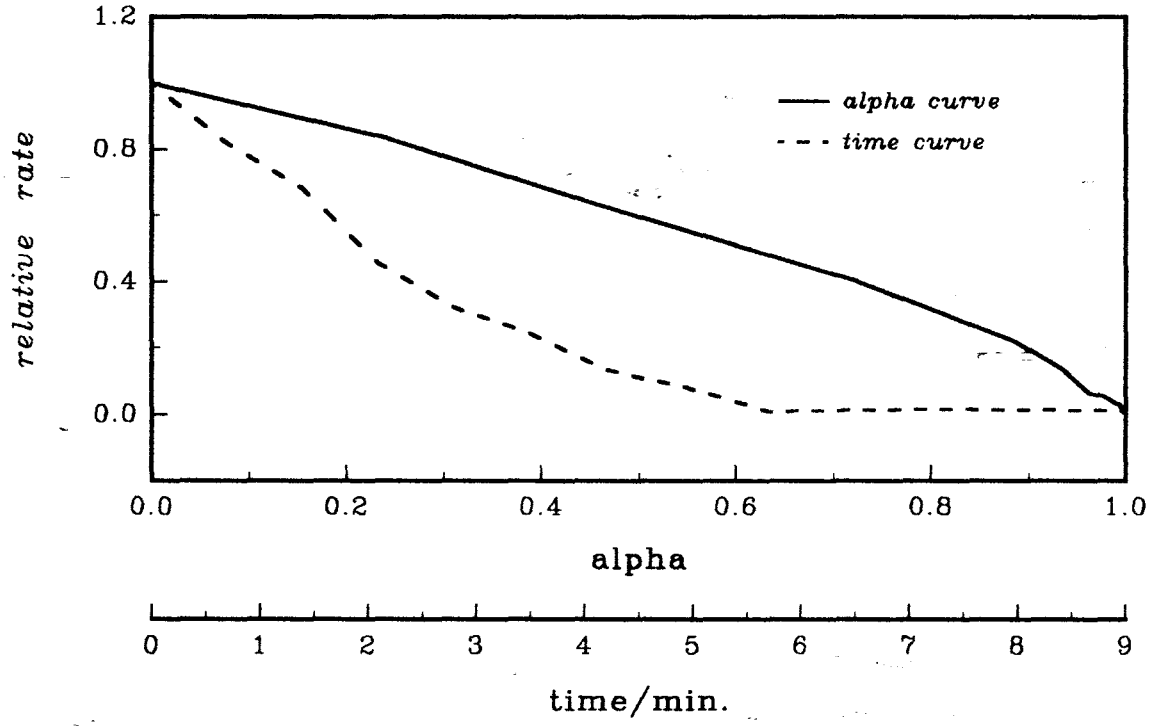

Figure 10.2.7c: Plots of rate versus alpha and rate versus time for the decomposition of $Ni(aa)Cl_2$ at 230°C.

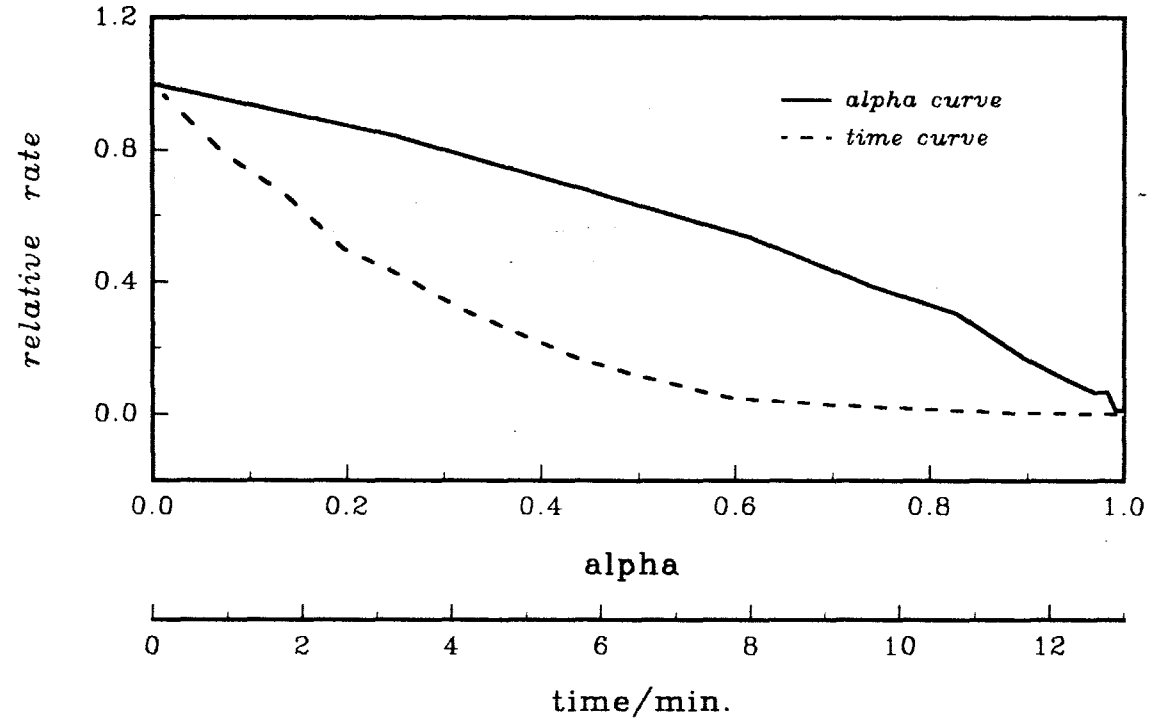

Figure 10.2.7d: Plots of rate versus alpha and rate versus time for the decomposition of $Ni(aa)Cl_2$ at 228°C.

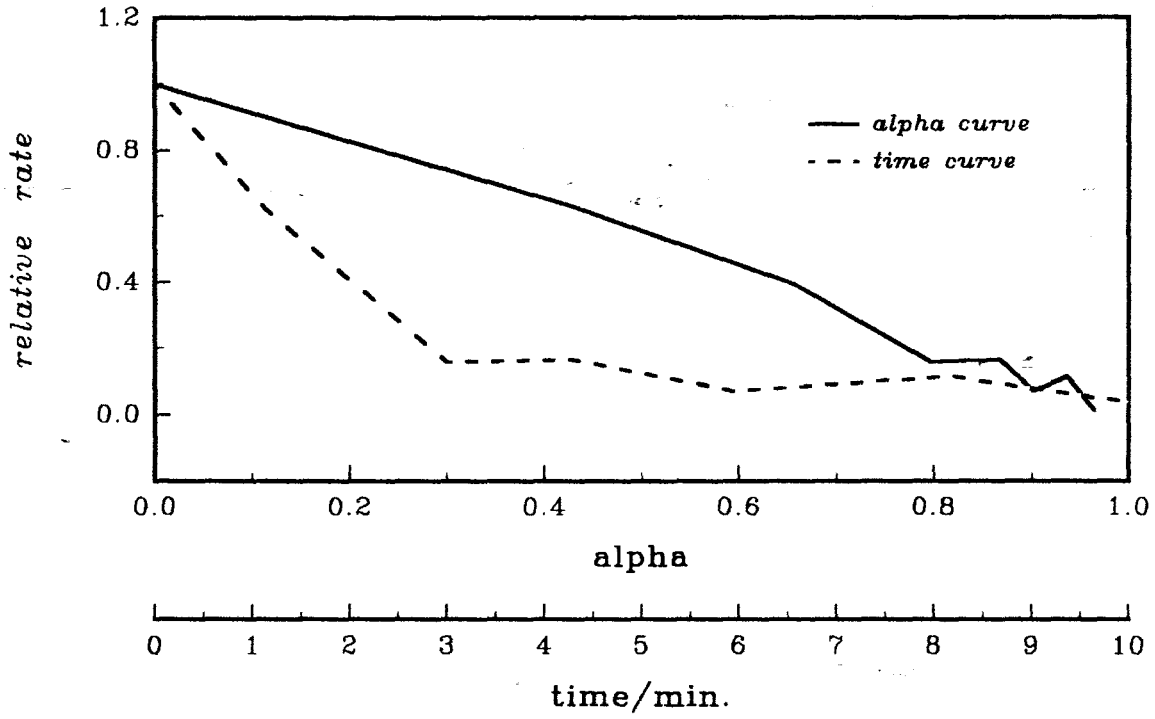

Figure 10.2.7e: Plots of rate versus alpha and rate versus time for the decomposition of $Ni(aa)Cl_2$ at 225°C.

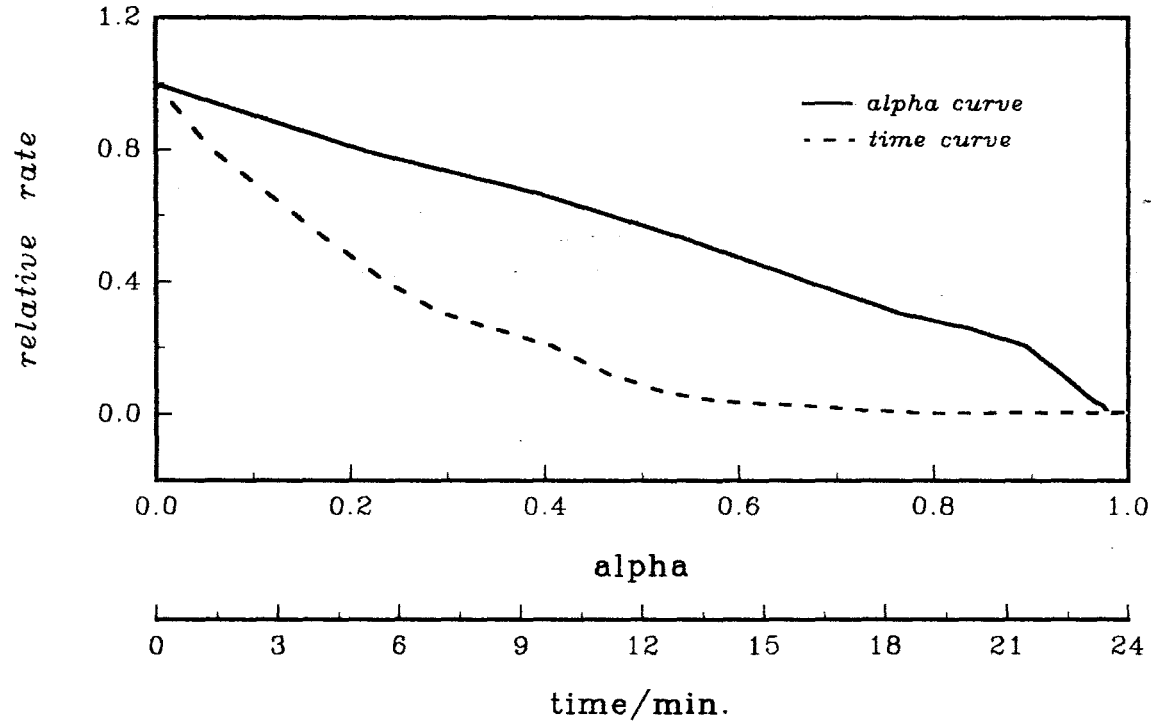

Figure 10.2.7f: Plots of rate versus alpha and rate versus time for the decomposition of $Ni(aa)Cl_2$ at 218°C.

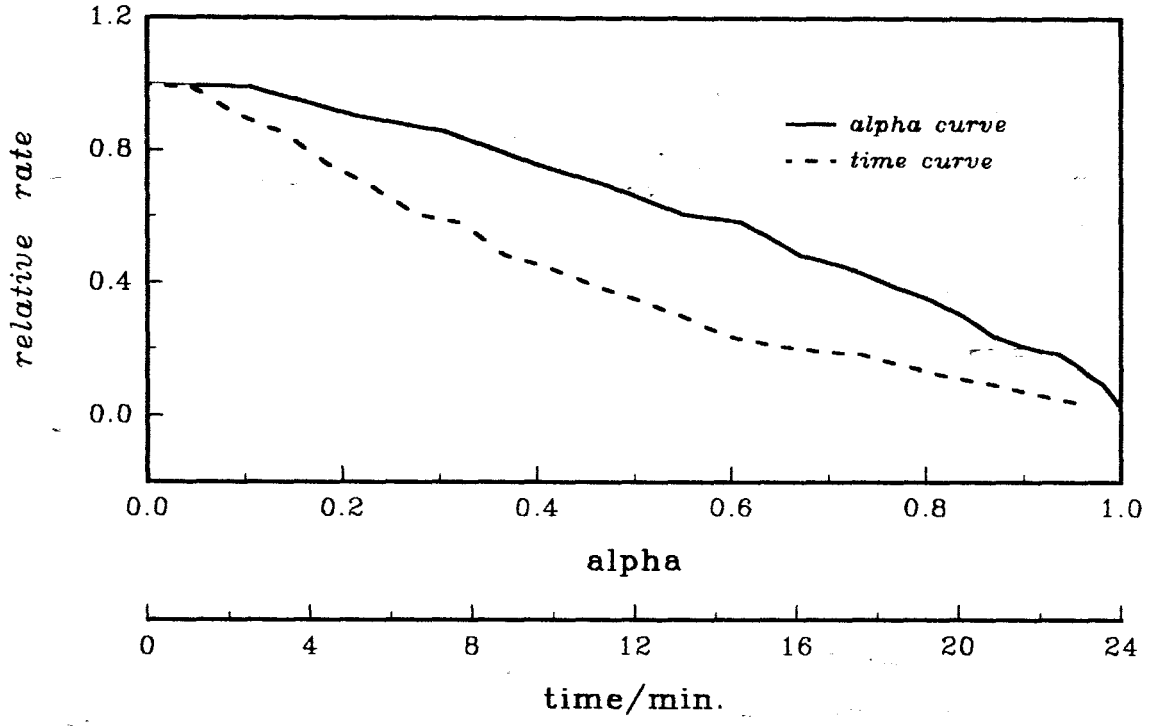

Figure 10.2.7g: Plots of rate versus alpha and rate versus time for the decomposition of $Ni(aa)Cl_2$ at 205°C.

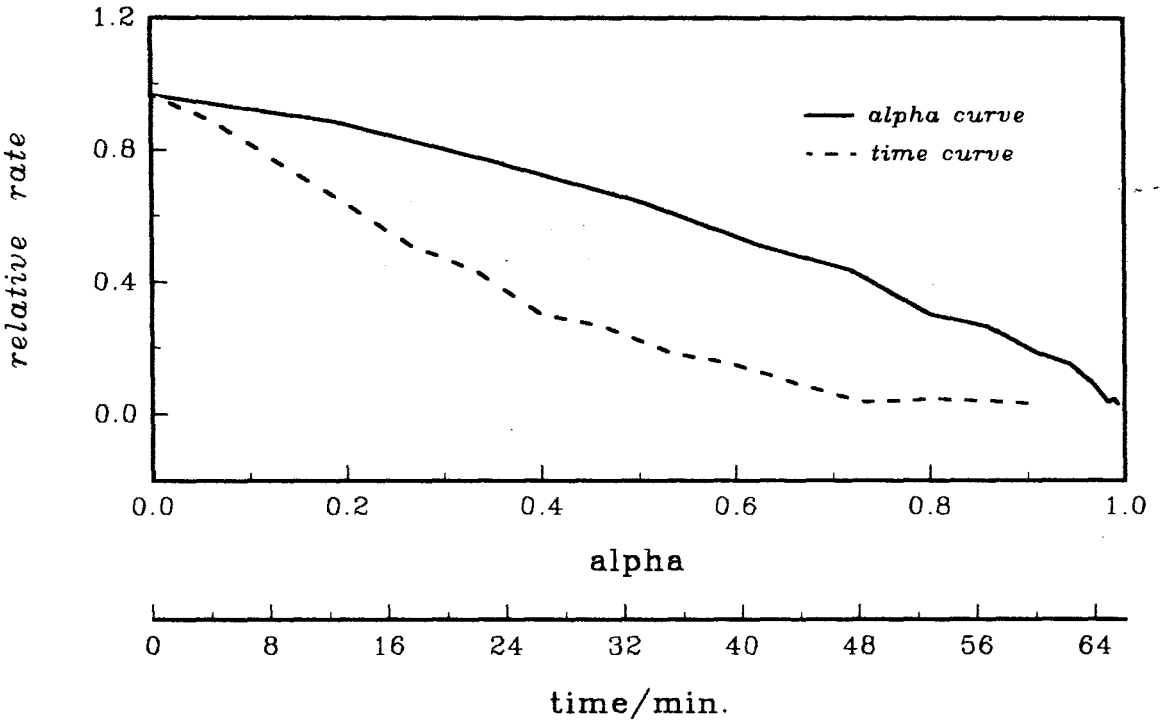

Figure 10.2.7h: Plots of rate versus alpha and rate versus time for the decomposition of $Ni(aa)Cl_2$ at 195°C.

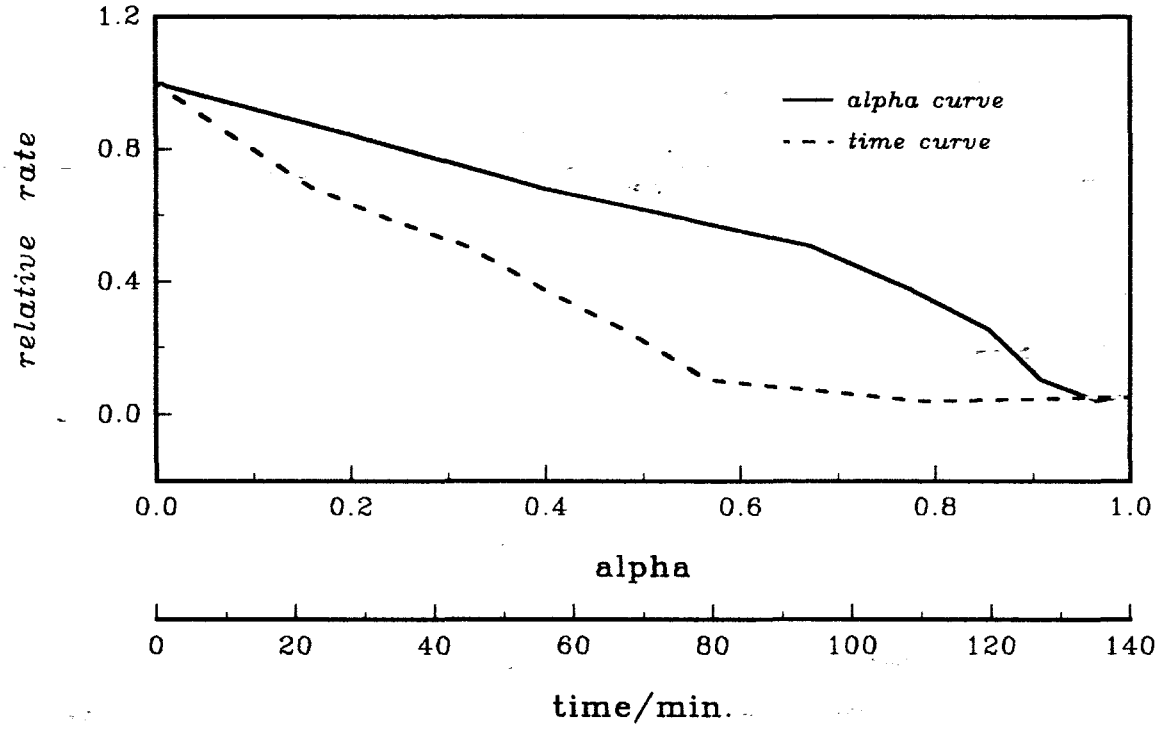

Figure 10.2.7i: Plots of rate versus alpha and rate versus time for the decomposition of $Ni(aa)Cl_2$ at 190°C.

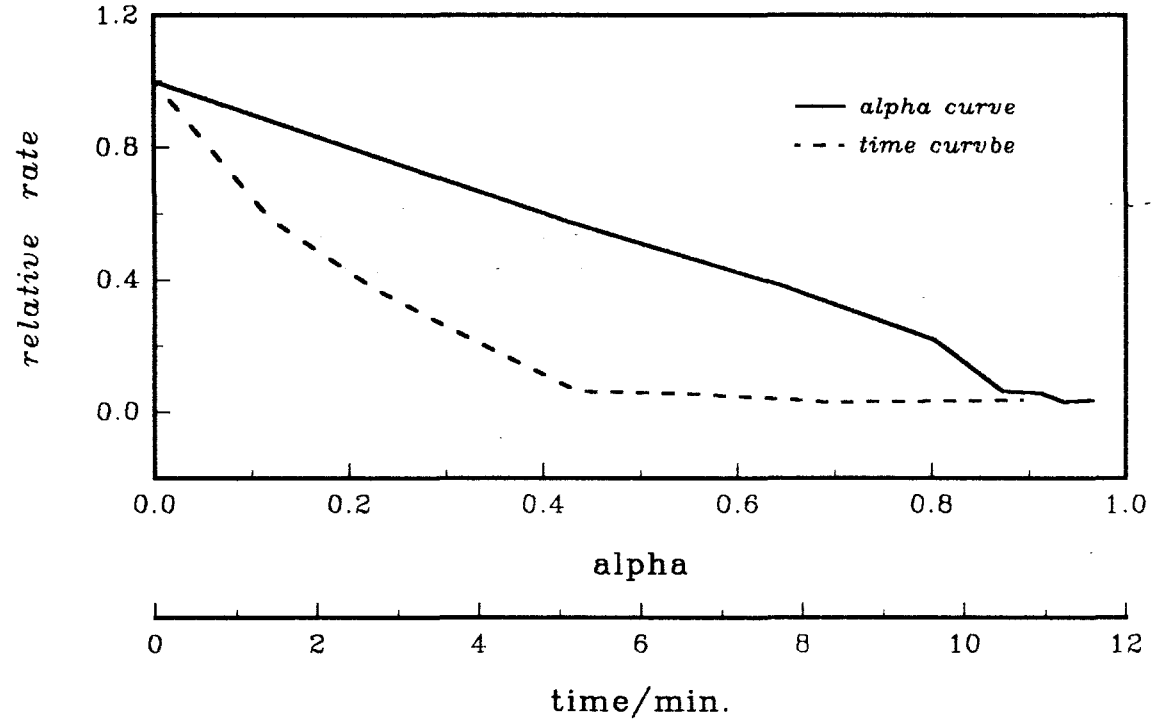

Figure 10.2.7j: Plots of rate versus alpha and rate versus time for the decomposition of $Ni(aa)Cl_2$ at 223°C.

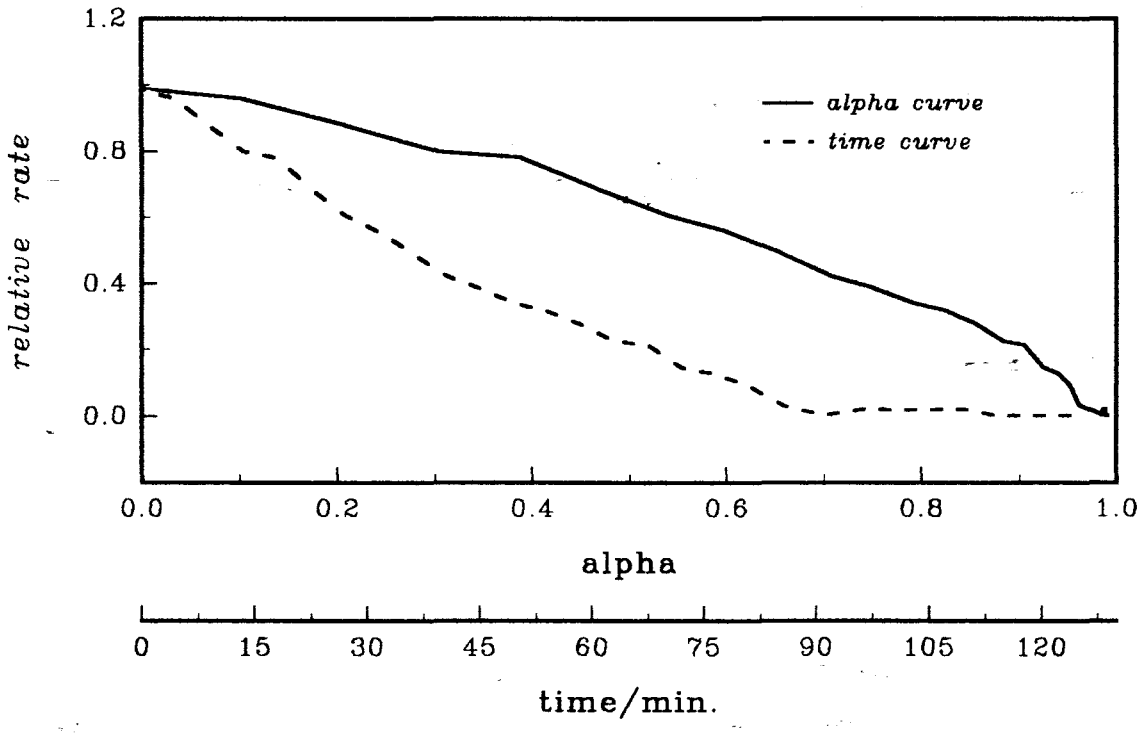

Figure 10.2.7k: Plots of rate versus alpha and rate versus time for the decomposition of $Ni(aa)Cl_2$ at 190°C.*

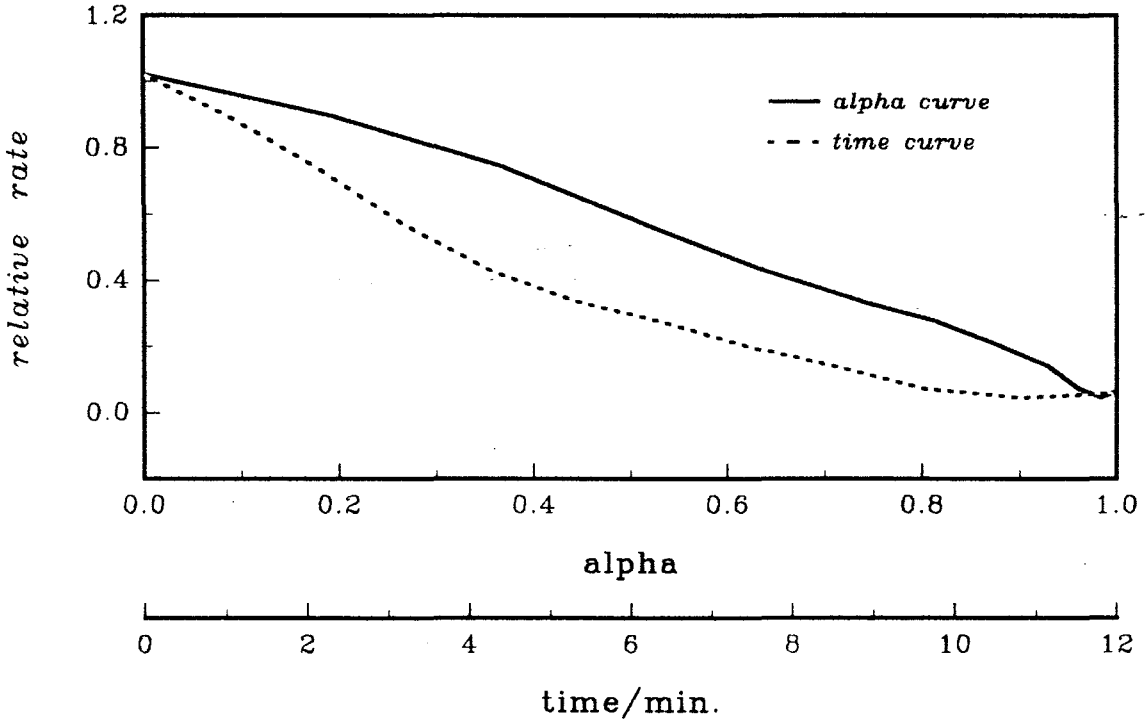

Figure 10.2.7l: Plots of rate versus alpha and rate versus time for the decomposition of $Ni(aa)Cl_2$ at 220°C.

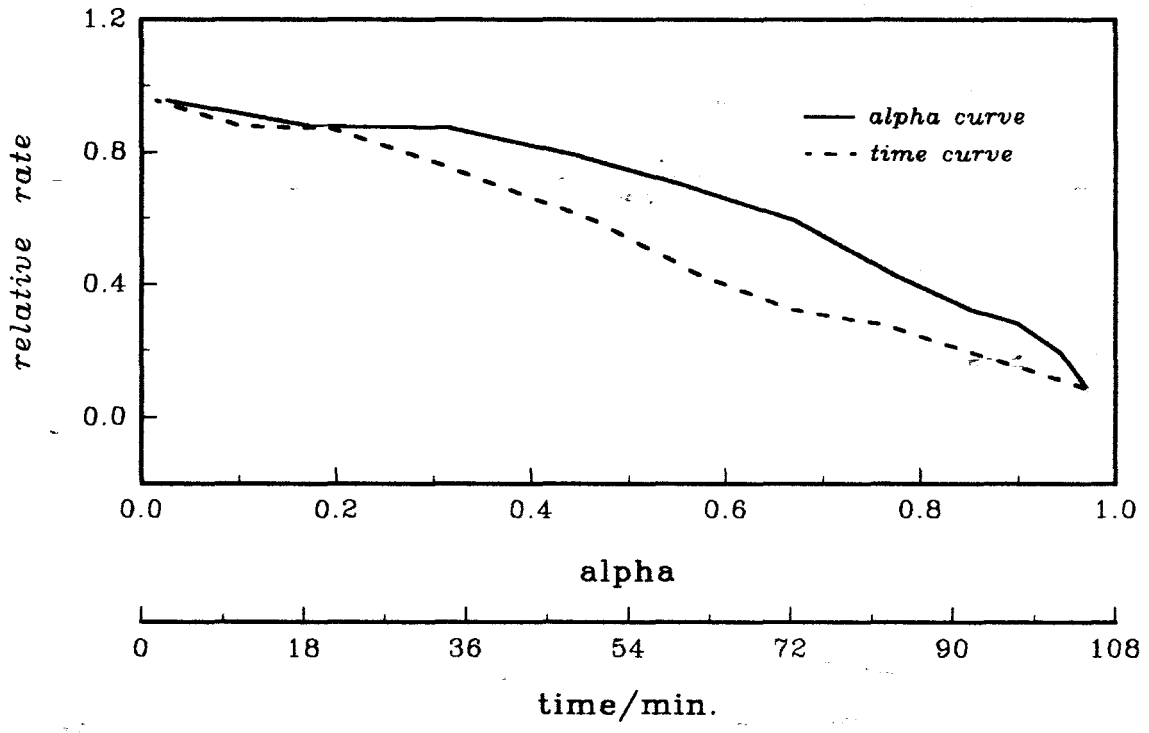

Figure 10.2.7m: Plots of rate versus alpha and rate versus time for the decomposition of $Ni(aa)Cl_2$ at 193°C.

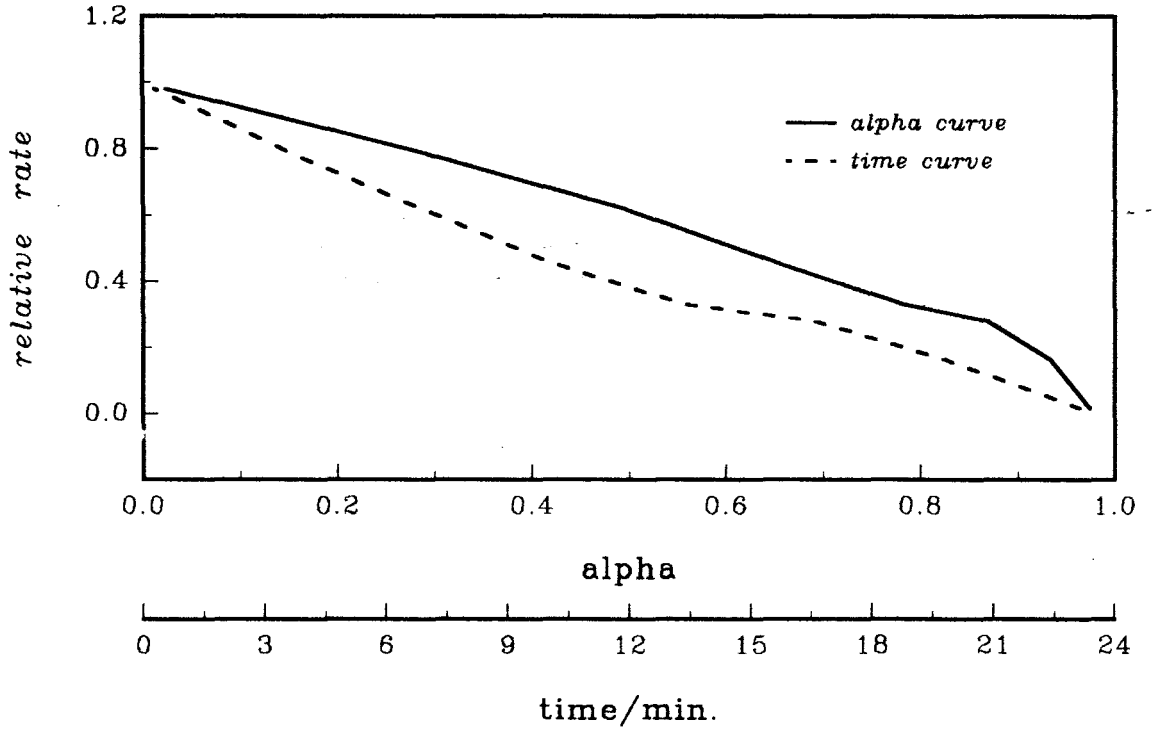

Figure 10.2.7n: Plots of rate versus alpha and rate versus time for the decomposition of $Ni(aa)Cl_2$ at 215°C.

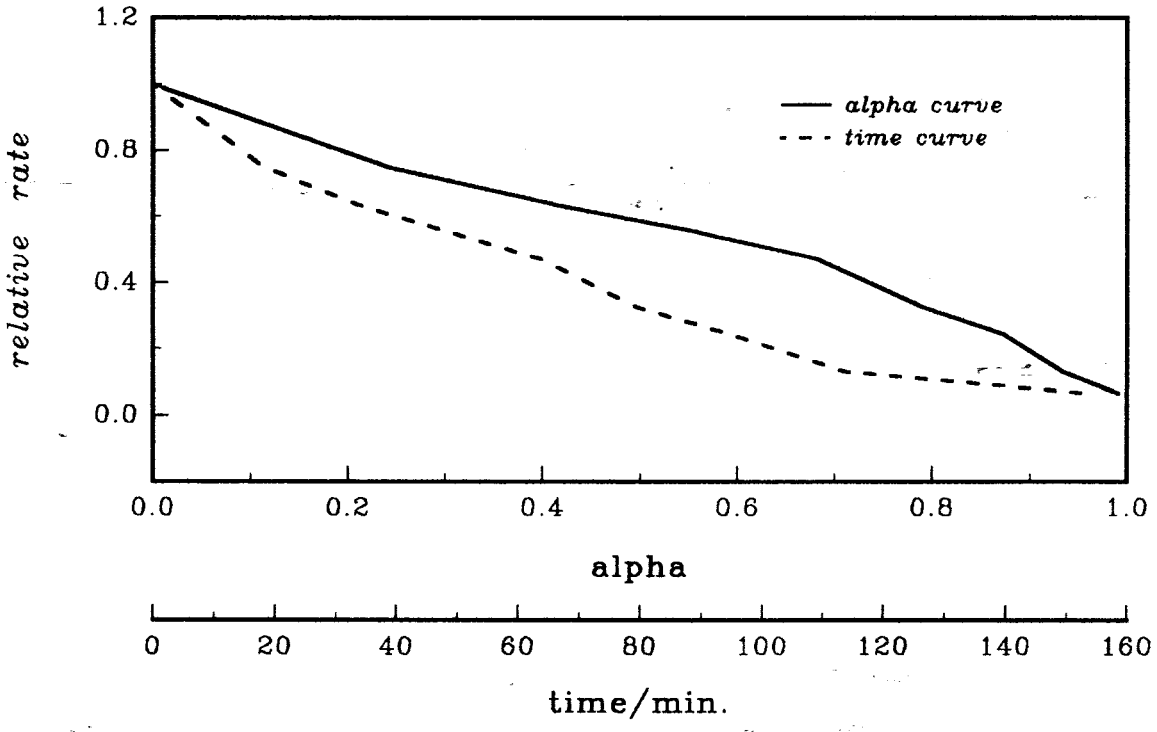

Figure 10.2.7o: Plots of rate versus alpha and rate versus time for the decomposition of $Ni(aa)Cl_2$ at 200°C.

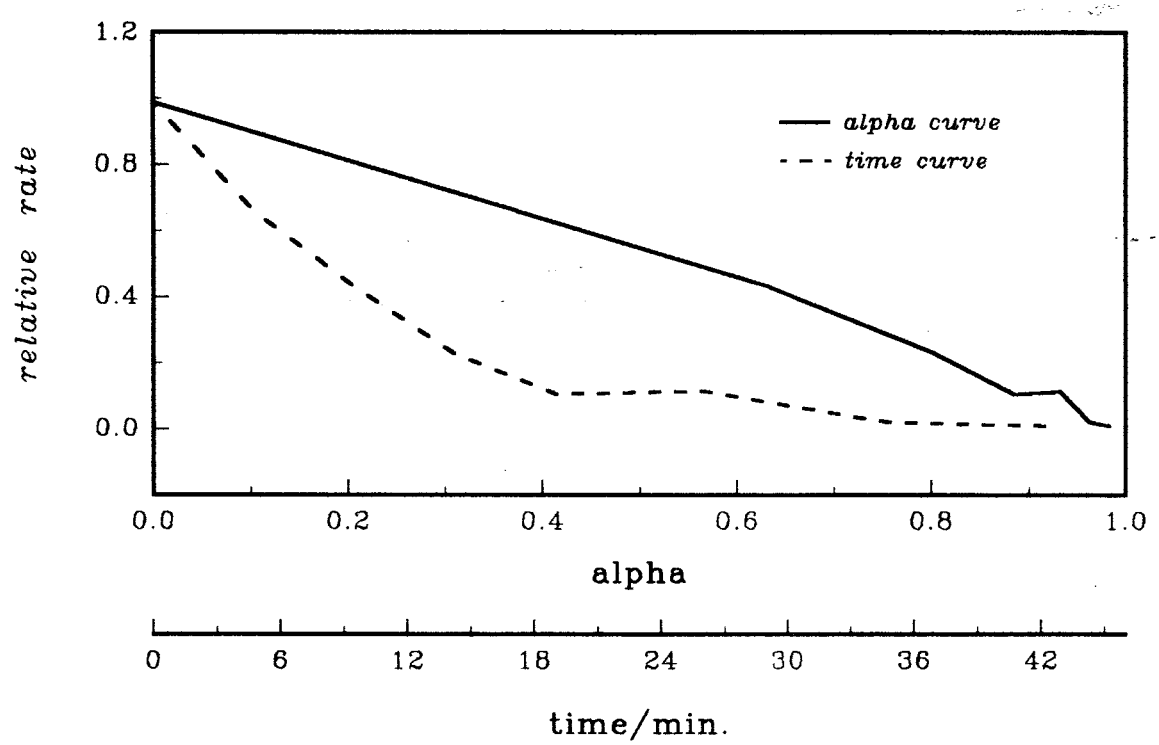

Figure 10.2.7p: Plots of rate versus alpha and rate versus time for the decomposition of $Ni(aa)Cl_2$ at 213°C.

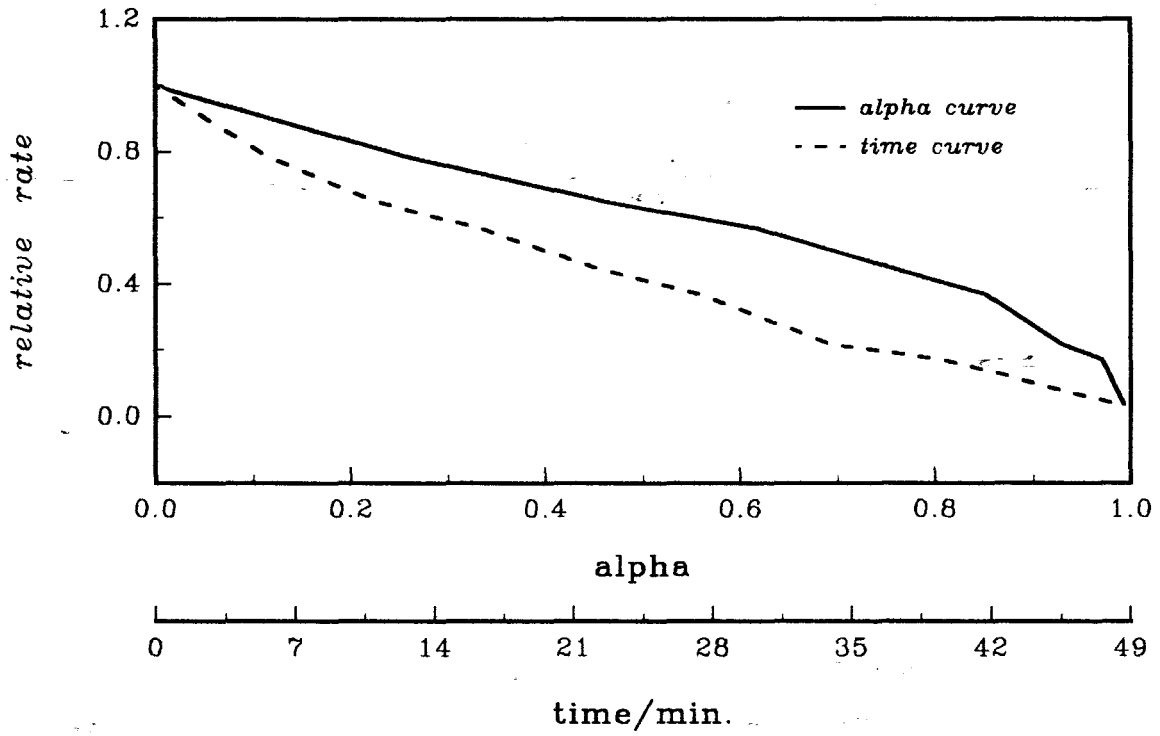

Figure 10.2.7q: Plots of rate versus alpha and rate versus time for the decomposition of $Ni(aa)Cl_2$ at 203°C.

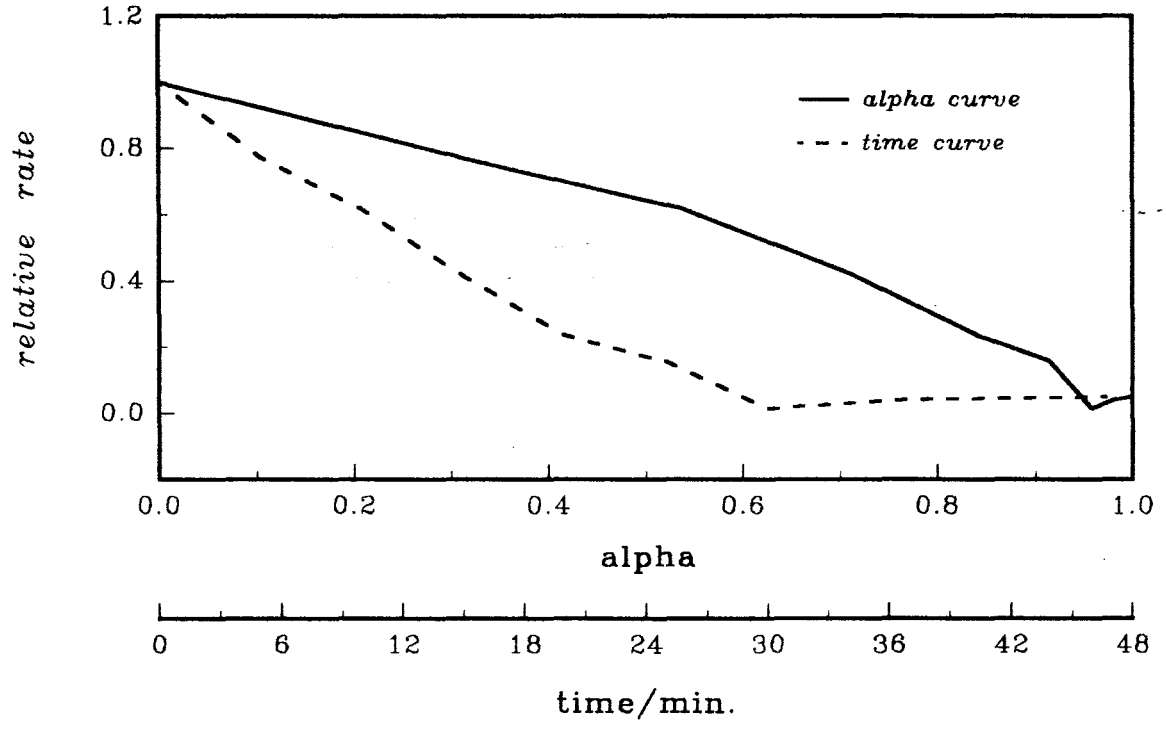

Figure 10.2.7r: Plots of rate versus alpha and rate versus time for the decomposition of $Ni(aa)Cl_2$ at 208°C.

APPENDIX IV

Chapter 10

Table 10.3.4b: Rate coefficients for the decomposition of Ni(*nma*)Cℓ_2 at different constant temperatures calculated using the **R2**, **R3** or **F1** rate expression over $0.00 \leq \alpha \leq 0.80$.

	R2 model		**R3 model**		**F1 model**	
T /°C	k / 10^{-3} s^{-1}	r	k / 10^{-3} s^{-1}	r	k / 10^{-3} s^{-1}	r
210	11.839 ± 0.035	0.9979	13.336 ± 0.014	0.9998	17.151 ± 0.067	0.9964
208	8.916 ± 0.023	0.9986	10.029 ± 0.010	0.9998	12.858 ± 0.061	0.9953
205	7.305 ± 0.044	0.9929	8.256 ± 0.031	0.9973	10.690 ± 0.022	0.9992
200	7.662 ± 0.038	0.9971	8.636 ± 0.002	0.9995	11.116 ± 0.053	0.9973
200*	4.294 ± 0.009	0.9991	4.824 ± 0.007	0.9995	6.172 ± 0.033	0.9936
198	3.639 ± 0.030	0.9853	4.126 ± 0.025	0.9922	5.363 ± 0.005	0.9993
195	3.952 ± 0.006	0.9991	4.025 ± 0.005	0.9997	5.154 ± 0.025	0.9938
193	2.919 ± 0.010	0.9973	3.289 ± 0.005	0.9994	4.232 ± 0.015	0.9969
190	2.919 ± 0.006	0.9991	3.281 ± 0.005	0.9994	4.201 ± 0.022	0.9932
188	2.172 ± 0.003	0.9994	2.440 ± 0.003	0.9995	3.121 ± 0.017	0.9928
185	1.694 ± 0.004	0.9982	1.907 ± 0.002	0.9997	2.450 ± 0.009	0.9959
183	0.689 ± 0.005	0.9773	0.784 ± 0.005	0.9853	1.029 ± 0.003	0.9952
180	1.073 ± 0.005	0.9949	1.211 ± 0.003	0.9984	1.564 ± 0.003	0.9986
178	0.840 ± 0.003	0.9954	0.947 ± 0.002	0.9984	1.220 ± 0.003	0.9978
175	0.678 ± 0.003	0.9950	0.765 ± 0.002	0.9984	0.987 ± 0.002	0.9984
175*	0.700 ± 0.003	0.9944	0.790 ± 0.002	0.9980	1.019 ± 0.002	0.9986
173	0.437 ± 0.002	0.9883	0.494 ± 0.002	0.9941	0.643 ± 0.001	0.9991
170	0.430 ± 0.001	0.9973	0.485 ± 0.001	0.9995	0.584 ± 0.002	0.9916
170*	0.489 ± 0.001	0.9971	0.550 ± 0.001	0.9994	0.708 ± 0.002	0.9972

* run in replicate

Table 10.3.6b: Rate coefficients for the decomposition of Ni(*nma*)Cℓ_2 at different constant temperatures calculated using the empirical **(B2)** rate expression, $\upsilon_r = 1 - (kt)^2$, over α ranges indicated.

	α-range: 0.05 - 0.75		α-range: 0.05 - 0.70	
T / °C	k / 10^{-3} s^{-1}	r	k / 10^{-3} s^{-1}	r
210	7.612 ± 0.089	0.9721	7.955 ± 0.103	0.9700
208	5.980 ± 0.069	0.9760	6.225 ± 0.080	0.9738
205	4.684 ± 0.061	0.9729	4.952 ± 0.070	0.9719
200	5.469 ± 0.082	0.9764	5.801 ± 0.086	0.9798
200*	2.585 ± 0.065	0.8884	2.602 ± 0.082	0.8531
198	2.519 ± 0.050	0.9329	2.799 ± 0.056	0.9398
195	2.435 ± 0.022	0.9827	2.496 ± 0.026	0.9789
193	1.943 ± 0.019	0.9802	2.010 ± 0.022	0.9782
190	2.042 ± 0.022	0.9757	2.053 ± 0.027	0.9673
188	1.319 ± 0.014	0.9749	1.333 ± 0.017	0.9673
185	1.037 ± 0.009	0.9803	1.072 ± 0.011	0.9776
183	0.582 ± 0.006	0.9586	0.591 ± 0.009	0.9359
180	0.800 ± 0.008	0.9751	0.848 ± 0.009	0.9774
178	0.563 ± 0.008	0.9432	0.563 ± 0.011	0.9205
175	0.437 ± 0.006	0.9521	0.453 ± 0.008	0.9392
175*	0.469 ± 0.005	0.9650	0.482 ± 0.006	0.9566
173	0.338 ± 0.004	0.9624	0.358 ± 0.004	0.9606
170	0.240 ± 0.005	0.9091	0.250 ± 0.006	0.8859
170*	0.302 ± 0.003	0.9531	0.311 ± 0.005	0.9394

* run in replicate

Table 10.3.7: Rate coefficients and values of b for the decomposition of N(*nma*)Cℓ_2 at different constant temperatures calculated using the empirical (**B2**) rate expression, $\ell n(1 - \upsilon_r) = b\ell n(t) + \ell n(k)$, over $0.05 \leq \alpha \leq 0.85$.

T / °C	slope = b	k / 10^{-3} s^{-1}	r
210	1.118 ± 0.020	7.822 ± 0.020	0.9795
208	1.289 ± 0.011	5.969 ± 0.011	0.9862
205	0.839 ± 0.011	4.600 ± 0.011	0.9682
200	1.272 ± 0.014	5.483 ± 0.014	0.9873
200*	1.516 ± 0.027	2.927 ± 0.027	0.9406
198	0.904 ± 0.014	2.957 ± 0.014	0.9563
195	1.552 ± 0.022	2.470 ± 0.022	0.9539
193	1.216 ± 0.114	1.986 ± 0.011	0.9810
190	1.962 ± 0.033	2.167 ± 0.033	0.9405
188	1.274 ± 0.017	1.278 ± 0.017	0.9584
185	1.040 ± 0.009	1.020 ± 0.009	0.9792
183	1.430 ± 0.018	0.610 ± 0.018	0.9368
180	1.367 ± 0.013	0.834 ± 0.013	0.9774
178	1.221 ± 0.025	0.571 ± 0.025	0.8874
175	1.127 ± 0.019	0.470 ± 0.019	0.9265
175*	1.113 ± 0.014	0.487 ± 0.014	0.9497
173	1.430 ± 0.022	0.367 ± 0.022	0.9237
170	0.946 ± 0.018	0.271 ± 0.018	0.9002
170*	1.022 ± 0.013	0.313 ± 0.013	0.9448

* run in replicate

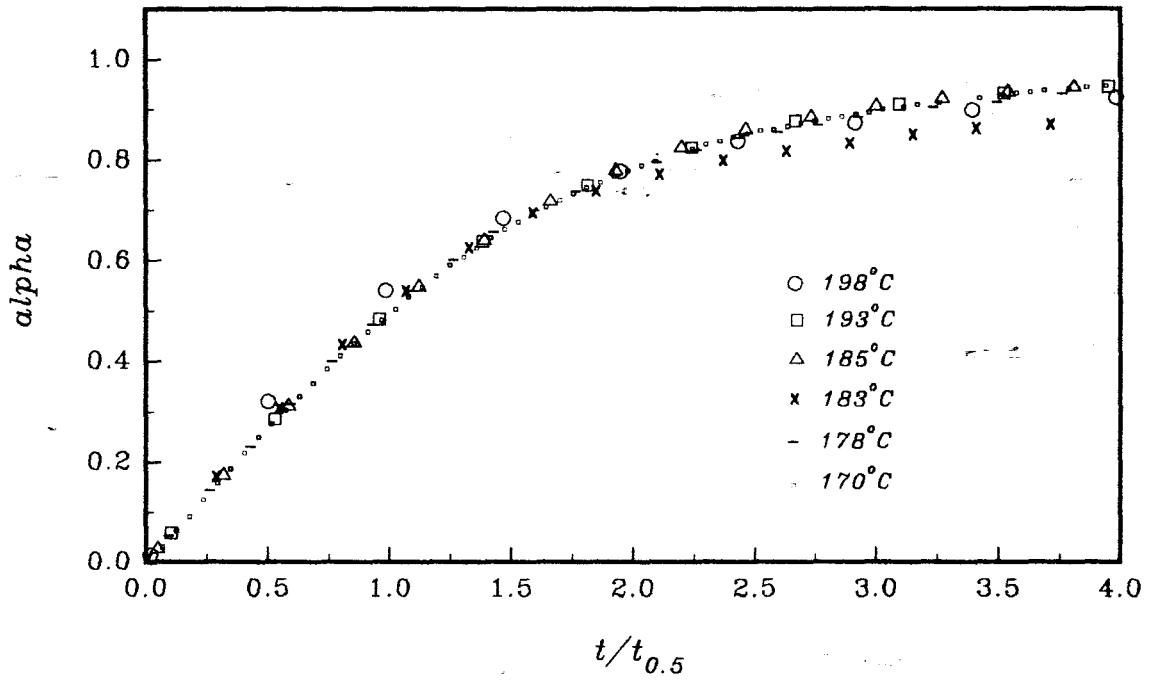

Figure 10.3.3b: Comparison of reduced-time plots for the decomposition of $Ni(nma)Cl_2$ at a series of constant temperatures.

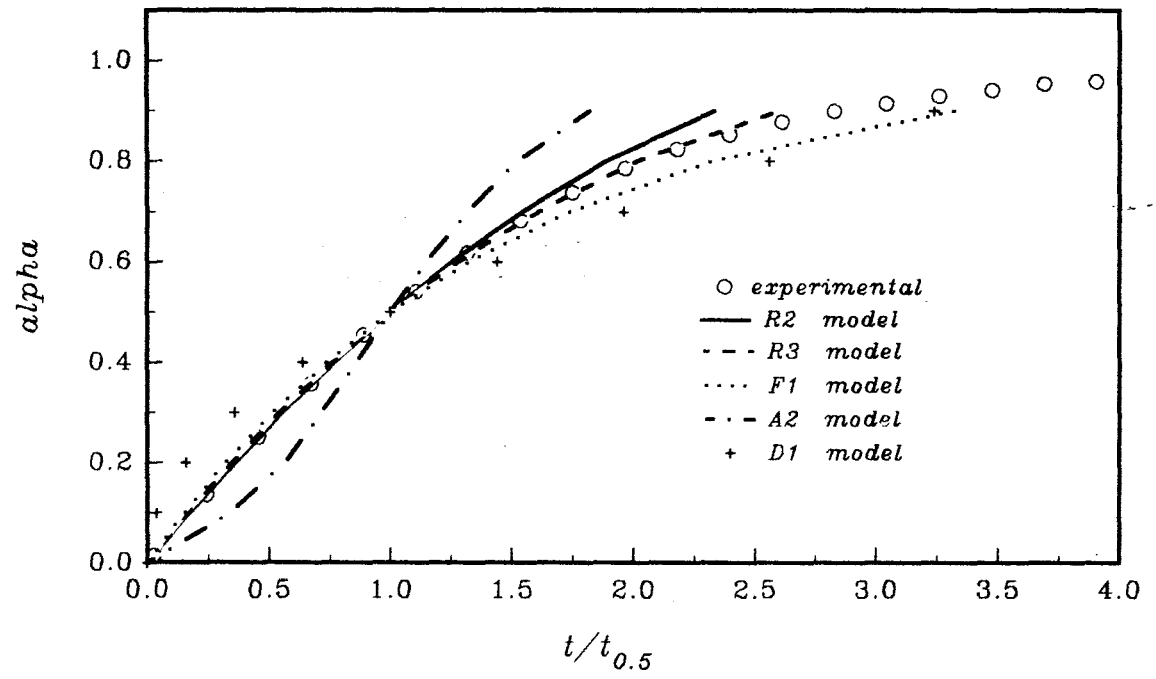

Figure 10.3.4b: Reduced-time plot for the decomposition of $Ni(nma)Cl_2$ at 210°C, compared with calculated plots for various kinetic models.

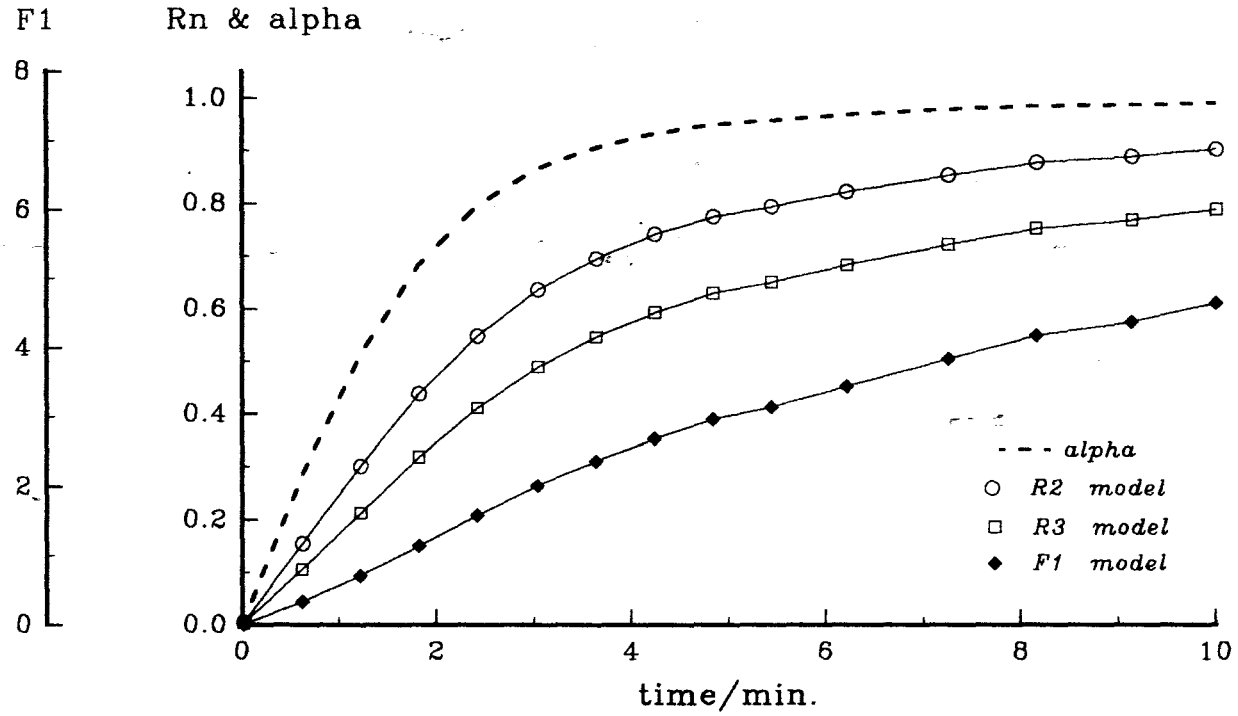

Figure 10.3.5b: Plots of $g(\alpha)$ versus time for the decomposition of $Ni(nma)Cl_2$ at 200°C. The α–time curve is included to show the range of α over which $g(\alpha)$ is approximately linear.

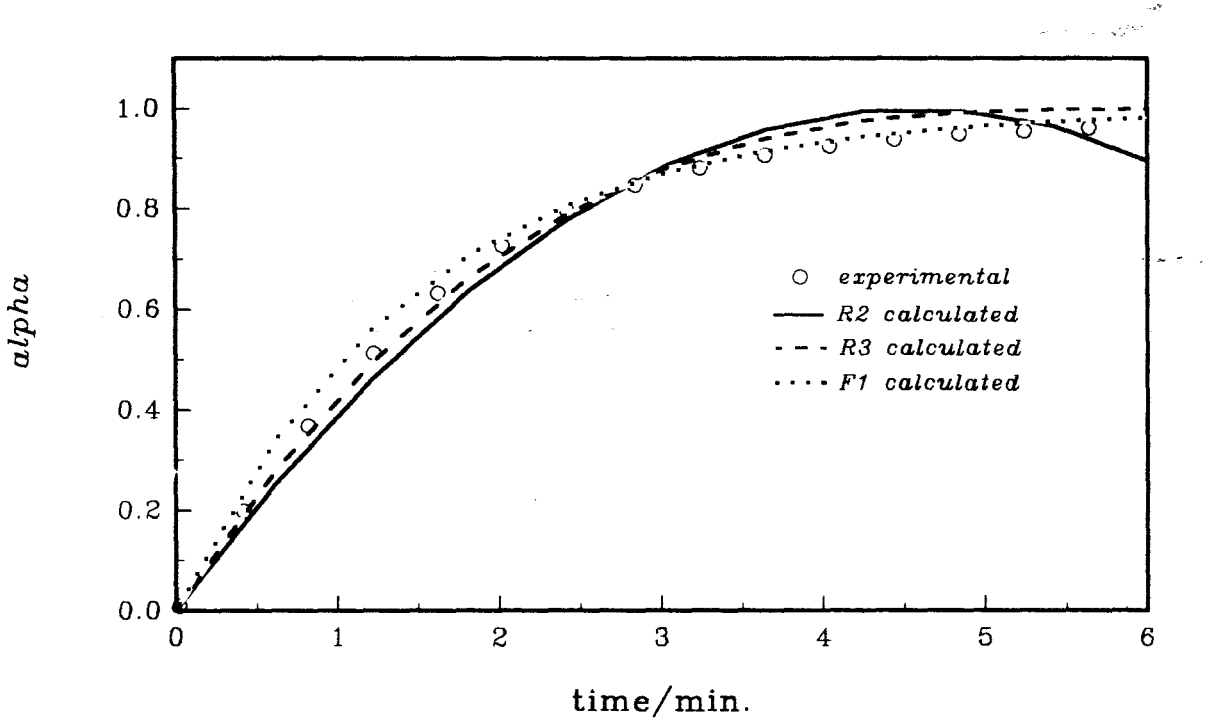

Figure 10.3.6b: Plots of $\alpha_{calc.}$ versus time using various kinetic models, compared with α_e versus time data for the decomposition of $Ni(nma)Cl_2$ at 200°C.

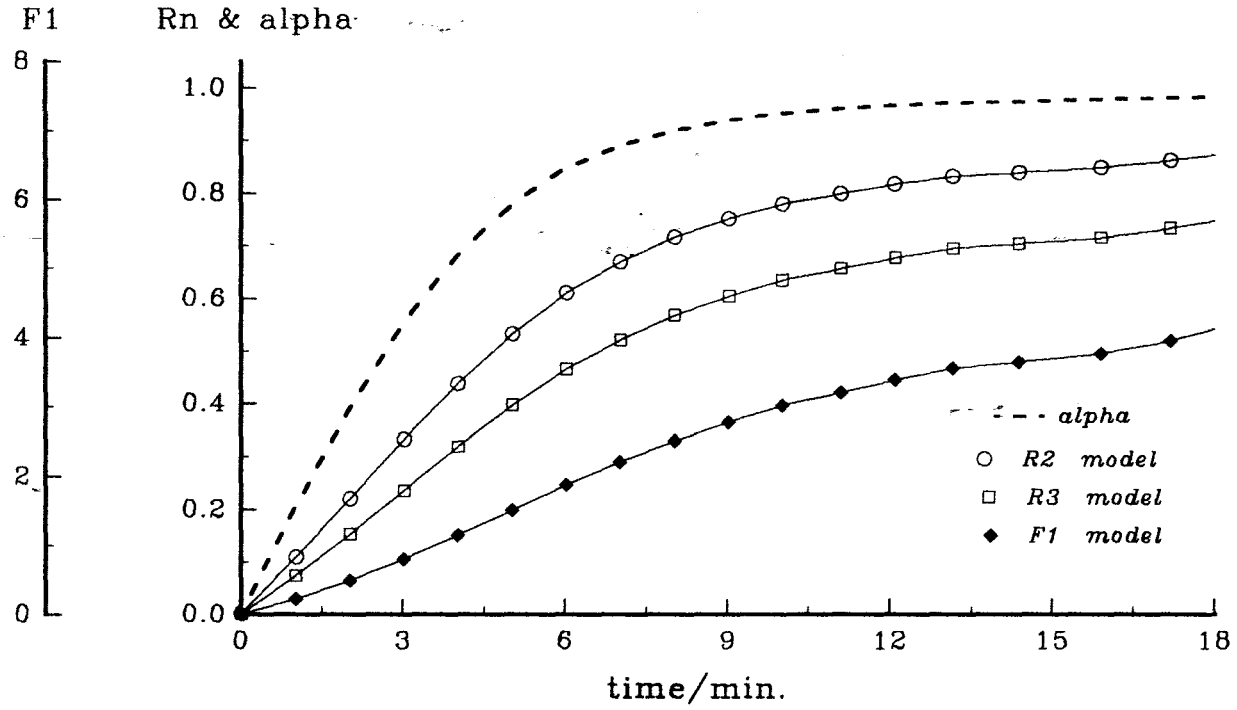

Figure 10.3.5c: Plots of g(α) versus time for the decomposition of $Ni(nma)Cl_2$ at 195°C. The α–time curve is included to show the range of α over which g(α) is approximately linear.

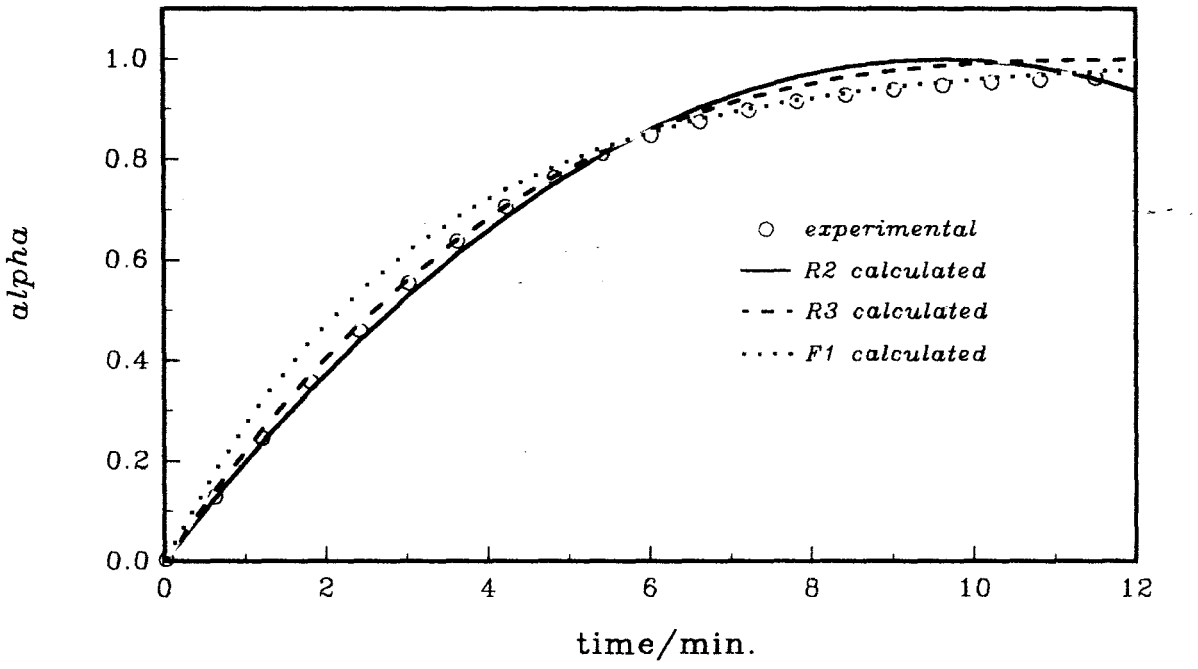

Figure 10.3.6c: Plots of $\alpha_{calc.}$ versus time using various kinetic models, compared with α_e versus time data for the decomposition of $Ni(nma)Cl_2$ at 195°C.

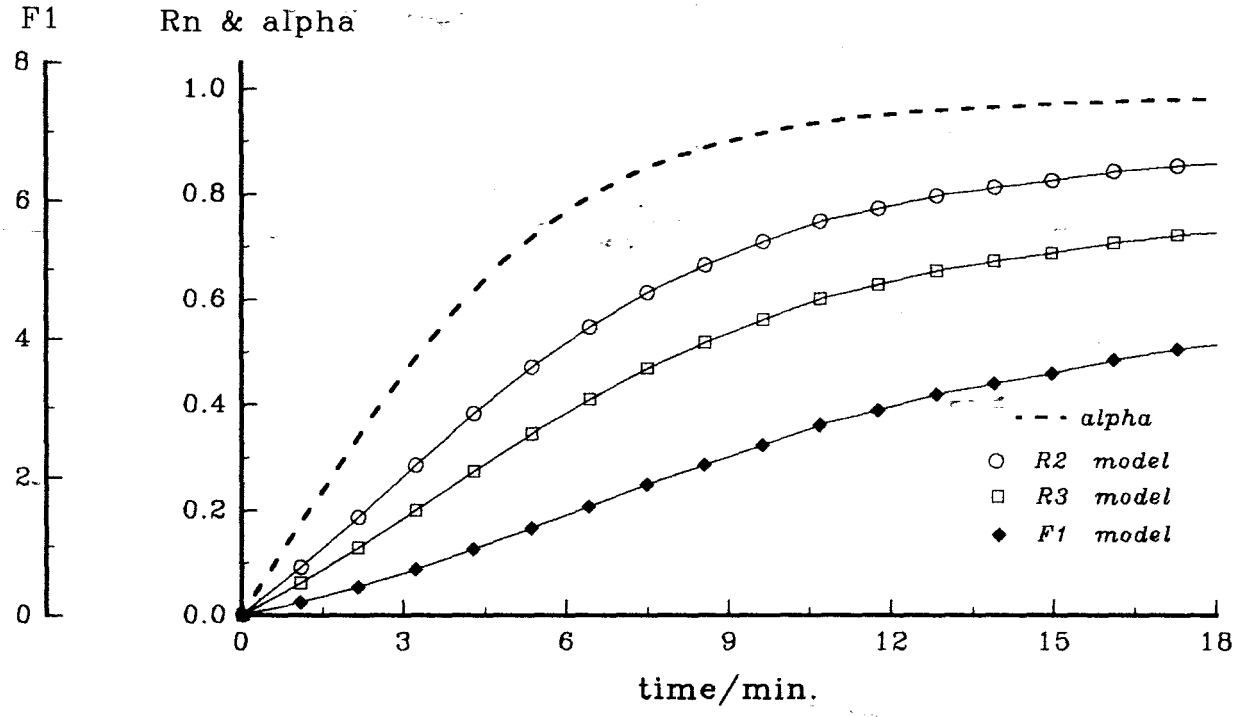

Figure 10.3.5d: Plots of $g(\alpha)$ versus time for the decomposition of $Ni(nma)Cl_2$ at 190°C. The α–time curve is included to show the range of α over which $g(\alpha)$ is approximately linear.

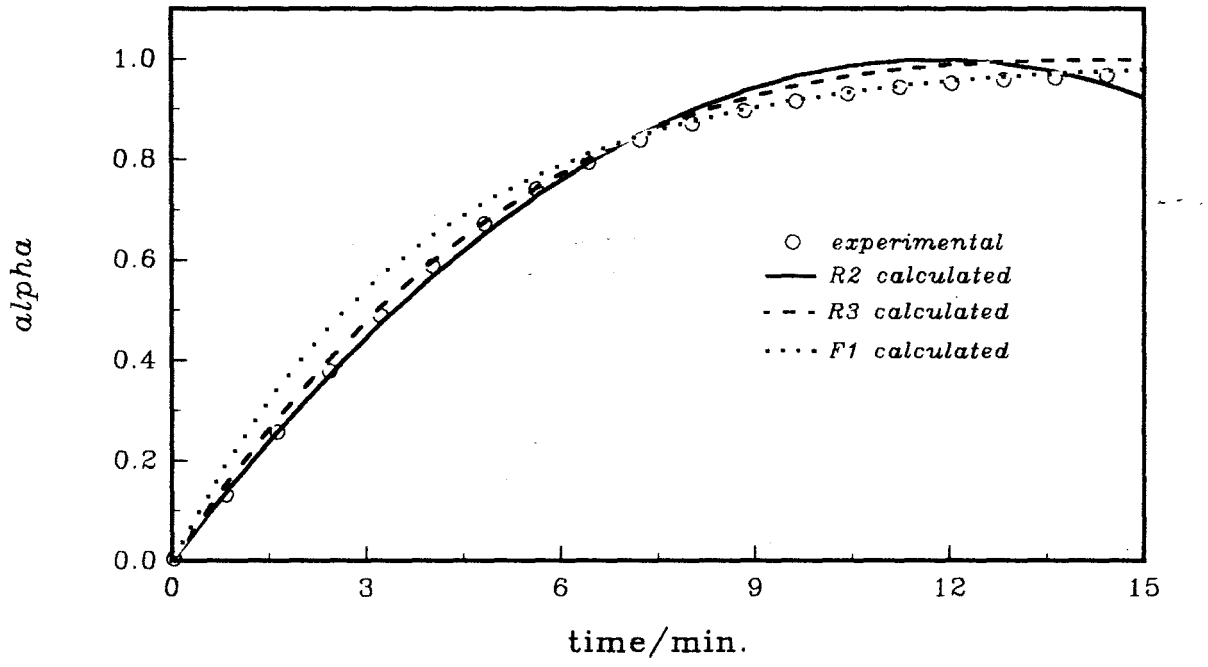

Figure 10.3.6d: Plots of $\alpha_{calc.}$ versus time using various kinetic models, compared with α_e versus time data for the decomposition of $Ni(nma)Cl_2$ at 190°C.

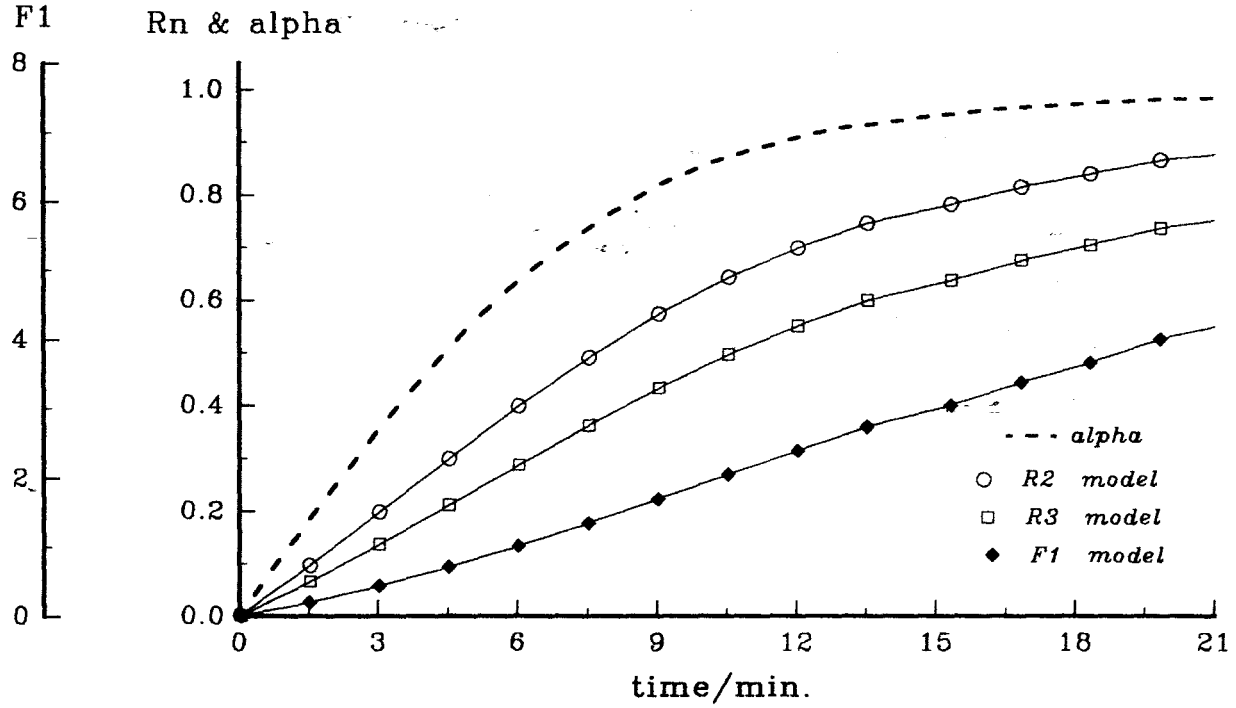

Figure 10.3.5e: Plots of $g(\alpha)$ versus time for the decomposition of $Ni(nma)Cl_2$ at 188°C. The α–time curve is included to show the range of α over which $g(\alpha)$ is approximately linear.

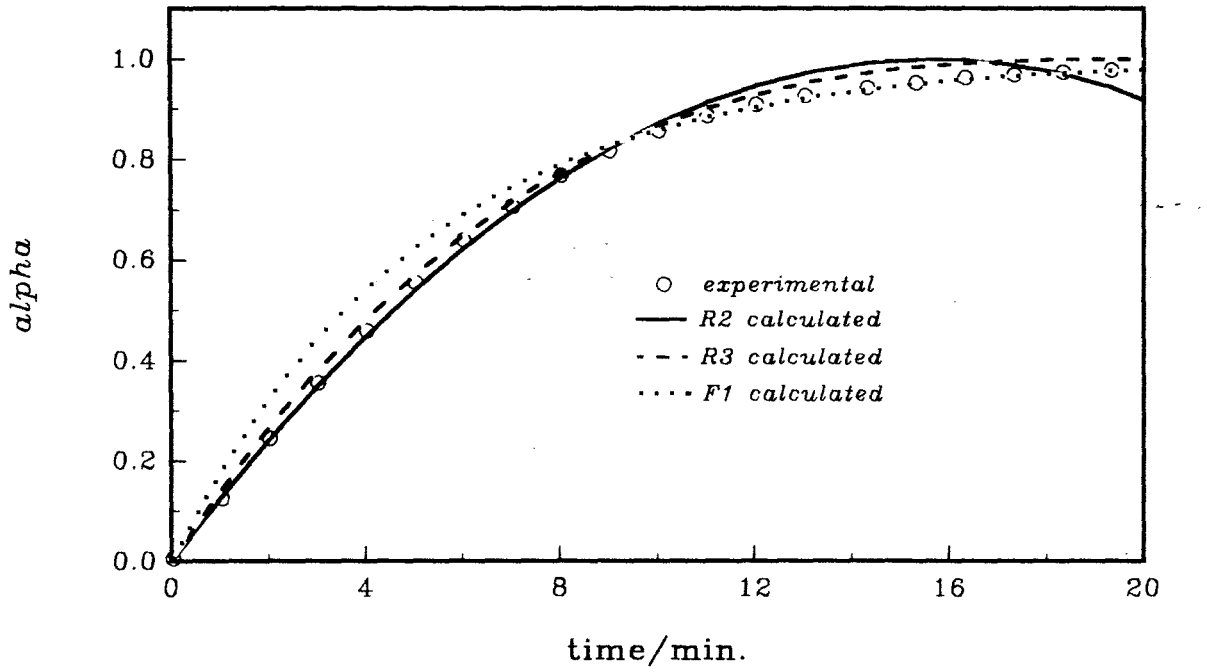

Figure 10.3.6e: Plots of $\alpha_{calc.}$ versus time using various kinetic models, compared with α_e versus time data for the decomposition of $Ni(nma)Cl_2$ at 188°C.

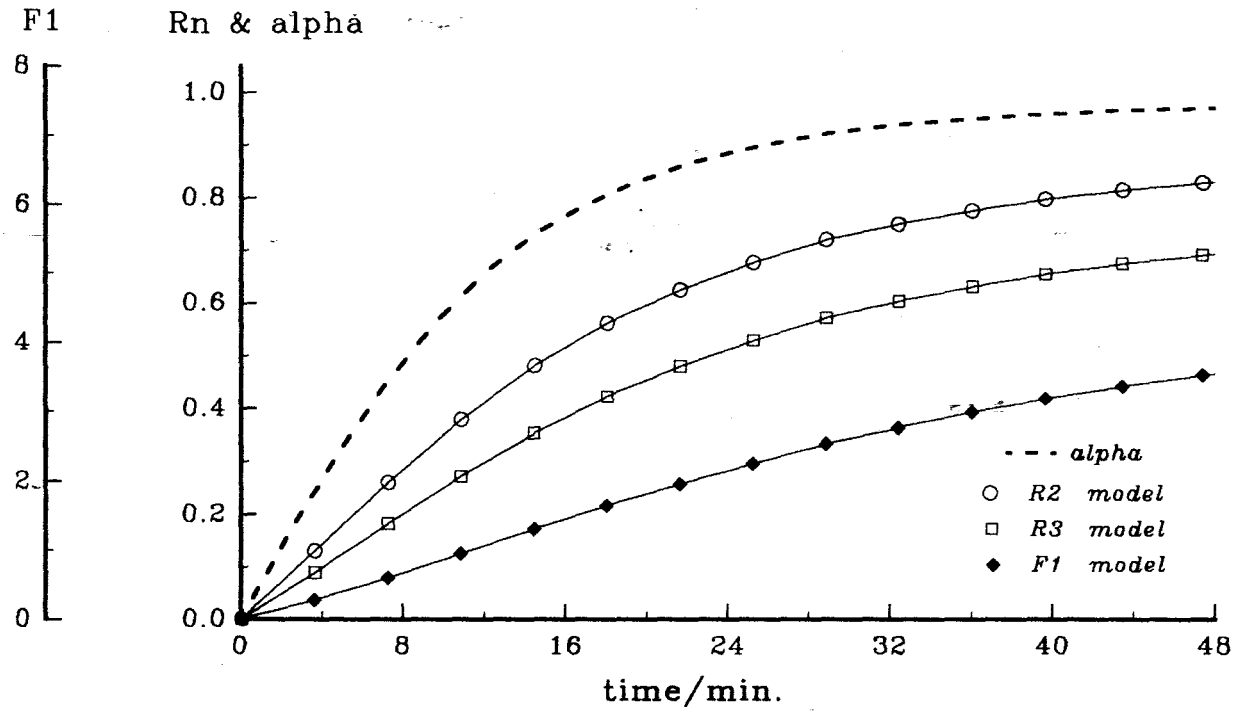

Figure 10.3.5f: Plots of $g(\alpha)$ versus time for the decomposition of $Ni(nma)Cl_2$ at 180°C. The α–time curve is included to show the range of α over which $g(\alpha)$ is approximately linear.

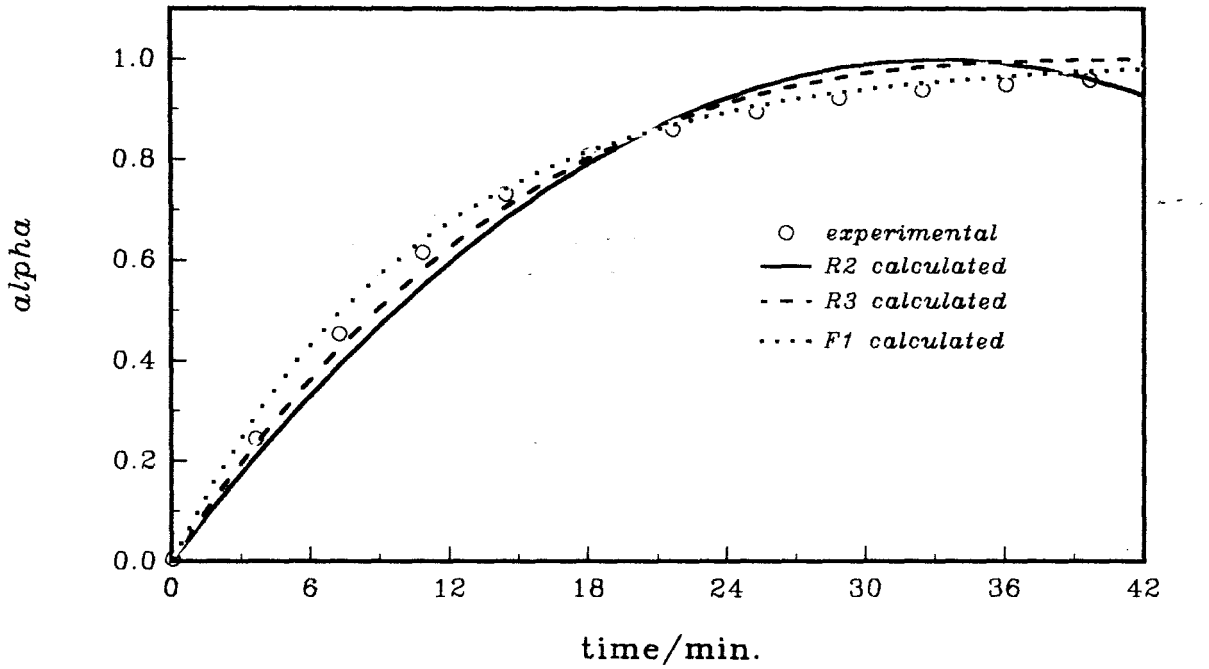

Figure 10.3.6f: Plots of $\alpha_{calc.}$ versus time using various kinetic models, compared with α_e versus time data for the decomposition of $Ni(nma)Cl_2$ at 180°C.

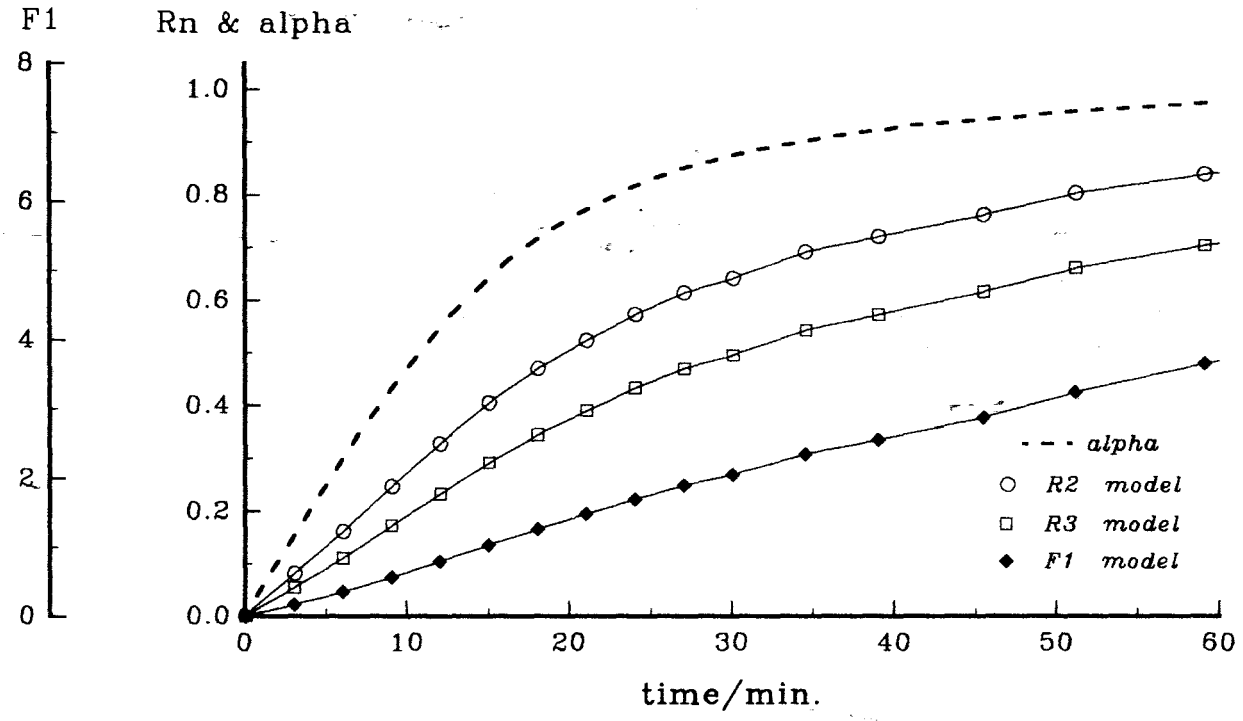

Figure 10.3.5g: Plots of $g(\alpha)$ versus time for the decomposition of $Ni(nma)Cl_2$ at 178°C. The α–time curve is included to show the range of α over which $g(\alpha)$ is approximately linear.

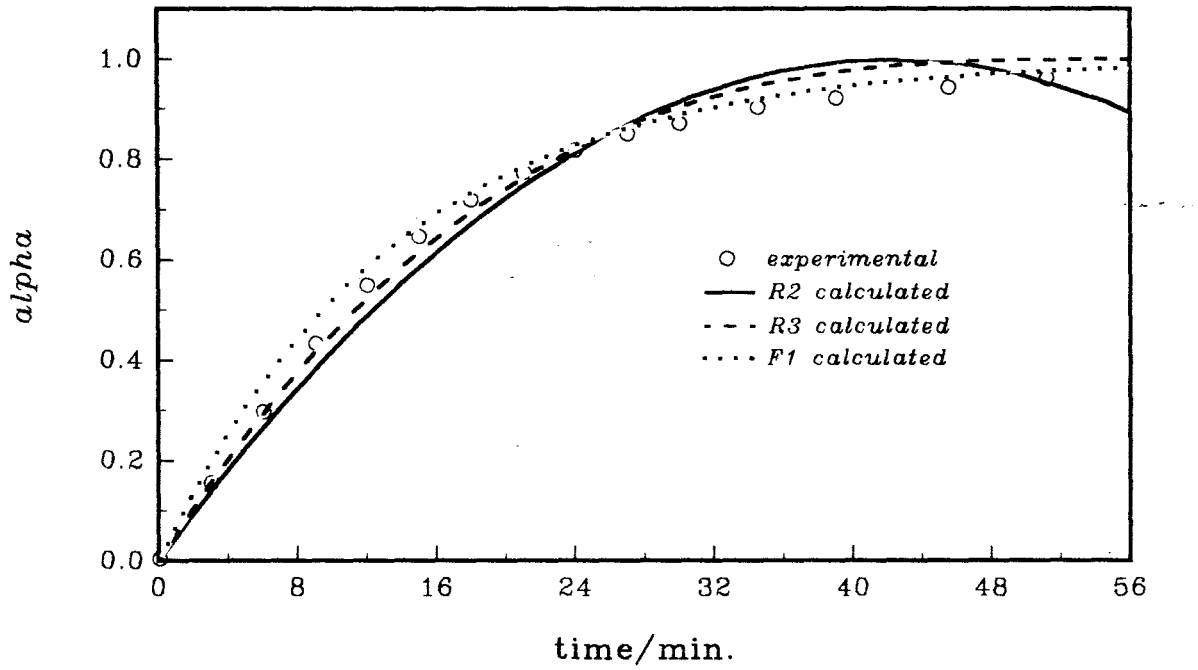

Figure 10.3.6g: Plots of $\alpha_{calc.}$ versus time using various kinetic models, compared to α_e versus time data for the decomposition of $Ni(nma)Cl_2$ at 178°C.

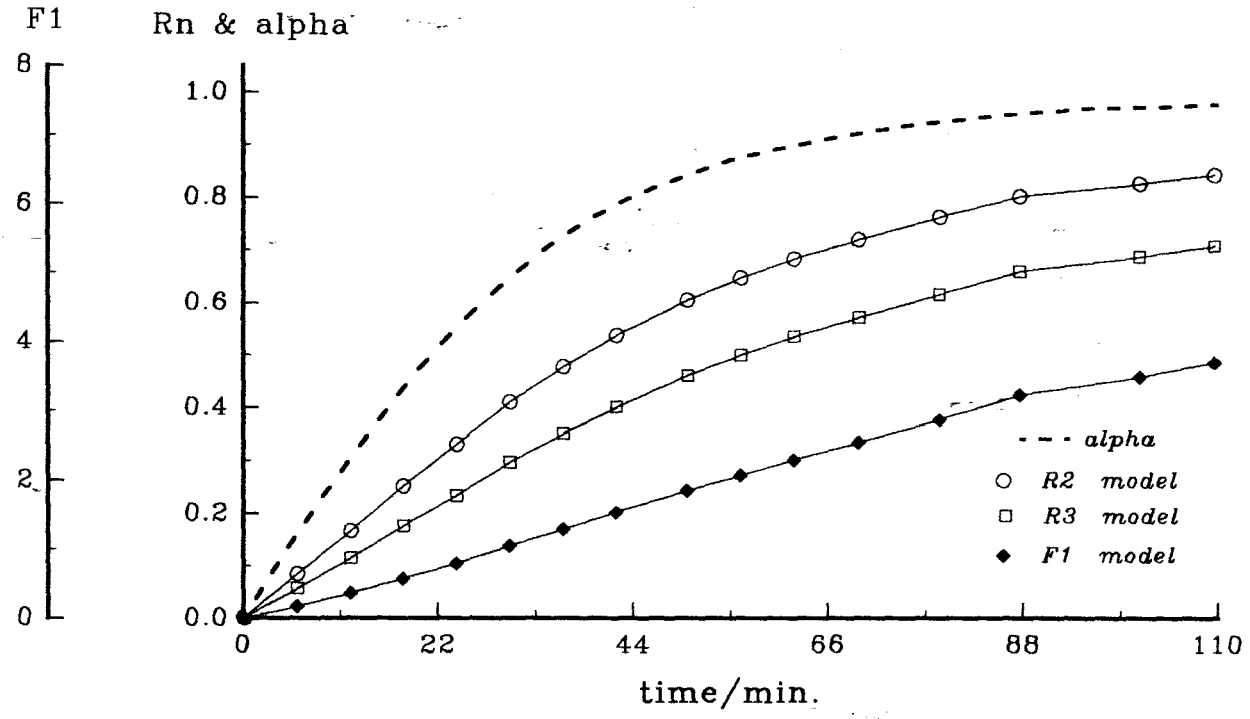

Figure 10.3.5h: Plots of $g(\alpha)$ versus time for the decomposition of $Ni(nma)Cl_2$ at 170°C. The α–time curve is included to show the range of α over which $g(\alpha)$ is approximately linear.

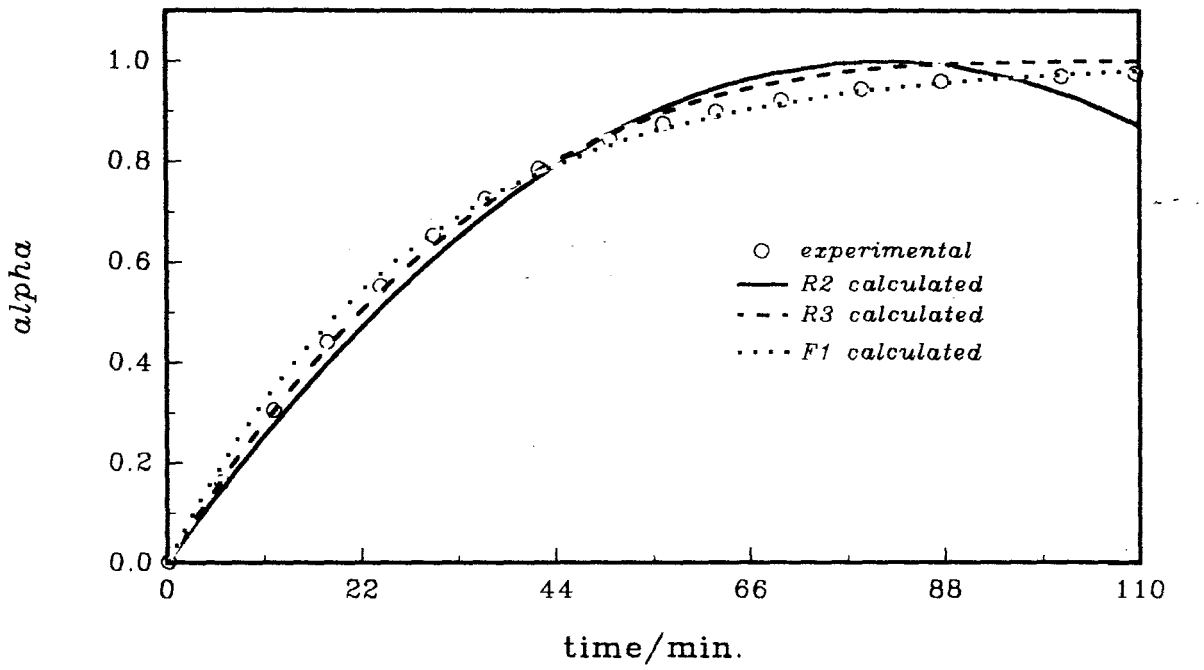

Figure 10.3.6h: Plots of $\alpha_{calc.}$ versus time using various kinetic models, compared with α_e versus time data for the decomposition of $Ni(nma)Cl_2$ at 170°C.

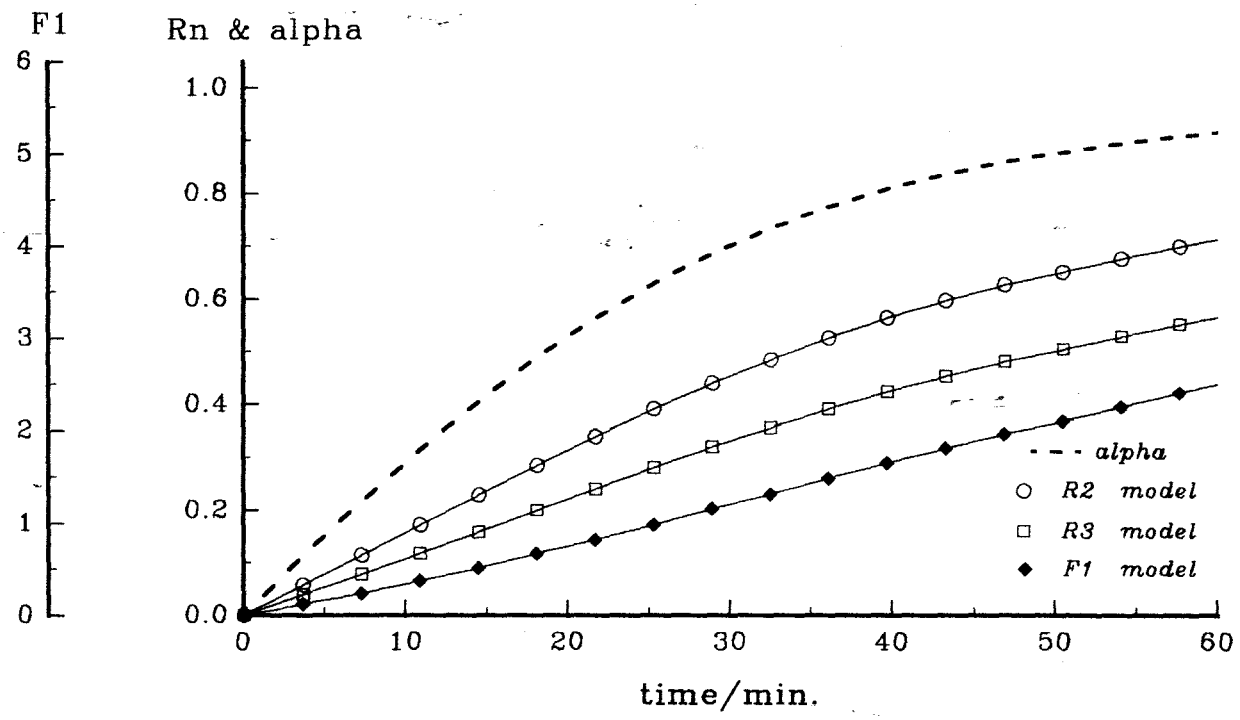

Figure 10.3.5i: Plots of $g(\alpha)$ versus time for the decomposition of $Ni(nma)Cl_2$ at 170°C.* The α–time curve is included to show the range of α over which $g(\alpha)$ is approximately linear.

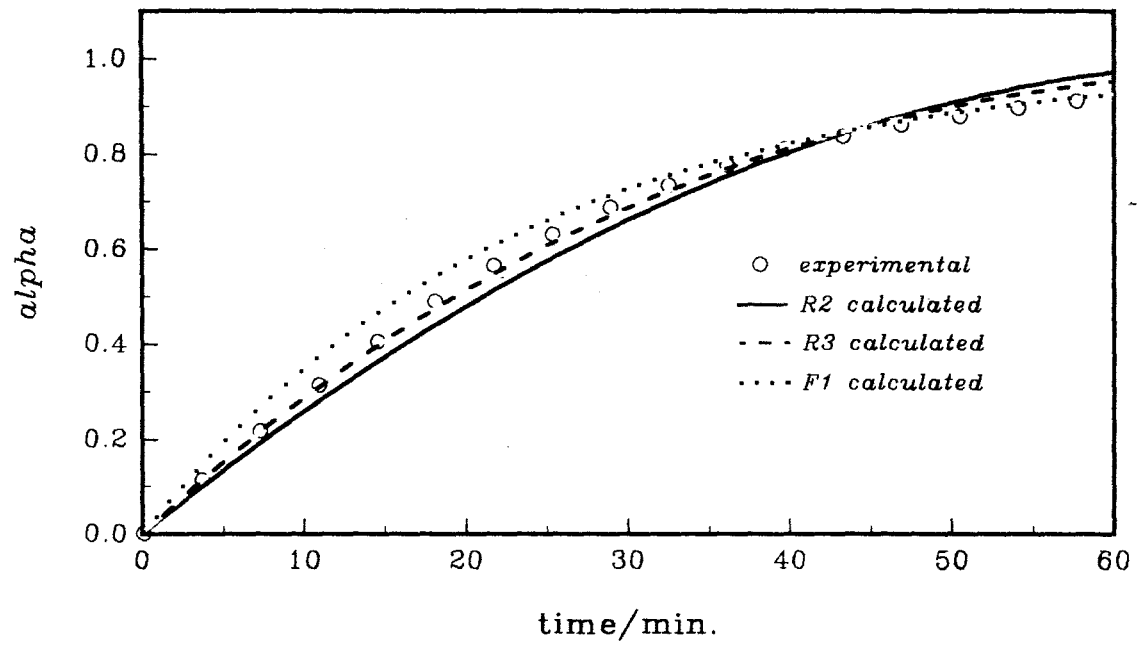

Figure 10.3.6i: Plots of $\alpha_{calc.}$ versus time using various kinetic models, compared with α_e versus time data for the decomposition of $Ni(nma)Cl_2$ at 170°C.*

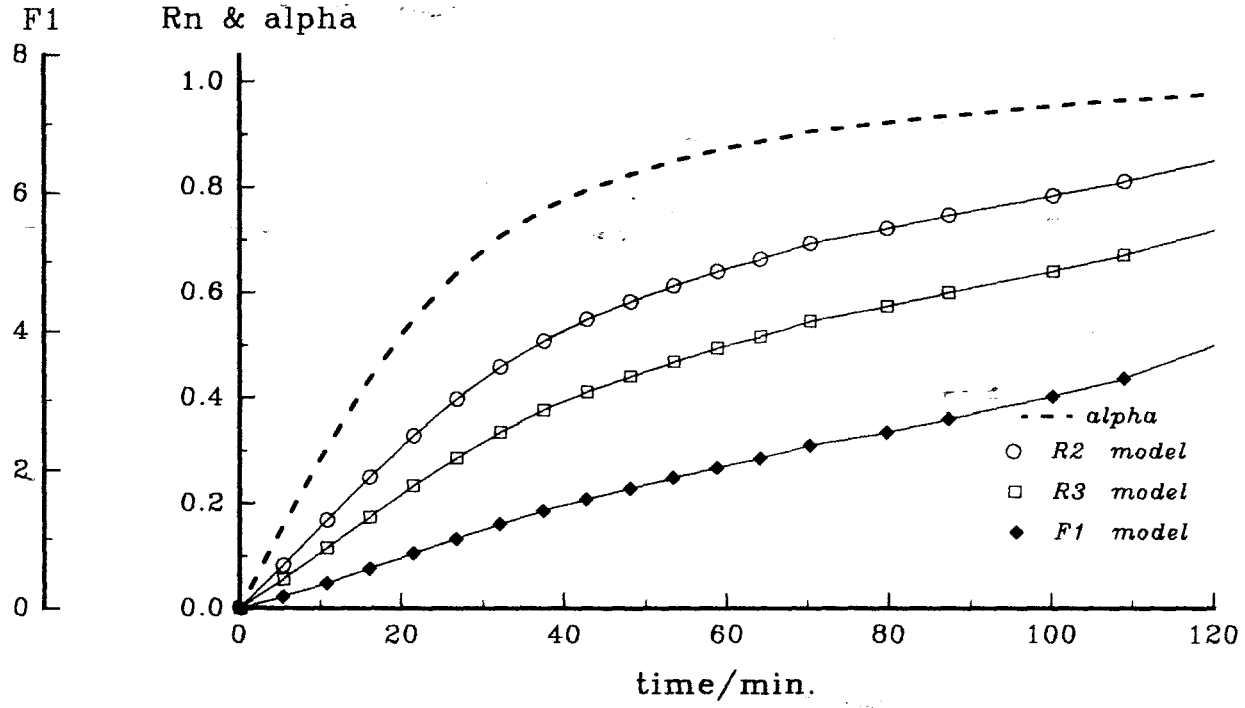

Figure 10.3.5j: Plots of $g(\alpha)$ versus time for the decomposition of $Ni(nma)Cl_2$ at 173°C. The α–time curve is included to show the range of α over which $g(\alpha)$ is approximately linear.

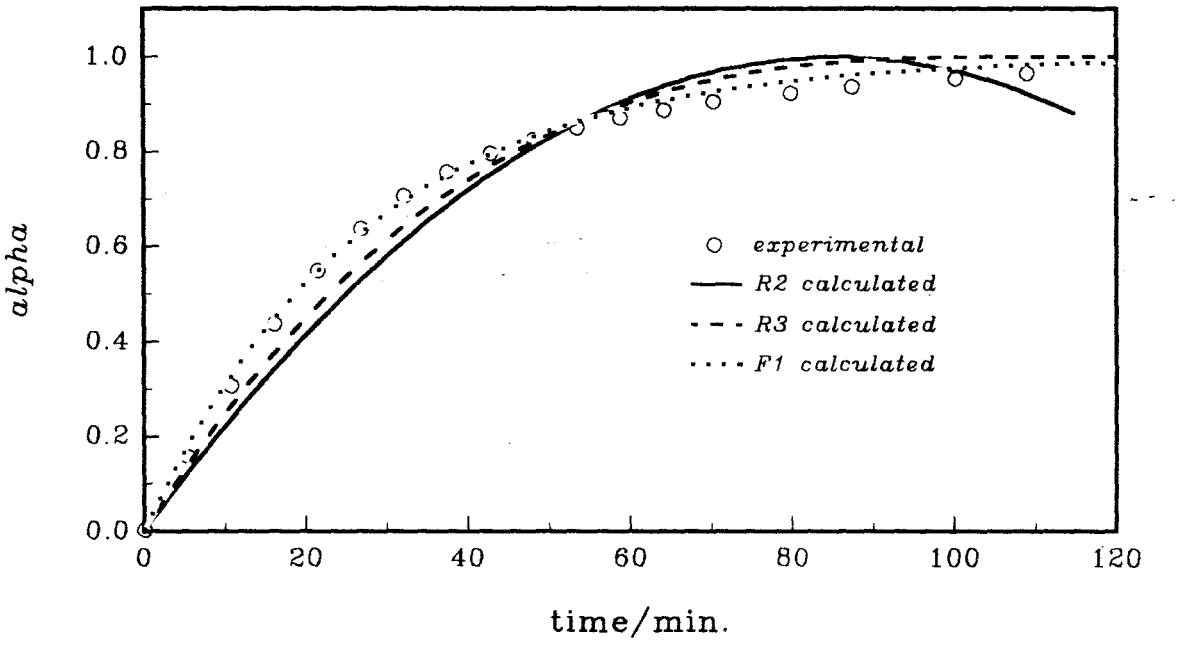

Figure 10.3.6j: Plots of $\alpha_{calc.}$ versus time using various kinetic models, compared with α_e versus time data for the decomposition of $Ni(nma)Cl_2$ at 173°C.

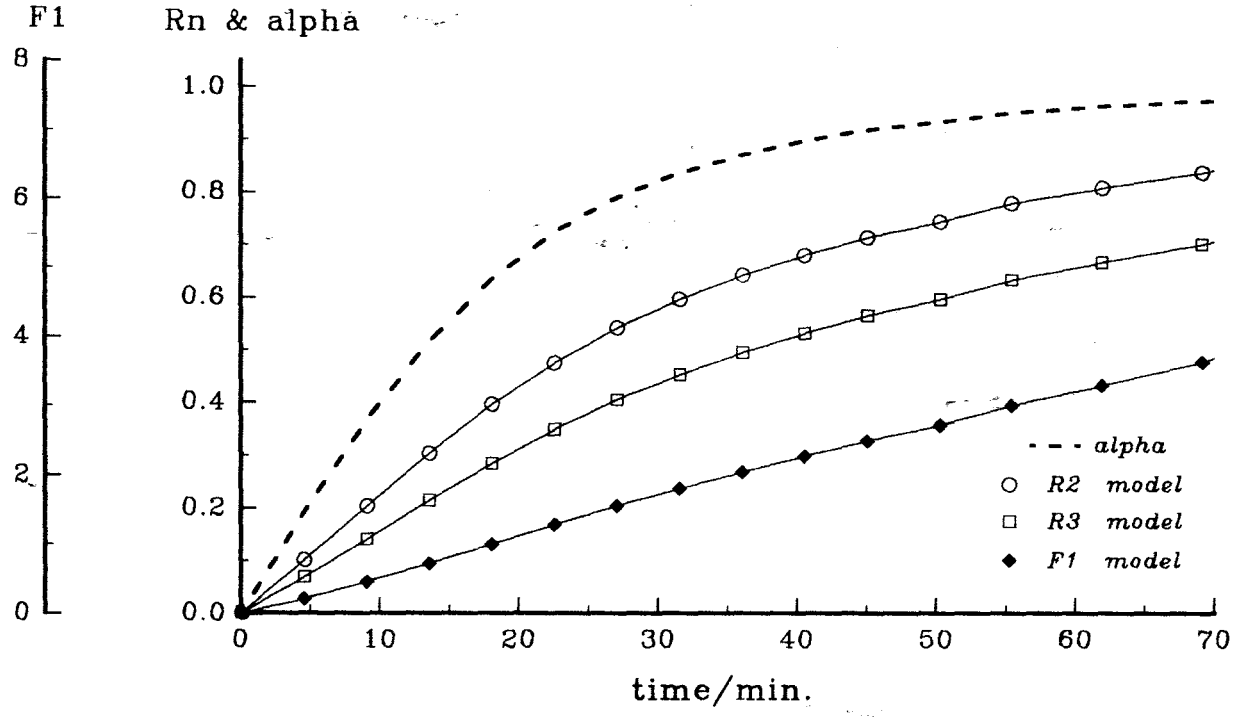

Figure 10.3.5k: Plots of $g(\alpha)$ versus time for the decomposition of $Ni(nma)Cl_2$ at 175°C. The α–time curve is included to show the range of α over which $g(\alpha)$ is approximately linear.

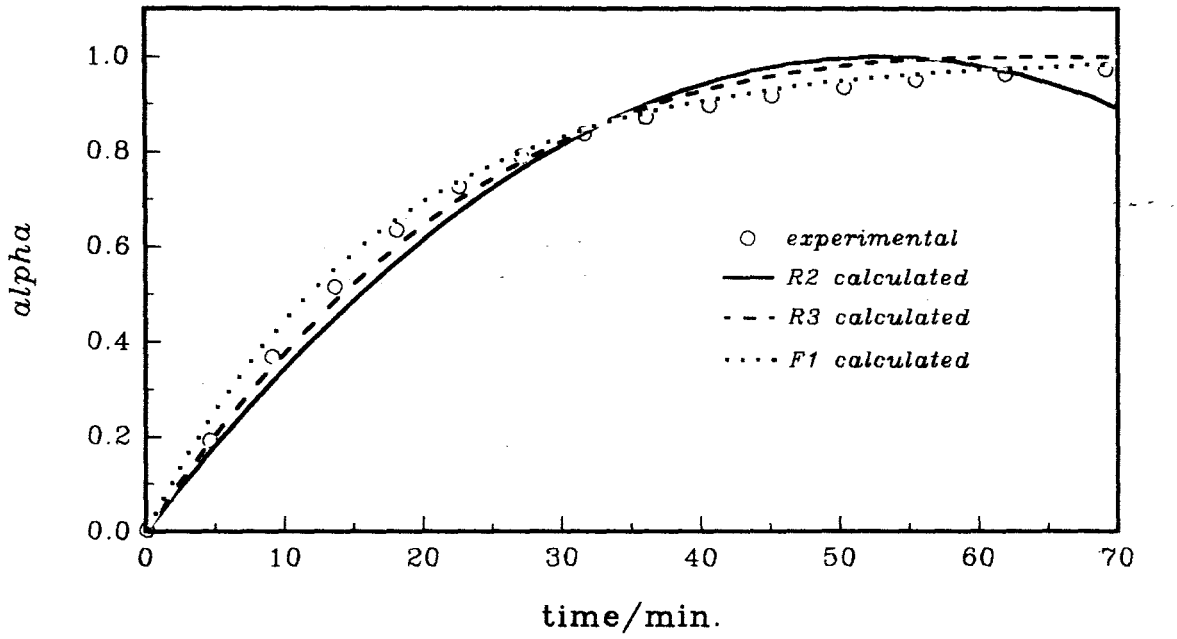

Figure 10.3.6k: Plots of $\alpha_{calc.}$ versus time using various kinetic models, compared with α_e versus time data for the decomposition of $Ni(nma)Cl_2$ at 175°C.

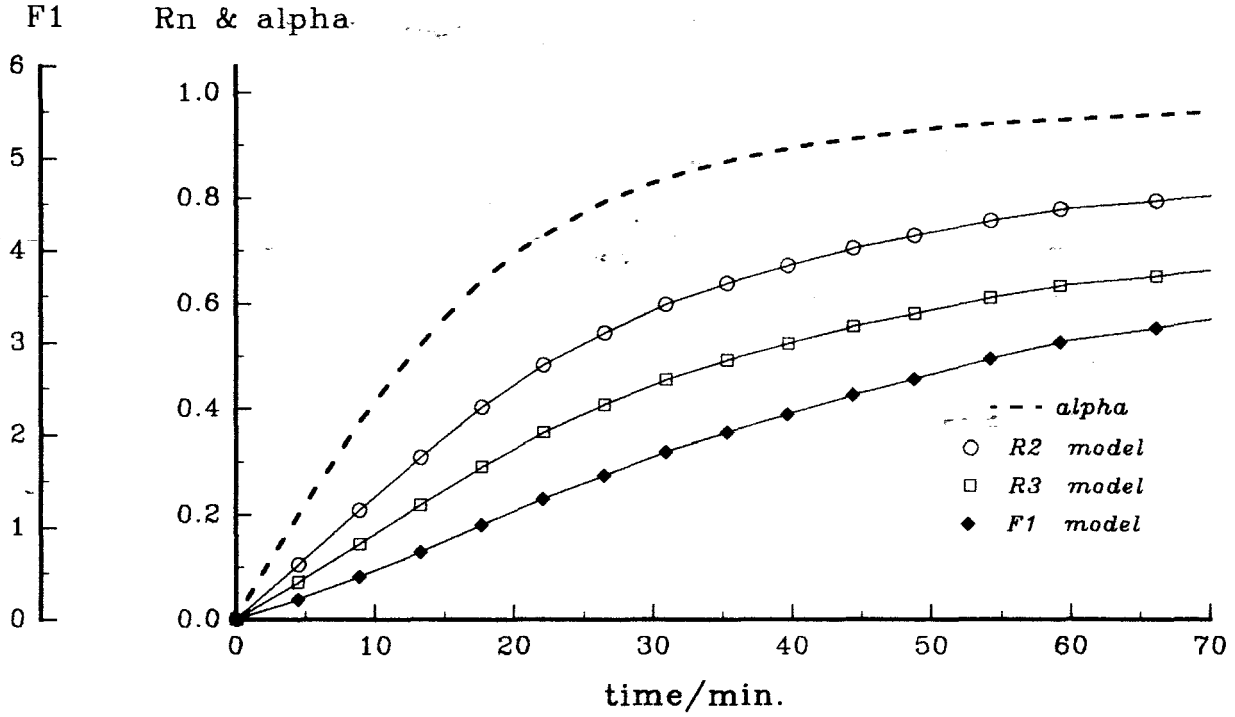

Figure 10.3.51: Plots of $g(\alpha)$ versus time for the decomposition of $Ni(nma)Cl_2$ at 175°C .* The α–time curve is included to show the range of α over which $g(\alpha)$ is approximately linear.

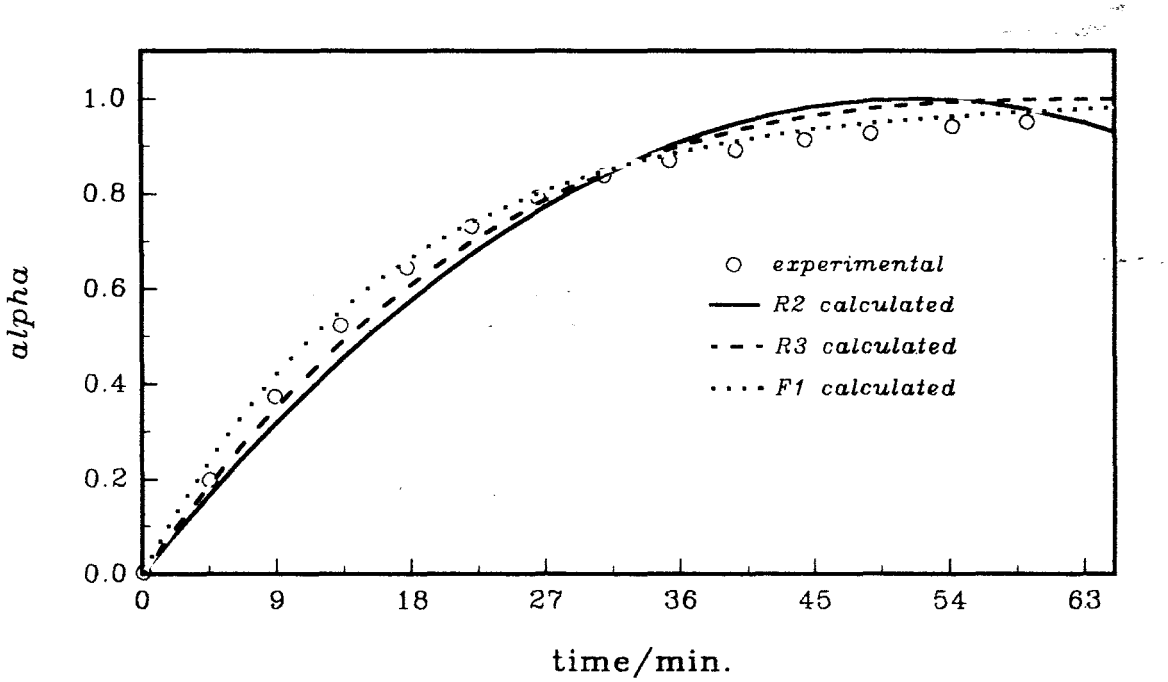

Figure 10.3.61: Plots of $\alpha_{calc.}$ versus time using various kinetic models, compared with α_e versus time data for the decomposition of $Ni(nma)Cl_2$ at 175°C .*

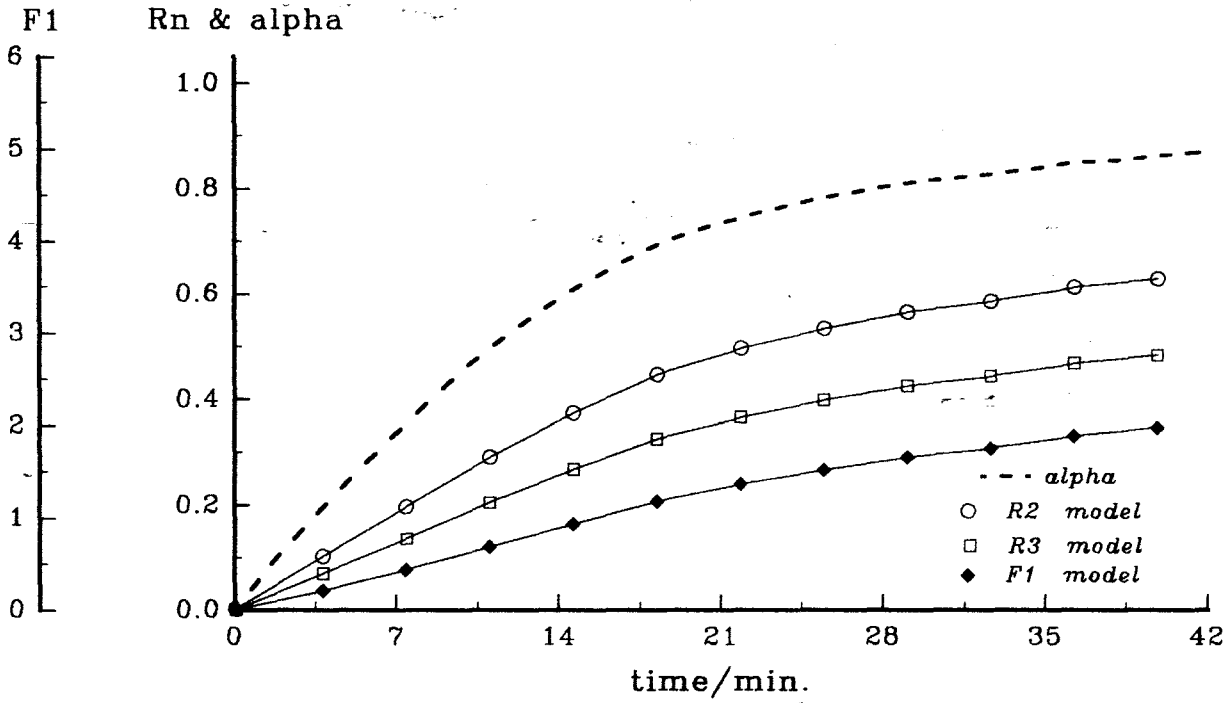

Figure 10.3.5m: Plots of $g(\alpha)$ versus time for the decomposition of $Ni(nma)Cl_2$ at 183°C. The α–time curve is included to show the range of α over which $g(\alpha)$ is approximately linear.

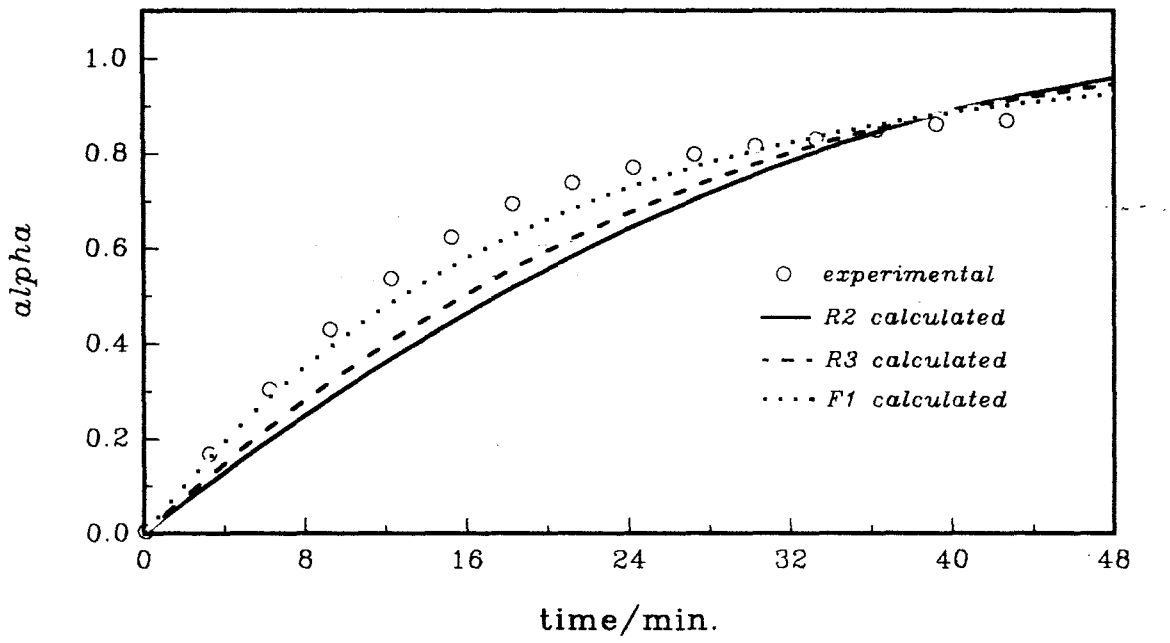

Figure 10.3.6m: Plots of $\alpha_{calc.}$ versus time using various kinetic models, compared with α_e versus time data for the decomposition of $Ni(nma)Cl_2$ at 183°C.

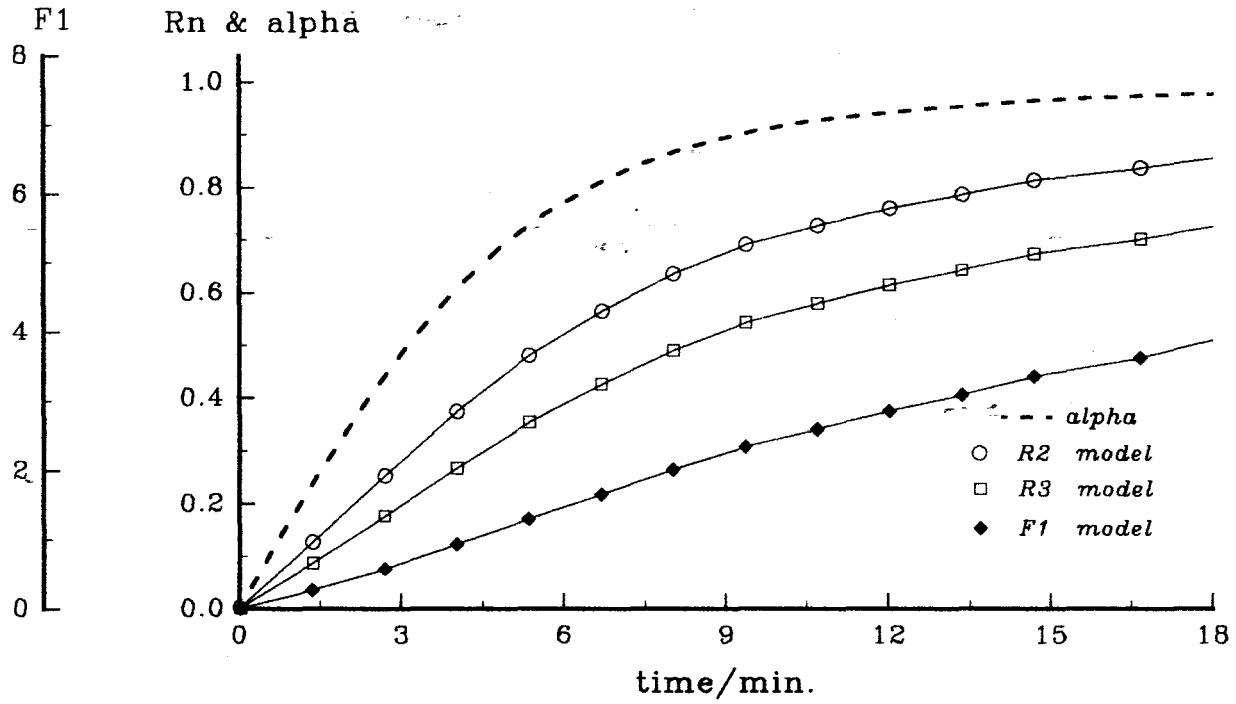

Figure 10.3.5n: Plots of $g(\alpha)$ versus time for the decomposition of $Ni(nma)Cl_2$ at 193°C. The α–time curve is included to show the range of α over which $g(\alpha)$ is approximately linear.

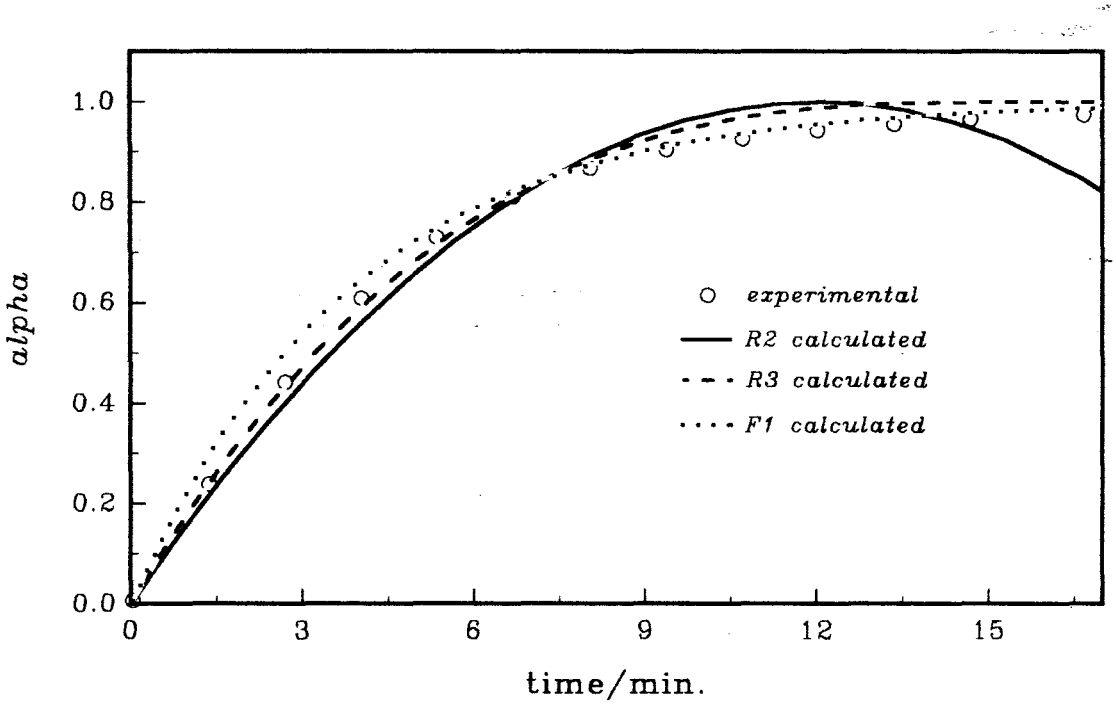

Figure 10.3.6n: Plots of $\alpha_{calc.}$ versus time using various kinetic models, compared with α_e versus time data for the decomposition of $Ni(nma)Cl_2$ at 193°C.

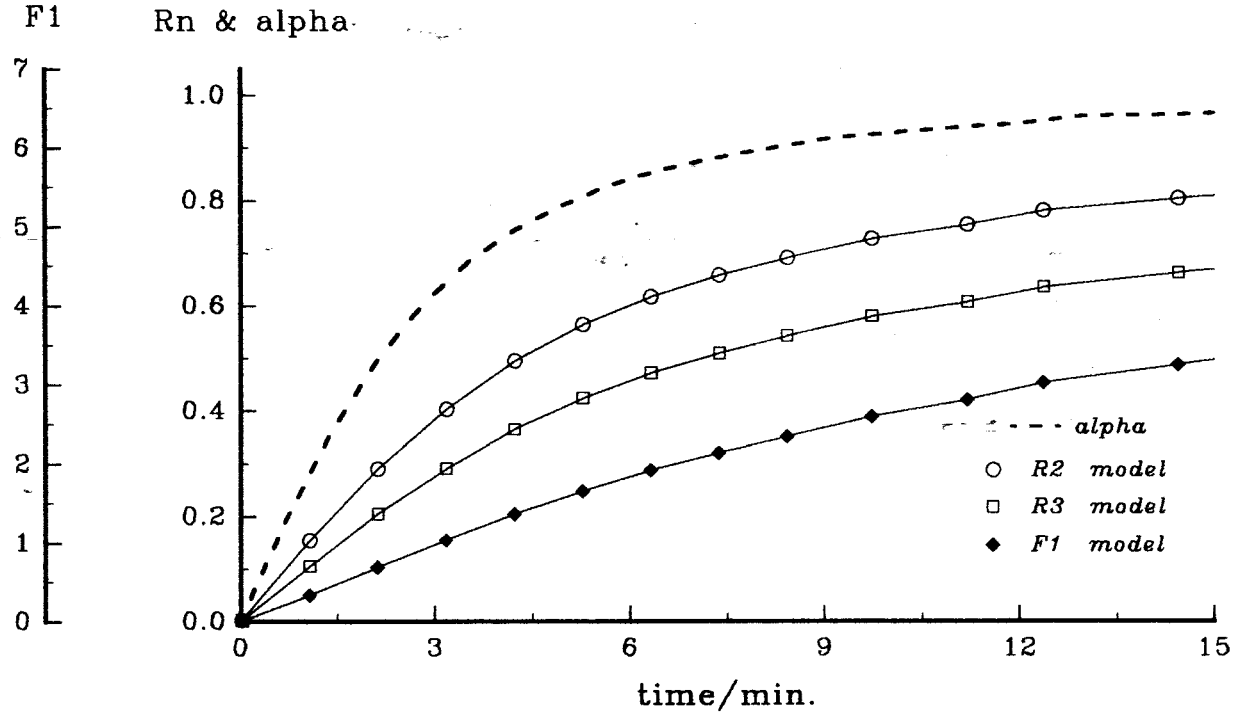

Figure 10.3.5o: Plots of $g(\alpha)$ versus time for the decomposition of $Ni(nma)Cl_2$ at 198°C. The α–time curve is included to show the range of α over which $g(\alpha)$ is approximately linear.

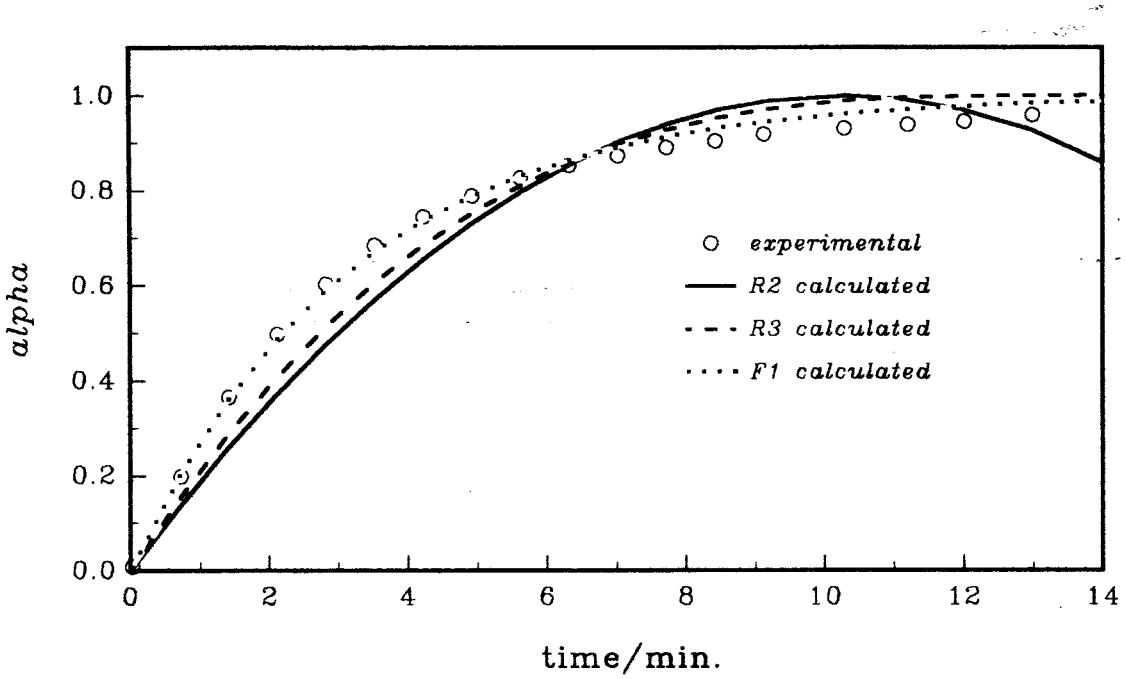

Figure 10.3.6o: Plots of $\alpha_{calc.}$ versus time using various kinetic models, compared with α_e versus time data for the decomposition of $Ni(nma)Cl_2$ at 198°C.

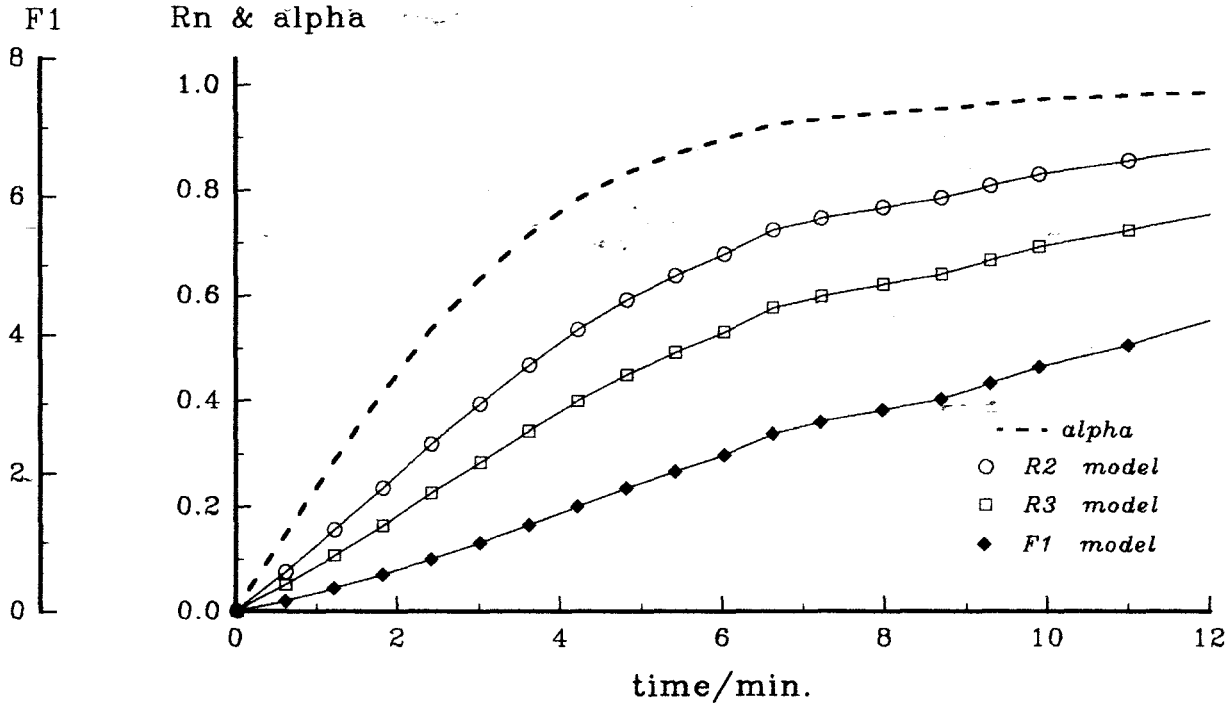

Figure 10.3.5p: Plots of g(α) versus time for the decomposition of $Ni(nma)Cl_2$ at 200°C.* The α–time curve is included to show the range of α over which g(α) is approximately linear.

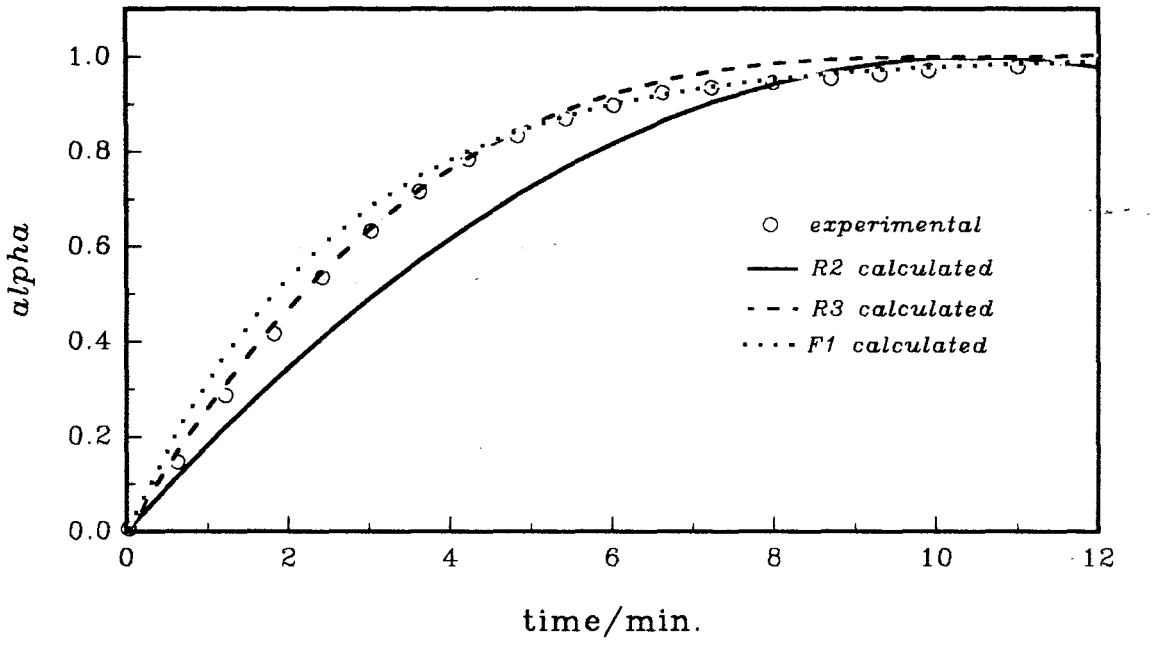

Figure 10.3.6p: Plots of $\alpha_{calc.}$ versus time using various kinetic models, compared with α_e versus time data for the decomposition of $Ni(nma)Cl_2$ at 200°C.*

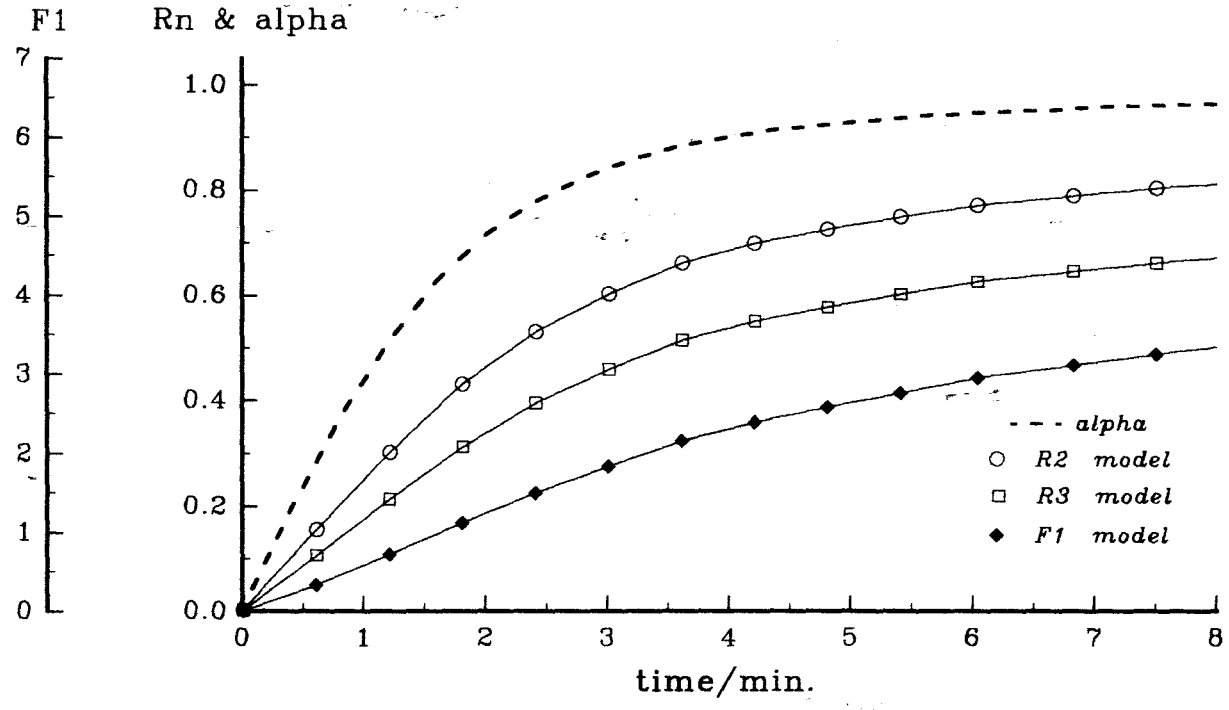

Figure 10.3.5q: Plots of $g(\alpha)$ versus time for the decomposition of $Ni(nma)Cl_2$ at 205°C. The α–time curve is included to show the range of α over which $g(\alpha)$ is approximately linear.

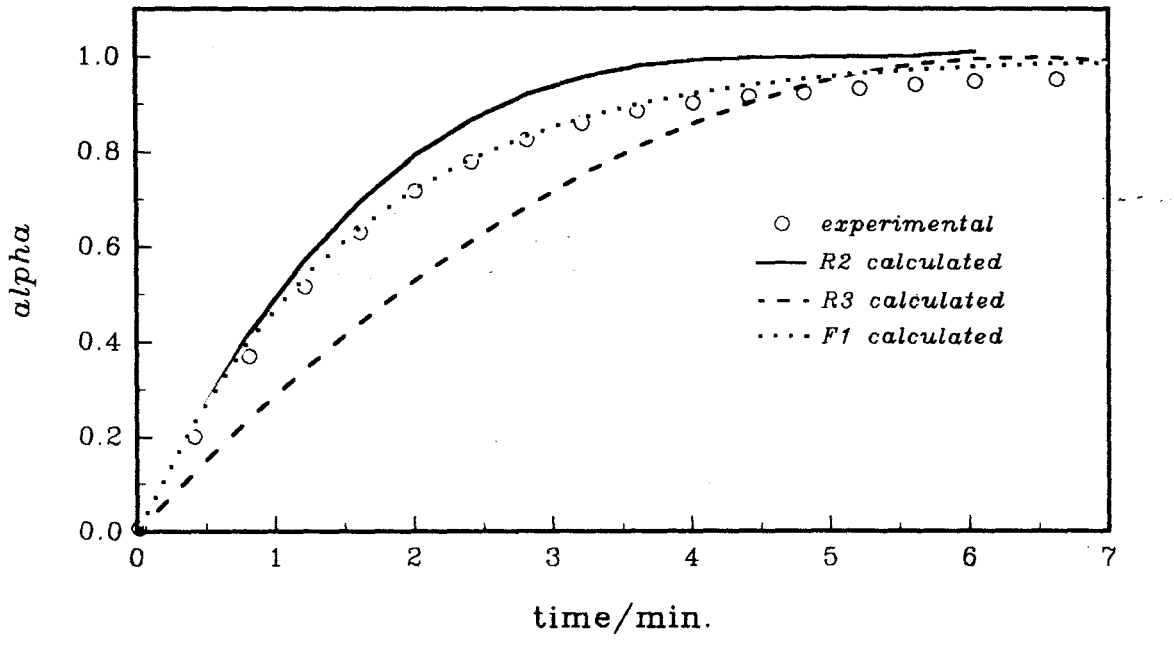

Figure 10.3.6q: Plots of $\alpha_{calc.}$ versus time using various kinetic models, compared with α_e versus time data for the decomposition of $Ni(nma)Cl_2$ at 205°C.

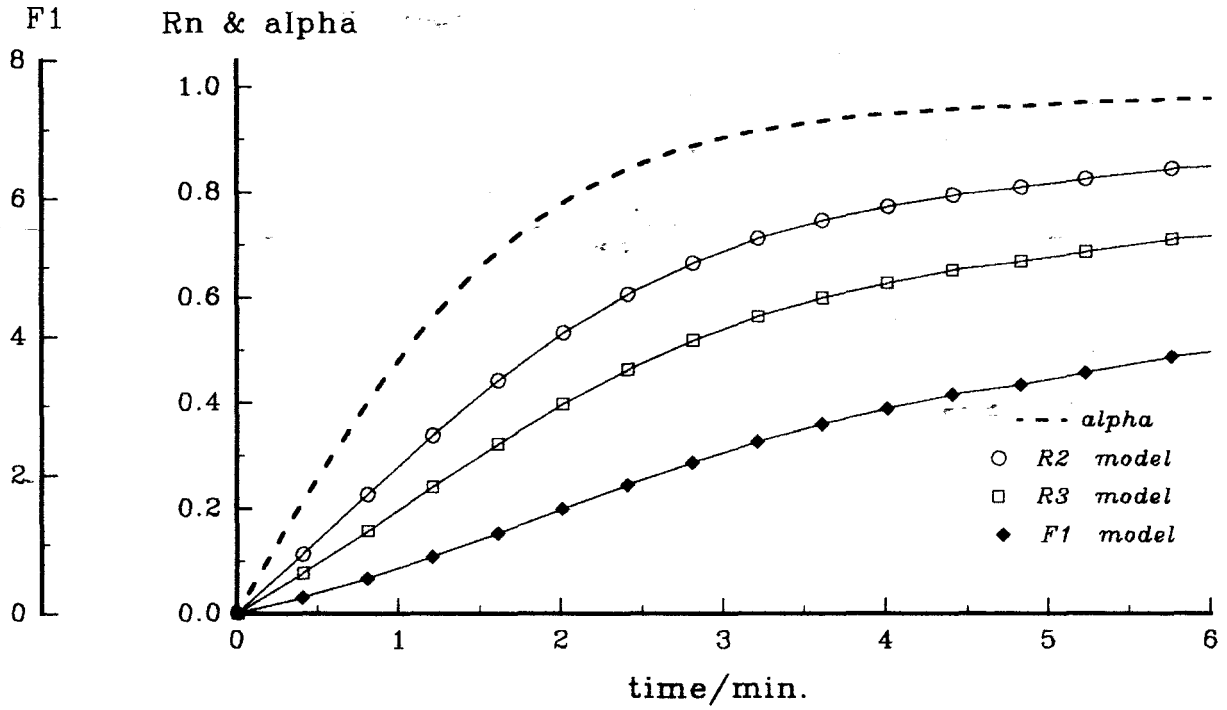

Figure 10.3.5r: Plots of $g(\alpha)$ versus time for the decomposition of $Ni(nma)Cl_2$ at 208°C. The α–time curve is included to show the range of α over which $g(\alpha)$ is approximately linear.

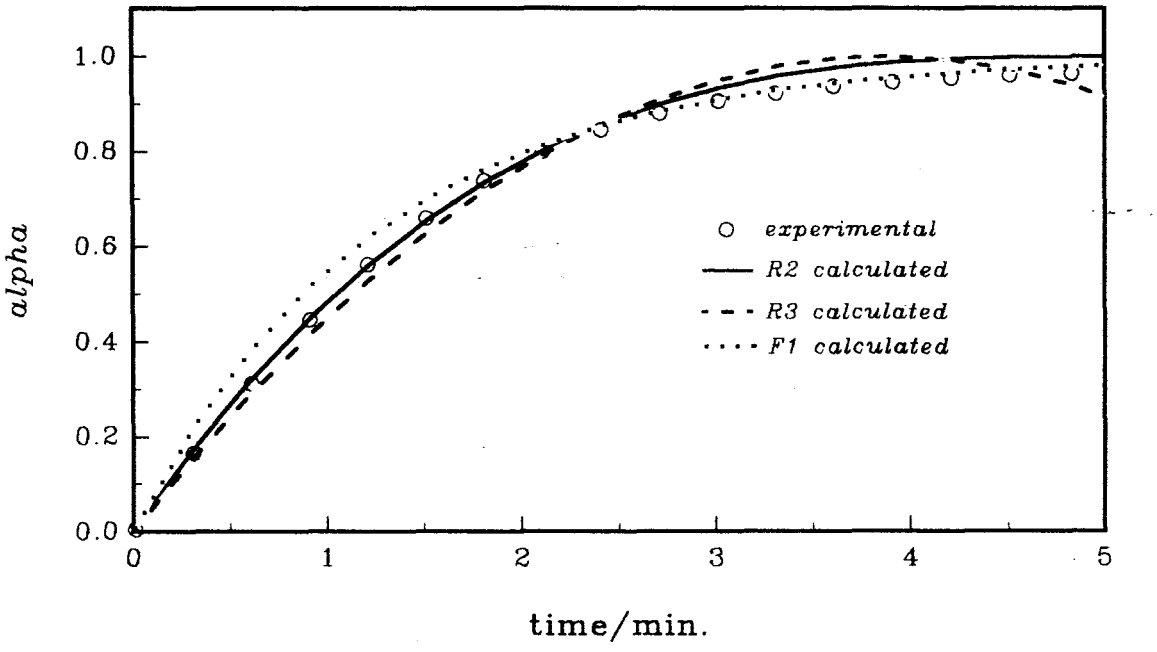

Figure 10.3.6r: Plots of $\alpha_{calc.}$ versus time using various kinetic models, compared with α_e versus time data for the decomposition of $Ni(nma)Cl_2$ at 208°C.

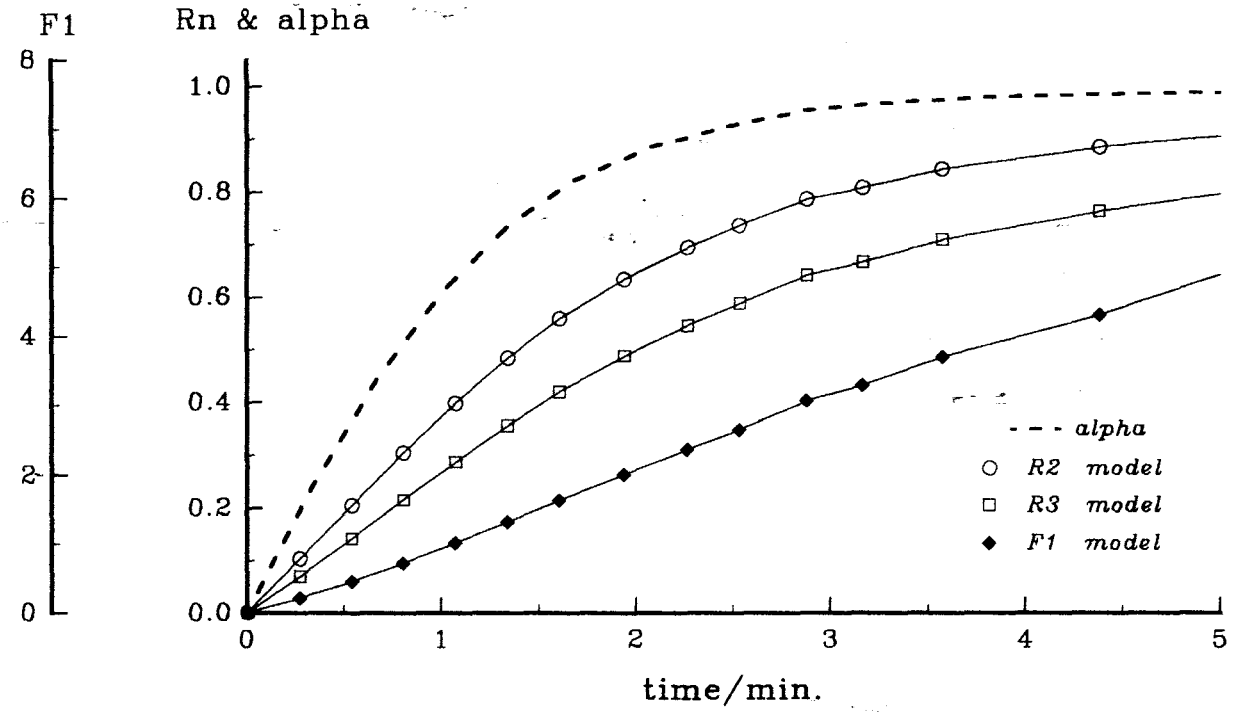

Figure 10.3.5s: Plots of $g(\alpha)$ versus time for the decomposition of $Ni(nma)Cl_2$ at 210°C. The α–time curve is included to show the range of α over which $g(\alpha)$ is approximately linear.

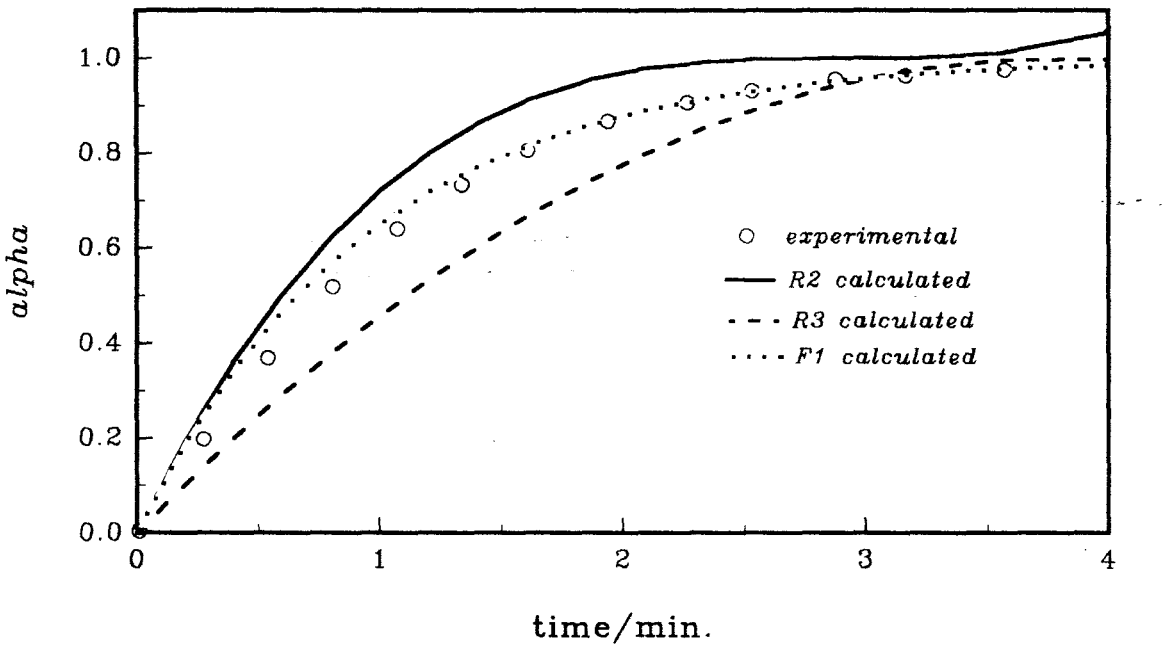

Figure 10.3.6s: Plots of $\alpha_{calc.}$ versus time using various kinetic models, compared with α_e versus time data for the decomposition of $Ni(nma)Cl_2$ at 210°C.

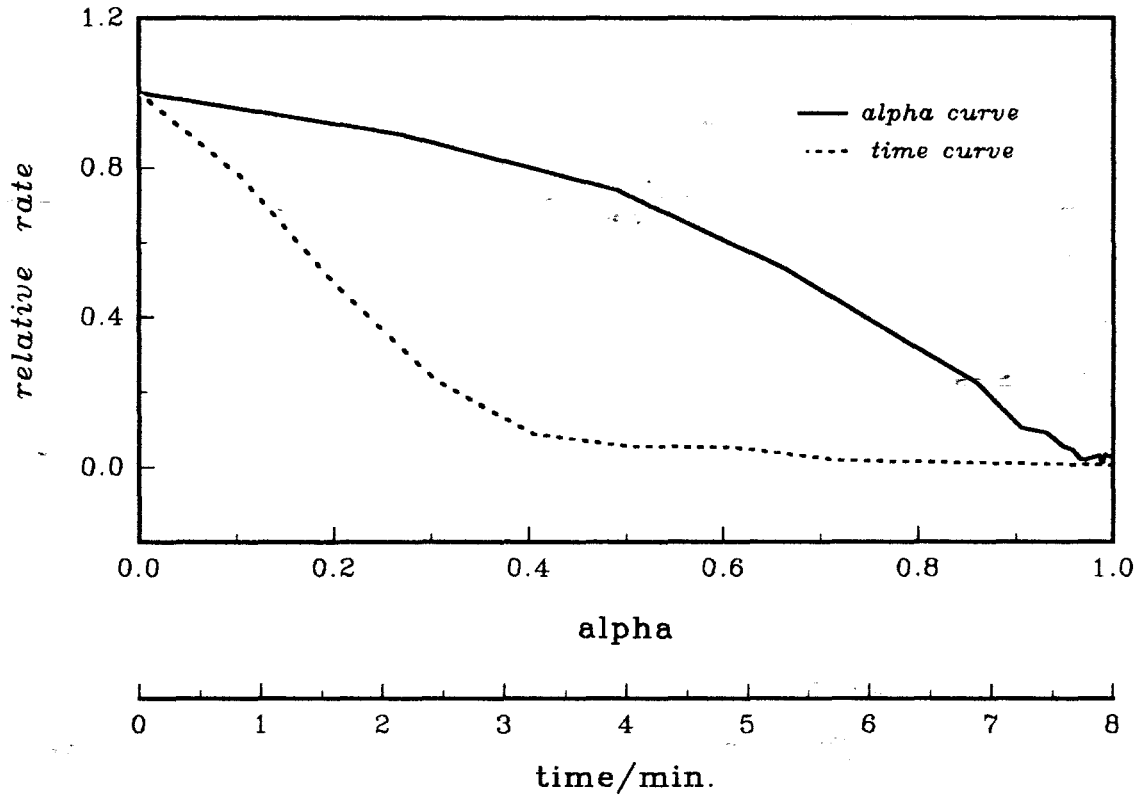

Figure 10.3.7b: Plots of rate versus alpha and rate versus time for the decomposition of $Ni(nma)Cl_2$ at 208°C.

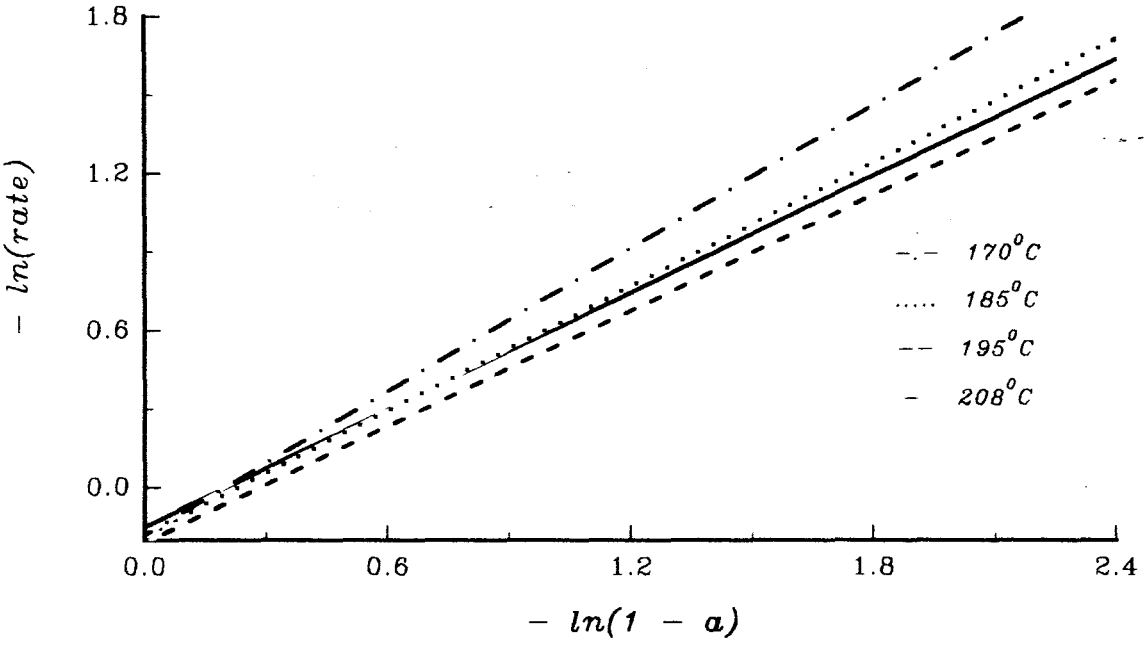

Figure 10.3.8b: Regression lines of ln(rate) versus $\ln(1 - \alpha)$ for the isothermal decomposition of $Ni(nma)Cl_2$.

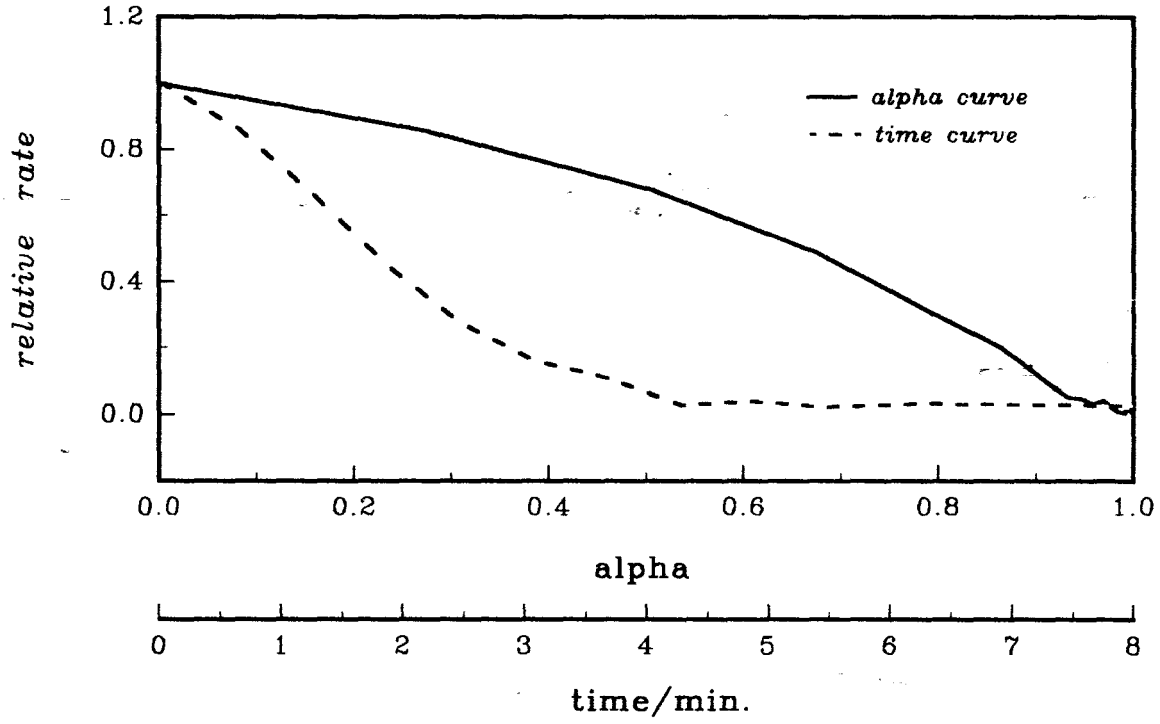

Figure 10.3.7c: Plots of rate versus alpha and rate versus time for the decomposition of $Ni(nma)Cl_2$ at 200°C.

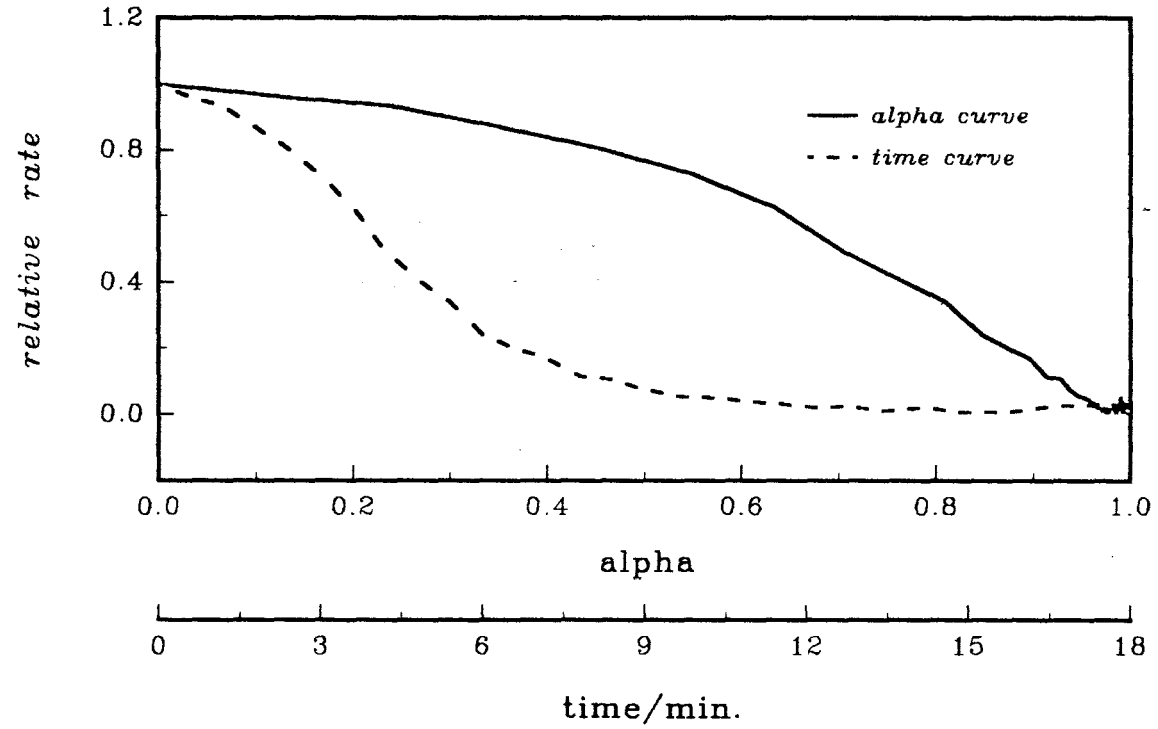

Figure 10.3.7d: Plots of rate versus alpha and rate versus time for the decomposition of $Ni(nma)Cl_2$ at 195°C.

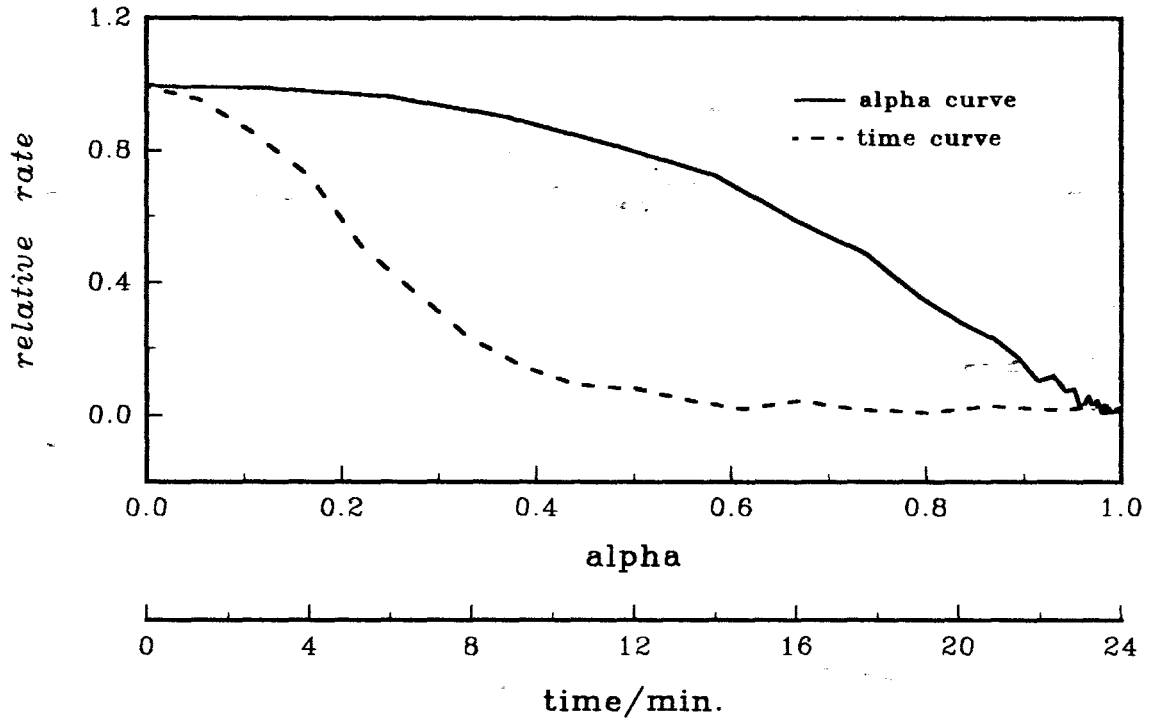

Figure 10.3.7e: Plots of rate versus alpha and rate versus time for the decomposition of $Ni(nma)Cl_2$ at 190°C.

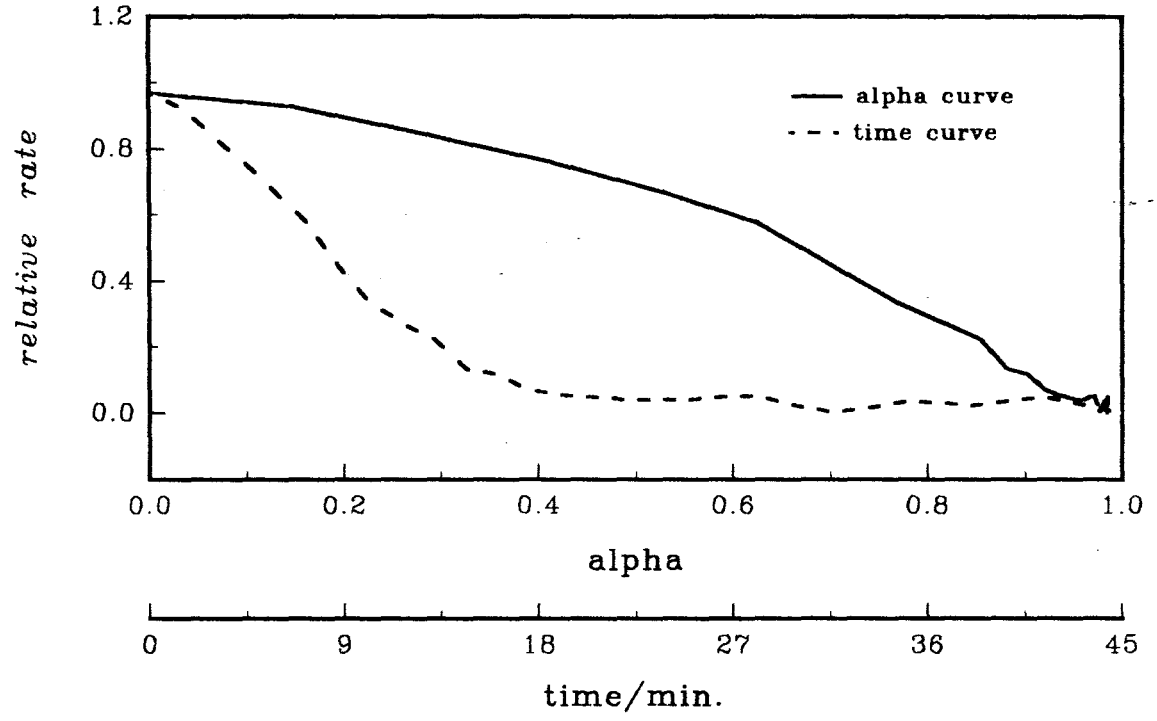

Figure 10.3.7f: Plots of rate versus alpha and rate versus time for the decomposition of $Ni(nma)Cl_2$ at 185°C.

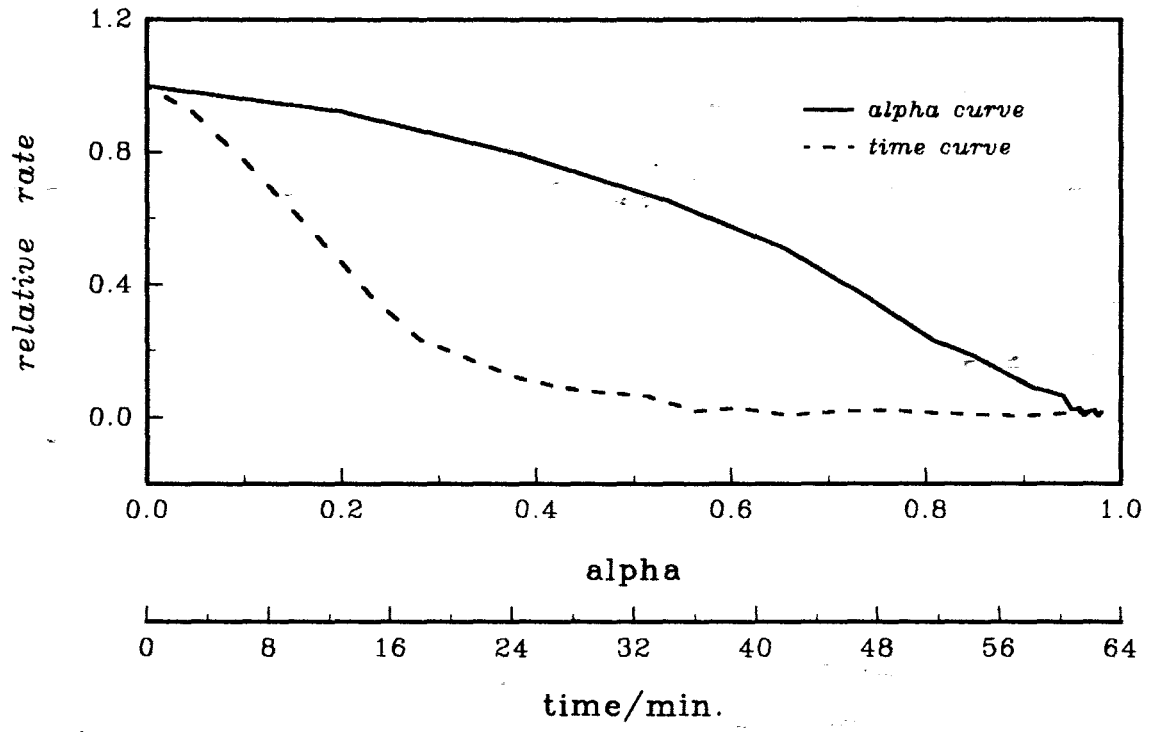

Figure 10.3.7g: Plots of rate versus alpha and rate versus time for the decomposition of $Ni(nma)Cl_2$ at 180°C.

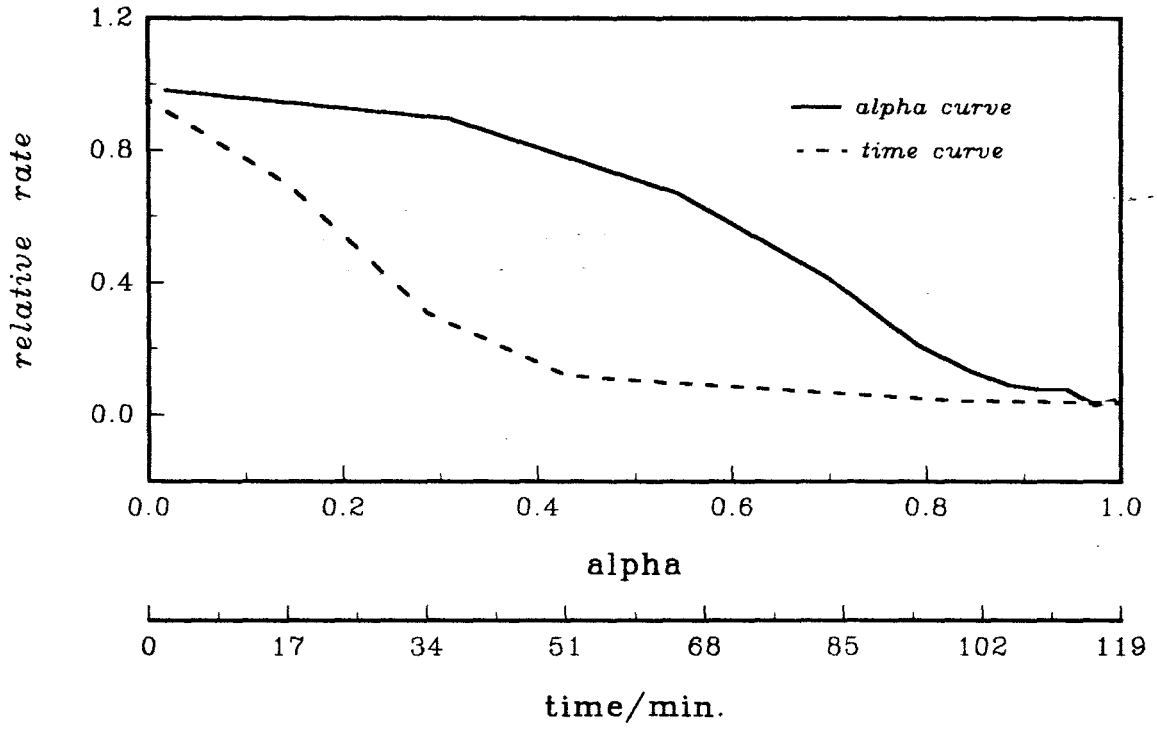

Figure 10.3.7h: Plots of rate versus alpha and rate versus time for the decomposition of $Ni(nma)Cl_2$ at 173°C.

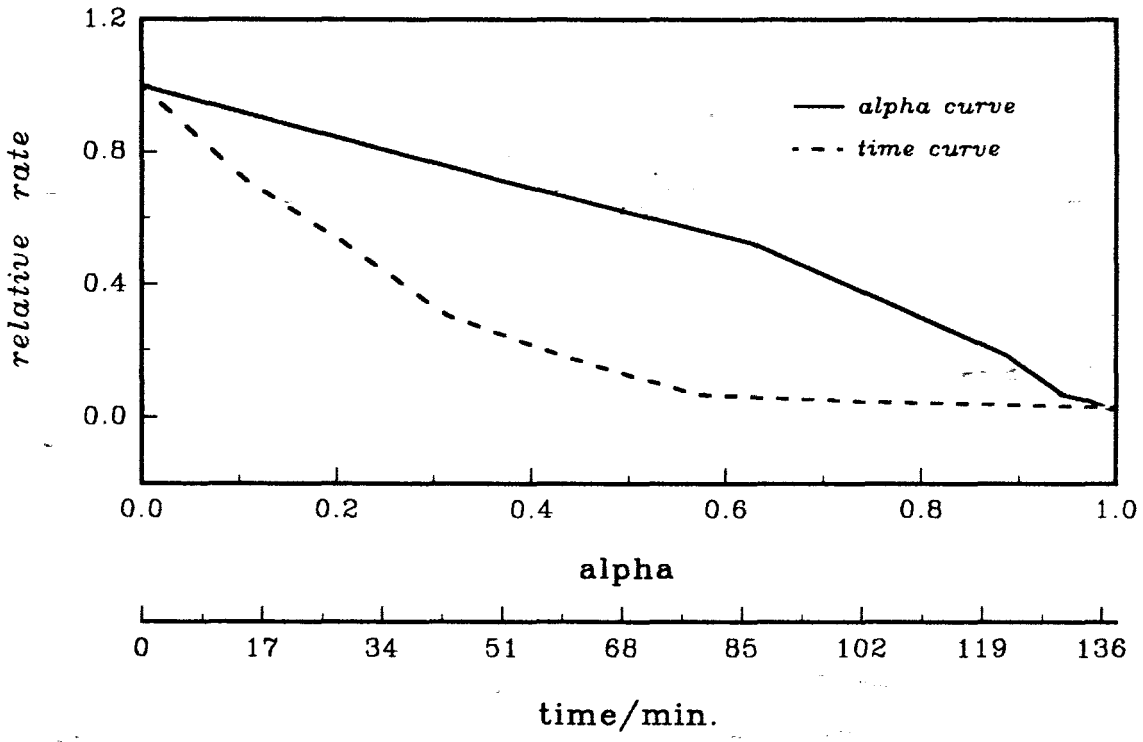

Figure 10.3.7i: Plots of rate versus alpha and rate versus time for the decomposition of $Ni(nma)Cl_2$ at 170°C.

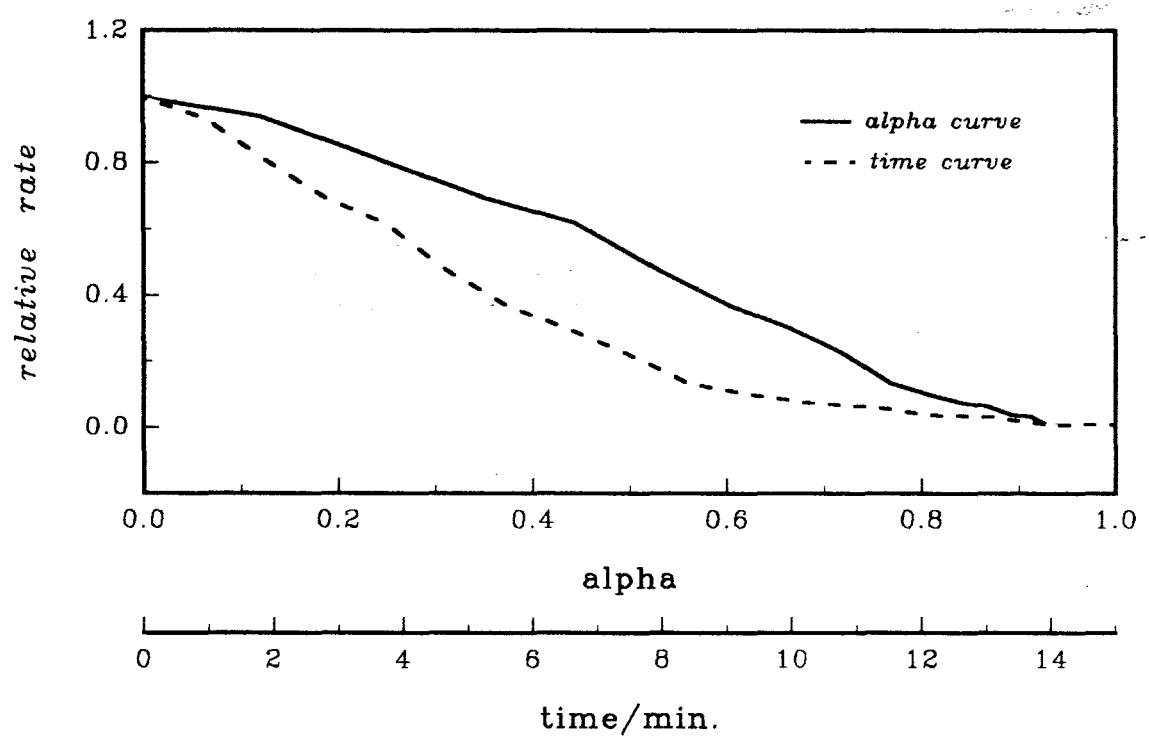

Figure 10.3.7j: Plots of rate versus alpha and rate versus time for the decomposition of $Ni(nma)Cl_2$ at 210°C.

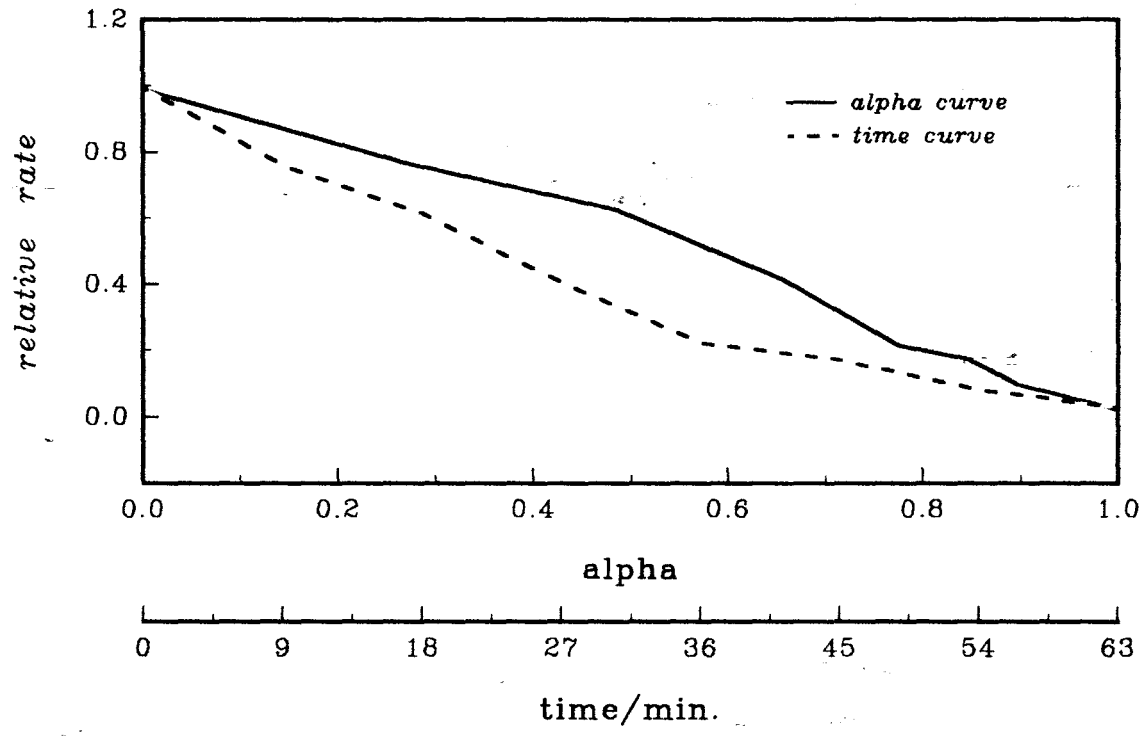

Figure 10.3.7k: Plots of rate versus alpha and rate versus time for the decomposition of $Ni(nma)Cl_2$ at 170°C.*

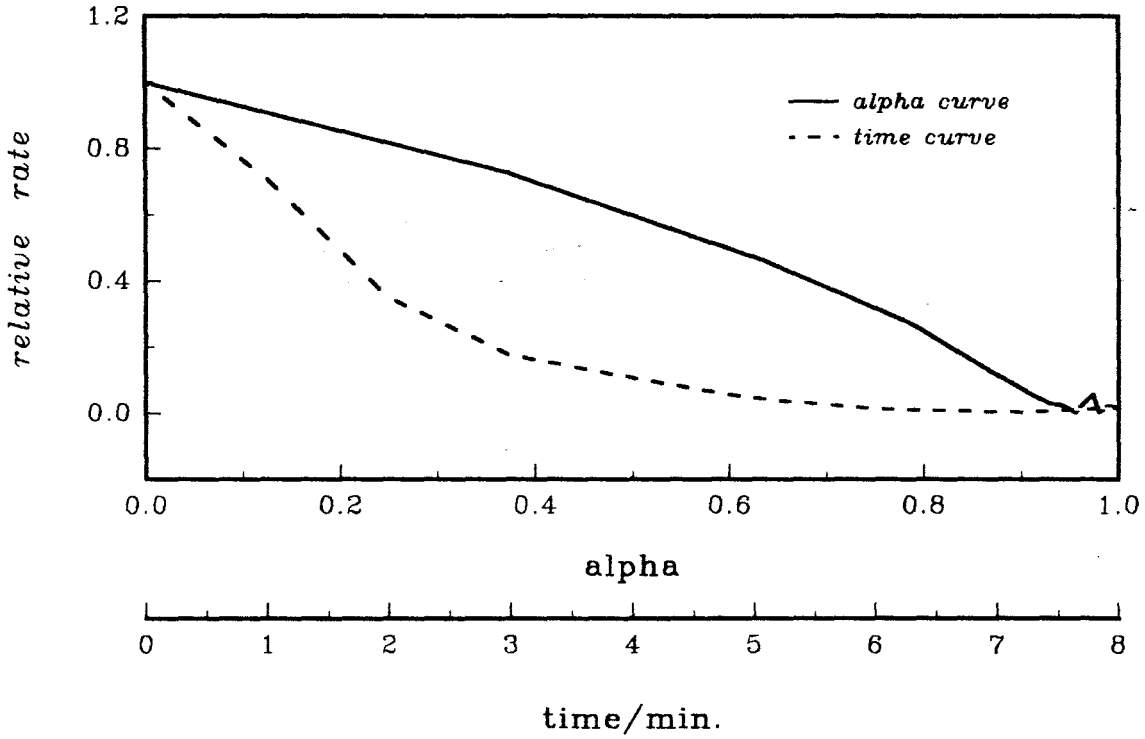

Figure 10.3.7l: Plots of rate versus alpha and rate versus time for the decomposition of $Ni(nma)Cl_2$ at 205°C.

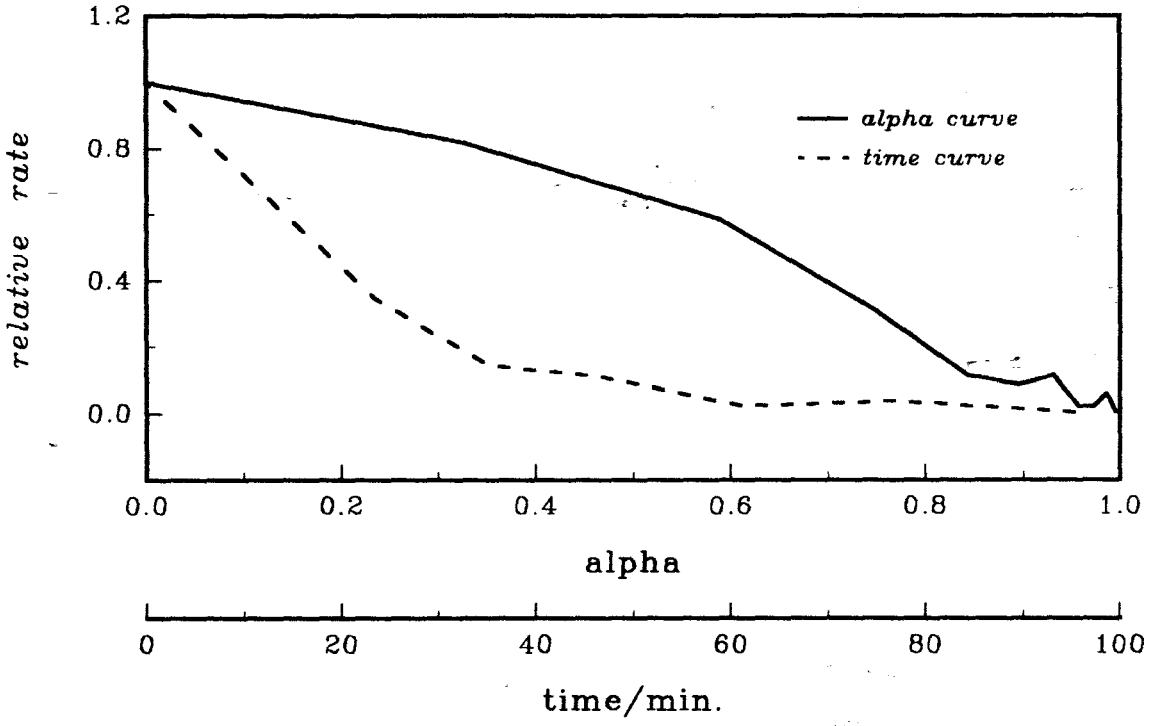

Figure 10.3.7m: Plots of rate versus alpha and rate versus time for the decomposition of $Ni(nma)Cl_2$ at 175°C.

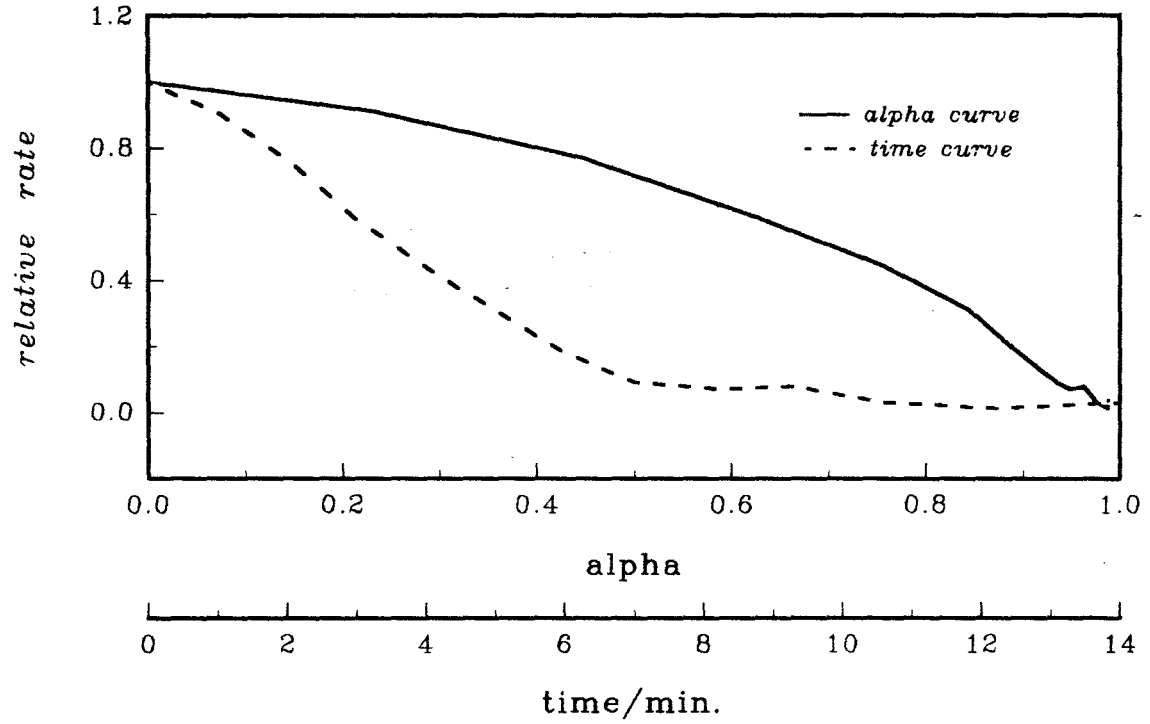

Figure 10.3.7n: Plots of rate versus alpha and rate versus time for the decomposition of $Ni(nma)Cl_2$ at 200°C.*

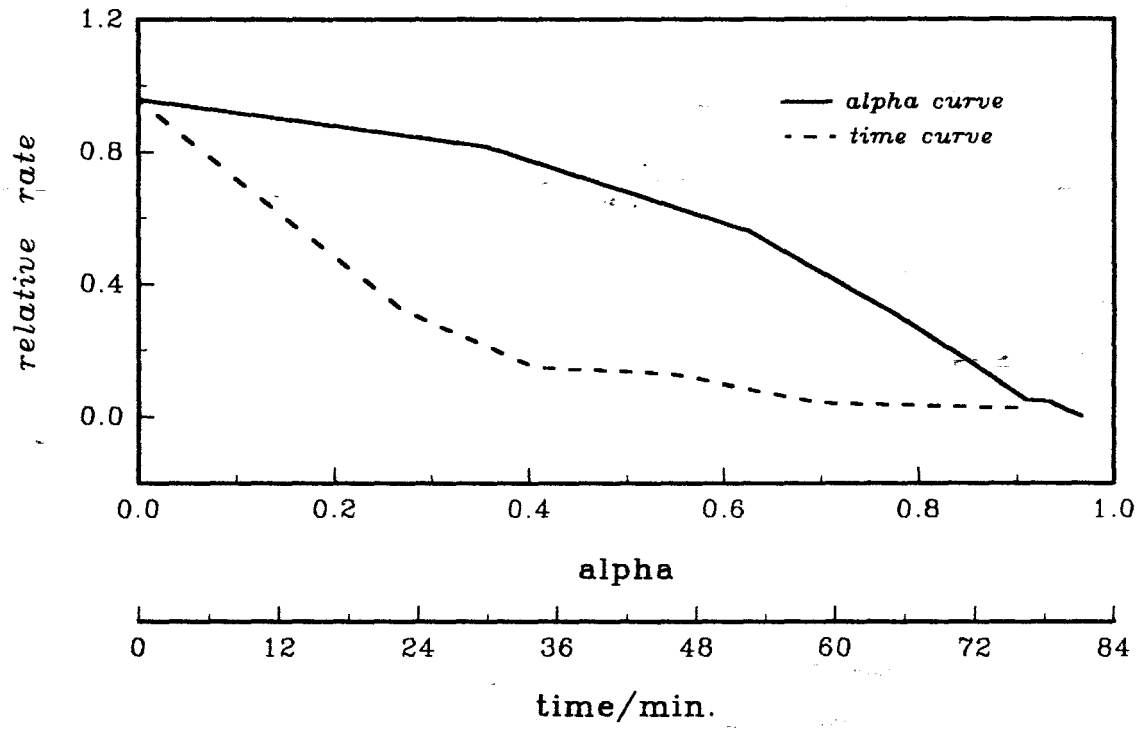

Figure 10.3.7o: Plots of rate versus alpha and rate versus time for the decomposition of $Ni(nma)Cl_2$ at 175°C.*

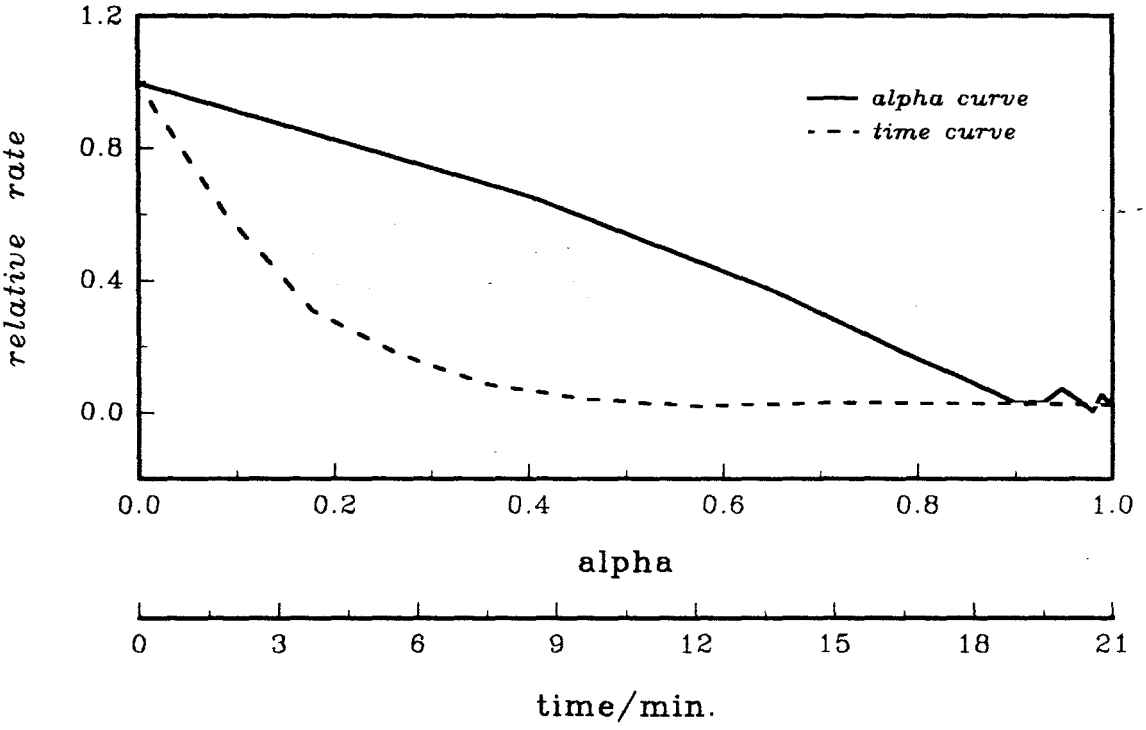

Figure 10.3.7p: Plots of rate versus alpha and rate versus time for the decomposition of $Ni(nma)Cl_2$ at 198°C.

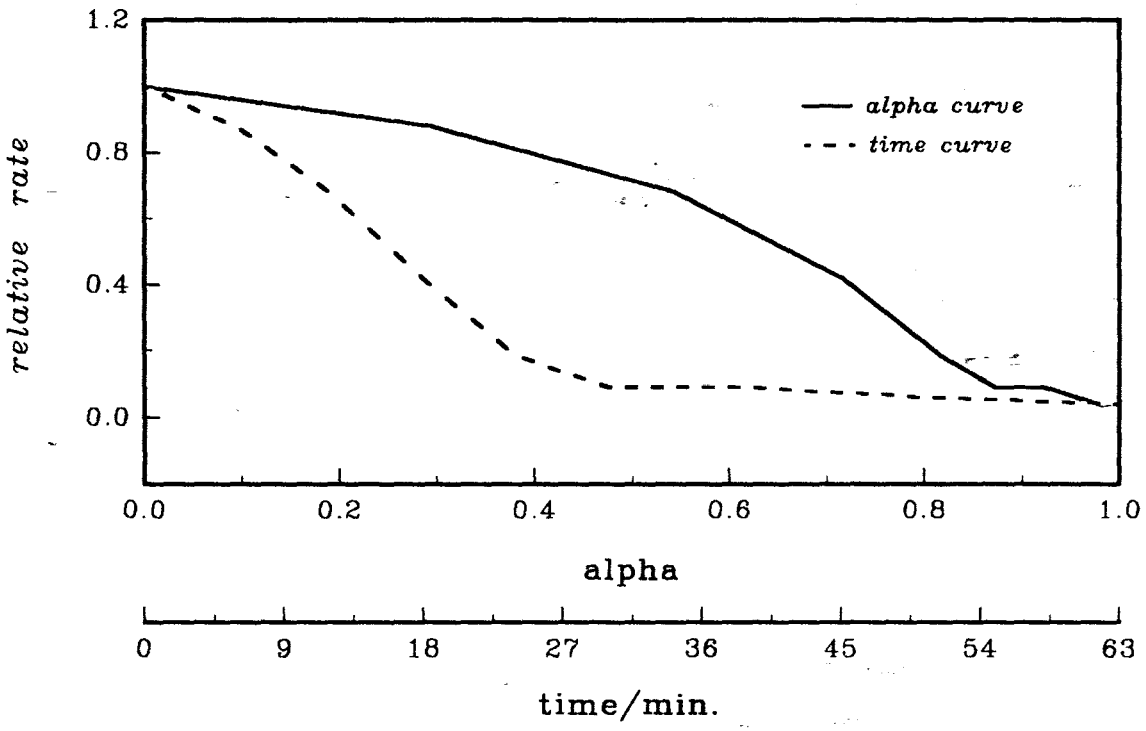

Figure 10.3.7q: Plots of rate versus alpha and rate versus time for the decomposition of $Ni(nma)Cl_2$ at 178°C.

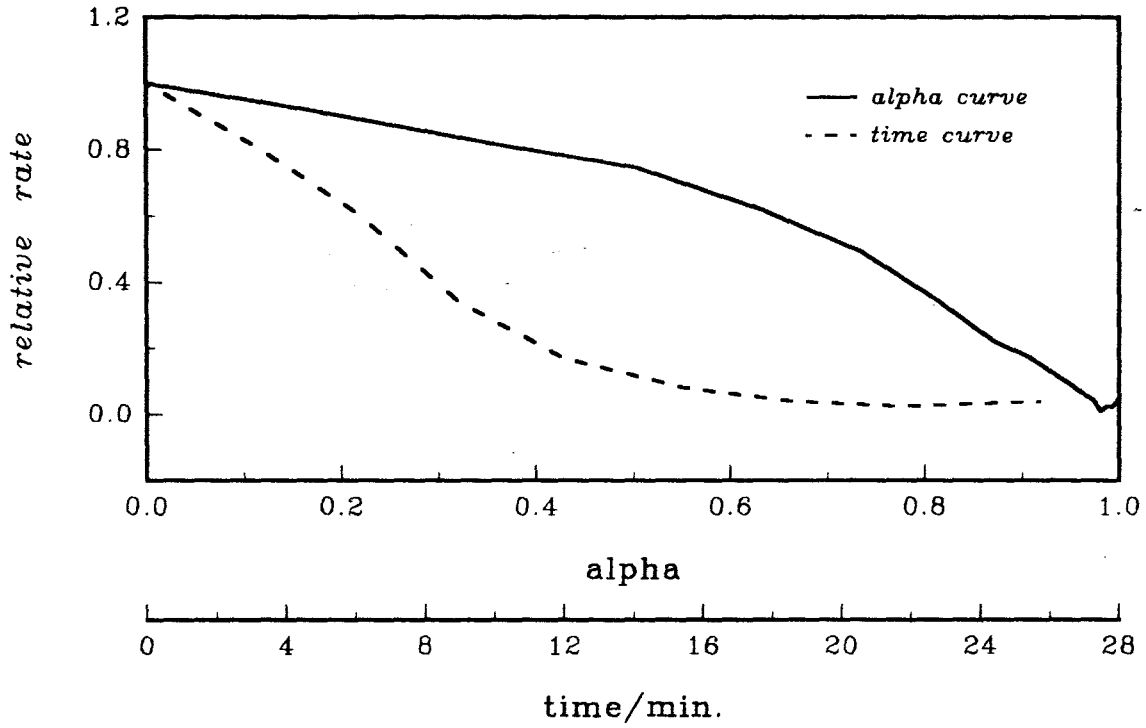

Figure 10.3.7r: Plots of rate versus alpha and rate versus time for the decomposition of $Ni(nma)Cl_2$ at 188°C.

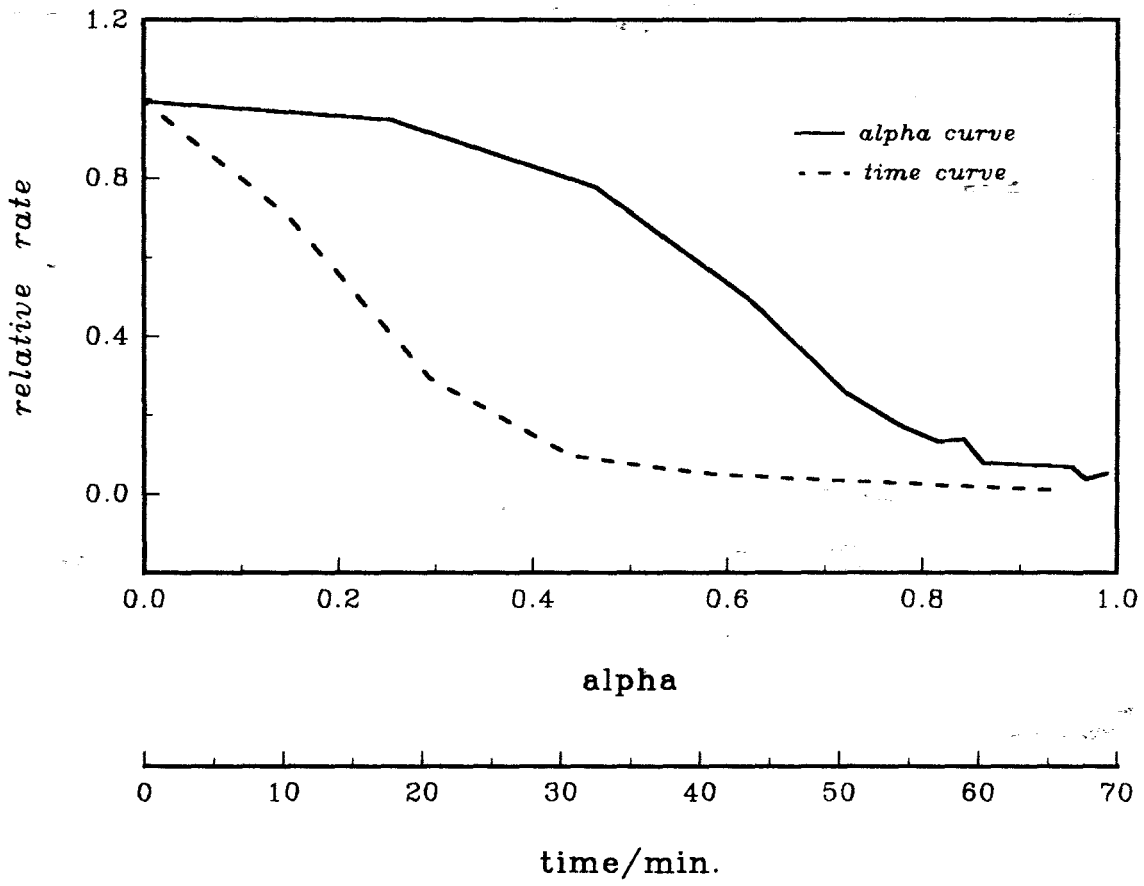

Figure 10.3.7s: Plots of rate versus alpha and rate versus time for the decomposition of $Ni(nma)Cl_2$ at 183°C.

APPENDIX V

Chapter 12

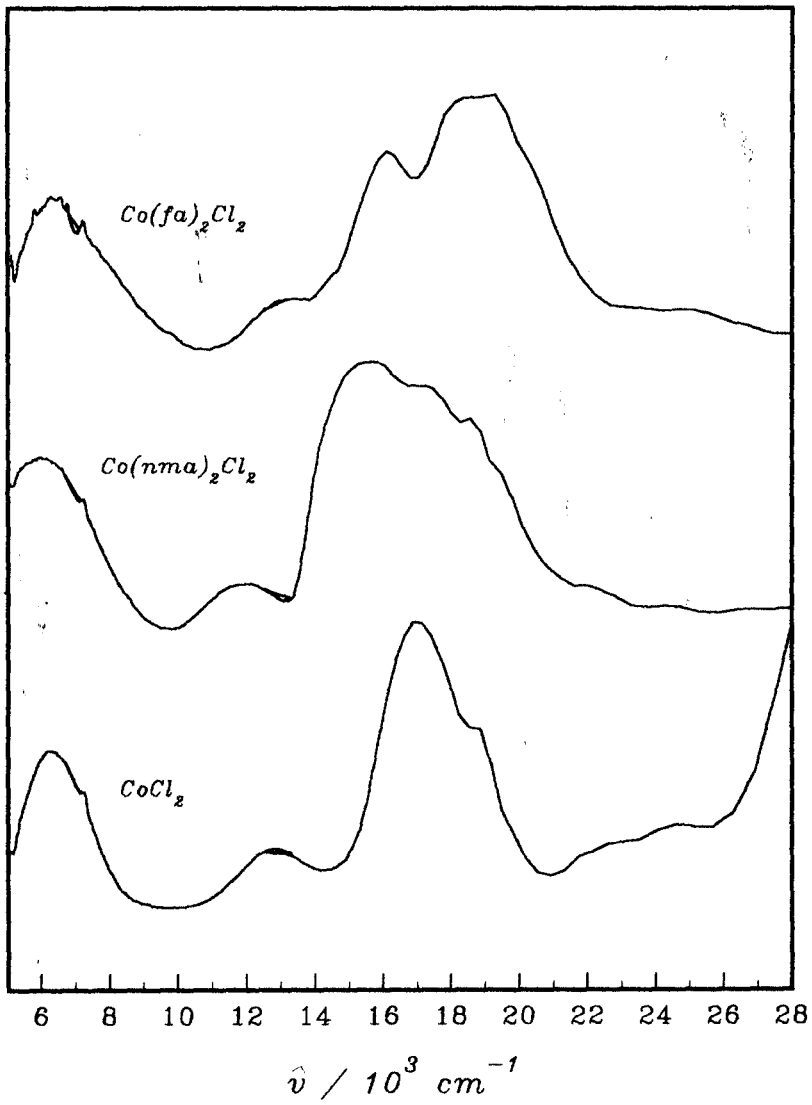

Figure 12.1.1: Diffuse reflectance spectra of octahedral CoL_2Cl_2 complexes and anhydrous $CoCl_2$.

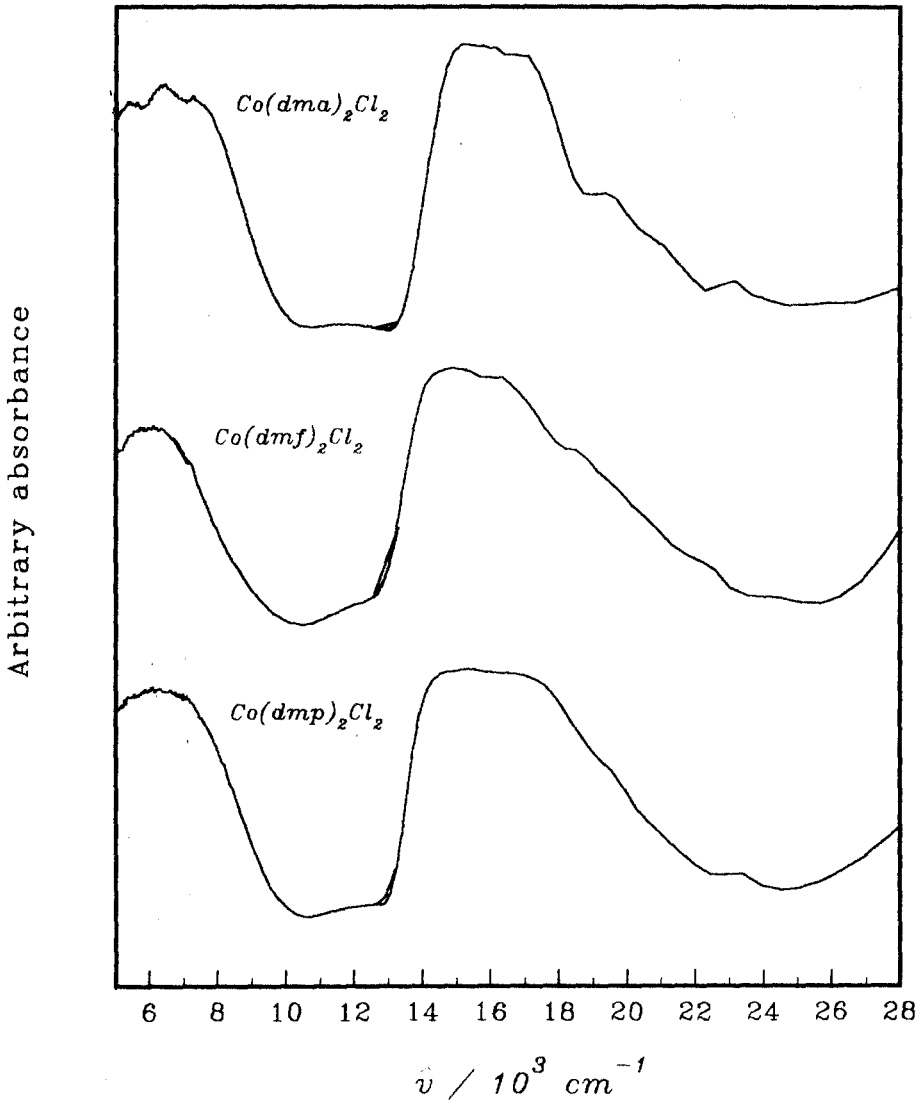

Figure 12.1.2: Diffuse reflectance spectra of tetrahedral CoL_2Cl_2 complexes.

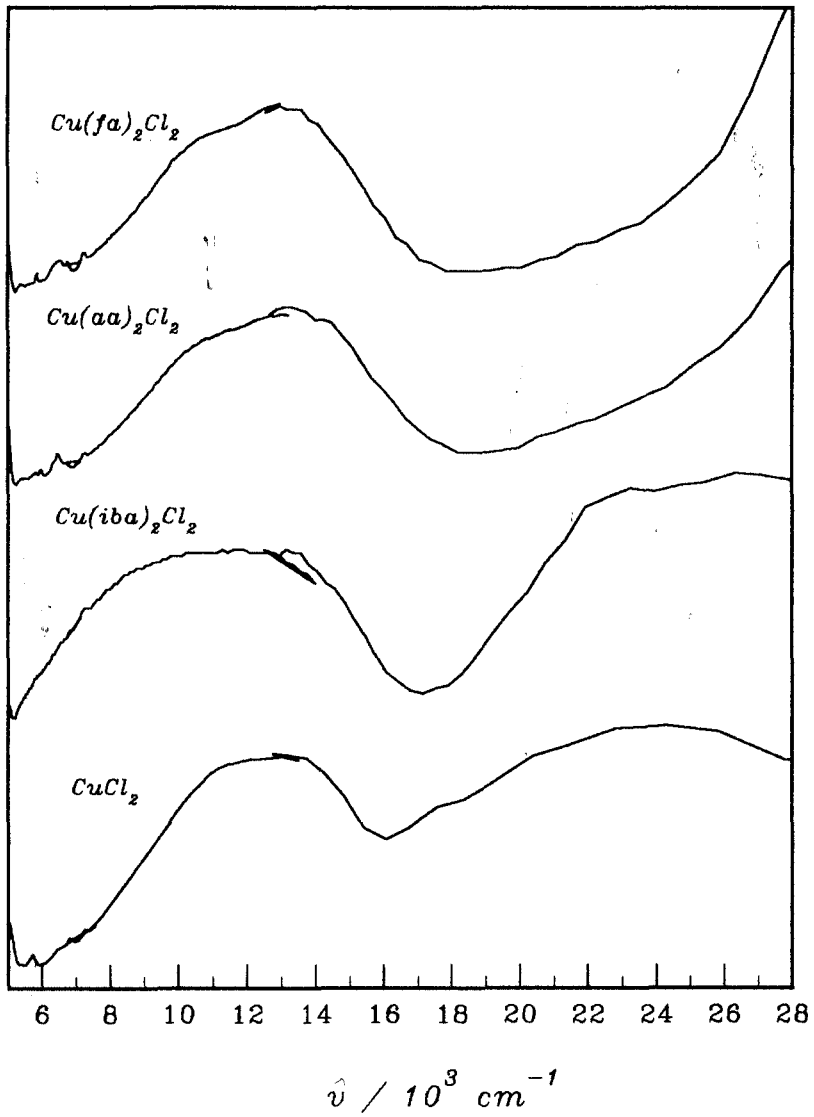

Figure 12.1.3: Diffuse reflectance spectra of CuL_2Cl_2 complexes, compared with spectrum of anhydrous $CuCl_2$.

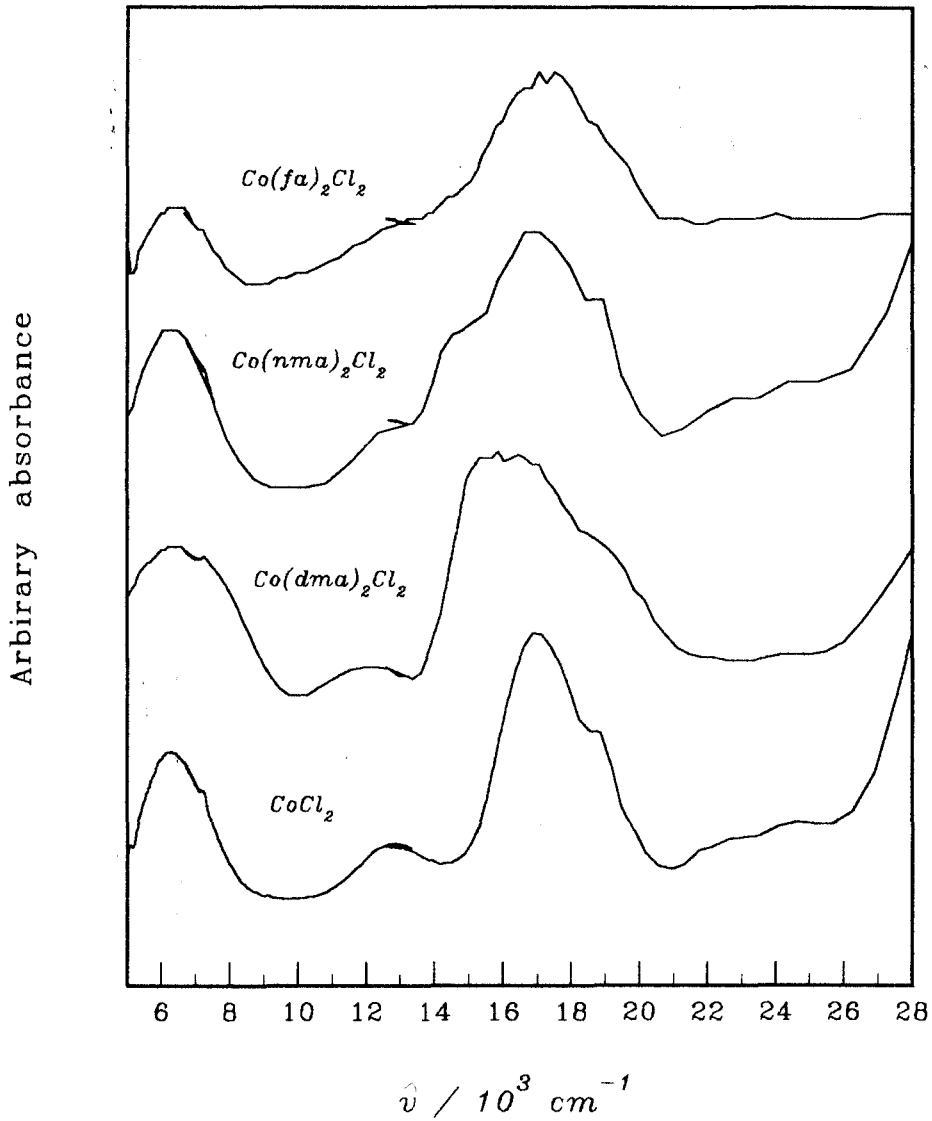

Figure 12.1.4: Spectra of decomposition residue of the cobalt–amide complexes, compared with the spectrum of anhydrous $CoCl_2$.

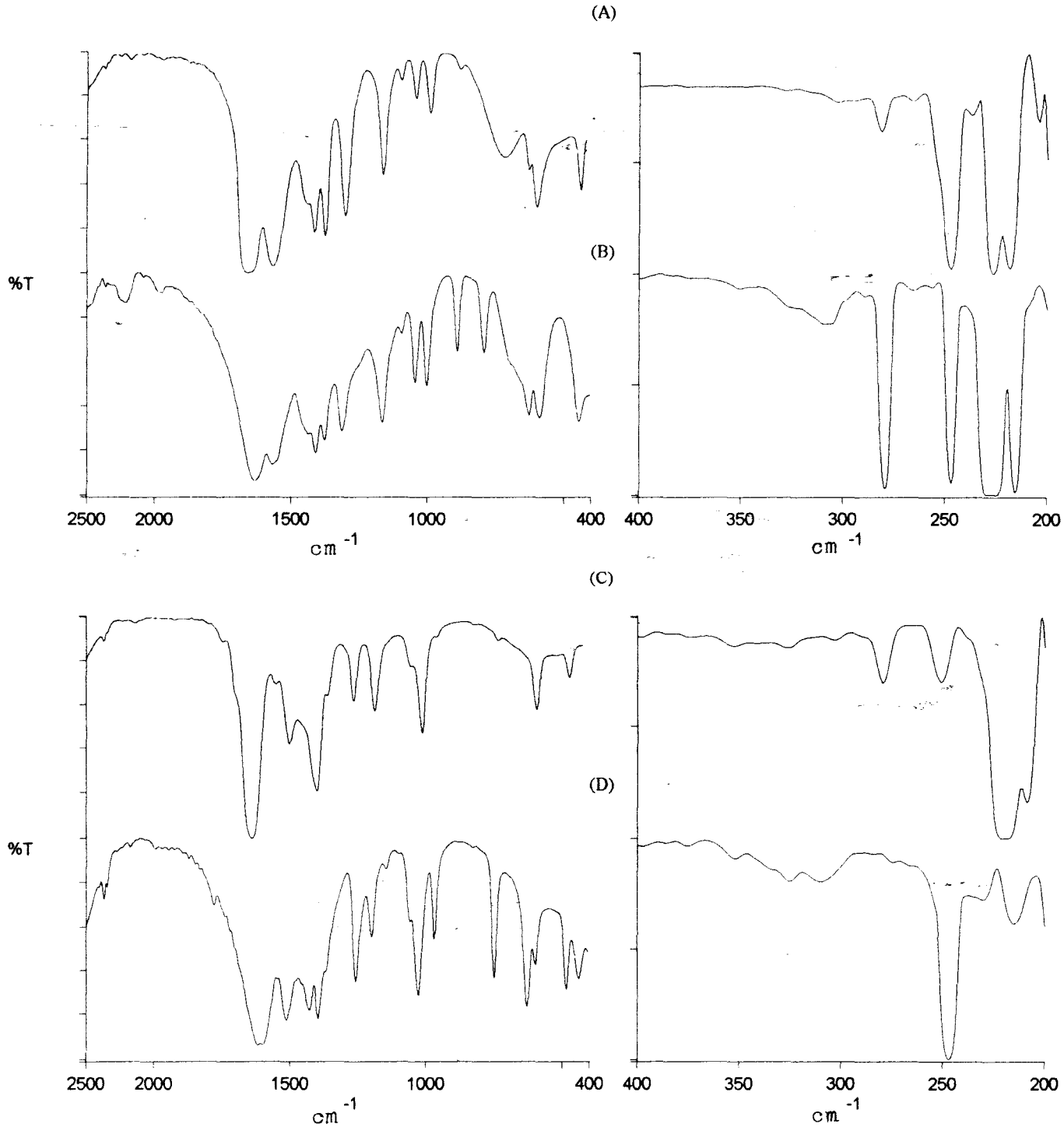

Figure 12.2.1: IR spectra of *nma* (A), Co(*nma*)$_2$Cℓ_2 (B), *dma* (C) and Co(*dma*)$_2$Cℓ_2 (D).

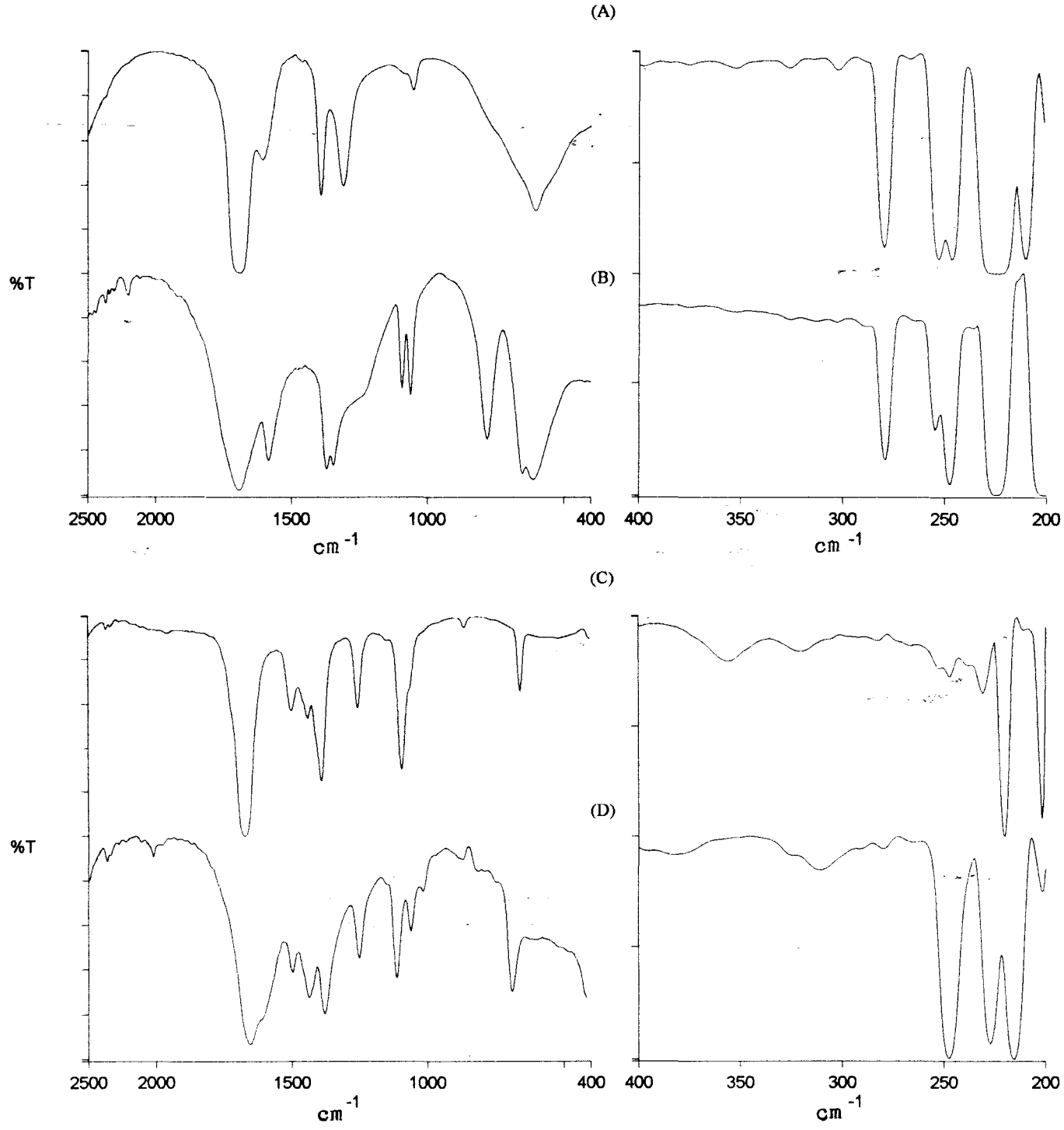

Figure 12.2.2: IR spectra of *fa* (A), $Co(fa)_2C\ell_2$ (B), *dmf* (C) and $Co(dmf)_2C\ell_2$ (D).

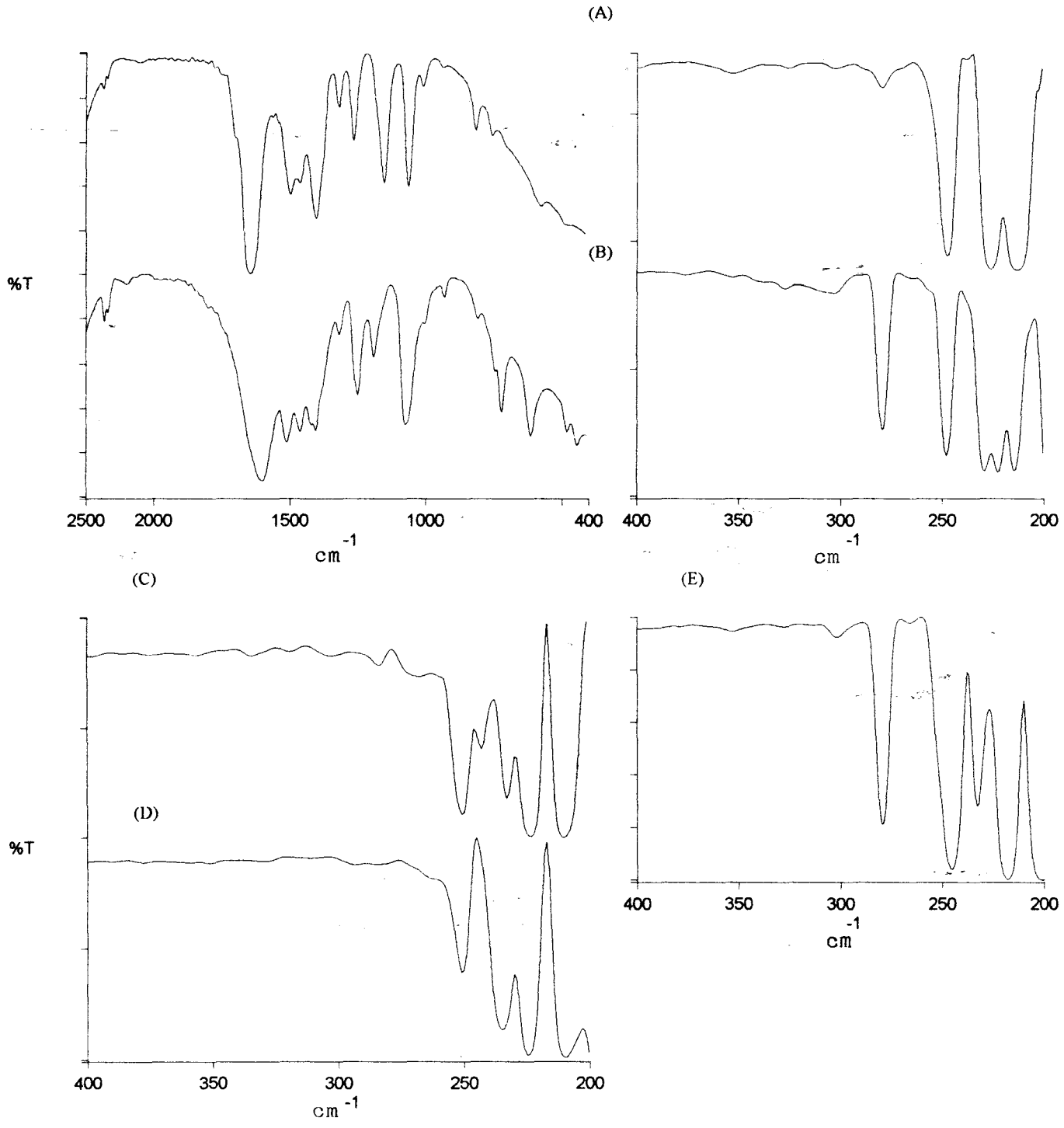

Figure 12.2.3: IR spectra of *dmp* (A), Co(*dmp*)$_2$Cℓ_2 (B), anhydrous CoCℓ_2 (C), NiCℓ_2 (D) and CuCℓ_2 (E).

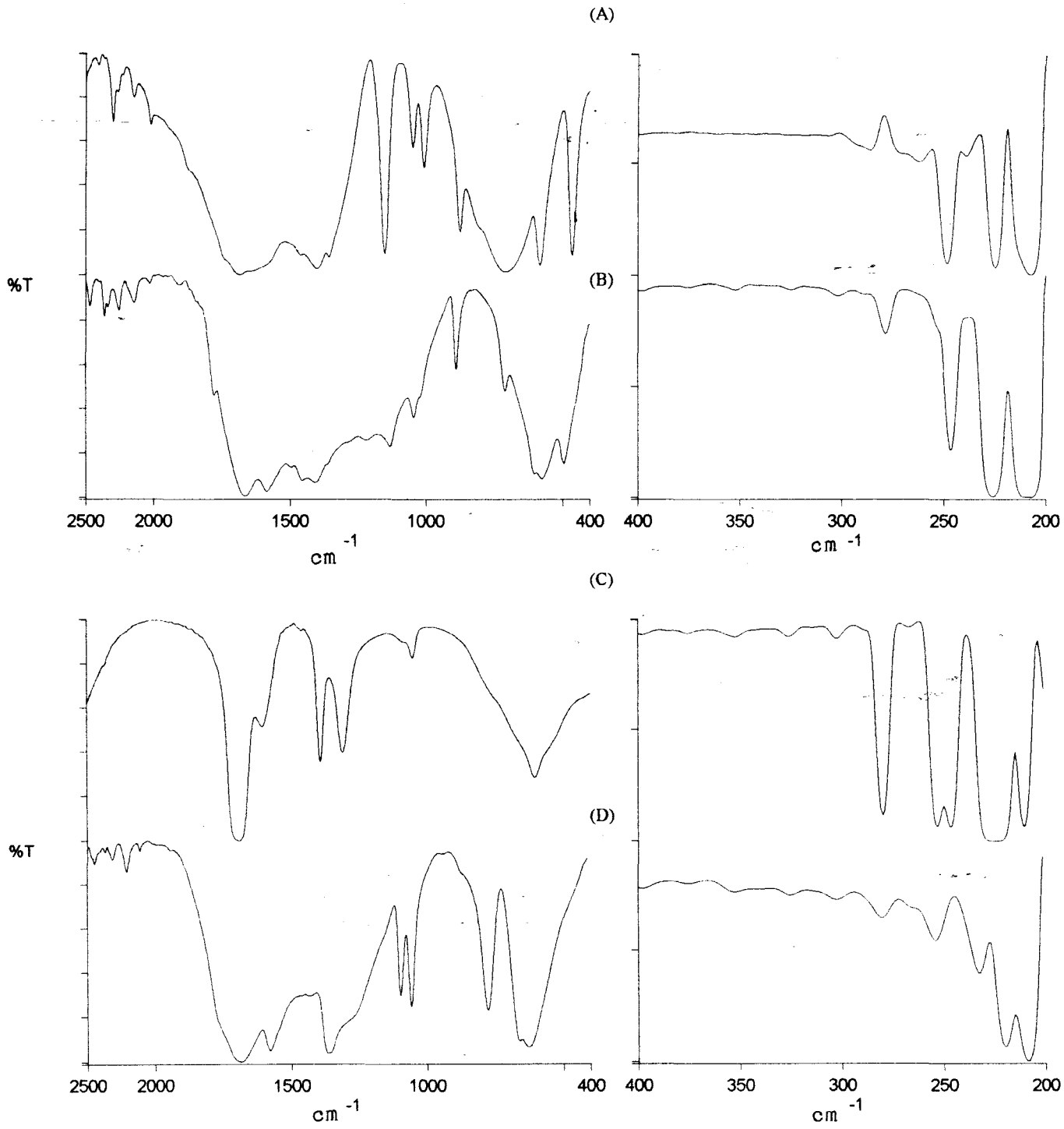

Figure 12.2.4: IR spectra of *aa* (A), $Cu(aa)_2C\ell_2$ (B), *fa* (C) and $Cu(fa)_2C\ell_2$ (D).

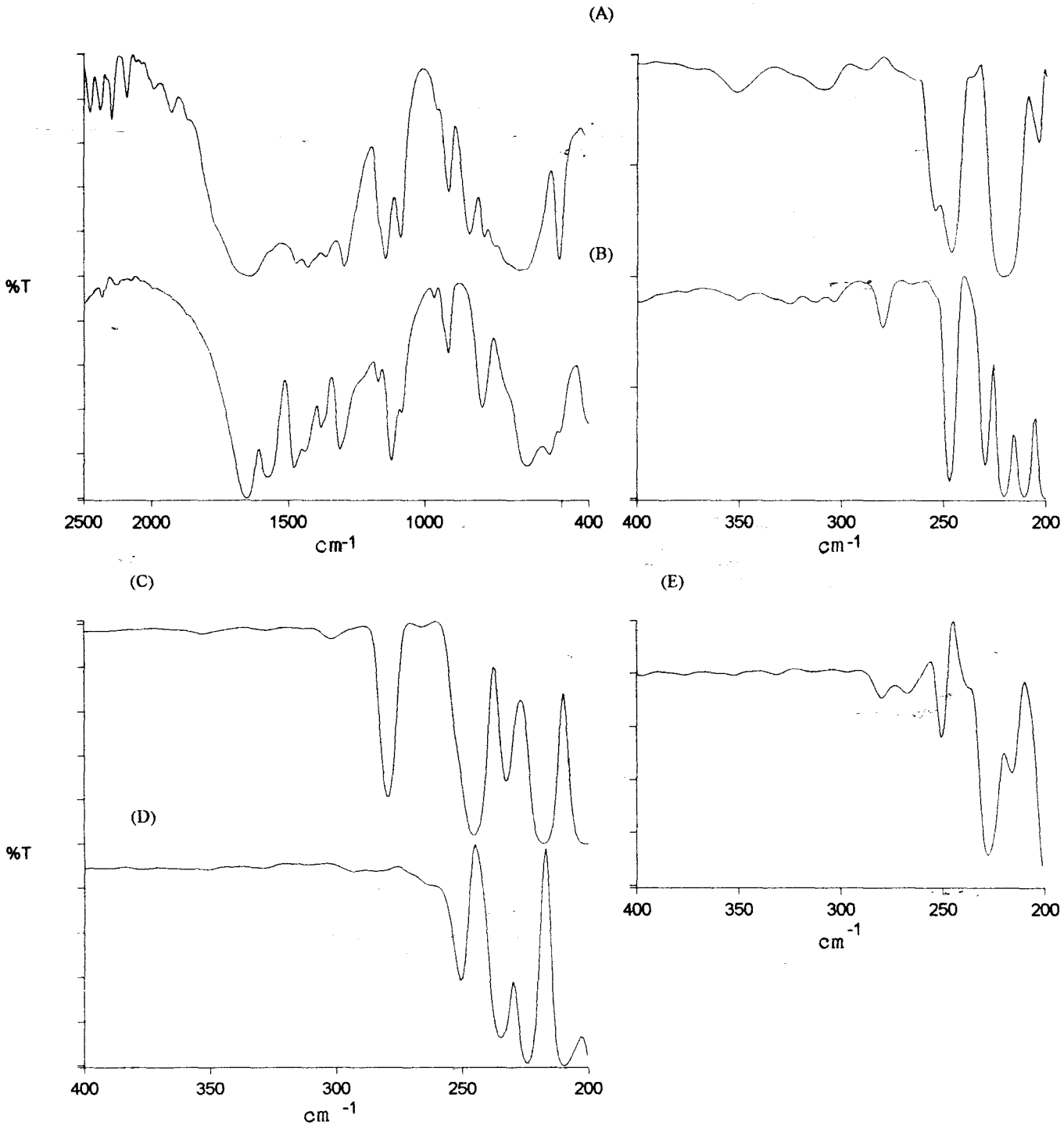

Figure 12.2.5: IR spectra of *iba* (A), Cu(*iba*)$_2$Cℓ_2 (B), anhydrous CuCℓ_2 (C), NiCℓ_2 (D) and CoCℓ_2 (D).